TESIS DE LA UNIVERSIDAD DE ZARAGOZA

2024

16

Gebrehiwet Abrham Gebreslase

Development of high-performance and stable electrocatalysts for alkaline water electrolysis

Director/es

Martínez Huerta, María Victoria

Lázaro Elorri, María Jesús

ISSN 2254-7606

Prensas de la Universidad Universidad Zaragoza

ISSN 2254-7606

Universidad Zaragoza
1542

Tesis Doctoral

DEVELOPMENT OF HIGH-PERFORMANCE AND STABLE ELECTROCATALYSTS FOR ALKALINE WATER ELECTROLYSIS

Autor

Gebrehiwet Abrham Gebreslase

Director/es

Martínez Huerta, María Victoria
Lázaro Elorri, María Jesús

UNIVERSIDAD DE ZARAGOZA
Escuela de Doctorado

Programa de Doctorado en Ingeniería Química y del Medio Ambiente

2023

DOCTORAL THESIS

DEVELOPMENT OF HIGH-PERFORMANCE AND STABLE ELECTROCATALYSTS FOR ALKALINE WATER ELECTROLYSIS

Gebrehiwet Abrham Gebreslase 2023

Thesis Directors

Maria Jesus Lázaro

Maria Victoria Martínez–Huerta

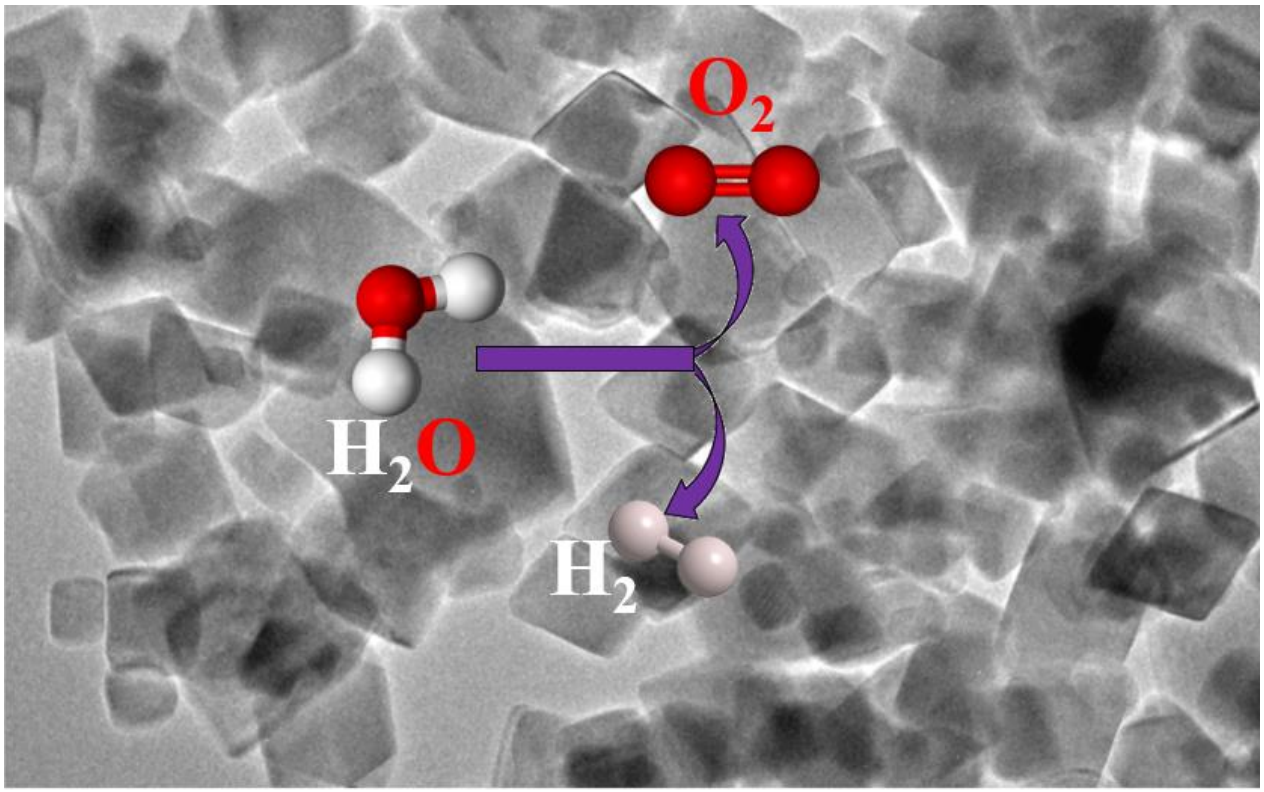

CSIC
Consejo Superior de Investigaciones Científicas

Universidad Zaragoza
1542

Instituto de Carboquímica_CSIC

C/ Miguel Luesma Castán, 4, 50018 Zaragoza. Spain

Telephone : +34 976 733 977

Fax: +34 976 733 318

www.icb.csic.es

UNIVERSIDAD DE ZARAGOZA

DEPARTMENT OF CHEMICAL AND ENVIRONMENTAL ENGINEERING

CONSEJO SUPERIOR DE INVESTIGACIONES CIENTÍFICAS (CSIC) -

INSTITUTO DE CARBOQUÍMICA (ICB)

DEVELOPMENT OF HIGH-PERFORMANCE AND STABLE ELECTROCATALYSTS FOR ALKALINE WATER ELECTROLYSIS

Doctoral Thesis

Gebrehiwet Abrham Gebreslase

2023

The doctors, Ms. María Jesús Lázaro Elorri, a Research Professor at the Instituto de Carboquímica of the Spanish National Research Council (Consejo Superior de Investigaciones Científicas -CSIC) and Ms. Maria Victoria Martínez–Huerta, a Tenured Scientist at the Instituto de Catálisis y Petroleoquímica of the Spanish National Research Council (Consejo Superior de Investigaciones Científicas -CSIC), report that the research work contained in this dissertation, entitled:

"**DEVELOPMENT OF HIGH-PERFORMANCE AND STABLE ELECTROCATALYSTS FOR ALKALINE WATER ELECTROLYSIS**" has been carried out by Mr.Gebrehiwet Abrham Gebreslase under our supervision at the Instituto de Carboquímica-CSIC.

The doctoral candidate has excelled in conducting research tasks to achieve the established objectives of the thesis, demonstrating remarkable initiative and perseverance in designing and executing experiments. Moreover, the candidate has made significant contributions to interpreting and discussing the results, formulating conclusions, and drafting publications and the doctoral thesis. The research mobility conducted at the Italian National Research Council - Institute for the Chemistry of OrganoMetallic Compounds (CNR-ICCOM), Pisa, Italy, and Institute of Organic Chemistry with Centre of Phytochemistry, Bulgarian Academy of Sciences, Sofia, Bulgaria has helped the candidate for his research work and in achieving the final goals of the thesis.

Hence, we authorize the presentation of this thesis for the PhD in Chemical and Environmental Engineering, and for the record, we sign this certificate.

Signature of the thesis supervisors

Signature: María Jesús Lázaro Elorri

Signature: María Victoria Martínez Huerta

Dr. Isabel Suelves Laiglesia, director of Instituto de Carboquímica of the Spanish National Research Council (Consejo Superior de Investigaciones Científicas –CSIC)

Reports that:

The present thesis entitled "**DEVELOPMENT OF HIGH-PERFORMANCE AND STABLE ELECTROCATALYSTS FOR ALKALINE WATER ELECTROLYSIS**" corresponds to the work carried out by Mr.Gebrehiwet Abrham Gebreslase at the Instituto de Carboquímica-CSIC, under the supervision of Ms. María Jesús Lázaro Elorri, and Ms. Maria Victoria Martínez–Huerta.

And I authorize the presentation of this thesis for the PhD in Chemical and Environmental Engineering, and for the record, I sign this certificate.

Signature

Isabel Suelves Laiglesia

“Stay positive tomorrow is a minute away”

Araya Zerihun

Acknowledgment

First of all, my heartfelt gratitude goes to Prof. Maria Jesus Lázaro (Instituto de Carboquímica–CSIC, Zaragoza, Spain) and Dr. Maria Victoria Martínez–Huerta (Instituto de Catálisis y Petroleoquímica–CSIC, Madrid, Spain), director of this thesis, for granting me the opportunity to pursue my PhD thesis under the fellowship of Marie Skłodowska–Curie Action –International Training Network (MSCA–ITN) in the project of Bimetallic catalyst knowledge-based development for energy applications (BIKE, Grant agreement ID: 813748). I would like to thank them for the continuous follow-up and supervision, including the recommendations, suggestions, and criticism I received during the work, which eventually empowered me to reach where I am today. Thank you so much for guiding and supporting me throughout the Thesis.

To David Sebastián, who extraordinarily helped me during the research work. I appreciate his expansive viewpoint, kind support, and encouragement he has provided me from the beginning. I have learned a lot from his kindness, amiable personality, magnificent wisdom, and knowledge he has. His broad scientific view, along with his inspiration for independence and creativity, has made him a persistently excellent mentor for me. Without his assistance, it would not have been easy to complete the doctoral thesis successfully. *Muchas gracias*, David. Thank you from the bottom of my heart.

To all fuel conversion group members, who have finished their work, and those who are proceeding with their research work. To David, Cinthia, Nicolas, Pedro, Antonio, Jose Manuel, Laura, Manuel, Irene, Sara, and other colleagues for their cooperation, pleasant connection, and for making the workplace delightful. Everyone has been kind and gracious enough. It is a wonderful group, full of pleasing people who are kind, friendly and open, and ready to cooperate whenever it is required. I extend my heartfelt gratitude to Maria Jesus (Menchu) for her unwavering supervision, meticulous reading, and insightful comments on my thesis. Her expert guidance and supervision enabled me to participate confidently in various workshops and conferences, and her astute management and organization skills were instrumental in facilitating my research secondment under the BIKE project in foreign countries. I am deeply appreciative of her steadfast dedication and commitment to my work and her overall support throughout the research process. I am especially thankful for her prompt and attentive assistance whenever I require her help. *Muchas gracias*, Menchu, for everything. Her mentorship and guidance will forever be cherished and remembered.

To Instituto de Catálisis y Petroleoquímica colleagues in the analysis service, I extend my heartfelt gratitude for their cooperation in characterizing materials whenever required. I am profoundly and overwhelmingly indebted to Maria Victoria (Marivi) for her unparalleled commitment, exceptional dedication, and magnificent contributions to my work. Despite our separate work locations, Marivi always made herself available to me, acting as a beacon of hope and a source of unwavering support. Her relentless optimism, kind and friendly are a testament to her remarkable character. I am deeply grateful for her unwavering support, thorough review, and perceptive feedback throughout my thesis work. Her exceptional attention to detail and insightful comments helped me refine my work and overcome any challenges I faced. Throughout my thesis work, she consistently exhibited exceptional problem-solving skills, which proved invaluable in overcoming challenges and obstacles. It was a privilege to have worked with someone of such remarkable qualities, and I am thankful for the wisdom, skills, and confidence she has imparted upon me. I cannot express in words my profound appreciation for Marivi's magnificent support and contributions to my work. Muchas gracias, Marivi.

To all Instituto de Carboquímica (ICB) staff, including the analysis service and characterization, administration, library, information technology center, maintenance, and cleaning service; for their cooperation, kindness, and politeness during the entire research work.

To Alessandro Fortunelli from Italian National Research Council - Institute for the Chemistry of OrganoMetallic Compounds (CNR-ICCOM), Pisa, Italy, for hosting me to conduct research mobility in his group. I would also like to thank Öyküm and Thantip (eve) for helping me during my stay at the institute. I would also like to thank all BIKE colleagues for designing and implementation of the BIKE project and for organizing numerous workshops and training.

To the Institute of Organic Chemistry with Centre of Phytochemistry, Bulgarian Academy of Sciences, Sofia, Bulgaria, for hosting me to perform research mobility for two months. My appreciation goes to Prof.TanyaTsoncheva, Dr. Boiko Tsyntsarski, Dr. Momtchil Dimitrov, Georgi Georgiev, and others who supported me during my stay at the institute. Thank you, Momtchil and Georgi, for making my stay in Bulgaria more enjoyable, for helping me to work in the lab smoothly, and also for exploring Bulgaria.

To Alberto Gonzalo callejo, a tutor of this doctoral Thesis from the Universisad de Zaragoza. Thank you for being so helpful whenever I needed it, particularly with the paperwork associated

with the university. His mentorship has been instrumental in my personal and academic growth, and I am deeply grateful for his help.

To all my family; my Father-Priest Abrham Gebreslase, my Mother-Mtslal Gebremichael, and all my brothers and sisters. It has been a difficult time to pass through the last three years. Starting with Covid-19 in 2020, I was not able to not travel to Ethiopia to visit them, and it got worse with the devastating genocidal war declared by the Ethiopian and Eritrean governments on November 03, 2020, against the Tigray (northern Ethiopia) region where all my relatives live. Such nightmare genocidal years in which I did not hear their voice for more than two years since the Ethiopian government cut off communication, shut down the electricity and water, froze all banks, bombed hospitals and schools, and destroyed all public and private infrastructure in the region. A government (Ethiopian), which is supposed to safeguard its citizen, has invited a foreign country of Eritrea to massacre/murder, gang rape its own people, pillage, and confiscate private and public properties. It has been a challenging time to remain calm and work efficiently in the face of the unprecedented humanitarian crisis on this scale, which has never been seen in humankind's history. Nevertheless, the resilience and perseverance of Tigray resistance fighters and my relatives against the invaders have inspired me to keep my head high and concentrate on my work. The sporadic messages and voices I had received from my mother, father, sisters, and brothers served as a source of inspiration and motivation for the tough two years. Thank you, mom (Adey), for being an inspiration and source of encouragement all the time, despite the fact you were going through a harsh time.

Last but not the least, I would like to express my gratitude to Mizan Tesfay for accompanying me during the Ph.D. period. There are no words for how much you mean to me. It would have been challenging to get through the past three years without her. I profoundly appreciate the inspiration, encouragement, and affection she has bestowed upon me. Her hard work and perseverance never cease to astound me, and I consider myself fortunate to meet her in my life.

Many thanks to everyone who has contributed to the thesis directly or indirectly.

¡Muchas gracias a todos los que han contribuido a la tesis directa o indirectamente!

ብጣዕሚ የመስግን ንኹሎም ኣብዚ ጽሑፍ ብቐጥታ ይኹን ብተዘዋዋሪ ኣበርክቶ ዝገበሩ።

Table of Contents

Table of Contents ..... **i**

Abstract ..... **iii**

Resumen ..... **vii**

Publication list ..... **xi**

Chapter I: General Introduction **1**

1. Introduction **2**

1.1. Water electrolysis: An Overview and Historical Background 5

1.2. Fundamentals of water electrolysis 6

1.2.1 Principles 6

1.2.2. Thermodynamics 7

1.2.3. Electrochemistry 8

1.3. Classification of water electrolysis technology 8

1.3.2. Alkaline water electrolysis 9

1.3.3. Proton Exchange Membrane Water Electrolysis 11

1.3.4. Anion Exchange Membrane Water Electrolysis 12

1.3.5. Solid oxide electrolysis 14

1.4. Fundamental reaction mechanism of water electrolysis 16

1.4.2. Hydrogen Evolution Reaction (HER) 19

1.4.3. Oxygen Evolution Reaction (OER) 20

1.5. Synthesis methods and evaluation criteria of electrocatalysts for OER/HER 22

1.5.2. Synthesis methods 22

1.5.3. Evaluation criterion of electrocatalyst for HER/OER 24

1.6. Electrocatalyst for alkaline water electrolysis 28

1.6.2. Electrocatalyst for Hydrogen Evolution Reaction 33

1.6.2.1. Precious metal-based electrocatalyst 34

1.6.2.2. Non-precious metal-based electrocatalyst 35

1.6.3. Electrocatalyst for Oxygen Evolution Reaction 38

1.6.3.1. Precious metal-based electrocatalyst 38

1.6.3.2. Non-precious metal-based electrocatalyst 40

References for chapter II 55

Chapter II: Objectives 83
1. Objectives and structure of the Thesis 84
1.1. Objectives 84
1.1.1. General objective 85
1.1.2. Specific objectives 85
1.2. The framework of the Doctoral Thesis 85
1.3. Structure of the Doctoral Thesis 86
Chapter III: Copies of the publications 87
Article I 89
Article II 90
Article III 91
Article IV 92
Article V 93
Chapter IV: Global discussion 95
1. Electrocatalyst for HER electrode 98
2. Electrocatalysts for OER electrode 99
3. Electrocatalyst testing in Anion exchange membrane water electrolysis 103
References for chapter IV 111
Chapter V: General Conclusions 115
General conclusions 116
Conclusiones generales 118
Appendixes 120
List of abbreviations 120

Abstract

Rapid industrialization and rising living standards around the world have led to an energy crisis and sever environmental pollution caused by the excessive use of conventional fossil fuels. Preventing further climate change and reducing carbon dioxide emissions have become the most critical challenges confronting modern society. This has sparked an intense interest in discovering and designing alternative energy sources with affordable, clean, and environmentally benign features. Hydrogen energy has been recognized as a viable alternative to fossil fuels and is pivotal in neutralizing carbon emissions. H_2 can be obtained using different approaches from different sources, including water, natural gas, coal, and biomass. The leading pathway for H_2 production remains via steam reforming of fossil fuels. Still, this method cannot achieve the future "carbon-neutral" energy system due to its reliance on fossil fuels and high CO_2 emissions.

H_2 production through water electrolysis driven by renewable energy is a clean and ultralow-carbon footprint route and has been regarded as the most promising approach for high-purity H_2 production. Two important half-reactions occur in water electrolysis: the Hydrogen evolution reaction (HER) on the cathode and the oxygen evolution reaction (OER) on the anode. Nonetheless, the sluggish kinetics and unfavorable thermodynamics of these reactions lead to enormous overpotential, which is the main challenge for mass hydrogen production. As a result, efficient electrocatalysts are required to ease the reaction energy barrier and expedite the reaction. To date, the most effective electrocatalysts for water electrolysis are primarily based on noble metals. For example, Pt-based electrocatalysts for HER and Ir- and Ru-derived electrocatalysts for OER. However, their scarcity and high cost obstruct them from sustainable use in large-scale applications. To circumvent this problem, in the last few decades, considerable efforts have been devoted to designing and developing electrocatalysts derived from transition metals combined with different materials such as carbon and heteroatoms, in which these materials exhibited appealing features such as good performance and availability, which made them a viable alternative to replacing the precious metals of Pt, Ir, and Ru.

This Thesis has focused on researching electrocatalysts derived from transition metals for both HER and OER electrodes. Two spinel oxides ($NiFe_2O_4$ and $CoFe_2O_4$) were prepared through hydrothermal methods for oxygen evolution reaction. They were used as precursors for further modification, in which through in situ polymerization of dopamine on the surface of the as-

prepared spinel oxides followed by carbonization have enabled to obtain an optimized property. The work has emphasized optimizing the electrochemical properties of these oxides by integrating them with multiple dopamine concentrations. The as-prepared $CoFe_2O_4$ powder was combined with various dopamine content (10, 20, 30, and 40 wt. %) and subjected to polymerization for 24 h and carbonization at 800 ^{0}C for 1 h under N_2 atmosphere. The effect of carbonized polydopamine on the overall physicochemical properties and electrochemical activity of $CoFe_2O_4$ electrocatalysts was systematically investigated. There was a noticeable change from a $CoFe_2O_4$ structure to a CoFe alloy when the ratio of $CoFe_2O_4$ to dopamine was optimized. The same procedure was employed to modify the $NiFe_2O_4$.

The morphology, crystalline structure, and chemical composition of the catalysts were characterized by scanning electron microscopy (SEM), transmission electron microscopy (TEM), X-ray diffraction (XRD), X-ray photoelectron spectroscopy (XPS), and inductively coupled plasma (ICP). The as-prepared electrocatalysts were measured for their electrochemical performance in a three-electrode system controlled by a potentiostat/galvanostat. In particular, $CoFe/NC_{30\%}$ (prepared with 30wt.% dopamine) electrocatalyst exhibits excellent catalytic activity towards OER, in which a small overpotential of 340 mV was required to generate a current density of 10 mA cm^{-2} in a 1.0 M KOH accompanied with outstanding durability. In the case of $NiFe_2O_4$, $NiFe/NC_{10\%}$ electrocatalyst that contains 10 wt. % dopamine showed a relatively higher catalytic activity for OER measured in 1 M KOH aqueous solution. It revealed a low overpotential (350 mV at 10 $mAcm^{-2}$), a low Tafel slope (56 $mVdec^{-1}$), a low charge transfer resistance, and a relatively higher electrochemically active surface area.

Moreover, a carbonaceous substance other than polydopamine was utilized to improve the electrochemical properties of CoFe. Carbon foam derived from petroleum pitch was synthesized and used to immobilize the Co and Fe electroactive metals. The bare carbon foam and heteroatom (P, N) co-doped carbon foam were produced through a simple thermal-chemical and carbonization process. The resulting composite materials were evaluated for their physical and chemical properties as well as electrochemical properties. The prepared electrocatalysts showed excellent electrocatalytic activity, faster reaction kinetics, and stability for OER electrodes, thanks to the carbon foam support that allowed for the immobilization of the Co and Fe electroactive metals. To generate a current density of 10 mA cm^{-2}, the synthesized CoFe@PN-CF electrocatalyst requires a

low overpotential of 320 mV, a low Tafel slope of 48 mV dec^{-1}, a relatively low charge transfer resistance, and a large electrochemically active surface area. Notably, it maintained stability for at least 20 hours, suggesting it could be used for large-scale water electrolysis.

In addition to the OER electrode, efforts have been devoted to designing and developing an electrocatalyst for the HER electrode. In this case, a stainless steel mesh (SSM) with a three-dimensional network structure was used as a substrate for growing transition metals. The commercial SSM material was transformed into an active and stable electrocatalyst through a hydrothermal and phosphorization process. Single and bimetals of Ni and Co were grown on the SSM substrate using hydrothermal method, and the resulting material was subjected to further phosphorization. Electrochemical analysis showed that the NiCoP@SSM catalyst has excellent catalytic activity for HER in 1 M KOH, with a current density of 10 mA cm^{-2} achieved at a low overpotential of 138 mV. This synthesis method provides a simple, binder-free, and scalable fabrication process.

Finally, the as-prepared electrocatalysts were evaluated for their performance in a single-cell anion exchange membrane water electrolysis. The results showed promising performance, particularly for the OER electrode. All electrocatalysts demonstrated attractive electroactivity. Among them, CoFe@PN-CF was found to have the highest activity, producing a current density of 0.45 Acm^{-2} at a cell potential of 1.8V when using CoFe@PN-CF in the anode and Pt/C in the cathode electrode.

Resumen

La rápida industrialización y el aumento de los estándares de vida en todo el mundo han provocado una crisis energética y una severa contaminación ambiental causada por el uso excesivo de combustibles fósiles convencionales. Prevenir un mayor cambio climático y reducir las emisiones de dióxido de carbono se han convertido en los desafíos más críticos que enfrenta la sociedad moderna. Esto ha provocado un gran interés en descubrir y diseñar fuentes de energía alternativas con características asequibles, limpias y ambientalmente benignas. El hidrógeno, como vector energético, se ha reconocido como una alternativa viable a los combustibles fósiles y juega un papel fundamental en la neutralización de las emisiones de carbono. El hidrógeno se puede obtener utilizando diferentes vías y diferentes fuentes, incluyendo agua, gas natural, carbón y biomasa. Actualmente, la vía principal para la producción de hidrógeno sigue siendo el reformado con vapor de agua de metano o gases licuados del petróleo. Sin embargo, este sistema no es "neutro en carbono" debido a su dependencia de los combustibles fósiles y las altas emisiones de CO_2.

La producción de hidrógeno a través de la electrólisis del agua impulsada por energías renovables es una ruta limpia y de huella de carbono ultra baja, y se ha considerado como el enfoque más prometedor para la producción de hidrógeno de alta pureza. En la electrólisis del agua ocurren dos importantes semi-reacciones: la reacción de evolución de hidrógeno (HER) en el cátodo y la reacción de evolución de oxígeno (OER) en el ánodo. Sin embargo, la cinética lenta y la termodinámica desfavorable de estas reacciones dan lugar a una enorme sobrepotencial, lo que representa el principal desafío para la producción masiva de hidrógeno. Por lo tanto, se requieren electrocatalizadores eficientes para facilitar la barrera energética de la reacción y acelerarla. Hasta la fecha, los electrocatalizadores más efectivos para la electrólisis del agua se basan principalmente en metales nobles. Por ejemplo, los electrocatalizadores a base de Pt para la HER y los electrocatalizadores derivados de Ir y Ru para la OER. Sin embargo, su escasez y alto costo impiden su uso sostenible en aplicaciones a gran escala. Para evitar este problema, en las últimas décadas se han dedicado esfuerzos considerables a diseñar y desarrollar electrocatalizadores derivados de metales de transición combinados con diferentes materiales, como carbono y heteroátomos, en los que estos materiales exhibieron características atractivas como un buen rendimiento y

disponibilidad, lo que los convierte en una alternativa viable para reemplazar los metales preciosos de Pt, Ir y Ru.

Esta tesis doctoral se ha centrado en investigar electrocatalizadores derivados de metales de transición para las reacciones de HER y OER. Dos óxidos de espinela ($NiFe_2O_4$ y $CoFe_2O_4$) se prepararon mediante el método hidrotermal para la reacción de evolución de oxígeno. Se utilizaron como precursores para una posterior modificación, en la cual la polimerización in situ de dopamina en la superficie de los óxidos de espinela seguida de carbonización permitió obtenerlos con propiedades optimizadas. El trabajo ha consistido en optimizar las propiedades electroquímicas de estos óxidos integrándolos con múltiples concentraciones de dopamina. La espinela $CoFe_2O_4$ preparada se combinó con varios contenidos de dopamina (10, 20, 30 y 40% en peso) y se sometió a polimerización durante 24 horas y carbonización a 800 ^{0}C durante 1 hora bajo atmósfera de N_2. Se investigó sistemáticamente el efecto de la polidopamina carbonizada en las propiedades fisicoquímicas y la actividad electroquímica de los electrocatalizadores de $CoFe_2O_4$. Se observó un cambio notable de una estructura de $CoFe_2O_4$ a una aleación de CoFe cuando se optimizó la proporción dopamina. El mismo procedimiento se utilizó para modificar el $NiFe_2O_4$.

La morfología, estructura cristalina y composición química de los catalizadores fueron analizadas por microscopía electrónica de barrido (SEM), microscopía electrónica de transmisión (TEM), difracción de rayos X (XRD), espectroscopía de fotoelectrones de rayos X (XPS) y plasma acoplado inductivamente (ICP). Para la caracterización electroquímica de los catalizadores se utilizó un sistema de tres electrodos controlado por un potenciostato/galvanostato. En particular, el electrocatalizador $CoFe/NC_{30\%}$ (preparado con un 30% en peso de dopamina) exhibía una excelente actividad catalítica hacia la OER, obteniendo un bajo sobrepotencial de 340 mV para generar una densidad de corriente de 10 mA cm^{-2} en una solución acuosa de KOH 1.0 M con una elevada durabilidad. En el caso de la espinela $NiFe_2O_4$, el electrocatalizador $NiFe/NC_{10\%}$ preparado con un 10% en peso de dopamina, mostró una actividad catalítica relativamente mayor para la reacción de evolución de oxígeno medida en una solución acuosa de KOH 1 M. Se obtuvo un bajo sobrepotencial (350 mV a 10 $mAcm^{-2}$), una baja pendiente de Tafel (56 $mVdec^{-1}$), una baja resistencia a la transferencia de carga y una superficie electroquímicamente activa relativamente mayor.

Además, se utilizó una sustancia carbonosa distinta al polidopamina para mejorar las propiedades electroquímicas de CoFe. Se sintetizó espuma de carbono a partir de brea de petróleo y se utilizó para inmovilizar los metales electroactivos Co y Fe. Las espumas de carbono con y sin dopar con heteroátomos (P, N) se sintetizaron mediante un proceso térmico-químico y de carbonización simple. Los materiales compuestos resultantes se caracterizaron para evaluar sus propiedades físicas, químicas y electroquímicas. Los electrocatalizadores preparados mostraron una excelente actividad electrocatalítica, cinética de reacción más rápida y estabilidad para la reacción de evolución de oxígeno, gracias al soporte de espuma de carbono que permitió la inmovilización de los metales electroactivos Co y Fe. Para generar una densidad de corriente de 10 mA cm^{-2}, el electrocatalizador sintetizado CoFe@PN-CF requería una baja sobretensión de 320 mV, una baja pendiente de Tafel de 48 mV dec^{-1}, una resistencia de transferencia de carga relativamente baja y una gran área superficial electroquímicamente activa. Es destacable que mantuvo su estabilidad durante al menos 20 horas, lo que sugiere que podría utilizarse para la electrólisis de agua a gran escala.

Además de la OER, se han dedicado esfuerzos a diseñar y desarrollar un electrocatalizador para la HER. En este caso, se utilizó una malla de acero inoxidable (SSM) con una estructura de red tridimensional como sustrato para cultivar metales de transición. El material comercial de SSM se transformó en un electrocatalizador activo y estable a través de un proceso hidrotérmico y de fosforización. Los metales únicos y bimetálicos de Ni y Co se cultivaron en el sustrato de SSM utilizando un método hidrotérmico, y el material resultante se sometió a una fosforización adicional. El análisis electroquímico mostró que el catalizador NiCoP@SSM tiene una excelente actividad catalítica para el HER en 1 M KOH, con una densidad de corriente de 10 mA cm^{-2} lograda con una baja sobretensión de 138 mV. Este método de síntesis proporciona un proceso de fabricación simple, sin aglutinantes y escalable.

Finalmente, se evaluaron los electrocatalizadores preparados en un electrolizador de agua de membrana de intercambio de aniones. Los resultados mostraron un rendimiento prometedor, especialmente para el electrodo OER. Todos los electrocatalizadores demostraron una electroactividad atractiva. Entre ellos, se determinó que CoFe@PN-CF presentaba la actividad más alta, produciendo una densidad de corriente de 0,45 Acm^{-2} a un potencial de célula de 1,8 V cuando se usa CoFe@PN-CF en el electrodo del ánodo y Pt/C en el electrodo del cátodo.

Publication list

This Doctoral Thesis, entitled "**DEVELOPMENT OF HIGH PERFORMANCE AND STABLE ELECTROCATALYSTS FOR ALKALINE WATER ELECTROLYSIS,**" carried out by **Mr. Gebrehiwet Abrham Gebreslase** and directed by **Dra. Mª María Jesús Lázaro** and **Dra. Mª Victoria Martínez Huerta** is presented by the modality of a **compendium of publications** with **international mention**.

The list of publications that make up the compendium is enclosed below. A review article pertinent to the research work carried out is also attached together with the research articles.

List of publications

(I) **G.A. Gebreslase**, M.V. Martínez-Huerta, D. Sebastián, M.J. Lázaro, NiCoP/CoP sponge-like structure grown on stainless steel mesh as a high-performance electrocatalyst for hydrogen evolution reaction, Electrochim. Acta. 438 (2023) 141538. https://doi.org/10.1016/j.electacta.2022.141538.

Impact factor 2021: 7.336; thematic area 2021: Electrochemistry (Q1)

(II) **G.A. Gebreslase**, M.V. Martínez-Huerta, D. Sebastián, M.J. Lázaro, Transformation of $CoFe_2O_4$ spinel structure into active and robust CoFe alloy/N-doped carbon electrocatalyst for oxygen evolution reaction, J. Colloid Interface Sci. 625 (2022) 70–82. https://doi.org/10.1016/j.jcis.2022.06.005.

Impact factor 2021: 9.965; thematic area 2021: Chemistry, physical (Q1).

(III) **G.A. Gebreslase**, D. Sebastián, M.V. Martínez-Huerta, M.J. Lázaro, Nitrogen-doped carbon decorated-$Ni_3Fe@Fe_3O_4$ electrocatalyst with enhanced oxygen evolution reaction performance, J. Electroanal. Chem. 925 (2022) 116887.

https://doi.org/10.1016/j.jelechem.2022.116887.

Impact factor 2021: 4.598; thematic area 2021: Chemistry, analytical (Q1), and Electrochemistry (Q2).

(IV) **G.A. Gebreslase**, D. Sebastián, M.V. Martínez-Huerta, T. Tsoncheva, B. Tsyntsarski, G. Georgiev, M.J. Lázaro, CoFe-loaded P, N co-doped carbon foam derived from petroleum pitch waste: an efficient electrocatalyst for oxygen evolution reaction https://doi.org/10.1016/j.cattod.2022.12.022

Impact factor 2021: 6.562; thematic area 2021: Chemistry, applied (Q1) and Chemistry, physical (Q2).

(V) **G.A. Gebreslase**, M.V. Martínez-Huerta, M.J. Lázaro, Recent progress on bimetallic NiCo and CoFe based electrocatalysts for alkaline oxygen evolution reaction: A review, J. Energy Chem. 67 (2022) 101–137. https://doi.org/10.1016/j.jechem.2021.10.009.
Impact factor 2021: 13.599; thematic area 2021: Chemistry, applied (Q1); Chemistry, physical (Q1)

All of the experimental works, analysis, and treatment of the generated data, as well as the writing of the manuscript, were contributed by the doctorate student in these publications, who appeared as the first author. All journals are indexed in the journal of citation report (*JCR*), and the information, including the impact factor and the thematic areas, was taken from the *JCR* website.

Oral and poster contribution

- **G. A. Gebreslase**, M. V. Martínez-Huerta, and M. J. Lázaro: VIII Symposium on Hydrogen, Fuel Cells, and Advanced Batteries, HYCELTEC; participated (in online mode) in an oral presenter with a research work entitled "In situ growth of NiCoP on stainless steel mesh as an enhanced electrocatalyst for hydrogen evolution reaction," July 10-13, 2022, held in Bueno Aires, Argentina.
- **G.A Gebreslase**, D.Sebastián, M.V.Martínez-Huerta, T.Tsonchevac, B.Tsyntsarski, G.Georgievc, M.J.Lázaro**:** 9th International Symposium on Carbon for Catalysis, CarboCat–IX**,** participated as a flash poster presentation with research work entitled "CoFe encapsulated in P, N co-doped carbon foam derived from petroleum pitch as a promising electrocatalyst for oxygen evolution reaction," Zaragoza, Spain, on June 28 – 30, 2022. Received an **award** of a certificate and pocket money for the best flash and poster presentation.
- **G. A. Gebreslase**, M. V. Martínez-Huerta, and M. J. Lázaro: European Hydrogen Energy Conference, participated in a Poster entitled "Facile synthesis of Nitrogen-doped carbon decorated-$Ni_3Fe@NiFe_2O_4$ electrocatalyst with enhanced OER performance", Madrid, Spain, 18-20 May 2022.
- **G. A. Gebreslase**, M. V. Martínez-Huerta, and M. J. Lázaro: 3rd International Workshop on Functional Nanostructured Materials, participated (in online mode) as an oral presenter with a research work entitled "Controllable preparation of $CoFe_2O$ /N-doped carbon electrocatalyst for an alkaline oxygen evolution reaction", Krakow, Poland, 6 -8 October 2021.

Workshop participation

- Workshop on catalysts for electrolyzers: BImetallic catalysts Knowledge-based development for Energy applications, took place at the Instituto de Catálisis y Petroleoquímica, CSIC (Madrid, Spain) on Wednesday 22 and at the Instituto de Carboquímica, CSIC (Zaragoza, Spain) from 23 to 24, June 2022.
- Workshop on Catalysis and design of advanced reactors, organized by Universitat Politecnica de catalunya (UPC), within the framework of MSCA-ITN-BIK, held on December 2021, in Barcelona, Spain.
- Workshop on Theoretical Approaches to NanoAlloy Catalysis, organized by the Technical University of Denmark (DTU), within the framework of MSCA-ITN-BIKE, performed online on March 16-19, 2021.
- Workshop on catalyst characterization and operando spectroscopy, organized by Karlsruhe Institute of Technology (KIT), within the framework of MSCA-ITN-BIKE, conducted online on January 14th and 15th, 2021.
- 2nd International Summer school on "Carbon nanomaterials and related systems: Synthesis, Characterization, Properties, and Applications in Energy," held in Jaca (Spain) from July 13-17, 2020.
- Workshop on Catalyst Manufacturing Technology, organized by Reading, UK, within the framework of MSCA-ITN-BIKE, performed online on September 8th, 9th, 15th, and 4th of December, 2020.
- Workshop on Preparation and Characterization of Catalysts for Hydrogen Production, organized by the Bulgarian academy of science, within the framework of MSCA-ITN-BIKE, performed online on March 9-13, 2020.
- Second International School on NanoAlloys (ISNA-2) organized within the Marie Skłodowska-Curie Action – International Training Network (MSCA-ITN) "Bimetallic catalyst knowledge-based development for energy applications (BIKE); held in Pisa Italy, January 20-24, 2020.

Chapter I: General Introduction

This chapter introduces the general introduction to the Ph.D. Thesis. A comprehensive review of water electrolysis, including the historical background, fundamentals of water electrolysis and classification of water electrolysis, electrochemical testing, the state of the art of electrocatalysts for Hydrogen Evolution Reaction (HER), and Oxygen Evolution Reaction (OER) is presented.

1.Introduction

The alarming energy crisis and environmental pollution induced by the rampant over-consumption of conventional fossil fuel, coal, and oil as a result of the rapid industrial growth and improvement of global human beings' living standards have sparked intense research enthusiasm in innovating and developing alternative energy systems [1]–[3]. According to the International Energy Agency (IEA) [4], global energy demand will continue to rise in the following decades, with fossil fuels continuing to dominate global energy use. Fossil fuels like oil, coal, and natural gas meet about 95% of the world's current energy needs. Carbon dioxide is the primary by-product of burning fossil fuels and is responsible for about 82% of the estimated greenhouse gas (GHG) emissions [5]. Simultaneously, there is a growing worldwide consensus that GHG emissions, which continue to rise, must be reduced to avoid hazardous GHG-induced climate impacts [6]–[8]. Supply energy security and climate change are two critical concerns regarding the future of the energy industry, raising the problem of determining the best strategy to reduce emissions while simultaneously delivering the energy needed to support the economy. In an effort to alleviate the impact of climate change, many nations around the world have planned decarbonization of the global economy as a top priority by the end of 2050.

To meaningfully respond to global warming by limiting the global temperature rise below 1.5 ^{0}C, the 'Paris Agreement' was drafted and ratified by 196 parties at the 21st conference of the parties (COP 21) in 2015 [9]. The Intergovernmental Panel on Climate Change (IPCC) estimates that GHG emissions must be brought down to 25–30 Gton of CO_2eq per year by 2030 to keep the global temperature rise below 1.5 ^{0}C [10]. This has propelled scientists, governments, and policy maker to discover and develop clean and environmentally friendly alternative renewable energy sources [11]–[13]. Thus, it is crucial to rapidly advance alternative green energy technologies to meet global energy demands and promote sustainable development. Over the last few decades, there has been an increasing interest and investment in the hydrogen economy worldwide to mitigate the prevailing energy dilemma. The hydrogen economy is a cutting-edge energy infrastructure that advocates the widespread use of H_2 to satisfy the energy requirements of the significant societal sectors [14]. It is described as a comprehensive solution to creating, storing, and providing energy, including all ultimate applications while achieving GHG reduction [15]. It is viewed as a viable option for achieving a low-carbon energy system. The capacity of hydrogen to reduce carbon

emissions and its expanding geopolitical and economic potential in the energy transition context are the main drivers for hydrogen production [16].

Hydrogen can be derived from fossil fuels, biomass, and water electrolysis with solar and wind energy, among other sources [17], [18]. Hydrogen is widely employed in petroleum refining, ammonia production, and other industries as a significant chemical raw material. Hydrogen can be used not only to power fuel cells but also to turn it into liquid fuel, making it a viable alternative to fossil and nuclear energy.

There are various hydrogen production techniques; each has advantages and disadvantages in developmental phases. The main hydrogen production techniques and their applications are presented in **Figure 1 [20]**. Hydrogen is obtained chiefly based on fossil fuel reformation (78%) and coal gasification (18%), while water electrolysis shares the remaining 4%. However, these conventional techniques (fossil fuel reforming and coal gasification) generate brown or grey hydrogen due to the usage of fossil fuels or the production of CO_2 from the methane gas reforming process. More crucially, steam reforming does not reduce reliance on finite fossil fuels or reduce pollution, so it fails to contribute to developing a low-carbon energy matrix. Blue hydrogen generation by CO_2 collection and conversion has been proposed. Still, the paradigm is now turning to hydrogen production via water electrolysis in conjunction with renewable energy towards eliminating fossil fuels and obtention of green hydrogen [11], [19].

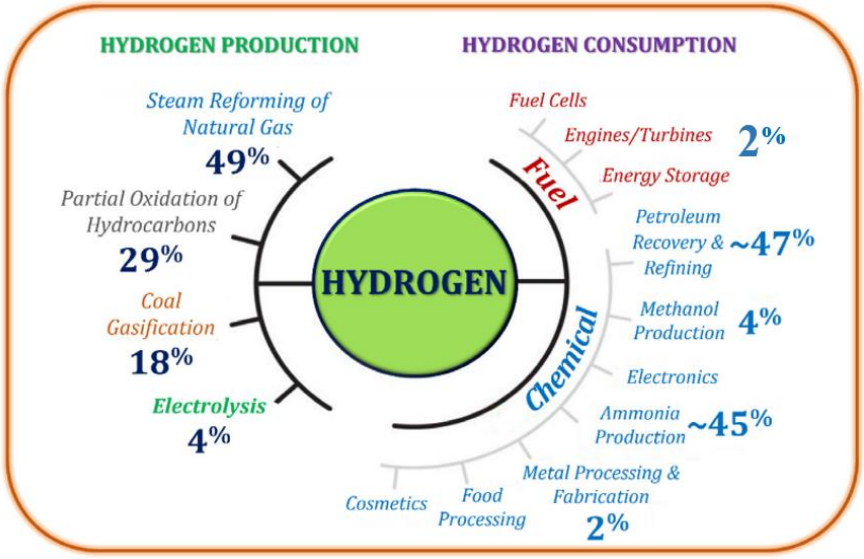

Figure 1. Main hydrogen production methods and applications [20].

Renewable energy sources combined with water electrolysis are promising solutions for large-scale hydrogen production. Despite its potential, water electrolysis remains a small part of hydrogen production. Water electrolysis produces high-quality hydrogen by converting water to hydrogen and oxygen. It can benefit from excess power from renewable energy sources. The increasing cost of energy has impacted the production of electrolytic hydrogen. However, this is expected to change with the growth of renewable energy sources such as photovoltaics and wind turbines. Electrolytic hydrogen can be produced from a renewable source, act as an energy carrier and storage medium, and overcome the intermittent nature of renewable energy [15], [21].

Because it generates pure hydrogen energy with no emissions of carbon dioxide, water electrolysis has been considered a potential strategy that can alleviate the impending crisis in the energy sector and the environmental catastrophe. The production of clean hydrogen energy by splitting water is a promising solution that may tackle the upcoming problem with energy and the environment. This technology uses water, a plentiful, inexpensive, and renewable resource, which appears to be the most environmentally friendly approach for hydrogen production [22]. **Figure 2** highlights an overview of the mass spectrum of the water electrolysis, comprising the water input and compact water electrolyzer design powered by different energy sources and furnishing O_2 and H_2 for various applications.

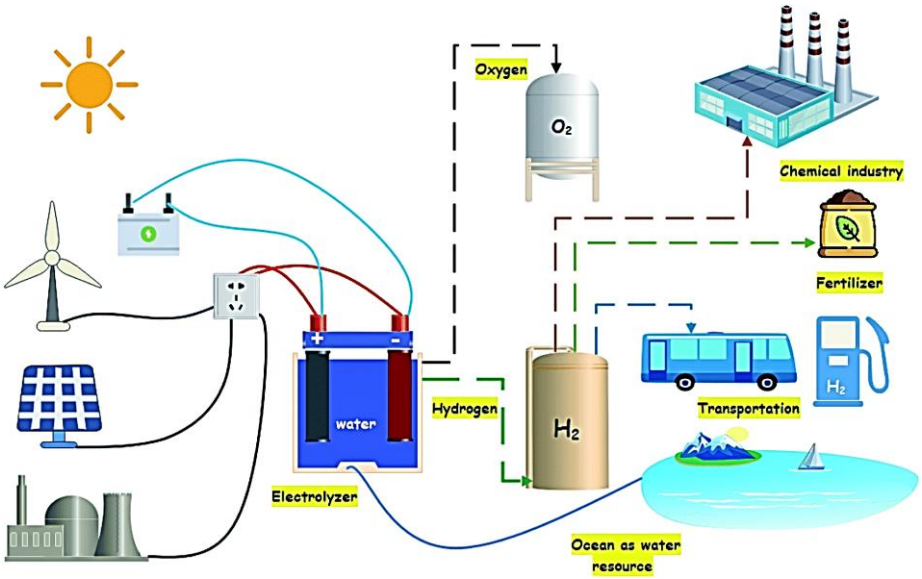

Figure 2. Schematic water electrolysis-based sustainable energy landscape representation for large-scale application [22].

1.1. Water electrolysis: An Overview and Historical Background

Water electrolysis can be described as splitting a water molecule into hydrogen and oxygen by applying an electric current. The first observations from experiments on the decomposition of water by electric discharges into "air inflammable" (flammable air), also known as hydrogen, and "air vital" (life-giving air), also known as oxygen gas, were published by Paets van Troostwyk and Deinman in 1789. Water electrolysis became a cost-effective technique for hydrogen production throughout the nineteenth century, thanks to advancements in electrodynamic generators such as the Gramme machine in 1869. Prof. D. Latchinof of Saint Petersburg, Dr. A d'Arsonval of the Collège de France in Paris, and Cdt Renard of the French military aerostation institution of Chalais have devised apparatus for the commercial synthesis of hydrogen and oxygen [23]. During 1885-1887, d'Arsonval utilized an electrolyzer to produce pure oxygen for his physiology experiments at the Collège de France. As an anode, a perforated iron cylinder was inserted within a cotton bag that also acted as a diaphragm. Dr. Schmidt presented a patent in 1900 that led to manufacturing the first industrial electrolyzer based on the filter-press concept. Asbestos fabric reinforced with rubber on the edges was utilized as diaphragm [23].

Then, Maschinenfabril Oerlikon developed and marketed the Schmidt bipolar electrolyzer in 1902. (Switzerland). More than 400 industrial electrolyzers were in use in the early twentieth century. Electrolyzers were primarily utilized in industrial applications to create hydrogen and oxygen for welding or cutting applications. In the 1920s and 1930s, more significant quantities of hydrogen were necessary to produce ammonia as precursors of fertilizer and explosives following the Haber process invention [23], [24]. This need for hydrogen, aided by the cheap cost of hydroelectricity in mountainous nations, sparked the development of water electrolysis technology, and the industrial market was dominated by three major companies: Oerlikon (Switzerland), Norsk Hydro in Glomfjord (Norway), and Cominco (Canada). Since the 1950s, the use of hydrocarbon energy in industry has increased. Large-scale hydrogen production was possible using coal gasification and natural gas steam reforming, which are substantially less expensive than electrolysis. The economic benefit of water electrolysis rapidly decreased, and the final large-scale plant in Norway (Glomfjord) was shut down in 1992. In 2010, industrial hydrogen production reached around 70 million tons annually from fossil fuels that do not use carbon capture and storage: 48% from natural gas, 30% from chemical and refinery off-gases, 18% from coal, and just 4% from electrolysis.

Recently, the large-scale development of renewable energy sources (solar and wind turbines) and the need for an effective mechanism to store energy rekindled international interest in water electrolysis. Improving water electrolysis efficiency and lowering capital expenditures are the two main priorities researcher work to diffuse more in the market [23], [25]. Water electrolysis technologies have been continuously developed and applied in industrial applications since the 18th century. Throughout this journey, several trends have impacted its development, and as a result, this journey can be generally divided into five generations [20], [26]. **Figure 3** illustrates the significant growth of each successive generation of water electrolysis and the difficulties encountered, technological advances, and other associated factors [26].

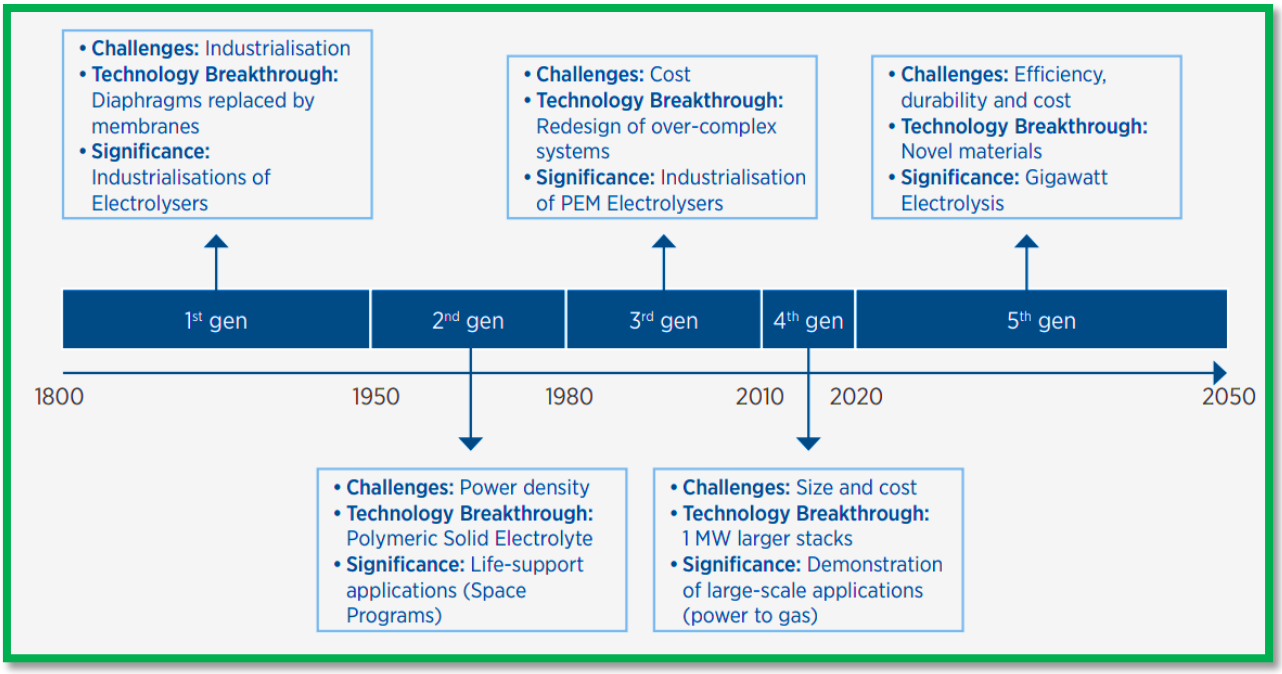

Figure 3. Evolution of water-electrolysis technology [26], where gen refers to generation.

1.2. Fundamentals of water electrolysis

1.2.1 Principles

Water electrolysis is a process of splitting water molecules into hydrogen and oxygen by applying a direct current across it. Current flows between two separate and immersed electrodes in an electrolyte to promote ionic conductivity. The electrodes must be corrosion resistant, have appropriate electric conductivity, have good catalytic properties, and be structurally durable. Because the electrolyte should not change during the process, it should not react with the electrodes.

Water electrolysis necessitates using a diaphragm or membrane/separator to prevent the hydrogen and oxygen that evolved at the electrodes from recombining. The diaphragm's electrical resistance protects the electrodes from being short-circuited. Nonetheless, the diaphragm should possess high ionic conductivity. Moreover, the diaphragms must have good physical and chemical stability [25].

The electrodes, diaphragm/separator, and electrolyte are the three most significant components of an electrolytic cell. In general, the global reaction of water electrolysis is described as follows.

$$H_2O\ (l) \rightarrow H_2\ (g) + \frac{1}{2}O_2\ (g) \qquad \text{Equation 1}$$

In the electrolysis process, the ions gain or release the electrons at the electrode's surface, forming a multiphasic gas–liquid–solid system. The cathode is the site of the reduction half-reaction. This electrode is polarized negatively when electrons from the external circuit flow into it. The oxidation half-reaction occurs in a second electrode, known as the anode. The outer circuit becomes positively polarized when the electrons leave the anode. Thus, the cathode produces hydrogen while the anode produces oxygen.

1.2.2. Thermodynamics

A water electrolyzer is an electrochemical device that transforms electric and thermal energy into chemical energy. The processes of an electrolytic cell can be explained using thermodynamic principles in terms of enthalpy change (ΔH), Gibbs' free energy change (ΔG), and thermal energy (Q). The ΔH refers to the energy required for the water electrolysis reaction, ΔG refers to the electric energy, and Q refers to the product of the process temperature (T) and the entropy change ΔS. Briefly, these thermodynamic parameters can be expressed as follows.

$$\Delta G = \Delta H - Q = \Delta H - T.\Delta S \qquad \text{Equation 2}$$

The electrolysis process is an endothermic ($\Delta H > 0$) and nonspontaneous chemical reaction (ΔG). The reversible cell voltage (V_{rev}) is the lowest voltage needed to start the electrolysis. This voltage can be expressed as a function of G as follows.

$$V_{rev} = \frac{\Delta G}{z.F} \qquad \text{Equation 3}$$

Where z is the number of electron moles transferred per hydrogen mole, and F is the Faraday constant (96 485 C/mol). The reversible cell voltages (V_{rev}) of an electrolytic cell at standard

conditions is about 1.23 V. Nevertheless, the energy consumption of the electrolysis process highly depends on temperature and pressure, in which variations in these parameters have a massive impact on the V_{rev}.

1.2.3. Electrochemistry

The cell voltage (V_{cell}) rises in relation to V_{rev} when a direct current is applied to an electrolysis cell to generate hydrogen. This is brought on by the irreversibility of the cell, primarily overvoltages and parasitic currents, which result in energy losses and reduce the efficiency of the cell. The V_{cell} can be expressed as the sum of the reversible voltage and the additional overvoltages in the electrolytic cell, as given below [25].

$$V_{cell} = V_{rev} + V_{ohm} + V_{act} + V_{con.} \qquad \text{Equation 4}$$

Where the V_{ohm} refers to the ohmic loss resulting from the resistance of the many cell elements (electrodes, interconnection, current collectors, electrolyte, diaphragm/separator, gas bubbles, etc.). V_{act} is an activation overvoltage due to the electrode kinetics. The charge transfers between the chemical species and the electrodes require substantial energy, which needs to be overcome to transfer from the reactants to the electrodes and vice versa. This depends on the catalytic properties of the electrode materials. V_{con} refers to concentration overvoltage caused by mass transport processes (such as convection and diffusion). Transport limitation diminishes reactant concentration while raising product concentration at the contact between the electrode and the electrolyte. V_{con} is often substantially lower than V_{ohm} and V_{act}, especially in the case of alkaline electrolysis. The I-V characteristic curve depicts the electrochemical behavior of an electrolytic cell by describing the relationship between cell voltage (V_{cell}) and current (I_{cell}).

1.3. Classification of water electrolysis technology

In the course of water electrolysis advancements, four distinct methods of water electrolysis were introduced, with main differences in the type of electrolyte, cell design, degree of maturity, working conditions, and ionic agents. The four types of water electrolysis are (1) Alkaline water electrolysis, (2) Anion Exchange Membrane electrolysis (AEM), (3) Proton Exchange Membrane water electrolysis (PEM), and (4) solid oxide electrolysis (SOE), as depicted in **Figure 4** [20][27]. The Alkaline and PEM water electrolysis are already commercialized, while the AEM and SOE technology are still under development at the lab scale. Nevertheless, the operating principles

remain the same for all methods. An electrolyte separates two electrodes to form an electrolysis cell. The chemical charges (anions (-) or cations (+)) created by one electrode are transported to the other electrode via a medium called an electrolyte. In the electrolysis process, pure water is a poor electrolyte because of its low conductivity; therefore, another electrolyte must be added to the solution to increase its conductivity. The descriptions of the four types of water electrolysis technologies, including historical background, working principles, and their features, along with pros and cons, are presented in the following subsections and **Tables 1 & 2**. Each technology possesses its limitations, as a result, there is no one technology that stands out as superior in every application; consequently, there is room for both competition and innovation, which should result in a reduction in overall costs. Critical materials, performance, stability, and maturity are some of the challenges faced by each technology.

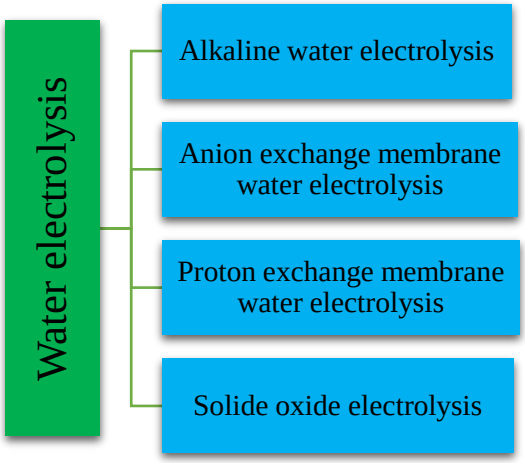

Figure 4. Classification of water electrolysis technology

1.3.2. Alkaline water electrolysis

Since Troostwijk and Diemann discovered the electrolysis phenomena in 1789, alkaline water electrolysis (AWE) has evolved into a well-developed technique for megawatt-scale hydrogen generation. It now represents the most extensive global electrolytic technology commercially [21]. Alkaline water electrolyzers are the most advanced commercial technology in the world due to their reliability, safety, and long lifetimes that can last up to 15 years [25]. The current lifetime of an alkaline water electrolysis system is 90,000 h, and the initial investment cost is between $500-1000/Kw. However, using corrosive (KOH) electrolytes and dealing with the moderate OH^- mobility in alkaline water electrolysis pose the most difficulties. Two distinct half-cell reactions

are involved in electrochemical water splitting: the hydrogen evolution reaction (HER) at the cathode and the oxygen evolution reaction (OER) at the anode. The two electrodes are submerged in a liquid alkaline electrolyte composed of a caustic potash solution containing 20-30% KOH. The two electrodes are separated by a diaphragm (**Figure 5**), separating the product gases for efficiency and safety. The diaphragm must be permeable to hydroxide ions and water molecules as well. Water is split to generate H_2 at the cathode and releases hydroxide anions, which flow through the diaphragm and recombine at the anode to form O_2 via the following mechanisms [15]:

Cathode: $2H_2O\ (l) + 2e^- \rightarrow H_2\ (g) + 2OH^-\ (aq)$ Equation 5

Anode: $2OH^-\ (aq) + \rightarrow H_2O(l) + \frac{1}{2} O_2\ (g) + 2e^-$ Equation 6

Diaphragms/separators, current collectors (gas diffusion layer), separator plates (bipolar plates), and end plates are the main parts of an alkaline water electrolysis cell. In the electrolysis of alkaline water, separators often take the form of perforated stainless-steel diaphragms covered in asbestos, zirconium dioxide, or nickel. Nickel mesh/foam is employed as gas diffusion layers, whereas bipolar and end plates are made of stainless steel or nickel-coated stainless steel separator plates [15]. Low partial load range, limited current density, and low operating pressure are the three main problems that alkaline electrolyzers typically face [21], [28].

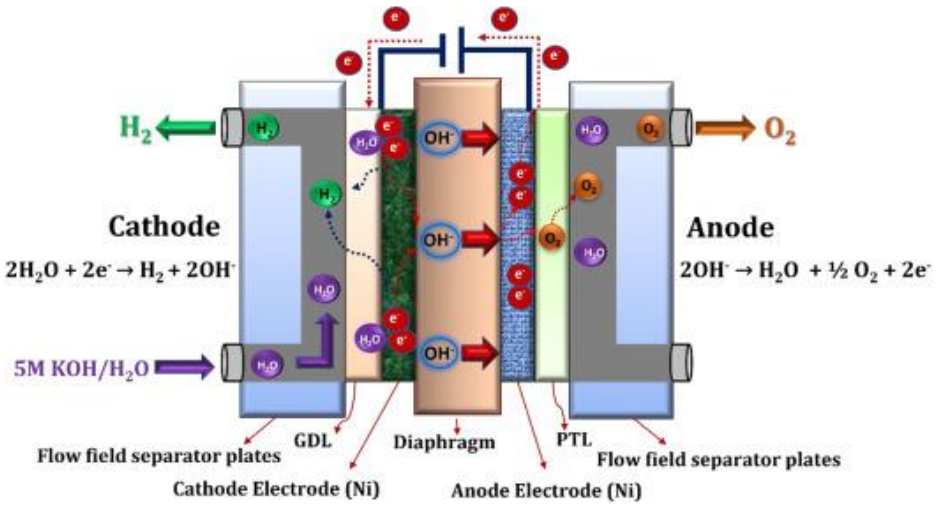

Figure 5. Schematic representation of alkaline electrolysis cell, adapted from [20].

1.3.3. Proton Exchange Membrane Water Electrolysis

Ion exchange polymers have been used in electrochemical applications since the late 1950s. The first water electrolyzer was made by General Electric in 1966 using a polymer membrane as the electrolyte. These membranes offer high proton conductivity, low gas crossover, compact system design, and high-pressure operation. The thin membrane (20-300 μm) thickness contributes to many of these advantages[21], [29].

Water electrolysis using a proton exchange membrane (PEM) is a promising technology with remarkable performance and stability that has been established in the market. The anode and cathode catalysts in PEM electrolysis are commonly IrO_2 and Pt, respectively. Instead of a liquid electrolyte, an acidic membrane is employed as a solid electrolyte (perfluorosulfonic acid membranes). The membrane transports H^+ cations from the anode to the cathode and separates H_2 and O_2 generated in the reaction.

In PEM, hydrogen and oxygen are split from water at their respective electrodes (hydrogen at the cathode and oxygen at the anode). Water is pumped to the anode, where it splits into oxygen (O_2), protons (H^+), and electrons (e^-), initiating PEM water electrolysis. The proton-conducting membrane transports these protons to the cathode side. The external power circuit, which supplies the reaction's driving force (cell voltage), is where the electrons leave the anode. The hydrogen is produced at the cathode side by recombining protons and electrons, as shown in **Figure 6** [29]. PEM electrolysis has advantages over alkaline electrolysis, such as faster kinetics of hydrogen evolution reaction and improved safety due to the absence of a caustic electrolyte. PEM can also operate at high pressure on the cathode side with atmospheric pressure on the anode side. However, the acidic cell environment requires expensive and rare materials that resist corrosion and low pH, such as noble metal catalysts like platinum group metals [30].

Besides, Ir consumption has recently surged due to its use in crucibles to manufacture LEDs for smartphones, tablets, televisions, and vehicles. It is assumed that the mass manufacturing of PEM electrolysis units will significantly impact Ir demand and, as a result, pricing. The primary distinction between the PEM and AWE is that the PEM electrolyzer can achieve substantially greater current densities, resulting in faster production rates and more compact systems [30]. The contrast and comparison between PEM and AWE are shown in **Table 1**. The gas diffusion layer, separator plates, and end plates are the most critical components PEM water electrolysis cell, along

with the membrane electrode assembly (consisting of the membrane and anode and cathode electrodes)[20].

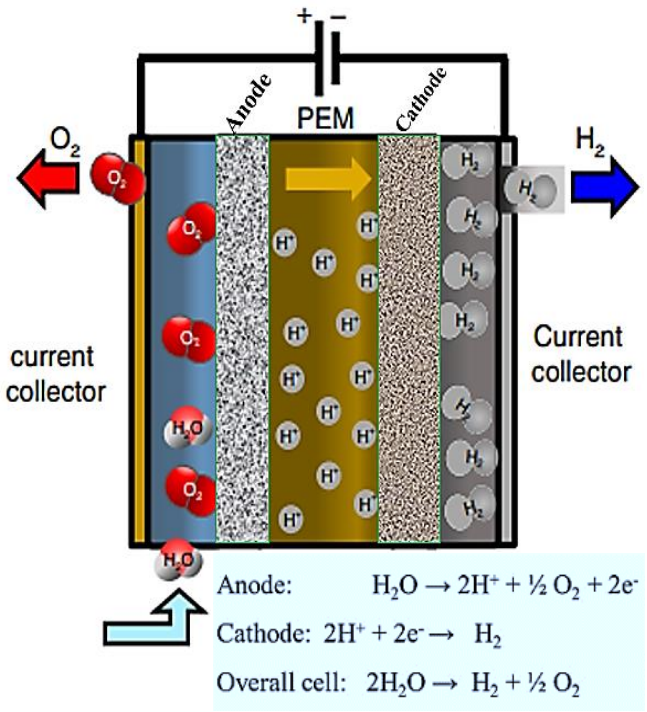

Figure 6. Schematic illustration of PEM water electrolysis adapted from Ref.[31] with slight modification.

1.3.4. Anion Exchange Membrane Water Electrolysis

An anion-exchange membrane water-electrolyte (AEMWE) is an emerging technology for producing green hydrogen energy. Due to its low cost and outstanding performance compared to the other standard electrolysis technologies, AEMWE has been the subject of intensive development by several research groups and institutes over the past few years. To address the drawbacks of the two electrolysis techniques discussed earlier, AEMWE integrates both AWE and PEMWE. AEMWE combines the less harsh environment of the alkaline electrolyzer and PEM electrolyzer with simplicity and good efficiency [20], [30]. The working principle of AEMWE lies in water reduction to produce hydrogen and hydroxide ions at the cathode. Then, hydroxide ions diffuse through the AEM and oxidize to generate water and oxygen at the anode by losing electrons, as shown in **Figure 7**. Water can be fed to both electrodes (anode and cathode), sometimes, water is only supplied to the cathode electrode. Schematically, AEMWE shares a similar configuration as a PEM cell with the dissimilarity that the membrane transports anions OH^- instead of protons

H^+. In that regard, the electrode reactions are identical to those of conventional alkaline cells. AEMWE produces hydrogen with better efficiency and purity than AWE, thanks to using AEM rather than a liquid electrolyte. Additionally, because non-noble metal-based materials can be applied, its cost can be lower than that of PEMWE. The advantage of AEMWE over the previous technology can be enlisted as follows [32]–[34].

- The AEM is thinner than the conventional diaphragm, enabling it to exhibit low ohmic losses.
- Compared to the PEM membrane, AEM is less expensive
- Because a concentrated KOH solution is not required, installation is less complicated and more straightforward.

Moreover, because of its fundamental design, the AEM electrolyzer doesn't need platinum-group metal (PGM) catalysts like PEM cells. Instead, transition-metal catalysts with adequate performances have been used in experiments, which reduces the cost. Additionally, improving the purity of generated gases at high pressure is a potential benefit over conventional alkaline electrolyzers currently being researched [32], [34]. However, it is claimed that the recently established AEM displays poor ionic conductivity and stability, meaning that its performance and durability still need to be improved to that of PEMWE [35], [36]. Investigating several commercial AEMs with good performance and durability is crucial. To get outstanding performance from AEMWE, it is decisive to explore the components of membrane-electrode assemblies (MEAs) and operating conditions in addition to developing a highly conductive, physically and chemically stable AEM [35]–[37]. Generally, the primary cell components of AEMMWE are membrane (separator), electrode materials, current collectors, gas diffusion layer (GDL), porous transport layer (PTL), separator plates (bipolar plates), and end plates. Transition metal-based electrocatalysts, particularly Nickel and NiFeCo alloy compositions, are commonly employed for both anode and cathode electrodes. As GDL for the anode and cathode, nickel foam/porous nickel mesh and carbon cloth are employed. The bipolar and end plates are stainless steel, while the separator plates are nickel-coated stainless steel. Technologies for water electrolysis using AEM are being developed up to the kW scale. Many laboratories and universities worldwide are engaged in developing AEM water electrolyzers [38].

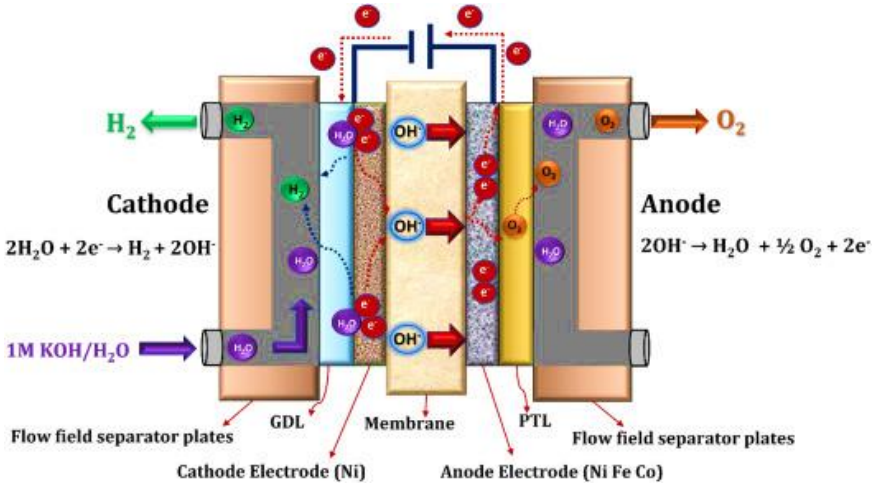

Figure 7. Schematic representation of AEM water electrolyzer; adapted from [20].

1.3.5. Solid oxide electrolysis

The solid oxide water electrolysis cell (SOEC) converts electrical energy into chemical energy through steam electrolysis at high temperatures (600-900°C). The technology is not new and has been studied since the 1960s. The SOEC operates by reducing water into hydrogen and oxide ions at the cathode. The oxide ions are further reduced to oxygen at the anode and the electrons drawn to the cathode through the external circuit. **Figure 8** depicts the underlying mechanism of solid oxide water electrolysis [25], [39]. The three components of the cell are the anode, cathode, and a dense ceramic electrolyte that conducts oxide ions. **Tables 1 and 2** summarize the different water electrolysis technologies and their specifications.

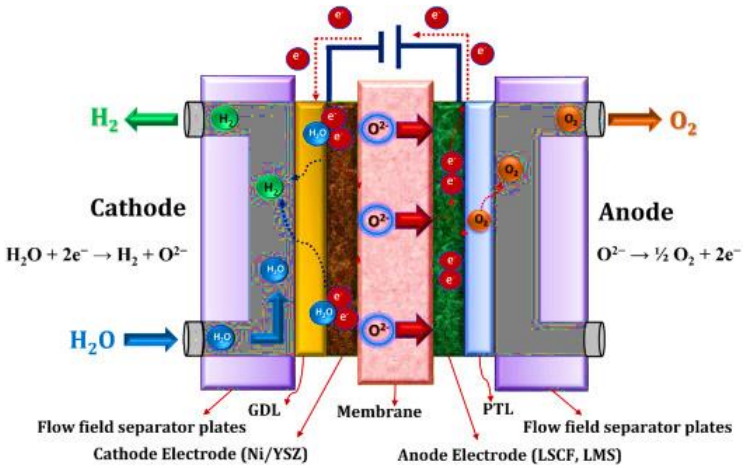

Figure 8. Schematic representation of solid oxide electrolysis cell, adapted from [20].

Overall, water electrolysis has advanced significantly in recent years, with each type having its strengths and weaknesses. Further research and development are ongoing to improve water electrolysis systems' efficiency, cost, and durability for hydrogen production.

Table 1. State-of-the-art specifications of different water electrolysis, taken from [21], [15].

Specification	Types of water electrolysis		
	Alkaline electrolysis	**PEM electrolysis**	**SOEs**
Cell temperature (°C)	60–80	50–80	900–1000
Cell pressure (bar)	<30	<30	<30
Current density (mA cm^{-2})	0.2–0.4	0.6–2.0	0.3–1.0
Cell voltage (V)	1.8–2.4	1.8–2.2	0.95–1.3
Power density (mW cm^{-2})	<1	<4.4	
Voltage efficiency HHV (%)	62–82	67–82	81–86
Specific energy consumption: Stack (kW h Nm^{-3})	4.2–5.9	4.2–5.6	-
Specific energy consumption: System (kW h Nm^{-3})	4.5–7.0	4.5–7.5	2.5–3.5
Lower partial load range (%)	20–40	0–10	-
Cell pressure (bar)	<3o	<70	1
Cell area (m^2)	>4	<0.03	<0.06
H_2 production rate: Stack-system (Nm^3 h^{-1})	<760	<10	<10
Lifetime stack (h)	<90,000	<20,000	8–20
Lifetime system (y)	20–30	10–20	-
H_2 purity (%)	99.5–99.9998%	99.9–99.9999	99.9–99.9999
Technology maturity	Widespread commercialization	Commercialized	Research & Development

Table 2. Pros and cons of the different water electrolysis technology (taken from [20], [21]).

Type of Electrolyzer	pros	Cons
AWE	✓ Well-established technology ✓ Possible to use non-noble catalysts ✓ High durability ✓ Relatively less expensive and cost-effective ✓ Stacks in the MW range	✓ Low current densities ✓ Crossover of gases (degree of purity) ✓ Low partial load range ✓ Low operational pressures ✓ Corrosive liquid electrolyte
AEMWE	✓ Noble metal-free electrocatalysts ✓ Low-concentrated (1M KOH) electrolyte	✓ Limited stability ✓ Emerging/not matured.
PEM	✓ High current densities ✓ High voltage efficiency ✓ Good partial load range ✓ Rapid system response ✓ High gas purity ✓ Compact system design	✓ High cost of components ✓ Acidic corrosive environment ✓ Low stability ✓ Stacks below the MW range ✓ Commercialization issue
SOEs	✓ High-pressure operation ✓ Utilizes non-noble catalysts ✓ High Efficiency >100% w/hot steam ✓ Efficiency up 100%; thermoneutral	✓ Durability issue (brittle ceramic) ✓ Bulky system design ✓ Laboratory stage

1.4. Fundamental reaction mechanism of water electrolysis

Electrochemical processes (reactions involving charge transfer) can be facilitated by a catalyst known as an electrocatalyst (**Equation 7**). It can serve as an electrode or be modified at the electrode's surface. The primary role of an electrocatalyst is to stimulate charge transfer between the electrode and the reactant by adsorbing the reactant on its surface to create the adsorbed intermediate. Electrocatalyst performance can be appropriately evaluated using a variety of kinetic

metrics, such as overpotential, exchange current density, and Tafel slope. These variables play an imperative role and can illuminate the electrochemical reaction's performance [40]. We briefly introduce these kinetic parameters in the following subsections before reviewing several electrocatalysts for water electrolysis.

$$O + ne^{-} \leftrightarrow R \qquad \text{Equation 7}$$

The most general equation of electrochemical kinetics, the Butler–Volmer equation, gives an approximation of the actual current density–overpotential relation for a reversible process. The Butler-Volmer equation is commonly used in electrochemical theory to represent the relationship between electrode potential (with respect to a suitable reference electrode) and current density. For a particular reaction (**Eq.8**), the total current (j) is the sum of the anodic current (j_a) and the cathodic current (j_c), and their contribution to the global current is shown in **Eq.9** [41].

$$j = j_c + j_a \qquad \text{Equation 8}$$

$$j = j_0[-e^{-\frac{\alpha nF\eta}{RT}} + e^{\frac{(1-\alpha)nF\eta}{RT}}] \qquad \text{Equation 9}$$

where the j, j_0, α, n, and η refers to the total current, exchange current density, transfer coefficient, number of electrons transferred, and overpotential, respectively, and the F, R, and T parameter represents Faraday's constant, the universal gas constant, and the absolute temperature, respectively. **Figure 9** illustrates the current-potential relationship at Butler–Volmer (B–V) and Tafel regions. The total current becomes equal to the product of $\frac{\alpha nF\eta}{RT}$ and j_0 at potentials much closer to the equilibrium potential, in which the Bulter–Volmer equation (**Eq. 9**) transforms to **eq. 10** using the linearized form.

$$j = j_0 \frac{\alpha nF\eta}{RT} \qquad \text{Equation 10}$$

The linearized Butler–Volmer equation can only be used for electrochemical processes that take place only at low current densities. Some examples of these processes are electroplating and electrochemical impedance spectroscopy (in which the overpotential is lower than approximately 25 mV at room temperature) [42].

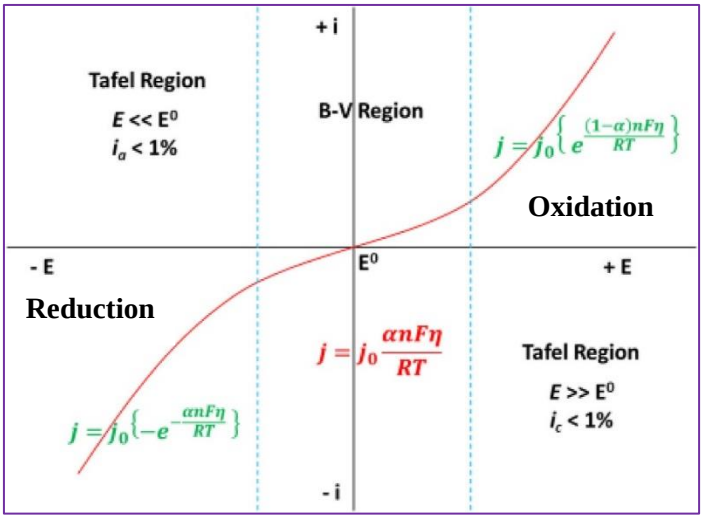

Figure 9. Schematic illustration of the current-potential relationship at Butler–Volmer (B–V) and Tafel regions [41].

When the overpotential is much higher, on the other hand, either oxidation (when E » E_{rev}) or reduction (when E « E_{rev}) takes over, then **Eq. (9)** changes into the well-known Tafel equations for oxidation (**Eq.12**) and reduction (**Eq.15**) When the E » E_{rev}, and η »0, the first exponential term of **Eq. (9)** (that is $e^{-\frac{\alpha nF\eta}{RT}}$) turned out to be negligible. Hence, **Eq. (9)** can be approximated as expressed in **Eq. (11)** and can further be transformed into **Eq.12.**

$$j = j_0\left[e^{\frac{(1-\alpha)nF\eta}{RT}}\right] \qquad \text{Equation 11}$$

$$j/j_0 = \left[e^{\frac{(1-\alpha)nF\eta}{RT}}\right]$$

$$ln(j) - ln(j_0) = e^{\frac{(1-\alpha)nF\eta}{RT}}$$

$$\eta = \frac{RT}{(1-\alpha)nF}ln(j) - \frac{RT}{(1-\alpha)nF}ln(j_0) \qquad \text{Equation 12}$$

Eq.12 can be simplified into **Eq.13**, which is equivalent to a straight line (y = mx +c).

$$\eta = a + log\ (j) \qquad \text{Equation 13}$$

On the other hand, when E « E_{rev} and η « 0, the second exponential term of **Eq.9** (that is $e^{\frac{(1-\alpha)nF\eta}{RT}}$) becomes zero. Therefore, the above **Eq. 9** can be approximated as stated in **Eq.14** and can further be transformed into **Eq.15**.

$$j = j_0[-e^{-\frac{\alpha nF\eta}{RT}}] \qquad \text{Equation 14}$$

$$\eta = \frac{RT}{\alpha nF} ln(-j) - \frac{RT}{\alpha nF} ln(j_0) \qquad \text{Equation 15}$$

Again, **Eq.15** can be simplified into **Eq.16**, which is equivalent to a straight line (y = mx +c).

$$\eta = a - log\ (j) \qquad \text{Equation 16}$$

In the above **Eqs.13 and 16,** the parameters 'a = $\frac{2.303RT}{\alpha nF}\log(j_0)$' represents the intercept of the linear line, which can be obtained by plotting η against log*(j).* It is referred to as the Tafel constant, and it can also function as an activity descriptor similar to j_0. Besides, 'b = $\frac{2.303RT}{\alpha nF}$' is the slope, also known as the Tafel slope, which provides extremely crucial information on the mechanism of the reaction being scanned and tells us how efficient the reaction is.

1.4.2. Hydrogen Evolution Reaction (HER)

The HER ($2H^+ + 2e^- \rightarrow H_2$) process is a two-electron transfer reaction on the electrode surface via two steps. The HER encompasses an intermediate reaction during the two-electron transfer. The generally acknowledged HER mechanism in alkaline media comprises three elementary reaction stages, as expressed below [43][44].

(Volmer, step 1) : $H_2O + e^- \rightleftarrows H_{ads} + OH^-$ Equation 17

(Heyrovsky, step 2): $H_{ads} + H_2O + e^- \rightleftarrows H_2 + OH^-$ Equation 18

(Tafel, step 3): $2H_{ads} \rightleftarrows H_2$ Equation 19

The global HER half-reaction can be written as follows:

$$2H_2O\ (l) + 2e^- \rightarrow H_{2\ (g)} + 2OH_{\ (aq)}^- \qquad \text{Equation 20}$$

In the Volmer process (step 1), hydrogen is adsorbed onto a free site on the electrode/catalyst surface after being released from the water molecule. Steps (2) and (3), respectively, involve the

electrochemical (Heyrovsky) and chemical (Tafel) generation of hydrogen. At low overpotentials, the Volmer step is followed by parallel Heyrovsky and Tafel steps. At high overpotentials, the Tafel step is essentially eliminated, and the reaction proceeds by the Volmer-Heyrovsky mechanism, as described by several writers [43].

In other words, if the covering surface of H_{ads} is low, it is preferable for individual H_{ads} to unite with an H^+ and an electron simultaneously to produce a molecule of H_2. This process is known as the Volmer Heyrovsky or atom-ion reaction. In the event of a wide coverage area of H_{ads}, two H_{ads} near one another on the electrode surface will recombine to produce molecular H_2. This process is known as the Volmer Tafel or combination reaction, as schematically illustrated in **Figure 10** [44].

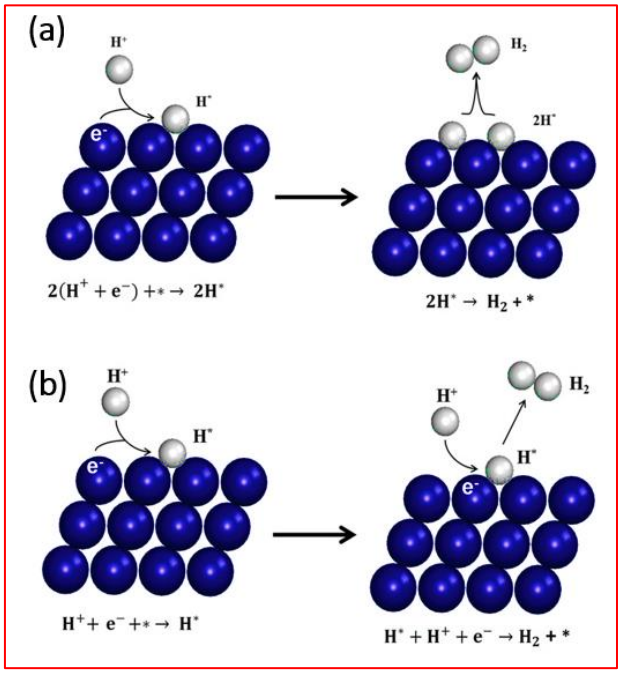

Figure 10. HER reaction mechanism on catalyst surface: (a) Volmer–Tafel mechanism, (b) Volmer–Heyrovsky. The * represents the active sites of the catalyst, and H^* denotes the adsorbed hydrogen to the catalyst's active site [45].

1.4.3. Oxygen Evolution Reaction (OER)

The OER process consists of four steps, each with one electron linked, whereas the HER is a two-electron-transfer process; as a result, the OER has slower kinetics and requires a large overpotential than the HER electrode. As a result, designing of electrocatalyst for OER is critical for effective water splitting. The synthesis of an electrocatalyst that is highly active, stable, and affordable is in

high demand from the perspective of accelerating the general market penetration of water electrolyzers. The suggested reaction mechanism for the OER under alkaline conditions is shown in **Figure 11** and expressed in **Eq.21-24** below [13][46].

$$4OH^- \rightarrow OH^* + 3OH^- + e^- \qquad \text{Equation 21}$$

$$OH^{*+} 3OH^- \rightarrow O^* + 2OH^- + H_2O + e^- \qquad \text{Equation 22}$$

$$O^* + 2OH^- + H_2O \rightarrow OOH^* + OH^- + H_2O + e^- \qquad \text{Equation 23}$$

$$OOH^* + OH^- + H_2O \rightarrow O_2 + 2H_2O + e^- \qquad \text{Equation 24}$$

Where* denotes the catalyst's active site and OH*, O*, and OOH* imply adsorbed intermediate species. The OER process typically consists of three stages. I) the process of water and hydroxyl ions adhering to the surface of the catalyst. II) the formation of an intermediate in the reaction, and III) the release of an oxygen molecule. OER is initiated at the metal site by the adsorption and discharge of OH^- anion at the anode surface, creating OH^- adsorbed species. Adsorbed OH species then underwent a redox reaction with the OH^- ion, releasing an electron and yielding H_2O and adsorbed atomic O. Adsorbed OOH species are then formed when an OH^- anion reacts with an adsorption-bound O atom. Adsorbed OOH species react with other OH^- anions, releasing an electron to create adsorbed O_2 and H_2O in the fourth phase. Last, O_2 is released from the adsorption process [47].

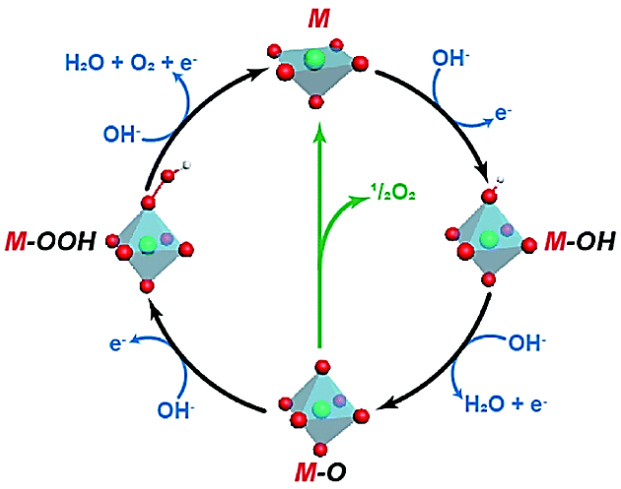

Figure 11. The OER mechanism under alkaline solution. The green line indicates a possible route for O_2 formation instead of M–OOH, taken from [48].

1.5. Synthesis methods and evaluation criteria of electrocatalysts for OER/HER

The structure, size, and morphology of an electrocatalyst, which are dictated by the synthesis method, significantly impact the catalyst's performance. The cation oxidation number/state, as well as the bulk and surface of the materials, may vary depending on the synthesis technique used. The size, shape, composition, and structure of a metal electrocatalyst are just a few of the physical elements that contribute to the formation of its unique qualities. Adjusting these factors could alter its properties and performance since electrocatalysts are highly sensitive to these parameters. This is because changing the size, for example, could affect the surface area, which is pivotal in electrocatalysis. In electrochemical water electrolysis, an electrocatalyst—typically a metal—interacts with an electrolyte to catalyze charge transfer. Therefore, the structure of the electrocatalyst not only influences the kinetics and catalysis of the electrochemical reaction but also the interaction with the components of the electrolyte and intermediate reactants, which in turn impacts the electrocatalytic activity. As a result, the catalyst surface structure, size, morphology, etc., play an essential role in catalyzing chemical reactions. Here, we highlight some of the most critical methods for preparing electrocatalyst materials and electrochemical characterization that has been widely practiced in the literature.

1.5.2. Synthesis methods

Without considering catalyst design and development concepts, achieving the appropriate level of catalytic performance appears to be complicated. In the ongoing research and development efforts to boost the electrocatalytic activity of materials, a great deal of attention has been focused on synthesis methods through various approaches. The difference in the synthesis method in a catalyst with a similar composition results in a change in the final performance of the catalyst. This is in addition to the fact that the synthesis method changes the morphology and structure of the catalyst. There are various ways to synthesize electrocatalysts for HER/OER electrodes [49]. In a broad sense, the approaches for synthesis can be divided into two major categories: physical and chemical methods (**Figure 12**). The bottom-up technique is used in chemical procedures, which means that an assembly of atoms or molecules generates various distribution sizes of nanostructured materials.

On the other hand, the top-down methodology utilized by the physical approaches involves the formation of nanostructures by unravelling their corresponding bulk material equivalents.

Chemical synthesis methods, including hydrothermal [50]–[52], solvothermal [53]–[55], sol-gel [56], co-precipitation [57], chemical vapour deposition[58], etc., are among the extensively used methods to synthesize bimetallic electrocatalysts. Different electrocatalysts for HER and OER were synthesized using chemical methods in this dissertation. As such, it is vital to highlight and briefly introduce these chemical synthesis methods in this review. A brief explanation of these methods is provided below.

The solvothermal method is a versatile process that uses high temperature and high pressure to create metal nanostructures with controlled shape and size [59]. It is mainly used with organic solvents and is called hydrothermal when the solvent is water. The process involves mixing precursors in a solvent, sealing the mixture, and heating it at a high temperature. The reaction can be finished in one step, and the product's quality is determined by adjusting parameters such as temperature, time, and pH. Both pressure and temperature speed up the chemical reaction, producing pure, homogeneous nanoparticles with a narrow size distribution [60].

One of the wet-chemical processes that are utilized in the production of nanostructured materials is the sol-gel method. The production of sol-gel requires several processes to be carried out, such as the hydrolysis of metal alkoxides to produce sol, condensation, ageing, and drying of the mixture. The nanoparticles are obtained through calcination, which is the last step [61]. The co-precipitation process involves subjecting the precursor metal to a heat treatment while it is dissolved in the provided solvent and combined with the precipitant. The precipitant can be removed using post-treatment methods through centrifugation and calcination processes. In this approach, particle aggregation and agglomeration can occur, significantly impacting the final electrocatalyst's performance [62]. In addition to the chemical synthesis methods, other physical methods, such as electrospinning [63], [64], laser ablation in liquid [51], and electrodeposition [65], etc., are also employed to synthesize electrocatalysts.

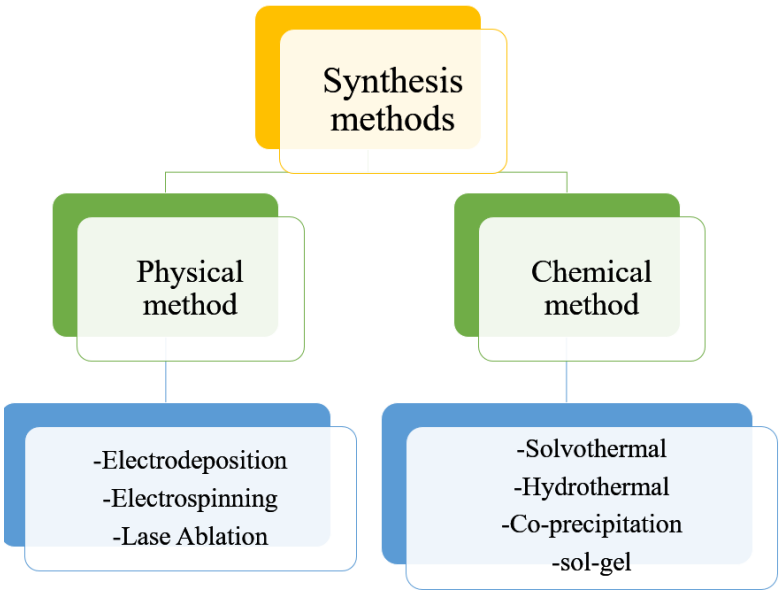

Figure 12. Classification of electrocatalyst synthesis methods.

1.5.3. Evaluation criterion of electrocatalyst for HER/OER

There are a variety of metrics that may be used to evaluate the electrochemical efficiency of an electrocatalyst material for HER/OER. Electrochemical experiments on a laboratory scale are typically carried out in a liquid environment, in a three-electrode cell controlled by a potentiostat/galvanostat. The three-electrode system consists of a working electrode (WE), counter electrode (CE), and reference electrode (RE). The WE is an electrode on which the reaction of interest occurs [66]; the RE is an electrode that serves as a point of reference in the context of potential control and measurement [67], and CE is used to close the current circuit in the electrochemical cell [68].

Determining testing methodologies and quantifiable criteria that allow for comparing different electrocatalyst materials under similar conditions is essential. Unfortunately, there is no defined standard for evaluating electrocatalysts or procedure for reporting results. The literature provides several characterizations for comparing and contrasting the catalytic activities of various catalysts, such as the overpotential, electrochemically active surface area, Faradaic efficiency, charge transfer resistance, Tafel slope, Turnover Frequency, exchange current density, and stability [40], [69], [70]. Due to the lack of a standard test technique, it isn't easy to make a valid and quantitative comparison of catalysts. Nevertheless, overpotential at a constant current density (10 mA cm^{-2}),

the Tafel slope, and at least one of the conventional stability tests are commonly employed to compare the performance of electrocatalysts.

The subsequent sub-section concisely discusses the most common parameters for evaluating catalytic activity and efficiency. These parameters include overpotential at specific current density, Tafel slope, faradic efficiency, turnover frequency, mass activity, electrochemical impedance spectroscopy (EIS), electrochemically active surface area (ECSA), and stability.

a) Overpotential

One of the most essential characteristics that determine the electrochemical performance of an electrocatalyst is the overpotential (η). For the OER, it is determined by the potential difference between the potential that is required to accomplish a given current density and the theoretical potential, which is 1.23 V ($\eta = E_{RHE} - 1.23$ V) [71]. In the case of HER, the theoretical potential is 0 V. The overpotential value required to achieve a current density of 10 mA cm^{-2} is commonly used as a reference, and a lower overpotential value indicates good catalytic performance. Generally, a catalyst with an overpotential in the range of 300–400 mV is considered an excellent catalyst for OER, whereas, for HER, the overpotential should approach zero.

b) Tafel slope

Tafel slope is utilized to determine the reaction kinetics of the catalyst coated on electrode materials. It is a tool that helps to gain an understanding of the reaction mechanism and kinetics, as well as to evaluate the electrochemical performance of several different catalysts [72], [73]. It is calculated by plotting the current response to the potential, as shown in **Eq.25.**

$$\eta = b \log \left(\frac{j}{j_0}\right) + a \qquad \text{Equation 25}$$

Where b represents the Tafel slope, η is overpotential, j is current density, and j_o is a current exchange density. The kinetics of the electron transport between the electrode and the analyte are shown by the exchange current density (j_0). A suitable electrocatalyst should have a small Tafel slope and a high current density.

c) Electrochemical active surface area (ECSA)

The electrode area available to the electrolyte utilized to transfer charges is known as the electrochemical active surface area (ECSA). In an electrode, the greater the electrochemically

active surface area, the greater the number of sites available for electrochemical reactions and, thus, faster kinetics. The ECSA can be determined by the double-layer capacitance (C_{dl}) measured through cyclic voltammetry (CV). The CV is recorded in the non-Faradic potential region at different scan rates (υ). The CV curve can be applied to quantify the double-layer charging current (i_c) using the following equation [74], [75].

$$i_c = \upsilon \times C_{dl} \qquad \text{Equation 26}$$

The slope of the graph of i_c vs υ represents the value of the C_{dl}. Based on this, ECSA can be determined using **Eq. (27)**:

$$ECSA = \frac{C_{dl}}{C_s} \qquad \text{Equation 27}$$

Where C_s is the specific capacitance of alkaline electrolyte (e.g., 0.04 mF·cm^{-2} used applied for 1.0 M KOH) [76].

d) Turnover frequency (TOF)

TOF is defined as the average number of moles of H_2 or O_2 evolved per active site and time unit. It allows for comparing different materials by measuring the particular activity of catalytic centers [69]. TOF can be evaluated using **Eq.28** [77]:

$$TOF\left(\frac{1}{s}\right) = \frac{J \times A}{4 \times F \times n} \qquad \text{Equation 28}$$

Where J (mA· cm^{-2}) represents the current density at a given overpotential, A is the active working electrode area, F is the Faradays constant (96,485 C· mol^{-1}), and n is the number of moles. High TOF represents a highly catalytic material. The most significant limitation of this metric is the difficulty of counting the active sites on the catalyst surface.

e) Mass activity

The mass activity indicates the current response normalized by the catalyst loading. The mass activity of the catalyst can be calculated as follows[77].

$$\text{mass activity} = j/m \qquad \text{Equation 29}$$

Where *j* is the measured current density ($mA \cdot cm^{-2}$) at a particular potential, and *m* is the mass loading of the working electrode ($mg \cdot cm^{-2}$).

f) Electrochemical impedance spectroscopy(EIS)

EIS is a valuable parameter for assessing the electrochemical properties of catalysts. It is used to establish a relationship between the trends in activity and the measured charge transfer resistances (R_{ct}). Moreover, it helps to study the resistance of the electrolyte solution [78]. Low R_{ct} means higher electrical conductivity, and materials that show low R_c are deemed to be suitable electrocatalysts for water electrolysis.

g) Faraday efficiency (FE)

The electrochemical performance of materials can be described using a metric called faradic efficiency (FE), which compares the proportion of real products to the percentage of theoretical products. It refers to the ratio of the amount of gas produced by the experiment to the amount determined theoretically [79]. This metric sheds light on the effectiveness of converting electrons into desired products.

h) Electrochemical stability

The stability of electrocatalysts is an essential component for large-scale applications. The chronoamperometry and the chronopotentiometry test are the two most frequent approaches used to investigate a catalyst's stability for both HER and OER. The underlying phenomena that occur during the electrochemical reaction are elusive, and the structure of the catalyst and the reaction mixture's composition undergo several changes during operation. Wang and co-workers [80] established a standard procedure to examine the actual catalyst activity and stability simultaneously. The objective is to compare the electrocatalyst activity and stability for OER. **Figure 13** shows a figure of merit for comparing the overpotential at 10 mA cm^{-2} at t =0 and t =10 h for different materials. Any data lying beyond 500 mV on either the x or y axis is not desirable for OER use. Catalysts with potential energy levels between 400 and 500 mV along both axis are optimal; however, materials that lie within this range along one axis but increase to higher than 500 mV after 10 hours cannot be employed for practical, and it is necessary to improve the stability. However, material between 300 and 400 mV along any axis is excellent for OER; this is especially true if the material begins in this range and maintains it after 10 hours of analysis. After 10 hours,

if it has moved to the 400-500 mV range, it is still adequate, but its stability has suffered. Furthermore, the ideal materials for OER use are those with an initial potential in the region of 200–300 mV (in literature, only a few materials lie in this range, at least from the x-axis). Based on this figure of merit, OER catalysts can be classified as either ideal (200–300 mV), excellent (300-400 mV), good (400-500 mV), or satisfactory (over 500 mV).

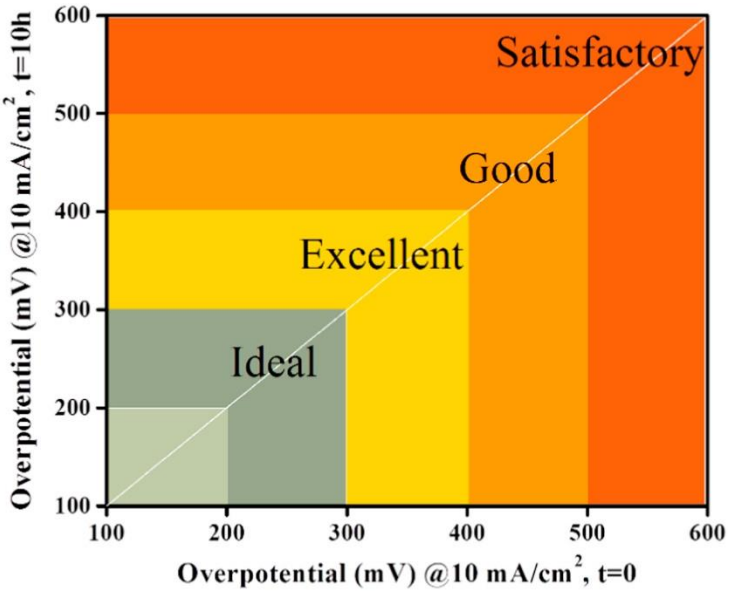

Figure 13. A figure of merit to compare electrocatalysts for OER

The following section presents the state-of-the-art and recent development of electrocatalysts for HER and OER. Significant focus was given to the theoretical understanding and the crucial factors which advance the catalytic activity toward HER/OER, such as the formation of crystal defects, impregnation into a different substrate containing high surface area, deposition/growing of electroactive metals in a conducive substrate, heteroatom doping, and alloy effect, etc.

1.6. Electrocatalyst for alkaline water electrolysis

Hydrogen production by electrolytic water splitting is perceived as a viable option to resolve the present energy and environmental issue. It has been intensively researched with an emphasis on availability and sustainability. Water electrolysis comprises two half-cell reactions (hydrogen evolution reaction (HER) at a cathode and oxygen evolution reaction (OER) at an anode. The equations below illustrate the OER and HER occur concurrently during water electrolysis [46].

(HER, Cathode): $4H_2O + 4e^- \rightarrow 2H_2 + 4OH^-$ Equation 30

(OER, Anode): $4OH^- \leftrightarrow 2H_2O + O_2 + 4e^-$ Equation 31

Overall: $2H_2O \rightarrow 2H_2 + O_2$ Equation 32

Both HER and OER are paramount for the complete efficiency of water electrolysis. The change in Gibbs free energy (G) for the water electrolysis process under normal conditions is 237.2 kJ mol^{-1}, corresponding to a cell voltage of 1.23V. However, due to the existence of an electrochemical kinetic barrier at both HER and OER electrodes, an extra overpotential is needed to initiate the reaction [44], [45]. The additional overpotential is utilized primarily to overcome various resistances in the system. These resistances include electrical resistance, mass transfer resistance, resistance caused by H_2 and O_2 bubbles, and intrinsic polarization resistance on both the anode and cathode surfaces[22]. In this regard, it is possible to circumvent this significant thermodynamic equilibrium potential by decorating the surface of the electrode with certain active catalytic materials. In general, electrocatalysts provide three primary functions for water splitting: a) stabilizing charge transfers and preventing their recombination; (b) providing active adsorption sites for the reactant species and (c) lowering the activation energies for oxidation and reduction of water. The development of scalable and robust electrocatalysts capable of driving water splitting with outstanding efficiency and durability is the primary obstacle to overcome in the field of hydrogen fuel to achieve a clean and sustainable energy conversion.

Currently, commercially available Pt/C electrocatalyst is used for HER, whereas IrO_2/RuO_2-based electrocatalysts are used for OER [81][44]. However, the rising cost and scarcity of these resources pose severe roadblocks to their widespread use [82], [83]. Thus, it is highly desired to investigate low-priced, efficient, and stable catalysts mainly constructed from earth-abundant metals. Significant interest has been in this area over the last several decades, leading to the exploration and development of a wide range of active catalysts derived from earth-abundant elements for HER/OER electrodes. Tremendous progress has been made in synthesizing and designing excellent non-noble metal-based catalysts for HER and OER.

Understanding the core theoretical and experimental ideas of the reactions that occur on the catalyst surface is absolutely necessary to develop electrocatalysts capable of expediting the reaction. Overpotential (η) is used to evaluate the performance of an electrocatalyst for HER and OER.

Several hypotheses have been put forward about the catalytic activity of materials for HER/OER. H-adsorption Gibbs free energy (G_{H^*}) and OH/O/OOH-adsorption free energies (G_{OH^*}, G_{O^*}, G_{OOH^*}) for the binding strength of reaction intermediates, where * denotes the active site on the surface of the catalyst, have been proposed to be highly correlated with the intrinsic catalytic activity of the HER/OER catalyst. When the current exchange density(j_e) for HER is plotted against structural parameters like G_{H^*} and the η for OER is plotted against the adsorbed oxygen reduction free energy of (G_{OH^*}, G_{O^*}, G_{OOH^*}) for different metal oxides, volcano-shaped diagrams are produced [45], as shown in **Figure 15**. It has been proposed that neither a strong nor a weak bond between reactant species and catalytic site contributes to electrocatalytic efficiency. The absence of consistent data is a significant issue with the volcano plot, as results obtained by several researchers on the same systems often differ by a large margin. Because of the scale relations, the volcano graphic is typically only used theoretically while discussing electrocatalysts for OER/HER [84].

The volcano plot for HER/OER represents the broad explanatory paradigm of the Sabatier principle in catalysis. It asserts that a catalyst may attain high catalytic activity when its surface has the appropriate binding energy for the produced intermediate species. An active catalyst will not bind intermediate species with an excessively strong or insufficiently weak force. If the reactant intermediates are weakly bound to the active sites, the catalyst surface will not be able to activate the active sites for a proper reaction. On the other hand, if they are strongly bound to the active sites, they will occupy and block the majority of the active catalytic sites, preventing effective reactions from occurring [45], [85], [86].

The most common and suitable descriptor for determining HER activities for various metals, nonmetals, and alloys is the computation of G_{H^*} on the catalyst surface. For the first time, in 1957, Parsons reported that HER catalysis is highly active on a catalyst surface with a G_{H^*} value close to zero [87]. As shown in **Figure 14a,** the pure metals (such as Pt, Rh, Re, and Ir) around the peak of the HER volcano plot have the optimum binding energy for hydrogen atoms. They have been demonstrated to possess excellent activity for HER since these metals are close to the optimum amount of hydrogen-binding energy, which makes it easiest from a thermodynamic point of view to go from reactants to intermediates to products. However, it has been shown that the volcano shape given by Sabatier's principle doesn't always accurately show how the HER current density

depends on the strength of the M–H bonds. This is notably true for the materials on the descending (right) branch of the Volcano plot, frequently coated with an oxide layer under conditions corresponding to the researched process. Hydrogen atoms are, therefore, not in primary contact with metallic state atoms but rather with these oxides. This was not considered when the initial HER Volcano plots were designed. The oxide coating can greatly slow the reaction rate, shifting the examined substances to the descending branch. Once the oxide-forming metals have been eliminated, linear dependency is nearly achievable [88].

In addition, it is essential to emphasize that the Volcano plot depicted in **Figure 14a** only analyzes the energy of hydride generation. Nonetheless, the position of the d-band center and the details of its interaction with hydrogen also play a crucial role in determining the catalytic activity. A surface's adsorbing potential is significantly affected by its d-band center. The change in the position of the center of the d-band relative to the Fermi level indicates a difference in the adsorption energy. Consequently, we can draw the following conclusion: the Volcano plot is an attempt to provide a theoretical comparison of pure metals based on a single criterion (M–H bond strength). A comparison of this kind can be seen as primarily instructive, as other elements influence the overall activity. Additional concerns are raised by the ambiguous state of affairs regarding metal oxides. It is actually much more complicated than that. Because there is a practically infinite number of alternatives for exact adjustment of the bonding energy and electron structure in alloys, complex compounds, and surface-modified electrocatalysts, the very generic comparison in the form of the Volcano plot becomes unsuitable [69]. Therefore, it is essential to streamline efforts to improve the electrocatalyst material. From the perspective of the catalysis/adsorption reaction system, density functional theory (DFT) has become an appealing technique for providing theoretical insights into the nature of a heterogeneous electrochemical reaction [89]. Step-by-step analysis of a chemical reaction can be used to determine its pathway, mechanism, and, ultimately, the rate-determining step.

When predicting the best attributes of a material (such as its surface energy, hydrogen binding/adsorption energy, the position of the d-band center, or electron density) for HER catalysis, DFT simulations are commonly utilized. And therefore, based on these criteria, the most promising candidate is selected to be subject to additional experimental analysis [90]. It's possible to quickly and economically evaluate various materials using this technology if adequate computational

power is available. Generally speaking, two distinct ways exist to incorporate DFT computations with experimental procedures. First, DFT simulations back up the experiment results and shed light on why a material might have improved catalytic activity [91]. The second method involves using DFT computations to foretell a catalyst's performance and propose the "optimal" structure/composition based on doping the various metals, surface modification, etc. Thus, the optimized material is designed, synthesized, and put through experimental testing [92]. The main things that limit the accuracy of DFT are the approximations that have to be made and the choice of functional, which are mathematical descriptions of electron density. Such mistakes can lead to serious errors, like underestimating the chemical reaction barriers and band gaps of materials or the excitation energies for dissociating and charge transfer.

For the OER electrode, the theoretical overpotential (η) vs. ($\Delta G_{O*} - \Delta G_{OH*}$) in the volcano plot reveals good agreement with the electrocatalytic activity for OER. As shown in **Figure 14b**, the metal oxides at or near the peak of OER volcano plots (such as IrO_2, Pt, and RuO_2) have optimal binding strengths with OER intermediate species and exhibit a small overpotential for OER [45] [93]. However, the efficient HER/OER materials found at or near the peak of HER/OER volcano plots are typically scarce and/or expensive noble metals/metal oxides, limiting their extensive commercial uses. As a result, many studies aiming to discover and develop effective HER/OER electrocatalysts have focused on Ni, Co, and Fe-based materials because of their proximity to noble metals in volcano plots and due to their high abundance in reserve, which reduces the cost.

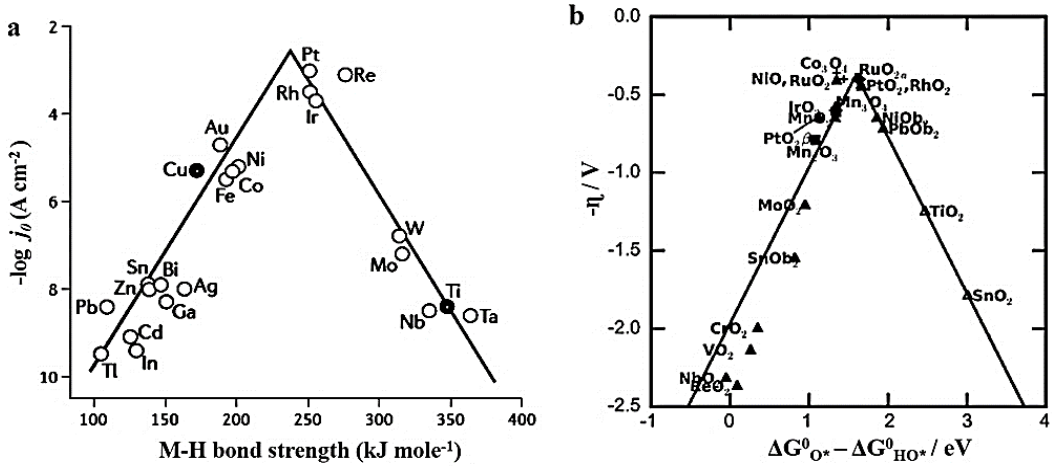

Figure 14. Volcano plots for a) hydrogen evolution reaction and b) oxygen evolution reaction [45]

A suitable electrocatalyst for water electrolysis should typically have the following features [45][94]:

- large surface area and plentiful active sites;
- high catalytic activity and optimum electrical contact to active sites;
- enlarged interstitial gaps and porosity between catalyst nanostructures for rapid charge transport and electrolyte permeation into the catalyst's interior;
- A surface with active properties that facilitates electrocatalyst adhesion and quick removal of byproducts.
- The catalyst needs to be chemically, electrochemically, and mechanically stable, and it has to tolerate harsh environments.
- Low overpotential for OER and HER electrode
- Lower energy barrier for intermediately adsorbed species, such as H*, O*, HO*, and HOO*, etc.
- Key factors in choosing electrocatalysts include their low material cost, facile synthesis, and minimal post-processing requirements at the commercial scale.

This report provides an overview of the development and fundamental mechanism of electrochemical HER/OER, as well as broad criteria for evaluating the catalytic activity of electrocatalysts in a scientific setting. A thorough review of the research into the design and development of catalysts based on earth-abundant transition metals (such as Ni, Co, Fe, and Mo) is provided. It summarizes the most critical parameters that affect OER/HER performance. Finally, we summarize the recent developments, provide a perspective on the future, and highlight the difficulties in developing cheap and efficient catalysts for water splitting.

1.6.2. Electrocatalyst for Hydrogen Evolution Reaction

It is vital to establish a consistent strategy for presenting and comparing the wide range of materials investigated as prospective electrocatalysts for the HER. In this case, the materials are presented in two categories: (i) precious metals-based catalysts and (ii) non-precious metal-based catalysts. In the following subsection, efforts have been devoted to recapitulating the electrocatalyst comprised of precious and non-precious metals for the HER electrode.

1.6.2.1. Precious metal-based electrocatalyst

Platinum-group metals (PGM) are considered a benchmark for HER electrode. The low-index single-crystal facets of Pt are the forefront electrocatalyst for HER. The activity trend is reported to be as follows: (111) < (100) < (110). The existence of reactive H_{opd} (overpotential deposition, weakly adsorbed state), found in the greatest concentration on the surface of the (110) atom, is deduced to be the cause of such phenomena. As a result, the activity of the Pt(110) surface is significantly higher than that of the other two surfaces [95], [84]. Because of their expensive cost and limited availability, noble metals are not suited for use in large industrial applications, despite having the highest catalytic activity for the HER. Therefore, a significant amount of effort has been put towards maximizing the electrocatalytic activity of Pt-based catalysts while simultaneously optimizing their geometric parameters and amount.

Supporting platinum nanoparticles on carbon with a high surface area is one approach to producing active electrocatalysts. The most popular Pt/C used in the industry is 20 wt. % Pt plated on carbon black has an overpotential of around 46 mV at 10 mA cm^{-2} in both alkaline and neutral solutions. Due to their high activity, Pt/C catalysts are still routinely used as a benchmark for newly-developed catalysts [96].

Atomic layer deposition is another strategy for reducing Pt consumption by producing controlled amounts of Pt nanoparticles, nanoclusters, or monolayers, reducing Pt loading to as little as one-tenth of typical levels [97], [98]. Nanoscaling Pt particles show promise but also have limits due to agglomeration or leaching, which reduces the active surface. However, isolating individual Pt atoms in a conductive matrix resolves this issue and has been successfully used in various electrochemical processes, including water electrolysis. This involves trapping individual Pt atoms in vacancies in the matrix of different supports like carbon vacancies in graphene or nitrogen vacancies in nitrides.

Mixing precious metals with cheaper ones can reduce their usage and enhance catalytic activity. Researchers have created ultrathin Pt-M alloy nanowires that perform better than Pt nanoparticle-based catalysts [99]. The improved performance is due to the "ligand effect" and "lattice strain effect" [100]. The atomic distribution within the catalyst structure is also vital for optimizing PGM-based catalysts [101].

Studies aimed at reducing precious metal loadings on AWE cells have limited possibilities and achieved significant reduction without impacting cell performance. However, the high cost and scarcity of precious metals remain the main obstacles to widespread use. The most promising approach for large-scale applications is to develop a catalyst based on abundant and inexpensive materials, where loading is not a significant cost concern.

1.6.2.2.Non-precious metal-based electrocatalyst

Energy conversion at large scales using AWEs requires using non-precious metal-based catalysts, as recapitulated in the previous subsection. Over the last few decades, significant time and energy has been invested in the quest for HER catalysts that are not based on precious metals. In particular, earth-abundant 3d transition metals (TMs), including Ni, Co, Mo, and Fe, have been shown to have the potential as catalytic materials for HER in alkaline electrolytes [102]–[105].

Nickel is widely researched for HER electrocatalysis. Ni-based materials are interesting because Ni is in the same group as Pt in the periodic table[106]. Improving the surface area of Ni catalysts through methods such as creating porous nanostructures and adding O-vacancies can boost HER activity [107]. Co-based materials are also popular in electrocatalysts research, with various shapes and chemical compositions studied Co-based catalysts have high conductivity and stability in alkaline media [108]. Performance can be improved by altering the catalyst's morphology and electrical structure through doping with non-metallic materials [109]. Cobalt-based catalysts are often prepared using wet chemistry, gas-solid reaction, electrodeposition, or template methods [110], [111].

Recent research has focused on transition metal sulfide (TMS) based electrocatalysts for HER. Cobalt sulfide created using various techniques and materials displays a wide variety of microscopic morphologies, from layers and grains to rods. Nanoparticles, nanosheets, etc., of cobalt sulfide, have recently been synthesized, and they give great exposed active sites and significantly increased conductivity [112], [113]. Nevertheless, due to the greater electronegativity of the S atom compared to the P atom, an extreme bond strength is produced between the S and H, which considerably increases the overpotential and reduces the efficiency of HER [114].

Many research studies based on Co-based catalysts have recently focused on Co-Mo alloys and their variants. High catalytic activity was demonstrated by the Co–Ni-Mo catalyst, which contained 45% Mo in the alloy, in which the addition of Ni increased the actual surface area, which led to an

increase in the catalytic activity of the ternary Co–Ni–Mo alloys (overpotential of 110 mV at 10 mA cm^{-2}, in comparison to 145 mV for the Co-Mo alloy) [115]. In addition to its use in alloys with other metals, cobalt is most frequently found in other compounds (such as sulfides and phosphides), where it can provide sufficient activity while also maintaining its stability under an alkaline environment. Moreover, Fe has applied for HER. It also has good HER activity (overpotentials can drop to roughly 260 mV at 10 mA cm^{-2}). It has been found that iron phosphides and iron sulfides both have high HER activity. However, there is limited literature on iron, either as a pure element or, in alloy form, as an electrocatalyst for HER. Pure Fe is sometimes used as a comparison material, but it can give different results depending on how it was prepared, its shape, or its surface area. Unfortunately, not much is known about pure Fe as a cathode material [45], [106], [116].

Steel materials are often used as bifunctional catalysts in total water splitting, but their catalytic activity is far inferior to other state-of-the-art catalysts [117]. Modifying the surface of steel-based materials, such as Fe-Mo and Fe-Co alloys, has increased activity. Creating microcracks on the surface by incorporating Mo can expand the available surface area, boosting activity. Fast solidification can also change the crystalline structure of Fe-based alloys to nano-crystalline or amorphous, which is more thermodynamically stable and has other desirable qualities. Molybdenum-containing compounds have also shown significant HER activity in alkaline electrolytes [118], [119]. Other transition metals, such as Tungsten [120]–[123] and Copper [124]–[126], have also been explored for use as catalysts.

Among the many metal structures listed above, metallic phosphides have been demonstrated to be promising candidates for HER catalysts for a long time. One of the reasons for this is that, unlike the activity of metal sulfides and selenides, the activity of phosphides is not restricted to the sites of crystal edges, and the HER can proceed in the bulk material as well [18], [127]–[133]. It is possible to further improve the catalytic activity of metal phosphides by appropriately doping the material with other elements. Nevertheless, under the influence of anodic polarization, the metal phosphides tend to undergo surface oxidation, which results in the formation of corresponding oxides and hydroxides [134]. Metal phosphides have recently garnered much interest because of their unique properties for HER. In Scopes, using keywords of "phosphide, alkaline, HER," it revealed that about 77 papers discussed metal phosphides for HER catalyst in alkaline media in

2015, while over 1660 works were published in 2022. These results point out the direction of the research in attempting to prepare sustainable electrocatalysts for HER electrode.

Substantial researchers have been devoted to preparing transition metal phosphides for HER. For example, Zhang and co-workers [135] prepared a nitrogen-doped NiCoP (denoted as N-NiCoP) nanowire arrays on carbon fiber paper skeleton (CFP) through a facile hydrothermal reaction followed by a phosphorization-nitrogenization process. Calculations based on density functional theory (DFT) and structural characterizations show that N dopant prefers to replace O defects in NiCoP lattice rather than P atoms. The N-NiCoP electrocatalyst offers better performance than the NiCoP counterpart. For N-NiCoP, the overpotentials to reach a current density of 100 $mA \cdot cm^{-2}$ was about 162.5 mV measured in 1 M KOH aqueous solution. It was reported that N doping is a viable and promising method for improving the HER performance of the NiCoP catalyst in alkaline electrolytes. Jiang and co-workers [136] prepared Co/NiCoP on carbon cloth through an electrochemical deposition and phosphorization approach, as shown in **Figure 15**. The Co/NiCoP-350 electrocatalyst exhibits a smaller overpotential of 54 mV to generate a current density of 10 mA cm^{-2} and a lower Tafel slope of 84 mV dec^{-1} than those of the electrocatalysts obtained under different calcination temperatures. More interestingly, the catalyst demonstrated appealing stability; it remained stable for about 30 h measured in 1 M KOH at a constant current density of 10 $mAcm^{-2}$.

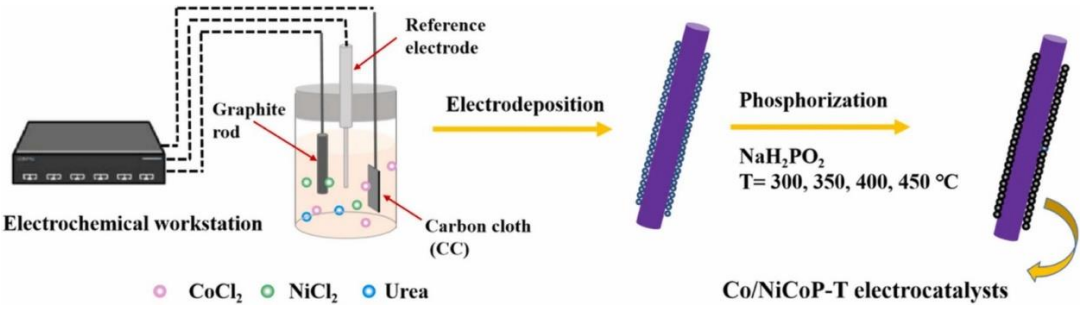

Figure 15. Schematic illustration of the Co/NiCoP electrocatalyst synthesis process adapted from [136].

Furthermore, many reports on synthesizing transition metallic phosphides for HER electrodes, including NiCoP nanowire arrays grown on 3D Ni foam (NiCoP NWAs/NF) [137], NiCoP nanostructures[138], NiCoP nanosheet arrays (NSAs) grown on 3D Ni foam [139], $(Ni_xFe_y)_2P$ nanoplates arrays grown on 3D nickel foams[140], have been reported. Bimetallic

ternary phosphides doped with additional metal elements can significantly improve the catalytic performance of HER compared to single metal binary phosphides. Electronic adjustment and synergistic effects contribute to the improved electrocatalytic performance of bimetallic ternary phosphides. As a result, in recent years, many studies on bimetallic ternary phosphides have been published in scientific journals.

1.6.3. Electrocatalyst for Oxygen Evolution Reaction

In this section, discussions on the current state of the art about electrocatalysts for OER are presented.

1.6.3.1.Precious metal-based electrocatalyst

To improve electrode kinetics and stability in different electrolyte solutions, scientists have been designing and developing a wide variety of catalysts. It has been demonstrated through experimentation that materials composed of iridium (Ir) and ruthenium (Ru) are more active toward OER in comparison to platinum (Pt) and palladium (Pd) (Pt < Pd <Ir < Ru). As of the current state of the art, the electrocatalysts for OER that are considered to be the benchmark are Ru, Ir, and their derivatives, due to their optimal interaction with the intermediates [141]. As a result, Ir and Ru-based catalysts will be the main points of discussion here. In the potential range of water electrolysis, the activity and stability of Ru and Ir thin films and the corresponding thermally oxidized RuO_2 and IrO_2 thin films, have been examined. It was reported that OER activity decreases as follows: $Ru > Ir \approx RuO_2 > IrO_2$, while dissolution increases as follows: $IrO_2 \ll RuO_2 < Ir \ll Ru$. It was discovered that the activity of both metals is more significant for OER than their oxides, but the dissolution is roughly two to three orders of magnitude more. There was also an approximately 30-fold difference in the quantity of dissolution between IrO_2 and RuO_2 under the same conditions, in which IrO_2 was more stable [142]. RuO_2 and IrO_2 have a rutile structure, with the metals in the center of an octahedral site and the oxygen atoms in the corners, with the octahedral connecting to one another by sharing corners. As a result of their high electrocatalytic activity toward OER in both acidic and alkaline solutions, RuO_2 and IrO_2 are frequently chosen as benchmark electrocatalysts for OER. Nevertheless, the sample preparation procedure and electrolyte condition significantly impact the OER performances of RuO_2 and IrO_2. For instance , rutile-type RuO2 displays remarkable OER catalytic activity in both acidic and basic electrolytes. However, given the high anodic potential, RuO_2 is extremely unstable in both

electrolytes, oxidizing to RuO_4 and dissolving in solution. A second common OER catalyst, IrO_2, also excels in this regard. However, IrO_2 likewise has the issue of being oxidized to IrO_3 and dissolved during OER, like RuO_2. IrO_2 is more stable than RuO_2, and it can maintain a higher anodic potential in both acidic and basic electrolytes [142].

It has been hypothesized how RuO_2 and IrO_2 are decomposed. Under anodic conditions, the (Ru^{4+}) O_2 will transform into the hydrous compound known as $RuO_2(OH)_2$ and deprotonates into the highly oxidized state known as (Ru^{8+}) O_4. In this case, (Ru^{8+}) O_4 is unstable in electrolyte and dissolves further into solution (along with a color change), thus causing RuO_2 catalysts to degrade. An explanation has also been provided for the scenario involving IrO_2. When the anodic potential is strong, a compound with a high oxidation state, (Ir^{6+}) O_3, will be produced. This compound will then be dissolved further in the electrolyte. In summary, the OER performance of IrO_2 is slightly lower but significantly more stable than RuO_2. To this end, an iridium-doped bimetallic oxide system, $Ru_xIr_{1-x}O_2$, was presented to increase RuO_2 stability. This technique proved to be highly efficient, and the incorporation of even a small amount of Ir into the sample was enough to significantly reduce the deterioration of stability without severely impacting the performance of OER [40], [143]–[145]. Synthesizing a core-shell-like structure ($IrO_2@RuO_2$) and then subjecting it to OER electrocatalysis is another way to improve electrocatalytic stability. It has been established that this core-shell shape can boost stability (1000^{th} cycles with 96.7% retention) and lower overpotential (300 mV) [146]. This is due to the contribution of the intrinsic activity of RuO_2 and the excellent stability of IrO_2. Despite being the benchmark for OER, both electrocatalysts are made from expensive metals, making mass production impractical [43]. Alternative OER electrocatalysts based on transition metal elements that are low-cost, highly active, and stable under oxidizing conditions have been the subject of intensive research and development activities, including the design, synthesis, and characterization of these electrocatalysts. Developing non-precious metal catalysts for oxygen-based processes has become a hot topic in electrochemical energy storage and conversion. Much attention is being paid to transition metal-based oxides, mixed metal oxides such spinels and perovskites, composites, layered structure type family, etc., and their composite as electrocatalysts for OER. The following section summarizes the non-precious metal-based electrocatalyst made up of earth-abundant transition metals.

1.6.3.2. Non-precious metal-based electrocatalyst

Transition metal-based OER electrocatalysts, such as transition-metal oxides (spinel, perovskite), sulfides, nitrides, carbide, and phosphides, have emerged as promising alternatives due to the structural and compositional oxygen-evolving complex active sites. Water splitting using transition metal is more practical because transition-metal elements are inexpensive, active, and stable over long periods in low oxidation conditions [13], [46], [147]. Numerous promising approaches have been taken to develop high-performance electrocatalysts for OER. Transition metal-containing metal oxide catalysts and other metal oxide families have been the subject of many studies for OER application [148]–[152]. Investigation into the OER activity of metal oxide catalysts incorporating transition metals and diverse metal oxide families has received significant attention and research in recent years. For example, metal oxides including, perovskite (ABO_3, where A stands for alkaline-earth and/or rare-earth metals and B stands for transition metals), spinel ($A'B'_2O_4$, where A′ stands for alkaline-earth and/or transition metals and B′ stands for group 13 elements and/or transition metals), layer structure type-family ($M(OH)_2$ and MOOH; M = Ni, Fe, Mn, and Co) have been discovered to demonstrate significant activity toward OER [13], [153], [40].

These oxides of transition metals are inexpensive, simple to synthesize, and safe for the ecosystem. In addition, they exhibit moderate conductivities and are stable in alkaline solutions, making them excellent candidates for OER electrocatalysis. Since transition metals can have different oxidation states and coordination environments (i.e., tetrahedral and octahedral sites), these oxide catalysts can possess rich combinations of transition metals in their structures, especially for perovskite- and spinel-type structures, resulting in entirely tunable OER behaviors. Because of their high OER activity, compounds of the layer structure type have also been the subject of much research. Doping has been shown to have a significant effect and be an efficient strategy for boosting OER activity for chemicals in this class. Metal oxides outside of the three groups mentioned above also exhibit momentous OER activity [13],[40], [68], [154]. Insightful findings have been gained from various attempts and systematic investigations based on these metal oxides, which help deduce the basic mechanism of OER. Non-oxide catalysts have also been reported as promising electrocatalytic materials for OER, and these materials could be good candidates for the overall water-splitting reaction. These catalysts include metal chalcogenides (TC, TC_2, T_9S_8, Ni_3C_2, T_3S_4, where T = Co and Ni, C = S, Se, and Te), metal pnictides (Co_2N, Ni_3N), and organometallics [155], [156] [40].

The following section presents a brief summary of the most researched earth-abundant transition metal-based electrocatalysts for OER.

Because of the mixed-valence states of $Co^{2+/3+/4+}$, the electrocatalysis of OER on cobalt oxide electrodes has been a subject of significant interest in the field of electrochemistry for a considerable amount of time. For example, Xu and co-workers [157] employed a ligand-assisted polyol reduction technique to prepare a synthetic oxygen-vacancy-containing porous cobalt oxide. This technique allows Co(OH)2 nanoplates to be efficiently converted into CoO_x while retaining their shape, and oxygen vacancies can be effectively created at tunable concentrations on the surface. OER performance is greatly enhanced by the vast surface area provided by the 2D porous structure and the abundance of active sites provided by oxygen vacancies, allowing overpotential values as low as 306 mV to produce a current density of 10 mA cm^{-2}. Zhao and co-workers[158] prepared CoO nanoparticles wrapped in a porous graphene sheet. The as-prepared electrocatalyst presents good OER activity with a low overpotential of 348 mV at 10 mA cm^{-2} and 79 mV dec^{-1} of the Tafel slope. The excellent OER activity may be attributed to the very porous structure of the composite material, in addition to the chemical and electrical interaction between the constituent parts. Moreover, Fe-doped CoO/C via electrospinning [159], CoO (OH) [160], etc., have been explored for their potential to catalyze the OER electrode. Besides, materials based on nickel are effective OER catalysts. The OER process has been reported to require a more significant potential and is often performed in an alkaline solution. Ni oxides are an excellent catalyst for OER because they are more stable and corrosion-resistant [161].

Manganese oxides also exhibit commendable OER activity, and it is yet another element that is found in abundance on Earth. For example, Meng and co-workers[162] synthesized MnO_2 with different crystal structures α-, β-, and δ-MnO2 and amorphous) and investigated the impact of the structure on OER activity. They looked into these materials' alkaline medium OER and ORR electrocatalytic activity. Their research shows that crystal shape significantly affects electrocatalytic performance. Regarding both OER, the activity was found as follows: α-MnO_2 > amorphous manganese oxide > β-MnO_2 > δ-MnO_2. At a current density of 10 $mAcm^{-2}$, α-MnO_2 showed an overpotential of 490 mV in OER experiments. The increased OER activity of α-MnO_2 was due to the mixed valences, plenty of di-μ-oxo bridges that function as proton sites, and the low charge transfer resistances.

Bimetals-based electrocatalysts are deemed to be more efficient in expediting reactions compared to their single-metal counterpart. This is because synergistic effects between the coupled metals, electronic structure modification, morphology, and crystallinity of the resultant product are imperative features of the electrochemical reaction process. Combining two or more metal species increases the availability of active sites and boosts electronic conductivity, both useful in electrocatalytic processes[163]. Besides, the valence and electronic states of metals can be manipulated greatly through the differential combination and tunable ratio of cations in bimetallic compounds. **Figure 16** shows the motive behind the synthesizing of bimetal-based electrocatalyst for OER. It expounds that bimetals are more efficient than their monometallic counterparts. Nevertheless, this depends on the type of metals employed, synthesis technique, morphology, and crystallinity of the resultant materials. Various optimization strategies of electrocatalysts have been practiced to shed light on the relationship between particle size, composition, phase, structure, and properties. Among the techniques are structural regulation, defect formation, phase engineering, chemical component optimization, interface regulation, doping regulation, in situ assemblies, alloying, and amorphization.

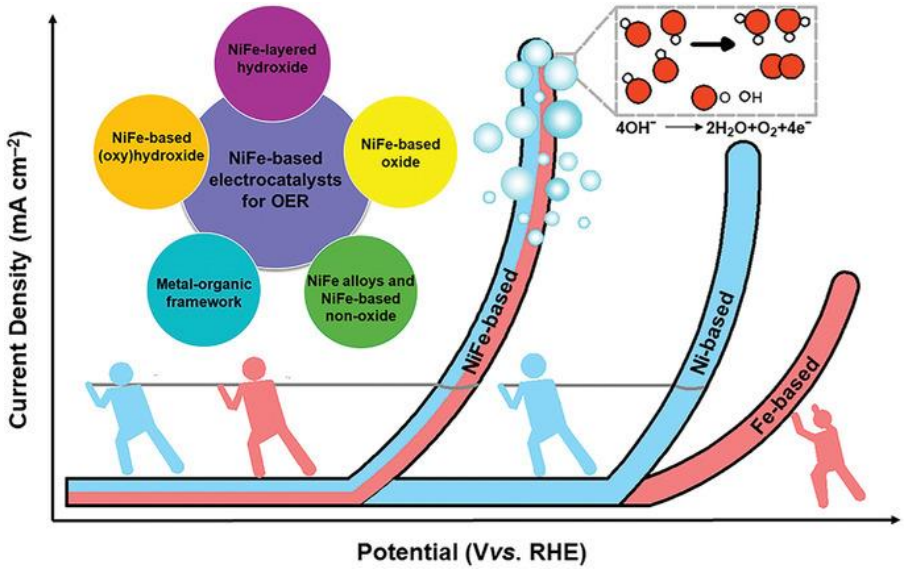

Figure 16. Schematic illustration of the bimetal coupling effect accelerates the OER process [46].

Over several decades, significant progress has been made in both the production and use of spinel-type materials, leading to substantial enhancements in their catalytic activity for OER. In contrast, reports of modifying spinel-type materials for OER are scarce.

Literature reports indicate that first-row transition metal compounds like Co, Ni, and Fe are viable and effective alternatives for electrochemical water splitting. Their high OER activity can be attributed to their ability to exist in multiple oxidation states ($M^{2+/3+/4+}$; M = active site, which need not be a metal atom). Co-based catalysts have been shown to take catalytic sites containing M^{4+}-containing species, while Fe and Ni-based catalysts have active sites containing M^{3+}comprising species. In addition, their OER activities are strongly affected by the composition, morphology, electron number of the transition metal, and oxygen surface binding energy. As a result, there is a wide range of options for altering the materials' chemical (oxidation state) and physical (roughness factor, conductivity) characteristics. Synthesizing bimetals oxide and integrating with carbonaceous materials to promote electrochemically active surface areas are among the most promising for achieving these features[164], [165]. This PhD. Thesis mainly focused on synthesizing high-performance and stable electrocatalysts employing transition bimetals modified by carbonaceous materials. As a result, it is important to recapitulate the recent development and progress made in applying oxides and alloys integrated with carbon for OER electrodes. The following paragraphs provide the state-of-the-art review related to bimetal oxides and alloys modified by carbon material.

Over the past few decades, significant progress has been made in the production and use of spinel-type materials, leading to substantial enhancements in their catalytic activity for OER [166]. Due to their low cost, good stability, outstanding redox performance, and appealing electrocatalytic activity, studies have shown that metal spinel oxides are attractive potential candidates for OER catalysts. Metal spinel oxides, such as $NiFe_2O_4$, are currently obtained primarily through high-temperature calcination, which typically results in significant aggregation, leading to the limited number of exposed active sites and unfavorable to electron transfer ability [167]. To this end, it is crucial to circumvent the aggregation problem and promote the exposed active areas. Incorporating these spinel oxide and carbon-based materials is one of the most effective methods for addressing these concerns.

Carbonaceous materials have been described as a possible option to tune the properties of metal oxide. Recently, carbon materials such as graphene[168], carbon nanotubes (CNT)[169], multi-wall carbon nanotubes (MWCNT) [58], carbon box [170], carbon cloth [163], carbon

nanofibers[171] have been used to enhance the conductivity of metallic electrocatalysts to facilitate the reaction and activity of the transition metal based electrocatalyst for OER.

Carbon materials are popular in energy tech due to their high surface area and desirable properties. The catalyst support is critical for large-scale OER electrodes, as it affects area, conductivity, and stability [172]. Its key benefits are chemical inertness, good electrical conductivity, and high specific surface area. Since the catalytic activity of carbon materials for OER is low, supplementary processes, such as heteroatom doping with *X* (X = N, S, or P), are incorporated to achieve the desired high catalytic performance. In addition to the metal elements' high inherent activity, the framework's heteroatom-doped carbon layers are also regarded as active sites because they provide strong support for dispersing metallic materials and facilitating electron/mass transfer [173]. Heteroatoms not only modify the electronic structure and increase the electric conductivity and wettability of the N-doped carbon matrix but also serve as coordination sites to immobilize metals and limit their aggregation during the electrochemical process thanks to the doped carbon support loaded metal or alloy hybrid catalyst [174]. In composites of metals and X-doped carbon materials, the electronic structure can be optimized, electron conductivity can be increased, and many active sites can be made available, eventually promoting the overall electrochemical performance.

The properties of metal oxide can be improved by combing it with conductive carbon support. **Figure 17** shows schematic representations of the integration of metal oxides and carbon supports, in which the metal oxides are well dispersed and immobilized in the carbon structure. Due to the uniform distribution of $NiFe_2O_4$ over the rGO-formed three-dimensional graphene network, the entire catalytic site is exposed, and rGO can enhance the ease electron transport channel in the electrocatalytic OER process (**Figure 17a**). Moreover, **Figure 17b** displays the schematic representation of the P-FeNiO/CNS hybrid catalyst synthesis process. First, the $NiFe/NiFe_2O_4$ embedded into a porous nitrogen-doped carbon nanosphere (denoted as FeNi-FeNiO/CNS) was obtained through an in situ phenolic resin polymerization of 3-aminophenol and formaldehyde in the presence of Fe and Ni salt solution. Then the resin was annealed at high temperatures. Based on its superior catalytic performance for OER, the FeNi-FeNiO/CNS produced at 800 °C was chosen for additional phosphating treatment to examine its structural evolution and electrochemical performance for OER. Structure evolution promotes the surface area

and active sites, which contributed to exhibiting the P-FeNiO/ CNS catalyst an enhanced activity [175].

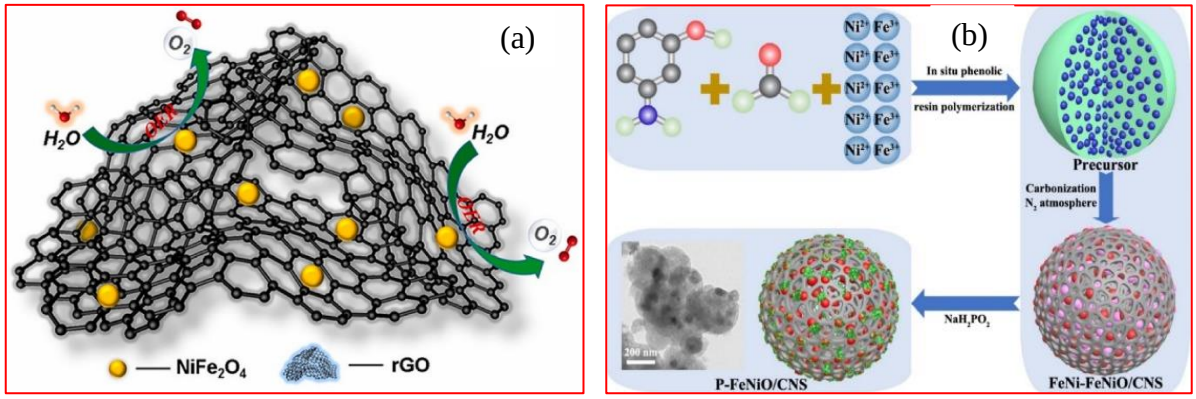

Figure 17. (a) schematic illustration of $NiFe_2O_4$ evenly dispersed on the three-dimensional graphene network, adapted from [167], and (b) schematic representation of the P-FeNiO/CNS hybrid catalyst synthesis process [175].

Substantial efforts have been reported in preparing spinel oxide and alloys integrated with carbonaceous materials. As electrode materials and catalyst supports, carbon-based materials have been the subject of extensive research due to their large pore size, good electrical conductivity, high specific surface area, and efficient mass transfer at the electrodes. Reports of numerous transition metal-based electrocatalysts for OER have been deposited or embedded in conductive carbon materials. For example, Raimundo and co-workers [176] reported NiFe nanoparticles embedded in carbon fibers-based electrocatalysts prepared by solution blow spinning method employing solutions of poly(vinyl pyrrolidone) and Ni and Fe nitrates precursors. The NiFe-carbon fibers are made up of NiFe nanoparticles that have sizes ranging from 4 to 12 nm, whereas the average diameter of carbon fibers is 827 nm. The synergistic impact between the carbon fibrillar matrix supporting the NiFe nanoparticles that act as the OER electrocatalytic center results in a low overpotential (296 mV) to generate a current density of 10 mA cm^{-2} and high chemical stability. Ma and co-workers[177] prepared an electrocatalyst made of FeNi alloy and $NiFe_2O_4$ confined on a carbonitride outer shell (denoted as FeNi/$NiFe_2O_4$@NC) through solvothermal method followed by one step annealing treatment. The optimized FeNi/$NiFe_2O_4$@NC-based electrocatalyst demonstrates superior electrocatalytic performances toward OER in alkaline media, with 10 mA cm^{-2} at an overpotential of 316 mV accompanied with excellent durability without decay after 5000

CV cycles. Moreover, preparing nanostructured metal oxides anchored on reduced graphene oxide can improve the electroactivity. For example, Umeshbabu and co-workers[178] prepared $NiCo_2O_4$ hexagonal nanoplates anchored on reduced graphene oxide sheets through a two-step solution-phase method for OER with enhanced electrocatalytic activity and stability. The OER electrocatalytic activity of the as-prepared $NiCo_2O_4$-rGO, $NiCo_2O_4$, and rGO electrodes was evaluated under alkaline conditions. Overpotential of only 300 mV is observed at current densities of 75 mA cm^{-2} during water oxidation, while a lower overpotential of 390 mV is needed to achieve a current density of 10 mA cm^{-2}. Synergistic solid effects between $NiCo_2O_4$ and rGO sheets are responsible for the enhanced electrocatalytic activity of $NiCo_2O_4$-rGO. In addition, to its conductivity, rGO also acts as a growth regulator for $NiCo_2O_4$ nanocrystals during the synthesis of $NiCo_2O_4$ nanoplates. It, therefore, improves the electrocatalytic activity and stability of the $NiCo_2O_4$-rGO hybrid in water oxidation processes. Besides, Geng and co-workers [179] prepared Co–Fe–O composites/reduced graphene oxide (rGO) hybrid structures through a hydrothermal route. They studied their composition-dependent electroactivity for OER in an alkaline solution. The overpotential and Tafel slope of the prepared catalysts are significantly lower compared to monometallic composition/rGO catalysts, suggesting synergistic effects. Li and co-workers[180] reported promising electrocatalysts made up of $CoFe_2O_4$ with spinel structure integrated with a three-dimensional (3D) porous graphene aerogel (GA) to form nitrogen-carbon doped $CoFe_2O_4$ (denoted as $CoFe_2O_4$@NC) composite materials. The strong interaction between nanosized $CoFe_2O_4$@NC and the graphitic carbon shell, along with the stability provided by the carbon shield, enhanced the OER synergistically. Graphene hydrogel was created using CoFe-PBA, and then subjected to heat treatments to obtain 3D porous graphene or aerogel-supported $CoFe_2O_4$. The resulting composite electrocatalyst ($CoFe_2O_4$@NC/GA-500) exhibited excellent stability and a smaller overpotential of 250 mV at a current density of 10 mA cm^{-2}.

Recently, dopamine, a biomolecule of various functional groups, has emerged as a promising carbon source for functionalizing materials. One unique property of dopamine is that it can self-polymerize at basic pH levels, resulting in the spontaneous deposition of polydopamine (PD) films on practically any surface [181]. In particular, PD stands out as a source of N-doped graphitized carbon because of its versatility as a composite nanomaterial, adaptability in terms of morphological tailoring, and potential for simple post-integration alterations. Dopamine is

anticipated to perform admirably in the processing of carbon-coating materials due to its robust and adaptable coating capabilities [182].

PDA can be prepared in three ways: enzymatic catalytic oxidation, electrochemical polymerization, or oxidation polymerization in solutions. The oxidation polymerization of dopamine (**Figure 18a**) can be done at room temperature in basic aqueous solutions, forming PD coating on various solid substrates, making solution oxidation the most general approach [182]. Although several different methods exist for generating PD, the precise mechanism of polymerization and the structure of the resulting compound still need to be discovered. Despite the extensive application of polydopamine, the molecular process responsible for the production of polydopamine has not been well explored. It has been hypothesized that the processes involved in the creation of polydopamine are pretty similar to those involved in the synthesis of melanin, which is made up of layered oligomeric proto-molecules that contain indolequinone units. It is likely that the derived carbon will have a structure that is analogous to the layered structure of its precursor [183]. It is generally agreed that numerous reactions and conversions take place during the polymerization process. These include the oxidation of dopamine to dopamine-quinone, intramolecular cyclization, rearrangement, and further oxidation into indole-quinone [184], [185]. The dopamine monomers were once thought to be oxidized, cyclized, and then covalently linked via aryl-aryl or other chemical bonding during an early stage of the structure analysis (**Figure 18b**)[186]. In 2011, Bernsmann and co-workers proposed that the process of PD production is similar to that of synthetic melanin. Dopamine oxidizes to 5,6-dihydroxyindole, which in turn breaks down into indolequinone. Multiple isomers of dimers and higher oligomers, including PD, are built from these two molecules by branching processes at locations 2, 3, and 7 (**Figure 18c**) [187]. Later, Dreyer and co-workers reported that PD is formed by the supramolecular aggregation of monomers linked together by covalent bonding and charge transfer, - stacking, and hydrogen bonding (**Figure 18d**) [188]. Finally, Hong and co-workers suggested that the formation of PD involves both the covalent bonding between the units and the non-covalent self-assembling of monomers or formed oligomers such as aromatic rings stacking on each other, leading to a typical structure of PD as presented in **Figure 18e**[183].

PD is a versatile carbon source due to its strong affinity to many solid surfaces, allowing for an easy thin coating. The transformation of PD into carbonized PD (c-PD) results in altered inorganic surfaces and improved functionalities. PD also can form covalent bonds or chemical bridges with

various organic molecules and transitional metal species due to its many functional groups, including catechol, amine, and imine. These functional groups allow PD to form complexes with different transition metal ions, including Fe^{3+}, Ni^{2+}, and Co^{2+}, thanks mainly to its catechol group, which makes coordination bonding possible between PD and the metal ions. PD is a unique biodegradable biopolymer distinguished by its great affinity to almost all solid materials (such as transition metals) via chemical binding because of the different functional groups. Additionally, it is a low-cost and environmentally-friendly carbon source. This opens up a wide range of possibilities for material modification, creating a wide variety of novel hybrid materials with distinctive structures and characteristics [182].

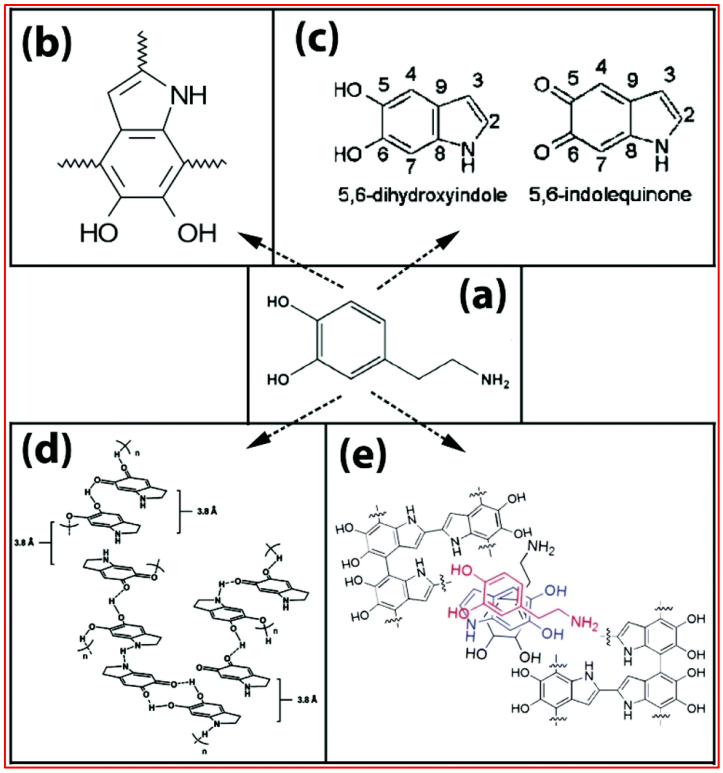

Figure 18. (a) Chemical structure of dopamine monomer, and (b-e) chemical structure of polydopamine proposed by different researcher groups: (b) Chen and co-workers [186], (c) Bernsmann and co-workers [187], (d) Dreyer and co-workers [188], and (e) Hong and co-workers [183].

Though dopamine has the potential to make materials more functional, there have been very few findings relating to dopamine-modified materials. A few reports, such as Gao and co-workers [189] applied dopamine to functionalize Fe_3O_4 nanoparticles for the magnetic separation of proteins; Yan

and co-workers [190] prepared polydopamine-derived porous carbon fiber/cobalt composites for oxygen reduction reactions(ORR); Tamakloe and co-workers [191] prepared PD-induced surface functionalization of carbon nanofibers for Pd deposition for OER and ORR electrodes; Zhou and co-workers[192] reported hollow carbon nanospheres doped with N and Fe-containing species prepared by Fe^{3+}-mediated polymerization of dopamine using a SiO_2 template, etc. Nevertheless, there are no reports on the application of dopamine to modify transition metals intended for OER electrodes for water electrolysis applications.

Apart from the carbon above sources, researchers have attempted to valorize industrial carbon-rich residues such as petroleum pitch. The tremendous potential of petroleum pitch (PP), a cheap and plentiful industrial leftover material, lies in its ability to serve as a carbon support and synthezise metal-encapsulated carbon compounds. Feedstock for electrodes for carbon finer synthesis, PP is a complex combination of polynuclear aromatic and aliphatic hydrocarbons. Making porous carbon foam (CF) from PP waste and other inexpensive materials is a cost-effective method of creating carbon support. CF is a sponge-like carbon with peculiar properties, including low density, high strength, a substantial exterior surface area thanks to its porous and open-cell structure, and controllable thermal and electrical conductivity [194]. Recently, some works have been extended toward converting these high-carbon precursors into high-value end products.

Table 3 summarizes studies on metal oxides, alloys, and composites for alkaline OER. Combining oxides with conductive materials possessing high surface area can improve electronic structure and overall electrochemical properties. Carbon support is necessary to immobilize the metal and prevent particle aggregation during reaction. However, the process of creating these materials is labor-intensive and costly. An easier method is needed for practical implementation. Although some successes have been reported, improving the electrochemical performance of Ni, Fe, and Co composites and alloys compared to reference electrocatalysts such as Ru- and Ir-based oxides is still necessary.

Table 3. Literature review of bimetal oxides, alloys, and composites (metals integrated with carbonaceous materials) based electrocatalyst for alkaline OER electrode; ***η*** represents overpotential, and ***b*** is Tafel slope.

Electrocatalyst	**Substrate**	***η* (mV) @10 mA·cm^{-2}**	***b* (mV/dec)**	**Stability remarks**	**Ref.**
CFO/rGO; Co/Fe (2:1)	GC	340	310	The current density decreased after about 10 h	[179]
CoFe-$CoFe_2O_4$/N-CNTs	GC	334	80	After 1000 cycles, a 12 mV overpotential increment was observed.	[196]
Fe_1Co_2-NC	GC	356	86.6	Smaller potential change (57 mV) after 12 h testing	[197]
FeCo-N/C	GC	370	52	Experienced 24% of anodic current attenuation during 30,000 s continued operation.	[198]
Co-Fe-1-1	CP	330	37	After 20 h continuous operation, a small overpotential rise (7%) was recorded.	[199]
Co_3O_{4-x} carbon@Fe_{2-y} Co_yO	GC	350	37.6	After 6000 cycles, a slight curve shift of about 20 mV at j = 50 mA/cm^2 was observed.	[200]
CoFe-MWCNTs	NF	300	84	Exhibited stable potential for about 3 h, and after 1000 cycles, a 10 mV potential shift was observed.	[201]

CoFe@NC-700	GC	380	110	After 1000 s operation at 1.60 V, a 7% current density decay was observed.	[202]
Fe−Co_3O_4 (Co/Fe = 32)	GC	486	--	Remained stable current after 10,000 s	[203]
$CoFe_2O_4$ nanoplates	GC	410	61	Stable polarization curve after 500 cycles	[204]
$CoFe_2O_4$	Au	374	35	Stable J of 10 mA cm^{-2} during 50 h measurements	[205]
$CoFe_2O_4$	NF	270	31	-	[65]
$CoFe_2$ - alloys/$CoFe_2O_4$	GC	300	73.34	Constant potential during 12 h measurement	[206]
$CoFe_2O_4$	NF	266	53	13.5% current density(20 $mAcm^{-2}$) attenuation after 24 h operation	[207]
CoFe2O4	GC	342	57.1	no attenuation after 1000 cycles, and no obvious J decay after 15 h operation	[208]
$CoFe_2O_4$ powders	NF	360	69.2	Stable various current densities for over 10, 000 s operation	[209]
$CoFe_2O_4$ NP	GC	335	76	Good J stability after 500 cycles	[210]
$CoFe_2O_4$/graphene	GC	300	68	83% retention of J of 10 $mAcm^{-2}$ after 30,000 s measurements	[56]
CoFe-MWCNTs	NF	300	84	Constant overpotential of 300 mV for 3 h operation	[58]
Fe-CoS/NC	GC	257	46.7	A stable J of 10 mA cm^{-2} for over 10 h operation, and only 2.82% decay was observed.	[211]
CoFe/SN-C	GC	270	-	Remained stable current density for over 5100 minutes	[212]

$Co_{0.8}Fe_{0.2}Ox/CNTs_{25wt\%}$	GC	280	49	The stable current density for about 8 h	[213]
$CoFe/Co_8FeS_8/CNT$	GC	290	38	Stable current for about 18 h	[214]
$CoFe_2O_4$/graphene	GC	300	68	About 83% relative current was reported after 30,000 s testing.	[215]
$Fe_3N@Co_4N@CoFe$	NF	225	48	Stable potential for about 20 h.	[216]
$Co_{5.47}N/Co_3Fe_7/NC$	GC	380	62.68	After 4000 CV cycles, 10 mV potential shift was recorded.	[217]
CoFe/N-HCS	NF	292	58	Retained a high relative current of 84.3% after 30 h operation.	[218]
CoFe-NCNFs	GC	323	63.9	The stable current density for about 10 h	[219]
$Co_{0.68}Fe_{0.32}O@NC/CC$	CC	260	58.9	After 10 h testing, about 95% current retention was recorded.	[220]
Fe-Co/NC-800	CP	279	42.7	Stable current for about 6 h	[221]
FeNiP@N-CFs	GC	300	47	A stable current density was observed for over 20 h at 1.55 V (vs RHE) applied potential.	[222]
NiFe/CNx	GC	360	59.1	Displayed a constant operating potential after running 10000 s, operated at j = 10 $mAcm^{-2}$.	[223]
NiFe@CN-G	GC	320	41	showed stable performance after 4 h operation, and a 76% retention of initial current density after 10 h.	[224]
FeNi@N-CNT	GC	300	47.7	Remained stable for about 10 h.	[225]

Ni_2Fe/rGO	GC	285	96	After 10 h test at the current density of 20 $mAcm^{-2}$, the potential increases by 40 mV.	[226]
$CoFe_2O_4$@N-CNFs	GC	349	80	Around 7.3% decrease of current density after 40000 s operation	[64]
$Co_3Fe_7O_x$/NPC	GC	328	31.4	The potential at a J = 10 mA cm^{-2} remained stable for about 15 h.	[227]
$FeCo_2$ P polyhedron	CFP	320	55	About 10% drop in the initial current density after a 12 h continuous test.	[228]
NiFe@NC	GC	360	81	Only decreased by 1.7% after 12 h operation.	[229]
NiCoFe-NC	GC	250	31	The J at 1.50 V increased at the initial of 4 h and then slightly declined in the following 20 h.	[230]
Co-Fe-N@MWCNT	GC	290	32	stable current-time curve and 3% attenuation after 20000 s.	[231]
$Co_{2.7}Fe_{0.3}O_4$ -NWs	CFP	342	64.4	After 100 h operation, it showed a stable J of 1000 mA cm^{-2}.	[232]
Ni/Co_3O_4@NC	GC	350	52.27	The polarization curve remained unaltered after 1000 cycles.	[233]

Where; GC: Glass carbon; CF: carbon nanofiber; NC: nitrogen-doped graphitized carbon shell; NCx: nitrogen-doped nanocarbon; NC-G: N-doped graphitic carbon shell; rGO: reduced graphene oxide; MWCNT: Multiwall carbon nanotube; CNT: carbon nanotube; NF: nickel foam; CP: Carbon paper; N-HCS: N-doped hollow carbon microspheres; NCNFs: N-doped carbon nanoflowers; CC: carbon cloth; NPC: porous carbon nanosheets; CFP: carbon fiber paper; NPs: nanoparticles; NW: nanowires.

In summary, finding an OER electrocatalyst with high performance, low cost, and stable properties is a puzzling phenomenon that needs more investigation, despite the significant progress accomplished so far. The ideal OER electrocatalyst should have high catalytic activity, low overpotential, good stability, and low cost. Noble metal-based catalysts, such as Ir and Ru oxides, have shown the best performance but are expensive and scarce, limiting their practical application. Therefore, there is an ongoing search for alternative electrocatalysts based on earth-abundant and low-cost materials, such as transition metals such as Co, Ni, and Fe. Numerous intriguing strategies have been devised to achieve superior OER electrocatalysts, which can potentially change the bottlenecks mentioned above. These include preparing nanostructured materials, doping heteroatoms into bimetals, preparing catalysts deposited in 3D/2D structured substrate, preparing bimetals with abundant oxygen defects/vacancies, and integrating a conductive material such as carbon into bimetals, and designing amorphous structure.

References for chapter II

[1] P. C. Stern, B. K. Sovacool, and T. Dietz, "Towards a science of climate and energy choices," *Nat. Clim. Chang.*, vol. 6, no. 6, pp. 547–555, 2016, doi: 10.1038/nclimate3027.

[2] S. Chu and A. Majumdar, "Opportunities and challenges for a sustainable energy future," *Nature*, vol. 488, no. 7411, pp. 294–303, 2012, doi: 10.1038/nature11475.

[3] S. Citation, *Climate Change*. Washington, D.C.: National Academies Press, 2014.

[4] IEA, "World Energy Outlook 2021 : Part of the World Energy Outlook," *Int. Energy Agency*, p. 386, 2021, [Online]. Available: https://www.iea.org/reports/world-energy-outlook-2021.

[5] A. Pareek, R. Dom, J. Gupta, J. Chandran, V. Adepu, and P. H. Borse, "Insights into renewable hydrogen energy: Recent advances and prospects," *Mater. Sci. Energy Technol.*, vol. 3, pp. 319–327, 2020, doi: 10.1016/j.mset.2019.12.002.

[6] A. Majumdar, J. M. Deutch, R. S. Prasher, and T. P. Griffin, "A framework for a hydrogen economy," *Joule*, vol. 5, no. 8, pp. 1905–1908, 2021, doi: 10.1016/j.joule.2021.07.007.

[7] P. C. Stern, K. B. Janda, M. A. Brown, L. Steg, E. L. Vine, and L. Lutzenhiser, "Opportunities and insights for reducing fossil fuel consumption by households and organizations," *Nat. Energy*, vol. 1, no. May, 2016, doi: 10.1038/nenergy.2016.43.

[8] S. Pacala and R. Socolow, "Stabilization wedges: Solving the climate problem for the next 50 years with current technologies," *Plan. Clim. Chang. A Read. Green Infrastruct. Sustain. Des. Resilient Cities*, vol. 305, no. August, pp. 55–61, 2018.

[9] P. Saravanan, M. R. Khan, C. S. Yee, and D.-V. N. Vo, "An overview of water electrolysis technologies for the production of hydrogen," in *New Dimensions in Production and Utilization of Hydrogen*, vol. 6, no. 7, Elsevier, 2020, pp. 161–190.

[10] IPCC, *Global Warming of 1.5°C*. Cambridge University Press, 2022.

[11] M. Ball and M. Weeda, "The hydrogen economy - Vision or reality?," *Int. J. Hydrogen Energy*, vol. 40, no. 25, pp. 7903–7919, 2015, doi: 10.1016/j.ijhydene.2015.04.032.

[12] G. F. Swiegers, R. N. L. Terrett, G. Tsekouras, T. Tsuzuki, R. J. Pace, and R. Stranger, "The prospects of developing a highly energy-efficient water electrolyser by eliminating or mitigating bubble effects," *Sustain. Energy Fuels*, vol. 5, no. 5, pp. 1280–1310, 2021, doi: 10.1039/d0se01886d.

[13] G. A. Gebreslase, M. V. Martínez-Huerta, and M. J. Lázaro, "Recent progress on bimetallic NiCo and CoFe based electrocatalysts for alkaline oxygen evolution reaction: A review," *J. Energy Chem.*, vol. 67, pp. 101–137, 2022, doi: 10.1016/j.jechem.2021.10.009.

[14] P. Woods, H. Bustamante, and K. Aguey-zinsou, "The hydrogen economy - Where is the water ?," *Energy Nexus*, vol. 7, no. July, p. 100123, 2022, doi: 10.1016/j.nexus.2022.100123.

[15] M. David, C. Ocampo-Martínez, and R. Sánchez-Peña, "Advances in alkaline water electrolyzers: A review," *J. Energy Storage*, vol. 23, no. April, pp. 392–403, 2019, doi: 10.1016/j.est.2019.03.001.

[16] K. J. Dillman and J. Heinonen, "A 'just' hydrogen economy: A normative energy justice assessment of the hydrogen economy," *Renew. Sustain. Energy Rev.*, vol. 167, no. March, p. 112648, 2022, doi: 10.1016/j.rser.2022.112648.

[17] F. Posso, A. Pulido, and J. C. Acevedo-Páez, "Towards The Hydrogen Economy: Estimation of green hydrogen production potential and the impact of its uses in Ecuador as a case study," *Int. J. Hydrogen Energy*, 2022, doi: 10.1016/j.ijhydene.2022.05.128.

[18] R. Gao *et al.*, "A comparative study on hybrid power-to-liquids/power-to-gas processes coupled with different water electrolysis technologies," *Energy Convers. Manag.*, vol. 263, no. May, p. 115671, 2022, doi: 10.1016/j.enconman.2022.115671.

[19] J. Yang *et al.*, "Non-precious electrocatalysts for oxygen evolution reaction in anion exchange membrane water electrolysis: A mini review," *Electrochem. commun.*, vol. 131, p. 107118, 2021, doi: 10.1016/j.elecom.2021.107118.

[20] P. Saravanan, M. R. Khan, C. S. Yee, and D.-V. N. Vo, "An overview of water electrolysis technologies for the production of hydrogen," in *Energy Reports*, vol. 8, Elsevier, 2020, pp. 161–190.

[21] M. Carmo, D. L. Fritz, J. Mergel, and D. Stolten, “A comprehensive review on PEM water electrolysis,” *Int. J. Hydrogen Energy*, vol. 38, no. 12, pp. 4901–4934, 2013, doi: 10.1016/j.ijhydene.2013.01.151.

[22] R. Andaveh, G. B. Darband, M. Maleki, and A. S. Rouhaghdam, “Superaerophobic/superhydrophilic surfaces as advanced electrocatalysts for the hydrogen evolution reaction: A comprehensive review,” *J. Mater. Chem. A*, vol. 10, no. 10, pp. 5147–5173, 2022, doi: 10.1039/d1ta10519a.

[23] N. Guillet and P. Millet, “Alkaline Water Electrolysis,” *Hydrog. Prod. By Electrolysis*, pp. 117–166, 2015, doi: 10.1002/9783527676507.ch4.

[24] W. Kreuter and H. Hofmann, “Electrolysis: the important energy transformer in a world of sustainable energy,” *Int. J. Hydrogen Energy*, vol. 23, no. 8, pp. 661–666, 1998, doi: 10.1016/S0360-3199(97)00109-2.

[25] A. Ursua, P. Sanchis, and L. M. Gandia, “Hydrogen Production from Water Electrolysis : Current Status and Future Trends,” *Proc. IEEE*, vol. 100, no. 2, pp. 410–426, 2012.

[26] IRENA, *Green Hydrogen Cost Reduction*. 2020.

[27] J. Chi and H. Yu, “Water electrolysis based on renewable energy for hydrogen production,” *Cuihua Xuebao/Chinese J. Catal.*, vol. 39, no. 3, pp. 390–394, 2018, doi: 10.1016/S1872-2067(17)62949-8.

[28] V. Schröder, B. Emonts, H. Janßen, and H. P. Schulze, “Explosion limits of hydrogen/oxygen mixtures at initial pressures up to 200 bar,” *Chem. Eng. Technol.*, vol. 27, no. 8, pp. 847–851, 2004, doi: 10.1002/ceat.200403174.

[29] S. Shiva Kumar and V. Himabindu, “Hydrogen production by PEM water electrolysis – A review,” *Mater. Sci. Energy Technol.*, vol. 2, no. 3, pp. 442–454, 2019, doi: 10.1016/j.mset.2019.03.002.

[30] H. A. Miller *et al.*, “Green hydrogen from anion exchange membrane water electrolysis: A review of recent developments in critical materials and operating conditions,” *Sustain. Energy Fuels*, vol. 4, no. 5, pp. 2114–2133, 2020, doi: 10.1039/c9se01240k.

[31] D. Li *et al.*, “Highly quaternized polystyrene ionomers for high performance anion exchange membrane water electrolysers,” *Nat. Energy*, vol. 5, no. 5, pp. 378–385, 2020, doi: 10.1038/s41560-020-0577-x.

[32] M. David, C. Ocampo-Martínez, and R. Sánchez-Peña, “Advances in alkaline water electrolyzers: A review,” *J. Energy Storage*, vol. 23, no. December 2018, pp. 392–403, 2019, doi: 10.1016/j.est.2019.03.001.

[33] C. C. Pavel *et al.*, “Highly efficient platinum group metal free based membrane-electrode assembly for anion exchange membrane water electrolysis,” *Angew. Chemie - Int. Ed.*, vol. 53, no. 5, pp. 1378–1381, 2014, doi: 10.1002/anie.201308099.

[34] H. Ito, N. Kawaguchi, S. Someya, and T. Munakata, “Pressurized operation of anion exchange membrane water electrolysis,” *Electrochim. Acta*, vol. 297, pp. 188–196, 2019, doi: 10.1016/j.electacta.2018.11.077.

[35] S. Y. Kang *et al.*, “High-performance and durable water electrolysis using a highly conductive and stable anion-exchange membrane,” *Int. J. Hydrogen Energy*, vol. 47, no. 15, pp. 9115–9126, 2022, doi: 10.1016/j.ijhydene.2022.01.002.

[36] W. You, E. Padgett, S. N. MacMillan, D. A. Muller, and G. W. Coates, “Highly conductive and chemically stable alkaline anion exchange membranes via ROMP of trans-cyclooctene derivatives,” *Proc. Natl. Acad. Sci. U. S. A.*, vol. 116, no. 20, pp. 9729–9734, 2019, doi: 10.1073/pnas.1900988116.

[37] Y. Chu, Y. Chen, N. Chen, F. Wang, and H. Zhu, “A new method for improving the ion conductivity of anion exchange membranes by using TiO2 nanoparticles coated with ionic liquid,” *RSC Adv.*, vol. 6, no. 99, pp. 96768–96777, 2016, doi: 10.1039/c6ra21355c.

[38] I. V. Pushkareva, A. S. Pushkarev, S. A. Grigoriev, P. Modisha, and D. G. Bessarabov, “Comparative study of anion exchange membranes for low-cost water electrolysis,” *Int. J. Hydrogen Energy*, vol. 45, no. 49, pp. 26070–26079, Oct. 2020, doi: 10.1016/j.ijhydene.2019.11.011.

[39] M. A. Laguna-Bercero, “Recent advances in high temperature electrolysis using solid oxide fuel cells: A review,” *J. Power Sources*, vol. 203, pp. 4–16, 2012, doi:

10.1016/j.jpowsour.2011.12.019.

[40] N. T. Suen, S. F. Hung, Q. Quan, N. Zhang, Y. J. Xu, and H. M. Chen, “Electrocatalysis for the oxygen evolution reaction: Recent development and future perspectives,” *Chem. Soc. Rev.*, vol. 46, no. 2, pp. 337–365, 2017, doi: 10.1039/c6cs00328a.

[41] S. Anantharaj and S. Noda, “How Properly Are We Interpreting the Tafel Lines in Energy Conversion Electrocatalysis?,” *Mater. Today Energy*, vol. 29, p. 101123, 2022, doi: 10.1016/j.mtener.2022.101123.

[42] M. Ghassemi, M. Kamvar, and R. Steinberger-Wilckens, “Fundamentals of electrochemistry,” *Fundam. Heat Fluid Flow High Temp. Fuel Cells*, pp. 75–99, 2020, doi: 10.1016/b978-0-12-815753-4.00004-x.

[43] M. Ďurovič, J. Hnát, and K. Bouzek, “Electrocatalysts for the hydrogen evolution reaction in alkaline and neutral media. A comparative review,” *J. Power Sources*, vol. 493, no. February, 2021, doi: 10.1016/j.jpowsour.2021.229708.

[44] V. Vij *et al.*, “Nickel-based electrocatalysts for energy-related applications: Oxygen reduction, oxygen evolution, and hydrogen evolution reactions,” *ACS Catal.*, vol. 7, no. 10, pp. 7196–7225, 2017, doi: 10.1021/acscatal.7b01800.

[45] S. Sultan *et al.*, “Single Atoms and Clusters Based Nanomaterials for Hydrogen Evolution, Oxygen Evolution Reactions, and Full Water Splitting,” *Adv. Energy Mater.*, vol. 9, no. 22, 2019, doi: 10.1002/aenm.201900624.

[46] J. Zhao, J. J. Zhang, Z. Y. Li, and X. H. Bu, “Recent Progress on NiFe-Based Electrocatalysts for the Oxygen Evolution Reaction,” *Small*, vol. 16, no. 51, pp. 1–23, 2020, doi: 10.1002/smll.202003916.

[47] Q. Zhao, Z. Yan, C. Chen, and J. Chen, “Spinels: Controlled Preparation, Oxygen Reduction/Evolution Reaction Application, and beyond,” *Chem. Rev.*, vol. 117, no. 15, pp. 10121–10211, 2017, doi: 10.1021/acs.chemrev.7b00051.

[48] Z. Cai, X. Bu, P. Wang, J. C. Ho, J. Yang, and X. Wang, “Recent advances in layered double hydroxide electrocatalysts for the oxygen evolution reaction,” *J. Mater. Chem. A*, vol. 7, no. 10, pp. 5069–5089, 2019, doi: 10.1039/c8ta11273h.

[49] A. Vazhayil, L. Vazhayal, J. Thomas, S. Ashok C, and N. Thomas, “A comprehensive review on the recent developments in transition metal-based electrocatalysts for oxygen evolution reaction,” *Appl. Surf. Sci. Adv.*, vol. 6, p. 100184, 2021, doi: 10.1016/j.apsadv.2021.100184.

[50] X. Guo, G. Liang, and A. Gu, “Construction of nickel-doped cobalt hydroxides hexagonal nanoplates for advanced oxygen evolution electrocatalysis,” *J. Colloid Interface Sci.*, vol. 553, pp. 713–719, Oct. 2019, doi: 10.1016/j.jcis.2019.05.072.

[51] X. Wang *et al.*, “Porous Cobalt-Nickel Hydroxide Nanosheets with Active Cobalt Ions for Overall Water Splitting,” *Small*, vol. 15, no. 8, p. 1804832, Feb. 2019, doi: 10.1002/smll.201804832.

[52] Y. Wang, C. Yang, Y. Huang, Z. Li, Z. Liang, and G. Cao, “Nickel induced electronic structural regulation of cobalt hydroxide for enhanced water oxidation,” *J. Mater. Chem. A*, vol. 8, no. 14, pp. 6699–6708, 2020, doi: 10.1039/D0TA00010H.

[53] J. Jiang, A. Zhang, L. Li, and L. Ai, “Nickel–cobalt layered double hydroxide nanosheets as high-performance electrocatalyst for oxygen evolution reaction,” *J. Power Sources*, vol. 278, pp. 445–451, Mar. 2015, doi: 10.1016/j.jpowsour.2014.12.085.

[54] Z. Wang, H. Wang, S. Ji, X. Wang, B. G. Pollet, and R. Wang, “Multidimensional regulation of Ni3S2@Co(OH)2 catalyst with high performance for wind energy electrolytic water,” *J. Power Sources*, vol. 446, no. October 2019, p. 227348, Jan. 2020, doi: 10.1016/j.jpowsour.2019.227348.

[55] F. Fievet *et al.*, “The polyol process: a unique method for easy access to metal nanoparticles with tailored sizes, shapes and compositions,” *Chem. Soc. Rev.*, vol. 47, no. 14, pp. 5187–5233, 2018, doi: 10.1039/c7cs00777a.

[56] Y. Ma *et al.*, “Reduced CoFe2O4/graphene composite with rich oxygen vacancies as a high efficient electrocatalyst for oxygen evolution reaction,” *Int. J. Hydrogen Energy*, vol. 45, no. 19, pp. 11052–11061, Apr. 2020, doi: 10.1016/j.ijhydene.2020.02.045.

[57] B. J. Waghmode, A. P. Gaikwad, C. V. Rode, S. D. Sathaye, K. R. Patil, and D. D. Malkhede, “Calixarene Intercalated NiCo Layered Double Hydroxide for Enhanced

Oxygen Evolution Catalysis," *ACS Sustain. Chem. Eng.*, vol. 6, no. 8, pp. 9649–9660, 2018, doi: 10.1021/acssuschemeng.7b04788.

[58] Z. Ali, M. Mehmood, J. Ahmed, A. Majeed, and K. H. Thebo, "CVD grown defect rich-MWCNTs with anchored CoFe alloy nanoparticles for OER activity," *Mater. Lett.*, vol. 259, p. 126831, 2020, doi: 10.1016/j.matlet.2019.126831.

[59] J. Lai, W. Niu, R. Luque, and G. Xu, "Solvothermal synthesis of metal nanocrystals and their applications," *Nano Today*, vol. 10, no. 2, pp. 240–267, Apr. 2015, doi: 10.1016/j.nantod.2015.03.001.

[60] G. Demazeau, "Solvothermal and hydrothermal processes: The main physico-chemical factors involved and new trends," *Res. Chem. Intermed.*, vol. 37, no. 2–5, pp. 107–123, 2011, doi: 10.1007/s11164-011-0240-z.

[61] N. Baig, I. Kammakakam, W. Falath, and I. Kammakakam, "Nanomaterials: A review of synthesis methods, properties, recent progress, and challenges," *Mater. Adv.*, vol. 2, no. 6, pp. 1821–1871, 2021, doi: 10.1039/d0ma00807a.

[62] S. Gyergyek, M. Drofenik, and D. Makovec, "Oleic-acid-coated CoFe 2O 4 nanoparticles synthesized by co-precipitation and hydrothermal synthesis," *Mater. Chem. Phys.*, vol. 133, no. 1, pp. 515–522, 2012, doi: 10.1016/j.matchemphys.2012.01.077.

[63] C. Alegre *et al.*, "Electrocatalysis of Oxygen on Bifunctional Nickel-Cobaltite Spinel," *ChemElectroChem*, vol. 7, no. 1, pp. 124–130, Jan. 2020, doi: 10.1002/celc.201901584.

[64] T. Li *et al.*, "Anchoring CoFe2O4 Nanoparticles on N-Doped Carbon Nanofibers for High-Performance Oxygen Evolution Reaction," *Adv. Sci.*, vol. 4, no. 11, 2017, doi: 10.1002/advs.201700226.

[65] C. Zhang *et al.*, "Electrodeposited nanostructured CoFe 2 O 4 for overall water splitting and supercapacitor applications," *Catalysts*, vol. 9, no. 2, 2019, doi: 10.3390/catal9020176.

[66] N. Elgrishi, K. J. Rountree, B. D. McCarthy, E. S. Rountree, T. T. Eisenhart, and J. L. Dempsey, "A Practical Beginner's Guide to Cyclic Voltammetry," *J. Chem. Educ.*, vol. 95, no. 2, pp. 197–206, 2018, doi: 10.1021/acs.jchemed.7b00361.

[67] M. Waleed Shinwari, D. Zhitomirsky, I. A. Deen, P. R. Selvaganapathy, M. Jamal Deen, and D. Landheer, "Microfabricated reference electrodes and their biosensing applications," *Sensors*, vol. 10, no. 3, pp. 1679–1715, 2010, doi: 10.3390/s100301679.

[68] C. Wei *et al.*, "Recommended Practices and Benchmark Activity for Hydrogen and Oxygen Electrocatalysis in Water Splitting and Fuel Cells," *Adv. Mater.*, vol. 31, no. 31, 2019, doi: 10.1002/adma.201806296.

[69] M. Ďurovič, J. Hnát, and K. Bouzek, "Electrocatalysts for the hydrogen evolution reaction in alkaline and neutral media. A comparative review," *J. Power Sources*, vol. 493, no. March, 2021, doi: 10.1016/j.jpowsour.2021.229708.

[70] F. Safizadeh, E. Ghali, and G. Houlachi, "Electrocatalysis developments for hydrogen evolution reaction in alkaline solutions - A Review," *Int. J. Hydrogen Energy*, vol. 40, no. 1, pp. 256–274, 2015, doi: 10.1016/j.ijhydene.2014.10.109.

[71] W. Zhang, D. Li, L. Zhang, X. She, and D. Yang, "NiFe-based nanostructures on nickel foam as highly efficiently electrocatalysts for oxygen and hydrogen evolution reactions," *J. Energy Chem.*, vol. 39, pp. 39–53, 2019, doi: 10.1016/j.jechem.2019.01.017.

[72] S. Trasatti, "Electrocatalysis in the anodic evolution of oxygen and chlorine," *Electrochim. Acta*, vol. 29, no. 11, pp. 1503–1512, Nov. 1984, doi: 10.1016/0013-4686(84)85004-5.

[73] J. Zhang *et al.*, "Surface engineering induced hierarchical porous Ni12P5-Ni2P polymorphs catalyst for efficient wide pH hydrogen production," *Appl. Catal. B Environ.*, vol. 282, no. September 2020, p. 119609, 2021, doi: 10.1016/j.apcatb.2020.119609.

[74] E. Cossar, M. S. E. Houache, Z. Zhang, and E. A. Baranova, "Comparison of electrochemical active surface area methods for various nickel nanostructures," *J. Electroanal. Chem.*, vol. 870, p. 114246, 2020, doi: 10.1016/j.jelechem.2020.114246.

[75] S. Trasatti and O. A. Petrii, "International Union of Pure and Applied Chemistry Physical Chemistry Division Commission on Electrochemistry: Real Surface Area Measurements in Electrochemistry," *Pure Appl. Chem.*, vol. 63, no. 5, pp. 711–734, 1991, doi: 10.1351/pac199163050711.

[76] S. K. Bikkarolla and P. Papakonstantinou, "CuCo2O4 nanoparticles on nitrogenated

graphene as highly efficient oxygen evolution catalyst," *J. Power Sources*, vol. 281, pp. 243–251, May 2015, doi: 10.1016/j.jpowsour.2015.01.192.

[77] F. Zheng *et al.*, "Fe/Ni bimetal organic framework as efficient oxygen evolution catalyst with low overpotential," *J. Colloid Interface Sci.*, vol. 555, pp. 541–547, 2019, doi: 10.1016/j.jcis.2019.08.005.

[78] S. Anantharaj and S. Noda, "Appropriate Use of Electrochemical Impedance Spectroscopy in Water Splitting Electrocatalysis," *ChemElectroChem*, vol. 7, no. 10, pp. 2297–2308, May 2020, doi: 10.1002/celc.202000515.

[79] B. Iandolo, B. Wickman, B. Seger, I. Chorkendorff, I. Zorić, and A. Hellman, "Faradaic efficiency of O2 evolution on metal nanoparticle sensitized hematite photoanodes," *Phys. Chem. Chem. Phys.*, vol. 16, no. 3, pp. 1271–1275, 2014, doi: 10.1039/c3cp54288b.

[80] M. Tahir *et al.*, "Electrocatalytic oxygen evolution reaction for energy conversion and storage: A comprehensive review," *Nano Energy*, vol. 37, no. February, pp. 136–157, 2017, doi: 10.1016/j.nanoen.2017.05.022.

[81] Z. Zhang, L. Cong, Z. Yu, L. Qu, and W. Huang, "Facial synthesis of Fe–Ni bimetallic N-doped carbon framework for efficient electrochemical hydrogen evolution reaction," *Mater. Today Energy*, vol. 16, p. 100387, 2020, doi: 10.1016/j.mtener.2020.100387.

[82] J. Jiang, A. Zhang, L. Li, and L. Ai, "Nickel-cobalt layered double hydroxide nanosheets as high-performance electrocatalyst for oxygen evolution reaction," *J. Power Sources*, vol. 278, pp. 445–451, 2015, doi: 10.1016/j.jpowsour.2014.12.085.

[83] Z. Guan, X. Zhang, J. Fang, X. Wang, W. Zhu, and Z. Zhuang, "Fe,Ni,S,N-doped carbon materials as highly active Bi-functional catalysts for rechargeable Zinc-Air battery," *Mater. Lett.*, vol. 258, p. 126826, 2020, doi: 10.1016/j.matlet.2019.126826.

[84] M. Plevová, J. Hnát, and K. Bouzek, "Electrocatalysts for the oxygen evolution reaction in alkaline and neutral media. A comparative review," *J. Power Sources*, no. March, 2021, doi: 10.1016/j.jpowsour.2021.230072.

[85] J. Greeley, T. F. Jaramillo, J. Bonde, I. Chorkendorff, and J. K. Nørskov, "Computational high-throughput screening of electrocatalytic materials for hydrogen evolution," *Nat.*

Mater., vol. 5, no. 11, pp. 909–913, 2006, doi: 10.1038/nmat1752.

[86] W. Sheng, M. Myint, J. G. Chen, and Y. Yan, "Correlating the hydrogen evolution reaction activity in alkaline electrolytes with the hydrogen binding energy on monometallic surfaces," *Energy Environ. Sci.*, vol. 6, no. 6, pp. 1509–1512, 2013, doi: 10.1039/c3ee00045a.

[87] B. Y. Roger, "THE RATE OF ELECTROLYTIC HYDROGEN EVOLUTION AND THE HEAT OF ADSORPTION OF HYDROGEN," pp. 1053–1063, 1957.

[88] A. R. Zeradjanin, J. P. Grote, G. Polymeros, and K. J. J. Mayrhofer, "A Critical Review on Hydrogen Evolution Electrocatalysis: Re-exploring the Volcano-relationship," *Electroanalysis*, vol. 28, no. 10, pp. 2256–2269, 2016, doi: 10.1002/elan.201600270.

[89] D. Weijing *et al.*, "The application of DFT in catalysis and adsorption reaction system," *Energy Procedia*, vol. 152, pp. 997–1002, 2018, doi: 10.1016/j.egypro.2018.09.106.

[90] Z. Liang, X. Zhong, T. Li, M. Chen, and G. Feng, "DFT Study on the Hydrogen Evolution Reaction for Different Facets of Co2P," *ChemElectroChem*, vol. 6, no. 1, pp. 260–267, 2019, doi: 10.1002/celc.201800601.

[91] A. C. Thenuwara, L. Dheer, N. H. Attanayake, Q. Yan, U. V. Waghmare, and D. R. Strongin, "Co-Mo-P Based Electrocatalyst for Superior Reactivity in the Alkaline Hydrogen Evolution Reaction," *ChemCatChem*, vol. 10, no. 21, pp. 4846–4851, 2018, doi: 10.1002/cctc.201801389.

[92] H. Wu, X. Zuo, S. P. Wang, J. W. Yin, Y. N. Zhang, and J. Chen, "Theoretical and experimental design of Pt-Co(OH)2 electrocatalyst for efficient HER performance in alkaline solution," *Prog. Nat. Sci. Mater. Int.*, vol. 29, no. 3, pp. 356–361, 2019, doi: 10.1016/j.pnsc.2019.05.009.

[93] Z. W. She, J. Kibsgaard, C. F. Dickens, I. Chorkendorff, J. K. Nørskov, and T. F. Jaramillo, "Combining theory and experiment in electrocatalysis: Insights into materials design," *Science (80-.).*, vol. 355, no. 6321, 2017, doi: 10.1126/science.aad4998.

[94] A. Raza, K. M. Deen, E. Asselin, and W. Haider, "A review on the electrocatalytic dissociation of water over stainless steel: Hydrogen and oxygen evolution reactions,"

Renew. Sustain. Energy Rev., vol. 161, no. February, p. 112323, 2022, doi: 10.1016/j.rser.2022.112323.

[95] N. M. Marković, S. T. Sarraf, H. A. Gasteiger, and P. N. Ross, "Surfaces in Alkaline Solution," *J. Chem. Soc. Faraday Trans.*, vol. 92, no. 20, pp. 3719–3725, 1996.

[96] B. You *et al.*, "Universal Surface Engineering of Transition Metals for Superior Electrocatalytic Hydrogen Evolution in Neutral Water," *J. Am. Chem. Soc.*, vol. 139, no. 35, pp. 12283–12290, 2017, doi: 10.1021/jacs.7b06434.

[97] W. Luo *et al.*, "Boosting HER Performance of Pt-Based Catalysts Immobilized on Functionalized Vulcan Carbon by Atomic Layer Deposition," *Front. Mater.*, vol. 6, no. October, pp. 1–10, 2019, doi: 10.3389/fmats.2019.00251.

[98] W. J. Lee *et al.*, "Atomic Layer Deposition of Pt Thin Films Using Dimethyl (N, N-Dimethyl-3-Butene-1-Amine- N) Platinum and O2 Reactant," *Chem. Mater.*, vol. 31, no. 14, pp. 5056–5064, 2019, doi: 10.1021/acs.chemmater.9b00675.

[99] M. E. Scofield *et al.*, "Role of chemical composition in the enhanced catalytic activity of Pt-based alloyed ultrathin nanowires for the hydrogen oxidation reaction under alkaline conditions," *ACS Catal.*, vol. 6, no. 6, pp. 3895–3908, 2016, doi: 10.1021/acscatal.6b00350.

[100] J. R. Kitchin, J. K. Nørskov, M. A. Barteau, and J. G. Chen, "Modification of the surface electronic and chemical properties of Pt(111) by subsurface 3d transition metals," *J. Chem. Phys.*, vol. 120, no. 21, pp. 10240–10246, 2004, doi: 10.1063/1.1737365.

[101] Q. Jia, W. Liang, M. K. Bates, P. Mani, W. Lee, and S. Mukerjee, "Activity descriptor identification for oxygen reduction on platinum-based bimetallic nanoparticles: In situ observation of the linear composition-strain-activity relationship," *ACS Nano*, vol. 9, no. 1, pp. 387–400, 2015, doi: 10.1021/nn506721f.

[102] F. Zeng, C. Mebrahtu, L. Liao, A. K. Beine, and R. Palkovits, "Stability and deactivation of OER electrocatalysts: A review," *J. Energy Chem.*, vol. 69, pp. 301–329, 2022, doi: 10.1016/j.jechem.2022.01.025.

[103] T. Feng, C. Ouyang, Z. Zhan, T. Lei, and P. Yin, "Cobalt doping VS2 on nickel foam as a

high efficient electrocatalyst for hydrogen evolution reaction," *Int. J. Hydrogen Energy*, vol. 47, no. 19, pp. 10646–10653, 2022, doi: 10.1016/j.ijhydene.2022.01.132.

[104] F. Keivanimehr *et al.*, "Electrocatalytic hydrogen evolution on the noble metal-free MoS2/carbon nanotube heterostructure: a theoretical study," *Sci. Rep.*, vol. 11, no. 1, pp. 1–9, 2021, doi: 10.1038/s41598-021-83562-w.

[105] K. Chen, B. Xu, L. Shen, D. Shen, and L. Guo, "Functions and performance of ionic liquids in enhancing electrocatalytic hydrogen evolution reactions : a comprehensive review," pp. 19452–19469, 2022, doi: 10.1039/d2ra02547g.

[106] J. Deng, P. Ren, D. Deng, L. Yu, F. Yang, and X. Bao, "Highly active and durable non-precious-metal catalysts encapsulated in carbon nanotubes for hydrogen evolution reaction," *Energy Environ. Sci.*, vol. 7, no. 6, pp. 1919–1923, 2014, doi: 10.1039/c4ee00370e.

[107] S. De, J. Zhang, R. Luque, and N. Yan, "Ni-based bimetallic heterogeneous catalysts for energy and environmental applications," *Energy Environ. Sci.*, vol. 9, no. 11, pp. 3314–3347, 2016, doi: 10.1039/c6ee02002j.

[108] J. Wang, W. Cui, Q. Liu, Z. Xing, A. M. Asiri, and X. Sun, "Recent Progress in Cobalt-Based Heterogeneous Catalysts for Electrochemical Water Splitting," *Adv. Mater.*, vol. 28, no. 2, pp. 215–230, 2016, doi: 10.1002/adma.201502696.

[109] R. Li *et al.*, "The urchin-like sphere arrays Co3O4 as a bifunctional catalyst for hydrogen evolution reaction and oxygen evolution reaction," *J. Power Sources*, vol. 341, pp. 250–256, 2017, doi: 10.1016/j.jpowsour.2016.10.096.

[110] Y. Shi and B. Zhang, "Recent advances in transition metal phosphide nanomaterials: Synthesis and applications in hydrogen evolution reaction," *Chem. Soc. Rev.*, vol. 45, no. 6, pp. 1529–1541, 2016, doi: 10.1039/c5cs00434a.

[111] W. Zhang, L. Cui, and J. Liu, "Recent advances in cobalt-based electrocatalysts for hydrogen and oxygen evolution reactions," *J. Alloys Compd.*, vol. 821, p. 153542, 2020, doi: 10.1016/j.jallcom.2019.153542.

[112] A. Sumboja *et al.*, "One-Step Facile Synthesis of Cobalt Phosphides for Hydrogen

Evolution Reaction Catalysts in Acidic and Alkaline Medium," *ACS Appl. Mater. Interfaces*, vol. 10, no. 18, pp. 15673–15680, 2018, doi: 10.1021/acsami.8b01491.

[113] Y. Pan, Y. Lin, Y. Chen, Y. Liu, and C. Liu, "Cobalt phosphide-based electrocatalysts: Synthesis and phase catalytic activity comparison for hydrogen evolution," *J. Mater. Chem. A*, vol. 4, no. 13, pp. 4745–4754, 2016, doi: 10.1039/c6ta00575f.

[114] S. Anantharaj, S. R. Ede, K. Sakthikumar, K. Karthick, S. Mishra, and S. Kundu, "Recent Trends and Perspectives in Electrochemical Water Splitting with an Emphasis on Sulfide, Selenide, and Phosphide Catalysts of Fe, Co, and Ni: A Review," *ACS Catal.*, vol. 6, no. 12, pp. 8069–8097, 2016, doi: 10.1021/acscatal.6b02479.

[115] A. Laszczyńska and I. Szczygieł, "Electrocatalytic activity for the hydrogen evolution of the electrodeposited Co–Ni–Mo, Co–Ni and Co–Mo alloy coatings," *Int. J. Hydrogen Energy*, vol. 45, no. 1, pp. 508–520, 2020, doi: 10.1016/j.ijhydene.2019.10.181.

[116] C. I. Müller *et al.*, "Electrochemical investigations on amorphous Fe-base alloys for alkaline water electrolysis," *Int. J. Hydrogen Energy*, vol. 39, no. 17, pp. 8926–8937, 2014, doi: 10.1016/j.ijhydene.2014.03.151.

[117] H. Schäfer and M. Chatenet, "Steel: The Resurrection of a Forgotten Water-Splitting Catalyst," *ACS Energy Lett.*, vol. 3, no. 3, pp. 574–591, 2018, doi: 10.1021/acsenergylett.8b00024.

[118] C. Lu *et al.*, "Molybdenum Carbide-Embedded Nitrogen-Doped Porous Carbon Nanosheets as Electrocatalysts for Water Splitting in Alkaline Media," *ACS Nano*, vol. 11, no. 4, pp. 3933–3942, 2017, doi: 10.1021/acsnano.7b00365.

[119] S. Upadhyay and O. P. Pandey, "Synthesis of Mo2C/MoC/C nanocomposite for hydrogen evolution reaction," *J. Solid State Electrochem.*, vol. 26, no. 2, pp. 559–564, 2022, doi: 10.1007/s10008-021-05096-5.

[120] D. Li *et al.*, "Defect-rich engineering of Ni-incorporated tungsten oxides micro-flowers on carbon cloth: A binder-free electrode for highly efficient hydrogen evolution reaction," *J. Power Sources*, vol. 520, no. July 2021, p. 230862, 2022, doi: 10.1016/j.jpowsour.2021.230862.

[121] M. Chen *et al.*, “In-situ phosphatizing of cobalt-molybdenum nanosheet arrays on self-supporting rGO/CNTs film as efficient electrocatalysts for hydrogen evolution reaction,” *Chem. Eng. J.*, vol. 422, no. May, p. 130355, 2021, doi: 10.1016/j.cej.2021.130355.

[122] S. Dong *et al.*, “A Review of the Application of Heterostructure Catalysts in Hydrogen Evolution Reaction,” *ChemistrySelect*, vol. 7, no. 14, 2022, doi: 10.1002/slct.202104041.

[123] M. Zeng and Y. Li, “Recent advances in heterogeneous electrocatalysts for the hydrogen evolution reaction,” *J. Mater. Chem. A*, vol. 3, no. 29, pp. 14942–14962, 2015, doi: 10.1039/c5ta02974k.

[124] A. Sajeev *et al.*, “Development of Cu3N electrocatalyst for hydrogen evolution reaction in alkaline medium,” *Sci. Rep.*, vol. 12, no. 1, pp. 1–13, 2022, doi: 10.1038/s41598-022-05953-x.

[125] N. H. Khdary, M. A. Ghanem, M. E. Abdelsalam, D. N. Khdary, and N. H. Alotaibi, “Copper-N-SiO2 nanoparticles catalyst for hydrogen evolution reaction,” *Int. J. Hydrogen Energy*, vol. 44, no. 41, pp. 22926–22935, 2019, doi: 10.1016/j.ijhydene.2019.06.186.

[126] J. Du, J. Wang, L. Ji, X. Xu, and Z. Chen, “A Highly Active and Robust Copper-Based Electrocatalyst toward Hydrogen Evolution Reaction with Low Overpotential in Neutral Solution,” *ACS Appl. Mater. Interfaces*, vol. 8, no. 44, pp. 30205–30211, 2016, doi: 10.1021/acsami.6b09975.

[127] A. S. Ansar, A. S. Gago, F. Razmjooei, R. Reißner, Z. Xu, and K. A. Friedrich, *Alkaline electrolysis—status and prospects*. Elsevier B.V., 2022.

[128] Q. Zhou, L. Liao, H. Zhou, D. Li, D. Tang, and F. Yu, “Innovative strategies in design of transition metal-based catalysts for large-current-density alkaline water/seawater electrolysis,” *Mater. Today Phys.*, vol. 26, no. May, p. 100727, 2022, doi: 10.1016/j.mtphys.2022.100727.

[129] H. Ikeda, R. Misumi, Y. Nishiki, Y. Kuroda, and S. Mitsushima, “Department of Chemistry and Life Science , Graduate School of Engineering Science , Division of Materials and Chemical Engineering , Faculty of Engineering , Yokohama Advanced Chemical Energy Research Center , Institute of Advanced Sciences , De Nora Perm,”

Electrochim. Acta, p. 141053, 2022, doi: 10.1016/j.electacta.2022.141053.

[130] H. K. Ju, S. Badwal, and S. Giddey, "A comprehensive review of carbon and hydrocarbon assisted water electrolysis for hydrogen production," *Appl. Energy*, vol. 231, no. September, pp. 502–533, 2018, doi: 10.1016/j.apenergy.2018.09.125.

[131] C. Huang, T. Ouyang, Y. Zou, N. Li, and Z. Q. Liu, "Ultrathin NiCo2P: X nanosheets strongly coupled with CNTs as efficient and robust electrocatalysts for overall water splitting," *J. Mater. Chem. A*, vol. 6, no. 17, pp. 7420–7427, 2018, doi: 10.1039/c7ta11364a.

[132] L. Zhang *et al.*, "Facile route of nitrogen doping in nickel cobalt phosphide for highly efficient hydrogen evolution in both acid and alkaline electrolytes," *Appl. Surf. Sci.*, vol. 512, no. November 2019, p. 145715, 2020, doi: 10.1016/j.apsusc.2020.145715.

[133] R. Zhang *et al.*, "Ternary NiCo2Px Nanowires as pH-Universal Electrocatalysts for Highly Efficient Hydrogen Evolution Reaction," *Adv. Mater.*, vol. 29, no. 9, pp. 2–7, 2017, doi: 10.1002/adma.201605502.

[134] P. Wang *et al.*, "Precise tuning in platinum-nickel/nickel sulfide interface nanowires for synergistic hydrogen evolution catalysis," *Nat. Commun.*, vol. 8, pp. 1–9, 2017, doi: 10.1038/ncomms14580.

[135] L. Zhang *et al.*, "Facile route of nitrogen doping in nickel cobalt phosphide for highly efficient hydrogen evolution in both acid and alkaline electrolytes," *Appl. Surf. Sci.*, vol. 512, no. November 2019, p. 145715, 2020, doi: 10.1016/j.apsusc.2020.145715.

[136] N. Jiang, S. J. Shi, Y. Y. Cui, and B. L. Jiang, "The effect of calcination temperature on the hydrogen evolution reaction performance of Co/NiCoP nano-heterojunction," *J. Alloys Compd.*, vol. 929, p. 167229, 2022, doi: 10.1016/j.jallcom.2022.167229.

[137] J. Li *et al.*, "Hierarchical NiCoP nanocone arrays supported on Ni foam as an efficient and stable bifunctional electrocatalyst for overall water splitting," *J. Mater. Chem. A*, vol. 5, no. 28, pp. 14828–14837, 2017, doi: 10.1039/c7ta03947f.

[138] C. Wang, J. Jiang, T. Ding, G. Chen, W. Xu, and Q. Yang, "Monodisperse Ternary NiCoP Nanostructures as a Bifunctional Electrocatalyst for Both Hydrogen and Oxygen Evolution

Reactions with Excellent Performance," *Adv. Mater. Interfaces*, vol. 3, no. 4, pp. 1–5, 2016, doi: 10.1002/admi.201500454.

[139] Y. Li, H. Zhang, M. Jiang, Y. Kuang, X. Sun, and X. Duan, "Ternary NiCoP nanosheet arrays: An excellent bifunctional catalyst for alkaline overall water splitting," *Nano Res.*, vol. 9, no. 8, pp. 2251–2259, 2016, doi: 10.1007/s12274-016-1112-z.

[140] S. Li *et al.*, "Self-supported ternary (NixFey)2P nanoplates arrays as an efficient bifunctional electrocatalyst for overall water splitting," *Electrochim. Acta*, vol. 319, pp. 561–568, 2019, doi: 10.1016/j.electacta.2019.07.022.

[141] A. Eftekhari, "Tuning the electrocatalysts for oxygen evolution reaction," *Mater. Today Energy*, vol. 5, pp. 37–57, 2017, doi: 10.1016/j.mtener.2017.05.002.

[142] S. Cherevko *et al.*, "Oxygen and hydrogen evolution reactions on Ru, RuO2, Ir, and IrO2 thin film electrodes in acidic and alkaline electrolytes: A comparative study on activity and stability," *Catal. Today*, vol. 262, pp. 170–180, Mar. 2016, doi: 10.1016/j.cattod.2015.08.014.

[143] L. E. Owe, M. Tsypkin, K. S. Wallwork, R. G. Haverkamp, and S. Sunde, "Iridium-ruthenium single phase mixed oxides for oxygen evolution: Composition dependence of electrocatalytic activity," *Electrochim. Acta*, vol. 70, pp. 158–164, 2012, doi: 10.1016/j.electacta.2012.03.041.

[144] A. T. Marshall and R. G. Haverkamp, "Electrocatalytic activity of IrO2-RuO2 supported on Sb-doped SnO2 nanoparticles," *Electrochim. Acta*, vol. 55, no. 6, pp. 1978–1984, 2010, doi: 10.1016/j.electacta.2009.11.018.

[145] F. I. Mattos-Costa, P. De Lima-Neto, S. A. S. Machado, and L. A. Avaca, "Characterisation of surfaces modified by sol-gel derived Ru<inf>x</inf>Ir<inf>1-x</inf>O<inf>2</inf> coatings for oxygen evolution in acid medium," *Electrochim. Acta*, vol. 44, no. 8–9, 1998.

[146] T. Audichon, T. W. Napporn, C. Canaff, C. Morais, C. Comminges, and K. B. Kokoh, "IrO2 Coated on RuO2 as Efficient and Stable Electroactive Nanocatalysts for Electrochemical Water Splitting," *J. Phys. Chem. C*, vol. 120, no. 5, pp. 2562–2573, 2016,

doi: 10.1021/acs.jpcc.5b11868.

[147] N. Yuan, Q. Jiang, J. Li, and J. Tang, “A review on non-noble metal based electrocatalysis for the oxygen evolution reaction,” *Arab. J. Chem.*, vol. 13, no. 2, pp. 4294–4309, 2020, doi: 10.1016/j.arabjc.2019.08.006.

[148] Z. Wu, P. Li, Q. Qin, Z. Li, and X. Liu, “N-doped graphene combined with alloys (NiCo, CoFe) and their oxides as multifunctional electrocatalysts for oxygen and hydrogen electrode reactions,” *Carbon N. Y.*, vol. 139, pp. 35–44, 2018, doi: 10.1016/j.carbon.2018.06.028.

[149] Y. Liu, C. Wang, S. Ju, M. Li, A. Yuan, and G. Zhu, “FeCo-based hybrid MOF derived active species for effective oxygen evolution,” *Prog. Nat. Sci. Mater. Int.*, vol. 30, no. February, pp. 185–191, 2020, doi: 10.1016/j.pnsc.2020.02.006.

[150] T. Oh, D. Park, and J. Kim, “CoFe 2 O 4 nanoparticles anchored on N/S co-doped mesoporous carbon spheres as efficient bifunctional electrocatalysts for oxygen catalytic reactions,” *Int. J. Hydrogen Energy*, vol. 44, no. 5, pp. 2645–2655, 2019, doi: 10.1016/j.ijhydene.2018.11.216.

[151] V. D. Silva, L. S. Ferreira, T. A. Simões, E. S. Medeiros, and D. A. Macedo, “1D hollow MFe 2 O 4 (M = Cu, Co, Ni) fibers by Solution Blow Spinning for oxygen evolution reaction,” *J. Colloid Interface Sci.*, vol. 540, pp. 59–65, 2019, doi: 10.1016/j.jcis.2019.01.003.

[152] J. Zhang, R. García-Rodríguez, P. Cameron, and S. Eslava, “Role of cobalt-iron (oxy)hydroxide (CoFeOx) as oxygen evolution catalyst on hematite photoanodes,” *Energy Environ. Sci.*, vol. 11, no. 10, pp. 2972–2984, 2018, doi: 10.1039/c8ee01346b.

[153] G. Abrham Gebreslase, M. Victoria Martínez-Huerta, D. Sebastián, and M. Jesús Lázaro, “Transformation of CoFe2O4 spinel structure into active and robust CoFe alloy/N-doped carbon electrocatalyst for oxygen evolution reaction,” *J. Colloid Interface Sci.*, 2022, doi: 10.1016/j.jcis.2022.06.005.

[154] M. J. Craig and M. García-Melchor, “Reaction descriptors for the oxygen evolution reaction: Recent advances, challenges, and opportunities,” *Curr. Opin. Electrochem.*, vol.

35, p. 101044, 2022, doi: 10.1016/j.coelec.2022.101044.

[155] C. Xia, Q. Jiang, C. Zhao, M. N. Hedhili, and H. N. Alshareef, “Selenide-Based Electrocatalysts and Scaffolds for Water Oxidation Applications,” *Adv. Mater.*, vol. 28, no. 1, pp. 77–85, 2016, doi: 10.1002/adma.201503906.

[156] Y. R. Zheng *et al.*, “An efficient CeO2/CoSe2 nanobelt composite for electrochemical water oxidation,” *Small*, vol. 11, no. 2, pp. 182–188, 2015, doi: 10.1002/smll.201401423.

[157] W. Xu *et al.*, “Porous cobalt oxide nanoplates enriched with oxygen vacancies for oxygen evolution reaction,” *Nano Energy*, vol. 43, no. November 2017, pp. 110–116, 2018, doi: 10.1016/j.nanoen.2017.11.022.

[158] N. Li, X. Liu, G. D. Li, Y. Wu, R. Gao, and X. Zou, “Vertically grown CoS nanosheets on carbon cloth as efficient hydrogen evolution electrocatalysts,” *Int. J. Hydrogen Energy*, vol. 42, no. 15, pp. 9914–9921, 2017, doi: 10.1016/j.ijhydene.2017.01.191.

[159] W. Li, M. Li, C. Wang, Y. Wei, and X. Lu, “Fe doped CoO/C nanofibers towards efficient oxygen evolution reaction,” *Appl. Surf. Sci.*, vol. 506, no. November 2019, p. 144680, Mar. 2020, doi: 10.1016/j.apsusc.2019.144680.

[160] B. S. Yeo and A. T. Bell, “Enhanced Activity of Gold-Supported Cobalt Oxide for the Electrochemical Evolution of Oxygen,” *J. Am. Chem. Soc.*, vol. 133, no. 14, pp. 5587–5593, Apr. 2011, doi: 10.1021/ja200559j.

[161] A. Vazhayil, L. Vazhayal, J. Thomas, S. Ashok C, and N. Thomas, “A comprehensive review on the recent developments in transition metal-based electrocatalysts for oxygen evolution reaction,” *Appl. Surf. Sci. Adv.*, vol. 6, p. 100184, Dec. 2021, doi: 10.1016/j.apsadv.2021.100184.

[162] Y. Meng, W. Song, H. Huang, Z. Ren, S.-Y. Chen, and S. L. Suib, “Structure–Property Relationship of Bifunctional MnO 2 Nanostructures: Highly Efficient, Ultra-Stable Electrochemical Water Oxidation and Oxygen Reduction Reaction Catalysts Identified in Alkaline Media,” *J. Am. Chem. Soc.*, vol. 136, no. 32, pp. 11452–11464, Aug. 2014, doi: 10.1021/ja505186m.

[163] C. Ray *et al.*, “Amorphous Phosphorus-Incorporated Cobalt Molybdenum Sulfide on

Carbon Cloth: An Efficient and Stable Electrocatalyst for Enhanced Overall Water Splitting over Entire pH Values," *ACS Appl. Mater. Interfaces*, vol. 9, no. 43, pp. 37739–37749, 2017, doi: 10.1021/acsami.7b11192.

[164] M. Plevová, J. Hnát, and K. Bouzek, "Electrocatalysts for the oxygen evolution reaction in alkaline and neutral media. A comparative review," *J. Power Sources*, vol. 507, no. May, 2021, doi: 10.1016/j.jpowsour.2021.230072.

[165] H. Osgood, S. V. Devaguptapu, H. Xu, J. Cho, and G. Wu, "Transition metal (Fe, Co, Ni, and Mn) oxides for oxygen reduction and evolution bifunctional catalysts in alkaline media," *Nano Today*, vol. 11, no. 5, pp. 601–625, 2016, doi: 10.1016/j.nantod.2016.09.001.

[166] H. Xu, J. Yuan, G. He, and H. Chen, "Current and future trends for spinel-type electrocatalysts in electrocatalytic oxygen evolution reaction," *Coord. Chem. Rev.*, vol. 475, p. 214869, 2023, doi: 10.1016/j.ccr.2022.214869.

[167] P. Zhang *et al.*, "A 3D rGO-supported NiFe2O4 heterostructure from sacrificial polymer-assisted exfoliation of NiFe-LDH for efficient oxygen evolution reaction," *Carbon N. Y.*, vol. 200, no. September, pp. 422–429, Nov. 2022, doi: 10.1016/j.carbon.2022.08.085.

[168] X. Han *et al.*, "Ultrasensitive Iron-Triggered Nanosized Fe–CoOOH Integrated with Graphene for Highly Efficient Oxygen Evolution," *Adv. Energy Mater.*, vol. 7, no. 14, 2017, doi: 10.1002/aenm.201602148.

[169] Y. Fang *et al.*, "Coaxial ultrathin Co1-yFeyOx nanosheet coating on carbon nanotubes for water oxidation with excellent activity," *RSC Adv.*, vol. 6, no. 84, pp. 80613–80620, 2016, doi: 10.1039/c6ra15624j.

[170] H. Ge, G. Li, J. Shen, W. Ma, X. Meng, and L. Xu, "Co4N nanoparticles encapsulated in N-doped carbon box as tri-functional catalyst for Zn-air battery and overall water splitting," *Appl. Catal. B Environ.*, vol. 275, no. April, p. 119104, Oct. 2020, doi: 10.1016/j.apcatb.2020.119104.

[171] W. Yang, J. Guo, J. Ma, N. Wu, J. Xiao, and M. Wu, "FeCo nanoalloys encapsulated in N-doped carbon nanofibers as a trifunctional catalyst for rechargeable Zn-air batteries and

overall water electrolysis," *J. Alloys Compd.*, vol. 926, p. 166937, Dec. 2022, doi: 10.1016/j.jallcom.2022.166937.

[172] M. Ďurovič, J. Hnát, M. Strečková, and K. Bouzek, "Efficient cathode for the hydrogen evolution reaction in alkaline membrane water electrolysis based on NiCoP embedded in carbon fibres," *J. Power Sources*, vol. 556, no. September 2022, p. 232506, Feb. 2023, doi: 10.1016/j.jpowsour.2022.232506.

[173] Q. Jin, L. Xiao, W. He, H. Cui, and C. Wang, "Self-supported metal (Fe, Co, Ni)-embedded nitrogen-doping carbon nanorod framework as trifunctional electrode for flexible Zn-air batteries and switchable water electrolysis," *Green Energy Environ.*, no. xxxx, 2022, doi: 10.1016/j.gee.2022.03.008.

[174] J. Chang *et al.*, "Applied Catalysis A , General Nickel iron alloy embedded , nitrogen doped porous carbon catalyst for efficient water electrolysis," *Appl. Catal. A, Gen.*, vol. 650, no. November 2022, p. 118984, 2023, doi: 10.1016/j.apcata.2022.118984.

[175] Z. Liu, B. Tang, X. Gu, H. Liu, and L. Feng, "Selective structure transformation for NiFe/NiFe2O4 embedded porous nitrogen-doped carbon nanosphere with improved oxygen evolution reaction activity," *Chem. Eng. J.*, vol. 395, no. April, p. 125170, Sep. 2020, doi: 10.1016/j.cej.2020.125170.

[176] R. A. Raimundo *et al.*, "Synthesis and characterization of NiFe-carbon fibers by solution blow spinning and application for the oxygen evolution reaction," *J. Phys. Chem. Solids*, vol. 160, no. July 2021, p. 110311, Jan. 2022, doi: 10.1016/j.jpcs.2021.110311.

[177] Y. Ma *et al.*, "Strongly Coupled FeNi Alloys/NiFe2O4@Carbonitride Layers-Assembled Microboxes for Enhanced Oxygen Evolution Reaction," *ACS Appl. Mater. Interfaces*, vol. 8, no. 50, pp. 34396–34404, 2016, doi: 10.1021/acsami.6b11821.

[178] E. Umeshbabu and G. Ranga Rao, "NiCo2O4 hexagonal nanoplates anchored on reduced graphene oxide sheets with enhanced electrocatalytic activity and stability for methanol and water oxidation," *Electrochim. Acta*, vol. 213, pp. 717–729, 2016, doi: 10.1016/j.electacta.2016.07.161.

[179] J. Geng, L. Kuai, E. Kan, Q. Wang, and B. Geng, "Precious-Metal-Free Co – Fe – O / rGO

Synergetic Electrocatalysts for Oxygen Evolution Reaction by a Facile Hydrothermal Route," pp. 1–7, doi: 10.1002/cssc.201403222.

[180] S. Li *et al.*, "CoFe2O4 nanoparticles@N-doped carbon coupled with N-doped graphene toward efficient electrochemical water oxidation," *Colloids Surfaces A Physicochem. Eng. Asp.*, vol. 626, no. May, p. 126898, 2021, doi: 10.1016/j.colsurfa.2021.126898.

[181] R. Liu *et al.*, "Dopamine as a carbon source: The controlled synthesis of hollow carbon spheres and yolk-structured carbon nanocomposites," *Angew. Chemie - Int. Ed.*, vol. 50, no. 30, pp. 6799–6802, 2011, doi: 10.1002/anie.201102070.

[182] J. Kong, S. I. Seyed Shahabadi, and X. Lu, "Integration of inorganic nanostructures with polydopamine-derived carbon: Tunable morphologies and versatile applications," *Nanoscale*, vol. 8, no. 4, pp. 1770–1788, 2016, doi: 10.1039/c5nr06711a.

[183] S. Hong, Y. S. Na, S. Choi, I. T. Song, W. Y. Kim, and H. Lee, "Non-covalent self-assembly and covalent polymerization co-contribute to polydopamine formation," *Adv. Funct. Mater.*, vol. 22, no. 22, pp. 4711–4717, 2012, doi: 10.1002/adfm.201201156.

[184] T. Łuczak, "Preparation and characterization of the dopamine film electrochemically deposited on a gold template and its applications for dopamine sensing in aqueous solution," *Electrochim. Acta*, vol. 53, no. 19, pp. 5725–5731, 2008, doi: 10.1016/j.electacta.2008.03.052.

[185] N. F. Della Vecchia, R. Avolio, M. Alfè, M. E. Errico, A. Napolitano, and M. D'Ischia, "Building-block diversity in polydopamine underpins a multifunctional eumelanin-type platform tunable through a quinone control point," *Adv. Funct. Mater.*, vol. 23, no. 10, pp. 1331–1340, 2013, doi: 10.1002/adfm.201202127.

[186] F. Yu *et al.*, "Experimental and theoretical analysis of polymerization reaction process on the polydopamine membranes and its corrosion protection properties for 304 Stainless Steel," *J. Mol. Struct.*, vol. 982, no. 1–3, pp. 152–161, 2010, doi: 10.1016/j.molstruc.2010.08.021.

[187] F. Bernsmann *et al.*, "Dopamine−Melanin Film Deposition Depends on the Used Oxidant and Buffer Solution," *Langmuir*, vol. 27, no. 6, pp. 2819–2825, Mar. 2011, doi:

10.1021/la104981s.

[188] D. R. Dreyer, D. J. Miller, B. D. Freeman, D. R. Paul, and C. W. Bielawski, “Elucidating the structure of poly(dopamine),” *Langmuir*, vol. 28, no. 15, pp. 6428–6435, 2012, doi: 10.1021/la204831b.

[189] F. Gao *et al.*, “Dopamine coating as a general and facile route to biofunctionalization of superparamagnetic Fe3O4 nanoparticles for magnetic separation of proteins,” *RSC Adv.*, vol. 4, no. 13, pp. 6657–6663, 2014, doi: 10.1039/c3ra46938g.

[190] J. Yan *et al.*, “Polydopamine-derived porous carbon fiber/cobalt composites for efficient oxygen reduction reactions,” *J. Mater. Chem. A*, vol. 3, no. 46, pp. 23299–23306, 2015, doi: 10.1039/c5ta06217a.

[191] W. Tamakloe, D. A. Agyeman, M. Park, J. Yang, and Y. M. Kang, “Polydopamine-induced surface functionalization of carbon nanofibers for Pd deposition enabling enhanced catalytic activity for the oxygen reduction and evolution reactions,” *J. Mater. Chem. A*, vol. 7, no. 13, pp. 7396–7405, 2019, doi: 10.1039/C9TA00025A.

[192] D. Zhou *et al.*, “Fe/N/C hollow nanospheres by Fe(iii)-dopamine complexation-assisted one-pot doping as nonprecious-metal electrocatalysts for oxygen reduction,” *Nanoscale*, vol. 7, no. 4, pp. 1501–1509, 2015, doi: 10.1039/c4nr06366j.

[193] G. A. Gebreslase, D. Sebastián, M. V. Martínez-Huerta, and M. J. Lázaro, “Nitrogen-doped carbon decorated-Ni3Fe@Fe3O4 electrocatalyst with enhanced oxygen evolution reaction performance,” *J. Electroanal. Chem.*, vol. 925, no. August, p. 116887, 2022, doi: 10.1016/j.jelechem.2022.116887.

[194] C. Chen, E. B. Kennel, A. H. Stiller, P. G. Stansberry, and J. W. Zondlo, “Carbon foam derived from various precursors,” *Carbon N. Y.*, vol. 44, no. 8, pp. 1535–1543, 2006, doi: 10.1016/j.carbon.2005.12.021.

[195] M. V. Martínez-huerta, T. Tsoncheva, B. Tsyntsarski, G. Georgiev, and M. J. L, “CoFe-loaded P , N co-doped carbon foam derived from petroleum pitch waste : An efficient electrocatalyst for oxygen evolution reaction,” no. December, 2022, doi: 10.1016/j.cattod.2022.12.022.

[196] D. Xu *et al.*, "N-doped bamboo-like CNTs combined with CoFe–CoFe2O4 as a highly efficient electrocatalyst towards oxygen evolution," *Int. J. Hydrogen Energy*, vol. 45, no. 11, pp. 6629–6635, 2020, doi: 10.1016/j.ijhydene.2019.12.180.

[197] Y. Lei *et al.*, "Electronic structure tuning of FeCo nanoparticles embedded in multi-dimensional carbon matrix for enhanced bifunctional oxygen electrocatalysis," *J. Alloys Compd.*, vol. 853, 2021, doi: 10.1016/j.jallcom.2020.157070.

[198] H. Shui, T. Jin, J. Hu, and H. Liu, "In Situ Incorporation Strategy for Bimetallic FeCo-Doped Carbon as Highly Efficient Bifunctional Oxygen Electrocatalysts," *ChemElectroChem*, vol. 5, no. 10, pp. 1401–1406, 2018, doi: 10.1002/celc.201800013.

[199] M. Xiong and D. G. Ivey, "Composition effects of electrodeposited Co-Fe as electrocatalysts for the oxygen evolution reaction," *Electrochim. Acta*, 2018, doi: 10.1016/j.electacta.2017.12.059.

[200] W. Xu, W. Xie, and Y. Wang, "Co3O4-x-Carbon@Fe2-yCoyO3 Heterostructural Hollow Polyhedrons for the Oxygen Evolution Reaction," *ACS Appl. Mater. Interfaces*, vol. 9, no. 34, pp. 28642–28649, 2017, doi: 10.1021/acsami.7b09213.

[201] Z. Ali, M. Mehmood, J. Ahmed, A. Majeed, and K. H. Thebo, "CVD grown defect rich-MWCNTs with anchored CoFe alloy nanoparticles for OER activity," *Mater. Lett.*, vol. 259, p. 126831, 2020, doi: 10.1016/j.matlet.2019.126831.

[202] Y. Wang, T. Hu, Y. Qiao, and Y. Chen, "Synergistic engineering of defects and architecture in CoFe@NC toward highly efficient oxygen electrode reactions," *Int. J. Hydrogen Energy*, vol. 45, no. 15, pp. 8686–8694, 2020, doi: 10.1016/j.ijhydene.2020.01.135.

[203] T. Grewe, X. Deng, and H. Tüysüz, "Influence of Fe doping on structure and water oxidation activity of nanocast Co3O4," *Chem. Mater.*, vol. 26, no. 10, pp. 3162–3168, 2014, doi: 10.1021/cm5005888.

[204] C. Mahala, M. D. Sharma, and M. Basu, "2D Nanostructures of CoFe2O4 and NiFe2O4: Efficient Oxygen Evolution Catalyst," *Electrochim. Acta*, vol. 273, pp. 462–473, 2018, doi: 10.1016/j.electacta.2018.04.079.

[205] C. You, Y. Ji, Z. Liu, X. Xiong, and X. Sun, “Ultrathin CoFe-Borate Layer Coated CoFe-Layered Double Hydroxide Nanosheets Array: A Non-Noble-Metal 3D Catalyst Electrode for Efficient and Durable Water Oxidation in Potassium Borate,” *ACS Sustain. Chem. Eng.*, vol. 6, no. 2, pp. 1527–1531, 2018, doi: 10.1021/acssuschemeng.7b03780.

[206] L. Wu, L. Shi, S. Zhou, J. Zhao, X. Miao, and J. Guo, “Direct Growth of CoFe2 Alloy Strongly Coupling and Oxygen-Vacancy-Rich CoFe2O4 Porous Hollow Nanofibers: an Efficient Electrocatalyst for Oxygen Evolution Reaction,” *Energy Technol.*, vol. 6, no. 12, pp. 2350–2357, 2018, doi: 10.1002/ente.201800298.

[207] S. Lei, Q. H. Li, Y. Kang, Z. G. Gu, and J. Zhang, “Epitaxial growth of oriented prussian blue analogue derived well-aligned CoFe2O4 thin film for efficient oxygen evolution reaction,” *Appl. Catal. B Environ.*, vol. 245, no. December 2018, pp. 1–9, 2019, doi: 10.1016/j.apcatb.2018.12.036.

[208] Y. Huang, W. Yang, Y. Yu, and S. Hao, “Ordered mesoporous spinel CoFe 2 O 4 as efficient electrocatalyst for the oxygen evolution reaction,” *J. Electroanal. Chem.*, vol. 840, no. April, pp. 409–414, 2019, doi: 10.1016/j.jelechem.2019.04.010.

[209] L. S. Ferreira *et al.*, “Structure, magnetic behavior and OER activity of CoFe2O4 powders obtained using agar-agar from red seaweed (Rhodophyta),” *Mater. Chem. Phys.*, vol. 237, no. April, p. 121847, 2019, doi: 10.1016/j.matchemphys.2019.121847.

[210] R. Valdez *et al.*, “Effect of betaine in the successful synthesis of CoFe 2 O 4 containing octahedron nanoparticles for electrocatalytic water oxidation,” *Appl. Surf. Sci.*, vol. 426, pp. 980–986, 2017, doi: 10.1016/j.apsusc.2017.07.232.

[211] C. Tian *et al.*, “Well-aligned arrangement CoFe nanoparticles assisted with cellulose nanofibrils for efficient oxygen evolution reaction,” *Appl. Surf. Sci.*, vol. 510, no. January, p. 145484, 2020, doi: 10.1016/j.apsusc.2020.145484.

[212] C. Li, E. Zhou, Z. Yu, H. Liu, and M. Xiong, “Tailor-made open porous 2D CoFe/SN-carbon with slightly weakened adsorption strength of ORR/OER intermediates as remarkable electrocatalysts toward zinc-air batteries,” *Appl. Catal. B Environ.*, vol. 269, no. December 2018, p. 118771, Jul. 2020, doi: 10.1016/j.apcatb.2020.118771.

[213] Y. Fang *et al.*, “Coaxial ultrathin Co1-yFeyOx nanosheet coating on carbon nanotubes for water oxidation with excellent activity,” *RSC Adv.*, vol. 6, no. 84, pp. 80613–80620, 2016, doi: 10.1039/c6ra15624j.

[214] B. Wang, Y. Hu, B. Yu, X. Zhang, D. Yang, and Y. Chen, “Heterogeneous CoFe–Co8FeS8 nanoparticles embedded in CNT networks as highly efficient and stable electrocatalysts for oxygen evolution reaction,” *J. Power Sources*, vol. 433, no. April, 2019, doi: 10.1016/j.jpowsour.2019.05.094.

[215] Y. Ma *et al.*, “Reduced CoFe2O4/graphene composite with rich oxygen vacancies as a high efficient electrocatalyst for oxygen evolution reaction,” *Int. J. Hydrogen Energy*, vol. 45, no. 19, pp. 11052–11061, 2020, doi: 10.1016/j.ijhydene.2020.02.045.

[216] Z. Cui *et al.*, “In situ integration of Fe3N@Co4N@CoFe alloy nanoparticles as efficient and stable electrocatalyst for overall water splitting,” *Electrochim. Acta*, vol. 395, p. 139218, 2021, doi: 10.1016/j.electacta.2021.139218.

[217] L. Li, J. Chen, S. Wang, Y. Huang, and D. Cao, “MOF-derived CoN/CoFe/NC bifunctional electrocatalysts for zinc-air batteries,” *Appl. Surf. Sci.*, vol. 582, no. November 2021, p. 152375, Apr. 2022, doi: 10.1016/j.apsusc.2021.152375.

[218] J. Li, Y. Kang, W. Wei, X. Li, Z. Lei, and P. Liu, “Well-dispersed ultrafine CoFe nanoalloy decorated N-doped hollow carbon microspheres for rechargeable/flexible Zn-air batteries,” *Chem. Eng. J.*, vol. 407, no. September 2020, p. 127961, Mar. 2021, doi: 10.1016/j.cej.2020.127961.

[219] S. Y. Lin, Y. P. Chen, Y. Cao, L. Zhang, J. J. Feng, and A. J. Wang, “Aminouracil-assisted synthesis of CoFe decorated bougainvillea-like N-doped carbon nanoflowers for boosting Zn–air battery and water electrolysis,” *J. Power Sources*, vol. 521, no. November 2021, p. 230926, 2022, doi: 10.1016/j.jpowsour.2021.230926.

[220] Y. Chong, Z. Pan, M. Su, X. Yang, D. Ye, and Y. Qiu, “1D/2D hierarchical Co1-xFexO@N-doped carbon nanostructures for flexible zinc–air batteries,” *Electrochim. Acta*, vol. 363, p. 137264, 2020, doi: 10.1016/j.electacta.2020.137264.

[221] W. Tan *et al.*, “Effect of carbonization temperature on electrocatalytic water splitting of

Fe-Co anchored on N-doped porous carbon," *J. Solid State Chem.*, vol. 302, no. July, p. 122435, 2021, doi: 10.1016/j.jssc.2021.122435.

[222] R. Mo, S. Wang, H. Li, J. Li, S. Yang, and J. Zhong, "Graphene layers-wrapped FeNiP nanoparticles embedded in nitrogen-doped carbon nanofiber as an active and durable electrocatalyst for oxygen evolution reaction," *Electrochim. Acta*, vol. 290, pp. 649–656, 2018, doi: 10.1016/j.electacta.2018.08.118.

[223] S. Ci *et al.*, "Rational design of mesoporous NiFe-alloy-based hybrids for oxygen conversion electrocatalysis," *J. Mater. Chem. A*, vol. 3, no. 15, pp. 7986–7993, 2015, doi: 10.1039/c5ta00894h.

[224] "ChemElectroChem - 2018 - Deng - Core Shell NiFe Nanoalloy with a Discrete N-doped Graphitic Carbon Cover for Enha.pdf." .

[225] Z. Tao, T. Wang, X. Wang, J. Zheng, and X. Li, "MOF-Derived Noble Metal Free Catalysts for Electrochemical Water Splitting," *ACS Appl. Mater. Interfaces*, vol. 8, no. 51, pp. 35390–35397, 2016, doi: 10.1021/acsami.6b13411.

[226] J. Geng, L. Kuai, E. Kan, Y. Sang, and B. Geng, "Hydrothermal Synthesis of a rGO Nanosheet Enwrapped NiFe Nanoalloy for Superior Electrocatalytic Oxygen Evolution Reactions," *Chem. - A Eur. J.*, vol. 22, no. 41, pp. 14480–14483, 2016, doi: 10.1002/chem.201602782.

[227] X. Lin *et al.*, "Precious-metal-free Co-Fe-O: X coupled nitrogen-enriched porous carbon nanosheets derived from Schiff-base porous polymers as superior electrocatalysts for the oxygen evolution reaction," *J. Mater. Chem. A*, vol. 4, no. 17, pp. 6505–6512, 2016, doi: 10.1039/c5ta10039a.

[228] J. Wang, J. Wang, M. Zhang, S. Li, R. Liu, and Z. Li, "Metal-organic frameworks-derived hollow-structured iron-cobalt bimetallic phosphide electrocatalysts for efficient oxygen evolution reaction," *J. Alloys Compd.*, vol. 821, p. 153463, 2020, doi: 10.1016/j.jallcom.2019.153463.

[229] L. Du *et al.*, "Nitrogen–doped graphitized carbon shell encapsulated NiFe nanoparticles: A highly durable oxygen evolution catalyst," *Nano Energy*, vol. 39, no. July, pp. 245–252,

2017, doi: 10.1016/j.nanoen.2017.07.006.

[230] W. J. Liu, X. Hu, H. C. Li, and H. Q. Yu, “Pseudocapacitive Ni-Co-Fe Hydroxides/N-Doped Carbon Nanoplates-Based Electrocatalyst for Efficient Oxygen Evolution,” *Small*, vol. 14, no. 34, pp. 1–11, 2018, doi: 10.1002/smll.201801878.

[231] T. Gao, Z. Jin, Y. Zhang, G. Tan, H. Yuan, and D. Xiao, “Coupling cobalt-iron bimetallic nitrides and N-doped multi-walled carbon nanotubes as high-performance bifunctional catalysts for oxygen evolution and reduction reaction,” *Electrochim. Acta*, vol. 258, pp. 51–60, 2017, doi: 10.1016/j.electacta.2017.07.172.

[232] Z. Ye *et al.*, “Cobalt-Iron Oxide Nanoarrays Supported on Carbon Fiber Paper with High Stability for Electrochemical Oxygen Evolution at Large Current Densities,” *ACS Appl. Mater. Interfaces*, vol. 10, no. 46, pp. 39809–39818, 2018, doi: 10.1021/acsami.8b15357.

[233] B. Dong *et al.*, “Synergistic effect of metallic nickel and cobalt oxides with nitrogen-doped carbon nanospheres for highly efficient oxygen evolution,” *Chinese J. Catal.*, vol. 41, no. 11, pp. 1782–1789, 2020, doi: 10.1016/S1872-2067(20)63621-X.

Chapter II: Objectives

This chapter presents the objectives and overall structure of the doctoral thesis.

1. Objectives and structure of the Thesis

1.1. Objectives

Water electrolysis is a promising technology that has the potential to produce carbon-free, clean and green hydrogen energy. The realization of water electrolysis depends significantly on the efficiency and performance of the electrocatalyst used. To be a sustainable and economically viable process, an efficient and high-performing electrocatalyst is vital to expedite the electrochemical reaction.

Precious-metal-based electrocatalysts, such as ruthenium, platinum, and iridium, have been employed in the state-of-the-art due to their relatively high activity and stability. However, the cost and scarcity of these materials have led to a pursuit of alternative, more environmentally friendly options. As the need for clean energy increases, the significance of developing and utilizing efficient and ecologically sustainable electrocatalysts for water electrolysis becomes more pressing. Recently, electrocatalysts made from transition metals such as Co, Ni, and Fe have shown great potential as a cost-efficient alternative to precious metal-based electrocatalysts. These electrocatalysts exhibit good performance in water electrolysis in basic media.

Various innovative approaches have been developed to achieve promising electrocatalysts to substitute precious metals. These techniques involve creating nanostructured materials, incorporating heteroatoms into bimetals, producing catalysts deposited on 3D/2D structured substrates, inducing abundant oxygen defects/vacancies in bimetals, and combining a conductive substance such as carbon with bimetals, as well as designing amorphous structures. Despite the extensive efforts made so far, the reported electrocatalysts still fall short of meeting the requirements for practical applications; as a result, there is still a pressing need for further research to develop highly active, stable, and economically viable electrocatalysts that can be applied in large-scale water electrolysis applications.

The focus of this PhD thesis has been on the investigation of transition metal-based electrocatalysts for water electrolysis, motivated by the recent advancements in the field of electrocatalysts developed from transition metals. Briefly, the general and specific objectives of the doctoral Thesis are provided as follows.

1.1.1. General objective

Development of high-performance, low-cost and stable bimetallic transition metal-based electrocatalysts for both reactions involved in an anion exchange membrane water electrolyzer: oxygen evolution reaction and hydrogen evolution reaction.

1.1.2. Specific objectives

- To synthesize electrocatalysts based on Ni, Fe and Co integrated with carbonaceous materials with different methods and optimized properties for oxygen evolution reaction in basic media.
- To explore the effect of heteroatoms dopant (such as nitrogen and phosphorus) on carbon structure and metal-impregnated carbon composites towards oxygen evolution reactions.
- To study the activity and stability of in situ-grown transition metals (Ni, Co) doped with phosphorus on stainless steel mesh conductive substrate for hydrogen evolution reaction in basic media.
- To characterize the as-prepared electrocatalysts using physicochemical techniques to study how their structural and morphological properties affect the activity measurements.

1.2. The framework of the Doctoral Thesis

This work was carried out at the "Fuel Energy Conversion" group at the Instituto de Carboquímica (ICB) in Zaragoza and the "Electrocatalysis for Energy and Environment" group at the Instituto de Catálisis y Petroleoquímica in Madrid, which are part of the Spanish National Research Council (CSIC). The doctoral thesis was funded by the European Union's Horizon 2020 Research and Innovation program under the Marie Skłodowska-Curie Actions - Innovative Training Networks (MSCA-ITN) as part of the "Bimetallic catalyst knowledge-based development for energy applications (BIKE)" project (Grant Agreement 813748).

During the study, secondments/mobilities were conducted at two different institutions. The first was at the Bulgarian Academy of Sciences in Sofia, Bulgaria, from April 15th, 2021 to June 15th, 2021, where they focused on synthesizing carbon-supported metal-based electrocatalysts for OER. The second was at the Italian National Research Council - Institute for the Chemistry of Organometallic Compounds in Pisa, Italy, from February 1st, 2021, to March 31st, 2021. The objective of this mobility was to gain experience in density-functional theory (DFT) based methods in catalytic research and to collaborate with researchers using advanced algorithms to perform atomic scale (predictive) modelling and simulations.

1.3. Structure of the Doctoral Thesis

This Doctoral Thesis comprises the scientific articles published in journals indexed in the *Journal of Citation Report* and the General introduction from which the research was carried out. The doctoral student was responsible for experimentation and data analysis and contributed to their writing.

Briefly, this Thesis is structured into five main chapters:

Chapter I: contains a general introduction to the historical background and development of water electrolysis. In this chapter, the fundamentals of water electrolysis technology, the category of water electrolysis, an electrocatalyst for alkaline hydrogen and oxygen evolution reaction, electrochemical testing, and the evaluation criterion of electrocatalysts are provided.

Chapter II: Comprise the objectives and the overall structure of the doctoral thesis.

Chapter III: Encompasses a copy of the research works published. This chapter contains four research works related to electrocatalysts for OER and HER and one comprehensive review paper pertinent to the OER.

Chapter IV: This chapter provides a global discussion of the research works. Besides, the electrocatalysts with the best performance from each article were tested in anion exchange membrane water electrolysis (AEMWE) to determine its potential for large-scale application; the analysis findings are reported in this chapter.

Chapter V: Entails the general conclusion of the thesis.

Chapter III: Copies of the publications

In this chapter, five articles, including one research article related to HER, three research articles related to OER, and one review article pertinent to OER, are attached.

The list of articles is provided as follows.

(I). NiCoP/CoP sponge-like structure grown on stainless steel mesh as a high-performance electrocatalyst for hydrogen evolution reaction (https://doi.org/10.1016/j.electacta.2022.141538)

(II). Transformation of $CoFe_2O_4$ spinel structure into active and robust CoFe alloy/N-doped carbon electrocatalyst for oxygen evolution reaction. (https://doi.org/10.1016/j.jcis.2022.06.005)

(III). Nitrogen-doped carbon decorated-$Ni_3Fe@Fe_3O_4$ electrocatalyst with enhanced oxygen evolution reaction performance (https://doi.org/10.1016/j.jelechem.2022.116887)

(IV). CoFe-loaded P, N co-doped carbon foam derived from petroleum pitch waste: an efficient electrocatalyst for oxygen evolution reaction (https://doi.org/10.1016/j.cattod.2022.12.022)

JOURNAL OF ENERGY CHEMISTRY

http://www.journals.elsevier.com/journal-of-energy-chemistry/

(V). Recent progress on bimetallic NiCo and CoFe based electrocatalysts for alkaline oxygen evolution reaction: A review (https://doi.org/10.1016/j.jechem.2021.10.009)

Article I

Electrochimica Acta 438 (2023) 141538

Contents lists available at ScienceDirect

Electrochimica Acta

journal homepage: www.journals.elsevier.com/electrochimica-acta

NiCoP/CoP sponge-like structure grown on stainless steel mesh as a high-performance electrocatalyst for hydrogen evolution reaction

Gebrehiwet Abrham Gebreslase [a], María Victoria Martínez-Huerta [b,*], David Sebastián [a], María Jesús Lázaro [a,*]

[a] Instituto de Carboquímica, CSIC. Miguel Luesma Castán 4, Zaragoza 50018, Spain
[b] Instituto de Catálisis y Petroleoquímica, CSIC. Marie Curie 2, Madrid 28049, Spain

ARTICLE INFO

Keywords:
Electrocatalyst
Phosphorization
NiCoP
Stainless steel mesh
Hydrogen evolution reaction

ABSTRACT

The stainless steel mesh (SSM) has received remarkable attention for hydrogen and oxygen evolution reactions. It was demonstrated that the SSM exhibits admirable performance towards oxygen evolution reaction (OER) electrocatalysis, while its catalytic activity for hydrogen evolution reaction (HER) remains quite low. This obstructs the utilization of SSM-based catalysts for sustainable complete water electrolysis. In this study, a facile hydrothermal route followed by a phosphorization process was adopted to transform commercially available SSM materials into high-performance and stable electrocatalysts for alkaline HER. We report an interconnected NiCoP-CoP sponge-like structure on SSM substrate without polymer binder. Benefiting from the 3D construction with high exposed surface area, close contact between electroactive species and conductive surface, and facilitated infiltration of electrolyte, the as-prepared NiCoP@SSM electrocatalyst brought an improved catalytic activity for HER, required a low overpotential of 138 mV to derive a current density of 10 $mAcm^{-2}$ in 1.0 M KOH aqueous solution. The high performance of the NiCoP@SSM catalyst has also unveiled fast reaction kinetics (presents a small Tafel slope of 74 mV/dec), a relatively large electrochemical active surface area (ECSA), and small charge transfer resistance. Furthermore, the NiCoP@SSM electrode also presented excellent stability during long-term measurements, making it one of the most encouraging HER electrodes to date. This research study paves the way for the development of HER-active electrocatalysts made from SSMs that are commercially available, low-cost, and highly active.

1. Introduction

With the motivation to circumvent the rising global energy demand and ecological disarrays because of the continuous consumption of fossil fuels, tremendous research efforts are being conducted in the realm of clean, green, and renewable energy sources, aiming at developing and designing more appealing, efficient energy storage and conversion system [1–3]. In this context, electrochemical water splitting, especially integrated with renewable energy, has become a distinctive approach for hydrogen production, which is considered as an ideal alternative energy carrier for the future due to its environmental friendliness, carbon-free, high energy density, and clean fuel [4–6]. However, the hydrogen evolution reaction (HER), one of the crucial half-reactions involved in water electrolysis, is kinetically indolent and demands high overvoltage to overcome the energy barrier. Electrocatalysts are necessary for this process to expedite the slow reaction kinetics. The state-of-the-art electrocatalyst utilized for HER often relies on Pt and its derivatives. Still, their high cost, low availability, and Pt poisoning glitches impact their use for the sustainable development of HER electrodes [7]. So far, about 4% of the total H_2 produced worldwide is shared from water electrolysis due to its high energy consumption, low efficiency, and expensive catalysts [8]. To this end, there is an urgent demand to develop catalysts with affordable, more efficient, and durable features using plentifully available materials to accelerate the reaction, reduce overvoltage, and boost overall energy efficiency.

To date, myriads of efforts have been devoted to preparing transition metal-based electrocatalysts (e.g., Ni, Co, Mo, and Fe) in the form of metal oxides, phosphides, sulfides, and nitrides, demonstrating promising alternatives to Pt due to their high abundance, low price, and modest HER catalytic activity [9–17]. In particular, transition metal phosphides (TMP), such as NiP, FeP, and CoP, have received extensive devotion recently due to their outstanding activity among the various

* Corresponding authors.
E-mail addresses: mmartinez@icp.csic.es (M.V. Martínez-Huerta), mlazaro@icb.csic.es (M.J. Lázaro).

https://doi.org/10.1016/j.electacta.2022.141538
Received 16 September 2022; Received in revised form 28 October 2022; Accepted 13 November 2022
Available online 16 November 2022

HER electrocatalysts reported [18–23]. TMPs retain excellent activity towards HER due to the electron transfer from the active metal into the P atoms, establishing a tailored active site surface to accelerate proton adsorption [24]. Incorporating P into the structure of transition metals induces a significant gain in terms of stability and chemical reactivity. The boosted catalytic activity of TMP towards HER has been correlated to the formation of a peculiar electronic structure prompted by the presence of the P atom, forming a "ligand effect". This is vital to dissociate molecular hydrogen and also endow moderate binding surface to adsorb the reaction intermediate, eventually stimulating the overall catalytic activity [25,26]. Henceforth, TMPs, encompassing inexpensiveness and good activity, are considered as a good candidate material to replace the precious HER catalysts. Despite the good activity of monometallic phosphides-based catalysts for HER, their unfavored hydrogen adsorption-free energy impacts their performance. To this end, researchers have been working to regulate the electronic structure and alter the intrinsic activity of TPMs by integrating with another metal, forming bimetal phosphides. Bimetallic-based catalysts frequently exhibit superb catalytic activity compared to the monometallic counterparts stemming from the synergistic effects between two catalytically active metals [27], emanating from the lattice strain variation, which induces different redox potentials and structural arrangement [28]. Moreover, the coupling effect of heteroatoms is also advantageous to further enlighten the material stability and adjust electronic structure [29]. Despite the much effort devoted to preparing bimetals doped with P atoms with a good performance, the performance of these alternative materials is still in further need of improvement to surpass the state-of-the-art HER catalysts.

Meanwhile, researchers have used two main strategies to evaluate the electrochemical performance of electrocatalysts. The first technique involves the usage of catalysts in powder form. In this case, an ink of catalyst is prepared by dispersing the powder in a solvent containing polymeric binder (e.g., Nafion). The resulting ink is coated/cast on glassy carbon. This technique has its own limitation: catalyst peeling off during long-term operation, and also the binder affects the activity of the catalyst by suppressing the active site and/or reducing the contact area between the active site and electrolyte [30,31]. The second technique involves the use of catalysts directly grown on three-dimensional (3D) conductive substrates such as nickel foam, copper foam, titanium mesh, graphene foam, stainless steel mesh, nickel foil, carbon cloth, etc., [31, 32]. Compared with the catalysts in powder form, catalyst directly grown on a conductive substrate has several advantages, including accelerated electron transfer from the catalytic materials to the substrate due to intimate contact between the active site and substrate, easy electrolyte penetration, it also circumvents the detaching/peeling of catalysts from the surface of the electrode during long term measurements, excellent conductivity, and mechanical stability [18,33].

In recent years, stainless steel mesh (SSM) has been employed as a substrate to grow electroactive materials on it because of its low-cost, excellent electrical conductivity, good chemical stability, good mechanical strength, and good corrosion resistance in alkaline media [34–38]. Two types of SSM, the 304 and 316, are used as electrocatalysts; however, the 316L-type SSM possesses better features, such as high stability and corrosion resistance structure even at high applied potential, compared to the 304 types, making it a suitable electrocatalyst substrate [39]. SSM material consists of Cr metal that passivates the SSM's outer layer, which distresses the electrochemical performance in energy and storage systems. As a result, researchers have attempted to improve the electrochemical properties of SSM material by subjecting it to various surface treatment techniques [40]. The SSM comprises chiefly Ni, Fe, Mo, Cr, and other impurities. The three former metals are demonstrated to be active for HER; hence, removing the inactive metal of Cr and enriching the surface of the electrode with active foreign material escorted by the intrinsically active elements in stainless steel would be a promising approach to stimulate the electrocatalytic properties of SSM.

The physicochemical and electrochemical properties of SSM can be transformed by surface modification and/or chemical etching to promote the surface area, and also doping of heteroatoms, such as P, can modify the surface by forming TMP [35]. Substantial efforts have been devoted to modifying SSM through different methods, including hydrothermal [33], thermo-selenization tuning method [35], and electrodeposition [41,42], for OER electrodes. For example, Shen and co-workers [40] prepared amorphous Ni (Fe)O_xH_y-coated nanocone arrays on SSM electrocatalyst through electrodeposition. The catalyst exhibited excellent activity and stability towards OER. The as-prepared electrode displayed a low overpotential of 280 and 303 mV to achieve high current densities of 500 and 1000 mA cm^{-2}. However, the catalyst's performance for the HER electrode was not reported. Zhang and co-workers [43] synthesized MoS_2@SSM catalyst via a hydrothermal route. The catalyst showed a low overpotential of 160 mV to achieve a current density of 10 mA cm^{-2} and a small Tafel slope of 61 mV dec^{-1} in 1.0 M KOH during HER measurements. The MoS_2@SSM catalyst was evaluated for its stability under a static potential of overpotential 160 mV for 18 h, and the catalyst maintains 85% of its initial current density. Yao and co-workers [38] prepared mesoporous (Fe/Ni)(P/S) dendritic nanorods on SSM through anodic oxidation and subsequent co-sulfuration/phosphorization method. The as-prepared catalyst displayed a low overpotential of 173 mV at 10 mA cm^{-2} and 270 mV at 100 mA cm^{-2}. Moreover, many works demonstrated the potential application of SSM for water electrocatalysis, primarily focusing on the OER electrode; however, the performance of SSM towards the HER electrode remains low. Rare works have been reported on modifying SSM substrates to catalyze HER, and their performance is still not promising [44]. Developing a high-performance, efficient, and robust SSM-based electrode with an affordable and facile route toward HER is still challenging. As a result, further research on the preparation of electroactive material on SSM substrate with excellent performance and stability is necessary to accelerate the HER electrode.

Herein, we employed 316-type SSM with a three-dimensional network structure substrate to grow NiCoP-CoP electroactive catalyst and transform it into a high-performance and stable electrode for HER through a hydrothermal route followed by phosphorization. This synthesis approach offers an easy, polymer-binder-free, and scalable fabrication process. The resulting NiCoP@SSM electrocatalyst reveals excellent performance and stability because of the intimate contact between the electroactive sites and conductive substrate, plentifully exposed active surface area, promoted mass and electron transportation, and robust structure. The as-prepared electrocatalyst, NiCoP@SSM, was used directly as a hydrogen-evolving cathode and displayed excellent catalytic activity with low overpotential (138 mV @ 10 mA cm^{-2}), a small Tafel slope (74 mV dec^{-1}), and long-term durability in 1.0 M KOH aqueous solution. This approach thus affords a facile, cost-effective, and scalable scheme for generating high-performance and stable electrocatalysts for alkaline HER electrodes.

2. Experimental section

2.1. Materials and chemicals

Stainless steel mesh (SSM, AISI 316 alloy, 0.103 mm nominal aperture, 0.066 mm wire diameter, 150 × 150 wires/inch), cobalt (II) nitrate hexahydrate (Alfa Aesar), nickel (II) nitrate hexahydrate (Alfa Aesar), urea (Sigma Aldrich), ammonium fluoride (NH_4F) (Sigma Aldrich), potassium hydroxide, 99.98% (metal basis), 85% min (Sigma Aldrich), and $NaH_2PO_2{\cdot}xH_2O$ (Sigma Aldrich). The water used in this work was ultrapure water (Milli-Q, 0.055 μS/cm, SIEMENS). All the chemical reagents were used as received without further modification.

2.2. Synthesis of NiCoP@SSM electrocatalysts

The hydrothermal method was employed to grow the NiCo

electroactive phase on the SSM substrate to obtain NiCo@SSM. Briefly, 2 mmol of Ni $(NO_3)_2{\cdot}6H_2O$, 4 mmol of Co $(NO_3)_2{\cdot}6H_2O$, 24 mmol of urea, and 12 mmol of NH_4F were mixed in 30 mL ultra-pure water to form a homogeneous solution via magnetic stirring for about 30 min. A piece of SSM (1 × 2 cm^2), which was cleaned by ultra-sonication (15 min each) sequentially in 3 M HCl, ethanol, and Milli-Q water, was immersed into the above solution. Then, the mixture was transferred into a 50 mL Teflon-lined stainless steel autoclave and maintained at 180 °C for 12 h. After cooling to room temperature, the NiCoOx uniformly grown on the SSM was removed, washed with ethanol and water, and dried at 70°C. For comparison purposes, monometallic counterparts of Co@SSM was also synthesized using the same procedure, except that Ni $(NO_3)_2{\cdot}6H_2O$ was absent. The NH_4F acts as a structure-directing agent surfactant and induces morphological change [45–47] in which the F^- ions can coordinate with M^{x+} metals to form complexes, and NH^{4+} ions act as a buffer to retain the solution at constant pH. The strong coordination between F^- ions and metal cation slows the release rate of metal ions and controls the precursor's growth and nucleation rate [48].

The NiCoP@SSM sample was obtained by phosphorization of the as-prepared NiCo@SSM precursor. Briefly, NiCo@SSM precursor and 2 g of $NaH_2PO_2{\cdot}xH_2O$ were put in the same ceramic boat, separated by 2 cm, and placed in the center of a horizontal tube reactor. Then, under N_2 flow, the reactor's temperature was increased to 350°C with a heating rate of 5°C min^{-1} and then up to 400°C at 1°C min^{-1} and maintained for 2 h to phosphatize the precursor. Finally, the reactor was cooled to room temperature, washed with water, and dried at 70°C to obtain NiCoP@SSM. The same procedure was followed to prepare CoP@SSM and NiP@SSM samples. For comparison purposes, the pristine SSM was also subjected to phosphorization, denoted as P@SSM, under the same condition to investigate its catalytic activity upon phosphorization. Moreover, the state-of-the-art Pt/C (40 wt. % Pt) deposited on SSM substrate (denoted Pt/C@SSM) was also prepared for comparison.

2.3. Physicochemical characterization

Scanning electron microscopy (SEM-EDX) was recorded in SEM Hitachi 3400N, EDX Röntec XFlash of Si (Li). A high-resolution transmission electron microscope (TEM) (a Tecnai F30) was utilized to observe the detailed morphology of the samples (at an accelerating voltage of 200 kV). X-ray diffraction (XRD) analyses were conducted in a Bruker D8 Advance diffractometer with Cu Kα of 1600 W. Crystallite sizes were calculated from the Scherrer equation applied to reflections (220) for NiCoO, (111) for NiCoP and (011) for CoP. X-ray photoelectron spectra (XPS) were obtained in a VG Escalab 200R spectrometer equipped with a hemispherical electron analyzer with Mg Kα (1253.6 eV) at 100 W with passing energy of 50 eV in the survey analysis and 20 eV in the high-resolution regions. The C 1s line at 284.6 eV was employed for charge correction of all XPS spectra. CasaXPS software was employed to perform peak fitting and quantification, and Shirley-type background was employed for all peaks. A 70%/30% Gaussian/Lorentzian line shape was used to deconvolute the high resolution for each component.

2.4. Electrochemical characterization

The electrochemical measurements were carried out at room temperature in a standard three-electrode electrochemical cell controlled by potentiostat/galvanostat AUTOLAB PGSTAT302. An aqueous solution of KOH (1 M) was used as an electrolyte. The set-up comprises carbon felt as the counter electrode, Ag/AgCl electrode as the reference electrode, and a 1 × 2 cm^2 of the as-prepared sample as the working electrode. The working electrode consisting of the samples was attached to a crocodile clip-type connector, and the active area was limited to 1 × 1 cm^2 by demarcating and covering the remaining surrounding area with Parafilm and scotch plastic tape. The actual surface area of the mesh was calculated according to the references [49,50] (Text S1, supporting information).

The linear sweep voltammetry (LSV) was performed for all samples at a scan rate of 5 mV s^{-1} in 1 M KOH aqueous solution. All potentials were converted to the reversible hydrogen electrode (RHE) using the Nernst formula of $E_{RHE} = E_{Ag/Agcl} + 0.197\ V + 0.059 \times pH$. Prior to the electrocatalytic activity measurement for HER, the working electrode was activated by continuous cyclic voltammogram (CV) scans until the variation of cycles was trivial. The HER polarization curve is plotted with an iR –correction. Tafel plots are obtained in the linear regions through Tafel equation fitting ($\eta = a + b \log j$), where η is the overpotential, b represents the Tafel slope, and j is the current density. In order to determine the electrochemical active surface areas (ECSA) of the samples, the double-layer capacitance (C_{dl}) was further measured by recording CV curves at various scan rates of 20, 40, 60, 80, and 100 mV s^{-1} in a potential range of 0.55–0.61 V vs. RHE. Electrochemical impedance spectroscopy (EIS) was measured at an overpotential of -138 mV in the frequency window from 100 kHz to 0.01 Hz at a 5 mV amplitude (rms). The electrochemical stability test for the best-performing sample (NiCoP@SSM) was measured by chronoamperometry at an overpotential of -138 mV for about 24 h.

3. Results and discussion

The schematic synthesis process of the NiCoP@SSM sample is shown in Scheme 1. Briefly, the NiCoP@SSM sample was obtained by hydrothermal route followed by a phosphorization process. First, the Ni and Co precursors were dissolved in water in the presence of urea and NH_4F. The mixture was transferred into an autoclave, pre-treated SSM was immersed, and subsequently subjected to a hydrothermal reaction. Then, the as-prepared NiCo@SSM sample was transformed into NiCoP@SSM material through the phosphorization process in the presence of a phosphorus precursor ($NaH_2PO_2.xH_2O$). Finally, the obtained product was washed and dried. Such *in situ* growth of electroactive materials on conductive SSM substrate would endow virtuous abundant active site and promote activity. The urea is used as a chelating agent, and NH_4F acts as a surfactant-morphology-controlling agent. In this case, the metal species first coordinate with the F^- ions, forming $M\text{-}F^{(2-x)-}{}_x$ complex intermediates. During the hydrothermal reaction, the Ni^{2+} and Co^{2+} ion react with CO_3^{2-} and OH^- ions, derived from the decomposition of urea, to form the NiCoOx precursor. The presence of NH_4F structure-directing agent enables to release of metal ions slowly, thus controlling the nucleation and growth rate [48,51].

X-ray diffraction (XRD) was applied to explore the crystallographic information of the samples. XRD patterns are shown in Fig. 1, and a summary of the detected crystalline phase for the different samples is presented in supporting information in Table S1. All of the samples exhibit the characteristic metallic alloy of NiFe on the SSM substrate. The Cr metal is observed in SSM and Co@SSM samples. The modified SSM shows extra diffraction peaks of weak intensity matching to distinct crystal structures based on synthesis design. Weak diffraction peaks of the surface structure may be attributed to the strong diffraction peaks of the bulk SSM substrate and the fact that *in situ* grown nanostructures are created as a thin coating on the surface; therefore, they are not notably identified by XRD [44]. The Co@SSM shows multiphase crystal structures which are of Fe_3O_4, Co, Co_3Mo, and $MoNi_4$ phases. For easiness, the sample is denoted as Co@SSM throughout the text; nevertheless, it must be kept in mind that Co@SSM consists of the mentioned phases. The NiCo@SSM sample displays diffraction peaks, which are attributed to the crystallographic plane of $Ni_{1.71}Co_{1.29}O_4$ with a cubic crystal system. This sample is denoted as NiCo@SSM throughout the manuscript text. In the case of the CoP@SSM sample, two additional crystal phases of CoP and Co_3O_4 are identified. Also, in this case, it must be bear in mind that the CoP@SSM sample comprises these phases, which is shortly denoted by CoP@SSM throughout the manuscript. Moreover, the NiCoP@SSM sample exhibited two additional phases of NiCoP and CoP. Metal phosphide formation verifies that $NaH_2PO_2.xH_2O$ successfully

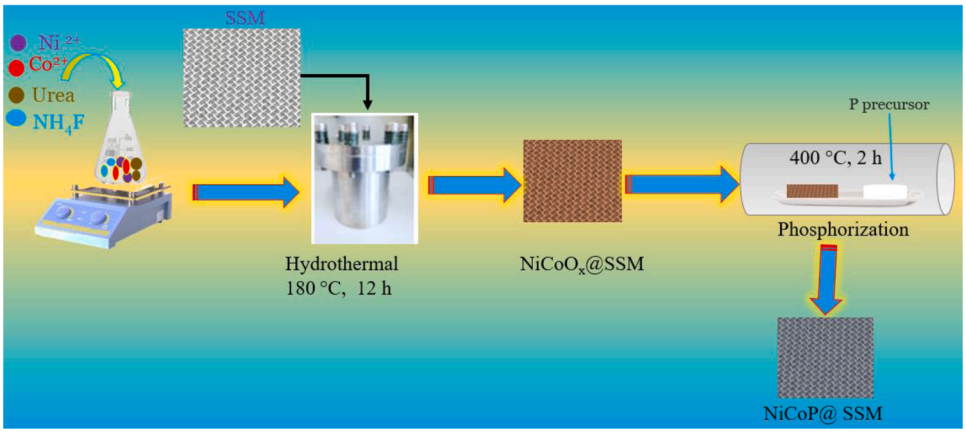

Scheme 1. Schematic illustration of the fabrication process of NiCoP@SSM electrocatalyst.

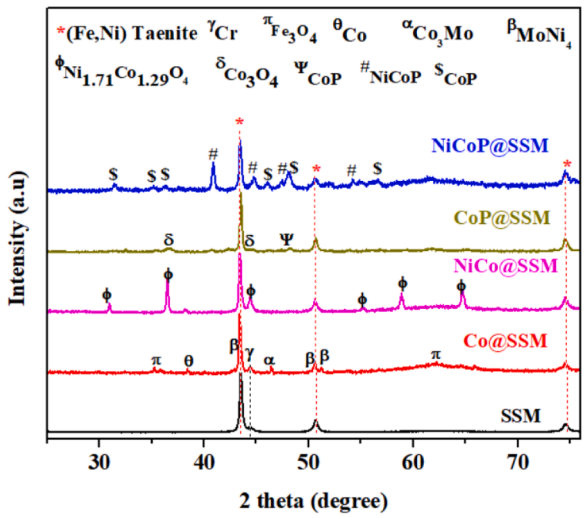

Fig. 1. X-ray diffraction (XRD) patterns of the different electrocatalyst.

phosphatizes the NiCo@SSM precursor. This sample NiCoP@SSM comprises NiCoP and CoP phases and is written as NiCoP@SSM throughout the text.

SEM image was used to observe the surface morphology of the samples. The SEM images of pristine SSM, Co@SSM, NiCo@SSM, CoP@SSM, and NiCoP@SSM samples are shown in Fig. 2. The surface of the pristine SSM sample is smooth without grain deposits on the surface. On the other hand, after the SSM substrate was subjected to hydrothermal reaction in the presence of Ni and Co precursor, the surface of SSM is entirely covered by different structures depending on the metal combinations. The Co@SSM sample exhibits a rough surface covered by entangled grains of particles (Fig. 2b), and the NiCo@SMM sample reveals a rough surface entirely covered by a spindle/rod-like structure (Fig. 2c). The SSM substrate can be activated by the F^- anion to generate more active sites for the nucleation and growth of the desired materials, further benefiting the intimate adhesion between the electroactive metals and the surface of the SSM substrate. Moreover, the samples subjected to phosphorization further changed their morphological appearance. The surface of the CoP@SSM sample contains a randomly and closely packed sheet-like structure (Fig. 2d), and the NiCoP@SSM sample contains a unique sponge-like structure (Fig. 2e, f). Fig. S1 (supporting information) shows the SEM images of the samples at low magnification in order to appreciate the surface morphology discrepancy.

Comparing the SEM images of the NiCo@SSM precursor (Fig. 2c) and the NiCoP@SSM (Fig. 2d) catalyst, the later catalyst shows a different microstructure with a sponge-like porous and rougher surface. This could be due to various factors: first, when the NiCo@SSM precursor was subjected to low-temperature gas phosphorization, the crystalline phase of NiCo@SSM was transformed from a single crystal phase of $Ni_{1.71}Co_{1.29}O_4$ into dual phases of NiCoP and CoP (NiCoP@SSM), which differs in chemical composition, crystal system, and crystallite size. The $Ni_{1.71}Co_{1.29}O_4$ has a cubic crystal system, while the NiCoP and CoP phases are hexagonal and orthorhombic crystal systems, respectively. The crystallite sizes were determined using the Scherrer equation applied to XRD patterns for NiCo@SSM and NiCoP@SSM related to the phases mentioned (NiCoO, NiCoP, and CoP). In this case, we assume that the evolution of the two different NiCoP and CoP phases with smaller crystallite size NiCoP (28.9 nm) and CoP (18.6 nm) relative to the $Ni_{1.71}Co_{1.29}O_4$ (44.7 nm) could be conjoining (via self-assembly or oriented attachment growth) to form a sponge-like structure. The formation of smaller crystallite size with porous structure could be likely due to the removal of interconnected pores during the long-time and relatively low-temperature phosphorization process. Besides, releasing H_2O gas and phosphine (PH_3) gas diffusion into the NiCo precursor during the phosphorization reaction can also contribute to the porous sponge-like structure [52]. This highlights the significance of $NaH_2PO_2{\cdot}xH_2O$ in constructing a unique sponge-like 3D interconnected structure. We can clearly observe that the hydrothermal reaction and/or phosphorization process has basically provided a rougher surface compared to the pristine SSM surface, which would eventually change the electrochemical performance. The sponge-like structures exhibited in the NiCoP@SSM sample are closely coupled with the SSM substrate, suggesting a robust mechanical strength. The porous architecture of the sponge and space/gap between the sponges could offer an environment for infiltration of the electrolyte (promoting reactants contact) and release of the evolved gases, which will eventually expedite mass and charge transfer, leading to enhanced activity.

To verify the elemental distribution of the sponge-like structure of the NiCoP@SSM sample, energy dispersive spectroscopy-scanning-transmission electron microscopy (EDS-STEM) was used. Fig. 2g displays the STEM image of a portion of the SSM covered with various elements, and Fig. 2 (h–n) displays the corresponding EDS elemental mapping. The structure is found to have uniform distribution and overlap of all the elements, proving that the sample is made up of the components Ni, O, Fe, Cr, P, Co, and Mo. From the optical photograph (Fig. S2), it is noticed that the color of the SSM mesh changed from silvery-white to dark brownish color (NiCo@SSM sample) and then finally reformed to black color (NiCo-CoP@SSM), indicating the successful growth of catalyst on the substrate.

TEM further unveiled the microstructure of the NiCoP@SSM sample. As shown in Fig. 3, at low and high magnification, the detailed sponge-

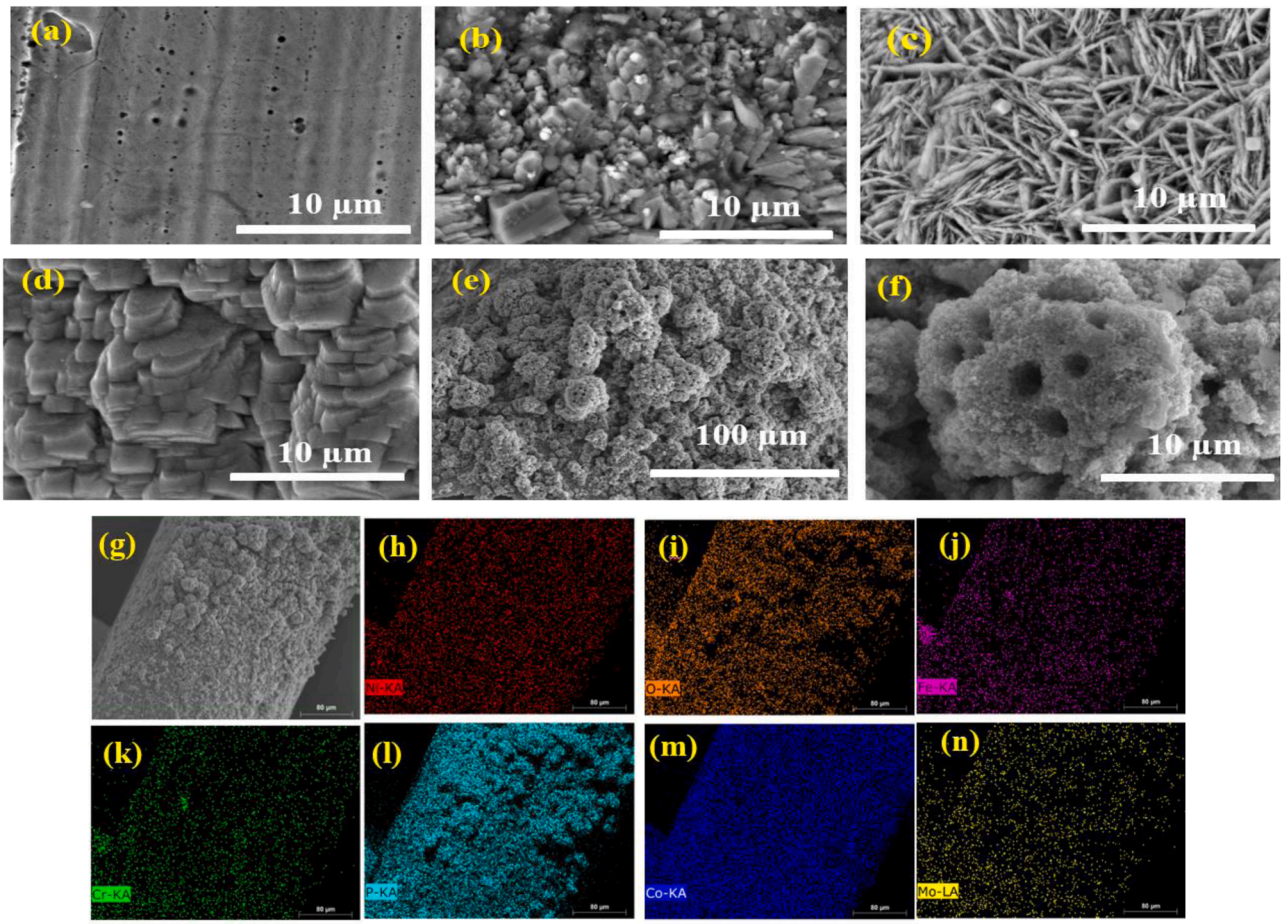

Fig. 2. SEM image of (a) Pristine SSM, (b) Co@SSM, (c) NiCo@SSM, (d) CoP@SSM, and (e) NiCoP@SSM at low magnification, (f) NiCoP@SSM at high magnification, and STEM image of (g) STEM image of NiCoP@SSM and (h–n) EDS elemental mapping images of Ni, O, Fe, Cr, P, Co, and Mo.

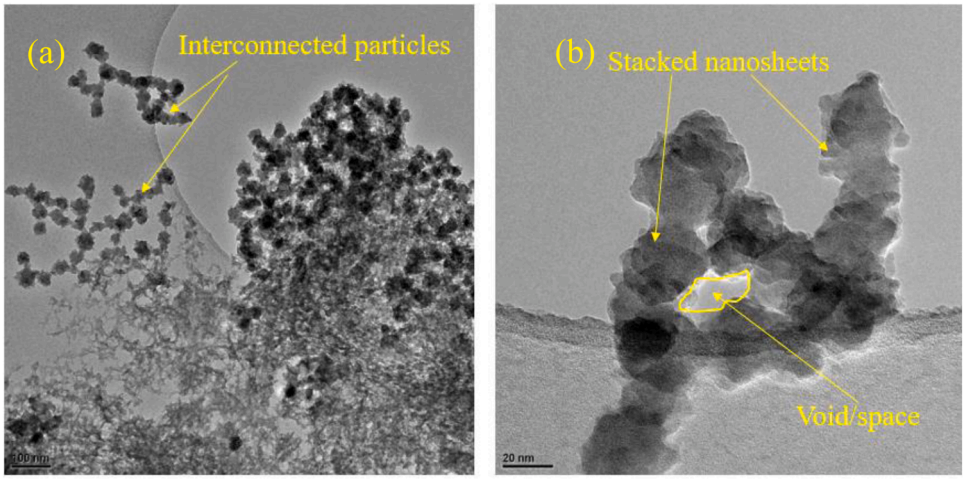

Fig. 3. TEM image of NiCoP@SSM (a) at low magnification and (b) at high magnification.

like structure of the sample encompasses interconnected grains and many stacked nanosheets. Fig. 3(a) presents a TEM image at low magnification, in which several small grains are interconnected with each other and ultrathin nanosheets are distributed on the surface, whereas Fig. 3(b) shows several stacked nanosheets forming a void/space in the middle with irregular and granular structure. It is vital to state that the sample for TEM analysis was obtained from the surface of the SSM substrate by ultrasonication treatment. In this case, the structure of the catalyst after ultrasonication application might alter to some extent, resulting in different morphology. As shown in Fig. 2(e), the SEM image of the NiCoP@SSM reveals the sample contains a porous sponge-like structure with an apparent void/space on the microstructure of the sponge, and the sponge-like microstructures are made up of a large number of irregular nanosheets. The voids/pores could result from the random stacking of the grains or nanosheets during the nucleation and growth.

X-ray photoelectron spectroscopy (XPS) was applied further to investigate the samples' elemental composition and valence states. The XPS survey spectra of all samples and the corresponding high-resolution spectra of the elements aimed at differentiating the appearance of the peaks on the surface are shown in Fig. S3. The pristine SSM surface comprises Fe 2p (Fig. S3a, c) and, to a certain extent of Cr element, as shown in the high resolution in Fig. S3e. Nevertheless, a very weak signal was observed for the other elements (Ni and Mo) (Fig. S3b and f), which are presented in the bulk material. It is important to mention the appearance of the C and O peaks in all samples could be attributed to the adsorption of adventitious CO_2 and O_2 on the surface of the mesh [53]. The XPS of the Co@SSM sample reveals the surface is composed of Ni, Co, and Fe (Fig. S3a–c), and the surface of the NiCo@SSM sample shows mainly of Ni and Co (Fig. S3a, b, and d) elements, which are grown by hydrothermal reaction. Besides, the surface of the composition of the CoP@SSM sample consists mainly of Co and P (Fig. S3d, and g) elements, which specifies that the hydrothermal reaction followed by the phosphating process enabled to deposit Co and P on the SSM substrate. Moreover, the XPS survey spectrum confirmed the Ni, Co, O, and P elements co-exist in the NiCoP@SSM sample (Fig. S3a). A clear appearance of peaks corresponding to the Ni, Co, and P elements can also be observed in the high-resolution spectra, as shown in Fig. S3b, d, and g.

The high-resolution spectrum of Ni 2p can be deconvoluted in three doublets. The peaks at 852.7 eV (for Ni $2p_{3/2}$) and at 870.1 eV (for Ni $2p_{1/2}$) are attributed to partially positive $Ni^{\delta+}$ in Ni-P bond [54]. The two peaks located at binding energy (BE) of 856.2 eV and 873.8 eV can be indexed to Ni $2p_{3/2}$ and Ni $2p_{1/2}$ of Ni^{2+}, while the two peaks at BE of 861.4 eV and 880.4 eV are related to the satellite peaks (Fig. S4a) [54, 55]. The deconvoluted high-resolution spectrum for Co 2p also contains $Co^{\delta+}$ (in Co-P bond) at BE of 778.9 eV and 793.8 eV attributed to the $Co2p_{3/2}$ and Co $2p_{1/2}$, respectively. The $Co^{\delta+}$ has a partial positive shift from that of Co metal (BE = 777.9 eV, $2p_{3/2}$). The peaks at BE of 782.0 eV and 798.04 eV are indexed to Co $2p_{3/2}$ and Co $2p_{1/2}$ of Co^{2+} (Fig. S4b). A partially positive charge of Co means there is a formation of Co-P bonds. Besides, satellite peaks are also observed at BE of 786.05 eV and 803.1 eV, corresponding to sat.$Co2p_{3/2}$ and Co $2p_{1/2}$, respectively [50]. Furthermore, the high-resolution spectrum of P 2p can be deconvoluted into three regions (Fig. S4c). The peaks at BE of 128.7 and 129.7 eV correspond to P $2p_{3/2}$ and P $2p_{1/2}$, which indicates a negative shift compared to elemental P (130.2 eV), which highlights the presence of a partial negative charge of $P^{\delta-}$ in the NiCoP@SSM sample. Likewise, the existence of a broad peak at a higher BE of 133.3 eV could be attributed to the oxidized P species [54] due to the exposure of the sample to air. The manifestation of a partial positive charge (δ^+) in both Ni and Co and a partial negative charge (δ^-) in P species unveils that there is a certain portion of Ni and Co electron density transferred to the P species [56].

The presence of $P^{\delta-}$ species that have a high affinity towards proton-acceptor, and consequently for hydrogen, and $Co^{\delta+}$/ $Ni^{\delta+}$ as hydride-acceptors that have a moderate interaction with hydrogen suggests that there will be a solid synergy/cooperativity to expedite the HER reaction. This is because P species have a high affinity for hydrogen. As a result, there is an expectation that it will give a high HER performance. The findings of the XPS examination provided further evidence that the phosphorization process resulted in the successful synthesis of nickel and cobalt phosphide (Ni-P and Co-P, respectively). In addition to Ni, Co, and P elements, we investigated to see if the metals Fe, Mo, and Cr are present on the surface. These elements are known to be present in the bulk of the SSM substrate. It was discovered that the XPS signal for these three metals is relatively low (Fig. S3c–f), which suggests that the surface of the catalyst does not consist of these elements and is instead mostly covered by materials containing Ni, Co, and P. In summary, the XPS analysis result reveals that the surface chemical composition of SSM substrate has been modified and transformed into Ni, Co, and P components, which are more active than Cr and Fe in catalyzing HER. Inductively coupled plasma atomic emission spectrometry (ICP-AES) analysis was used to examine the elemental composition of the NiCoP@SSM samples. The NiCoP@SSM sample contains Co (3.0 wt. %), Cr (18.8 wt.%), Fe (68.36 wt.%), Mo (0.14 wt.%), Ni (8.8 wt.%) and P (1.0 wt.%).

The electrochemical performance of the pristine SSM and the modified SSM was conducted by linear scan voltammetry (LSV) using a three-electrode system in 1.0 M KOH aqueous solution at a scan rate of 5 mV s^{-1}. For comparison, the state-of-the-art Pt/C (40 wt.% Pt) deposited on SSM substrate, pristine SSM, Co@SSM, NiCo@SSM, CoP@SSM, and NiCoP@SSM samples were prepared and evaluated their electrocatalytic activity for alkaline HER. All LSV curves were corrected by iR against the ohmic resistance and normalized to the submerged geometric area of the electrode. As presented by the LSV curve in Fig. 4a, the NiCoP@SSM catalyst exhibited an outstanding catalytic activity for HER, requiring only 138 mV overpotential (η) to produce a cathodic current density of 10 mA cm^{-2} (η_{10} is used as a benchmark for electrocatalytic performance comparison). Whereas, at the same cathodic current density, the overpotential for Pt/C@SSM, pristine SSM, Co@SSM, NiCo@SSM, and CoP@SSM were 44 mV, 534 mV, 305 mV, 277 mV, and 193 mV, respectively. The NiCoP@SSM catalyst presented a superior catalytic activity, revealing the lowest overpotential compared to the other as-prepared samples except with that of the commercial Pt/C@SSM-based catalyst, as shown in Fig. 4b.

In an effort to study the reaction mechanism of HER, the Tafel slope was determined. Tafel slope (b) is the intrinsic property of a catalyst that is closely related to the rate of HER. The Tafel slope was determined from the HER polarization curve based on the Tafel equation ($\eta = b \log j + a$), where j, η, b, and a are the current density, overpotential, Tafel slope, and a constant, respectively [57]. Generally, the reaction mechanism for alkaline HER comprises three elementary reaction steps, as expressed below, where * stands for an active site [58].

$$H_2O + e^- \rightarrow OH^- + H^* \ (\text{Volmer},\ b = 120\ \text{mV/dec}) \quad (1)$$

$$H^* + H_2O + e^- \rightarrow OH^- + H_2(g) \ (\text{Heyrovsky},\ b = 40\ \text{mV/dec}) \quad (2)$$

$$2H^* \rightarrow 2^* + H_2(g) \ (\text{Tafel},\ b = 30\ \text{mV/dec}) \quad (3)$$

The HER follows either the Volmer-Heyrovsky mechanism or the Volmer-Tafel mechanism, and the mechanism and the rate-determining step can be estimated from the Tafel slope magnitude. As shown in Table 1 and Fig. S5a, the pristine SSM catalyst possesses a Tafel slope of 207 $mVdec^{-1}$, whereas the Pt/C@SSM, Co@SSM, NiCo@SSM, CoP@SSM, and NiCoP@SSM showed a Tafel slope of 88, 108, {102,164}, 102, and 74 $mVdec^{-1}$, respectively. These data indicate that the HER kinetics of NiCoP@SSM catalyst follows the Volmer-Heyrovsky mechanism (Volmer step: $H_2O + e^- \rightarrow OH^- + H^*$ and Heyrovsky step: $H_2O + H^* + e^- \rightarrow H_2\uparrow + OH^-$), and the Heyrovsky reaction is the rate-limiting step [59]. The Tafel slope of the NiCoP@SSM catalyst is much smaller than that of other catalysts, signifying that it retains a faster charge transfer kinetics. As a result, it can effectively boost the catalytic activity of the electrode.

Electrochemical impedance spectroscopy (EIS) was also performed to investigate the interface behavior and electrocatalytic kinetics. Nova software was used to fit the curves, and the fitting values of each component are shown in Table 1, and the equivalent circuit diagram is presented in Fig. S6. Figs. S5b and S7 show the Nyquist plot of all catalysts with a semi-circle arc. The arc diameter of the Nyquist plot embodies the sum of charge transfer resistance (R_{ct}) and series resistance (R_s); the latter can be determined from the intersection point in the high-frequency region on the left side and the X-axis. As shown in Table 1, the R_s is more or less comparable in all experiments since the same electrolyte (1 M KOH) was used for all HER measurement. The slight difference could be originated from the gas bubbles accumulated in the electrolyte during the actual reaction, which could have slightly influenced the resistance. Nevertheless, a significant discrepancy can be seen in the value of R_{ct}, in which the NiCoP@SSM catalyst exhibited the lowest value (≈ 11 Ω.cm^2) among the samples, indicating that the

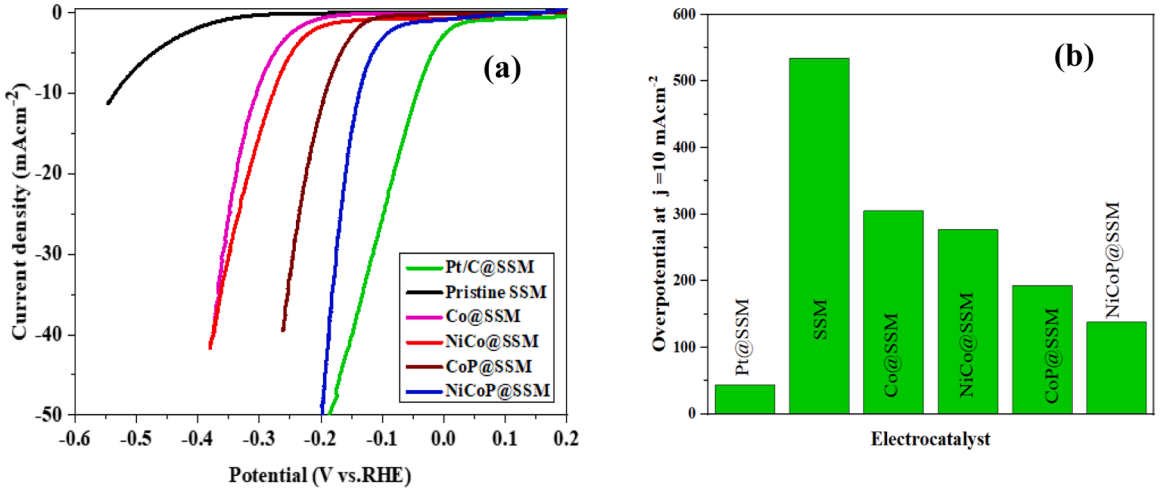

Fig. 4. Electrochemical performance of different electrocatalysts. (a) HER polarization curve, and (b) overpotential at 10 mA cm^{-2} current density.

Table 1
Summary of electrochemical characteristics of the different electrocatalysts.

Electrocatalyst	Tafel slope (mVdec^{-1})	R_s (Ω. cm^2)	R_{ct} (Ω. cm^2)	EDL capacitance (mFcm^{-2})
Pristine SSM	207	7.2	4483.8	0.093
Co@SSM	108	7.98	494.4	0.47
NiCo@SSM	{102,164}	7.2	282.6	1.43
CoP@SSM	102	8.58	36.24	1.67
NiCoP@SSM	74	7.86	10.98	4.58

phosphorization of the NiCo@SSM leads to promotes the charge transfer rate between the electrode and electrolyte interface by reducing the resistance in the interface of the material surface, eventually enhancing the electrochemical reaction kinetics. According to the SEM image (Fig. 2e), the NiCoP@SSM sample possesses a porous sponge-like structure with certain gaps within the sponge-like structure, and this could offer a space for infiltration of the electrolyte and discharge of the evolved hydrogen, which will eventually accelerate mass and charge transfer, leading to promoted HER performance.

To enlighten the origin of the high activity towards hydrogen evolution, the electrochemical active surface area (ECSA) of the as-prepared catalysts was investigated. The ECSA was estimated by determining the electrochemical double-layer capacitance measured using cyclic voltammetry (CV). It is generally recognized that the ECSA has a linear relationship with the electrical double layer (EDL) capacitance caused by the interfacial charging process [60], and cyclic voltammetry (CV) is the most practiced approach to calculate the EDL capacitance of catalysts. The CV measurements were recorded at various scan rates (20, 40, 40, 60, 80, and 100 mV s^{-1}) in the potential range of 0.55 to 0.61 V vs. RHE, and the corresponding CV curves are presented in Fig. S8. The EDL capacitance was determined by plotting the $\Delta J = (J_a - J_c)/2$ at 0.58 V vs. RHE against the various scan rate, in which the linear slope is the EDL capacitance Accordingly, the EDL capacitance values for the pristine SSM, Co@SSM, NiCo@SSM, CoP@SSM and NiCoP@SSM were 0.093, 0.47, 1.43, 1.67, and 4.58 mFcm^{-2}, respectively (Fig. S9). The largest EDL of the NiCoP@SSM sample (Table 1) means that it retains the largest ECSA due to its unique porous sponge-like structure and rough scale structure. It demonstrated that the synergetic effect of the two metals followed by phosphorization led to achieving a high ECSA, which can expose abundant active sites, thus lifting the overall HER performance.

According to the findings that were presented earlier, the NiCoP@SSM electrocatalyst possesses greater catalytic activity and is significantly more effective than the vast majority of SSM-based electrocatalysts that have been published in the scientific literature (Table 2). The unique and porous sponge structure can endow appropriate contact with the electrolyte and intermediate species, ensuing in rich active sites for HER. This work demonstrates a feasible method for converting widely available SSM substrates into high-performance and durable HER electrocatalysts.

The electrocatalytic stability is an important parameter to take into account for large-scale applications. To this end, chronoamperometry (I vs. t at specific potential) was measured to evaluate the stability of the best-performing electrocatalyst of NiCoP@SSM. As shown in Fig. 5a, NiCoP@SSM exhibited a very slight current attenuation after 24 continuous operations at -138 mV overpotential in a 1 M KOH aqueous solution. Specifically, after 24 h operation, 90% current retention was recorded, demonstrating its good stability. Besides, the HER polarization curve before and after stability measurement was also recorded and compared. As shown in Fig. 5b, the catalytic activity after long-term measurement presents a trivial decay, signifying its splendid HER stability. Henceforth, the catalyst offers outstanding kinetics after stability measurements. The slight decrease in catalytic activity after 24 h continuous stability measurements could be originated from the

Table 2
Performance comparisons of SSM-based electrocatalysts for HER electrode reported in the literature.

Catalyst	Overpotential (mV) at j =10 mAcm^{-2}	Tafel slope (mV/dec)	Stability measurement	Refs.
NiCoP@SSM	138	74	90% current retention after 24 h operation	This work
NiSx/SS	258	100	Remained stable up to 2000 cycles	[61]
NiP@SSM	149	80	95% overpotential retention after 25 h test	[36]
SSM	209.8	115.6	Good stability after 2000 cycles.	[62]
MoS_2/SSM	160	61	85 % current retention after 18 h test	[43]
NASSM	146	60.1	26 mV increase after 100 h operation	[63]
EASS-Ar/H_2	370	-	Remained stable for about 100 h operation	[64]

Where; NASSM: N-doped anodized stainless-steel mesh; EASS: Etched and anodized stainless steel.

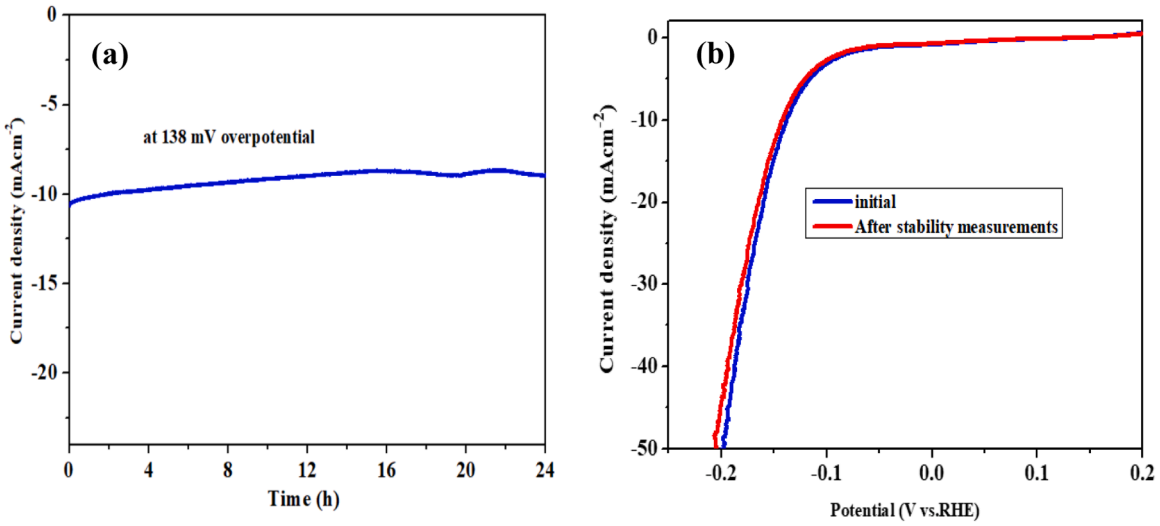

Fig. 5. (a) Chronoamperometry stability test at an overpotential of -138 mV for 24 h, and (b) HER polarization curve of NiCoP@SSM catalyst before and after stability test.

accumulation of bubbles in the porous sponge-like structure, which hinders the interaction between the electrolyte and the catalytic surface. When HER occurs at electrocatalytic interfaces, it releases gas bubbles, which in turn appear as an undesired increase in overpotential and simultaneously impair the activity of the electrocatalytic materials. Henceforth, the slight potential increment after long-term stability measurements likely arose from the gas bubble effect rather than from restructuring or deformation of the morphology or crystalline structure of the catalyst, as it was corroborated by SEM and XRD analysis results after the stability test.

Furthermore, the NiCoP@SSM sample was further characterized by XRD, SEM, and TEM after the stability test to investigate its physicochemical properties. After the stability test, a scanning electron microscope (SEM) analysis was carried out in order to appraise the morphological feature of the NiCoP@SSM electrocatalyst. As can be seen in Fig. 6a, the sponge-like structure that was seen in the NiCoP@SSM before the stability test appears to have a comparable morphology when compared to the SEM image that was obtained after the stability test. This reveals that its microstructure is exceptionally stable, as there was no substantial aggregation even when subjected to a harsh alkaline environment. The transmission electron micrograph further revealed that the structure of the sample that was noticed prior

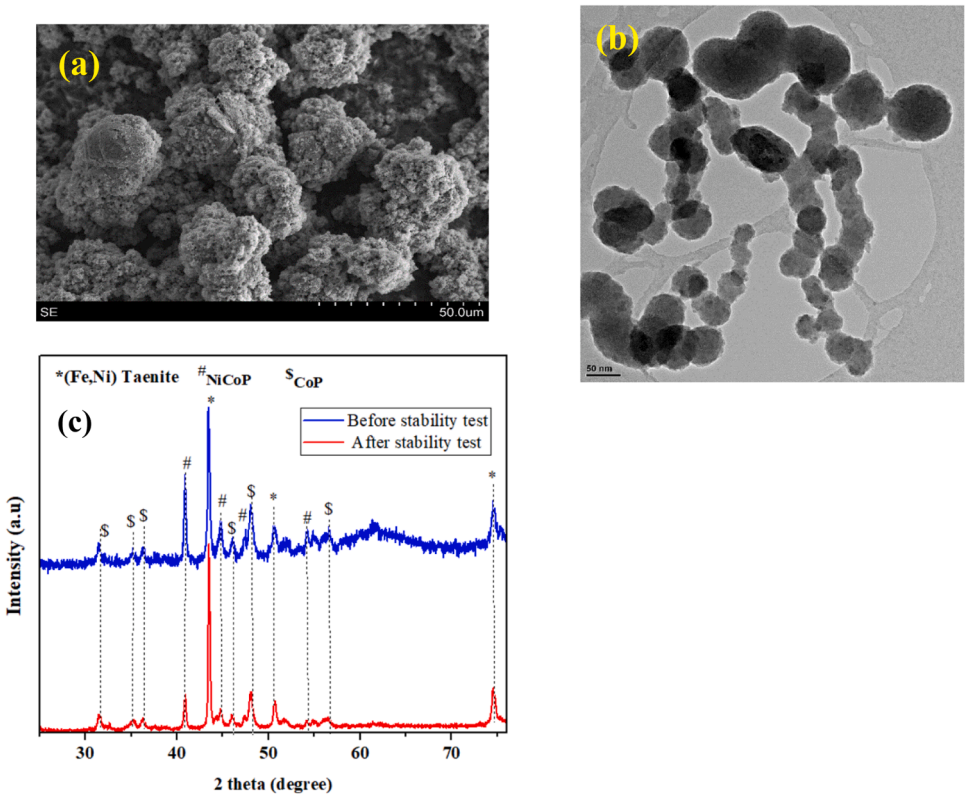

Fig. 6. SEM morphological characterization of NiCoP@SSM sample: (a) after stability test; TEM image of NiCoP@ SSM sample (b) after stability test, and (c) XRD pattern of NiCoP@SSM sample after stability measurements.

to the stability test is comparable to the morphology of the sample that was observed after the stability assessment (Fig. 6b). XRD was further used to assess the crystalline phases. Again, the XRD pattern of the sample before and after stability measurement remained intact/similar, as shown in Fig. 6c, demonstrating its excellent crystalline phase stability. The intact morphology and unaltered crystallinity of the sample further highlight its commendable properties for long–term application.

In short, the NiCoP@SSM catalyst exhibited excellent HER performance, which can be attributed to the following noteworthy features: primarily, surface enrichment of SSM with NiCoP/CoP species endows more active sites on the surface and makes the composite intrinsically more favorable for HER, as demonstrated by the lowered overpotential. The NiCoP/CoP sponge-like structure comprises the electroactive phase of NiCoP and CoP, and the coupling effect of these inter-connected phases could offer more active sites, resulting in enhanced HER activity. Secondly, the *in situ* growth of sponge-like structures on the conducive 3D substrate ensures high conductivity. The use of polymeric binders (such as Nafion) for powder-based electrocatalysts tempts to influence the charge transportation during the reaction. In this case, the electrocatalyst was prepared without a binder, which not only prominently enhances the conductivity of the electrode but also amplifies the active site for hydrogen evolution. Thirdly, the SSM substrate with an open mesh structure substantially improves the electrolyte diffusion, and the porous sponge-like structure bargains a large ECSA bringing more active sites, resulting in enhanced HER. Fourthly, the relatively low charge transfer of the sample could partially contribute to the enhanced HER performance. Moreover, the $P^{\delta-}$ species in the NiCoP@SSM sample with a high affinity towards proton-acceptor and $Co^{\delta+}$/ $Ni^{\delta+}$ as hydride-acceptor with moderate interaction towards hydrogen demonstrates that there is a substantial synergetic effect to expedite the reaction. Fig. S10 shows the HER polarization curve of the mono and bimetals of Ni and Co. As it is ostensible, there is a synergetic effect between the electroactive metals of Ni and Co. The NiCo@SSM catalyst exhibits higher catalytic activity for HER relative to the monometal counterparts, suggesting a coupling effect between Ni and Co. The pristine SSM was also subjected to phosphorization to obtain a P@SSM sample to explore its catalytic activity for HER. As shown in Fig. S7, the P@SSM sample exhibits a relatively higher catalytic activity than the pristine SSM. Nevertheless, the role of P was further pronounced when it was incorporated into the as-prepared NiCo@SSM, resulting in NiCoP@SSNM with excellent catalytic activity for HER. The P dopant has played a crucial role in further improving the HER performance by optimizing the electronic structure of the bimetals, altering the morphology, improving the conductivity, and providing the synergistic impact between metal and metal phosphide. Henceforth, we can appreciate the contribution of the Ni/Co metals and P in the NiCoP@SSM catalyst, in which the Ni/Co metals are the major electroactive elements that largely contribute to the observed HER performance, while the P dopant has further altered the overall physicochemical and progressed the overall electrochemical activity of electroactive metals.

4. Conclusions

In summary, a NiCoP/CoP hybrid electrocatalyst with a peculiar sponge-like structure was successfully fabricated on a three-dimensional stainless steel mesh substrate through a hydrothermal route followed by a phosphorization process. Electrochemical results reveal that the NiCoP@SSM catalyst presents a splendid catalytic activity for HER in 1 M KOH aqueous solution. In particular, the catalyst required a low overpotential of 138 mV to derive a current density of 10 mA cm^{-2}. Moreover, it exhibited the smallest Tafel slope, relatively low charge transfer resistance, and the largest ECSA of the series. More interestingly, it showed excellent stability during 24 h continuous operation. The high performance of the NiCoP@SSM catalyst could be attributed to many factors; firstly, the 3D of SSM provides a large surface area and myriads of active catalytic sites during the reaction; secondly, the synergetic effect of Ni and Co and the electronic hybridization between these metals and phosphorus can optimize the energy barrier of a redox reaction and can change the electronic structure, which effectively expedites the electrocatalysis. Moreover, considering the $P^{\delta-}$ species in the NiCoP and CoP structure with a high affinity towards proton-acceptor, hence for hydrogen, and also $Co^{\delta+}$/ $Ni^{\delta+}$ as hydride-acceptor with moderate interaction with hydrogen, it shows that there is a substantial synergetic effect to expedite the catalytic process. This study presents an effective approach for transforming commercially available SSM substrates into high-performance and durable HER electrocatalysts for practical application.

Appendix A. Supplementary data

Supporting information is enclosed in a separate document.

CRediT authorship contribution statement

Gebrehiwet Abrham Gebreslase: Data curation, Writing – original draft. **María Victoria Martínez-Huerta:** Conceptualization, Supervision, Writing – review & editing. **David Sebastián:** Supervision, Writing – review & editing. **María Jesús Lázaro:** Project administration, Funding acquisition.

Declaration of Competing Interest

The authors declare that they have no known competing financial interests or personal relationships that could have appeared to influence the work reported in this paper.

Data availability

No data was used for the research described in the article.

Acknowledgments

The authors wish to acknowledge the grants PID2020-115848RB-C21 and PID2020-115848RB-C22 funded by MCIN/AEI/10.13039/501100011033.

Supplementary materials

Supplementary material associated with this article can be found, in the online version, at doi:10.1016/j.electacta.2022.141538.

References

[1] J. Chow, R.J. Kopp, P.R. Portney, Energy resources and global development, Science 302 (2003) 1528–1531, https://doi.org/10.1126/science.1091939, 80-.
[2] A. Jahanger, M. Usman, M. Murshed, H. Mahmood, D. Balsalobre-Lorente, The linkages between natural resources, human capital, globalization, economic growth, financial development, and ecological footprint: the moderating role of technological innovations, Resour. Policy 76 (2022), 102569, https://doi.org/10.1016/j.resourpol.2022.102569.
[3] M. Usman, A. Jahanger, M.S.A. Makhdum, D. Balsalobre-Lorente, A. Bashir, How do financial development, energy consumption, natural resources, and globalization affect Arctic countries' economic growth and environmental quality? An advanced panel data simulation, Energy 241 (2022), 122515, https://doi.org/10.1016/j.energy.2021.122515.
[4] G.A. Gebreslase, M.V. Martínez-Huerta, M.J. Lázaro, Recent progress on bimetallic NiCo and CoFe based electrocatalysts for alkaline oxygen evolution reaction: a review, J. Energy Chem. 67 (2022) 101–137, https://doi.org/10.1016/j.jechem.2021.10.009.
[5] X. Hu, X. Tian, Y.W. Lin, Z. Wang, Nickel foam and stainless steel mesh as electrocatalysts for hydrogen evolution reaction, oxygen evolution reaction and overall water splitting in alkaline media, RSC Adv. 9 (2019) 31563–31571, https://doi.org/10.1039/c9ra07258f.
[6] R. Zahra, E. Pervaiz, M. Yang, O. Rabi, Z. Saleem, M. Ali, S. Farrukh, A review on nickel cobalt sulphide and their hybrids: earth abundant, pH stable electro-catalyst

for hydrogen evolution reaction, Int. J. Hydrog. Energy. 45 (2020) 24518–24543, https://doi.org/10.1016/j.ijhydene.2020.06.236.
[7] D. Duan, J. Feng, S. Liu, Y. Wang, X. Zhou, MOF-derived cobalt phosphide as highly efficient electrocatalysts for hydrogen evolution reaction, J. Electroanal. Chem. 892 (2021), 115300, https://doi.org/10.1016/j.jelechem.2021.115300.
[8] X. Kong, Q. Gao, S. Bu, Z. Xu, D. Shen, B. Liu, C.S. Lee, W. Zhang, Plasma-assisted synthesis of nickel-cobalt nitride–oxide hybrids for high-efficiency electrochemical hydrogen evolution, Mater. Today Energy 21 (2021), 100784, https://doi.org/10.1016/j.mtener.2021.100784.
[9] S. Chen, Y. Pan, Enhancing catalytic properties of noble metal@MoS_2/WS_2 heterojunction for the hydrogen evolution reaction, Appl. Surf. Sci. 591 (2022), 153168, https://doi.org/10.1016/j.apsusc.2022.153168.
[10] Z. Zeng, X. Chen, K. Weng, Y. Wu, P. Zhang, J. Jiang, N. Li, Computational screening study of double transition metal carbonitrides M′2M″CNO2-MXene as catalysts for hydrogen evolution reaction, NPJ Comput. Mater. 7 (2021) 80, https://doi.org/10.1038/s41524-021-00550-4.
[11] M. Zhu, X. Bai, Q. Yan, Y. Yan, K. Zhu, K. Ye, J. Yan, D. Cao, X. Huang, G. Wang, Iron molybdenum selenide supported on reduced graphene oxide as an efficient hydrogen electrocatalyst in acidic and alkaline media, J. Colloid Interface Sci. 602 (2021) 384–393, https://doi.org/10.1016/j.jcis.2021.06.038.
[12] Y. Lu, C. Yue, Y. Li, W. Bao, X. Guo, W. Yang, Z. Liu, P. Jiang, W. Yan, S. Liu, Y. Pan, Y. Liu, Atomically dispersed Ni on Mo2C embedded in N, P codoped carbon derived from polyoxometalate supramolecule for high-efficiency hydrogen evolution electrocatalysis, Appl. Catal. B Environ. 296 (2021) 120336, https://doi.org/10.1016/j.apcatb.2021.120336.
[13] B. Zhang, W. Xu, S. Liu, X. Chen, T. Ma, G. Wang, Z. Lu, J. Sun, Enhanced interface interaction in Cu_2S@Ni core-shell nanorod arrays as hydrogen evolution reaction electrode for alkaline seawater electrolysis, J. Power Sources. 506 (2021), 230235, https://doi.org/10.1016/j.jpowsour.2021.230235.
[14] H. Liu, J. Shang, L. Zeng, B. Cao, H. Geng, J. Lang, X. Cao, H. Gu, A setaria-shaped Pd/Ni-NC electrocatalyst for high efficient hydrogen evolution reaction, Chem. Eng. J. Adv. 6 (2021), 100101, https://doi.org/10.1016/j.ceja.2021.100101.
[15] J. Li, X. Zhou, Z. Xia, Z. Zhang, J. Li, Y. Ma, Y. Qu, Facile synthesis of CoX (X = S, P) as an efficient electrocatalyst for hydrogen evolution reaction, J. Mater. Chem. A 3 (2015) 13066–13071, https://doi.org/10.1039/c5ta03153b.
[16] M. Ren, X. Guo, S. Huang, Transition metal atoms (Fe, Co, Ni, Cu, Zn) doped RuIr surface for the hydrogen evolution reaction: a first-principles study, Appl. Surf. Sci. 556 (2021), https://doi.org/10.1016/j.apsusc.2021.149801.
[17] B. Adegbemiga Yusuf, M. Xie, W. Yaseen, C. Judith Oluigbo, J. Xie, Y. Xu, Ni nanoparticles oriented on MoO_2@BC nanosheets with an outstanding long-term stability for hydrogen evolution reaction, Chem. Eng. Sci. 246 (2021), 116868, https://doi.org/10.1016/j.ces.2021.116868.
[18] X. Gao, K. Lu, J. Chen, J. Min, D. Zhu, M. Tan, NiCoP–CoP heterostructural nanowires grown on hierarchical Ni foam as a novel electrocatalyst for efficient hydrogen evolution reaction, Int. J. Hydrog. Energy 46 (2021) 23205–23213, https://doi.org/10.1016/j.ijhydene.2021.03.155.
[19] C. Hu, C. Lv, S. Liu, Y. Shi, J. Song, Z. Zhang, J. Cai, A. Watanabe, Nickel phosphide electrocatalysts for hydrogen evolution reaction, Catalysts 10 (2020), https://doi.org/10.3390/catal10020188.
[20] Z. Zhang, J. Hao, W. Yang, J. Tang, Defect-rich CoP/Nitrogen-doped carbon composites derived from a metal-organic framework: high-performance electrocatalysts for the hydrogen evolution reaction, ChemCatChem 7 (2015) 1920–1925, https://doi.org/10.1002/cctc.201500398.
[21] W. Xiao, X. Li, C. Fu, X. Zhao, Y. Cheng, J. Zhang, Morphology and distribution of *in-situ* grown MoP nanoparticles on carbon nanotubes to enhance hydrogen evolution reaction, J. Alloy. Compd. 877 (2021), 160214, https://doi.org/10.1016/j.jallcom.2021.160214.
[22] R. Zhang, X. Wang, S. Yu, T. Wen, X. Zhu, F. Yang, X. Sun, X. Wang, W. Hu, Ternary $NiCo_2P_x$ nanowires as pH-universal electrocatalysts for highly efficient hydrogen evolution reaction, Adv. Mater. 29 (2017), https://doi.org/10.1002/adma.201605502.
[23] C. Karaman, O. Karaman, N. Atar, M.L. Yola, Tailoring of cobalt phosphide anchored nitrogen and sulfur co-doped three dimensional graphene hybrid: boosted electrocatalytic performance towards hydrogen evolution reaction, Electrochim. Acta. 380 (2021), https://doi.org/10.1016/j.electacta.2021.138262.
[24] D. Gao, J. Guo, H. He, P. Xiao, Y. Zhang, Geometric and electronic modulation of fcc NiCo alloy by Group-VI B metal doping to accelerate hydrogen evolution reaction in acidic and alkaline media, Chem. Eng. J. 430 (2022), 133110, https://doi.org/10.1016/j.cej.2021.133110.
[25] G. Zhang, G. Wang, Y. Liu, H. Liu, J. Qu, J. Li, Highly active and stable catalysts of phytic acid-derivative transition metal phosphides for full water splitting, J. Am. Chem. Soc. 138 (2016) 14686–14693, https://doi.org/10.1021/jacs.6b08491.
[26] J.A. Rodriguez, P. Liu, Desulfurization reactions on metal carbides and phosphides: complex role of C and P sites, ACS Natl. Meet. B. Abstr. (2007) 4575–4583.
[27] B. Fang, Z. Qi, F. Liu, C. Zhang, C. Li, J. Ni, J. Lin, B. Lin, L. Jiang, Activity enhancement of ceria-supported Co-Mo bimetallic catalysts by tuning reducibility and metal enrichment, J. Catal. 406 (2022) 231–240, https://doi.org/10.1016/j.jcat.2022.01.015.
[28] P. Strasser, S. Koh, T. Anniyev, J. Greeley, K. More, C. Yu, Z. Liu, S. Kaya, D. Nordlund, H. Ogasawara, M.F. Toney, A. Nilsson, Lattice-strain control of the activity in dealloyed core-shell fuel cell catalysts, Nat. Chem. 2 (2010) 454–460, https://doi.org/10.1038/nchem.623.
[29] H. Wang, S. Tao, Fabrication of a porous NiFeP/Ni electrode for highly efficient hydrazine oxidation boosted H2evolution, Nanoscale Adv. 3 (2021) 2280–2286, https://doi.org/10.1039/d1na00043h.
[30] G.A. Gebreslase, M.V. Martínez-Huerta, D. Sebastián, M.J. Lázaro, Transformation of $CoFe_2O_4$ spinel structure into active and robust CoFe alloy/N-doped carbon electrocatalyst for oxygen evolution reaction, J. Colloid Interface Sci. 625 (2022) 70–82, https://doi.org/10.1016/j.jcis.2022.06.005.
[31] X. Chen, G. Zeng, T. Gao, Z. Jin, Y. Zhang, H. Yuan, D. Xiao, *In situ* formation of high performance Ni-phytate on Ni-foam for efficient electrochemical water oxidation, Electrochem. Commun. 74 (2017) 42–47, https://doi.org/10.1016/j.elecom.2016.09.010.
[32] N.K. Chaudhari, H. Jin, B. Kim, K. Lee, Nanostructured materials on 3D nickel foam as electrocatalysts for water splitting, Nanoscale 9 (2017) 12231–12247, https://doi.org/10.1039/c7nr04187j.
[33] Q. Zhang, H. Zhong, F. Meng, D. Bao, X. Zhang, X. Wei, Three-dimensional interconnected Ni(Fe)OxHy nanosheets on stainless steel mesh as a robust integrated oxygen evolution electrode, Nano Res. 11 (2018) 1294–1300, https://doi.org/10.1007/s12274-017-1743-8.
[34] Q. Chen, R. Zhu, J. Wang, K. Yu, X. Sheng, Z. Xu, Y. Sun, J. Shen, Q. Zhang, *In-situ* etching of stainless steel: $NiFe_2O_4$ octahedral nanoparticles for efficient electrocatalytic oxygen evolution reaction, J. Alloy. Compd. 911 (2022), 165141, https://doi.org/10.1016/j.jallcom.2022.165141.
[35] Y. Xiao, T. Hu, X. Zhao, F.X. Hu, H. Bin Yang, C.M. Li, Thermo-selenizing to rationally tune surface composition and evolve structure of stainless steel to electrocatalytically boost oxygen evolution reaction, Nano Energy 75 (2020), 104949, https://doi.org/10.1016/j.nanoen.2020.104949.
[36] Y. Gao, T. Xiong, Y. Li, Y. Huang, Y. Li, M.S.J.T. Balogun, A simple and scalable approach to remarkably boost the overall water splitting activity of stainless steel electrocatalysts, ACS Omega 4 (2019) 16130–16138, https://doi.org/10.1021/acsomega.9b02315.
[37] Y. Hu, H. Yang, J. Chen, T. Xiong, M.S.J.T. Balogun, Y. Tong, Efficient hydrogen evolution activity and overall water splitting of metallic Co_4N nanowires through tunable d-orbitals with ultrafast incorporation of FeOOH, ACS Appl. Mater. Interfaces 11 (2019) 5152–5158, https://doi.org/10.1021/acsami.8b20717.
[38] M. Yao, H. Hu, N. Wang, W. Hu, S. Komarneni, Quaternary (Fe/Ni)(P/S) mesoporous nanorods templated on stainless steel mesh lead to stable oxygen evolution reaction for over two months, J. Colloid Interface Sci. (2019), https://doi.org/10.1016/j.jcis.2019.11.032.
[39] Y. Lyu, R. Wang, L. Tao, Y. Zou, H. Zhou, T. Liu, Y. Zhou, J. Huo, S.P. Jiang, J. Zheng, S. Wang, *In-situ* evolution of active layers on commercial stainless steel for stable water splitting, Appl. Catal. B Environ. 248 (2019) 277–285, https://doi.org/10.1016/j.apcatb.2019.02.032.
[40] M. Kim, J. Ha, Y.T. Kim, J. Choi, Stainless steel: a high potential material for green electrochemical energy storage and conversion, Chem. Eng. J. 440 (2022), 135459, https://doi.org/10.1016/j.cej.2022.135459.
[41] D. Li, Y. Li, B. Zhang, Y.H. Lui, S. Mooni, R. Chen, S. Hu, H. Ni, Insertion of platinum nanoparticles into MoS_2 nanoflakes for enhanced hydrogen evolution reaction, Materials 11 (2018), https://doi.org/10.3390/ma11091520 (Basel).
[42] G.R. Zhang, L.L. Shen, P. Schmatz, K. Krois, B.J.M. Etzold, Cathodic activated stainless steel mesh as a highly active electrocatalyst for the oxygen evolution reaction with self-healing possibility, J. Energy Chem. 49 (2020) 153–160, https://doi.org/10.1016/j.jechem.2020.01.025.
[43] K. Zhang, Y. Liu, B. Wang, F. Yu, Y. Yang, L. Xing, J. Hao, J. Zeng, B. Mao, W. Shi, S. Yuan, Three-dimensional interconnected MoS_2 nanosheets on industrial 316L stainless steel mesh as an efficient hydrogen evolution electrode, Int. J. Hydrog.n Energy 44 (2019) 1555–1564, https://doi.org/10.1016/j.ijhydene.2018.11.172.
[44] J. Ekspong, T. Wågberg, Stainless steel as a bi-functional electrocatalyst-A top-down approach, Materials 12 (2019) 6–9, https://doi.org/10.3390/ma12132128 (Basel).
[45] H. Zhang, C. Lu, H. Hou, Y. Ma, S. Yuan, Facile morphology-controlled synthesis of Co_3O_4 nanostructure on carbon cloth and their morphology-dependent pseudocapacitive performances, J. Alloy. Compd. 797 (2019) 970–977, https://doi.org/10.1016/j.jallcom.2019.05.206.
[46] J. Yan, X. Zhang, W. Zheng, L.Y.S. Lee, Interface engineering of a 2D-C_3N_4/NiFe-LDH heterostructure for highly efficient photocatalytic hydrogen evolution, ACS Appl. Mater. Interfaces (2021), https://doi.org/10.1021/acsami.1c03240.
[47] L. Wu, J. Zhang, S. Wang, Q. Jiang, R. Feng, S. Ju, W. Zhang, F. Song, Silver decorated hydroxides electrocatalysts for efficient oxygen evolution reaction, Chem. Eng. J. 442 (2022), 136168, https://doi.org/10.1016/j.cej.2022.136168.
[48] L. Cheng, M. Xu, Q. Zhang, G. Li, J. Chen, Y. Lou, NH_4F assisted and morphology-controlled fabrication of $ZnCo_2O_4$ nanostructures on Ni-foam for enhanced energy storage devices, J. Alloy. Compd. 781 (2019) 245–254, https://doi.org/10.1016/j.jallcom.2018.11.402.
[49] B.S. Zakaria, B.R. Dhar, Characterization and significance of extracellular polymeric substances, reactive oxygen species, and extracellular electron transfer in methanogenic biocathode, Sci. Rep. 11 (2021) 1–13, https://doi.org/10.1038/s41598-021-87118-w.
[50] Y. Li, J. Liu, C. Chen, X. Zhang, J. Chen, Preparation of NiCoP hollow quasi-polyhedra and their electrocatalytic properties for hydrogen evolution in alkaline solution, ACS Appl. Mater. Interfaces 9 (2017) 5982–5991, https://doi.org/10.1021/acsami.6b14127.
[51] X. Wu, X. Han, X. Ma, W. Zhang, Y. Deng, C. Zhong, W. Hu, Morphology-controllable synthesis of Zn-Co-mixed sulfide nanostructures on carbon fiber paper toward efficient rechargeable zinc-air batteries and water electrolysis, ACS Appl. Mater. Interfaces 9 (2017) 12574–12583, https://doi.org/10.1021/acsami.6b16602.
[52] Y. Zhang, L. Sun, L. Zhang, X. Li, J. Gu, H. Si, L. Wu, Y. Shi, C. Sun, Y. Zhang, Highly porous oxygen-doped NiCoP immobilized in reduced graphene oxide for

supercapacitive energy storage, Compos. Part B Eng. 182 (2020), 107611, https://doi.org/10.1016/j.compositesb.2019.107611.
[53] G.K. Sharma, B. Ranjan, D. Kaur, Electrochemical kinetics of 2D-MoS_2 sputtered over stainless-steel mesh: insights into the Na^+ ions storage for flexible supercapacitors, Ceram. Int. 48 (2022) 23404–23414, https://doi.org/10.1016/j.ceramint.2022.04.332.
[54] S. Maity, D.K. Singh, D. Bhutani, S. Prasad, U.V. Waghmare, S. Sampath, E. Muthusamy, High surface area NiCoP nanostructure as efficient water splitting electrocatalyst for the oxygen evolution reaction, Mater. Res. Bull. 140 (2021), 111312, https://doi.org/10.1016/j.materresbull.2021.111312.
[55] T. Chen, M. Qian, X. Tong, W. Liao, Y. Fu, H. Dai, Q. Yang, Nanosheet self-assembled NiCoP microflowers as efficient bifunctional catalysts (HER and OER) in alkaline medium, Int. J. Hydrog. Energy. 46 (2021) 29889–29895, https://doi.org/10.1016/j.ijhydene.2021.06.121.
[56] C. Wang, J. Jiang, T. Ding, G. Chen, W. Xu, Q. Yang, Monodisperse ternary NiCoP nanostructures as a bifunctional electrocatalyst for both hydrogen and oxygen evolution reactions with excellent performance, Adv. Mater. Interfaces 3 (2016) 1–5, https://doi.org/10.1002/admi.201500454.
[57] J. Zhu, L. Hu, P. Zhao, L.Y.S. Lee, K.Y. Wong, Recent advances in electrocatalytic hydrogen evolution using nanoparticles, Chem. Rev. 120 (2020) 851–918, https://doi.org/10.1021/acs.chemrev.9b00248.
[58] T. Shinagawa, A.T. Garcia-Esparza, K. Takanabe, Insight on Tafel slopes from a microkinetic analysis of aqueous electrocatalysis for energy conversion, Sci. Rep. 5 (2015) 13801, https://doi.org/10.1038/srep13801.
[59] Z. Qiu, C.W. Tai, G.A. Niklasson, T. Edvinsson, Direct observation of active catalyst surface phases and the effect of dynamic self-optimization in NiFe-layered double hydroxides for alkaline water splitting, Energy Environ. Sci. 12 (2019) 572–581, https://doi.org/10.1039/c8ee03282c.
[60] G. Li, L. Anderson, Y. Chen, M. Pan, P.Y. Abel Chuang, New insights into evaluating catalyst activity and stability for oxygen evolution reactions in alkaline media, Sustain. Energy Fuels 2 (2018) 237–251, https://doi.org/10.1039/c7se00337d.
[61] J.S. Youn, S. Jeong, I. Oh, S. Park, H.D. Mai, K.J. Jeon, Enhanced electrocatalytic activity of stainless steel substrate by nickel sulfides for efficient hydrogen evolution, Catalysts 10 (2020) 1–9, https://doi.org/10.3390/catal10111274.
[62] Y. Liu, K. Zhang, D. Zhang, W. Dong, T. Jiang, H. Zhou, L. Li, B. Mao, Industrial stainless steel meshes for efficient electrocatalytic hydrogen evolution, J. Energy Storage 41 (2021), 102844, https://doi.org/10.1016/j.est.2021.102844.
[63] M. Yao, B. Sun, N. Wang, W. Hu, S. Komarneni, Self-generated N-doped anodized stainless steel mesh for an efficient and stable overall water splitting electrocatalyst, Appl. Surf. Sci. 480 (2019) 655–664, https://doi.org/10.1016/j.apsusc.2019.03.036.
[64] M. Kim, J. Ha, N. Shin, Y.T. Kim, J. Choi, Self-activated anodic nanoporous stainless steel electrocatalysts with high durability for the hydrogen evolution reaction, Electrochim. Acta 364 (2020), 137315, https://doi.org/10.1016/j.electacta.2020.137315.

Supporting Information

for

NiCoP/CoP sponge-like structure grown on stainless steel mesh as a high-performance electrocatalyst for hydrogen evolution reaction

Gebrehiwet Abrham Gebreslase[a], María Victoria Martínez-Huerta[b*], David Sebastián[a], María Jesús Lázaro[a*]

[a] *Instituto de Carboquímica, CSIC. Miguel Luesma Castán 4, 50018, Zaragoza, Spain.*

[b] *Instituto de Catálisis y Petroleoquímica, CSIC. Marie Curie 2, 28049, Madrid, Spain.*

[*]Corresponding authors.

E-mail addresses: mmartinez@icp.csic.es (M.V. Martínez-Huerta), mlazaro@icb.csic.es (M.J. Lázaro)

Text S1. Estimation of the actual surface area of the working electrode

The actual surface area (S) of the working electrode mesh was estimated according to the reference [1], [2].

$$S = 2\pi bdn(n+1) + \frac{3}{2}\pi d^2(n+1)^2$$

Where; (b) is the pore size, and (d) is the wire diameter, (n) is the number of mesh. The segments are considered as a cylindrical shape, and the area lost at the junction (cross-over of the segments) is assumed to be ¼.

Example: The actual surface area for the pristine SSM sample is calculated as follows.

In 1 ×1 cm^2 area; n =12, b = 0.54 mm, and d = 0.6 mm.

$$S = 2\pi bdn(n+1) + \frac{3}{2}\pi d^2(n+1)^2$$

Accordingly,

$$S\ (cm^2) = 2\pi * 0.054 * 0.06 * 12(12+1) + \frac{3}{2}\pi * 0.06^2(12+1)^2$$

$S = 6.04\ cm^2$

Table S1. X-ray diffraction (XRD) analysis result

catalyst	Crystalline Phases
Pristine SSM	(Fe, Ni) Taenite (JCPDS, #47-1417), and Cr (JCPDS, #89-4055)
Co@SSM	(Fe, Ni) Taenite (JCPDS, #47-1417), Fe_3O_4 (JCPDS, #82-1533); Co (JCPDS, #70-2633); Co_3Mo (JCPDS, #29-0488), and $MoNi_4$ (JCPDS, #65-5480)
NiCo@SSM	(Fe, Ni) Taenite (JCPDS, #47-1417) and $Ni_{1.71}Co_{1.29}O_4$ (JCPDS, #40-1191)
CoP@SSM	(Fe, Ni) Taenite (JCPDS, #47-1417), CoP (JCPDS, #65-1474), and Co_3O_4 (JCPDS, #01-1152)
NiCoP@SSM	(Fe, Ni) Taenite (JCPDS, #47-1417), CoP (JCPDS, #89-2598), and NiCoP (JCPDS, #71-2336)

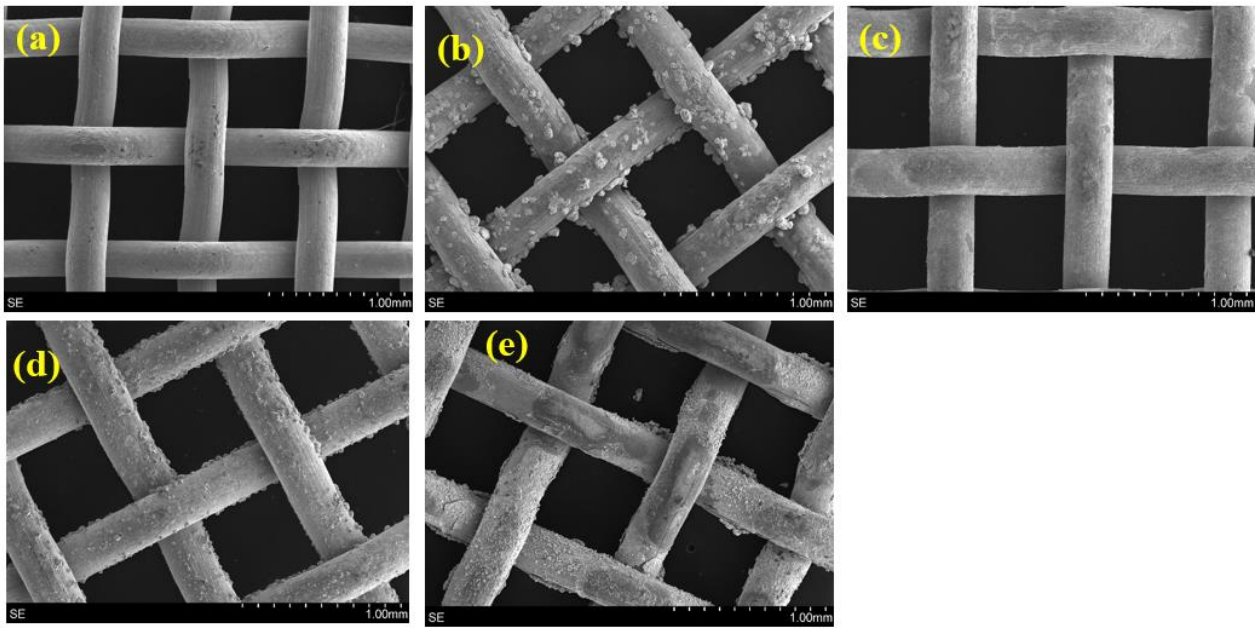

Figure S1. SEM image of (a) Pristine SSM, (b) Co@SSM, (c) NiCo@SSM, (d) CoP@SSM and (e)NiCoP@SSM

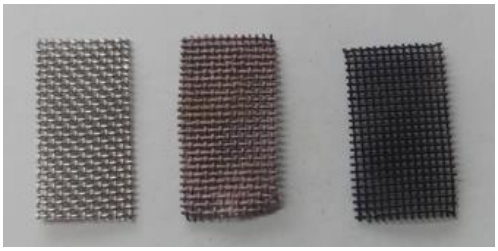

Figure S2.Optical photograph of pristine SSM (left), NiCo@SSM (middle) and NiCoP-CoP@SSM (in the right).

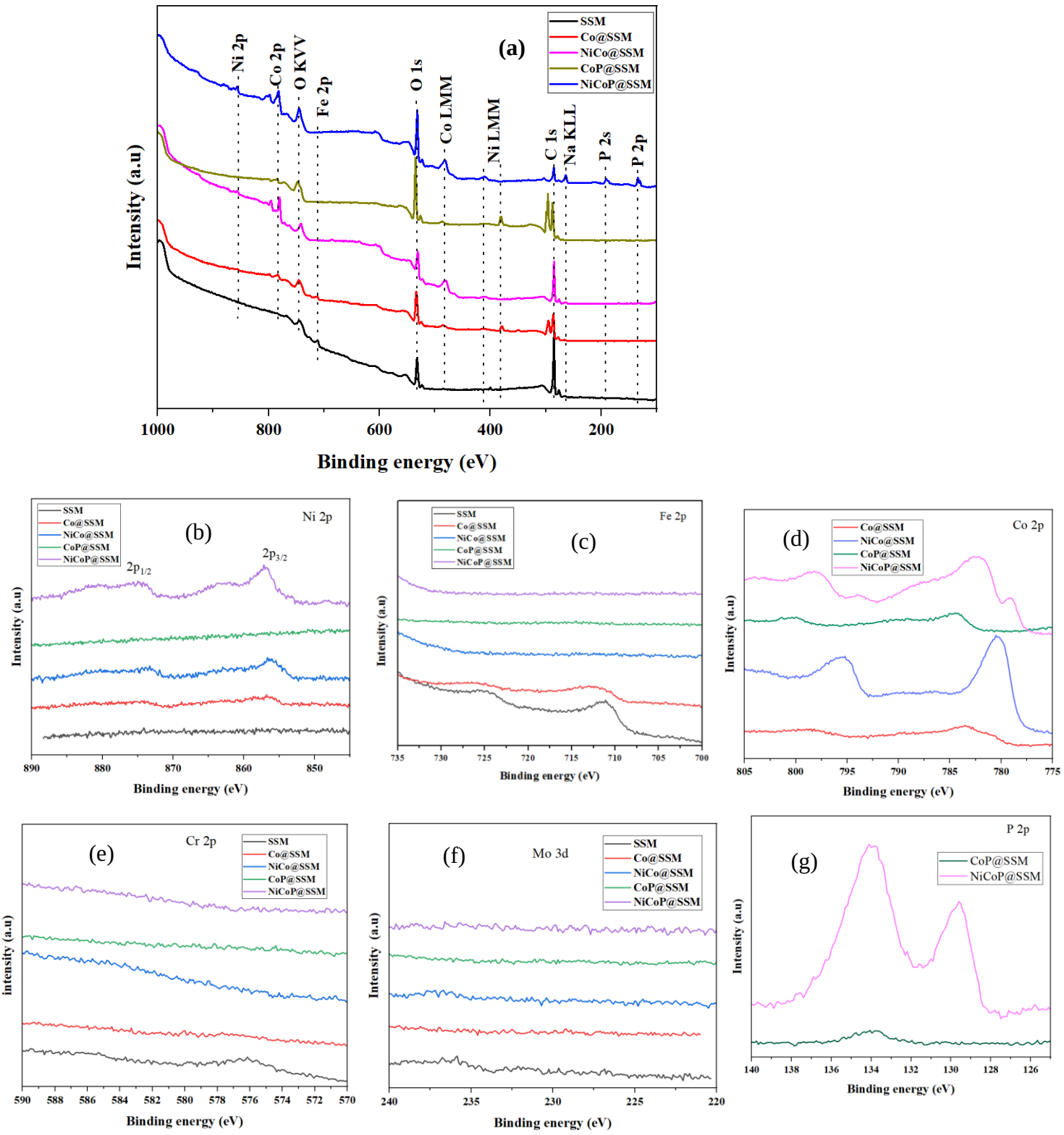

Figure S3. (a)XPS survey spectra of the various samples and high resolution spectra (b) Ni 2p, (c) Fe 2p, (d) Co 2p, (e) Cr 2p, (f) Mo 3d and (g) P 2p of the different samples.

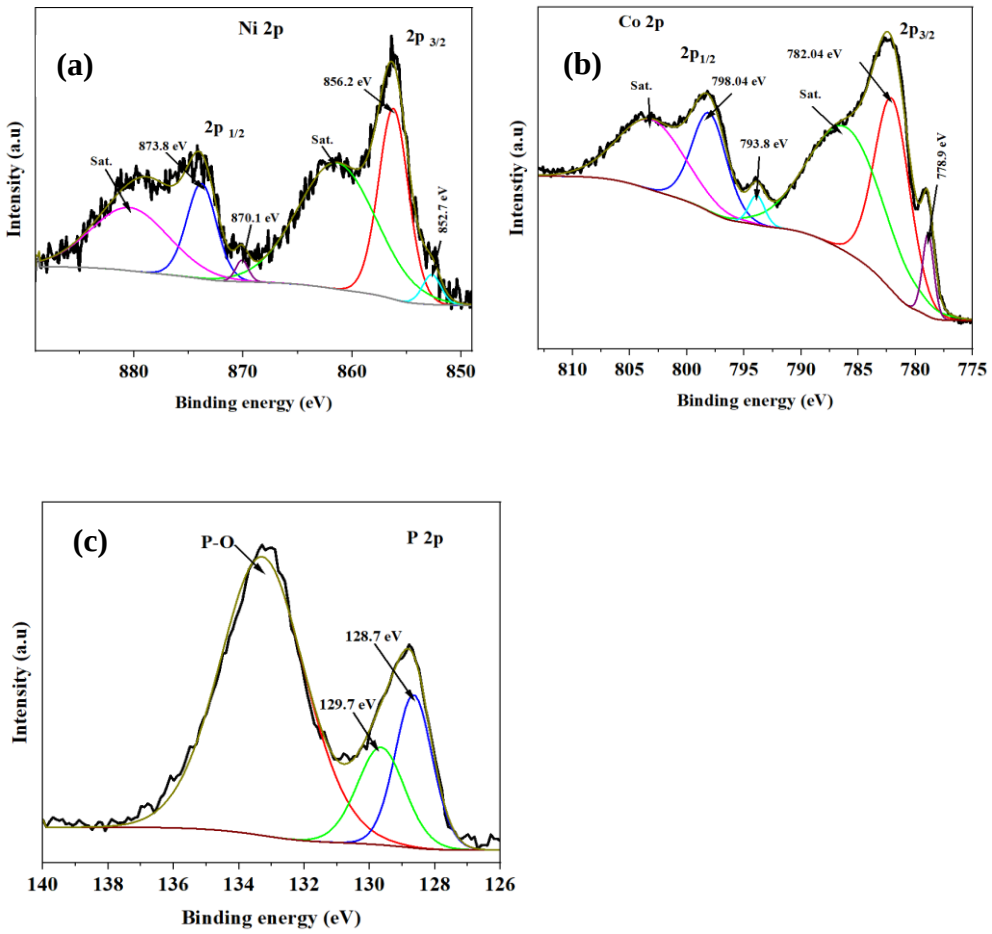

Figure S4 . XPS high-resolution spectra of (a) Ni 2p, (b) Co 2p and (c) P 2p of NiCoP@SSM catalyst.

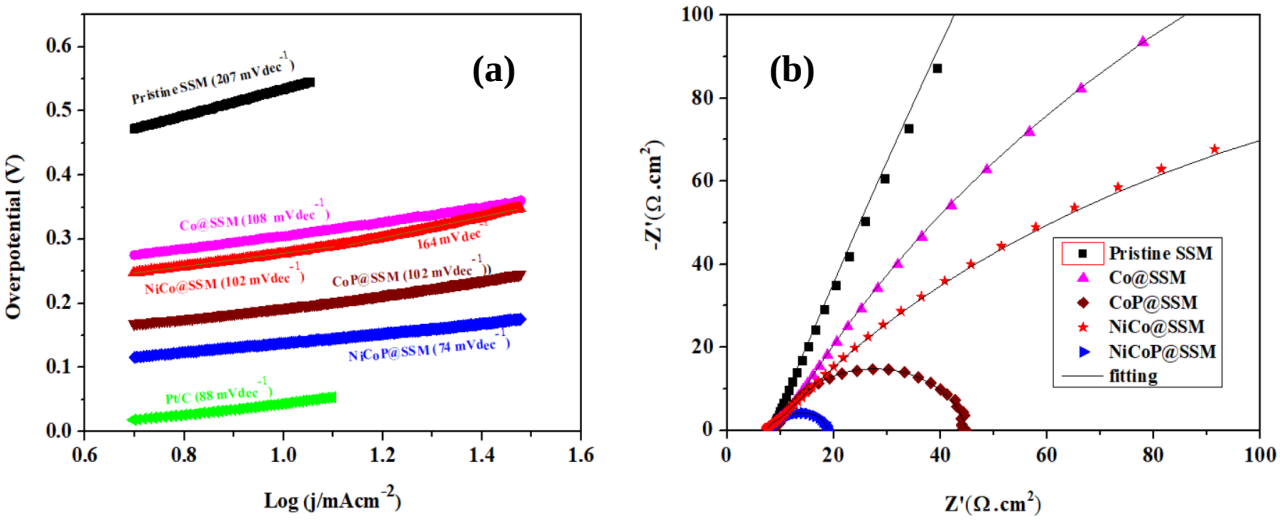

Figure S5. (a) Tafel slopes, (b) Nyquist plot measured at 138 mV overpotential.

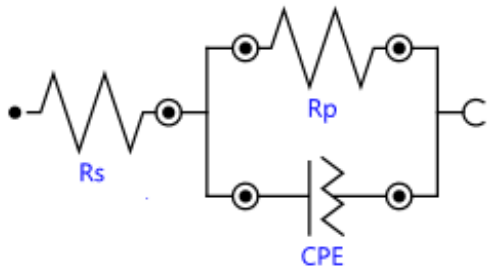

Figure S6. Equivalent circuit diagram used to fit the EIS result.

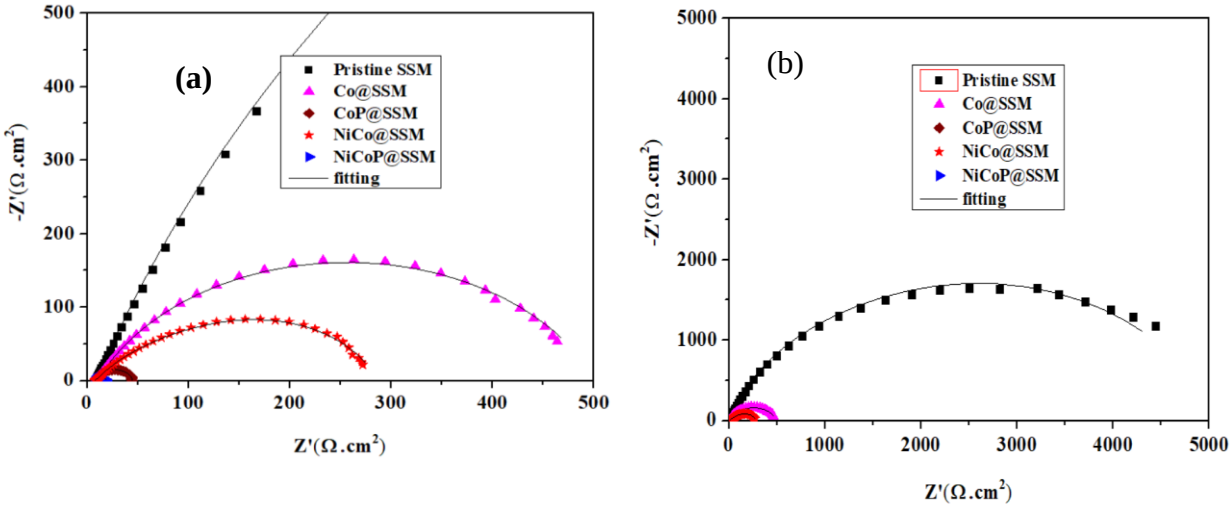

Figure S7. Nyquist plot of various samples at different X and Y values: (a) at low scale and (b) large scale.

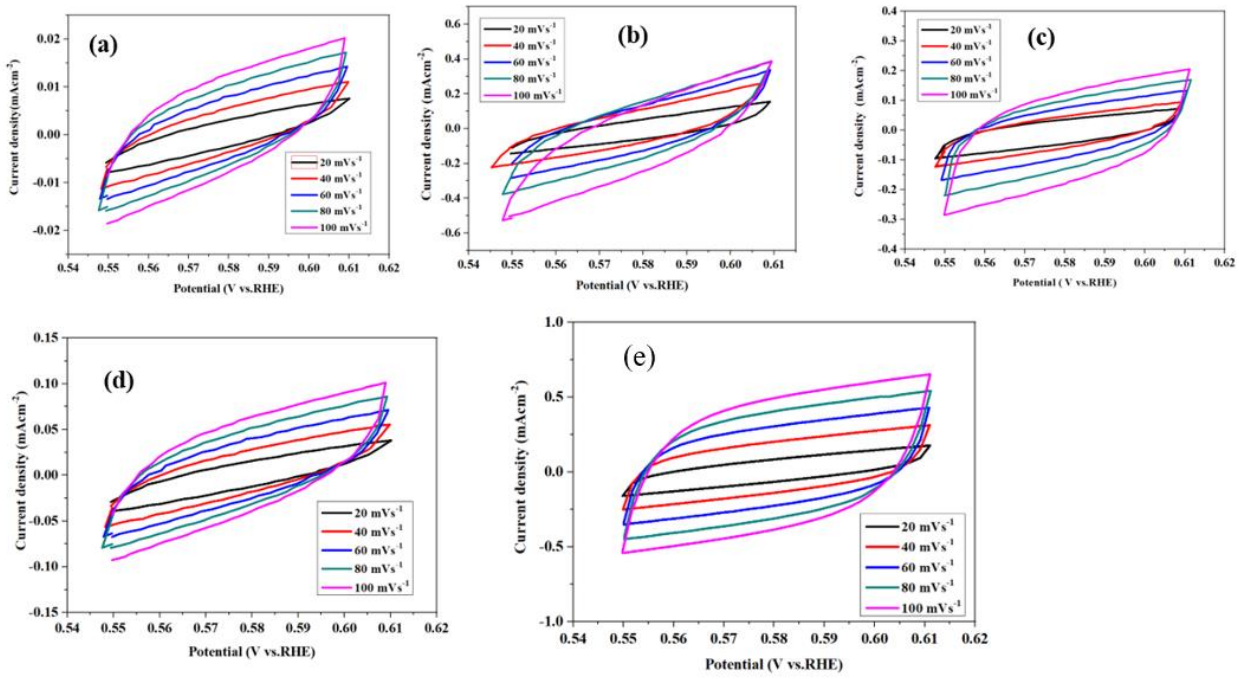

Figure S8. Cyclic voltammogram of the as-prepared catalyst at different scan rates.

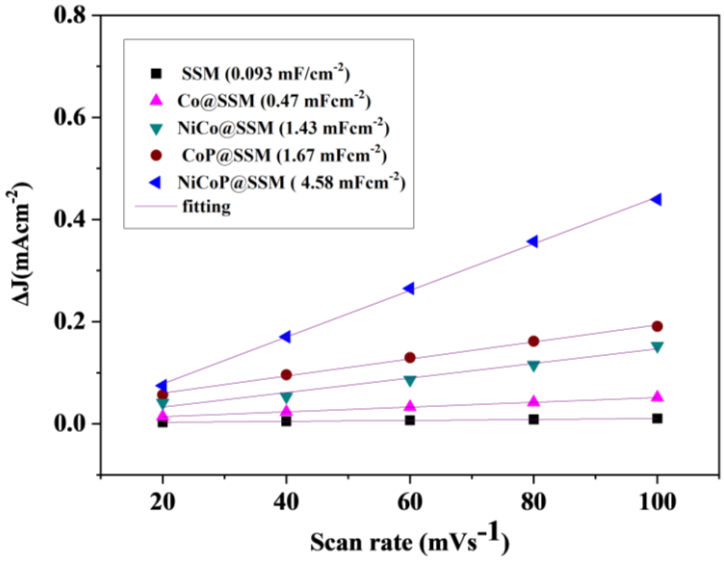

Figure S9. Fitted electrochemical C_{dl} of the current at different scan rates, measured in 1.0 M KOH

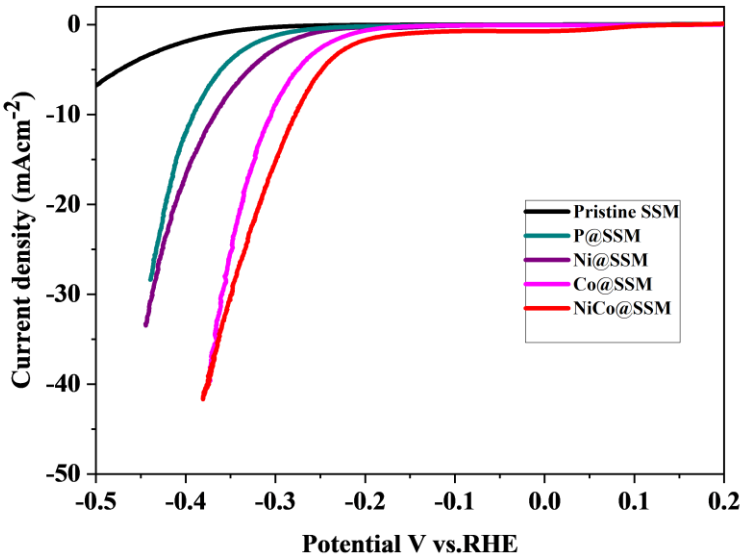

Figure S10. HER Polarization curve comparison of mono and bimetals of Ni and Co.

References

[1] Y. Zhang, M. D. Merrill, and B. E. Logan, "The use and optimization of stainless steel mesh cathodes in microbial electrolysis cells," *Int. J. Hydrogen Energy*, vol. 35, no. 21, pp. 12020–12028, 2010, doi: 10.1016/j.ijhydene.2010.08.064.

[2] B. S. Zakaria and B. R. Dhar, "Characterization and significance of extracellular polymeric substances, reactive oxygen species, and extracellular electron transfer in methanogenic biocathode," *Sci. Rep.*, vol. 11, no. 1, pp. 1–13, 2021, doi: 10.1038/s41598-021-87118-w.

Article II

Journal of Colloid and Interface Science 625 (2022) 70–82

Contents lists available at ScienceDirect

Journal of Colloid and Interface Science

journal homepage: www.elsevier.com/locate/jcis

Transformation of $CoFe_2O_4$ spinel structure into active and robust CoFe alloy/N-doped carbon electrocatalyst for oxygen evolution reaction

Gebrehiwet Abrham Gebreslase [a], María Victoria Martínez-Huerta [b,*], David Sebastián [a], María Jesús Lázaro [a,*]

[a] Instituto de Carboquímica, CSIC. Miguel Luesma, Castán 4, 50018 Zaragoza, Spain
[b] Instituto de Catálisis y Petroleoquímica, CSIC. Marie Curie 2, 28049 Madrid, Spain

GRAPHICAL ABSTRACT

By controlling and optimizing the ratio of $CoFe_2O_4$ and dopamine, a transformation of the $CoFe_2O_4$ spinel structure to CoFe alloy/N-doped carbon was observed. The optimized composite exhibits an excellent catalytic activity and stability towards OER.

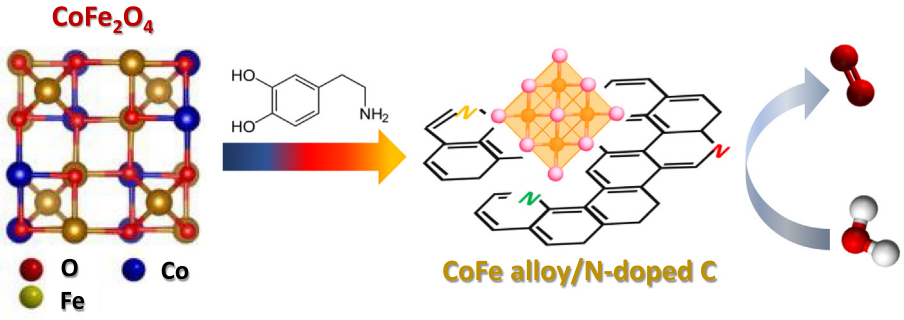

ARTICLE INFO

Article history:
Received 25 March 2022
Revised 24 May 2022
Accepted 2 June 2022
Available online 6 June 2022

Keywords:
$CoFe_2O_4$
CoFe
Dopamine
N-doped carbon
Electrocatalysts
Oxygen evolution reaction

ABSTRACT

Electrochemical water splitting is an environmentally benign technology employed for H_2 production; however, it is critically hampered by the sluggish kinetics of the oxygen evolution reaction (OER) at the positive electrode. In this work, nitrogen-doped carbon-coated CoFe electrocatalysts were synthesized via a three-step route comprising (1) hydrothermal reaction, (2) *in-situ* polymerization of dopamine and (3) carbonization. The effect of carbonized polydopamine on the overall physicochemical properties and electrochemical activity of CoFe catalysts was systematically studied. By controlling and optimizing the ratio of $CoFe_2O_4$ and dopamine contents, a transformation of the $CoFe_2O_4$ structure to CoFe alloy was observed. It was found that $CoFe/NC_{30\%}$ (prepared with 30% dopamine) exhibits an excellent catalytic activity towards OER. A small overpotential of 340 mV was required to generate a current density of 10 mA cm^{-2} in a 1.0 M KOH electrolyte. More importantly, the $CoFe/NC_{30\%}$ catalyst reflected exceptional durability for at least 24 h. This research sheds light on the development of affordable, highly efficient, and durable electrocatalysts for OER.

* Corresponding authors.
E-mail addresses: mmartinez@icp.csic.es (M.V. Martínez-Huerta), mlazaro@icb.csic.es (M.J. Lázaro).

https://doi.org/10.1016/j.jcis.2022.06.005
0021-9797/

1. Introduction

Due to the ever-growing energy demand and environmental deterioration, innovating and developing efficient and viable energy conversion and storage systems is indispensable. Electrochemical water splitting driven by electricity is one of the most promising strategies to store surplus renewable energy in the form of hydrogen [1–3]. It has captivated remarkable attention because of its high cleanliness and environmental friendliness. Water splitting comprises two half-reactions: hydrogen evolution reaction (HER) and oxygen evolution reaction (OER) [4,5]. These two half-reactions are kinetically slow, demanding a certain overpotential to derive the reaction process. Predominantly, the efficiency of water splitting is precluded by the OER, which requires high overpotential originating from the multi-electron/proton couple reaction [6,7]. Therefore, developing and using an electrocatalyst is crucial to expedite the reaction. At present, the state-of-the-art precious metal based electrocatalysts (e.g., RuO_2 or IrO_2) show good catalytic activity towards OER. However, their scarcity and unaffordable cost obstruct this technology from a sustainable large-scale application [8–11]. Hence, developing an affordable and chemically stable OER electrocatalyst with splendid activity and efficiency is vital for the development of water splitting systems.

In recent years, earth-abundant transition metals, chiefly Ni, Co, Fe, Cu, and Mn-based oxides, alloys, phosphides, sulfides, and hydroxides, have been demonstrated as the most potential electrocatalysts for OER because of their abundant reserves, low cost and considerable electrochemical activity, and stability [9,12–18]. Compared with single metal oxides, a myriad of studies revealed that bimetallic oxides and alloys of CoFe [19,20], NiCo [21,22], and NiFe [23] have superior catalytic activity towards OER electrocatalysis due to the different redox potential, synergetic effect, adjustable electronic structure, and structural ordering triggered by the dissimilarity of the lattice strain [20,24] The combination of two transition metals has recently attracted prodigious attention for oxygen electrodes due to their low cost, metal–metal solid coordination, and remarkable stabilization compared to their monometallic counterparts [25]. However, the electrochemical performance of the most reported bimetallic-based electrocatalysts is unsatisfactory for sustainable water splitting applications. This is caused by the fact that bimetal oxides and alloys possess low surface area, poor electrical conductivity, and the tendency of particle aggregation during preparation and dissolution during the electrolysis rigorously affects the performance.

One of the best strategies to circumvent these concerns is to integrate bimetals with carbon materials such as graphene, carbon nanotube, carbon nanofiber etc., to promote their conductivity and electrocatalytic stability and also facilitate the charge transfer of the hybridized system, thus boosting the overall OER performance [11,23,26]. Carbon materials are an interesting option to disperse metals, preventing the nanoparticles' dissolution and aggregation, minimizing the electrical resistance, and increasing the density (or number) of active sites [20]. Besides, integrating heteroatoms such as N into carbon can augment electrical conductivity and modify the electronic structure of the carbon matrix [26]. The nitrogen dopant promotes the catalytic activity of materials by inducing a relatively more positive charge for neighboring carbon atoms, which is essential to expedite the adsorption of intermediate reactants. The combination of N-doped carbon and metal oxides/alloys results in a favorable bond due to the high affinity of nitrogen toward the metal, which can remarkably stimulate interfacial electron transfer between the surface of the electrocatalyst and the intermediate reactants [27]. Nowadays, bimetallic formulations encapsulated in N-doped carbon-based materials are evolving as a new class of promising electrocatalysts for OER due to their low-cost and substantial catalytic activity [28].

Polydopamine (PD) is reported as an ideal carbon source and surface functionalizing agent among the various carbon sources [29]. PD is a peculiar biodegradable biopolymer characterized by its excellent affinity to almost all solid materials (such as transition metals) via chemical binding stemming from its different functional groups (e.g., it contains catechol, imine, amine…). Besides, it is an eco-friendly and cost-effective carbon source, which endows plenty of prospects to modify materials [30–32]. PD can easily be converted to a peculiar type of carbon, nitrogen-doped graphitized carbon, at high pyrolysis temperature. The graphitization of carbon enhances the electrical conduction of the materials, and nitrogen doping promotes electron transport which further boosts the electrical conductivity [31]. Moreover, it was revealed that PD has a particular tendency of adsorption towards Fe and Co transition metals [33]. Considering the above merits, integrating the virtue of PD with the spinel-phase bimetallic oxide (such as $CoFe_2O_4$) could be a rational approach to obtaining a satisfactory electrocatalyst for OER with superb activity and noticeable structural stability. Substantial works have reported that $CoFe_2O_4$ integrated with carbon material (such as graphene or nanotube) exhibits excellent performance [11,34–37]. Complex multistep processes are generally used in these works, which are energy and time-consuming synthesis procedures to integrate catalytically active metals into carbon support [26]. Hence, it is crucial to find an economical and facile synthesis procedure to combine bimetals with conductive carbon substrates. In literature, few research works have been devoted to synthesizing composite Co, Fe, and CoFe bimetallic catalysts modified by dopamine for oxygen reduction and evolution reactions for different applications [28,33,38,39]. However, to the best of our knowledge, there is no report on studying the electrocatalytic activity of composite electrocatalysts prepared by integrating $CoFe_2O_4$ and dopamine for water oxidation.

Herein, we report the synthesis and electrocatalytic characterization of composite materials consisting of nitrogen-doped carbon-coated CoFe (hereafter: CoFe/NC) bimetals as active and robust electrocatalysts for alkaline OER. The composite materials are prepared by a facile hydrothermal route and in situ polymerization of dopamine on the surface of $CoFe_2O_4$ followed by carbonization at high temperature. The effect of carbonized polydopamine on the structural and electrocatalytic activity of the CoFe catalysts was systematically scrutinized. The as-prepared electrocatalysts were characterized by physicochemical and electrochemical techniques, including X-ray diffraction (XRD), electron microscopy, inductively coupled plasma (ICP), X-ray photoelectron spectroscopy (XPS), and a three-electrode system for electrochemical analysis (OER). Our experimental findings indicate that dopamine promotes the transformation of $CoFe_2O_4$ spinel structure towards the CoFe/N-doped carbon catalyst, which significantly stimulates the OER performance. Integration of an optimized dopamine (30 wt%) content with $CoFe_2O_4$, results in a CoFe alloy catalyst with a low overpotential of 340 mV at 10 mA cm^{-2} and a Tafel slope of 77 mV dec^{-1}, which is comparable to the activity of the benchmark IrO_2 catalyst.

2. Experimental

2.1. Materials and reagents

Cobalt (II) nitrate hexahydrate (Alfa Aesar), iron (III) nitrate hydrate (Riedel de-Haen, Sigma Aldrich), dopamine hydrochloride (MW = 189.64 g/mol, Sigma Aldrich), tris(hydroxymethyl aminomethane) (ACS, reagent ≥99.8%%, MW = 121.14 g/mol, Sigma

Aldrich), potassium hydroxide (Analytical grade, Fischer scientific), potassium hydroxide pellets, 85% (Alfa Aesar), ultrapure water (Mili-Q, 0.055 μS/cm, SIEMENS), Nafion ®Perfluorinated resin solution (5 wt%, Sigma Aldrich), commercial IrO_2 powder, 99 % (Alfa Aesar). All the reagents used in this study were analytical grade and were used without further modification.

2.2. Synthesis of electrocatalysts

First, a spinel oxide of $CoFe_2O_4$ was prepared by hydrothermal method[40]. Briefly, $Fe(NO_3)_3{\cdot}9H_2O$ (7.6 mmol) and $Co(NO_3)_2{\cdot}6H_2O$ (3.8 mmol) were dissolved in 30 mL of deionized water (stirred for 30 min), followed by the addition of 30 mL of a 2 M KOH aqueous solution and stirred at room temperature for 2 h. The prepared mixture was transferred into a Teflon-lined stainless steel autoclave and maintained at 180 °C for 22 h. The autoclave was removed from the oven and cooled naturally to room temperature, and the product was washed with ethanol and water and dried at 60 °C overnight. The cobalt iron oxide composites were prepared through a simple polymerization reaction of dopamine with $CoFe_2O_4$ followed by carbonization. In this case, 0.4 g of the prepared $CoFe_2O_4$ was dispersed in 50 mL tris(tris(hydroxymethyl) aminomethane)-buffer (Tris-HCl, 10 mM, pH 8.5) by sonication for 30 min to form a suspension. Then, the necessary amount of dopamine hydrochloride was added to the above mixture in order to vary the concentration relative to the spinel $CoFe_2O_4$ (10, 20, 30, and 40 wt%). The mixture was stirred at room temperature for 24 h to polymerize the dopamine. Next, the product was centrifuged, washed with deionized water, and dried at 60 °C overnight. Finally, the as-prepared product was calcined at 800 °C for 1 h at a heating rate of 5 °C/min under N_2 atmosphere to obtain CoFe/NCx, where x stands for the mass fraction of dopamine hydrochloride relative to $CoFe_2O_4$.

2.3. Physicochemical characterization

The weight percentages of the metals were acquired by inductively coupled plasma atomic emission spectroscopy (ICP-AES) in a Xpectroblue-EOP-TI FMT26 (Spectro). The X-ray diffraction (XRD) analyses were carried out in a Bruker D8 Advance diffractometer with Cu Kα radiation operating at 1600 W. Scanning electron microscopy (SEM) studies were also obtained in a SEM Hitachi 3400 N microscope. Chemical analyses were performed by energy-dispersive X-ray (EDX) spectroscopy with an EDX Röntec XFlash Si (Li) coupled to SEM. Ultra-high resolution imaging (HRTEM) analysis was made in Titan Cube (CEOS Company). X-ray photoelectron spectroscopies (XPS) were acquired on a Kratos AXIS Supra system equipped with a hemispherical electron energy analyzer operating with mono Al Kα (1486.7 eV) at 120 W (8 mA/15 kV. Analysis area = 2 × 1 mm), base pressure 10^{-9} Torr. A high-resolution spectrum was acquired with pass energy of 20 eV and 0.1 eV step. The C 1s line at 284.6 eV was used to correct all XPS spectra. CasaXPS software was used to perform peak fitting and quantification, and Shirley-type background was employed for all peaks. Gaussian/Lorentzian (GL: 30%) line shapes were used for each component.

2.4. Electrochemical measurements

All electrochemical performance measurements were conducted in a three-electrode system controlled by a potentiostat/galvanostat AUTOLAB PGSTAT302 at room temperature. A high surface glassy-carbon rod, a reversible hydrogen electrode (RHE), and a rotating ring disk electrode (RRDE) with a glassy carbon disk (diameter = 5 mm) and a Pt ring were employed as counter, reference, and working electrode, respectively. The overpotential (η) value was determined by $\eta = E_{RHE} - 1.23$ V. All the applied potentials were corrected by the ohmic drop considering iR_s, where R_s is the series resistance of the system. An ink of 20 μL was deposited drop by drop cast onto the glassy carbon disk to prepare the working electrode. The ink was prepared by dispersing and sonicating 5.4 mg of catalyst in 518 μL isopropanol/water (1: 3) with 22 μL of Nafion solution. A commercial IrO_2 catalyst was also deposited on the working electrode following the same procedure for comparison purposes. A 1 M KOH aqueous solution was used as a supporting electrolyte throughout the experiment. All OER measurements were conducted in a N_2-saturated 1 M KOH aqueous solution. In the beginning, cyclic voltammetry (CV) was performed at a scan rate of 100 mV s^{-1} in the potential range of 0.05–1.0 V vs. RHE for about 50 cycles. Besides, three CV were carried out at a scan rate of 20 mV s^{-1} in the potential range of 0.05–1.1 V vs. RHE. Before recording OER polarization curve, 10 CV were carried out at a scan rate of 5 mV s^{-1} in the potential range of 1.1–1.8 V vs. RHE at 1600 rpm. The electrochemically active surface area (ECSA) of the electrocatalysts was scrutinized from the electrochemical double-layer capacitance (C_{dl}) by performing CV from 1.1 to 1.23 V vs. RHE at a scan rate of 20 mV s^{-1}. Electrochemical impedance spectroscopy (EIS) was measured at 1.6 V vs. RHE in the frequency range of 100 kHz to 0.01 Hz at a 5 mV amplitude (rms). Chronopotentiometry (at current density (j) of 10 mA cm^{-2}) was employed to evaluate the long-term stability of the most active composite electrocatalyst.

3. Results and discussion

3.1. Synthesis and structural characterization of electrocatalysts

The synthesis process for the nitrogen-doped carbon-coated CoFe electrocatalysts is illustrated in Scheme 1. The typical synthesis procedure employed in this framework is based on three consecutive step-reactions. First, $CoFe_2O_4$ spinel oxide was prepared by facile hydrothermal route; second, polymerization of dopamine on the surface of the prepared spinel oxide was performed; and third, the carbonization process was implemented at 800 °C for one hour under N_2 atmosphere, leading to the formation of N-doped carbon-coated CoFe. For comparison, different mass ratios of dopamine were mixed with the pristine $CoFe_2O_4$ in order to investigate the optimum amount.

XRD was used to investigate the crystalline structure of the prepared electrocatalysts. As shown in Fig. 1, a single phase of spinel-type $CoFe_2O_4$ (JCPDS, #22-1086) was successfully prepared by the hydrothermal route for the pristine CoFe. The sharp diffraction peaks at 2θ of 30.25°, 35.63°, 37.27°, 43.31°, 53.74°, 57.29°, 62.9°, 74.5°, and 90.24° correspond to (2 0 0), (3 1 1), (2 2 2), (4 0 0), (4 2 2), (5 1 1), (4 4 0), (5 3 3), and (7 3 1) crystal planes of face-centered cubic (FCC) structure of $CoFe_2O_4$ [26,41]. Upon incorporating 10% of dopamine into the pristine $CoFe_2O_4$, the same spinel crystal structure prevails but contains few impurities of Fe metal. The peaks at 2θ = 45.04°, 65.6°, and 83.1° are related to (1 1 0), (2 0 0) and (2 1 1) crystalline planes of cubic iron metal (JCPDS, #65-4899). However, incorporating a higher dopamine content immensely alters the crystal structure, resulting in CoFe alloys and iron oxide. Specifically, the catalyst with a dopamine content greater than or equal to 20% presents a crystal structure of CoFe alloy with traces of FeO or Fe_3O_4. The diffraction peaks of CoFe/$NC_{20\%}$, CoFe/$NC_{30\%}$, and CoFe/$NC_{40\%}$ at 2θ of 44.88°, 65.31°, 82.74° and 99.48° are related to the (1 1 0), (2 0 0), (2 1 1) and (2 0 2) planes of the crystalline cubic CoFe alloy (JCPDS, #49-1568) [42]. The diffraction peaks of CoFe/$NC_{20\%}$ and CoFe/$NC_{30\%}$ observed at 2θ of 36.343°, 42.2° and 61.2° are related to (1 1 1), (2 0 0), and (2 2 0) planes of crystalline cubic FeO (JCPDS, #46-1312).

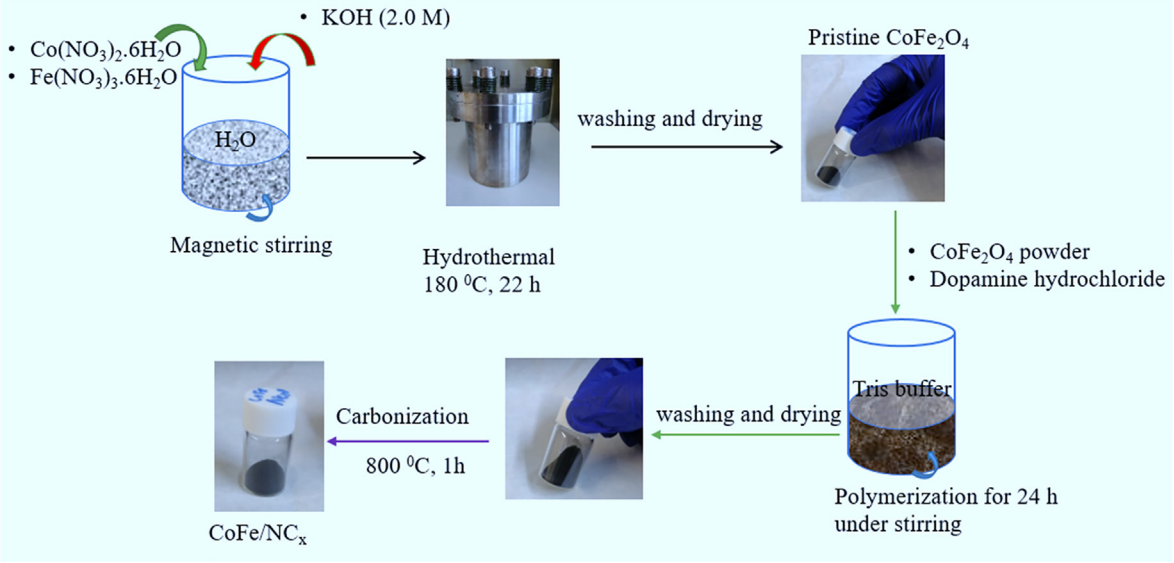

Scheme 1. Schematic illustration of the synthesis process of pristine $CoFe_2O_4$ and $CoFe/NC_x$ composite electrocatalysts.

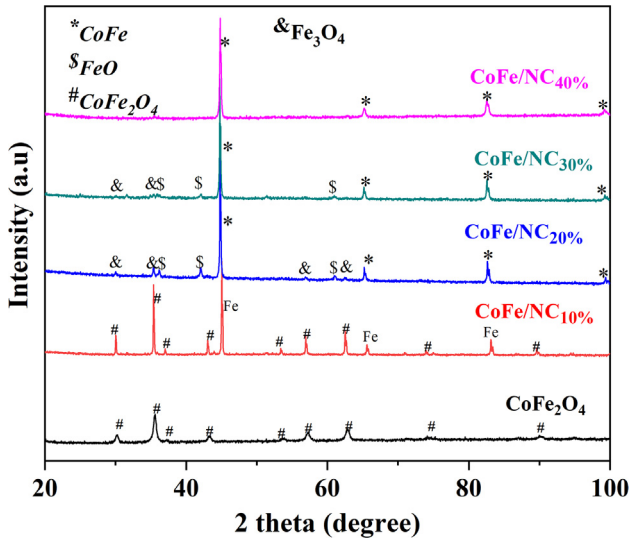

Fig. 1. XRD patterns of the as-prepared electrocatalysts.

Moreover, $CoFe/NC_{20\%}$ and $CoFe/NC_{30\%}$ contain additional phase of Fe_3O_4 (JCPDS, #82-1533), reflecting a multiphase structure formation by using these dopamine contents. The percentages of CoFe alloys and oxides for the sample in which CoFe alloy appeared are also calculated to elucidate the ratio of CoFe alloy and oxides. As shown in **Table S1**, the ratio of CoFe alloy and oxides for the $CoFe/NC_{20\%}$ and $CoFe/NC_{30\%}$ samples was found to be 9.34 and 11.47, respectively, while $CoFe/NC_{40\%}$ sample encompasses 100% of CoFe alloy. From the diffractograms, no prominent diffraction peak of graphitic carbon was identified, indicating a low degree of crystallinity of carbon, which was further confirmed by Raman spectroscopy.

Polydopamine (PD) has the ability to form complexes with many transition metals, including Co^{2+} and Fe^{3+}, since it possesses various functional groups (e.g., catechol, imine, and amine). Because of its strong and versatile binding ability, dopamine is an imperative carbon source to functionalize and transform various materials. Notably, thanks to the catechol group that assists PD in coordinating with Co^{2+} and Fe^{3+}, combining different dopamine contents with metal ions could ultimately offer various structures, morphologies, and functionalities. The amount of PD coated on the surface of metals alters the overall crystallinity phase [31,43]. The XRD pattern (Fig. 1) showed an apparent phase transformation from $CoFe_2O_4$ spinel oxide into CoFe alloy, depending on the amount of dopamine mixed with the spinel oxide precursor. The CoFe alloy formation at high dopamine content could be ascribed to the ability of dopamine to form a complex with Co^{2+} and Fe^{3+} and reduce these metal species, since the reactivity of PD relies on the concentration of the functional group, pH, and carbonization temperature. The active catechol group in PD oxidizes into the quinine group, releasing electrons and protons, and it was demonstrated that Fe^{3+} could oxidize catechol to form quinine species [31]. Increasing dopamine content enriches the concentration of the catechol group, which potentially plays a crucial role in transforming the crystalline phase. Hence, it is presumed that diverse functional groups in the PD play a crucial role in transforming the $CoFe_2O_4$ into CoFe alloy upon changing the content of PD and carbonizing at high temperatures. In summary, the $CoFe_2O_4$ coordinated with PD could form carbon-coated CoFe alloy upon mixing with high content of PD followed by thermal treatment.

SEM and TEM were used to examine the morphology and structure of the prepared electrocatalysts (Fig. 2, **Figures S1-S3**). Fig. 2 **(a)** presents the SEM image of the pristine $CoFe_2O_4$ electrocatalyst, indicating that the spinel particles are too small to be observed by SEM. In this regard, the TEM image (Fig. 2**(c)**) revealed that the as-prepared pristine $CoFe_2O_4$ contains octahedron-like structure nanoparticles with varying sizes in the range from 3 to 45 nm (average diameter of 9.5 nm). However, incorporating a certain amount of polydopamine into the pristine $CoFe_2O_4$ significantly changes the particle size and morphologies. $CoFe/NC_{10\%}$ sample exhibits a mixture of octahedral-like structure and non-distinct morphology with a larger particle size than the pristine. Relatively larger particles with ostensibly octahedral-like structure and irregular sheet shape can be observed in the other series of catalysts while increasing the dopamine concentration from 10 to 40 % (Figure S2). Trivial change in morphology and phase composition was observed after 20% dopamine incorporation, except that $CoFe/NC_{40\%}$ sample exhibits pure CoFe alloy, as revealed by the XRD (Fig. 1).

The particle size distribution for all electrocatalysts is presented in the supporting information (**Figure S3**). The other composite electrocatalysts show a larger particle size and different

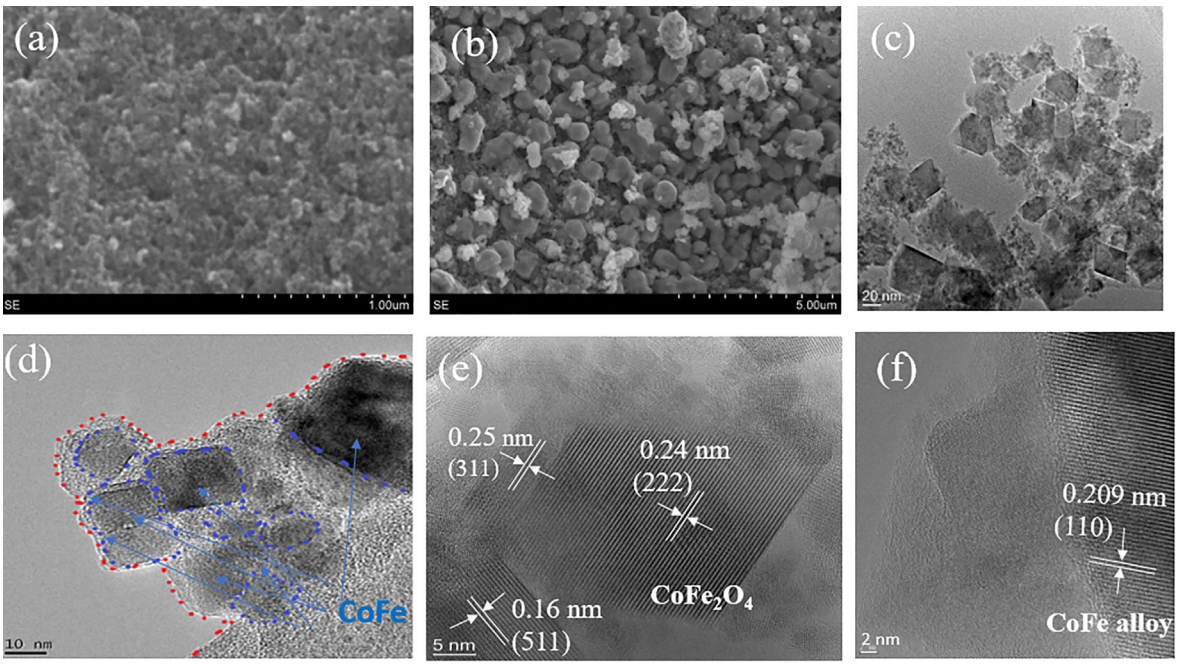

Fig. 2. SEM images of (a) pristine $CoFe_2O_4$, (b) $CoFe/NC_{30\%}$; TEM images of (c) pristine $CoFe_2O_4$, (d) $CoFe/NC_{30\%}$; HRTEM images with and lattice fringe analyses of (e) pristine $CoFe_2O_4$, and (f) $CoFe/NC_{30\%}$ (CoFe alloy).

morphology than the pristine $CoFe_2O_4$ catalyst. The resulting composite materials' particle size increases with increasing dopamine content. Notably, the particle size of $CoFe/NC_{10\%}$ spans from 5 to 30 nm with an average particle size of 16 nm, while the $CoFe/NC_{20\%}$ $CoFe/NC_{30\%}$, and $CoFe/NC_{40\%}$ unveils large particle size with an average of 18, 18.2 and 33 nm, respectively.

Focusing on $CoFe/NC_{30\%}$, the SEM image indicates a larger nanoparticle than the pristine $CoFe_2O_4$ with a tangled and irregular shape (Fig. 2**(b)**). TEM observation displayed in Fig. 2**(d)** reveals that the composite $CoFe/NC_{30\%}$ possesses a mixture of octahedral-like structure and some irregular shape nanoparticles with a larger size ranging from 10 to 50 nm (average diameter of 18.2 nm, **Figure S3**). Many black nanoparticles appear surrounded by an amorphous carbon layer, forming a "core-shell" network structure. These carbon network structures are known to enhance conductivity and expedite mass transfer, thus boosting electrocatalytic activity [44]. Furthermore, the high-resolution TEM (HR-TEM) images disclose several well-resolved lattice fringes for both pristine and composite materials (Fig. 2**(e) and (f)**, respectively). The pristine $CoFe_2O_4$ exhibits some kinds of lattice fringe spacing of 0.24, 0.25, and 0.16 nm, which are assigned to the (2 2 2), (3 1 1), and (5 1 1) planes, respectively, of the cubic structure of the spinel, as shown in Fig. 2**(e)** [45]. Whereas, the HRTEM image of $CoFe/NC_{30\%}$ displays a lattice fringe of 0.209 nm, which corresponds to (1 1 0) crystal planes of CoFe alloy, as shown in Fig. 2 **(f)** [44].

X-ray photoelectron spectroscopy (XPS) analysis was employed to acquire further information on the catalyst surface, including the oxidation state of the different species. It is worth mentioning that the data must be interpreted considering its shortcomings since the oxidation state of the catalyst surface could likely change during the electrochemical reaction process. The XPS results revealed the existence of Co, Fe, and O for all electrocatalysts, and in addition, both N and C were detected in the composite CoFe/NC electrocatalysts (Fig. 3 **and Figure S4**). It is imperative to state that Fe 2p overlaps intensely with the Co LMM Auger peak and Co 2p overlaps strongly with the Fe LMM Auger peak, when the Al Kα X-ray source is used in XPS analysis [46,47]. Specifically, cobalt Auger bands are located at around 698, 713 and 771 eV and iron Auger bands are located at around 784, 834, and 888 eV [48], in which Co LMM (at 713 eV) overlaps with the main Fe 2p peak and Fe LMM (at 784 eV) overlaps with the main Co 2p peak. This impacts for a correct quantitative analysis of the sample's composition. Nevertheless, the XPS analysis result provides information about the surface's composition.

The XPS spectra of Fe 2p (**Figure S4**) display a complex profile with four spin–orbit doublets, including metallic iron, oxidized iron (II and III), and shakeup satellite peaks in the composite samples. Focusing on the $CoFe/NC_{30\%}$, the small first peak at lower binding energy (Fe $2p_{3/2}$ ca. 708.2 eV) is attributed to metallic iron. The two most intense peaks corresponding to Fe $2p_{3/2}$ at ca. 710.5 eV and 713.4 eV are assigned to Fe (II) and Fe (III)/Co Auger band, respectively, while the fourth doublet with higher binding energy is ascribed to satellite peak. The Fe (II) and Fe (III) are attributed to different bonding states of iron, like Fe^{2+}–O/N and Fe^{3+}–O/N bonds, reflecting the presence of inevitable partial surface oxidation due to exposure to air [49]. The binding energy for all elemental species of Fe 2p and Co 2p is provided in **Table S 2**. It is worth mentioning that the iron species' binding energy for the composites show a slightly positive shift, indicating a stronger interaction between Fe and N-doped carbon [5].

Figures S4 (b) shows the XPS high-resolution spectrum of Co 2p, which is fitted with three pairs of spin–orbit doublets and a pair of satellite peaks. In the composite samples, the doublet peak at lower binding energy (Co $2p_{3/2}$ ca. 777.6 ± 1 eV) is attributed to metallic cobalt. The other three doublet peaks at higher binding energy (Co $2p_{3/2}$ ca. 780, ca. 783, and ca. 787 eV) correspond to Co^{3+}, Co^{2+}/Fe Auger band and satellite peaks [44,49], respectively.

The C 1s XPS high-resolution spectra for the CoFe/NC-based electrocatalysts are shown in Fig. 3 **(a).** The high-resolution XPS of C 1s can be resolved into three peaks for all composite electrocatalysts. The peaks at binding energy (BE) of ca. 284.6, 285.9, and 288.1 eV correspond to the carbon bonded to oxygen or nitrogen atoms in the forms C—C, C—N (C—O), and C═O, respectively [50,51]. Moreover, an additional peak at BE ca. 283 eV was observed which is attributed to metallic carbides [52,53]. The

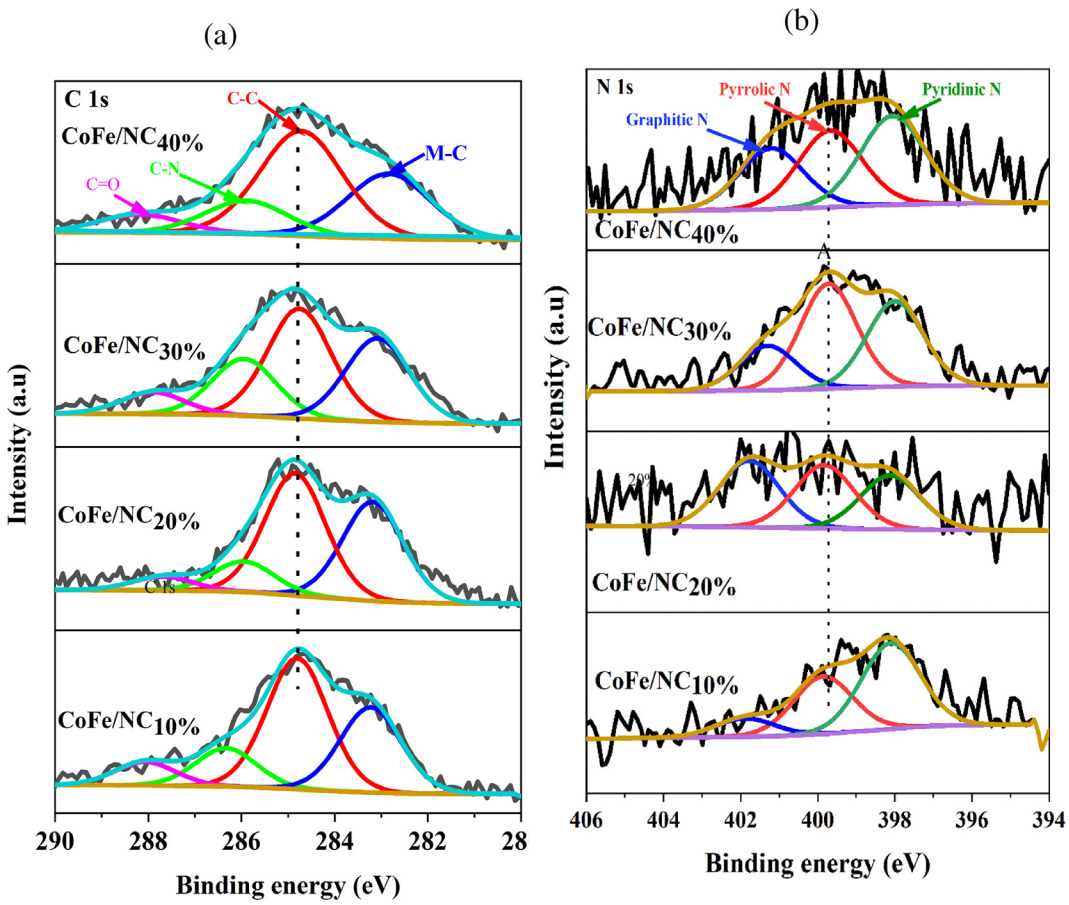

Fig. 3. XPS high-resolution spectra of (a) C 1s, (b) N 1s for all electrocatalysts.

C—N bond further unraveled the existence of nitrogen-doped carbon in the composite. The presence of the N dopant in the carbon structure can alter and promote the electronic structure of carbon, thus enhancing the electron conductivity of the materials [54]. Moreover, the appearance of the carbide in the composte electrocatalyst could partilay contribute to the promoted catalytic activity compare with the pristine $CoFe_2O_4$.

Fig. 3 **(b)** shows the high-resolution N 1s spectra, deconvoluted into various peaks. The peaks at a binding energy of ca. 398, ca. 399, and ca. 401 eV are assigned to pyridine-N, pyrrolic-N, and graphitic-N, respectively [55]. When a nitrogen atom is doped into carbon, the carbon's spin density and charge distribution are altered by the neighboring N dopant, prompting an activation region on the carbon surface [50]. The activated region can be directly involved in the catalytic reaction and promote the catalytic activity.

The metal content of the as-prepared electrocatalysts was investigated by inductively coupled plasma-atomic emission spectroscopy (ICP-AES). The result disclosed that the atomic ratio of the two metals (Fe/Co) is approximately 2 (**Table S3**), which is in good agreement with the stoichiometry of the initial precursors used to synthesize the spinel oxide.

3.2. OER performance measurements

The electrocatalytic activity of the prepared electrocatalysts and IrO_2 were measured in a three-electrode cell with an electrolyte of N_2-deaerated 1 M KOH aqueous solution by CV measurements under a scan rate of 5 mVs^{-1}. Fig. 4**(a)** displays the OER polarization curves of various electrocatalysts (positive-going scan). The pristine $CoFe_2O_4$ electrocatalyst presents an overpotential of 440 mV to derive a current density of 10 mA cm^{-2}. Incorporating carbonized polydopamine into the spinel remarkably alters the overall catalytic activity. To produce the same current density, the composite materials display smaller overpotential (η_{10}): $CoFe/NC_{10\%}$ (360 mV), $CoFe/NC_{20\%}$ (360 mV), $CoFe/NC_{30\%}$ (340 mV) and $CoFe/NC_{40\%}$ (390 mV). Among the various prepared composite electrocatalysts, $CoFe/NC_{30\%}$ was considerably more catalytically active for OER and presented analogous activity compared to the reference electrocatalyst of IrO_2 (η_{10} = 350 mV), as shown in Fig. 4**(a).**

Moreover, aiming to evaluate the reaction kinetics of the various electrocatalysts, the Tafel slope of these electrocatalysts was determined. Tafel slope bears the OER kinetics of each material and is used to assess the rate-determining step (rds). It is worth mentioning that it is crucial to select an appropriate potential or current range in determining the Tafel slope. Tafel slope should be calculated from the range where the currents are generated from the faradic reaction kinetics. Both high potential and low potential windows dramatically affect the Tafel slope value. This is because the inevitable oxygen bubbles block the active sites and increase mass resistance at high potential, and the contribution of the non-faradic capacitive current is significant at low potential; hence, these two extreme conditions should be avoided [56,57]. Tafel slope can be expressed as follows: overpotential $\eta = a + b \log(j)$ [56].where j represents the current density, b means the Tafel slope, and a is constant. Lower values of b reveal a lower increment of overpotential with the increase of current density during the reaction, suggesting faster reaction kinetics for the *rds*. In this work, the selected log (j) range takes into account

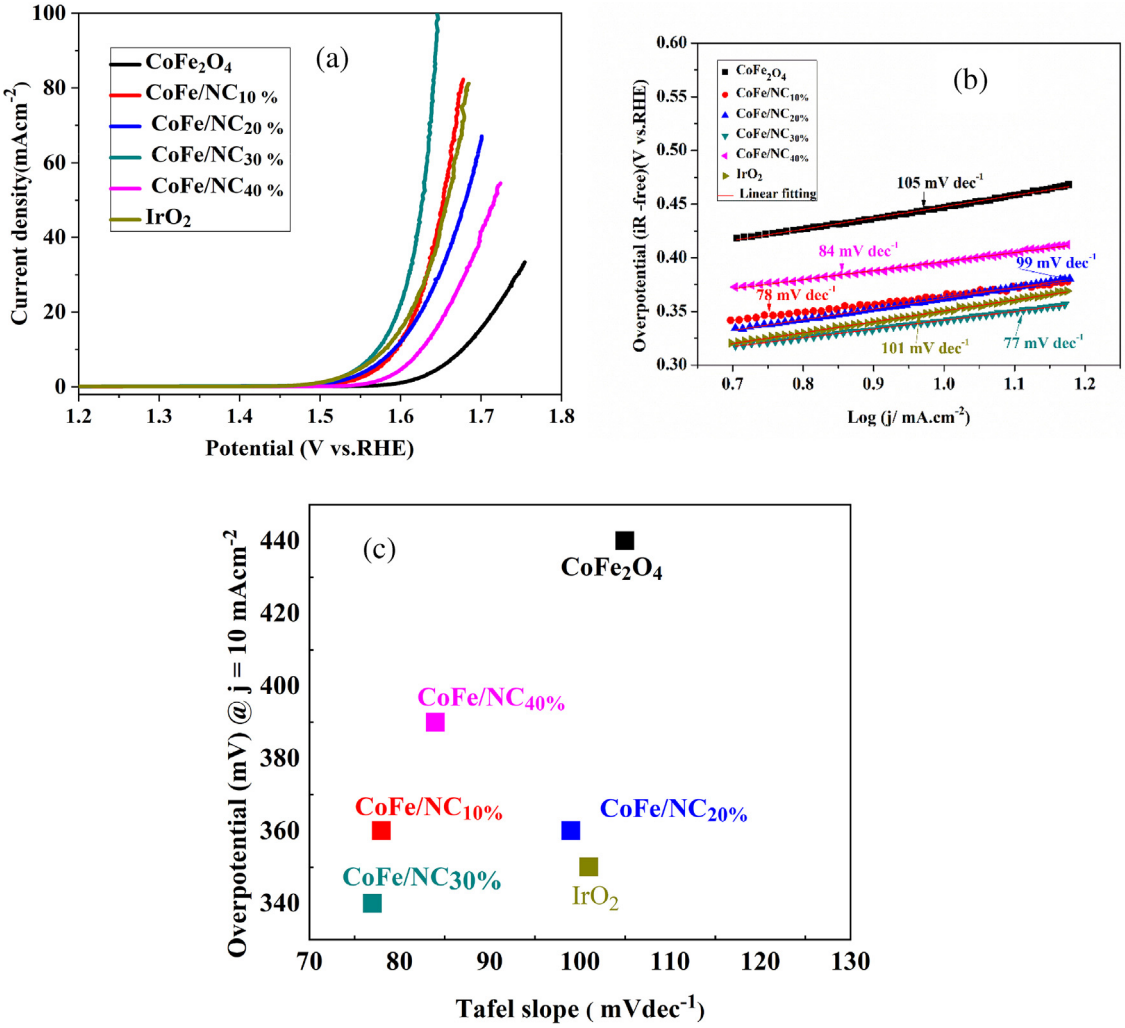

Fig. 4. (a) OER polarization curve of the various electrocatalyst tested in 1.0 M KOH at a scan rate of 5 mV s^{-1}, (b) Tafel plots derived from the OER polarization curve, (c) Overpotential vs. Tafel slope comparison of various electrocatalysts.

the 10 mA cm^{-2} current density, which is used as a benchmark to compare catalysts. As shown in Fig. 4**(b),** there is a remarkable change in the Tafel slope when comparing the pristine $CoFe_2O_4$ and composite electrocatalysts, in which the spinel presents a higher Tafel slope of 106 mV dec^{-1}. In contrast, the composite catalysts of $CoFe/NC_{10\%}$ (78 mV dec^{-1}), $CoFe/NC_{20\%}$ (99 mV dec^{-1}), $CoFe/NC_{30\%}$ (77 mV dec^{-1}), and $CoFe/NC_{40\%}$ (84 mV dec^{-1}) show lower Tafel slopes. It is well documented that OER comprises four sequences of steps with four electron transfer reactions and contains several intermediates such as MO, MOOH (where M is the active site). Many researchers have reported a profound insight on Tafel slope determination for OER in alkaline media [56,57], considering the following reaction mechanism.

$$M + OH^- \leftrightarrow MOH + e^-, \text{ with a Tafel slope of } 120 \text{ mV dec}^{-1} \quad (1)$$

$$MOH + OH^- \leftrightarrow MO^- + H_2O, \text{ with a Tafel slope of } 60 \text{ mV dec}^{-1} \quad (2)$$

$$MO^- \rightarrow MO + e^-, \text{ with a Tafel slope of } 45 \text{ mV dec}^{-1} \quad (3)$$

$$2MO \rightarrow 2M + O_2, \text{ with a Tafel slope of } 19 \text{ mV dec}^{-1} \quad (4)$$

Each step has a corresponding Tafel slope value, highlighting the overall reaction rate. According to the Tafel slope markers above, the pristine $CoFe_2O_4$ electrocatalyst with a Tafel slope of 106 mV dec^{-1} indicates that the reaction determining steps are given by equations (1) and (2). Nevertheless, it could be predominantly determined by the adsorption of the reacting species of OH^- onto the spinel oxide surface (equation (1)). For the composite-based electrocatalysts, the Tafel slope was lower than the pristine $CoFe_2O_4$ but still determined by both reaction mechanisms of equations (1) and (2). In this case, the decrease of Tafel slope can be associated with the selective adsorption of some of the intermediates species during the different reaction steps [57,58]. The lower Tafel slope of the composite electrocatalysts (principally $CoFe/NC_{10\%}$ and $CoFe/NC_{30\%}$) in the selected region of current density reflects low overpotential loss. This can stem from the augmented bond strength for OH^- adsorption on the catalyst surface, which expedites the electron reaction; thus, a high current density can be achieved at a relatively lower overpotential.

Materials that exhibit low overpotential and Tafel slope are regarded as ideal electrocatalysts for OER. Fig. 4**(c)** summarizes the overpotential at 10 mA cm^{-2} (η_{10}) vs. Tafel slope of the various electrocatalysts, which is helpful to captivate the electrochemical discrepancy among the samples. Among the investigated catalyts,

$CoFe/NC_{30\%}$ is located at the left bottom of the graph, thus presenting the lowest Tafel slope and overpotential, demonstrating its good electrochemical performance for OER.

Exchange current density (j_0) is also an important parameter to evaluate the catalytic efficiency of materials. The exchange current density reveals the intrinsic rate of electron transfer kinetics between the electrode and reactants at zero overpotential. It is directly proportional to the active catalytic area. Larger exchange current density usually indicates a faster reaction and a suitable electrocatalyst for the desired response [57,59]. The magnitude of the current exchange density was determined from the Tafel plot (log j vs. E) by extrapolating the linear correlation to $\eta = 0$. Table 1 summarizes the calculated electrokinetic parameters of OER for the various electrocatalysts. The polydopamine-modified CoFe exhibited higher exchange current density, signifying enhanced intrinsic catalytic activity. Both $CoFe/NC_{30\%}$ and $CoFe/NC_{10\%}$ present a comparable Tafel slope. The value of the exchange-current density of $CoFe/NC_{30\%}$ was determined to be 5.7×10^{-2} mA cm^{-2}, which is more than two-fold greater than that of $CoFe/NC_{10\%}$. This result reveals that $CoFe/NC_{30\%}$ retains a larger active specific surface area, which is more favorable to the enhanced catalytic activity. It is noteworthy to mention that $CoFe/NC_{20\%}$ displays a higher exchange current density of the same order of magnitude than IrO_2. Still, these two catalysts exhibit a higher Tafel slope, which results in slower kinetics at practical overpotential.

The above electrochemical results demonstrate that an optimum amount of polydopamine is imperative to achieve a satisfactory electrocatalyst. A carbon layer that uniformly surrounds or wraps the entire surface of CoFe nanoparticles could lead to the formation of the desired electrocatalyst with good conductivity and activity. On the one hand, a low carbon content may not fully cover the entire CoFe nanoparticle, leading to a non-uniform coating of the active metals. Such materials might exhibit deficient electronically conducting networks. On the other hand, a high amount of carbon would diminish the content of the electroactive materials. It could also possibly mask the electroactive materials impacting the contact between the active site and electrolyte, increasing the polarization resistance, thus negatively influencing the electrocatalytic activity. Hence, the above OER test results reveal that $CoFe/NC_{30\%}$ displays promising electrocatalytic activity among all samples, owing to the appropriate content of PD integrated with CoFe active materials. Such an optimum combination of carbon and active materials aids in lowering the polarization resistance of the electrocatalyst and the diffusion and mass transport of electrolyte ions, leading to improved electrocatalytic performance.

The electrocatalytic activity of the material is highly controlled by the number of active sites exposed and the intrinsic catalytic activity of each site [60]. Hence, it is important to estimate the actual electrochemically active surface area of the prepared electrocatalyst. Electrochemical surface areas (ECSAs) were further used to study the activity difference of the as-prepared electrocatalysts. The ECSAs of the electrocatalysts can be determined from their electric double-layer capacitance (C_{dl}) using cyclic voltammetry. In literature, the standard CV techniques are generally employed to investigate the capacitance on a material surface. The ECSAs of the prepared electrocatalysts were determined according to ref. [56]. As shown in Fig. 5**(a)**, the specific capacitance value for the pristine $CoFe_2O_4$, $CoFe/NC_{10\%}$, $CoFe/NC_{20\%}$, $CoFe/NC_{30\%}$, and $CoFe/NC_{40\%}$ is determined to be 0.22, 0.91, 0.38, 1.94 and 0.87 F g^{-1}, respectively. A catalyst with higher C_{dl} has a higher ECSAs value since C_{dl} is linearly proportional to the ECSA [56]. The $CoFe/NC_{30\%}$ electrocatalyst with the highest C_{dl} (1.94 F g^{-1}) value of the series reveals that the tailored nitrogen-doped carbon has remarkably upgraded ECSA, positively influencing the overall OER catalytic activity. The following equation was applied to calculate the ECSA magnitude for each sample explicitly; $ECSA = C_{dl}/C_s$, where C_s is the specific capacitance and is usually assumed to be 0.04 mF cm^{-2} in 1.0 M KOH electrolyte [61,62]. The specific capacitance and ECSA values for the various electrocatalysts are shown in **Table S4**. To evaluate the inherent activity of the active site, we have plotted ECSA normalized polarization curve. As shown in **Figure S5**, the intrinsic activity of $CoFe/NC_{20\%}$ is higher than that of $CoFe/NC_{30\%}$, which discloses a reversed profile trend compared to the geometric area normalized polarization curve (Fig. 4**a**). Such circumstances reflect that the improved $CoFe/NC_{30\%}$ mainly originates from the increased ECSA. Compared to $CoFe/NC_{30\%}$ sample, the $CoFe/NC_{20\%}$ sample showed an apparent higher ECSA normalized current density (j_{ECSA}). This could be due to the excessive active sites assembled on a small surface leading to low efficiency of the active site. As a result, $CoFe/NC_{20\%}$ exhibits relatively higher j_{ECSA} of OER but unfavorable OER normalized by the geometric area of the electrode. On the other hand, the large ECSA and favorable geometric normalized OER activity of $CoFe/NC_{30\%}$ uncover that many active sites are substantially distributed on the surface, and atomic utilization is efficiently enhanced, promoting the overall OER activity. Such phenomena have also been reported in literature [63,64].

The mass activity was also considered to determine the performance of the as-prepared electrocatalysts. It portrays the current response normalized by the loaded amount of the electrocatalyst. The mass activity (A g^{-1}) was calculated according to the following equation: mass activity = j/m [65], where j (mA cm^{-2}) is the current density at a given overpotential and m is the mass loading (1 mg cm^{-2}) of catalyst on the glassy carbon. As shown in Fig. 5 **(b)**, the $CoFe/NC_{30\%}$ catalyst exhibits a mass activity of 10 A g^{-1} at an overpotential of 340 mV, which is much higher than the other electrocatalysts. This result attests that $CoFe/NC_{30\%}$ electrocatalyst is highly active for oxygen evolution.

Moreover, the Faradaic oxygen efficiencies for $CoFe/NC_{30\%}$ electrocatalyst were determined to estimate the OER contribution to the overall measured current from the disk. It is defined as follows. Faradaic oxygen efficiency $\varepsilon = (4/n_{ORR}) \cdot j_{ring}/(N \cdot j_{disk})$ [66], where $(4/n_{ORR})$ represents the ratio of the number of electrons transferred in the OER at the disk electrode and in the ORR at the ring electrode ($n_{ORR} = 4$ for the Pt ring), N is the RRDE collection efficiency, and j_{ring} and j_{disk} are the ring and disk currents, respectively.

The RRDE collection efficiency N (0.248) was determined from the ring and disk current ratios in 10 mM $K_3[Fe(CN)_6]$ + 1 M $NaNO_3$ solution. This value is in good agreement with the theoretical value given by the manufacturer (0.25). A constant ring potential of 0.4 V vs. RHE was chosen for the RRDE studies of the OER, which is enough to reduce the oxygen evolved from the disk. Fig. 6**(a)** shows the disk and ring current measurements for the best composite electrocatalyst ($CoFe/NC_{30\%}$), and Fig. 6**(b)** presents the values of Faradaic oxygen efficiencies of $CoFe/NC_{30\%}$ at different potentials. At 1.51 V vs. RHE applied potential, the highest Faradaic efficiency (83%) was obtained and gradually decreased to 48% when the applied disk potential increased to 1.55 V vs. RHE, as shown in Fig. 6**(b)**. The decreasing Faradaic efficiency could be attributed

Table 1
Summary of electrokinetic parameters of OER for the various electrocatalysts.

Electrocatalyst	η –iR-free @ 10 mA cm^{-2}(mV)	j_0 (mA cm^{-2})	Tafel slope (mV dec^{-1})
$CoFe_2O_4$	440	5.4×10^{-4}	105
$CoFe/NC_{10\%}$	360	2.0×10^{-4}	78
$CoFe/NC_{20\%}$	360	2.4×10^{-3}	99
$CoFe/NC_{30\%}$	340	5.7×10^{-4}	77
$CoFe/NC_{40\%}$	390	2.0×10^{-4}	84
IrO_2	350	3.4×10^{-3}	101

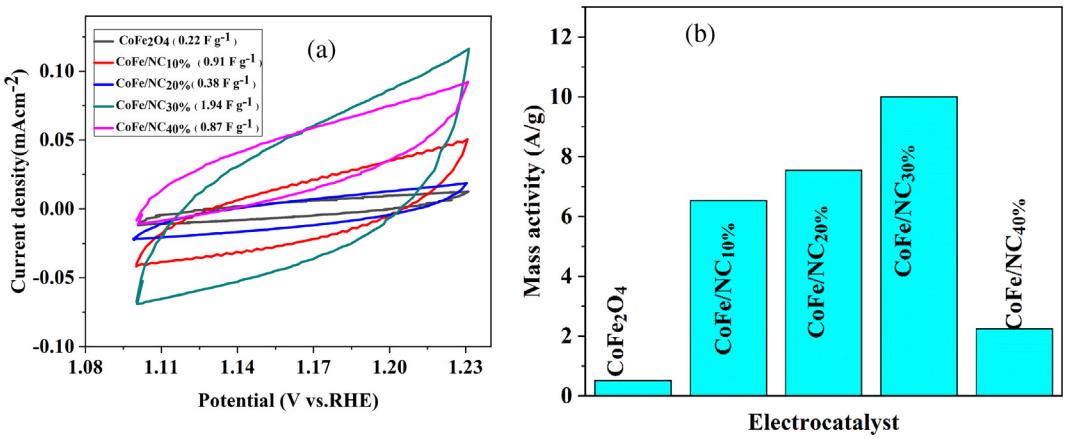

Fig. 5. (a) Cyclic voltammograms of various electrocatalysts measured in 1 M KOH at a scan rate of 20 mV s^{-1}. The measurement was conducted using RDE in idle mode. The specific capacitance values for the corresponding electrocatalyst are displayed in the legend, determined according to the ref. [56], and (b) plot of mass activity of the different electrocatalysts calculated at an overpotential of 340 mV.

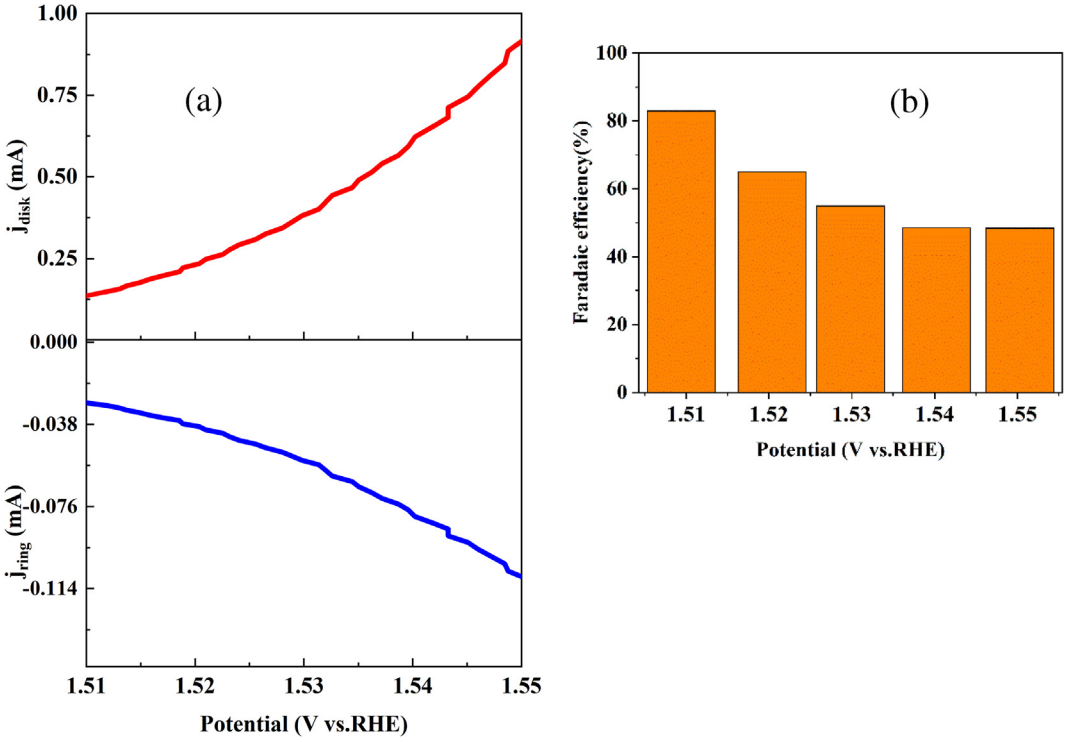

Fig. 6. (a) Disk and ring currents of $CoFe/NC_{30\%}$ catalyst deposited on RRDE plotted as functions of the applied disk potential. (b) Profile of faradaic oxygen efficiencies of $CoFe/NC_{30\%}$ electrocatalyst in 1 M KOH at 1600 rpm under N_2 saturation.

to the undissolved oxygen bubbles that evolve at relatively high applied disk potential. Apparently, substantial bubbles were generated at high potentials that could discharge to the electrolyte without having much contact in the ring since the Pt ring electrode cannot collect the majority of the oxygen in the gas bubbles. Hence, the Faradaic efficiency achieved at relatively low applied disk potential (83%) is dominantly ascribed to the OER rather than the other non-OER reaction such as carbon oxidation, oxidation of nanoparticles etc. This could be more representative of the OER efficiency of the $CoFe/NC_{30\%}$ catalyst.

Electrochemical impedance spectroscopy (EIS) was measured to investigate the reaction kinetics at the electrode/electrolyte interface. It is an essential analytical, diagnostic tool that assists in evaluating various resistances related to the charge transfer process in the electrical double layer. It helps estimate the charge transfer resistance (R_{ct}) attributed to the reaction kinetics and series resistance (R_s) mainly caused by ion conduction at the electrolyte [56]. The OER process is remarkably related to its surface's charge transfer resistance (R_{ct}). Materials that exhibit lower charge transfer resistance are favorable for OER. Fig. 7 shows the Nyquist plot of the different electrocatalysts, measured at 1.6 V vs. RHE in 1 M KOH solution and 1600 rpm. The corresponding charge transfer resistance (R_{ct}) and solution resistance (R_s) for all samples determined from EIS measurement are shown in **Table S5**. The value of R_{ct} for the as-prepared electrocatalyst was determined to be as follows: pristine $CoFe_2O_4$ (96.4 Ω cm^2), $CoFe/NC_{10\%}$ (3.47 Ω cm^2), $CoFe/NC_{20\%}$ (4.6 Ω cm^2), $CoFe/NC_{30\%}$ (1.48 Ω cm^2), and $CoFe/NC_{40\%}$ (62.7 Ω cm^2). As it is apparent, the $CoFe/NC_{30\%}$ reveals the lowest

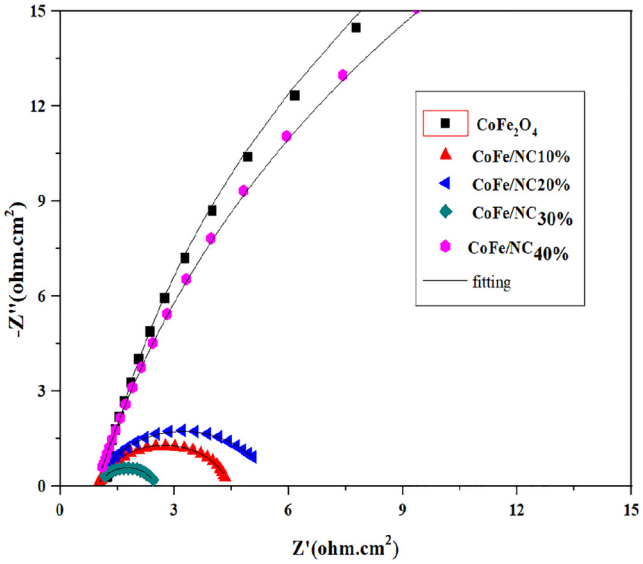

Fig. 7. EIS spectra of the pristine CoFe and CoFe/NC composite electrocatalysts measured at 1.6 V vs. RHE in a 1.0 M KOH aqueous solution.

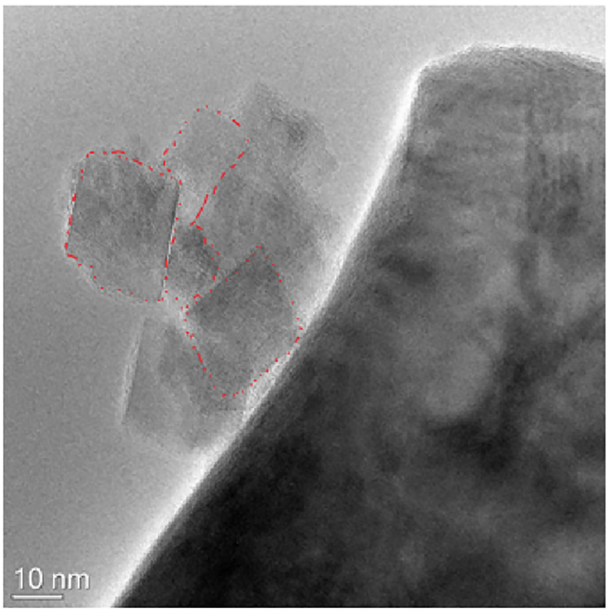

Fig. 9. TEM image of $CoFe/NC_{30\%}$ catalyst after stability measurement.

R_{ct} (1.48 Ω.cm^2) among all the electrocatalysts, demonstrating its prompt charge transfer and favorable reaction kinetics for OER [67], which is consistent with the OER polarization curve.

Apart from the activity, long-term durability is another imperative parameter to evaluate electrocatalyst for extensive large-scale applications. The long-term durability experiment of $CoFe/NC_{30\%}$ for OER was conducted by chronopotentiometry (CP). As shown in Fig. 8**(a)**, the $CoFe/NC_{30\%}$ electrocatalyst displayed outstanding durability at a constant current density of 10 mA cm^{-2} tested in a 1 M KOH electrolyte. The $CoFe/NC_{30\%}$ curve showed a constant potential without a pronounced increase of potential after 24 h continuous measurements, demonstrating its excellent catalytic durability under OER conditions. Besides, the OER polarization curve of $CoFe/NC_{30\%}$ (Fig. 8**(b)**) after the 24 h stability test almost overlaps with the initial OER polarization curve, proving its excellent stability. In order to assess the catalyst structural robustness or morphological change after the stability test, the $CoFe/NC_{30\%}$ catalyst was characterized by TEM. As shown in Fig. 9, the $CoFe/NC_{30\%}$ catalyst after 24 h continuous OER measurements at a current density of 10 mA cm^{-2} demonstrated a typical octahedral-like structure supplemented with another sheet-like shape. The resembling morphology of the $CoFe/NC_{30\%}$ catalyst before and after the OER durability test indicates that the as-prepared catalyst holds a robust structure. This could be stemmed from the N-doped carbon coating layer that keeps the active metals from dissolving and transforming into another structure and phase during the electrocatalysis under a strong alkaline environment.

The outstanding OER catalytic activity of $CoFe/NC_{30\%}$ could be attributed to numerous factors: (i) the synergetic/coupling effect between CoFe and the N-doped carbon, with optimum content of dopamine; (ii) the improved electronic conductivity stemmed from the in-situ formed N-doped carbon, as attested by the reduced charge transfer resistance in the EIS analysis.

In CoFe bimetallic-based electrocatalyst, various explanations regarding the active sites for OER have been reported in the published literature. For example, Zhu and co-workers reported that Fe sites are the leading active site for catalysis, while Co species offers conductive networks and favorable synergetic effects for Fe sites [68]. Other authors suggested that both Fe and Co sites can be concurrently involved in the catalytic process, known as the two-site catalytic mechanism [69]. Carbon materials are used as

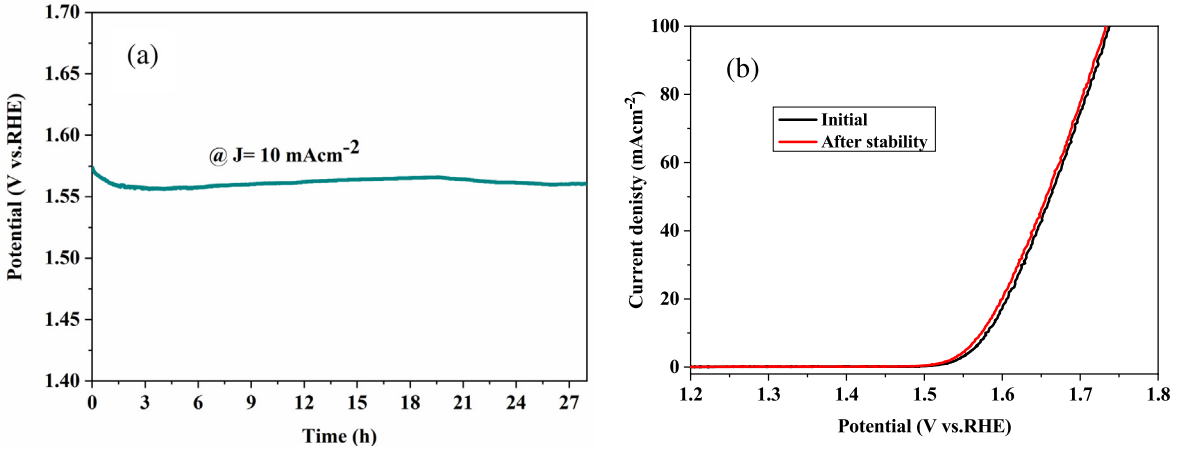

Fig. 8. (a) Chronopotentiometry stability test of $CoFe/NC_{30\%}$ conducted at j = 10 mA cm^{-2} in 1 M KOH at room temperature and rotation speed of 1600 rpm, and (b) OER polarization curve recorded before and after the stability measurements.

Table 2
Comparison of OER electrocatalytic activity of CoFe-based electrocatalysts reported in the literature. The η_{10} (mV) refers to the overpotential required to generate a j of 10 mA cm^{-2}.

Electrocatalyst	Substrate	η_{10} (mV)	Tafel slope (mV dec^{-1})	Stability remark	Ref.
$CoFe/NC_{30\%}$	GCE	340	77	Showed stable potential of 1.57 V @ j = 10 mA cm^{-2} for about 24 h.	This work
FeCo-N/C	GCE	370	52	Experienced 24% of anodic current attenuation during 30,000 s continuous operation.	[70]
Co-Fe-1–1	CP	330	37	After 20 h continuous operation, a small overpotential rise (7%) was observed.	[71]
Co_3O_{4-x} carbon@Fe_{2-y} Co_yO	GCE	350	37.6	After 6000 cycles, a slight curve shift of about 20 mV at j = 50 mA/cm^2 was observed.	[72]
CoFe-MWCNTs	NF	300	84	Exhibited stable potential for about 3 h, and after 1000 cycles, a 10 mV potential shift was observed.	[73]
CoFe-$CoFe_2O_4$/N-CNTs	GCE	334	80	After 1000 cycles, a 12 mV overpotential increment was observed.	[36]
CoFe@NC-700	GCE	380	110	After 1000 s operation at 1.60 V, a 7% current density decay was observed.	[24]
$CoFe_2O_4$/graphene	GCE	300	68	About 83% relative current was reported after 30,000 s testing.	[34]
Fe_3N@Co_4N@CoFe	NF	225	48	Stable potential for about 20 h.	[74]
$Co_{5.47}N/Co_3Fe_7$/NC	GCE	380	62.68	After 4000 CV cycles, 10 mV potential shift was recorded.	[75]
CoFe/N-HCS	NF	292	58	Retained a high relative current of 84.3% after 30 h operation.	[25]
CoFe-NCNFs	GCE	323	63.9	Stable current density for about 10 h	[76]
Fe_1Co_2-NC	GCE	356	86.6	Smaller potential change (57 mV) after 12 h testing	[77]
$Co_{0.68}Fe_{0.32}O$@NC/CC	CC	260	58.9	After 10 h testing, about 95% current retention was recorded.	[78]
Fe-Co/NC-800	CP	279	42.7	Stable current for about 6 h	[79]

Where; MWCNT: Multiwall carbon nanotube; NC: Nitrogen-doped carbon, GCE: glassy carbon electrode; NF: nickel foam; CP: Carbon paper; N-HCS: N-doped hollow carbon microspheres; NCNFs: N-doped carbon nanoflowers; CC: carbon cloth.

a substrate to disperse or coat metal/metal oxides and are essential to promote conductivity and enrich active sites [20]. Doping nitrogen into carbon lattice could remarkably increase the positive charge density of the adjacent carbon atoms because of its higher electronegativity and ability to donate electrons [44]. Some researchers have attempted to elucidate the role of CoFe alloys and the nitrogen-doped carbon (NC) during the OER process. Wang and co-workers investigated the role of CoFe alloy and NC in OER. The adsorption free energies of the oxygen intermediates (OOH*, O*, and OH*) on CoFe alloy, graphitic N doping (NC), and CoFe/NC were calculated and revealed the role of the individual and combined species for OER. The rate-determining step of OER was identified to be the formation of OOH* intermediate, and it was found that coupled CoFe/NC exhibits the lowest adsorption energy of OOH* intermediate, reflecting the most preferred OER free-energy pathway due to the synergetic promotion of both CoFe alloy and NC in CoFe/NC. Hence, the high electrocatalytic performance of the CoFe/NC catalyst achieved in this work could be related to the synergetic effect of CoFe bimetals and nitrogen-doped carbonized polydopamine.

The as-developed electrocatalyst was compared with similar materials recently reported in the literature, and $CoFe/NC_{30\%}$ surpassed several previously reported electrocatalysts. As it is apparent from Table 2, our catalyst ($CoFe/NC_{30\%}$) outshines over the recently published papers, including CoFe alloys, in terms of its exceptional stability. The noticeable electrocatalytic superiority of $CoFe/NC_{30\%}$ catalyst will make its prospective to be used for hydrogen generation in electrochemical water electrolysis.

4. Conclusions

In summary, CoFe/N-doped carbon ($CoFe/NC_x$) electrocatalysts were synthesized by sequential steps of the hydrothermal route, in situ polymerization of dopamine followed by carbonization. Results demonstrated that incorporating different dopamine content with $CoFe_2O_4$ spinel oxides greatly influences the physicochemical and electrochemical properties. Among the obtained $CoFe/NC_x$ electrocatalyst, the $CoFe/NC_{30\%}$ sample displayed excellent catalytic activity and stability for alkaline oxygen evolution reaction (OER); it presented a small overpotential of 340 mV to derive a 10 mA cm^{-2} current density, a small Tafel slope of 77 mV dec^{-1} and exhibited exceptional electrochemical stability for about 24 h. In contrast with the recently reported CoFe/NC-based electrocatalysts for OER (Table 2), the optimized $CoFe/NC_{30\%}$ electrocatalyst showed better stability, remaining unchanged for at least 24 h. The excellent OER activity and stability of $CoFe/NC_{30\%}$ could be stemmed from: (i) the synergetic effect of CoFe and N-doped carbon coating layer, and (ii) the reduced charge transfer resistance, as a result of the optimized dopamine content integration, as corroborated by the electrochemical impedance spectroscopy analysis. This study could open a new avenue for developing high-performance, affordable and stable electrocatalysts for large-scale OER electrodes.

CRediT authorship contribution statement

Gebrehiwet Abrham Gebreslase: Data curation, Writing – original draft. **María Victoria Martínez-Huerta:** Conceptualization, Writing – review & editing. **David Sebastián:** Supervision. **María Jesús Lázaro:** Project administration, Funding acquisition.

Declaration of Competing Interest

The authors declare that they have no known competing financial interests or personal relationships that could have appeared to influence the work reported in this paper.

Acknowledgements

Financial support from the European Union's Horizon 2020 Research and Innovation programme under the Marie Skłodowska-Curie Actions-Innovative Training Networks (MSCA-ITN) Grant Agreement 813748 are gratefully acknowledged. The authors wish to acknowledge the grants PID2020-115848RB-C21 and PID2020-115848RB-C22 funded by MCIN/AEI/10.13039/5011 00011033. Authors also acknowledge the use of instrumentation as well as the technical advice provided by the National Facility ELECMI ICTS, node "Laboratorio de Microscopias Avanzadas" at Universidad de Zaragoza.

Appendix A. Supplementary material

Supplementary data to this article can be found online at https://doi.org/10.1016/j.jcis.2022.06.005.

References

[1] B. Looney, Statistical Review of World Energy globally consistent data on world energy markets. and authoritative publications in the field of energy, Rev. World Energy Data. 70 (2021) 8–20.

[2] J. Chi, H. Yu, Water electrolysis based on renewable energy for hydrogen production, Cuihua Xuebao/Chinese, J. Catal. 39 (2018) 390–394, https://doi.org/10.1016/S1872-2067(17)62949-8.

[3] S.G. Simoes, J. Catarino, A. Picado, T.F. Lopes, S. di Berardino, F. Amorim, F. Gírio, C.M. Rangel, T. Ponce de Leão, Water availability and water usage solutions for electrolysis in hydrogen production, J. Clean. Prod. 315 (2021) 128124.

[4] T. Zhang, J. Du, P. Xi, C. Xu, Hybrids of Cobalt/Iron Phosphides Derived from Bimetal-Organic Frameworks as Highly Efficient Electrocatalysts for Oxygen Evolution Reaction, ACS Appl. Mater. Interfaces 9 (2017) 362–370, https://doi.org/10.1021/acsami.6b12189.

[5] Q. Huang, C. Li, Y. Tu, Y. Jiang, P. Mei, X. Yan, Spinel CoFe2O4 /carbon nanotube composites as efficient bifunctional electrocatalysts for oxygen reduction and oxygen evolution reaction, Ceram. Int. 47 (2021) 1602–1608, https://doi.org/10.1016/j.ceramint.2020.08.276.

[6] R. Duan, Y. Li, S. Gong, Y. Tong, Z. Li, W. Qi, Hierarchical CoFe oxyhydroxides nanosheets and Co2P nanoparticles grown on Ni foam for overall water splitting, Electrochim. Acta 360 (2020), https://doi.org/10.1016/j.electacta.2020.136994 136994.

[7] S. Weiß, M. Ertl, S.D. Varhade, A.V. Radha, W. Schuhmann, J. Breu, C. Andronescu, Trivalent iron rich CoFe layered oxyhydroxides for electrochemical water oxidation, Electrochim. Acta 350 (2020), https://doi.org/10.1016/j.electacta.2020.136256 136256.

[8] S. Xie, F. Li, S. Xu, J. Li, W. Zeng, Cobalt/iron bimetal-organic frameworks as efficient electrocatalysts for the oxygen evolution reaction, Chinese, J. Catal. 40 (2019) 1205–1211, https://doi.org/10.1016/S1872-2067(19)63384-X.

[9] Y. Zhang, M. Yang, X. Jiang, W. Lu, Y. Xing, Self-supported hierarchical CoFe-LDH/NiCo2O4/NF core-shell nanowire arrays as an effective electrocatalyst for oxygen evolution reaction, J. Alloys Compd. 818 (2020), https://doi.org/10.1016/j.jallcom.2019.153345 153345.

[10] Y.Z. Su, Q.Z. Xu, G.F. Chen, H. Cheng, N. Li, Z.Q. Liu, One dimensionally spinel NiCo2O4 nanowire arrays: Facile synthesis, water oxidation, and magnetic properties, Electrochim. Acta 174 (2015) 1216–1224, https://doi.org/10.1016/j.electacta.2015.06.092.

[11] Q. Huang, C. Li, Y. Tu, Y.u. Jiang, P. Mei, X. Yan, Spinel CoFe2O4 /carbon nanotube composites as efficient bifunctional electrocatalysts for oxygen reduction and oxygen evolution reaction, Ceram. Int. 47 (2) (2021) 1602–1608.

[12] L. Ji, Y. Wei, P. Wu, M. Xu, T. Wang, S. Wang, Q. Liang, T.J. Meyer, Z. Chen, Heterointerface Engineering of Ni2P-Co2P Nanoframes for Efficient Water Splitting, Chem. Mater. 33 (2021) 9165–9173, https://doi.org/10.1021/acs.chemmater.1c02609.

[13] K. Malaie, M.R. Ganjali, Tuning CoFe and NiFe spinel oxide compositions by a fast glycine-nitrate autocombustion for oxygen evolution electrocatalysts and implications from their cyclic voltammograms on the role of Fe, Mater. Chem. Phys. 253 (2020), https://doi.org/10.1016/j.matchemphys.2020.123339 123339.

[14] R. Zhang, S. Cheng, N.a. Li, W. Ke, N, S-codoped graphene loaded Ni-Co bimetal sulfides for enhanced oxygen evolution activity, Appl. Surf. Sci. 503 (2020) 144146.

[15] M.S. Burke, L.J. Enman, A.S. Batchellor, S. Zou, S.W. Boettcher, Oxygen evolution reaction electrocatalysis on transition metal oxides and (Oxy)hydroxides: activity trends and design principles, Chem. Mater. 27 (2015) 7549–7558, https://doi.org/10.1021/acs.chemmater.5b03148.

[16] B. Aghabarari, J.M. Luque-Centeno, M. Capel-Sánchez, M.J. Lázaro Elorri, M.V. Martínez-Huerta, Ni-based composites from chitosan biopolymer a one-step synthesis for oxygen evolution reaction, Catalysts 9 (2019) 471.

[17] C. He, X. Han, X. Kong, M. Jiang, D. Lei, X. Lei, Fe-doped Co 3 O 4 @C nanoparticles derived from layered double hydroxide used as efficient electrocatalyst for oxygen evolution reaction, J. Energy Chem. 32 (2019) 63–70, https://doi.org/10.1016/j.jechem.2018.06.014.

[18] G.A. Gebreslase, M.V. Martínez-Huerta, M.J. Lázaro, Recent progress on bimetallic NiCo and CoFe based electrocatalysts for alkaline oxygen evolution reaction: A review, J. Energy Chem. 67 (2022) 101–137, https://doi.org/10.1016/j.jechem.2021.10.009.

[19] A. Samanta, C.R. Raj, Bifunctional nitrogen-doped hybrid catalyst based on onion-like carbon and graphitic carbon encapsulated transition metal alloy nanostructure for rechargeable zinc-air battery, J. Power Sources. 455 (2020), https://doi.org/10.1016/j.jpowsour.2020.227975 227975.

[20] Z. Wu, P. Li, Q. Qin, Z. Li, X. Liu, N-doped graphene combined with alloys (NiCo, CoFe) and their oxides as multifunctional electrocatalysts for oxygen and hydrogen electrode reactions, Carbon N. Y. 139 (2018) 35–44, https://doi.org/10.1016/j.carbon.2018.06.028.

[21] H. Shi, G. Zhao, Water oxidation on spinel NiCo2O4 nanoneedles anode: microstructures, specific surface character, and the enhanced electrocatalytic performance, J. Phys. Chem. C 118 (2014) 25939–25946, https://doi.org/10.1021/jp508977j.

[22] B. Cui, H. Lin, J.-B. Li, X. Li, J. Yang, J. Tao, Core-ring structured NiCo2O4 nanoplatelets: synthesis, characterization, and electrocatalytic applications, Adv. Funct. Mater. 18 (2008) 1440–1447, https://doi.org/10.1002/adfm.200700982.

[23] S. Kang, K. Ham, J. Lee, Moderate oxophilic CoFe in carbon nano fi ber for the oxygen evolution reaction in anion exchange membrane water electrolysis, Electrochim. Acta. 353 (2020), https://doi.org/10.1016/j.electacta.2020.136521 136521.

[24] Y. Wang, T. Hu, Y. Qiao, Y. Chen, Synergistic engineering of defects and architecture in CoFe@NC toward highly efficient oxygen electrode reactions, Int. J. Hydrogen Energy. 45 (2020) 8686–8694, https://doi.org/10.1016/j.ijhydene.2020.01.135.

[25] J. Li, Y. Kang, W. Wei, X. Li, Z. Lei, P. Liu, Well-dispersed ultrafine CoFe nanoalloy decorated N-doped hollow carbon microspheres for rechargeable/flexible Zn-air batteries, Chem. Eng. J. 407 (2021), https://doi.org/10.1016/j.cej.2020.127961 127961.

[26] T. Li, Y. Lv, J. Su, Y.i. Wang, Q. Yang, Y. Zhang, J. Zhou, L. Xu, D. Sun, Y. Tang, Anchoring CoFe2O4 Nanoparticles on N-Doped Carbon Nanofibers for High-Performance Oxygen Evolution Reaction, Adv. Sci. 4 (11) (2017) 1700226.

[27] Z.Q. Liu, H. Cheng, N. Li, T.Y. Ma, Y.Z. Su, ZnCo2O4 quantum dots anchored on nitrogen-doped carbon nanotubes as reversible oxygen reduction/evolution electrocatalysts, Adv. Mater. 28 (2016) 3777–3784, https://doi.org/10.1002/adma.201506197.

[28] X. Ma, H. Chai, Y. Cao, J. Xu, Y. Wang, H. Dong, D. Jia, W. Zhou, An effective bifunctional electrocatalysts: controlled growth of CoFe alloy nanoparticles supported on N-doped carbon nanotubes, J. Colloid Interface Sci. 514 (2018) 656–663, https://doi.org/10.1016/j.jcis.2017.12.081.

[29] X. Liu, T. Zhang, Y. Qu, G. Tian, H. Yue, D. Zhang, S. Feng, Carbonized polydopamine coated single-crystalline NiFe2O4 nanooctahedrons with enhanced electrochemical performance as anode materials in a lithium ion battery, Electrochim. Acta. 231 (2017) 27–35, https://doi.org/10.1016/j.electacta.2017.02.020.

[30] R. Liu, S.M. Mahurin, C. Li, R.R. Unocic, J.C. Idrobo, H. Gao, S.J. Pennycook, S. Dai, Dopamine as a carbon source: The controlled synthesis of hollow carbon spheres and yolk-structured carbon nanocomposites, Angew. Chemie - Int. Ed. 50 (2011) 6799–6802, https://doi.org/10.1002/anie.201102070.

[31] J. Kong, S.I. Seyed Shahabadi, X. Lu, Integration of inorganic nanostructures with polydopamine-derived carbon: Tunable morphologies and versatile applications, Nanoscale. 8 (2016) 1770–1788, https://doi.org/10.1039/c5nr06711a.

[32] J. Kong, W.A. Yee, L. Yang, Y. Wei, S. Lei Phua, H. Guan Ong, J. Ming Ang, X. Li, X. Lu, Highly electrically conductive layered carbon derived from polydopamine and its functions in SnO2-based lithium ion battery anodes, Chem. Commun. 48 (2012) 10316–10318, https://doi.org/10.1039/c2cc35284b.

[33] J. Yan, H. Lu, Y. Huang, J. Fu, S. Mo, C. Wei, Y.E. Miao, T. Liu, Polydopamine-derived porous carbon fiber/cobalt composites for efficient oxygen reduction reactions, J. Mater. Chem. A. 3 (2015) 23299–23306, https://doi.org/10.1039/c5ta06217a.

[34] Y. Ma, H. Zhang, J. Xia, Z. Pan, X. Wang, G. Zhu, B. Zheng, G. Liu, L. Lang, Reduced CoFe2O4/graphene composite with rich oxygen vacancies as a high efficient electrocatalyst for oxygen evolution reaction, Int. J. Hydrogen Energy. 45 (2020) 11052–11061, https://doi.org/10.1016/j.ijhydene.2020.02.045.

[35] W. Yan, W. Bian, C. Jin, J.H. Tian, R. Yang, An efficient Bi-functional electrocatalyst based on strongly coupled CoFe2O4/carbon nanotubes hybrid for oxygen reduction and oxygen evolution, Electrochim. Acta. 177 (2015) 65–72, https://doi.org/10.1016/j.electacta.2015.02.044.

[36] D. Xu, B. Liu, G. Liu, K. Su, C. Yang, H. Tong, D. Qian, J. Li, N-doped bamboo-like CNTs combined with CoFe–CoFe2O4 as a highly efficient electrocatalyst towards oxygen evolution, Int. J. Hydrogen Energy 45 (2020) 6629–6635, https://doi.org/10.1016/j.ijhydene.2019.12.180.

[37] B. Zhang, H. Wang, Z. Zuo, H. Wang, J. Zhang, Tunable CoFe-based active sites on 3D heteroatom doped graphene aerogel electrocatalysts: Via annealing gas regulation for efficient water splitting, J. Mater. Chem. A 6 (2018) 15728–15737, https://doi.org/10.1039/c8ta05705b.

[38] X. Zhang, Y. Wang, S. Dong, M. Li, Dual-site polydopamine spheres/CoFe layered double hydroxides for electrocatalytic oxygen reduction reaction, Electrochim. Acta 170 (2015) 248–255, https://doi.org/10.1016/j.electacta.2015.04.170.

[39] C. Li, E. Zhou, Z. Yu, H. Liu, M. Xiong, Tailor-made open porous 2D CoFe/SN-carbon with slightly weakened adsorption strength of ORR/OER intermediates as remarkable electrocatalysts toward zinc-air batteries, Appl. Catal. B Environ. 269 (2020), https://doi.org/10.1016/j.apcatb.2020.118771 118771.

[40] X. Liu, T. Zhang, Y. Qu, G. Tian, H. Yue, D. Zhang, S. Feng, Carbonized polydopamine coated single-crystalline NiFe 2 O 4 nanooctahedrons with enhanced electrochemical performance as anode materials in a lithium ion battery, Electrochim. Acta 231 (2017) 27–35, https://doi.org/10.1016/j.electacta.2017.02.020.

[41] Y. Bide, M.R. Nabid, B. Etemadi, Facile synthesis and catalytic application of selenium doped graphene/CoFe2O4 for highly efficient and noble metal free dehydrogenation of formic acid, Int. J. Hydrogen Energy 41 (2016) 20147–20155, https://doi.org/10.1016/j.ijhydene.2016.08.108.

[42] A. Samanta, C.R. Raj, Catalyst support in oxygen electrocatalysis: a case study with CoFe alloy electrocatalyst, J. Phys. Chem. C. 122 (2018) 15843–15852, https://doi.org/10.1021/acs.jpcc.8b02830.

[43] H. Li, J. Xi, A.G. Donaghue, J. Keum, Y. Zhao, K. An, E.R. McKenzie, F. Ren, Synthesis and catalytic performance of polydopamine supported metal nanoparticles, Sci. Rep. 10 (2020) 1–7, https://doi.org/10.1038/s41598-020-67458-9.
[44] H.J. Niu, S.S. Chen, J.J. Feng, L. Zhang, A.J. Wang, Assembled hollow spheres with CoFe alloyed nanocrystals encapsulated in N, P-doped carbon nanovesicles: An ultra-stable bifunctional oxygen catalyst for rechargeable Zn-air battery, J. Power Sources. 475 (2020), https://doi.org/10.1016/j.jpowsour.2020.228594 228594.
[45] T. Zhang, Z. Li, L. Wang, Z. Zhang, S. Wang, Spinel CoFe2O4 supported by three dimensional graphene as high-performance bi-functional electrocatalysts for oxygen reduction and evolution reaction, Int. J. Hydrogen Energy. 44 (2019) 1610–1619, https://doi.org/10.1016/j.ijhydene.2018.11.120.
[46] M. Fantauzzi, F. Secci, M. Sanna Angotzi, C. Passiu, C. Cannas, A. Rossi, Nanostructured spinel cobalt ferrites: Fe and Co chemical state, cation distribution and size effects by X-ray photoelectron spectroscopy, RSC Adv. 9 (2019) 19171–19179, https://doi.org/10.1039/c9ra03488a.
[47] J. Sun, P. Song, H. Zhou, L. Lang, X. Shen, Y. Liu, X. Cheng, X. Fu, G. Zhu, A surface configuration strategy to hierarchical Fe-Co-S/Cu2O/Cu electrodes for oxygen evolution in water/seawater splitting, Appl. Surf. Sci. 567 (2021), https://doi.org/10.1016/j.apsusc.2021.150757 150757.
[48] D. Briggs, X-ray photoelectron spectroscopy (XPS), Handb. Adhes. Second Ed. (2005) 621–622, https://doi.org/10.1002/0470014229.ch22.
[49] Y. Wang, D. Liu, Z. Liu, C. Xie, J. Huo, S. Wang, Porous cobalt-iron nitride nanowires as excellent bifunctional electrocatalysts for overall water splitting, Chem. Commun. 52 (2016) 12614–12617, https://doi.org/10.1039/c6cc06608a.
[50] X. Wang, B. Zheng, D. Yang, B. Sun, W. Zhang, Y. Chen, Self-assembled CoFe nanoparticle-embedded carbon nanowires as efficient nonprecious catalyst for overall water splitting, Energy Technol. 7 (2019) 1–8, https://doi.org/10.1002/ente.201801061.
[51] T. Takagaki, Y. Igari, T. Takaoka, I. Kusunoki, XPS study of the reaction of the Si (100) surface with a C 2 H 4 beam, Appl. Surf. Sci. 92 (1996) 287–290, https://doi.org/10.1016/0169-4332(95)00243-X.
[52] J. Sun, H. Xu, G. Liu, P. Zhu, R. Fan, Y. Yoneyama, N. Tsubaki, Green synthesis of rice bran microsphere catalysts containing natural biopromoters, ChemCatChem. 7 (2015) 1642–1645, https://doi.org/10.1002/cctc.201500375.
[53] X. Ma, K. Li, X. Zhang, B. Wei, H. Yang, L. Liu, M. Zhang, X. Zhang, Y. Chen, The surface engineering of cobalt carbide spheres through N, B co-doping achieved by room-temperature: In situ anchoring effects for active and durable multifunctional electrocatalysts, J. Mater. Chem. A. 7 (2019) 14904–14915, https://doi.org/10.1039/c9ta03762d.
[54] X. Gu, C. Wu, S. Wang, L. Feng, Cobalt fluoride/nitrogen-doped carbon derived from ZIF-67 for oxygen evolution reaction, Catal. Commun. 162 (2022), https://doi.org/10.1016/j.catcom.2021.106394 106394.
[55] Z. Peng, H. Wang, X. Xia, X. Zhang, Z. Dong, Integration of CoFe alloys and Fe/Fe3C nanoparticles into N-doped carbon nanosheets as dual catalytic active sites to promote the oxygen electrocatalysis of Zn-air batteries, ACS Sustain. Chem. Eng. 8 (2020) 9009–9016, https://doi.org/10.1021/acssuschemeng.0c01729.
[56] G. Li, L. Anderson, Y. Chen, M. Pan, P.-Y. Abel Chuang, New insights into evaluating catalyst activity and stability for oxygen evolution reactions in alkaline media, Sustain. Energy Fuels. 2 (2018) 237–251, https://doi.org/10.1039/C7SE00337D.
[57] T. Shinagawa, A.T. Garcia-Esparza, K. Takanabe, Insight on Tafel slopes from a microkinetic analysis of aqueous electrocatalysis for energy conversion, Sci. Rep. 5 (2015) 1–21, https://doi.org/10.1038/srep13801.
[58] J.C. Ruiz-Cornejo, J.F. Vivo-Vilches, D. Sebastián, M.V. Martínez-Huerta, M.J. Lázaro, Carbon nanofiber-supported tantalum oxides as durable catalyst for the oxygen evolution reaction in alkaline media, Renew. Energy. 178 (2021) 307–317, https://doi.org/10.1016/j.renene.2021.06.076.
[59] N.T. Suen, S.F. Hung, Q. Quan, N. Zhang, Y.J. Xu, H.M. Chen, Electrocatalysis for the oxygen evolution reaction: Recent development and future perspectives, Chem. Soc. Rev. 46 (2017) 337–365, https://doi.org/10.1039/c6cs00328a.
[60] D. Zhu, J. Liu, L. Wang, Y. Du, Y. Zheng, K. Davey, S.Z. Qiao, A 2D metal-organic framework/Ni(OH) 2 heterostructure for an enhanced oxygen evolution reaction, Nanoscale. 11 (2019) 3599–3605, https://doi.org/10.1039/c8nr09680e.
[61] J. Zhao, X. Wang, F. Chen, C. He, X. Wang, Y. Li, R. Liu, X. Chen, Y. Hao, M. Yang, F. Li, A one-step synthesis of hierarchical porous CoFe-layered double hydroxide nanosheets with optimized composition for enhanced oxygen evolution electrocatalysis, Inorg. Chem. Front. 7 (2020) 737–745, https://doi.org/10.1039/C9QI01394F.
[62] Y. Zhang, X. Gao, L. Lv, J. Xu, H. Lin, Y. Ding, C. Wang, Tailoring π-symmetry electrons in cobalt–iron phosphide for highly efficient oxygen evolution, Electrochim. Acta. 341 (2020), https://doi.org/10.1016/j.electacta.2020.136029 136029.
[63] Y. Dang, P. Han, Y. Li, Y. Zhang, Y. Zhou, Low-crystalline mixed Fe-Co-MOFs for efficient oxygen evolution electrocatalysis, J. Mater. Sci. 55 (2020) 13951–13963, https://doi.org/10.1007/s10853-020-05026-2.
[64] X. Huang, L. Gong, H. Xu, J. Qin, P. Ma, M. Yang, K. Wang, L. Ma, X. Mu, R. Li, Hierarchical iron-doped CoP heterostructures self-assembled on copper foam as a bifunctional electrocatalyst for efficient overall water splitting, J. Colloid Interface Sci. 569 (2020) 140–149, https://doi.org/10.1016/j.jcis.2020.02.073.
[65] Y.R. Hong, S. Mhin, K.M. Kim, W.S. Han, H. Choi, G. Ali, K.Y. Chung, H.J. Lee, S.I. Moon, S. Dutta, S. Sun, Y.G. Jung, T. Song, H.S. Han, Electrochemically activated cobalt nickel sulfide for an efficient oxygen evolution reaction: Partial amorphization and phase control, J. Mater. Chem. A. 7 (2019) 3592–3602, https://doi.org/10.1039/c8ta10142f.
[66] I.S. Filimonenkov, C. Bouillet, G. Kéranguéven, P.A. Simonov, G.A. Tsirlina, E.R. Savinova, Carbon materials as additives to the OER catalysts: RRDE study of carbon corrosion at high anodic potentials, Electrochim. Acta. 321 (2019) 134657.
[67] Y. Wu, Y. Gao, H. He, P. Zhang, Electrodeposition of self-supported Ni–Fe–Sn film on Ni foam: An efficient electrocatalyst for oxygen evolution reaction, Electrochim. Acta. 301 (2019) 39–46, https://doi.org/10.1016/j.electacta.2019.01.151.
[68] G. Zhu, X. Xie, X. Li, Y. Liu, X. Shen, K. Xu, S. Chen, Nanocomposites based on CoSe 2 -decorated FeSe 2 nanoparticles supported on reduced graphene oxide as high-performance electrocatalysts toward oxygen evolution reaction, ACS Appl. Mater. Interfaces. 10 (2018) 19258–19270, https://doi.org/10.1021/acsami.8b04024.
[69] B.o. Zhang, X. Zheng, O. Voznyy, R. Comin, M. Bajdich, M. García-Melchor, L. Han, J. Xu, M. Liu, L. Zheng, F.P. García de Arquer, C.T. Dinh, F. Fan, M. Yuan, E. Yassitepe, N. Chen, T. Regier, P. Liu, Y. Li, P. De Luna, A. Janmohamed, H.L. Xin, H. Yang, A. Vojvodic, E.H. Sargent, Homogeneously dispersed multimetal oxygen-evolving catalysts, Science 352 (6283) (2016) 333–337.
[70] H. Shui, T. Jin, J. Hu, H. Liu, In situ incorporation strategy for bimetallic FeCo-doped carbon as highly efficient bifunctional oxygen electrocatalysts, ChemElectroChem. 5 (2018) 1401–1406, https://doi.org/10.1002/celc.201800013.
[71] M. Xiong, D.G. Ivey, Composition effects of electrodeposited Co-Fe as electrocatalysts for the oxygen evolution reaction, Electrochim. Acta. 260 (2018) 872–881.
[72] W. Xu, W. Xie, Y. Wang, Co3O4-x-Carbon@Fe2-yCoyO3 heterostructural hollow polyhedrons for the oxygen evolution reaction, ACS Appl. Mater. Interfaces. 9 (2017) 28642–28649, https://doi.org/10.1021/acsami.7b09213.
[73] Z. Ali, M. Mehmood, J. Ahmed, A. Majeed, K.H. Thebo, CVD grown defect rich-MWCNTs with anchored CoFe alloy nanoparticles for OER activity, Mater. Lett. 259 (2020), https://doi.org/10.1016/j.matlet.2019.126831 126831.
[74] Z. Cui, X. Liang, P. Wang, P. Zhou, Q. Zhang, Z. Wang, Z. Zheng, Y. Liu, Y. Dai, B. Huang, In situ integration of Fe3N@Co4N@CoFe alloy nanoparticles as efficient and stable electrocatalyst for overall water splitting, Electrochim. Acta. 395 (2021), https://doi.org/10.1016/j.electacta.2021.139218 139218.
[75] L. Li, J. Chen, S. Wang, Y. Huang, D. Cao, MOF-derived CoN/CoFe/NC bifunctional electrocatalysts for zinc-air batteries, Appl. Surf. Sci. 582 (2022), https://doi.org/10.1016/j.apsusc.2021.152375 152375.
[76] S.Y. Lin, Y.P. Chen, Y. Cao, L. Zhang, J.J. Feng, A.J. Wang, Aminouracil-assisted synthesis of CoFe decorated bougainvillea-like N-doped carbon nanoflowers for boosting Zn–air battery and water electrolysis, J. Power Sources. 521 (2022), https://doi.org/10.1016/j.jpowsour.2021.230926 230926.
[77] Y. Lei, R. Huang, H. Xie, D. Zhang, X. Liu, Y. Si, N.a. Li, Electronic structure tuning of FeCo nanoparticles embedded in multi-dimensional carbon matrix for enhanced bifunctional oxygen electrocatalysis, J. Alloys Compd. 853 (2021) 157070.
[78] Y. Chong, Z. Pan, M. Su, X. Yang, D. Ye, Y. Qiu, 1D/2D hierarchical Co1-xFexO@N-doped carbon nanostructures for flexible zinc–air batteries, Electrochim. Acta. 363 (2020), https://doi.org/10.1016/j.electacta.2020.137264 137264.
[79] W. Tan, S. Xie, J. Yang, J. Lv, J. Yin, C. Zhang, J. Wang, X. Shen, M. Zhao, M. Zhang, G. He, L. Yang, Effect of carbonization temperature on electrocatalytic water splitting of Fe-Co anchored on N-doped porous carbon, J. Solid State Chem. 302 (2021), https://doi.org/10.1016/j.jssc.2021.122435 122435.

Supporting Information

for

Transformation of $CoFe_2O_4$ spinel structure into active and robust CoFe alloy/N-doped carbon electrocatalyst for oxygen evolution reaction

Gebrehiwet Abrham Gebreslase[a], María Victoria Martínez-Huerta[b*], David Sebastián[a], María Jesús Lázaro[a*]

[a] *Instituto de Carboquímica, CSIC. Miguel Luesma Castán 4, 50018, Zaragoza, Spain.*
[b] *Instituto de Catálisis y Petroleoquímica, CSIC. Marie Curie 2, 28049, Madrid, Spain.*

[*]Corresponding authors.
E-mail addresses: mmartinez@icp.csic.es (M.V. Martínez-Huerta), mlazaro@icb.csic.es (M.J. Lázaro)

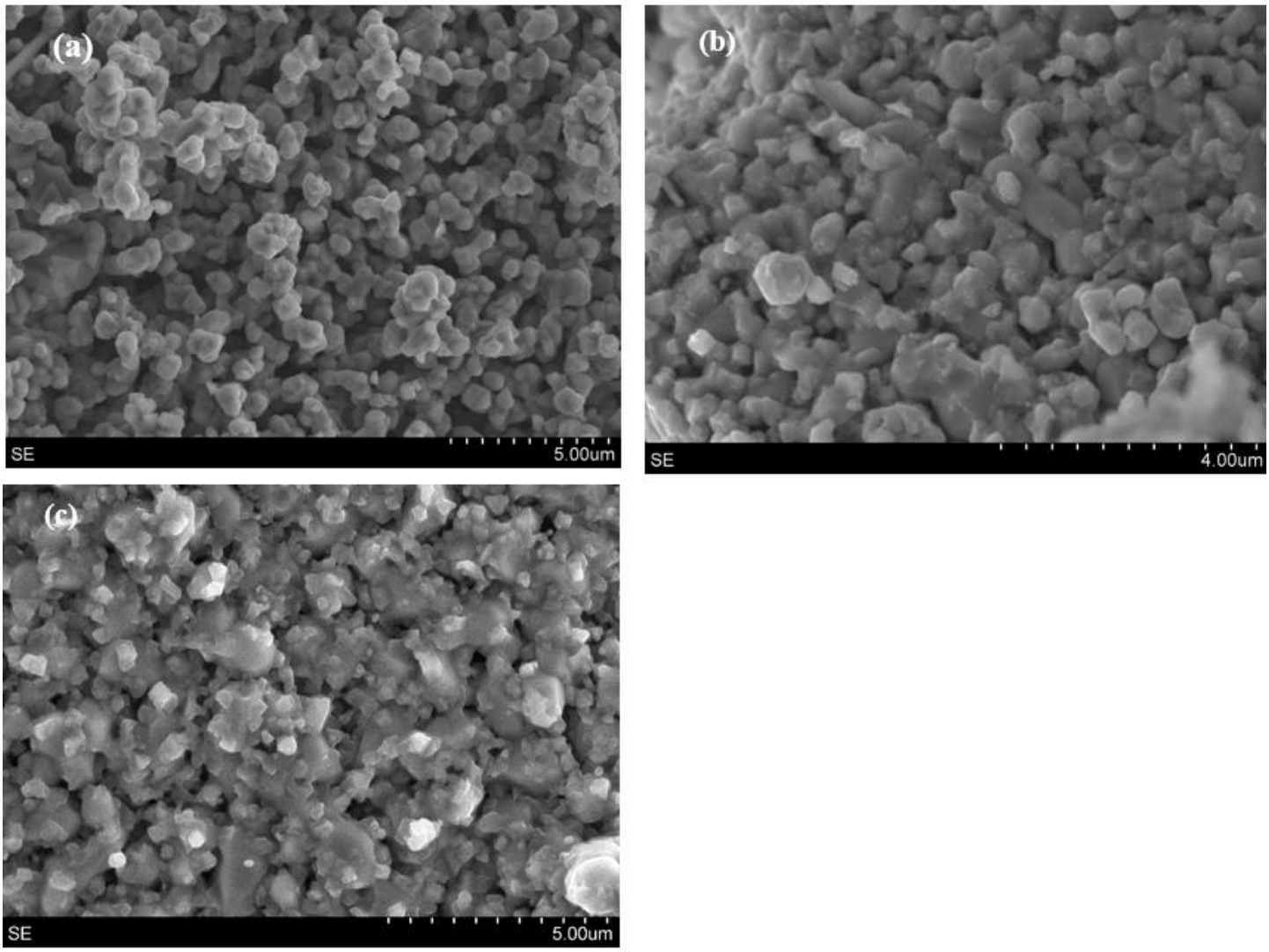

Figure S 1. SEM images of (a) $CoFe/NC_{10\%}$, (b) $CoFe/NC_{20\%}$, and (c) $CoFe/NC_{40\%}$.

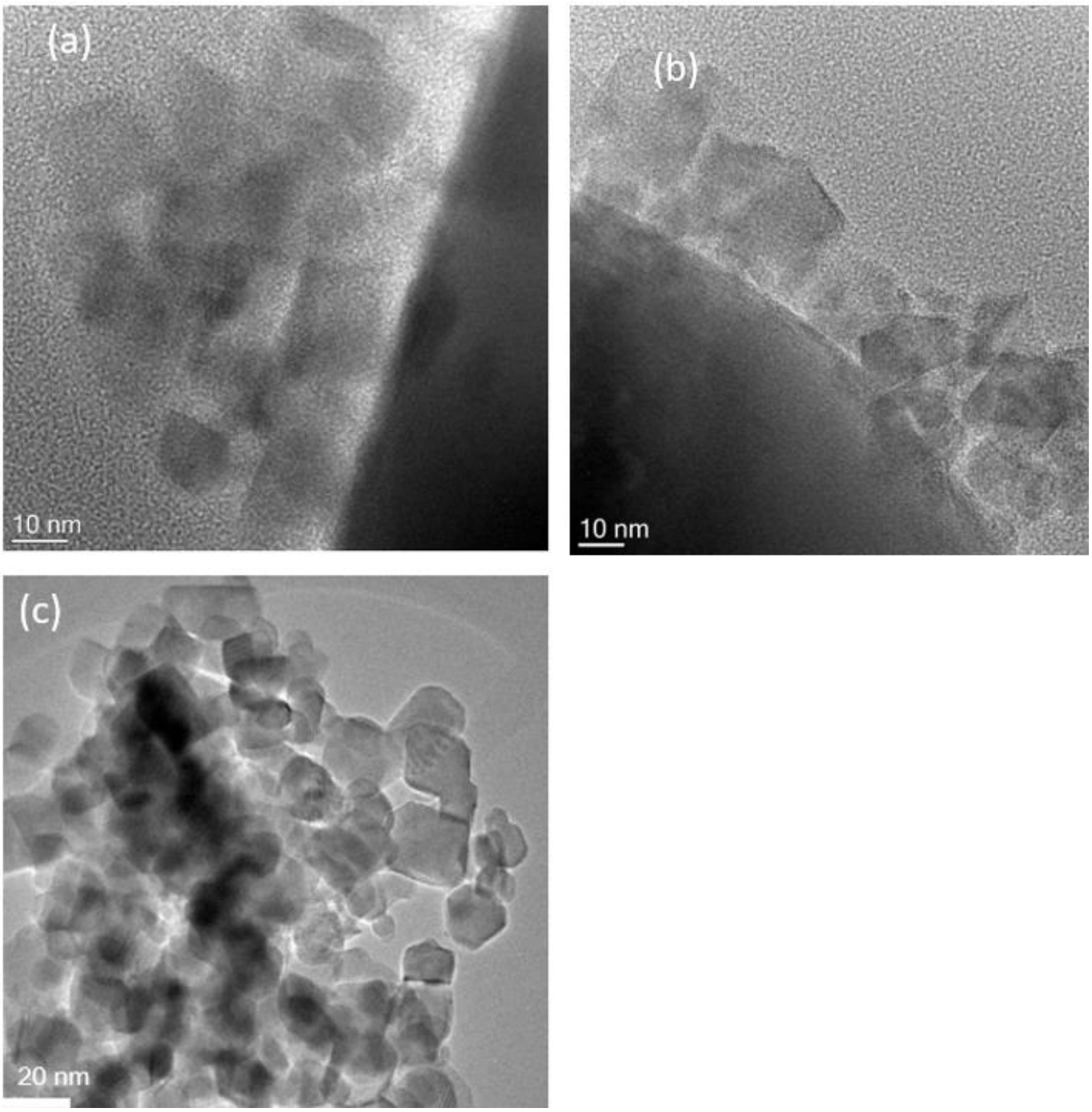

Figure S 2.TEM images of (a) $CoFe/NC_{10\%}$, (b) $CoFe/NC_{20\%}$, and (c) $CoFe/NC_{40\%}$

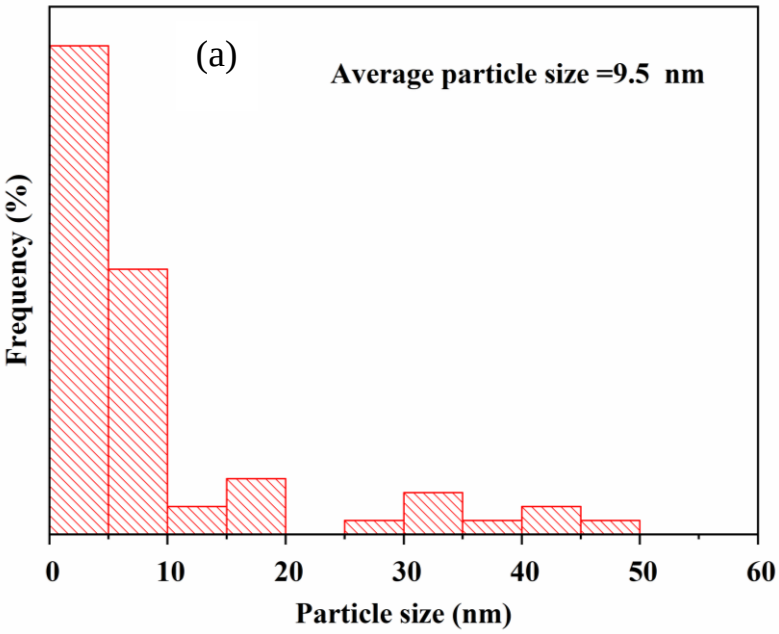
(a)
Average particle size =9.5 nm
Frequency (%)
0
10
20
30
40
50
60
Particle size (nm)

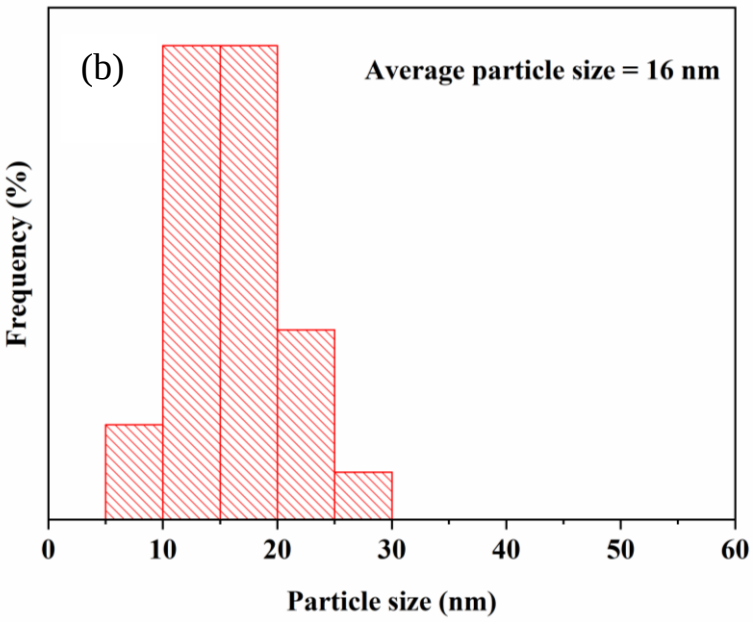
(b)
Average particle size = 16 nm
Frequency (%)
0
10
20
30
40
50
60
Particle size (nm)

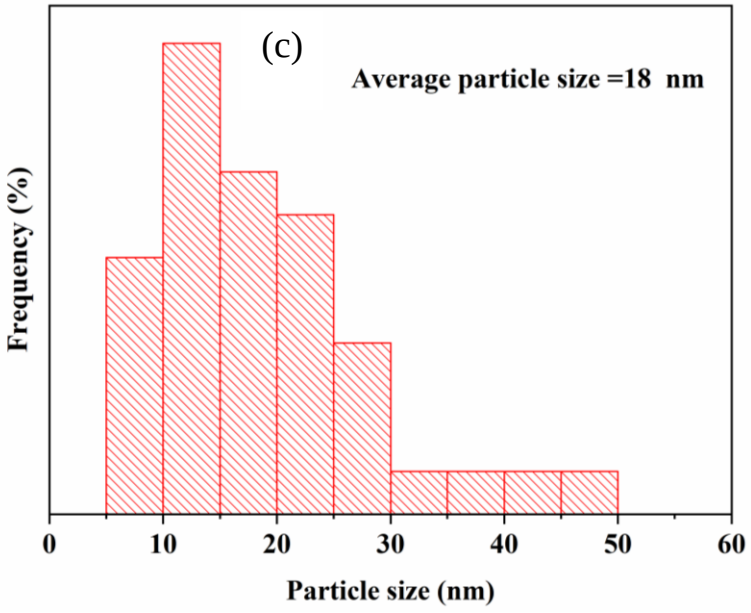
(c)
Average particle size =18 nm
Frequency (%)
0
10
20
30
40
50
60
Particle size (nm)

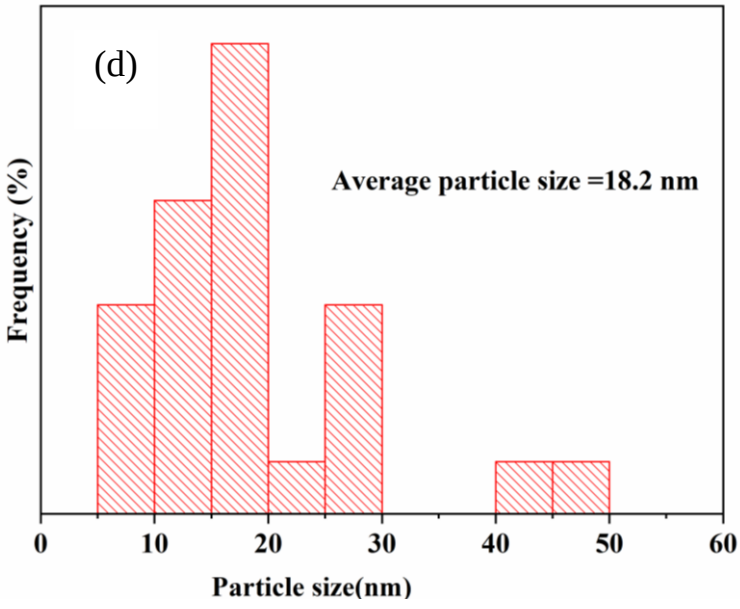
(d)
Average particle size =18.2 nm
Frequency (%)
0
10
20
30
40
50
60
Particle size(nm)

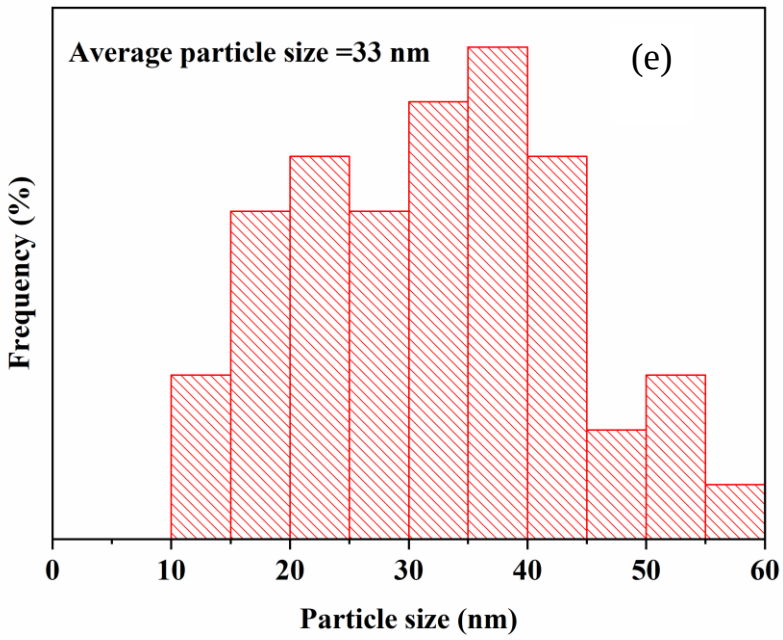

Figure S 3. Particle size distribution of the various electrocatalyst: (a) $CoFe_2O_4$, (b) $CoFe/NC_{10\%}$, (c) $CoFe/NC_{20\%}$,(d) $CoFe/NC_{30\%}$, and (e) $CoFe/NC_{40\%}$.

Table S 1. Amount of CoFe alloys and oxides in the composite samples, determined from the XRD analysis.

Catalyst	**CoFe alloy (%)**	**Oxides (%)**	**CoFe alloy /oxides ratio**
$CoFe/NC_{20\%}$	90.6	9.4	9.34
$CoFe/NC_{30\%}$	91.98	8.02	11.47
$CoFe/NC_{40\%}$	100	-	100% CoFe alloy

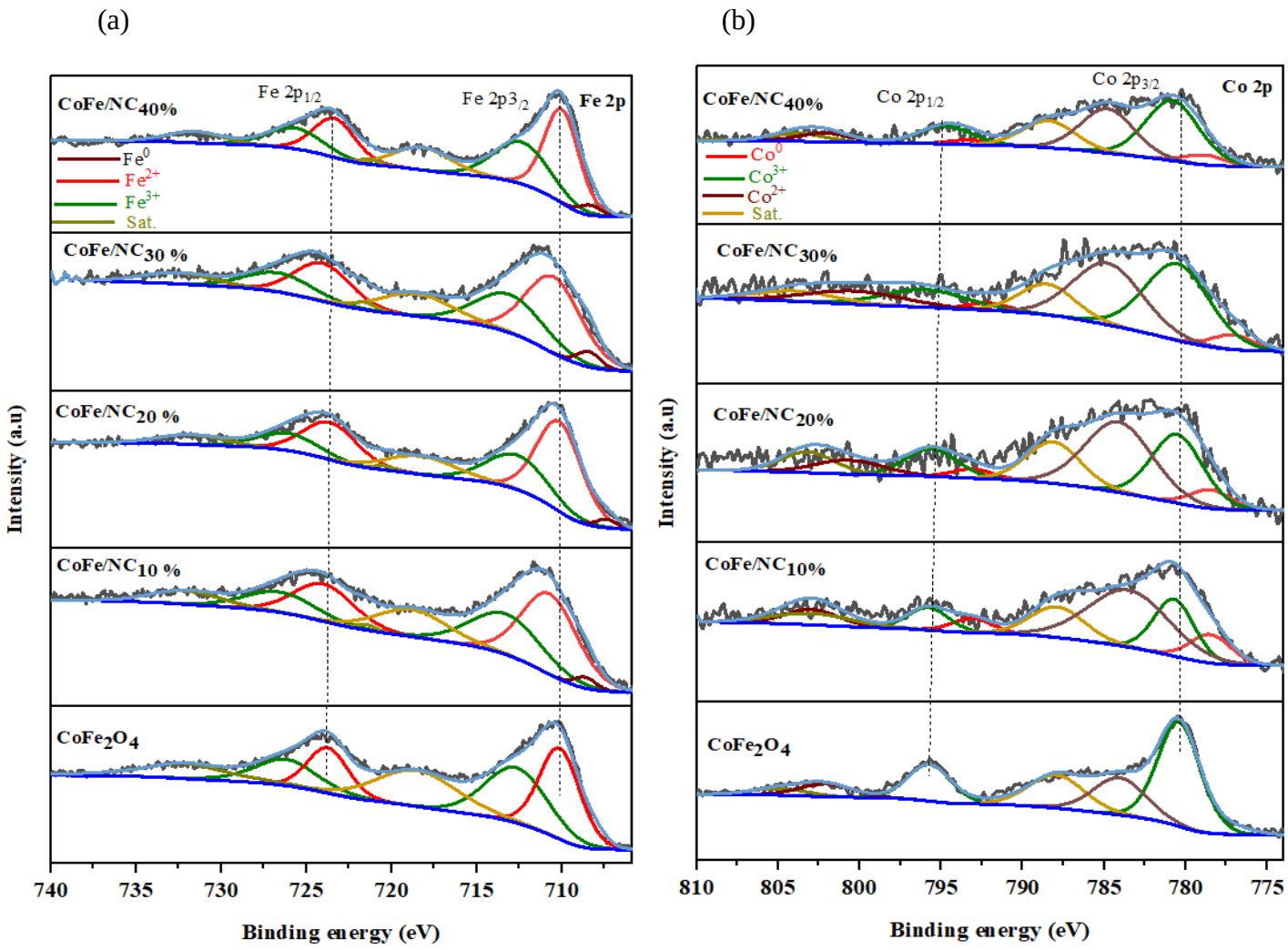

Figure S 4. XPS high resolution spectra of (a) Fe 2p, (b) Co 2p, for all electrocatalysts

Table S 2. XPS analysis results of the electrocatalysts

Catalyst	BE of Fe $2p_{3/2}$ (eV)	Corresponding Fe species	BE of Co $2p_{3/2}$ (eV)	Corresponding Co species
$CoFe_2O_4$	710.0	Fe^{2+}	780.3	Co^{3+}
	712.8	Fe^{3+}	784.1	Co^{2+}
	718.4	Sat.	787.7	Sat.
$CoFe/NC_{10\%}$	707.8	Fe^{0}	777.6	Co^{0}
	710.4	Fe^{2+}	780.1	Co^{3+}
	713.1	Fe^{3+}	783.2	Co^{2+}
	718.5	Sat.	787.4	Sat.
$CoFe/NC_{20\%}$	707.0	Fe^{0}	777.8	Co^{0}
	710.0	Fe^{2+}	779.8	Co^{3+}
	712.8	Fe^{3+}	783.6	Co^{2+}
	718.3	Sat.	787.7	Sat.
$CoFe/NC_{30\%}$	708.2	Fe^{0}	777.3	Co^{0}
	710.5	Fe^{2+}	780.7	Co^{3+}
	713.4	Fe^{3+}	783.9	Co^{2+}
	718.5	Sat.	788.4	Sat.
$CoFe/NC_{40\%}$	707.5	Fe^{0}	777.5	Co^{0}
	710. 0	Fe^{2+}	779.6	Co^{3+}
	712.8	Fe^{3+}	783.8	Co^{2+}
	718.3	Sat.	787.5	Sat.

Table S 3. Elemental composition of the prepared electrocatalysts

Samples	**Co (wt.%)**	**Fe (wt. %)**	**Fe/Co ratio**
$CoFe_2O_4$	20.8	40.2	1.93
$CoFe/NC_{10\%}$	24	51.8	2.16
$CoFe/NC_{20\%}$	28.4	57.4	2.02
$CoFe/NC_{30\%}$	28.7	57	1.99
$CoFe/NC_{40\%}$	30.1	58.4	1.94

Table S 4. Specific capacitance and ECSA values for the various eletrocataysts

Sample	C_{dl} (mF)	C_{dl} (F/g)	Cs (mF/cm^2)	ECSA (cm^2)
$CoFe_2O_4$	0.22	0.22	0.04	5.5
$CoFe/NC_{10\%}$	0.91	0.91	0.04	22.75
$CoFe/NC_{20\%}$	0.38	0.38	0.04	9.5
$CoFe/NC_{30\%}$	1.94	1.94	0.04	48.5
$CoFe/NC_{40\%}$	0.87	0.87	0.04	21.75

Table S 5. Charge transfer resistance (R_{ct}) and solution resistance (R_s) determined from EIS measurement

Electrocatalyst	Rs ($\Omega.cm^2$)	Rct ($\Omega.cm^2$)
$CoFe_2O_4$	1.14	96.4
$CoFe/NC_{10\%}$	1.0	3.47
$CoFe/NC_{20\%}$	0.94	4.6
$CoFe/NC_{30\%}$	1.03	1.48
$CoFe/NC_{40\%}$	0.96	62.7

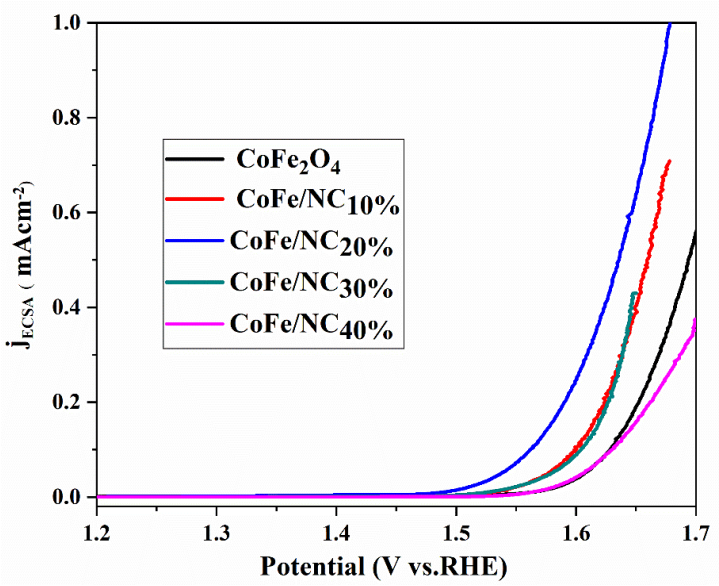

Figure S 5. ECSA-normalized polarization curve

Article III

Journal of Electroanalytical Chemistry 925 (2022) 116887

Contents lists available at ScienceDirect

Journal of Electroanalytical Chemistry

journal homepage: www.elsevier.com/locate/jelechem

Nitrogen-doped carbon decorated-$Ni_3Fe@Fe_3O_4$ electrocatalyst with enhanced oxygen evolution reaction performance

Gebrehiwet Abrham Gebreslase [a], David Sebastián [a], María Victoria Martínez-Huerta [b,*], María Jesús Lázaro [a,*]

[a] Instituto de Carboquímica, CSIC. Miguel Luesma Castán 4, 50018 Zaragoza, Spain
[b] Instituto de Catálisis y Petroleoquímica, CSIC, Marie Curie 2, 28049 Madrid, Spain

ARTICLE INFO

Keywords:
Electrocatalyst
Oxygen evolution reaction
NiFe
Dopamine
N-doped carbon

ABSTRACT

High performance, durable and inexpensive electrocatalyst for oxygen evolution reaction (OER) is of great importance for tenable hydrogen production via water electrolysis. Although spinel oxides (AB_2O_4, A, B = metal) represent a class of promising candidates for OER, their intrinsically poor electrical conductivity impacts their electrochemical performance. Herein, we employed a facile approach to transform an intrinsically low active $NiFe_2O_4$ into nitrogen-doped carbon decorated $Ni_3Fe@Fe_3O_4$ catalyst with improved activity and stability for alkaline OER. Initially, a pristine $NiFe_2O_4$ octahedron-like structure was synthesized by a hydrothermal route. Then, series electrocatalysts were prepared by incorporating the pristine $NiFe_2O_4$ with different dopamine concentrations via *in-situ* polymerizations of dopamine followed by carbonization. The morphology, crystalline structure, and chemical composition of the catalysts were characterized by scanning electron microscopy (SEM), transmission electron microscopy (TEM), X-ray diffraction (XRD), X-ray photoelectron spectroscopy (XPS), and inductively coupled plasma (ICP). The OER electrocatalysis performance was measured in a standard three-electrode system. The effect of the carbonized dopamine on the electrocatalytic activity and structure of the $NiFe_2O_4$ precursor was systematically investigated. Among several NiFe electrocatalysts, the one with 10 wt% of dopamine ($NiFe/NC_{10\%}$) exhibited a relatively higher catalytic activity for OER tested in 1.0 M KOH; unveiled low overpotential (350 mV at 10 $mAcm^{-2}$ current density), a low Tafel slope (56 $mVdec^{-1}$), low charge transfer resistance, relatively higher electrochemically active surface area. Most prominently, it remained stable for at least 12 h. This work provides a new perspective for functionalizing metal oxides and affords a facile synthesis approach, low-cost, high-performance, and robust electrocatalyst for alkaline OER electrodes.

1. Introduction

Electrochemical water splitting (EWS) plays a pivotal role in producing renewable and green hydrogen energy, especially when integrated with other renewable energy sources, such as electricity and solar. Hydrogen is distinguished by its high calorific value, ecological friendliness, and zero greenhouse emission when it is used. EWS is widely considered as one of the most stimulating next-generation energy storage and conversion systems, principally to furnish green hydrogen energy [1–3]. Regrettably, the practical application and performance of EWS is remarkably hindered by the focal electrochemical reaction process occurring at the electrode, particularly the oxygen evolution reaction (OER). OER is a kinetically sluggish reaction that markedly governs water electrolysis' efficiency. It consists of four consecutive reaction processes (four-electron transfer process), which demand a high overpotential to overcome the energy barrier [4–7]. To this end, developing a high-performance and durable electrocatalyst is essential to circumvent the sluggish reaction kinetics of OER, thus facilitating the EWS. Precious metals such as RuO_2 and IrO_2 and their derivatives are the benchmark electrocatalysts for OER. However, their high cost and low earth abundance limit their usage for large-scale and practical applications [8,9]. Moreover, the stability of these metal oxides is also a major concern. For example, apart from dissolving during the OER reaction, RuO_2 tends to oxidize to form RuO_4 and IrO_2 oxidizes to form IrO_3, affecting the overall efficiency [5]. Therefore, exploring alternative materials with cost-effective, abundant reserves, stable, and highly efficient electrocatalyst is vital for the penetration of EWS in the market.

Considerable efforts have been devoted to preparing efficient electrocatalysts using earth-abundant transition metals (e.g., Ni, Fe, Mn,

* Corresponding authors.
E-mail addresses: mmartinez@icp.csic.es (M.V. Martínez-Huerta), mlazaro@icb.csic.es (M.J. Lázaro).

https://doi.org/10.1016/j.jelechem.2022.116887
Received 30 August 2022; Received in revised form 26 September 2022; Accepted 7 October 2022
Available online 12 October 2022

Co, etc.) [10–16]. Metal oxides [17–19], sulfides [20–24], alloys [11,25,26], phosphides [27–33], nitrides [34], selenides [35] etc., have been amongst the most researched electrocatalysts for OER and for overall water splitting. Particularly, the bimetallic $NiFe_2O_4$ spinel structure has been reported as a profound potential for OER electrocatalysis because of its suitable adsorption/desorption of intermediate species of OER, low cost, high natural abundance, ample valence states, and ecological benignity [36–38]. However, the spinel structure possesses poor electrical conductivity and low surface area, which impede its widespread application [39–41]. Moreover, many of the synthesized metal oxides are in powder form; as a result, they tend to aggregate during the electrochemical reaction process, deteriorating the structural stability and utilization of the catalyst [42].

Myriads of research findings demonstrated that OER activities massively rely on the active sites and conductivity of the materials. One way to transfigure and amplify the active site is by tailoring the electrocatalyst's crystallinity and morphology structure with a larger electroactive surface area that would eventually endow abundant active sites. This can be achieved by designing nanostructured materials (nanowires, nanosheets, mesoporous, nanorods, etc…) [18]. Besides, the number of active sites in electrocatalysts can be supplemented through different strategies such as creating defect structures, surface engineering, doping heteroatoms, and tailoring porosity [40]. For example, Lim and co-workers [40] prepared $NiFe_2O_4$ spinel nanoparticles, with plentiful oxygen vacancies, through a hydrothermal route followed by hydrogen treatment. The as-prepared electrocatalyst revealed a lower overpotential of 389 mV to derive a current density of 10 $mAcm^{-2}$. Mahala and co-workers [43] developed 2D nanostructures of $NiFe_2O_4$ for OER, demanding an overpotential of 460 mV to generate a current density of 10 $mAcm^{-2}$ using a 1.0 M NaOH aqueous solution.

On the other hand, the conductivity of metallic electrocatalysts can be promoted by integrating with carbon or metals—this aids in regulating the electronic structure and promoting the intrinsic conductivity [18,39,44,45]. Substantial research works have been performed to prepare NiFe integrated with carbon materials comprising a high surface area. It was demonstrated that integrating metal oxide with conductive carbon materials (such as graphene, carbon nanotube, etc.) can enhance the catalytic activity and stability since the carbon material offers a virtuous coordinating environment with good conductivity, high surface area, and robust electrochemical stability [46,47]. Carbon materials provide physical support for the discrete metals and metal oxide and offer a charge transport channel, propagating overall performance. Doping heteroatoms such as nitrogen into carbon can also further alter the electronic structure of the catalyst and offers abundant defects as an active site, which eventually galvanize the overall catalytic activity [48]. The resulting outstanding performance of the combined materials stems from the synergetic effect between the carbon and metal/metal oxide [49]. Although innumerable outstanding results have been accomplished on bimetals, NiFe integrated with various carbonaceous materials towards OER electrocatalysis, the preparation methods for the carbon support are complex, unsafe, and energy-consuming steps. Hence, it is imperative to pursue alternative methods and carbon sources to synthesize NiFe integrated with carbon with inexpensive, easy, and mild synthesis routes to provide unique structures and enhanced conductivity for OER under alkaline electrolytes. The use of polydopamine (PDA) as a surface functionalizing agent has recently received remarkable attention because of its excellent and flexible agent for coating various surface materials. PDA is a mussel adhesive-inspired biomimetic synthetic polymer with admirable affinity to numerous solid surfaces [50]. It is characterized by its prospect of offering nitrogen-doped carbon after carbonization at high temperatures. Moreover, polydopamine also has the capability to adsorb on the surface of a transition metal such as Ni^{2+} and $Fe^{3+/2+}$, due to its diverse functional groups (e.g., imine, catechol, amine), which allows coordinating with the metal ions [50–52]. This provides a meaningful opportunity to functionalize and synthesize materials with desired structure and properties. In our previous work [11], we reported CoFe decorated nitrogen-doped carbon (CoFe/NC) catalyst prepared by incorporating $CoFe_2O_4$ and polydopamine. Carbonized polydopamine altered the crystalline structure and electrochemical activity of $CoFe_2O_4$, in which incorporating 30 % PDA presented excellent catalytic activity and stability for alkaline OER. Nevertheless, there is no report that elucidates the effect of polydopamine on the physicochemical properties and OER activity of $NiFe_2O_4$ spinel oxide.

Herein, considering the merits of polydopamine, we synthesized nitrogen-doped carbon derived from polydopamine decorated $Ni_3Fe@NiFe_2O_4$ (hereafter NiFe/NC) composite electrocatalyst with excellent and tailored activity towards OER. The nanocomposite was obtained by hydrothermal synthesis of spinel oxide of $NiFe_2O_4$, in situ polymerization of various dopamine content (5, 10, 20, and 30 wt%) on the $NiFe_2O_4$ surface, followed by carbonization at high temperature. The as-prepared $NiFe/NC_{10\%}$ electrocatalyst presented excellent catalytic activity towards OER under alkaline electrolyte, in which a low overpotential, small Tafel slope, and outstanding durability have been recorded. The presence of the carbon layer and the evolution of Ni_3Fe and Fe_3O_4 phases progressed the catalytic activity of the sample.

2. Experimental section

2.1. Chemical reagents

Iron (III) nitrate hydrate (98 %, Riedel de-Haen, Sigma Aldrich), Nickel (II) nitrate hexahydrate (≥97.0 %, Alfa Aesar), dopamine hydrochloride. (MW = 189.64 g/mol, Sigma Aldrich), tris(hydroxymethyl aminomethane)(ACS, reagent > =99.8 %, MW = 121.14 g/mol, Sigma Aldrich)). Potassium hydroxide (Analytical grade, Fischer scientific), Potassium hydroxide, pellets, 85 % (Alfa Aesar), Ultrapure water (Q2, 0.055 μS/cm, SIEMENS), Nafion ®Perfluorinated resin solution (5 wt%, Sigma Aldrich), commercial IrO_2 powder, 99 % (Alfa Aesar). All the chemical reagents were used as received without further modification.

Electrocatalyst synthesis.

2.2. Synthesis of $NiFe_2O_4$ electrocatalyst

A facile one-step hydrothermal route was employed to synthesize $NiFe_2O_4$ nanoparticles. Typically, Fe $(NO_3)_3{\cdot}9H_2O$ (7.6 mmol) and Ni $(NO_3)_2{\cdot}6H_2O$ (3.8 mmol) were dissolved in 30 mL of deionized water and stirred for half an hour. Subsequently, 30 mL of a 2 M KOH solution was added and stirred for 2 h. The resulting mixture was transferred into a Teflon-lined stainless steel autoclave and maintained at 180 °C for 22 h. The precipitate was cooled to room temperature and collected by centrifugation. The product was washed with ethanol and water several times and dried at 60 °C overnight.

2.3. Synthesis of dopamine-modified $NiFe_2O_4$ composite electrocatalyst

The composite electrocatalysts were prepared by mixing $NiFe_2O_4$ with dopamine hydrochloride, in situ polymerization, followed by carbonization at high temperatures. Specifically, 0.4 g of the prepared $NiFe_2O_4$ was dispersed in 50 mL Tris (tris(hydroxymethyl) aminomethane)-buffer (Tris-HCl, 10 mM, pH 8.5) by ultrasonication for half an hour to form a suspension. Next, a different mass fraction of dopamine hydrochloride relative to the spinel $NiFe_2O_4$ (5, 10, 20, and 30 wt%) was added to the above mixture and stirred at room temperature for 24 h. Then, the product was centrifuged, washed with deionized water, and dried at 60 °C overnight. Finally, the as-prepared product was carbonized at 800 °C for 1 h at a 5 °C min^{-1} heating rate

under N_2 atmosphere. Throughout the manuscript, the samples are designated as NiFe/NC_x, where × refers to the mass fraction of dopamine (x = 5, 10, 20, and 30 wt%) relative to the $NiFe_2O_4$ precursor and NC refers to nitrogen-doped carbon.

2.4. Physicochemical characterization

Scanning electron microscopy (SEM-EDX) was obtained in SEM Hitachi 3400 N, EDX Röntec XFlash de Si (Li). Ultra-high resolution imaging (HRTEM) analysis was conducted in Titan Cube (CEOS Company). The metal's weight percentage was acquired by inductively coupled plasma atomic emission spectroscopy (ICP-AES) in a Xpectroblue-EOP-TI FMT26 (Spectro). The X-ray diffraction (XRD) analyses were analyzed in a Bruker D8 Advance diffractometer with Cu Kα of 1600 W. X-ray photoelectron spectroscopies (XPS) were acquired on a Kratos AXIS Supra system equipped with a hemispherical electron energy analyzer operating with mono Al Kα (1486.7 eV) at 120 W (8 mA/15 kV. Analysis area = two × one mm), base pressure 10^{-9} Torr. Survey scans were recorded from 0 to 1200 eV with Pass Energy/step (Wide: 160 eV/1.0 eV, Regions: 20 eV/0.1 eV. The C 1 s line at 284.6 eV was employed to correct all XPS spectra. CasaXPS software was used to perform peak fitting and quantification, and Shirley-type background was employed for all peaks. Gaussian and Lorentzian (GL: 30 %) line shapes were used for each component.

2.5. Electrochemical measurements

The electrochemical performance of the electrocatalyst was measured in a three-electrode system controlled by potentiostat/galvanostat AUTOLAB PGSTAT302 at room temperature. 1.0 M KOH aqueous solution was used as an electrolyte. Glassy-carbon (GC) rod, reversible hydrogen electrode (RHE), and rotating ring disk electrode (RRDE) with a glassy carbon disk (diameter = 5 mm) were used as a counter, reference, and working electrode, respectively. A 20 μL ink solution was deposited drop by drop on the GC working electrode. The ink catalyst solution was prepared by dispersing 4.8 mg of electrocatalyst in 461 μL isopropanol/water (1: 1) solvent containing 19.48 μL of Nafion solution (5 wt%), followed by ultrasonication for 15 min.

To perform OER measurement, first, the electrolyte was de-aerated with N_2 for about 30 min. Next, all electrocatalysts were subjected to 50 cyclic voltammetry cycles between 0.05 and 1.0 V vs RHE at a 100 mV/s scan rate for surface activation. In addition, three cyclic voltammetry was carried out at a scan rate of 20 mV/s in the potential range of 0.05–1.1 vs RHE. OER polarization curve for all electrocatalysts was obtained after 10 cycles of CV in the potential scope of 1.1–1.8 V vsRHE at a scan rate of 5 mV/s at 1600 rpm. The CV curves were corrected by $V = V_{measured} - iR_s$, where $V_{measured}$ is the measured potential, and R_s is the solution resistance determined by the electrochemical impedance spectroscopy (EIS). Electrochemical impedance spectroscopy was measured at 1.60 V vs RHE in the frequency range of 100 kHz to 0.01 Hz at a 5 mV amplitude. To evaluate and compare the electrochemically active surface area (ECSA) of the various electrocatalyst, cyclic voltammetry (CV) measurements were carried out in the non-faradaic potential window of 1.1–1.23 V vsRHE at a scan rate of 20 mV/s. In this case, the catalysts' electrical double layer capacitances (C_{dl}) is determined from the integrated area of CV, and it has been demonstrated that C_{dl} is directly proportional to the ECSA [53]. The electrochemical stability of the best composite electrocatalyst was scrutinized using chronopotentiometry at 10 $mAcm^{-2}$ current density.

3. Results and discussion

The composite electrocatalysts were prepared via three sequential steps as schematically represented in Scheme 1. Firstly, spinel oxide of $NiFe_2O_4$ was synthesized through a hydrothermal route. Subsequently, the obtained $NiFe_2O_4$ powder was mixed with different content of dopamine hydrochloride and subjected to polymerize on the surface of the spinel oxide for 24 h under stirring. Lastly, NiFe/NCx was gradually obtained by carbonizing the resultant product.

The surface morphology and structure of the electrocatalysts was observed by SEM and TEM. The SEM images shown in Fig. S1(a–e), reveal there is an apparent discrepancy in surface morphology between the samples. Fig. S1(a) shows the SEM image for the pristine $NiFe_2O_4$ sample in which a rough surface is observed, but it remained challenging to observe particle size and shape clearly, due to its small size and limitation of the SEM resolutions. To this end, we employed TEM to visualize the particle size and shape. The TEM image in Fig. 1(a) indicates that the as-prepared pristine $NiFe_2O_4$ encompasses an octahedral-like structure with uneven particle size in the range of 20–120 nm. Overlapping nucleation and the growing process could be the reason for the broad-size particle distribution. Moreover, Ost-

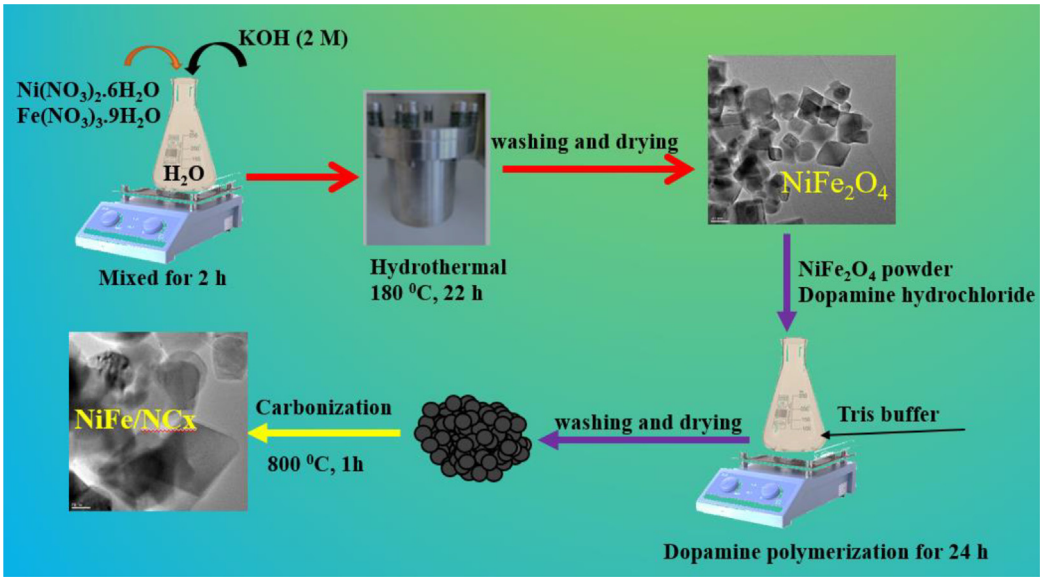

Scheme 1. Schematic illustration of the synthesis process employed to obtain $NiFe_2O_4$ and NiFe/NC_x composite electrocatalysts.

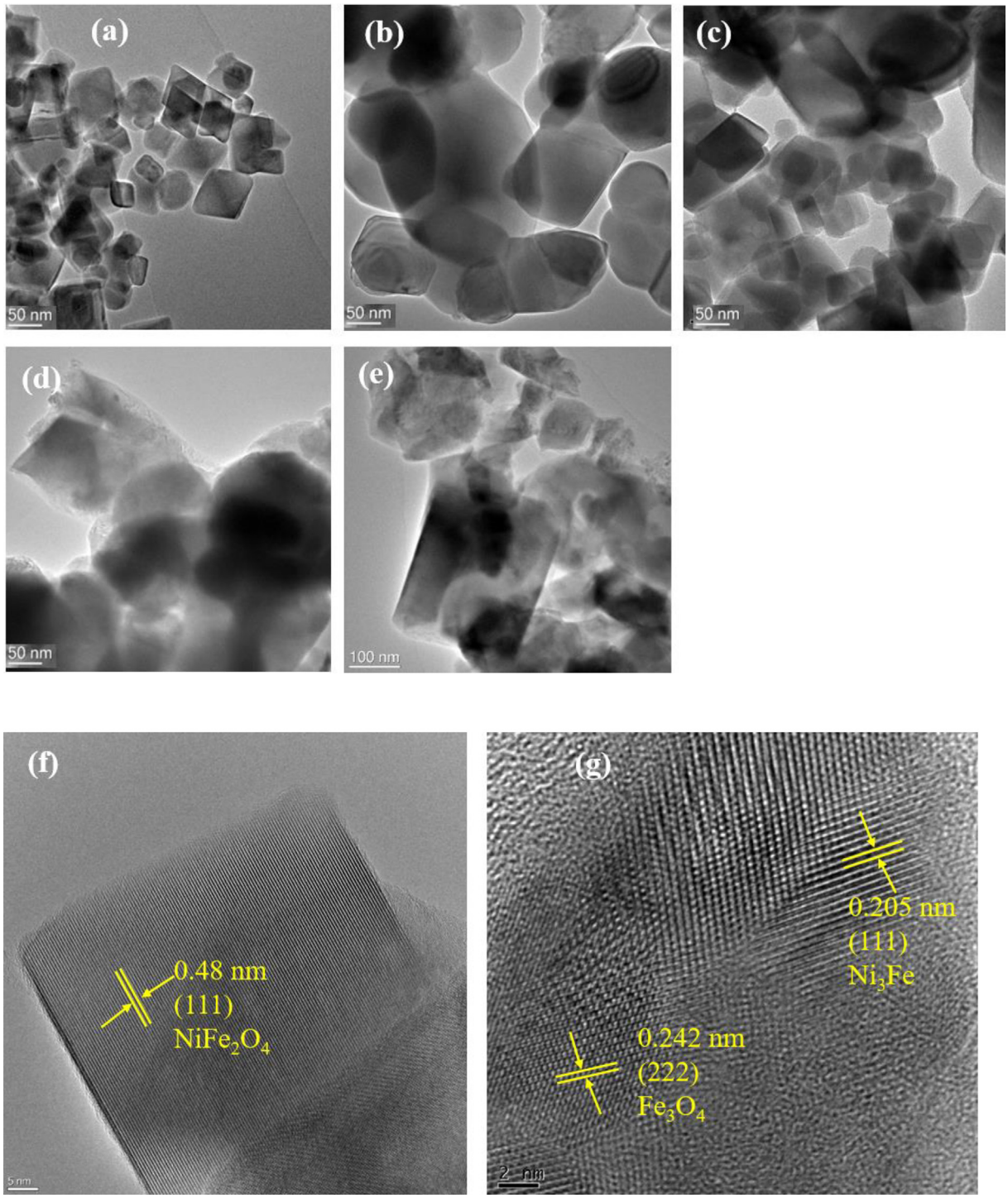

Fig. 1. TEM image of (a) $NiFe_2O_4$, (b) $NiFe/NC_{5\%}$, (c) $NiFe/NC_{10\%}$, (d) $NiFe/NC_{20\%}$, (e) $NiFe/NC_{30\%}$ (f) HRTEM image of $NiFe_2O_4$, and (g) HRTEM image $NiFe/NC_{10\%}$ sample.

wald ripening because of the long-time thermal treatment can also contribute to the relatively broad size distribution [54,55]. In contrast, the surface images of the composite electrocatalysts show different morphologies compared to the pristine, as shown in Fig. S1(a–e) and Fig. 1(a–e). Integrating dopamine as a carbon source into the pristine $NiFe_2O_4$ ultimately altered the overall morphology and particle size. The composite samples (Fig. 1(b–e)) reveal an irregular texture and an entangled network without distinct characteristic morphology, which could be originated from the nitrogen-doped carbon framework derived from the thermal carbonization of the polydopamine. The particle size of the composite samples has exhibited a remarkable increase compared to the pristine $NiFe_2O_4$ precursors. The particle size distribution of the pristine and the composite samples is presented in the supporting information in Fig. S2. The average particle size of the pristine $NiFe_2O_4$ is about 53 nm, while the average particle size of $NiFe/NC_{5\%}$, $NiFe/NC_{10\%}$, $NiFe/NC_{20\%}$, and $NiFe/NC_{30\%}$ is determined to be 132, 55, 137, and 110 nm, respectively. It is apparent from this information that there is a clear particle size difference between the samples depending on the dopamine contents. The $NiFe/NC_{5\%}$ sample shows a bigger particle size than that of $NiFe/NC_{10\%}$, possibly due to the dis-

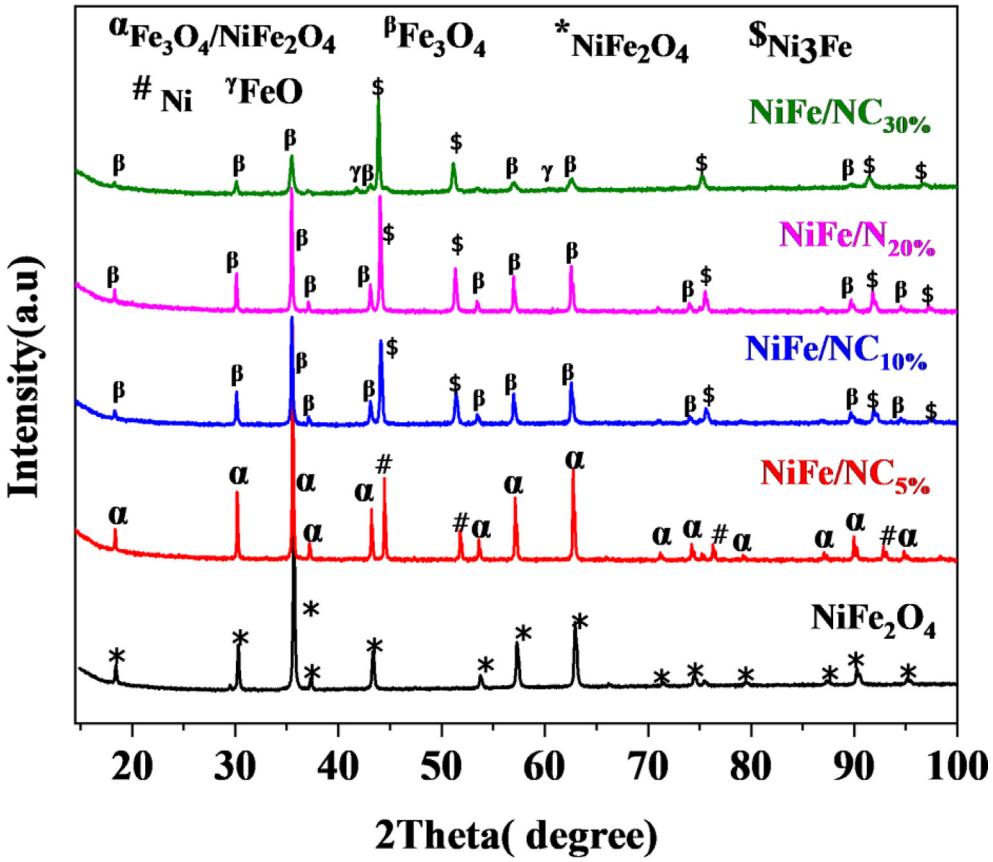

Fig. 2. XRD pattern for the various electrocatalyst.

similarity of crystal phase evolved in each sample. XRD analysis (Fig. 2) unveiled that NiFe/$NC_{5\%}$ contains $NiFe_2O_4$, Ni, and Fe_3O_4 phases, while NiFe/$NC_{10\%}$ comprises mainly Ni_3Fe and Fe_3O_4 crystal phases. The evolution of dissimilar crystal phases can lead to the formation of different particle sizes, depending on the nature of surface chemistries and particle growth. Moreover, the particle size of the NiFe/$NC_{20\%}$ sample is much larger than the NiFe/$NC_{10\%}$ sample, which could be due to the dopamine content difference, in which a high amount of carbonized polydopamine coating layer can encapsulate many units, leading to the formation of bigger particles. A similar trend was also observed in the crystallinity size determined from the XRD analysis (Table 1). Emphasizing on NiFe/$NC_{10\%}$ sample, the SEM image (Fig. S1(c)) reveals a rough surface with a granular framework. Observation of particle size and microstructure of the particles via SEM was challenging. The TEM image of NiFe/$NC_{10\%}$ discloses the product contains a mixture of octahedral-like structure and an irregular structure with a larger particle size (varying from 10 to 120 nm). The apparent morphology and particle size difference observed between the nanocomposite and pristine $NiFe_2O_4$ electrocatalysts suggest an intimate interaction between the dopamine and the spinel oxide, which altered the microstructure and crystallinity of the resultant nanocomposites.

Table 1
Summary of phase components, lattice parameters, weight percentage, and crystalline size of each phase obtained from XRD quantitative analysis.

Sample	Phases	Lattice parameters (a) (Å)	Amount (wt. %)	Crystallite size (nm)
$NiFe_2O_4$	$NiFe_2O_4$	8.35	100	53.3
NiFe/$NC_{5\%}$	Ni	3.53	5.93	113.3
	$NiFe_2O_4$	8.37	74.6	113.3
	Fe_3O_4	8.39	19.47	–
NiFe/$NC_{10\%}$	Fe_3O_4	8.39	67.55	59.5
	Ni_3Fe	3.55	32.45	53.2
NiFe/$NC_{20\%}$	Fe_3O_4	8.39	64.92	97.7
	Ni_3Fe	3.56	35.08	75.2
NiFe/$NC_{30\%}$	Fe_3O_4	8.39	49.83	21.5
	Ni_3Fe	3.57	39.02	49.0
	FeO	4.33	8.97	15.8
	Ni	3.51	2.18	11.0

To investigate and compare the crystal structure of pristine $NiFe_2O_4$ and carbon-modified $NiFe_2O_4$, we employed fast Fourier transform and inversed fast Fourier transform on a selected area of HRTEM images using ImageJ software to get information on its lattice fringe space. Fig. 1(f) shows the HRTEM images of $NiFe_2O_4$, in which the lattice spacing of 0.48 nm corresponds to the (1 1 1) plane of $NiFe_2O_4$. The HRTEM image NiFe/$NC_{10\%}$ is shown in Fig. 1(g). The lattice fringe spacing of 0.205 nm corresponds to the (1 1 1) plane of Ni_3Fe. Besides, the lattice fringe space of 0.242 nm can be assigned to the (2 2 2) plane of Fe_3O_4. This result reveals that the NiFe/$NC_{10\%}$ sample consists of two crystal phases, which is in agreement with the XRD analysis result. The formation of Ni_3Fe alloy could be due to the partial reduction of the $NiFe_2O_4$ by dopamine, and they are presented together in close contact with Fe_3O_4. Such heterogeneous materials usually exhibit stable activity during catalysis [7]. The formation of Ni_3Fe closely contacted with the Fe_3O_4, and the coating of the carbonized polydopamine layer could be favorable for electron transfer, promoting conductivity and catalytic activity.

X-ray diffraction (XRD) measurement was applied to examine the samples' composition, concentration, and crystal phases. As shown in Fig. 2, the pristine $NiFe_2O_4$ sample reveals a pure spinel oxide ($NiFe_2O_4$) structure. The major diffraction peaks located at (2θ =) 18.4°,

30.3°, 35.7°, 37.3°, 43.4°, 53.8°, 57.4°, 63.0°, 71.5°, 74.6°, 75.6°, 79.6°, 87.4°, 90.4° and 95.3° correspond to the (1 1 1), (2 2 0), (3 1 1), (2 2 2), (4 0 0), (4 2 2), (5 1 1), (4 4 0), (6 2 0), (5 3 3), (6 2 2), (4 4 4), (6 4 2), (7 3 1), and (8 0 0) planes of a cubic spinel $NiFe_2O_4$ structure (*Fd*-3 m, JCPDS, #44–1485), respectively. No other peak was observed, revealing that a pure nickel ferrite phase was formed. In the case of the composite samples, different compositions and crystalline phases were obtained. The $NiFe/NC_{5\%}$ sample comprises a standard XRD pattern of nickel-metal (*Fm*-3 m, JCPDS, #87–0712) and a mixture of $NiFe_2O_4$ and iron oxide (Fe_3O_4, JCPDS, #65–3107). The major reflection peaks at (2θ =) 44. 5°, 51.8°, 76.4°, and 92.9° correspond to (1 1 1), (2 0 0), (2 2 0), and (3 1 1) crystal plane reflections of nickel, respectively. The contribution of (weight percentage, wt. %) of each phase (Ni metal, Fe_3O_4, and $NiFe_2O_4$) was calculated to estimate the amount presented in the sample (Table 1). It is important to mention that the diffraction peak of Fe_3O_4 and $NiFe_2O_4$ have similar XRD diffraction patterns, with slight diffraction angle differences. To differentiate which structure was presented in the samples, the chemical composition of metals was estimated by coupling both XRD and ICP analysis. The ICP analysis result was used as a foundation/threshold to estimate the corresponding phase concentration that could avail in the product and identify the possible phase structure ($NiFe_2O_4$, Fe_3O_4, or both). Accordingly, it was found that the $NiFe/NC_{5\%}$ sample contains Ni (5.93 %), Fe_3O_4 (19.52 %), and $NiFe_2O_4$ (74.6 %) phases, indicating the product comprises a multi-phase crystalline structure. On the other hand, $NiFe/NC_{10\%}$ and $NiFe/NC_{20\%}$ encompass an alloy of Ni_3Fe and Fe_3O_4. The five characteristic peaks at (2θ =) 44.1°,51.4°, 75.6°, 92.0°, and 97.0° correspond to (1 1 1), (2 0 0), (2 2 0), (3 1 1), and (2 2 2) cubic crystal planes of Ni_3Fe (*Pm*-3 m, JCPDS #65–3244). It is important to notice the difference between $NiFe/NC_{10\%}$ and $NiFe/NC_{20\%}$ samples in terms of weight percentage contribution and crystalline size of each phase, in which less amount of Ni_3Fe was observed for the $NiFe/NC_{10\%}$ sample, and also the crystallite size is relatively small compared to the $NiFe/NC_{20\%}$ sample (Table 1). Moreover, $NiFe/NC_{30\%}$ sample possesses a multi-phase crystallographic structure, including Ni_3Fe, Fe_3O_4, FeO, and a trace of Ni metal. The reflection peaks at (2θ =) 36.1°, 41.93°, and 60.8° are attributed to the crystallographic planes (1 1 1), (0 0 2), and (0 2 2) of FeO (JCPDS, #06–0615), respectively. The crystallite size in this sample is smaller than the other composite counterparts, which could be due to the segregation of a certain percentage of Fe_3O_4 particles. The appearance of Ni_3Fe crystal structure in the composite samples could be due to the reduction of the $NiFe_2O_4$ precursor by the carbonized polydopamine. From these XRD analysis results, we can conclude that incorporating dopamine and carbonization at high temperatures has influenced the overall crystal structure of the $NiFe_2O_4$ precursor, which could ultimately offer different catalytic activity based on the type of crystal structure, quantity, and composition. Adding a low dopamine content results in a mixture of $NiFe_2O_4$ and Fe_3O_4 with a dominant $NiFe_2O_4$ crystal structure, while a further increase of dopamine content has led to the formation of an alloy of Ni_3Fe and Fe_3O_4 phases, differing in weight percentage, unit cell parameter, and crystalline size. Table 1 shows a summary of phase components, lattice parameters, weight percentage, and crystalline size of each phase obtained from the XRD analysis. The lattice parameter (a) for the pristine $NiFe_2O_4$ was determined to be 8.35 Å, while it has slightly increased to 8.37 Å in the $NiFe/NC_{5\%}$ sample. Moreover, after dopamine concentration increased, a phase transformation from $NiFe_2O_4$ to Ni_3Fe (a = 3.56 ± 0.01) and Fe_3O_4 (a = 8.39 Å) crystal structure was observed. The absence of graphitic carbon in the XRD pattern (Fig. 2) could be due to a low crystallinity degree of the carbon material.

The electrocatalytic performance of material relies on its surface. In this case, X-ray photoelectron spectroscopy (XPS) is a vital technique to unravel the surface chemistry of materials. The surface composition and valence states of the pristine and nanocomposite catalysts were explored by the surface-sensitive XPS technique. The high-resolution XPS analysis of Ni 2p and Fe 2p for all samples and C 1 s and N 1 s for the nitrogen-doped carbon-modified $NiFe_2O_4$ is shown in Fig. 3. The XPS spectrum of Ni 2p (Fig. 3a) can be resolved into three doublets for the pristine $NiFe_2O_4$, while four doublets were obtained for the composite electrocatalysts. Looking at pristine $NiFe_2O_4$, the first two peaks of Ni $2p_{3/2}$ at binding energy (BE) of ca. 855 and 856.6 eV are attributed to Ni^{2+} and Ni^{3+}, while the third doublet at higher BE ca.861.3 eV corresponds to shake up satellites. In the case of nanocomposite catalysts, the peaks are slightly shifted to higher binding energy, indicating a strong bond interaction between nitrogen-doped carbon and metals. Notably, for the $NiFe/NC_{10\%}$ catalyst, the peaks of Ni $2p_{3/2}$ shifted to 855.5, 856.8, and 861.3 eV, which can be assigned to Ni^{2+}, Ni^{3+}, and shake-up satellite, respectively. Moreover, an apparent metallic nickel was observed in all composite electrocatalysts at a lower BE of ca. 852 eV [56,57]. The relative concentration of the deconvoluted chemical species of Ni 2p (Ni^{2+}, Ni^{3+}, and Ni^0) revealed that there is an actual appearance of metallic nickel after integrating dopamine with the $NiFe_2O_4$ precursor, and the relative concentration of Ni^{2+} is higher than Ni^{3+}species, as shown in Table S1.

Fig. 3b shows the high–resolution XPS spectra of Fe 2p, in which two pairs of spin–orbit signals and two shake-up satellites are unveiled for all catalysts. The peaks at BE ca. 710, 712, and 718 eV can be assigned to Fe^{2+}, Fe^{3+}, and shake-up satellites, respectively [57–59]. Again, it is essential to mention that the binding energy for the composite catalysts indicated a slight shift towards higher binding energy, suggesting an intimate interaction between the carbon and Fe metal. Moreover, the relative concentration of the deconvoluted Fe^{3+} chemical species is higher than the Fe^{2+}counterpart in all samples. The results demonstrate that the chemical composition of nanocomposite catalyst contains Ni^0, Ni^{3+}, Ni^{2+}, Fe^{2+}, and Fe^{3+}. The XPS analysis for Ni 2p and Fe 2p is shown in Table S1, which explicitly outlines the corresponding binding energy for the different doublets in each sample and the relative concentration of the deconvoluted chemical species. To examine the chemical state of the carbonized polydopamine, the XPS of C 1 s and N 1 s was also evaluated.

The high resolution of C 1 s can be deconvoluted into three prominent peaks (Fig. 3(c)). The peaks at BE of ca. 284.6, 286.2, and 288.4 eV are assignable to the aromatic linked carbon (C—C/C═C), the C bonded with nitrogen or oxygen (C—N/C—O), and O–C═O/C═O, respectively [57,60,61]. The C—N bond confirms the existence of nitrogen-doped carbon material, which is vital for ion transfer in the interface due to its favorable electrical conductivity.

The deconvolution analysis of the N 1 s spectrum leads to three prominent peaks (Fig. 3d) corresponding to different nitrogen species. The peaks positioned at BE of ca. 398, 399.3, and 401.0 eV can be assigned to pyridinic N, pyrrolic N, and graphitic N, respectively. [62,63]. It is decisive to outline that the sample $NiFe/NC_{10\%}$ possesses a relatively high pyridinic-N and graphitic N content compared to the other samples. It was demonstrated that pyridinic-N and graphitic N are among the N atoms considered as potential active sites for OER [64]. The graphitic carbon is beneficial to improve the durability of catalysts [65], and the pyridinic-N facilitates the adsorption of intermediates of water oxidation (OH–, OOH–) due to its ability to accept an electron from the adjacent carbon, thus leading to enhanced catalytic activity [66].

ICP –AES was used to study the composition and metal ratio of the as-prepared pristine and nanocomposite materials, and the results are presented in Table S2. It revealed that the weight ratio of iron to nickel is about 2, which agrees with the initial ratio of Fe and Ni.

To probe the OER electrocatalytic activity, all the as-prepared electrocatalysts were tested in 1.0 M KOH alkaline solution using a three-electrode system at a scan rate of 5 mVs^{-1}. For comparison, the pristine $NiFe_2O_4$ and dopamine $NiFe_2O_4$ modified samples were measured for their corresponding catalytic activity for OER. As illuminated in

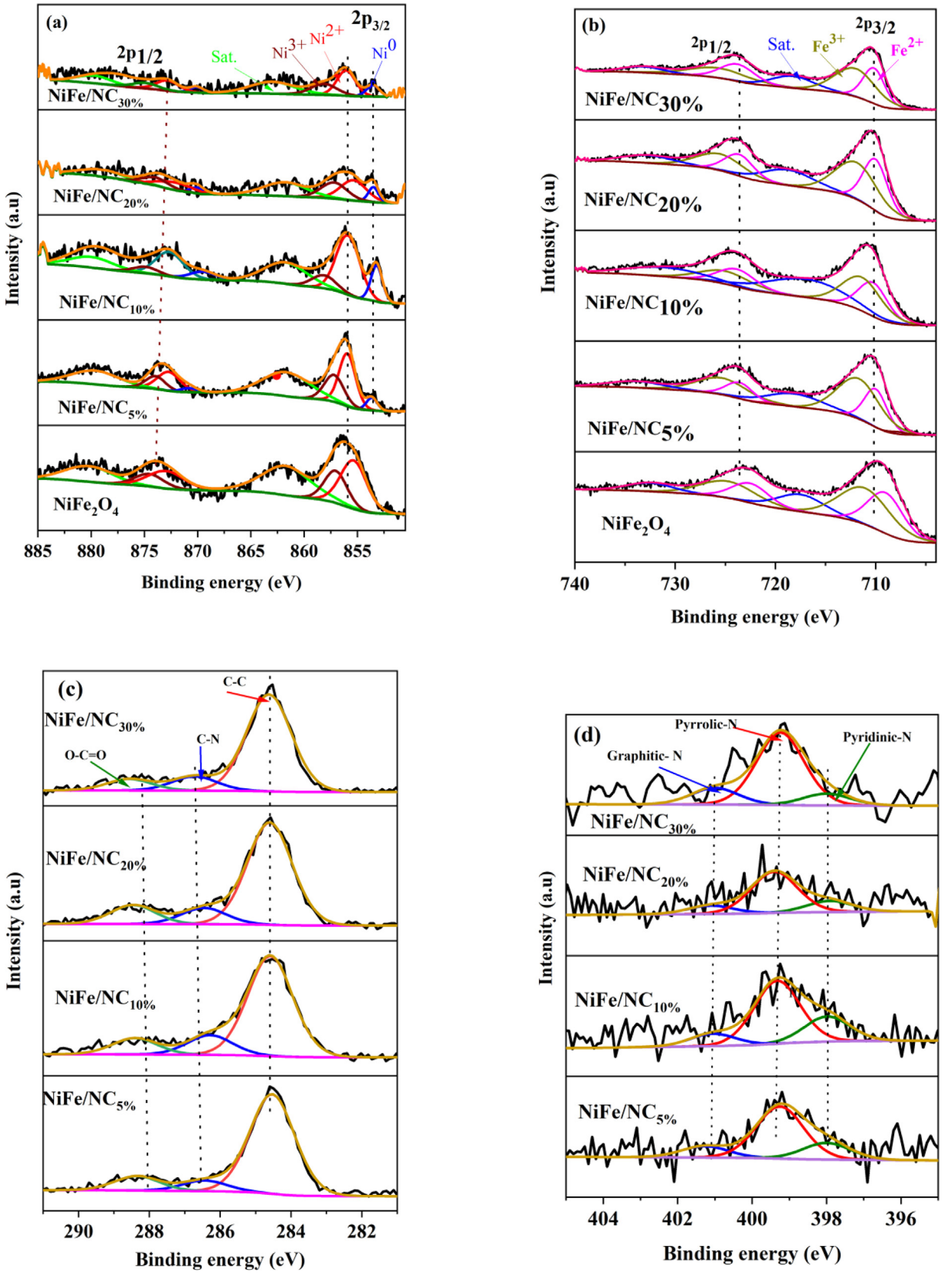

Fig. 3. High resolution XPS spectra of (a) Ni 2p, (b) Fe 2p, (c) C 1 s, and (d) N 1 s.

Fig. 4(a), $NiFe/NC_{10\%}$ displays higher catalytic activity for OER than the other catalysts. Particularly, $NiFe/NC_{10\%}$ electrocatalyst only needs 350 mV of overpotential to obtain a current density of 10 $mAcm^{-2}$, which is relatively lower than the other prepared electrocatalysts. The pristine $NiFe_2O_4$, $NiFe/NC_{5\%}$, $NiFe/NC_{20\%}$, and $NiFe/NC_{30\%}$ electrocatalysts require an overpotential of 540 mV, 420 mV,

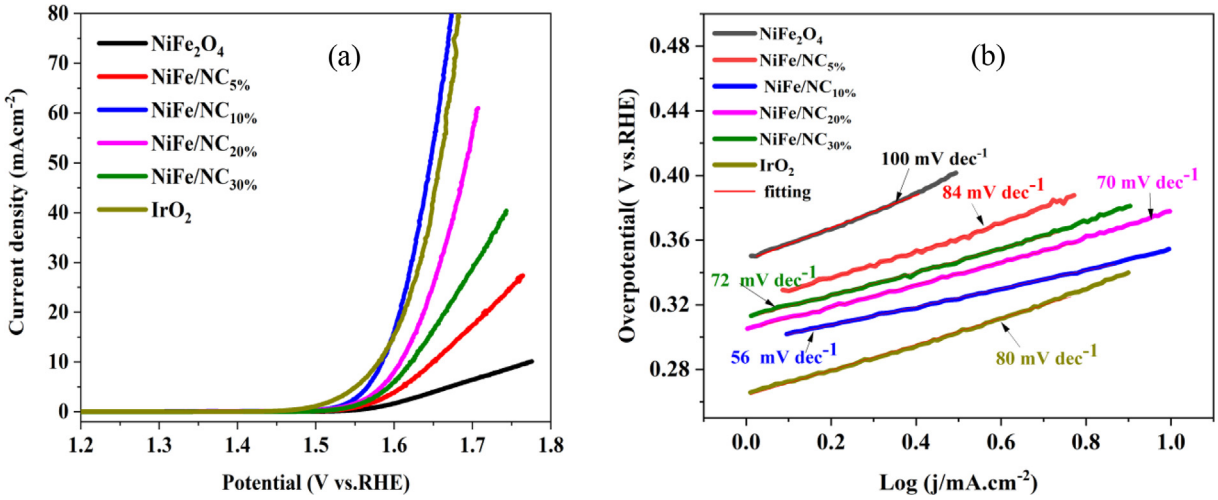

Fig. 4. Electrochemical measurements in 1.0 M KOH electrolyte: (a) OER polarization curve of different electrocatalysts at a 5 mVs^{-1} scan rate and (b) Tafel plot.

370 mV, and 390 mV, respectively, to derive the same current density. The OER activity of IrO_2 is also measured and used as a benchmark to compare the prepared catalysts' performance. $NiFe/NC_{10\%}$ and commercial IrO_2 exhibited a comparable performance for OER, as it is apparent from Fig. 4(a). More fascinatingly, $NiFe/NC_{10\%}$ catalyst shows a profound higher current density with increasing applied potential, which outsmarted the other catalysts prepared following the same synthesis condition. The coating layer of dopamine on the surface of bimetals could be the rationale for the promoted catalytic activity of the resulting nanocomposite samples. The $NiFe/NC_{10\%}$ sample presented the most active towards OER with the optimum combination of dopamine and $NiFe_2O_4$ precursor, which evidently unveils the effect of dopamine amount in modulating the microstructure, active sites, conductivity, and activity of $NiFe_2O_4$ precursor. Adding more dopamine leads to the formation of bigger particle sizes. Also, the electroactive metals could be covered by a thicker carbon layer, which increases the polarization resistance of the catalyst and deteriorates the activity. On the other hand, low dopamine may not fully cover the entire metal, leading to a non-uniform coating of the active metals; as a result, a compromised activity could be achieved.

To study the intrinsic activity of the samples, the OER kinetics of all catalysts was explored by the Tafel plot. As shown in Fig. 4(b), the corresponding Tafel slope of $NiFe_2O_4$, $NiFe/NC_{5\%}$, $NiFe/NC_{10\%}$, $NiFe/NC_{20\%}$, $NiFe/NC_{30\%}$, and IrO_2 was determined to be 100, 84, 56, 70, 72, and 80 mV/dec, respectively. The low Tafel slope of $NiFe/NC_{10\%}$ further highlights its extraordinary catalytic activity. Tafel slope is correlated to the rate-determining steps. It is well accepted that the OER process comprises four consecutive steps. The proposed reaction pathways for OER under alkaline solution are given as follows [10,67].

$$M + OH^- \rightarrow M - OH + e^- \quad (1)$$

$$M - OH + OH^- \rightarrow M - O + H_2O + e^- \quad (2)$$

$$M - O + OH^- \rightarrow M - OOH + e^- \quad (3)$$

$$M - OOH + OH^- \rightarrow M + O_2 + H_2O + e^- \quad (4)$$

where 'M' denotes an active site on the surface; the value of the Tafel slope varies depending on the rate of determining steps. It differs from 120 $mVdec^{-1}$ for step (1) if the first electron transfer is the rate-determining step, and it is less than 120 $mVdec^{-1}$, if the rate-determining step is one of the subsequent steps. If the rate-determining steps approach the end of the reaction steps, it is considered a sign of a good electrocatalyst. It has been reported that a Tafel slope near 60 $mVdec^{-1}$ reveals that the rate-determining step is located at the end of the multi-electron transfer reaction step (4) [68], suggesting good catalytic activity. Herein, $NiFe/NC_{10\%}$ presented a low Tafel slope of 56 $mVdec^{-1}$, unveiling the rate-determining step presides at the end of reaction steps. This indicates that optimum dopamine content can commendably transform and tune the intrinsic catalytic activity of the spinel oxide. The optimized carbonized polydopamine plays a crucial role in altering the material's functionality and amplifying the OER activity. Integrating low and high polydopamine concentration with the spinel $NiFe_2O_4$ leads to lower activity. Therefore, it is necessary to optimize the content of polydopamine to obtain a tailored and promising electrocatalyst. A thicker layer of carbon on the surface of metal particles would lessen the electrocatalytic activity of the materials due to the barrier of electron transfer between the carbon layer and active metals. Hence, developing a suitable route to synthesize desired carbon layer thickness on a surface of metals particle is imperative to advance electrocatalyst for OER application remarkably [35].

Fig. 5(a) illustrates the different electrocatalysts comparisons considering both overpotential and Tafel slope. Materials with lower overpotential and small Tafel slope are ideal electrocatalysts for OER. $NiFe/NC_{10\%}$ catalyst shows both lower overpotential and small Tafel slope among the electrocatalyst series, demonstrating its favorable features towards OER. The CV method is commonly employed to evaluate the surface capacitance of catalysts. Fig. 5(b) shows the CV profile of the prepared electrocatalysts, measured in the potential range of 0.05 and 1.10 V vs RHE at the scan rate of 20 mVs^{-1}. The CV curve presents a non-rectangular behavior at the selected potential region and scan rate. The non-rectangular shapes of the CV curves reveal that the resulting capacitive behavior is mainly characteristic of the pseudocapacitance process [69,70]. From Fig. 5b, we can observe an apparent discrepancy with respect to the integrated area under the CV curve in which the $NiFe/NC_{10\%}$ sample showed a relatively higher area. It is noteworthy to mention that the evolution of the capacitive profile is in accordance with the anodic OER profile (Fig. 4a), suggesting that the nitrogen-doped carbon coating plays a key role in modifying the intrinsic feature of pristine $NiFe_2O_4$.

The catalyst's electrochemical active surface area (ECSA) was estimated through the CV technique to further explore the intrinsic electrochemical features. It is apparent that ECSA has a linear relationship with the electrical double layer (EDL) due to the interfacial charging process. In this case, a potential window in which no faradic or no oxidation/reduction reaction occurs is meticulously selected. The recorded current is attributed only to the surface-controlled capacitance. As shown in Fig. 6(a), interestingly, the NiFe/

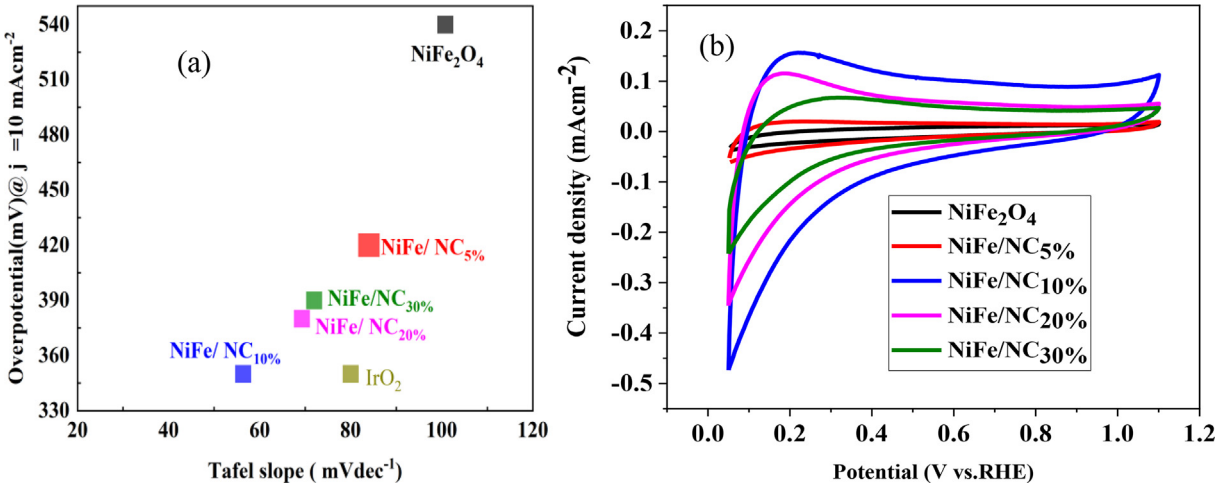

Fig. 5. (a) Comparison of overpotential at j = 10 mAcm^{-2} and (b) cyclic voltammograms (CV) of the as-prepared electrocatalyst in the potential range of 0.05–1.10 V vsRHE at 20 mVs^{-1} scan rate.

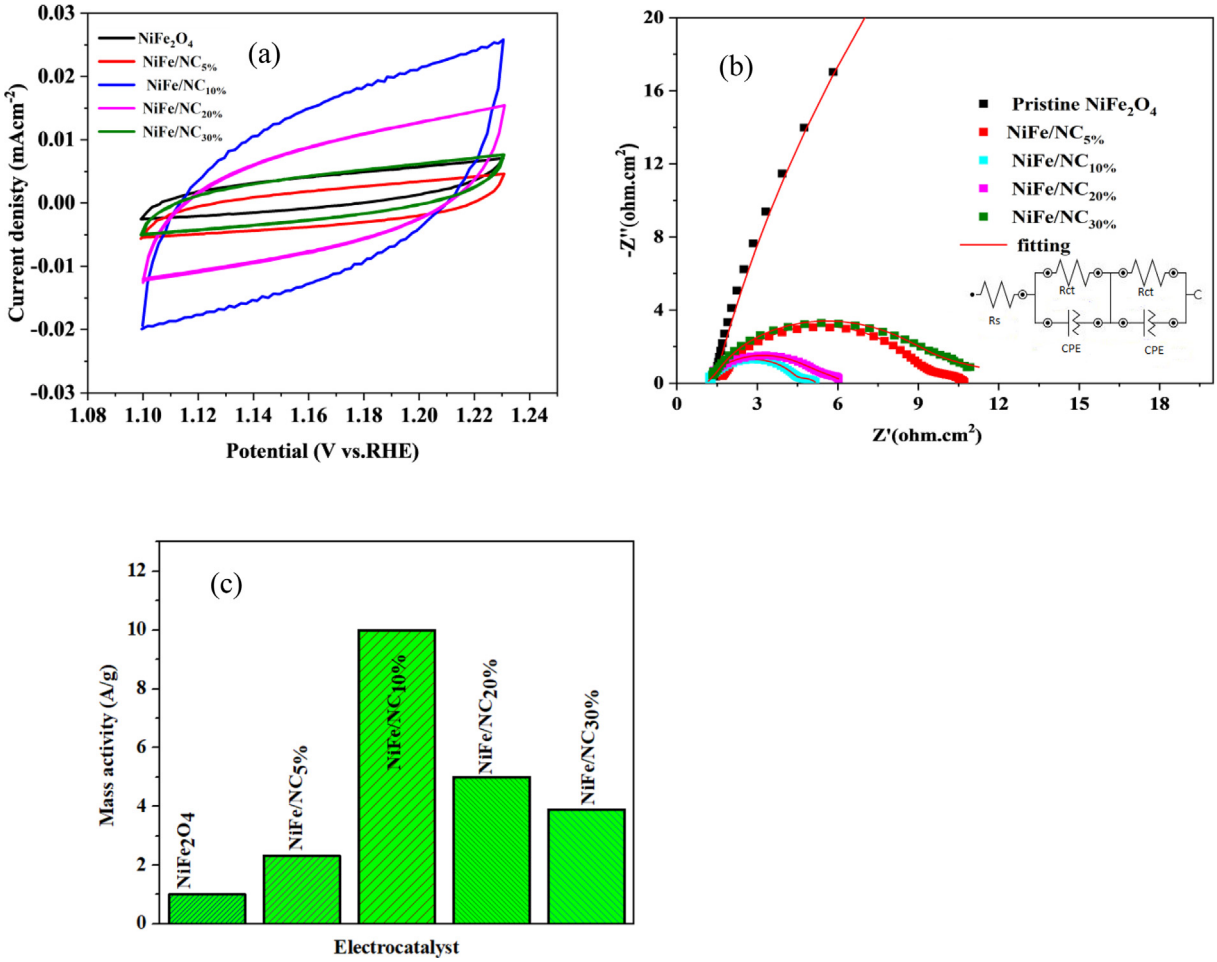

Fig. 6. (a) CV profile of the as-synthesized electrocatalysts measured in 1 M KOH in the non-faradaic region (from 1.10 to 1.23 V vs RHE) at a scan rate of 20 mV s^{-1}, (b) Nyquist plots conducted at 1.60 V vs RHE and (c) comparison of the mass activity of the different electrocatalysts determined at 350 mV overpotential.

$NC_{10\%}$ sample presents a relatively higher EDL capacitance. The capacitance value for the pristine $NiFe_2O_4$, NiFe/$NC_{5\%}$, NiFe/$NC_{10\%}$, NiFe/$NC_{20\%}$, NiFe/$NC_{30\%}$ was determined to be 0.10, 0.12, 0.57, 0.34 and 0.3 mFcm^{-2}, respectively. The relatively higher ECSA of NiFe/$NC_{10\%}$ could provide abundant active sites readily available for the reactants, ultimately expediting the OER electrocatalysis.

Electrochemical impedance spectroscopy (EIS) was utilized to review the charge transfer resistance of the as-prepared catalysts. The Nyquist plots of the different electrocatalysts are shown in Fig. 6(b). Impedance spectra can be best elucidated with the help of an equivalent circuit model, comprising of the following circuit elements: uncompensated solution resistance (R_s), charge transfer resistance (R_{ct}), and constant phase elements (CPE) [71]. As shown in Fig. 6(b), the Nyquist plot is fitted with equivalent circuit mode (Fig. 6b, inset), where the intersection of the semi-circle in the X-axis reflects the resistance of the solution (R_s). The magnitude of the semi-circle reveals the charge transfer resistance (R_{ct}) between the electrolyte and catalyst during the OER, and the constant phase elements (CPE) is related to pseudocapacitance [72,73]. A material with a lower value of R_{ct} would have favorable charge transfer between the surface catalyst and reaction intermediate, ensuing in promoted catalytic performance [74]. The R_{ct} magnitude for the different electrocatalysts is tabulated in Table S3, in which the corresponding R_{ct} value for the various electrocatalysts is given as follows in decreasing order: $NiFe_2O_4$ < NiFe/$NC_{30\%}$ > NiFe/$NC_{5\%}$ > NiFe/$NC_{20\%}$ > NiFe/$NC_{10\%}$. Among the samples, NiFe/$NC_{10\%}$ presents the lowest R_{ct} value, suggesting excellent electrical conductivity or the smallest charge transfer resistance, leading to enhanced OER. In contrast, the pristine $NiFe_2O_4$ possesses high R_{ct}; as a result, it shows a sluggish response towards OER. More stimulatingly, both EIS analysis and kinetics agree with the OER polarization profile. The relatively prominent electrochemical activity of NiFe/$NC_{10\%}$ could be stemmed from the faster electron process, enlarged surface area, and tailored surface functionality.

The mass activity was also taken into account when determining the performance of the as-prepared electrocatalysts. The current response normalized by the electrocatalyst load is represented by mass activity. The mass activity (A g^{-1}) was calculated using the following equation: mass activity = j/m [75], where j (mA cm^{-2}) refers to the current density at a given overpotential (350 mV), and m is the mass of catalyst (mg cm^{-2}) on the electrode. Fig. 6c shows the profile of mass activity measured at 350 mV overpotential. Accordingly, the NiFe/$NC_{10\%}$ electrocatalyst exhibits the highest mass activity of 10 A g^{-1} at a 350 mV overpotential. This finding indicates that the NiFe/$NC_{10\%}$ electrocatalyst is suitable for catalyzing OER.

Similar materials that have recently been reported in the literature were compared to the as-prepared electrocatalyst. As shown in Table 2, the NiFe/$NC_{10\%}$ catalyst outperformed for the many similar electrocatalysts reported, principally in terms of its excellent stability. NiFe/$NC_{10\%}$ catalyst has the potential to be used in electrochemical water electrolysis for hydrogen generation due to its demonstrated electrocatalytic superiority.

Where; CF: carbon nanofiber; NC*: nitrogen-doped graphitized carbon shell; NC**: nitrogen-codoped porous carbon; NCx: nitrogen-doped nanocarbon; NC-G: *N*-doped graphitic carbon shell; rGO: reduced graphene oxide.

Furthermore, the faradaic OER contribution to the global anodic current registered in the disk was determined by faradaic oxygen efficiencies (ε) using the following expression: $\varepsilon = (4/n_{ORR})\, I_{ring}/(N.I_{disk})$ [76], where n_{ORR} is the number of electrons transferred in the oxygen reduction reaction (ORR) at the ring electrode ($n_{ORR} = 4$ for the Pt ring), N is the RRDE collection efficiency, I_{ring} and I_{disk} are the ring and disk current, respectively. The RRDE collection efficiency N was determined to be 0.248, as reported in our previous paper [77].

The Faradaic efficiency of the catalyst was determined using chronoamperometry measurements. Initially, the disk and ring currents were measured at E = 0 V vs RHE for 1 min, and then, a constant potential of 1.52 V vs RHE (equivalent to 1 $mAcm^{-2}$ OER current density) was applied at the disk while the Pt ring was maintained at 0.4 V vs RHE. The Faradaic efficiency was measured at 1 $mAcm^{-2}$ for the reason that this disk-current density is sufficiently high to produce dissolved oxygen while maintaining a low local bubble formation rate on the disk electrode surface [78]. As shown in Fig. 7(a and b), the catalyst did not produce current at 0 V vs RHE subjected for 1 min. When 1.52 V was applied at the disk electrode, a current density equivalent to 1 $mAcm^{-2}$ was registered at the disk (Fig. 7a). The O_2 generated at the disk electrode diffuses towards the surrounding Pt ring electrode, on which it becomes rapidly reduced. Therefore, a current is generated at the Pt ring, as it is apparent in Fig. 7b. Fig. 7c displays the corresponding profile of Faradaic efficiency as a function of time. The Faradic oxygen efficiency was found to be about 98 % at the beginning and slowly decreased with increasing time. The decrease of efficiency through time could be due to the decay of the ring current, which is evident from the Pt ring current profile (Fig. 7b). Likely, this emanates from the oxygen bubble formation with elapsing time. Only dissolved oxygen can be collected at the Pt ring electrode, and the local oxygen saturation and bubble formation at the disk electrode could negatively affect the efficiency [79]. Therefore, the Faradaic efficiency estimated at the beginning of the chronoamperometric test at 1.52 V vs RHE, accounting for 98 %, is representative of the OER faradaic efficiency of the NiFe/$NC_{10\%}$ electrocatalyst, which is predominantly attributed to the OER rather than other by-products such as carbon and nanoparticle oxidation reaction. The faradaic efficiency of IrO_2 was also determined with the same method in order to compare with our sample. As shown in Fig. S3 in the supporting information, the faradaic efficiency of the IrO_2 catalyst is around 99 %, which is in agreement with what is reported in the literature [79]. The same trend of decreasing faradic efficiency has also been observed. This could be due to the accumulation of undissolved oxygen bubbles in the vicinity of the electrodes, limiting the transfer of dissolved oxygen from the disk to the ring and resulting in a reduced ring current [76]. In summary, the as-prepared NiFe/$NC_{10\%}$ and the commercial IrO_2 electrocatalyst exhibited a comparable faradaic efficiency, suggesting that NiFe/$NC_{10\%}$ is an efficient catalyst for expediting OER.

Stability measurement is another crucial parameter to elucidate materials' potential for practical application. The stability NiFe/$NC_{10\%}$ electrocatalyst was evaluated by chronopotentiometry measurements (E-t) at a constant current density (j = 10 $mAcm^{-2}$) under 1.0 M KOH aqueous solution. As shown in Fig. 8(a), the NiFe/$NC_{10\%}$ sample revealed a stable potential during 12 h continuous measurement, suggesting its promising prospect for practical application. This

Table 2
Comparison of OER electrocatalytic activity of similar NiFe-based electrocatalysts reported in the literature. The η_{10} (mV) stands for the overpotential required to produce a current density of 10 mA cm^{-2}.

Electrocatalyst	η_{10} (mV)	Tafel slope (mV dec^{-1})	Stability remark	References
NiFe@$NC_{10\%}$	350	56	Showed stable potential for at least 12 h, operated at j = 10 $mAcm^{-2}$.	This work
NiFe@NC*	360	81	Only decreased by 1.7 % after 12 h operation.	[83]
FeNi-NC**	380	115	presented high stability with about 92 % retention after 10,000 s of continuous test	[84]
FeNiP@*N*-CFs	300	47	A stable current density was observed for over 20 h at 1.55 V (vs RHE) applied potential.	[85]
NiFe/CNx	360	59.1	Displayed a constant operating potential after running 10000 s, operated at j = 10 $mAcm^{-2}$.	[86]
NiFe@CN-G	320	41	showed stable performance after 4 h operation, and a 76 % retention of initial current density after 10 h.	[87]
FeNi@*N*-CNT	300	47.7	Remained stable for about 10 h.	[88]
Ni_2Fe/rGO	285	96	After 10 h test at the current density of 20 $mAcm^{-2}$, the potential increases by 40 mV.	[89]

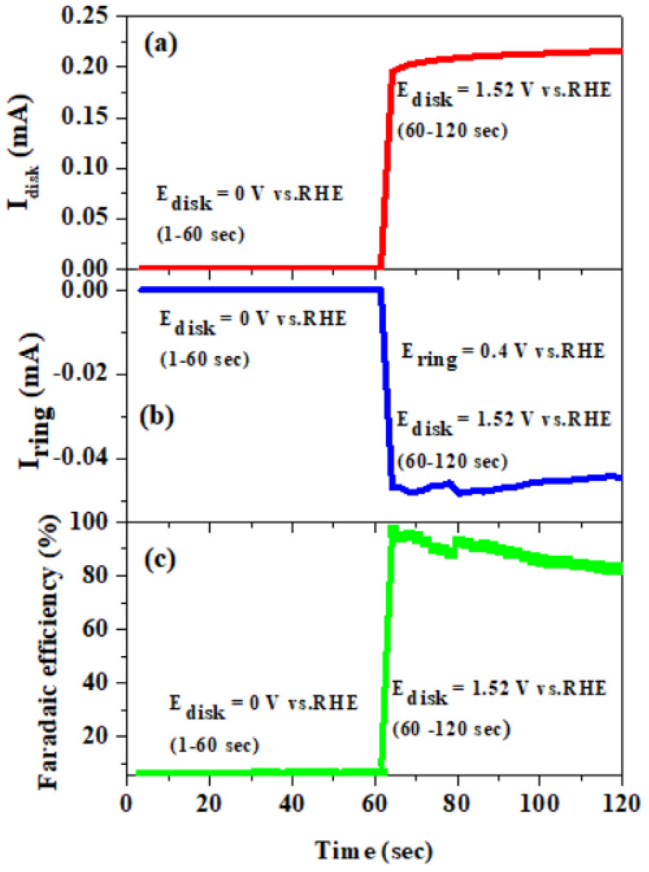

Fig. 7. Chronoamperometry measurement of NiFe/$NC_{10\%}$ catalyst on RRDE at 1600 rpm in N_2-saturated 1.0 M KOH at a constant potential of 1.52 V vsRHE: (a) disk current, (b) ring current at E_{ring} = 0.4 V vsRHE, and (c) Oxygen faradaic efficiency profile.

could be due to the carbon coating layer that prevents the electroactive species from dissolving and deactivating upon exposure to a harsh working environment. The OER polarization curve was also obtained after the long-term stability test to compare its catalytic activity with the initial curve. As shown in Fig. 8(b), the OER polarization curve after the stability test has almost overlapped with the initial OER profile, signifying its excellent catalytic stability. For comparison, the stability of the IrO_2 catalyst was also measured under the same condition. It displays that the potential increased after a few hours (as shown in Fig. 8(a), indicating the unstable characteristics of IrO_2.

Furthermore, the TEM image of the spent NiFe/$NC_{10\%}$ catalyst (Fig. 9) reveals no apparent morphological changes compared to the fresh catalyst. These results demonstrate that the nitrogen-doped carbon-coated $Ni_3Fe@Fe_3O_4$ is efficient and durable for water oxidation under a harsh alkaline environment. The carbon layer can act as shielding to protect the metal nanoparticles from dissolving and leaching in the alkaline electrolyte, leading to a stable microstructure. All these findings underlined the potential of carbonized polydopamine to functionalize and transform $NiFe_2O_4$ to another crystal phase with an improved OER activity and stability.

What is the active site for OER? The OER reaction mechanism based on NiFe-based electrocatalyst is still in debate; nevertheless, several researchers have been reporting their discoveries and outlooks. In NiFe electrocatalyst, the commonly surfaced view is that Fe acts as an active site for OER and becomes more pronounced active in the presence of Ni. For example, Mirabella and co-workers [80] studied the Ni incorporated Fe_3O_4 for OER and revealed that the OER intermediates are located on Fe sites, and the Ni metal has a promoting effect on the Fe active site. Other researchers, such as Zhang and co-workers [67], reported that both Ni and Fe sites could act as active sites for OER, which was determined using density functional theory (DFT) calculations. In NiFe decorated by carbonaceous materials, the mono-metals and bimetals coordinated with carbon can act as an active site for OER. Bai and co-workers [81] reported that Ni_3Fe-based active sites are more prominent active than mono-metals counterparts towards OER, revealing that bimetals can form different active sites for OER depending on the combination and crystal phase evolved. M—C—N (M: metals) has been reported as an essential reaction center where active sites are located for trapping OER intermediates. Moreover, the active sites for OER can also be found at the surface defects [82]. Henceforth, the combination of active sites of Ni_3Fe and Fe_3O_4 decorated by a carbon layer would be an appealing approach to provide a heterostructured catalyst with favorable reaction kinetics and stability toward OER.

The excellent electrocatalytic activity and stability of NiFe/$NC_{10\%}$ could be attributed to the following features: (i) the tailored surface functionality and structural character of the N doped carbon assembled with dual phases (Ni_3Fe and Fe_3O_4) could expose amply accessible active sites, expedite mass diffusion and electron transfer, thus stimulating OER activity. (ii) The *N*-doped carbon alters the morphology, particle size, crystal phase, and electronic structure of $NiFe_2O_4$,

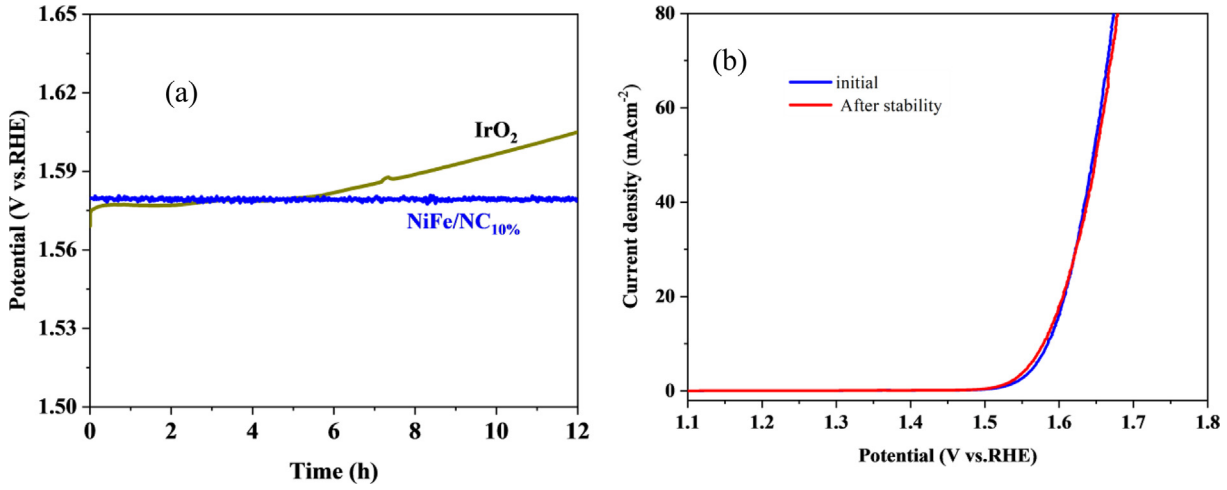

Fig. 8. (a) Chronopotentiometry stability test of NiFe/$NC_{10\%}$ and IrO_2 electrocatalyst conducted at j = 10 $mAcm^{-2}$ in 1.0 M KOH at a rotation speed 1600 rpm, (b) OER polarization curve of NiFe/$NC_{10\%}$ before and after stability measurements.

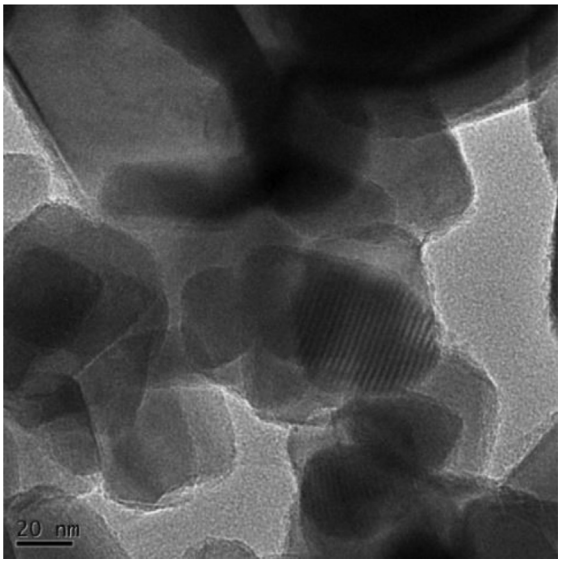

Fig. 9. TEM image of $NiFe/NC_{10\%}$ electrocatalyst after stability measurements.

which can positively contribute to the improved OER activity. (iii) The synergetic/coupling effect of the evolved Ni_3Fe alloy and Fe_3O_4 together with the *N*-doped carbon can potentially enhance the OER activity and durability. All the above aspects could contribute to the outstanding OER electrocatalytic performance of $NiFe/NC_{10\%}$ electrocatalyst.

4. Conclusions

In summary, a spinel oxide of $NiFe_2O_4$ was transformed into nitrogen-doped carbon-decorated $Ni_3Fe@NiFe_2O_4$ nanocomposite (NiFe/NCx) electrocatalysts through three subsequent steps comprising hydrothermal, polymerization, and carbonization. The as-prepared electrocatalysts were evaluated for their electrocatalytic performance. Results indicated that integrating carbonized polydopamine with the $NiFe_2O_4$ appreciably altered physicochemical properties and improved the OER electrocatalytic activity and stability. The optimum combination of dopamine and $NiFe_2O_4$ precursor was 10 wt% of dopamine relative to the $NiFe_2O_4$ precursor ($NiFe/NC_{10\%}$). Features such as microstructure, particle size, crystal phase, and electronic structure of $NiFe_2O_4$ can be transfigured by controlling the dopamine concentration. The $NiFe/NC_{10\%}$ catalyst displays a relatively lower overpotential of 350 mV to derive a current density of 10 $mAcm^{-2}$ and a smaller Tafel slope of 56 mV/dec during OER measurement in 1.0 KOH electrolyte, which is the best performing catalyst among the as-prepared samples. The improvement could be stemmed from the favorable conductivity network and enhanced electrical conductivity resulting from the optimum carbon coating and the electroactive sites of Ni_3Fe and Fe_3O_4. The reported NiFe/NC catalyst can be a non-precious alternative material to advance the development of electrocatalysts for green hydrogen production by water electrolysis. Our effort also provides a new perspective on transforming transition metal oxides into active and robust electrocatalysts for pragmatic electrochemical water electrolysis.

CRediT authorship contribution statement

Gebrehiwet Abrham Gebreslase: Investigation, Visualization, Writing – original draft. **David Sebastián:** Methodology, Writing – review & editing. **María Victoria Martínez-Huerta:** Conceptualization, Supervision, Writing – review & editing. **María Jesús Lázaro:** Supervision, Writing – review & editing, Funding acquisition.

Data availability

No data was used for the research described in the article.

Declaration of Competing Interest

The authors declare that they have no known competing financial interests or personal relationships that could have appeared to influence the work reported in this paper.

Acknowledgments

Financial support from the European Union's Horizon 2020 Research and Innovation programme under the Marie Skłodowska-Curie Actions–Innovative Training Networks (MSCA-ITN) Grant Agreement 813748 are gratefully acknowledged. Authors also acknowledge the use of instrumentation as well as the technical advice provided by the National Facility ELECMI ICTS, node "Laboratorio de Microscopias Avanzadas" at Universidad de Zaragoza. Authors acknowledge also Isaías Fernández for the fruitful discussion on XRD results.

Appendix A. Supplementary data

Supplementary data to this article can be found online at https://doi.org/10.1016/j.jelechem.2022.116887.

References

[1] M. David, C. Ocampo-Martínez, R. Sánchez-Peña, J. Energy Storage 23 (2019) 392–403.
[2] K. Zeng, D. Zhang, Prog. Energy Combust. Sci. 36 (2010) 307–326.
[3] L. Meng, H. Xuan, X. Liang, Y. Li, J. Yang, P. Han, J. Alloys Compd. 919 (2022) 165877.
[4] C. Cheng, D. Li, T. Zhao, D. Wang, D. Zhong, G. Hao, G. Liu, J. Li, Q. Zhao, Int. J. Hydrogen Energy 46 (2021) 14407–14417.
[5] T. Li, Y. Lv, J. Su, Y. Wang, Q. Yang, Y. Zhang, J. Zhou, L. Xu, D. Sun, Y. Tang, Adv. Sci. 4 (2017) 1700226.
[6] Z. Fu, S. Liu, Z. Mai, Z. Tang, D.D. Qin, Y. Tian, X. Wang, Chem. - An Asian J. 15 (2020) 3568–3574.
[7] M.Y. Gao, J.R. Zeng, Q.B. Zhang, C. Yang, X.T. Li, Y.X. Hua, C.Y. Xu, J. Mater. Chem. A 6 (2018) 1551–1560.
[8] H.A. Bandal, A.R. Jadhav, A.H. Tamboli, H. Kim, Electrochim. Acta 249 (2017) 253–262.
[9] Y. Li, S. Yang, H. Li, G. Li, M. Li, L. Shen, Z. Yang, A. Zhou, Colloids Surf. A Physicochem. Eng. Asp. 506 (2016) 694–702.
[10] G.A. Gebreslase, M.V. Martínez-Huerta, M.J. Lázaro, J. Energy Chem. 67 (2022) 101–137.
[11] G. Abrham Gebreslase, M. Victoria Martínez-Huerta, D. Sebastián, M. Jesús Lázaro, J. Colloid Interface Sci. (2022).
[12] J. Mohammed-Ibrahim, J. Power Sources 448 (2020) 227375.
[13] T. Wang, W. Xu, H. Wang, Electrochim. Acta 257 (2017) 118–127.
[14] H. Osgood, S.V. Devaguptapu, H. Xu, J. Cho, G. Wu, Nano Today 11 (2016) 601–625.
[15] J.S. Kim, B. Kim, H. Kim, K. Kang, Adv. Energy Mater. 8 (2018) 1–26.
[16] C. Qin, A. Fan, D. Ren, C. Luan, J. Yang, Y. Liu, X. Zhang, X. Dai, M. Wang, Electrochim. Acta 323 (2019) 134756.
[17] H. Chen, J. Yan, H. Wu, Y. Zhang, S. Liu, J. Power Sources 324 (2016) 499–508.
[18] J. Zhang, Y. Jiang, Y. Wang, C. Yu, J. Cui, J. Wu, X. Shu, Y. Qin, J. Sun, J. Yan, H. Zheng, Y. Zhang, Y. Wu, Electrochim. Acta 321 (2019) 134652.
[19] J.C. Ruiz-Cornejo, J.F. Vivo-Vilches, D. Sebastián, M.V. Martínez-Huerta, M.J. Lázaro, Renew. Energy 178 (2021) 307–317.
[20] H. Fan, Y. Ma, W. Chen, Y. Tang, L. Li, J. Wang, J. Alloys Compd. 894 (2021) 162533.
[21] X. Zhang, Y. Xue, Q. Yan, K. Zhu, K. Ye, J. Yan, D. Cao, X. Huang, G. Wang, Mater. Today Energy 21 (2021) 1–7.
[22] Y. Yang, H. Meng, S. Yan, H. Zhu, W. Ma, C. Wang, F. Ma, Z. Hu, J. Alloys Compd. 874 (2021) 159874.
[23] Y. Xue, M. Liu, Y. Qin, Y. Zhang, X. Zhang, J. Fang, Chinese Chem. Lett. (2021).
[24] K. Ao, Q. Wei, W.A. Daoud, A.C.S. Appl, Mater. Interfaces 12 (2020) 33595–33602.
[25] Z. Chen, X. Liu, T. Shen, C. Wu, L. Zu, L. Zhang, Int. J. Hydrogen Energy 46 (2021) 37736–37745.

[26] D. Lim, E. Oh, C. Lim, S.E. Shim, S.H. Baeck, Catal. Today 352 (2020) 27–33.
[27] T. Wang, X.Z. Fu, S. Wang, Green Energy Environ. (2021).
[28] C. Teng, N. Zhang, X. Gao, X. Li, Z. Wu, W. Wang, M. Zhi, Z. Hong, Mater. Today Energy 11 (2019) 192–198.
[29] Y. Wu, Y. Li, M. Yuan, Z. Lü, L. Xu, B. Wei, J. Alloys Compd. 847 (2020) 156363.
[30] R. Li, J. Xu, C. Lu, Z. Huang, Q. Wu, J. Ba, T. Tang, D. Meng, W. Luo, Electrochim. Acta 357 (2020) 136873.
[31] P. Bhanja, Y. Kim, B. Paul, Y.V. Kaneti, A.A. Alothman, A. Bhaumik, Y. Yamauchi, Chem. Eng. J. 405 (2021) 126803.
[32] N.L.W. Septiani, Y.V. Kaneti, K.B. Fathoni, K. Kani, A.E. Allah, B. Yuliarto, H.K. Nugraha, Z.A. Dipojono, D. Alothman, Y.Y. Golberg, Chem. Mater. 32 (2020) 7005–7018.
[33] N.L.W. Septiani, Y.V. Kaneti, K.B. Fathoni, Y. Guo, Y. Ide, B. Yuliarto, X. Jiang, N. Nugraha, H.K. Dipojono, D. Golberg, Y. Yamauchi, J. Mater. Chem. A 8 (2020) 3035–3047.
[34] S. Hu, S. Wang, C. Feng, H. Wu, J. Zhang, H. Mei, A.C.S. Sustain, Chem. Eng. 8 (2020) 7414–7422.
[35] Y. Guo, C. Zhang, J. Zhang, K. Dastafkan, K. Wang, C. Zhao, Z. Shi, A.C.S. Sustain, Chem. Eng. 9 (2021) 2047–2056.
[36] S. Kang, K. Ham, J. Lee, Electrochim. Acta 353 (2020) 136521.
[37] N.T. Suen, S.F. Hung, Q. Quan, N. Zhang, Y.J. Xu, H.M. Chen, Chem. Soc. Rev. 46 (2017) 337–365.
[38] Y. Huang, J.J. Wang, Y. Zou, L.W. Jiang, X.L. Liu, W.J. Jiang, H. Liu, J.S. Hu, Chinese J. Catal. 42 (2021) 1395–1403.
[39] G. Liu, K. Wang, X. Gao, D. He, J. Li, Electrochim. Acta 211 (2016) 871–878.
[40] D. Lim, H. Kong, N. Kim, C. Lim, W.S. Ahn, S.H. Baeck, ChemNanoMat 5 (2019) 1296–1302.
[41] H. Yang, Y. Liu, S. Luo, Z. Zhao, X. Wang, Y. Luo, Z. Wang, J. Jin, J. Ma, ACS Catal. 7 (2017) 5557–5567.
[42] Y. Shi, X. Feng, H. Guan, J. Zhang, Z. Hu, Int. J. Hydrogen Energy 46 (2021) 8557–8566.
[43] C. Mahala, M.D. Sharma, M. Basu, Electrochim. Acta 273 (2018) 462–473.
[44] D. Li, S. Liu, G. Ye, W. Zhu, K. Zhao, M. Luo, Z. He, Green Chem. 22 (2020) 1710–1719.
[45] P. Stelmachowski, J. Duch, D. Sebasti, Materials (Basel). (2021) 1–44.
[46] Y. Feng, H. Zhang, Y. Zhang, X. Li, Y. Wang, ACS. Appl. Mater. Interfaces 7 (2015) 9203–9210.
[47] H. Wang, H. Dai, Chem. Soc. Rev. 42 (2013) 3088.
[48] Z. Li, X. Wu, X. Jiang, B. Shen, Z. Teng, D. Sun, G. Fu, Y. Tang, Adv. Powder Mater. (2021).
[49] S. Farid, S. Ren, C. Hao, Inorg. Chem. Commun. 94 (2018) 57–74.
[50] J. Kong, S.I. Seyed Shahabadi, X. Lu, Nanoscale 8 (2016) 1770–1788.
[51] J. Yan, H. Lu, Y. Huang, J. Fu, S. Mo, C. Wei, Y.E. Miao, T. Liu, J. Mater. Chem. A 3 (2015) 23299–23306.
[52] W. Tamakloe, D.A. Agyeman, M. Park, J. Yang, Y.M. Kang, J. Mater. Chem. A 7 (2019) 7396–7405.
[53] G. Li, L. Anderson, Y. Chen, M. Pan, P.-Y. Abel Chuang, Sustain, Energy Fuels 2 (2018) 237–251.
[54] Z. Xing, Z. Ju, J. Yang, H. Xu, Y. Qian, Nano Res. 5 (2012) 477–485.
[55] X. Liu, T. Zhang, Y. Qu, G. Tian, H. Yue, D. Zhang, S. Feng, Electrochim. Acta 231 (2017) 27–35.
[56] J. Lian, Y. Wu, H. Zhang, S. Gu, Z. Zeng, X. Ye, Int. J. Hydrogen Energy 43 (2018) 12929–12938.
[57] L. Liu, S. Hu, K. Gao, Cellulose 27 (2020) 1021–1031.
[58] F. Te Tsai, H.C. Wang, C.H. Ke, W.F. Liaw, A.C.S. Appl, Energy Mater. 1 (2018) 5298–5307.
[59] J. Zeng, T. Song, M. Lv, T. Wang, J. Qin, H. Zeng, RSC Adv. 6 (2016) 54964–54975.
[60] Y. Xu, W. Tu, B. Zhang, S. Yin, Y. Huang, M. Kraft, R. Xu, Adv. Mater. 29 (2017).
[61] Y. Liu, J. Li, F. Li, W. Li, H. Yang, X. Zhang, Y. Liu, J. Ma, J. Mater. Chem. A 4 (2016) 4472–4478.
[62] Z. Peng, H. Wang, X. Xia, X. Zhang, Z. Dong, A.C.S. Sustain, Chem. Eng. 8 (2020) 9009–9016.
[63] Z. Shang, Z. Chen, Z. Zhang, J. Yu, S. Tan, F. Ciucci, Z. Shao, H. Lei, D. Chen, J. Alloys Compd. 740 (2018) 743–753.
[64] Y. Liu, F. Li, H. Yang, J. Li, P. Ma, Y. Zhu, J. Ma, ChemSusChem 11 (2018) 2358–2366.
[65] A. Samanta, C.R. Raj, J. Phys. Chem. C 122 (2018) 15843–15852.
[66] C. Alegre, C. Busacca, A. Di Blasi, O. Di Blasi, A.S. Aricò, V. Antonucci, V. Baglio, ChemElectroChem 7 (2020) 124–130.
[67] Z. Zhang, X. Yan, J. Liu, B. Liu, Z.G. Gu, Sustain, Energy Fuels 5 (2021) 2668–2677.
[68] S.Y. Lee, H. Jung, S.Y. Chae, H.S. Oh, B.K. Min, Y.J. Hwang, Electrochim. Acta 281 (2018) 684–691.
[69] M. Kumar, A. Subramania, K. Balakrishnan, Electrochim. Acta 149 (2014) 152–158.
[70] A. Shaheen, S. Hussain, G.J. Qiao, M.H. Mahmoud, H. Fouad, M.S. Akhtar, J. Nanoelectron. Optoelectron. 16 (2022) 1357–1362.
[71] Y. Wang, J. Li, B. Zhang, W. Hou, X. Xu, J. Mater. Sci. Mater. Electron. 30 (2019) 19984–19993.
[72] Z. Xiao, Y.C. Huang, C.L. Dong, C. Xie, Z. Liu, S. Du, W. Chen, D. Yan, L. Tao, Z. Shu, G. Zhang, H. Duan, Y. Wang, Y. Zou, R. Chen, S. Wang, J. Am. Chem. Soc. 142 (2020) 12087–12095.
[73] G.I. Cubillos, E. Romero, A. Umaña-Perez, Sci. Rep. 11 (2021) 1–19.
[74] H.A. Bandal, A.R. Jadhav, H. Kim, J. Alloys Compd. 726 (2017) 875–884.
[75] Y.R. Hong, S. Mhin, K.M. Kim, W.S. Han, H. Choi, G. Ali, K.Y. Chung, H.J. Lee, S.I. Moon, S. Dutta, S. Sun, Y.G. Jung, T. Song, H.S. Han, J. Mater. Chem. A 7 (2019) 3592–3602.
[76] I.S. Filimonenkov, C. Bouillet, G. Kéranguéven, P.A. Simonov, G.A. Tsirlina, E.R. Savinova, Electrochim. Acta 321 (2019).
[77] G.A. Gebreslase, M.V. Martínez-Huerta, D. Sebastián, M.J. Lázaro, J. Colloid Interface Sci. 625 (2022) 70–82.
[78] C.C.L. McCrory, S. Jung, J.C. Peters, T.F. Jaramillo, J. Am. Chem. Soc. 135 (2013) 16977–16987.
[79] I.S. Filimonenkov, S.Y. Istomin, E.V. Antipov, G.A. Tsirlina, E.R. Savinova, Electrochim. Acta 286 (2018) 304–312.
[80] F. Mirabella, M. Müllner, T. Touzalin, M. Riva, Z. Jakub, F. Kraushofer, M. Schmid, M.T.M. Koper, G.S. Parkinson, U. Diebold, Electrochim. Acta 389 (2021) 138638.
[81] X. Bai, Y. Ma, Q. Wang, J. Guan, Int. J. Hydrogen Energy 47 (2022) 2304–2312.
[82] Q. Yue, C. Liu, Y. Wan, X. Wu, X. Zhang, P. Du, J. Catal. 358 (2018) 1–7.
[83] L. Du, L. Luo, Z. Feng, M. Engelhard, X. Xie, B. Han, J. Sun, J. Zhang, G. Yin, C. Wang, Y. Wang, Y. Shao, Nano Energy 39 (2017) 245–252.
[84] L. Yang, X. Zeng, D. Wang, D. Cao, Energy Storage Mater. 12 (2018) 277–283.
[85] R. Mo, S. Wang, H. Li, J. Li, S. Yang, J. Zhong, Electrochim. Acta 290 (2018) 649–656.
[86] S. Ci, S. Mao, Y. Hou, S. Cui, H. Kim, R. Ren, Z. Wen, J. Chen, J. Mater. Chem. A 3 (2015) 7986–7993.
[87] C. Deng, K.H. Wu, J. Scott, S. Zhu, R. Amal, D.W. Wang, ChemElectroChem 5 (2018) 732–736.
[88] Z. Tao, T. Wang, X. Wang, J. Zheng, X. Li, A.C.S. Appl, Mater. Interfaces 8 (2016) 35390–35397.
[89] J. Geng, L. Kuai, E. Kan, Y. Sang, B. Geng, Chem. - A Eur. J. 22 (2016) 14480–14483.

Supporting information

for

Nitrogen-doped carbon decorated-$Ni_3Fe@Fe_3O_4$ electrocatalyst with enhanced oxygen evolution reaction performance

Gebrehiwet Abrham Gebreslase[a], David Sebastián[a], María Victoria Martínez-Huerta[b*], María Jesús Lázaro[a*]

[a] *Instituto de Carboquímica, CSIC. Miguel Luesma Castán 4, 50018, Zaragoza, Spain.*
[b] *Instituto de Catálisis y Petroleoquímica, CSIC. Marie Curie 2, 28049, Madrid, Spain.*

* Corresponding authors: mmartinez@icp.csic.es, mlazaro@icb.csic.es

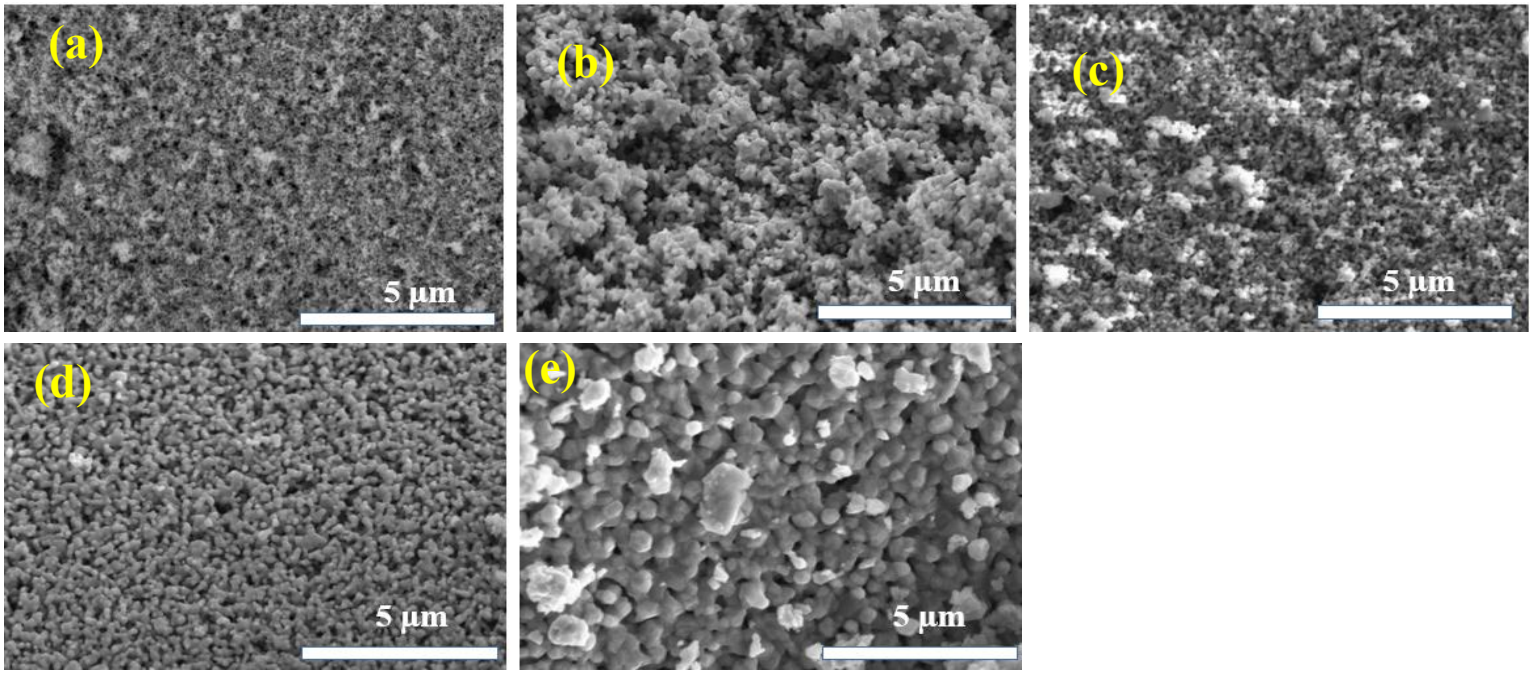

Figure S1. SEM images of (a) pristine $NiFe_2O_4$, (b) $NiFe/NC_{5\%}$, (c) $NiFe/NC_{10\%}$, (d) NiFe $NiFe/NC_{20\%}$, and (e) $NiFe/NC_{30\%}$.

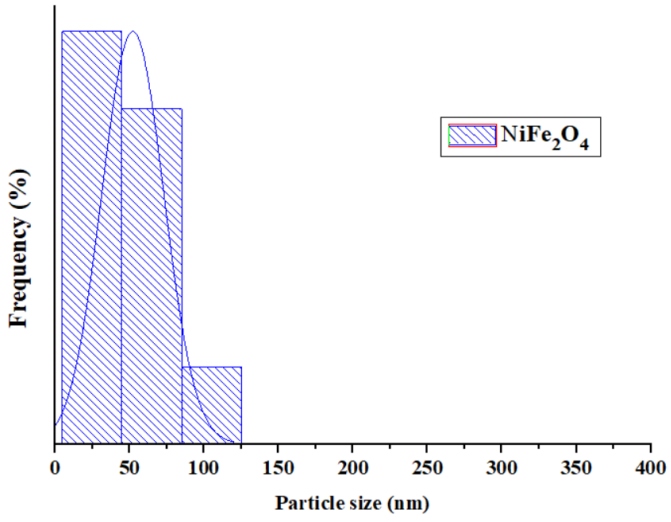

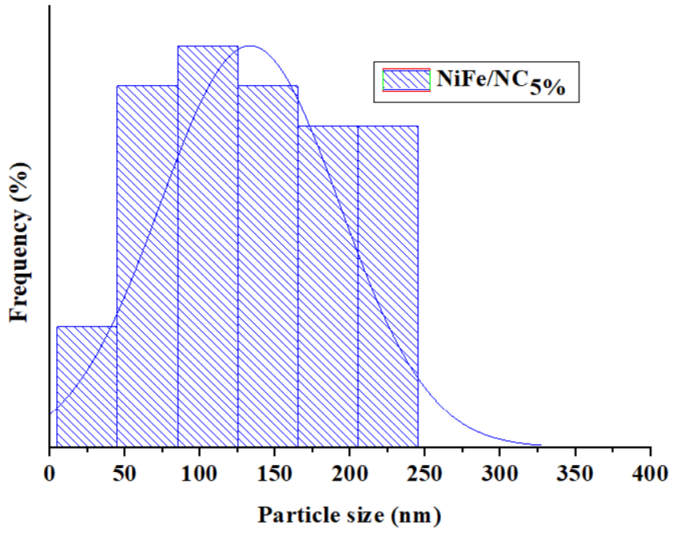

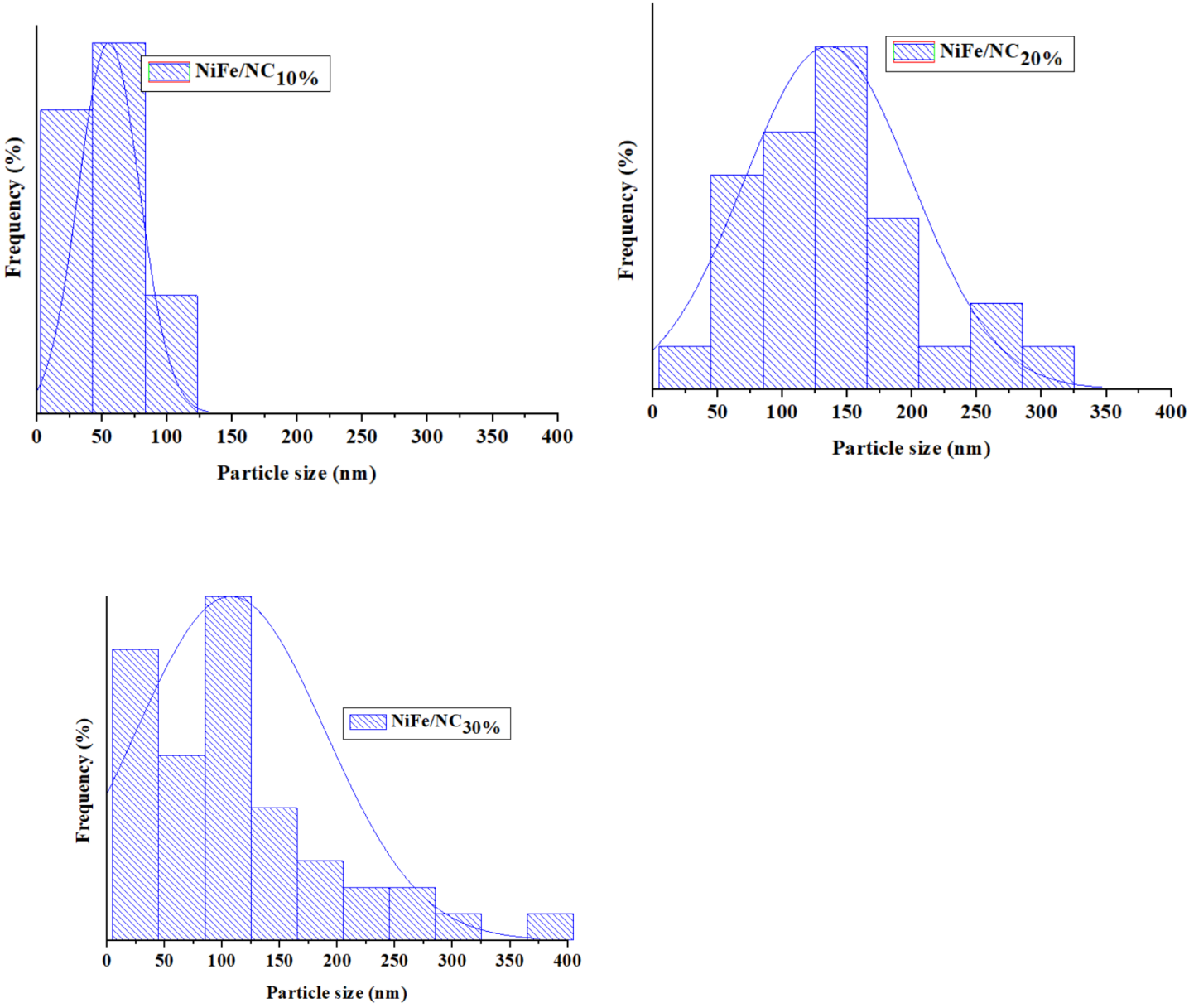

Figure S2. Particle size distribution of the various electrocatalyst

Table S1. XPS analysis result

Catalyst	BE of Ni $2p_{3/2}$ (eV)	Deconvoluted Ni species and percentage (%)	BE of Fe $2p_{3/2}$ (eV)	Deconvoluted Fe species and percentage (%)
$NiFe_2O_4$	854.9	Ni^{2+} (63.58)	709.3	Fe^{2+} (43.59)
	856.6	Ni^{3+}(36.42)	711.6	Fe^{3+}(56.41)
	861.3	Sat.	717.5	Sat.
NiFe/NC$_{5\%}$	852.3	Ni^{0} (8.91)	710.0	Fe^{2+}(33.75)
	855.5	Ni^{2+}(56.62)	712.0	Fe^{3+} (66.25)
	856.8	Ni^{3+}(34.47)	717.6	Sat.
	861.3	Sat.		
NiFe/NC$_{10\%}$	852.2	Ni^{0} (19.71)	710.0	Fe^{2+} (44.57)
	855.4	Ni^{2+} (65.27)	712.0	Fe^{3+}(55.43)
	857.5	Ni^{3+} (15.02)	717.7	Sat.
	861.2	Sat.		
NiFe/NC$_{20\%}$	852.3	Ni^{0} (13.75)	710.3	Fe^{2+} (44.36)
	855.4	Ni^{2+}(48.17)	711.9	Fe^{3+}(55.64)
	856.8	Ni^{3+}(38.09)	717.8	Sat.
	861.4	Sat.		
NiFe/NC$_{30\%}$	852.3	Ni^{0}(16.36)	710.0	Fe^{2+} (39.98)
	855.5	Ni^{2+}(51.60)	711.8	Fe^{3+} (60.02)
	857.6	Ni^{3+}(32.05)	717.7	Sat.
	861.5	Sat.		

Note: The value in parenthesis indicates the relative concentration of the corresponding chemical species in each sample.

Table S 2. Metal composition analysis results from inductively coupled plasma atomic emission spectroscopy (ICP-AES) analysis.

Samples	Fe (wt. %)	Ni (wt. %)	The ratio of Fe/Ni
$NiFe_2O_4$	54	26.35	2.05
$NiFe/NC_{5\%}$	50.2	24.6	2.04
$NiFe/NC_{10\%}$	52	25.2	2.06
$NiFe/NC_{20\%}$	53	26.1	2.03
$NiFe/NC_{30\%}$	54.9	26.5	2.07

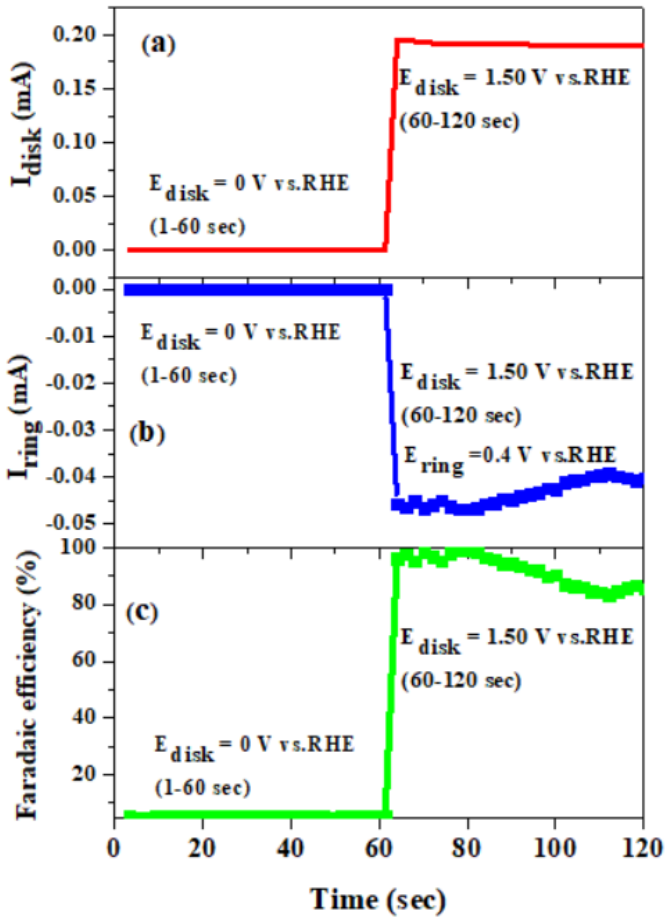

Figure S 3. Chronoamperometry measurement of IrO_2 catalyst supported on RRDE at 1600 rpm in N_2-saturated 1.0 M KOH at constant potential of 1.50 V vs.RHE: (a) disk current, (b) ring current at E_{ring} = 0.4 V vs.RHE, and (c) Oxygen faradaic efficiency profile.

Table S 3. Charge transfer resistance (R_{ct}) values obtained from the impedance analysis result

Samples	R_{ct} **(ohm.cm^2)**
$NiFe_2O_4$	266.17
$NiFe/NC_{5\%}$	9.64
$NiFe/NC_{10\%}$	4.04
$NiFe/NC_{20\%}$	5.78
$NiFe/NC_{30\%}$	11.98

Article IV

Catalysis Today xxx (xxxx) xxx

Contents lists available at ScienceDirect

Catalysis Today

journal homepage: www.elsevier.com/locate/cattod

CoFe-loaded P, N co-doped carbon foam derived from petroleum pitch waste: An efficient electrocatalyst for oxygen evolution reaction

Gebrehiwet Abrham Gebreslase [a], David Sebastián [a], María Victoria Martínez-Huerta [b,*], Tanya Tsoncheva [c], Boiko Tsyntsarski [c], Georgi Georgiev [c], María Jesús Lázaro [a,*]

[a] Instituto de Carboquímica, CSIC. Miguel Luesma Castán 4, 50018, Zaragoza, Spain
[b] Instituto de Catálisis y Petroleoquímica, CSIC. Marie Curie 2, 28049, Madrid, Spain
[c] Institute of Organic Chemistry with Centre of Phytochemistry, Bulgarian Academy of Sciences, Acad. G. Bontchev, block 9, Sofia, 1113, Bulgaria

ARTICLE INFO

Keywords:
Electrocatalysts
Oxygen evolution reaction
CoFe
Carbon foam
And P
N co-doped carbon foam
Petroleum pitch

ABSTRACT

Designing and developing affordable, high-performance, and stable electrocatalysts for oxygen evolution reaction (OER) is decisive for pragmatic water electrolysis to produce green hydrogen energy. In this work, we report cobalt and iron incorporated in phosphorus and nitrogen co-doped carbon foam (CF) derived from petroleum pitch as a promising electrocatalyst for alkaline OER. The P, N heteroatoms co-doped carbon foam (PN-CF) was first synthesized via thermo-chemical treatment of low-cost petroleum pitch in the presence of melamine (N source) and sodium hypophosphite (P source) precursors, followed by carbonization. Then, mono and bimetals of Co and Fe were impregnated into the as-prepared composite carbon foam (PN-CF) substrate, followed by further carbonization. Among the different catalysts, the bimetallic CoFe integrated with the PN-CF (CoFe@PN-CF) reveals an outstanding electrocatalytic activity (320 mV overpotential at j = 10 mA·cm^{-2}), low Tafel slope (48 mV·dec^{-1}), and excellent durability during OER measurement in 1 M KOH aqueous solution. The superb performance of the CoFe@PN-CF catalyst stems from the synergetic effect of the bimetals confined on phosphorus and nitrogen co-doped carbon foam support with high specific surface area, highly porous structure, and formation of graphitic domains, which enhances the electrical conductivity. This work sheds light on the potential for valorizing petroleum pitch and provides a facile synthesis approach to synthesizing a low-cost, high-performance, and durable electrocatalyst for alkaline OER.

1. Introduction

Water electrolysis powered by renewable energy sources (e.g., wind, solar, geothermal) has been considered as a significant milestone in developing clean, green, and renewable hydrogen energy sources that might substitute fossil fuels [1–3]. Hydrogen evolution reaction (HER) and oxygen evolution reaction (OER) are the two fundamental reaction steps in water electrolysis. However, the kinetics of OER is a very sluggish process compared to the HER due to the multi-electron complex step (four-electron transfer) reactions. Yet, one of the largest hurdles impeding the performance of water electrolysis is the OER electrode with high overpotential [4]. As a result, it is paramount to exploit and use electrocatalysts to expedite the slow reaction. Currently, the benchmark electrocatalysts are limited to noble metal oxides (IrO_2 and RuO_2). However, their application is hampered due to their high price, poor durability, and limited abundance [5]. To this end, one of the most important research works in the field of electrocatalysis is the development of a low-cost, stable, and high-performance electrocatalyst capable of substituting precious metals.

So far, considerable efforts have been devoted to developing electrocatalysts based on the 3d transition metals (Ni, Co, Fe, Mo, etc.), including oxides [6], phosphides [7], (oxy)hydroxides [8], nitrides [9], sulfides [10], carbides [11], layered double hydroxides (LDHs) [12], etc.; nevertheless, the preparation of OER electrocatalysts retaining high activity and stability that can be obtained through facile and scalable approach is still challenging. Transition metals are still far from fulfilling the ideal features required for OER electrocatalysis due to their aggregation tendency during synthesis, low surface area, and unsatisfactory conductivity [13]. Transition metal oxide-based catalysts have been the primary focus of the majority of recent attempts to design efficient and cost-effective OER electrocatalysts. This is due to the fact that metal species are generally considered to be the active sites for

* Corresponding authors.
E-mail addresses: mmartinez@icp.csic.es (M.V. Martínez-Huerta), mlazaro@icb.csic.es (M.J. Lázaro).

https://doi.org/10.1016/j.cattod.2022.12.022
Received 3 October 2022; Received in revised form 22 November 2022; Accepted 22 December 2022
Available online 23 December 2022

electrochemical OER. On the other hand, researchers have been attempting to design and develop carbon-based metal-free electrocatalysts for OER in the last few years [14]. Organic-based electrocatalysts have the benefit of being inexpensive, good electrically and thermally conductors, easy to tune, and present high surface area [15,16]. However, developing highly efficient OER catalytic systems that need little to no metal for OER electrodes remains challenging. In an attempt to obtain cost-effective and earth-abundant materials, Mirzakulova and co-workers [17] reported entirely carbon (N(5)-ethyl--flavinium ions) based electrocatalyst for OER. Oxygen evolution was detected when carbon was used as an OER electrode. The OER is predicted to occur via a peroxide intermediate generated between the oxidized flavin pseudobase and the oxidized carbon electrode based on spectroelectrochemical data and the calculation of density functional theory results. Despite the low OER activity achieved, this finding has opened up a new avenue for designing and developing carbon-based metal-free electrocatalysts for OER. These results prompted further investigation of carbon-based electrocatalysts for water oxidation by Zhao and co-workers [31]. They prepared nitrogen-doped graphite nanomaterials from a nitrogen-rich polymer. The as-prepared material shows a low overpotential of 380 mV at a current density of 10 mA cm^{-2} in an alkaline solution. The electrochemical and physicochemical analysis revealed that the superb OER activity of nitrogen-doped carbon material originates from pyridinic-N- or/and quaternary-N-related active sites. Carbon-based metal-free OER electrocatalysts are not common in the scientific literature because they are prone to chemical and electrochemical degradation [18,19], which is related to the strong oxidizing conditions of OER. Nonetheless, the number of publications on carbon-based metal-free electrocatalysts for OER has recently increased, with an emphasis on 3D structures and doping with heteroatoms [20].

For many years, carbonaceous materials (such as graphene, porous carbon, carbon nanotubes, and other nanostructures) have been widely utilized as metal support. Carbon is vital for stabilizing the metal nanoparticles, enhancing surface area, increasing the exposed active sites, and improving stability during long-time measurements [21]. Combining transition metal and carbon can circumvent the shortfalls mentioned above. Doping heteroatoms (e.g., N, P, S) into carbon structure can further alter the surface chemistry and electronic configuration [22], resulting in enhanced performance. Recent research revealed that nitrogen-doped carbon-based electrodes modified with transition metals offer metal-nitrogen (M-Nx) species, widely regarded as effective active sites that tremendously change the reaction kinetics [23]. The dopant can alter the electronic properties of the carbon, increase the number of active sites, and maintain the carbon skeleton. It has been reported that the N atom doped in the C skeleton exits in the forms of graphitic N, pyridinic N, and pyrrolic N, which plays a crucial role in catalysis [24]. Besides, the presence of the heteroatom in the carbon structure reduces the adsorption barrier of reactants by restructuring the charge and spin density of the carbon atom, thus promoting reaction efficiency [25]. For example, due to the difference in electronegativity of N (3.04) and C (2.55), N with higher electronegativity breaks the electroneutrality of carbon to form charged sites (C^{+}) in the carbon skeleton. N is n-dopant that can improve carbon's conductivity by donating electrons, bringing the Fermi level nearer to the conduction band. Due to the similarity in atomic radius, N (70 pm) and C (77 pm), N can easily integrate into the carbon lattice, thus forming a strong N-C covalent bond, promoting the stability of N-doped carbon [26]. Moreover, adding P dopant to carbon structure can further alter the conductivity due to its higher electron-donating ability and larger atomic radius (110 pm). In this case, charged P^{+} species are formed when P is integrated with carbon due to the smaller electronegativity of P (2.19) compared to C (2.55) [27]. The P atoms also play a crucial role in tailoring the local charge density and adjusting the charge state of the host surface [28]. In this regard, integrating both heteroatom dopants into carbon can revolutionize the carbon's microstructure, conductivity, and functionality. The synergy of metal incorporated with the heteroatom (P, N) co-doped carbon could effectively regulate the local electronic structure and optimize the adsorption and desorption of the reactant intermediates, ultimately bringing an ideal platform for preparing highly active and robust electrocatalysts.

From the prospect of OER electrocatalyst design point of view, the materials should encompass abundant exposed active sites to furnish high catalytic activity and stability during the reaction process. Moreover, a facile and cost-effective synthesis approach is urgently needed for large-scale applications. Combining transition metal and heteroatoms-doped carbon is a promising approach to disperse electroactive metal in the carbon structure, thus increasing activity and stability. Therefore, configuring and fabricating 3d transition metals and heteroatom-doped carbon composite metals is vital to promoting OER via suitable doping effect and surface structure tailoring [29]. Numerous research works have reported on different transition metals integrated with heteroatom-doped carbon support to enhance stability and encourage charge transfer efficiency during OER catalysis [9,30,31]. Despite the substantial efforts made on this approach, developing a facile, reliable, and low-cost carbon precursor for preparing metal-integrated with heteroatom-doped carbon with high OER activity and durability is still a considerable challenge.

Petroleum pitch (PP), an inexpensive and abundant industrial residue material, has vast potential for preparing carbon support and synthesizing metal-encapsulated carbon materials for different applications. PP is a complex mixture of polynuclear aromatic and aliphatic hydrocarbons and has been studied widely as feedstock for electrodes and carbon finer synthesis. These aromatic molecules are not welcome in today's pursuit of energy at lower carbon prices. Transforming these high-carbon precursors into a high-value-added product has recently received significant courtesy [32]. Preparing porous carbon foam (CF) from low–cost and waste material of PP offers an economical way to produce carbon support. CF is sponge-like carbon material with peculiar characteristics: lightweight, good strength, large external surface area with a porous and open-cell structure, and tailorable thermal and electrical conductivity [33]. Moreover, CF contains an open-pore structure, in which macropores are connected with each other and contain space/holes on their cell wall, which is advantageous for integrating other foreign materials to change their functionalities [34]. The carbon foam with profuse porous architecture, large surface area, and promoted mass transfer capability is imperative for hosing metals [35].

Considering these merits, we fabricated and explored composite materials composed of Co/Fe incorporated with P, N co-doped carbon foam (PN-CF) derived from petroleum pitch with high activity and stability for alkaline oxygen evolution reaction. The composite carbon support was synthesized through direct thermo-chemical oxidation of low-cost petroleum pitch in the presence of melamine (N source) and sodium hypophosphite (P source) precursors, followed by thermal treatment. The Co and Fe metals were incorporated into PN-CF via a simple impregnation method followed by further thermal treatment. The selected metals of Fe and Co are regarded as excellent candidates for OER electrocatalysis in alkaline electrolytes due to their low cost, abundant reserves, and relatively high activity [36,37]. The carbon foam support without heteroatoms was also investigated to individuate the effect of the heteroatom on carbon morphology and functionality. The performance of the prepared catalysts is characterized by using both physicochemical and electrochemical properties, intended to obtain detailed insight into the characteristics of naturally abundant carbon sources (petroleum pitch) to diffuse their potential application for water electrocatalysis. This research work unravels a new avenue for transforming industrial waste products of petroleum pitch into high-performance electrocatalysts for OER.

2. Experimental section

2.1. Synthesis of carbon foam and P, N co-doped carbon foam

The carbon foam (CF) was synthesized through the following procedure: petroleum pitch (50 g) precursor was heated until the melting state and further subjected to controlled thermo-chemical treatment at 120–200 °C under atmospheric pressure, whereas 10 mL HNO_3 (65 wt. %, Sigma Aldrich) was added by drops to the mixture under continuous stirring until solidification. Then, the obtained solid product was calcined at 850 °C at a heating rate of 10 °C/min for 1 h under N_2 atmosphere. The same procedure was employed to prepare P, N co-doped carbon foam (PN-CF), except that the process was performed in the presence of $NaH_2PO_2{\cdot}xH_2O$ (amount = 5 wt. % relative to the CF content) (Sigma Aldrich) and melamine (amount = 10 wt. % relative to the CF content) (Sigma Aldrich).

2.2. Synthesis of Co, Fe, and CoFe @ P, N co-doped carbon foam

The catalysts were synthesized by impregnation of the as-prepared P, N co-doped carbon foam with cobalt nitrate ($Co(NO_3)_2$ $6H_2O$ (Alfa Aesar)), iron nitrate ($Fe(NO_3)_3$ $9H_2O$ (Sigma Aldrich)) or both as metal precursors. In order to enhance the hydrophilicity and dispersion of the PN-CF in water, the PN-CF was ground to a fine powder using a ball mill. Then, chemical oxidation of the fine powder of CF (4 g) with concentrated HNO_3 (50 mL) (Panreac, 65 wt. %) at 80 °C for 1 h under reflux was applied. The resulting product was washed with deionized water and dried overnight at 70 °C. Subsequently, 1.5 g of the oxidized PN-CF was dispersed by sonication in 80 mL Milli-Q water. Cobalt nitrate and iron nitrate (1:2 metal ratio) were added to the above solution. The resulting mixture was vigorously stirred using a magnetic stirrer at 80 °C until the solvent completely evaporated. The total metal content relative to the carbon material was fixed at 20 wt. %. Finally, the obtained product was subjected to carbonization at 950 °C for 90 min with a heating rate of 10 °C/min in a nitrogen atmosphere. For comparison purposes, single metal Fe and Co were impregnated into the carbon foam; additionally, catalysts with different ratios of Co/Fe loaded into the PN-CF were also prepared. Moreover, bimetal incorporated with carbon foam without heteroatom dopant was also prepared. The acquired catalysts were washed with ultrapure water and dried overnight at 70 °C. Throughout the manuscript, CF stands for carbon foam, PN-CF represents phosphorus and nitrogen co-doped carbon foam, Fe@PN-CF, Co@PN-CF, and CoFe@PN-CF indicate iron and cobalt monometals, and iron and cobalt bimetals impregnated into PN-CF, respectively. CoFe@PCF denotes cobalt and iron bimetals impregnated into carbon foam.

2.3. Physicochemical characterization

X-ray diffraction (XRD) analysis was carried out in a Bruker D8 Advance diffractometer with Cu Kα radiation at 1600W. The weight percentages of the metals were acquired by inductively coupled plasma atomic emission spectroscopy (ICP-AES) in a Xpectroblue-EOP-TI FMT26 (Spectro). Elemental analysis of as-synthesized material was performed in a CHNS-O Analyzer Thermo FlashEA 1112. Scanning electron microscopy (SEM) studies were obtained in a SEM Hitachi 3400 N microscope. N_2 physisorption measurements were conducted in ASAP2020 (Micromeritics) to evaluate the specific surface area. The specific surface area was determined by the multiple-point Brunauere-Emmette-Teller (BET) approach. The micropore area and pore volume were acquired by applying the t-plot method. A high-resolution transmission electron microscope (TEM) (a Tecnai F30) was used to observe the detailed morphology of the samples, operated at an accelerating voltage of 200 kV. X-ray photoelectron spectroscopies (XPS) were acquired on a Kratos AXIS Supra system equipped with a hemispherical electron energy analyzer operating with Mg (1253.6 eV) at 300 W (20 mA, 15 kV. Analysis area = 1.75 ×2.75 mm). The high-resolution spectrum was acquired with passing energy of 20 eV and 0.1 eV steps, and the survey spectrum was recorded with passing energy of 50 eV and 0.5 eV steps. The C 1 s line at 284.6 eV was used to correct all XPS spectra. CasaXPS software was used to perform peak fitting and quantification, and Shirley-type background was employed for all peaks. Gaussian/Lorentzian (GL: 30 %) line shapes were employed for each component.

2.4. Electrochemical measurement

All electrochemical performance measurements were conducted in a three-electrode system controlled by a potentiostat/galvanostat AUTO LAB PGSTAT302 at room temperature. Glassy carbon rods and Ag/AgCl were used as counter and reference electrodes. A rotating disk electrode (RDE, diameter = 5 mm) or rotating ring-disk electrode (RRDE, disk diameter = 5 mm, Pt ring) coated with a thin catalyst layer was used as a working electrode. The catalyst ink was prepared by dispersing and sonicating 6 mg of catalyst in 588 μL isopropanol/water (1: 1) with 12 μL of Nafion solution (10 wt. %). The working electrode was prepared by drop-casting an ink of 20 μL on the glassy carbon disk and drying under N_2 flow. A 1 M KOH solution was used as the electrolyte for OER electrochemical measurements. The OER activity of the samples was evaluated by linear sweep voltammetry (LSV) at a scan rate of 5 mV s^{-1} in N_2 de-aerated 1 M KOH aqueous solution. The applied potentials were converted to a reversible hydrogen electrode (RHE) according to following the equation [38]:

$$E_{RHE} = E_{Ag\,/\,AgCl} + 0{\cdot}197 + 0{\cdot}059 \times pH$$

The overpotential (η) value was determined by $\eta = E_{RHE} - 1.23$ V. All the applied potentials were corrected by the ohmic drop considering iR_s, where R_s is the series resistance of the system. Prior to electrochemical measurements, the electrolyte was saturated by N_2 gas flow for at least half an hour. Prior to the OER test, certain cyclic voltammetry (CV) was performed: first, 20 cycles were performed in the 0.05–1.0 V vs. RHE potential window at a scan rate of 100 mV s^{-1}; second, three cycles were carried out at a scan rate of 20 mV s^{-1} in the potential range of 0.05–1.1 V vs. RHE; third, 10 cycles of OER polarization curve was recorded in the potential range 1.1–1.8 V vs. RHE 5 mV s^{-1} at 1600 rpm, and then, linear sweep voltammetry (LSV) was measured for further OER performance evaluation. The LSV of the electrocatalytic electrode was converted into a Tafel plot using overpotential (η) vs. log j. relation ($\eta = b\,log|\,j\,| + a$); herein, the Tafel slope (b) reflects the reaction mechanism of the catalyst. The electrochemically active surface area (ECSA) of the electrocatalysts was elucidated from the electrochemical double-layer capacitance (C_{dl}) by performing CV from 1.1 to 1.16 V vs. RHE at various scan rates (20, 40, 60, 80, and 100 mVs^{-1}). Electrochemical impedance spectroscopy (EIS) was measured at 1.6 V vs. RHE in the frequency range of 100 kHz to 0.01 Hz at a 5 mV amplitude (rms). The faradaic oxygen efficiency of the best-performing as-prepared electrocatalyst and commercial IrO_2 was determined by amperometry measurement at 1 $mAcm^{-2}$ current density. Moreover, chronopotentiometry (at j = 10 mA cm^{-2}) and LSV were employed to analyze the durability and activity of the most active electrocatalyst after and before the stability test.

3. Results and discussion

3.1. Electrocatalyst synthesis

The synthesis procedure employed to prepare the carbon foam (CF), heteroatom (P, N) co-doped carbon foam (PN-CF), and metal (Fe, Co) impregnated carbon foam (M@PN-CF) is illustrated in Scheme 1. Firstly, carbon foam was prepared from petroleum pitch through thermo-chemical treatment. It was obtained with or without the addition of the heteroatom precursors to study the effect of the heteroatoms on the

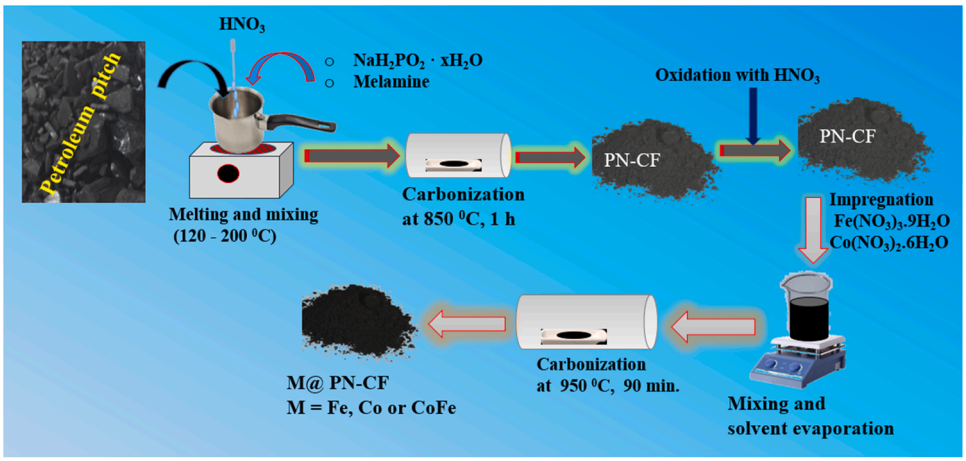

Scheme 1. Schematic illustration of the preparation process of metal-impregnated carbon foam.

morphology and structure of carbon foam. Then, the as-prepared carbon foam was oxidized with concentrated nitric acid to enhance its hydrophilicity or to dispersion in water in the subsequent impregnation process. Finally, transition metals of iron nitrate (Fe source) and cobalt nitrate (Co source) were impregnated with the as-prepared carbon foam, followed by carbonization at high temperatures. To demonstrate the impact of the active metal species on the performance of the resultant composite materials, mono and bimetals of Co and Fe were impregnated into carbon foam support, and their potential for OER was thoroughly investigated. Benefiting from the porous and excellent structural stability of carbon foam support and the coupling effect of Co/Fe metals, the prepared composite electrode may offer promising electrocatalytic performance for OER.

3.2. Structure and morphology characterization

The scanning electron microscopy (SEM) images of the CF, PN-CF, Fe@PN-CF, Co@PN-CF, CoFe@PN-CF, and CoFe@CF are shown in Fig. 1. From Fig. 1a, the CF mainly reveals an amorphous structure and rough surface supplemented with tiny holes due to random aggregation of the porous carbon matrix. The tiny holes on the surface entail the occurrence of abundant pores, which are beneficial for immobilizing the metal species. The SEM image also displays an appearance of cracks on the surface, which is a characteristic of successfully developed carbon foam [39]. The SEM image of P, N co-doped CF is shown in Fig. 1b, presenting an altered microstructure compared with the pristine CF. It displays an irregularly tangled network and a rough surface without distinct characteristic morphology, which could result from heteroatoms fused in carbon foam during the thermal process. In the case of metal-incorporated carbon foam, as for the Fe@PN-CF (Fig. 1 c), Co@PN-CF (Fig. 1d), and CoFe@CF (Fig. 1f), it exhibits a rough surface containing a grainy carbon framework with widespread small bright spherical particles, which reveals the incorporation of metallic nanoparticles due to the thermal reduction of metal nitrates. The supplemented electron around the immobilized metal particles delocalizes the adjacent local carbon shell, thereby forming higher brightness in the area confining the metal particles [38]. The clear difference between the metal-embedded CF and pristine CF suggests that metal impregnation

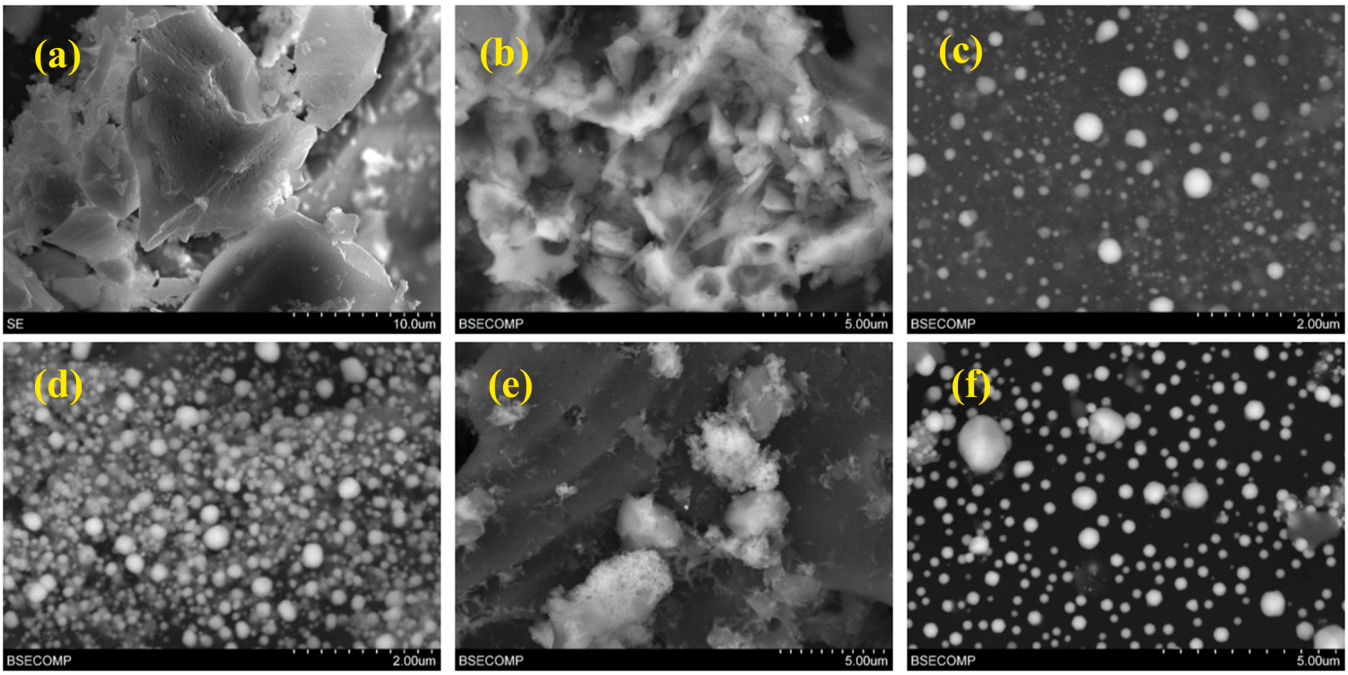

Fig. 1. SEM images of CF (a), PN-CF (b), Fe@PN-CF (c), Co@PN-CF (d), CoFe@PN-CF (e), and CoFe@CF (f).

remarkably changes the morphology of the carbon support. The CoFe@PN-CF (Fig. 1e) displays a different microstructure than the other metal-incorporated carbon foam. A mixture of prominent large irregular, and bright spots and a worm-like structure was observed in this case. The altered morphologies of CoFe@PN-CF relative to the other suggest the intimate interaction between the CoFe and PN-CF, which involves the charge distribution within the network CoFe@PN-CF; it integrates the polarity and electron donor and acceptor character of the CF shell, lifts the interfacial bonding between the metal and carbon foam, promotes the affinity of the surface to electrolyte and normalizes the adsorption energy for the intermediate reactants [38]. The carbon foam shields the metal particle from erosion and phase alteration during electrocatalysis in a harsh environment. Further heteroatoms doping into carbon could galvanize the catalytic activity of the carbon material by reducing the surface work function and monitoring the adsorption of reactants on the surface [38]. The synergy/coupling effect of Co/Fe metal and PN dopants can promote the overall catalytic activity of the resulting composite electrocatalyst.

The surface morphology of carbon foam and metal-impregnated carbon foam was further studied by transmission electron microscopy (TEM). The composition and elemental mapping of the corresponding elements of the samples were also analyzed by scanning-transmission electron microscope (STEM) together with energy dispersive spectroscopy (EDS). Fig. 2 shows a comparison of TEM images of the different samples. The morphology of carbon foam presents a typical amorphous structure due to the random aggregation of a porous carbon matrix. Layer by layer sheet-like structure with an irregular arrangement was observed in the CF sample, as shown in Fig. 2(a) and Fig. 2S(a). The TEM image of the PN-CF sample is shown in Fig. 2(b) and Fig. 2S(b), in which an amorphous carbon that involves defects or vacancies on its surface was observed. The apparent morphology difference relative to pristine CF suggests that the microstructure of resulting composite carbon derived from petroleum pitch in the presence of nitrogen and phosphorous precursors is prominently altered by PN incorporation. Inserting dopants in the carbon matrix could crack the carbon network, generating defects/vacancies. Moreover, the bubble evolution while adding a foaming agent of HNO_3 during the thermo-chemical reaction could contribute to the evolved cracks. The defects/vacancies presented on the carbon matrix can be a crucial hosting site for impregnating metals. In the case of metal-impregnated carbon foam, the morphology looked different. In line with the SEM image of the Fe@PN-CF sample (Fig. 1(c)), the TEM image of the Fe@PN-CF sample (Fig. 2(c)) shows a widespread distribution of dark spots throughout the carbon matrix. The dark spots are iron nanoparticles immobilized on the carbon microstructure. Apart from the dark spots of iron nanoparticles, a ligamentous fold-like structure was also observed, as shown in Fig. 2(c) and Figure S1 (c). Similar morphology was also detected in the Co@PN-CF sample, in which carbon-encapsulated cobalt nanoparticles appeared as black spots throughout the surface (Fig. 2(d)). Moreover, detailed observation by TEM reveals the Co@PN-CF sample also contains a ligamentous fold-like structure, as shown in Figure S1(d). Meanwhile, the morphology of the CoFe@PN-CF sample exhibits different features. As shown in Fig. 2(e) and Figure S1(e), ultra-small particles are immobilized in the heteroatoms co-doped carbon foam supports. It appeared like a fractured surface with alternative white and black spots, which is closely related to the incorporation of metal atoms within the carbonaceous network. On the other hand, the CoFe@CF sample presents dim spherical particles surrounded by amorphous carbon bright background. The chemical composition of these spherical particles was revealed by STEM, in which the spherical particles are an alloy of CoFe enclosed by a carbon layer. Besides, it can be attributed to the non-uniform distribution of defects on the composite surface. It is important to mention that an effort to determine the lattice fringe of the metal particles was challenging due to the fact that the metal particles are covered by the carbon layer, which affects the transmission of the electron beam through the metal particles; as a result, it is difficult to obtain a precise atomic spacing in which metal particles are intruded in the carbon network and surrounded by carbon sheet layer [38]. In the high-resolution TEM image of CoFe@PN-CF shown in Figure S1(e), no clear lattice fringes are detected, and this conforms to the low-crystalline feature observed in the XRD analysis (Fig. 3). STEM-EDS element mapping of the CoFe@PN-CF sample was performed to elucidate the distribution of Co, Fe, C, N, and P atoms. The bulk structure contains Co, Fe, C, N, O, and P atoms, in which almost all atoms are uniformly distributed in the whole matrix, as displayed in Fig. 2(g-n). The elemental mappings confirm that heteroatoms (P, N) and metals (Co, Fe) are effectively doped and homogeneously distributed throughout CoFe@PN-CF composite sample. It is believed that such composite material can be a far-reaching catalyst for water oxidation. The P, N dopants are crucial for modifying the electrons donor/acceptor feature of the carbon, and the immobilized Co and Fe particles on the P, N doped carbon matrix are electroactive sites; hence, it is presumed that CoFe@PN-CF materials can deliver an augmented electrocatalytic activity of CoFe@PN-CF towards OER.

The N_2 adsorption-desorption measurements were conducted to measure the sample's textual properties. Table 1 shows a snapshot of the textural properties of the different materials. The pristine CF presents the highest BET-specific surface area and total pore volume. On the other hand, the mono and bimetal incorporated CF showed a relatively lower surface area. Particularly, the BET-specific surface area of the material is given as follows in decreasing order: CF > CoFe@CF > Co@PN-CF > Fe@PN-CF > CoFe@PN-CF. The total pore volume at $p/p^0 = 0.99$ was evaluated, and it was found that CF and CoFe@CF retain the highest values as presented below in decreasing order: CF > CoFe@CF > Fe@PN-CF > Co@PN-CF > CoFe@PN-CF. It is apparent from Table 1 that the incorporation of the heteroatoms substantially influenced the surface area and the microporosity textures. The micropore contribution was determined by the t-plot method. Accordingly, it was found that all materials contain a significant amount of micropores (both in terms of surface area and pore volume). The microporosity contribution of the CF sample was about 94 % (in terms of surface area), while it has decreased in the other samples. in which the microporosity contribution (in terms of surface area) of the materials is presented as follows in decreasing order: CF > CoFe@CF > CoFe@PN-CF > Co@PN-CF > Fe@PN-CF. Microporosity contribution (in terms of pore volume) of the materials was also determined. The CF and CoFe@CF sample contains about 87 % and 75 %, respectively, while the Co@PN-CF, CoFe@PN-CF, and Fe@PN-CF present about 39 %, 28 %, and 16 %, respectively. These results indicate that the incorporated Co and Fe metals and co-doped P/N dopants cause a more condensed structure and exhibit remarkable differences in the porosity distribution.

The crystal structure of the prepared samples was characterized by XRD. As shown in Fig. 3, the XRD pattern of carbon foam exhibits two apparent weak and broad diffraction peaks between $2\theta = 20–30^0$ and $40–50^0$, corresponding to the C (002) and C (100) diffraction plane of carbon, respectively. This discloses that the sample encompasses aromatic carbon sheets organized randomly or with a low degree of graphitization [40,41]. The crystal structure of the P, N heteroatoms modified carbon foam shows a noticeably unlike diffraction peak compared to the original carbon foam, suggesting the heteroatoms play a crucial role in transforming carbon foam precursor into different crystallinity, composition, and structure. The PN-CF sample contains a mixture of $Na_4P_2O_7$ (JCPDS, #10–0187 and #02–0248), P (JCPDS, #02–0266), and C_3N_4 (JCPDS, #50–0848) crystal structures. In the P, N incorporated carbon foam (PN-CF), the diffraction peaks of the carbon foam are imperceptible due to the higher intensity of heteroatoms relative to the carbon material. Apparently, low crystallinity is observed in all subsequent samples due to the nature of the amorphous carbon foam substrate. Moreover, in the mono metal and bimetals embedded carbon foam samples, the diffraction peaks belonging to PN-CF or CF are invisible, possibly due to the lower intensity relative to the strong peaks attributed to the metals. The Fe@PN-CF sample presents two major crystal phases (Fe_3P and Fe_2P). The reflection peaks at $2\theta = 35.75^0$,

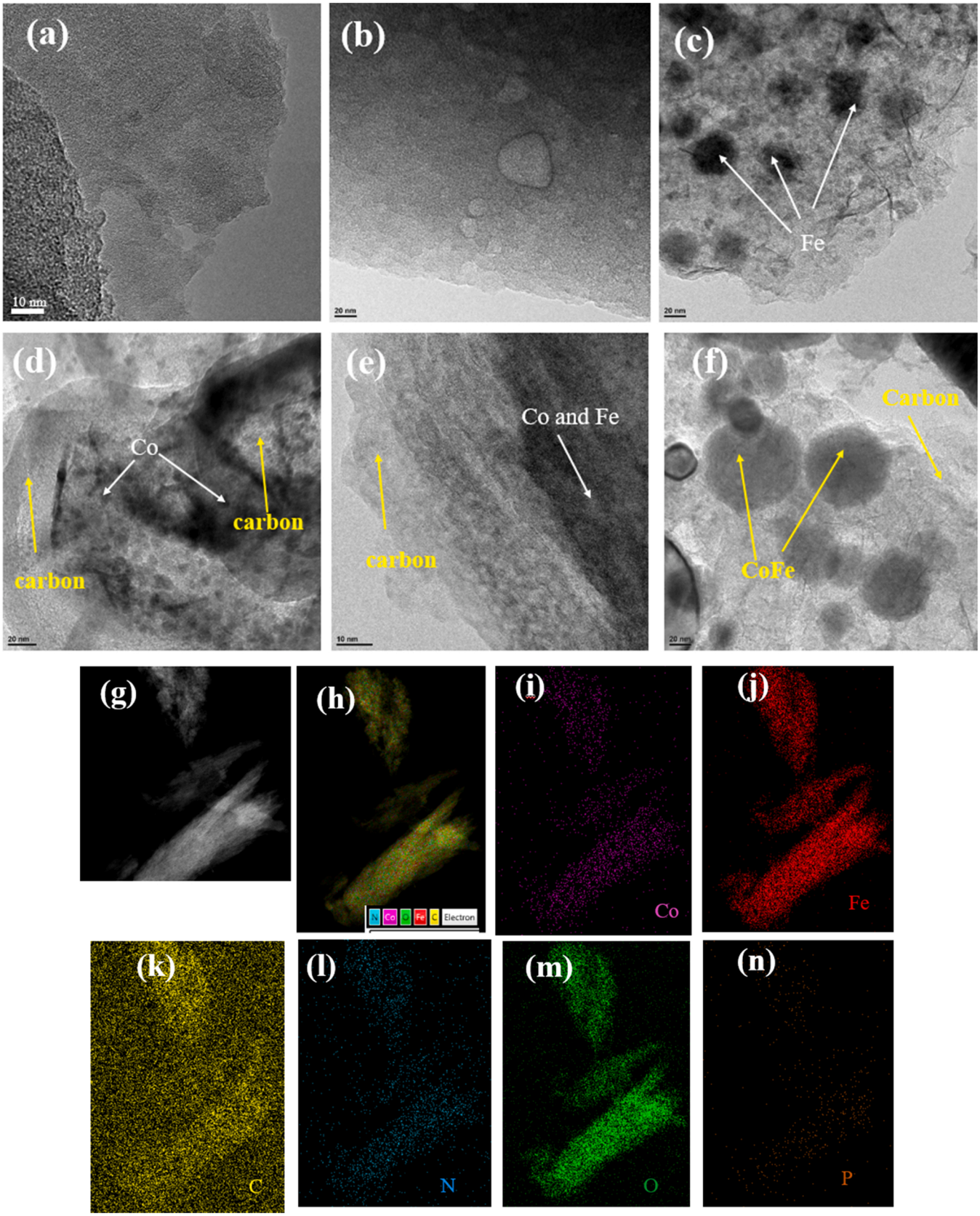

Fig. 2. TEM images of (a) pristine CF, (b) PN-CF, (c) Fe@PN-CF, (d) Co@PN-CF, (e) CoFe@PN-CF, (f) CoFe@ CF and (g) STEM image of CoFe@PN-CF and (h-n) EDS elemental mapping images of Co, Fe, C, N, O and P.

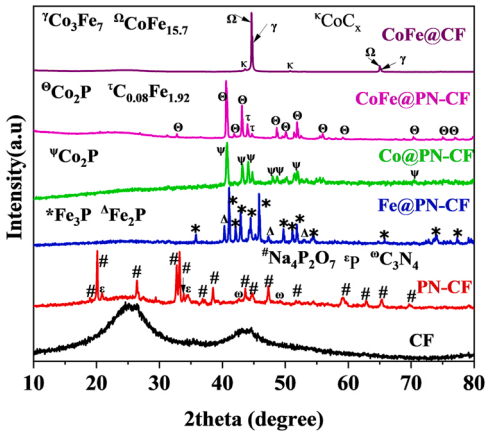

Fig. 3. XRD patterns of the different samples.

Table 1
Textural properties of the different materials determine by N_2 physisorption.

Catalyst	BET-specific surface area (m^2/g)	Micropore area (m^2/g)*	Total pore volume (cm^3/g) @ at p/p^0 = 0.99	Micropore volume (cm^3/g)*	Meso/macropore volume (cm^3/g)
CF	386	364 (94 %)	0.163	0.141 (87 %)	0.022
Fe@PN-CF	73	41 (56 %)	0.108	0.017 (16 %)	0.091
Co@PN-CF	135	99(73 %)	0.103	0.040 (39 %)	0.063
CoFe@PN-CF	55	41 (74 %)	0.063	0.018 (28 %)	0.045
CoFe@CF	290	268 (92 %)	0.143	0.107 (75 %)	0.036

* The values in parenthesis present the percentage of micropore contribution with respect to the total surface area or total pore volume.

41.03^0, 42.06^0, 42.88^0, 44.45^0, 45.8^0, 49.69^0, 51.09^0, 51.81^0, 54.36^0, 65.74^0, 74.05^0, and 77.3^0 can be indexed to the diffraction of the peak of Fe_3P, which correspond to the (301), (321), (330), (112), (420), (141), (222), (150), (312), (341), (161), (532), and (143) crystal planes of tetragonal Fe_3P (JCPDS, #87–2712). The diffraction peaks at $2\theta = 40.3^0$, 47.29, and 52.95^0 are attributed to hexagonal Fe_2P (JCPDS, #88–1803), which correspond to the (111), (210), and (002) crystallographic planes of Fe_2P. The XRD pattern of the Co@PN-CF sample contains a typical diffraction peak located at $2\theta = 40.72^0$, 43.3^0, 44.07^0, 49.7^0, 50.38^0, 52.65^0, and 69.02 assigned to Co_2P (JCPDS, #32–0306), which correspond to (121), (211), (130), (221), (310), (230), and (222) diffraction crystal planes of orthorhombic Co_2P. The XRD pattern of the CoFe@PN-CF sample reveals two major crystal phases. The appearance of reflection peaks at $2\theta = 31.64^0$, 32.92^0, 40.73^0, 42.06^0, 44.08, 48.72^0, 49.71^0, 52.03^0, 56.20^0, 69.02^0, 70.53^0, 75.34^0, and 77.02^0 are attributed to the (200), (111), (121), (220), (130), (031), (221), (002), (320), (222), (132), (312) and (051) crystallographic planes of orthorhombic Co_2P (JCPDS, #06–0595). Besides, the reflections at $2\theta = 44.02^0$ and 44.84^0 can be indexed to the (101) and (110) crystallographic planes of tetragonal $C_{0.08}Fe_{1.92}$ (JCPDS, #44–1291). Moreover, for comparison purposes and to appreciate the effect of heteroatoms (P, N) on the resulting crystal phase evolution, the CoFe@CF sample was also prepared and characterized by XRD. As shown in Fig. 3, the sharp diffraction peaks located at $2\theta = 44.75^0$ and 65.11^0 corresponds to the (110) and (200) crystallographic planes of cubic Co_3Fe_7 (JCPDS, #48–1816). The reflection peaks at $2\theta = 44.65^0$ and 64.99^0 can be indexed to the (110) and (200) crystallographic planes of cubic $CoFe_{15.7}$ (JCPDS, #65–7519). In addition, the diffraction peaks at $2\theta = 43.54^0$ and 50.77^0 can be attributed to the (111) and (200) crystal planes of cubic CoC_x (JCPDS, #44–0962). The XRD patterns of the CoFe@CF sample obtained after incorporating heteroatoms apparently indicates the conversion of CoFe alloy into cobalt phosphide and $C_{0.08}Fe_{1.92}$.

Raman spectroscopy was further applied to elucidate the structural changes in the materials. Raman affords information on the structure of carbon-carbon bonds and reveals the materials' crystallographic and vibration information. The peak intensity ratio of D and G (I_D/I_G) is typically employed to appraise the disorder or the graphitization degree of materials [42]. As shown in Fig. 4, the peaks are deconvoluted into four peaks (D, D', G and D'') using Lorentzian curve fitting. The corresponding Raman shift (cm^{-1}) of the deconvoluted peaks is tabulated in Table 2. The peaks at 1350–1354 and 1581–1582 cm^{-1} are related to the D and G bands. The G band is related to the E_{2g} vibration mode of graphite and is associated with the stretch vibration of sp^2-bonded carbon atoms. The D band reveals imperfections in sp^2 carbon structures and results from the breathing modes of six-atom rings and appears in the existence of the disordered structure. D' band is related to disorder in graphite, and D'' band appears only in amorphous carbon and is connected to interstitial defects [38,43,44]. As shown in Table 2, the ratio of I_D/I_G for all samples is higher than 1, reflecting an amorphous structural material. The ratio of I_D/I_G for the pristine carbon foam was about 1.60. This value was increased to 1.74 upon incorporating P and N into CF, reflecting the dopants increased the disorder or created defects in the carbon structure. On the other hand, the ratio of I_D/I_G for Fe@PN-CF, Co@PN-CF, CoFe@PN-CF, and CoFe@CF samples is found to be 1.42, 1.28, 1.11, and 1.18, respectively, which suggests a positive contribution to the graphitization of carbon structure after incorporating mono/bimetals followed by secondary carbonization. Notably, CoFe@PN-CF presented the lowest I_D/I_G ratio. In this situation, it can be presumed that the coupling effect of the bimetals together with the P, N co-doped carbon foam accompanied by secondary carbonization is more favorable for the formation of graphitic carbon, which eventually stimulates the conductivity, reducing the charge transfer resistance during the electrochemical reaction and henceforth facilitates OER kinetics. From a practical perspective, materials with a higher graphitization degree are

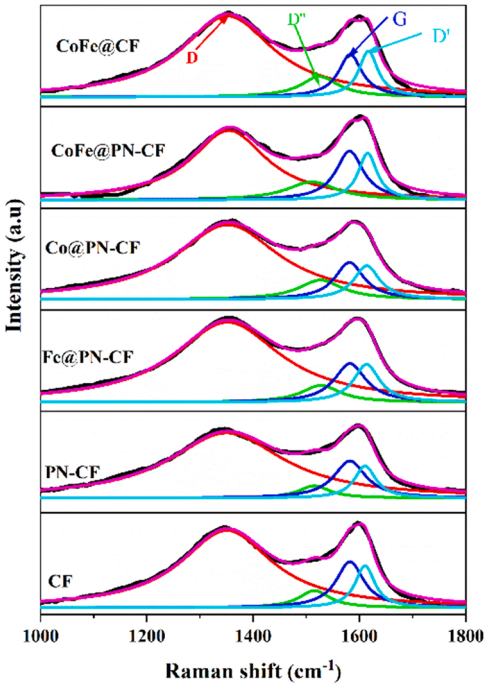

Fig. 4. Raman spectra of the different samples.

Table 2
Raman shift (cm^{-1}) of the deconvoluted peaks (shown in Fig. 4) and I_D/I_G ratio comparison.

samples	D	D"	G	D'	I_D/I_G
CF	1350	1515	1582	1610	1.60
PN-CF	1350	1515	1582	1611	1.74
Fe@PN-CF	1352	1526	1582	1613	1.42
Co@PN-CF	1352	1526	1581	1613	1.28
CoFe@PN-CF	1354	1510	1582	1615	1.11
CoFe@CF	1352	1525	1583	1616	1.18

better for water oxidation in which the electrical conductivity highly depends on the degree of graphitization.

X-ray photoelectron spectroscopy (XPS) was further applied to analyze the surface elemental chemical compositions of the as-prepared catalysts. The XPS survey spectra confirm that the elements of Co, Fe, C, N, P, and O co-existed on the surface of the CoFe@PN-CF sample, as shown in Fig. 5a. This indicates the successful doping of P, N, Co, and Fe into the carbon structure. A high-resolution XPS spectrum was further applied to the selected elements to study the respective oxidation state. The high-resolution spectra of Co 2p can be decomposed into three doublets. As shown in Fig. 5b, the XPS peaks at binding energy (BE) of 780 eV, 781.7, and 786.8 eV are ascribed to the Co^{3+}, Co^{2+}, and shake-up satellite of Co $2p_{3/2}$, respectively. The peaks at a higher binding

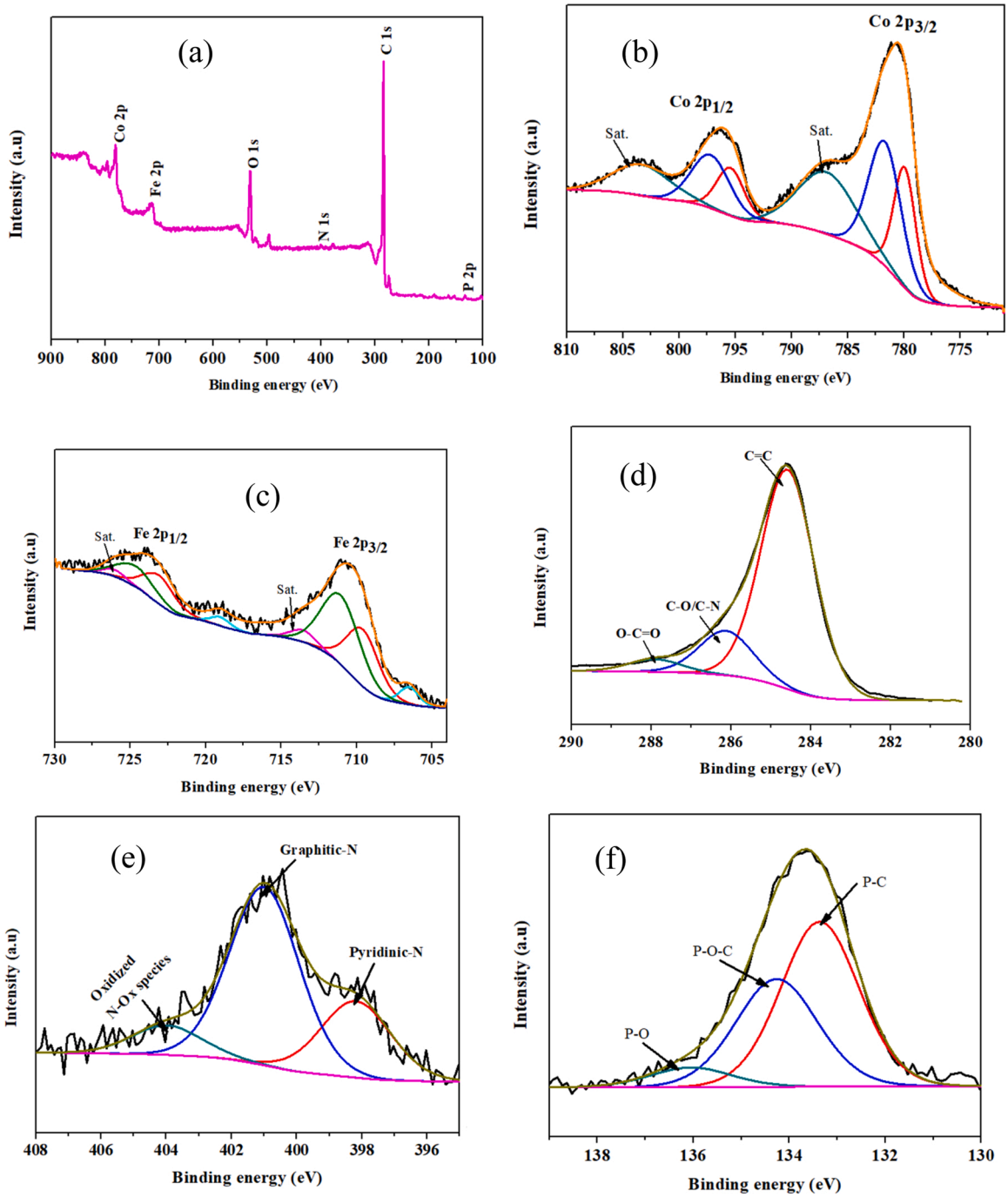

Fig. 5. (a) XPS survey spectra of CoFe@PN-CF, (b) High resolution of spectrum of Co 2p, (c) Fe 2p, (d) C 1 s, (e) N 1 s, and (f) P 2p.

energy of 795.4, 797.2, and 803.4 eV correspond to the Co^{3+}, Co^{2+}, and shake-up satellite of Co $2p_{1/2}$, respectively [42]. Likewise, the peaks corresponding to Fe^0 (706.5 and 719.91 eV), Fe^{2+} (709.7 and 723.4 eV), and Fe^{3+} (711.3 and 725.0 eV) appear in Fe 2p high-resolution spectra. Besides, the peaks at BE of 713.8 and 726.3 eV are attributed to the shake-up satellite of Fe 2p (Fig. 5c) [45]. Moreover, the high-resolution XPS spectra of C 1s can be fitted into three main peaks; the peaks at 284.6, 286.2, and 288.0 eV are assigned to the C-C, C-N/C═O, and O-C═O, respectively (Fig. 5d) [46]. This result indicates the incorporation of a nitrogen atom into the carbon structure. The high-resolution XPS spectrum of N 1s exhibits three major characteristic peaks at about 398.2, 400.0, and 404.0, which are assignable to the pyridinic-N, graphitic-N and oxidized- N groups, respectively (Fig. 5e) [47]. The presence of the pyridinic-N functional group can efficiently promote the adsorption capacity of OH^- [48] and can serve as an active site by anchoring the metals. The graphitic N is essential for promoting the conductivity of the composites [38]. It was demonstrated that the pyridinic N and graphitic N were reported to create a positive charge on adjacent sp^2-hybridized carbon atoms, providing more active sites and high stability; as a result, expediting the OER performance [23,25].

Furthermore, the high-resolution XPS of P 2p shows three prominent characteristic peaks; the peaks at BE of 133.4, 134.4, and 136.3 eV can be assigned to P-C, P-O-C, and P-O, respectively (Fig. 5**f**), further confirming the incorporation of P to the carbon and the inevitable oxidation the sample's surface in the air [26,49,50]. Meanwhile, we have also investigated and compared the XPS spectra of the other samples (Figure S2, Supporting information). The XPS spectrum of Fe 2p from the three samples (Fe@PN-CF, CoFe@PN-CF, and CoFe@CF) is shown in Figure S2a, whereas the Co 2p spectra (from Co@PN-CF, CoFe@PN-CF, and CoFe@CF) are shown in Figure S2b. It highlights the presence of Fe and Co on the surface of the corresponding samples. Besides, the XPS spectra of C 1 s (Figure S2c) and N1s ((Figure S2d) are also recorded and showed similar characteristic peaks in all samples. Finally, the XPS spectra for the P 2p segment are also shown in Figure S2e, which again exhibit similar characteristic peaks with slight differences in the PN-CF sample. The weak peak appeared at about 130 eV designates the presence of P^0 ($P_{3/2}$ and $P_{1/2}$) in the PN-CF sample, while it appeared in oxidized forms in the other composites prepared by impregnating metals with the PN-CF substrate. The co-doping of the N and P atoms could induce reasonable adjustment of the electronic structures in the carbon structure of the carbon foam, ultimately creating plenty of active sites readily available for the OER reactants [50].

The samples were characterized by ICP and elemental analysis to better explore the composition. As shown in Table 3, the pristine carbon foam support contains about 71 % C, 1.6 % H, and 2.91 % N. After adding the melamine as N precursor to the CF, the concentration of the N content has prominently increased. The pristine CF has about 3 wt. % of N content, while it is doubled after adding 10 wt. % of melamine, indicating N-enrichment of the composite carbon. Besides, ICP revealed the presence of a P atom in the bulk composite, in which the PN-CF support shows the highest P content of 4.2 %, and the metal-impregnated PN-CF sample reveals about 2 wt. %. The presence of N and P in the final product could modify the target electrocatalyst's overall physicochemical and electrochemical properties. The initial concentration of the metal content was about 20 wt. % relative to the bulk carbon foam support, while it has increased in the final product. For example, initially, the metal content (Co+Fe) of the CoFe@PN-CF sample was about 20 wt. % relative to the composite carbon foam. After impregnation, followed by carbonization at 950 ^{0}C, the metal loading increased to 29.7 wt. % (Table 3). This is due to the fact that, after carbonization of the mixture at high temperature, the carbon content of the carbon support was decreased due to decomposition; therefore, it is expected to increase the relative metal content.

Table 3
Composition from ICP and Elemental analysis of the samples.

	Elemental analysis (wt. %)			ICP (wt. %)		
Sample	C	H	N	Fe	Co	P
CF	71	1.6	2.9	-	-	-
PN-CF	58	2.1	6.1	-	-	4.2
Fe@PN-CF	57	0.6	5.2	33	-	2.05
Co@PN-CF	49	0.5	5.8	-	32	2.1
CoFe@PN-CF	42	2.0	6.0	19	10	2.3
CoFe@CF	61	0.6	1.3	15	7.8	-

3.3. Electrochemical characterization

The electrocatalytic OER performance of the pristine CF, PN-CF support and all-metal (Fe, Co, CoFe) incorporated carbon foam was explored in a three-electrode cell system under an alkaline electrolyte, as shown in Fig. 6a. The carbon support (CF and PN-CF) was evaluated for its OER activity for a pertinent comparison. As shown in Fig. 6a, both carbon support present low OER activity in the applied potential range. Regarding the metal-incorporated carbon foam, all samples show a substantial progressive activity towards OER. The monometallic Co incorporated with the PN-CF support (Co@PN-CF) exhibits an outstanding OER activity, while Fe@PN-CF presents lower activity than Co@PN-CF. Interestingly, excellent water oxidation was achieved upon incorporating CoFe bimetals into PN-CF (CoFe@PN-CF). Fig. 6b highlights the various metal-embedded carbon foam electrocatalyst with their corresponding overpotential at $j = 10$ mAcm^{-2}. The CoFe@PN-CF electrocatalyst requires a small overpotential of 320 mV to yield a current density of 10 mAcm^{-2}, which is superior to that of the reference IrO_2 electrocatalyst (η_{10} = 350 mV). On the other hand, Fe@PN-CF and Co@PN-CF sample demands a 420 and 360 mV overpotential, respectively, to derive the same current density. Carbon foam without doping heteroatoms was also prepared, and CoFe bimetals were embedded into it and evaluated the OER performance. In this case, the CoFe@CF catalyst requires an overpotential of 380 mV to derive 10 mAcm^{-2}. This comparison manifests the promising OER activity of the CoFe@PN-CF electrode boosted by the encapsulated CoFe bimetal nanoparticles in the PN-CF support. The notable OER activity of the CoFe@PN-CF catalyst could be emanated from the synergetic effect of the bimetals, an optimized ratio of Co/Fe, and a higher graphitic phase of PN-CF in the presence of CoFe alloy nanoparticle, which is vital to amplify conductivity and the altered microstructure of CoFe alloy embedded PN-CF compared to the monometallic counterpart. On the other hand, the effect of the Co/Fe ratio towards OER activity was investigated. Various electrocatalysts were prepared by varying the ratio of Co and Fe aimed at investigating the OER activity. In particular, four catalysts (Co_1Fe_1@PN-CF, Co_1Fe_2@PN-CF, Co_2Fe_1@PN-CF, and Co_1Fe_3@PN-CF) are prepared and tested for their OER performance. Figure S4 compares the OER polarization curve of CoFe@PN-CF prepared with different ratios of Co/Fe. It is apparent that Co_1Fe_2@PN-CF has the best OER catalytic performance. This suggests the important role of the bimetals, depending on the combination, which affects its electronic structure and conductivity. Hence, the CoFe@PN-CF sample is the best-performing electrocatalyst in this work, and the Co_1Fe_2@PN-CF (denoted as CoFe@PN-CF throughout the manuscript) catalyst was further analyzed considering its superior activity via both physicochemical and electrochemical characterization together with the other metal-free carbon foam and mono-metal loaded carbon foam samples. The relatively higher OER performance of CoFe@PN-CF may be attributed to the redistribution of π-electrons spin between Co and Fe (via the bridging O^{2-}), leading to optimized adsorption/desorption characteristics of the intermediate species on the surface, which eventually improves the electrocatalytic kinetics [51]. Besides, the excellent OER activity of the synthesized CoFe@PN-CF electrocatalyst is ascribed to the presence of the nitrogen, phosphorous, and transition metal sites. They act as proton and hydride acceptor sites, which may facilitate oxygen evolution by forming oxy/hydroxides during the OER. In an alkaline environment, metal-oxy/hydroxides are formed via the following mechanism [25].

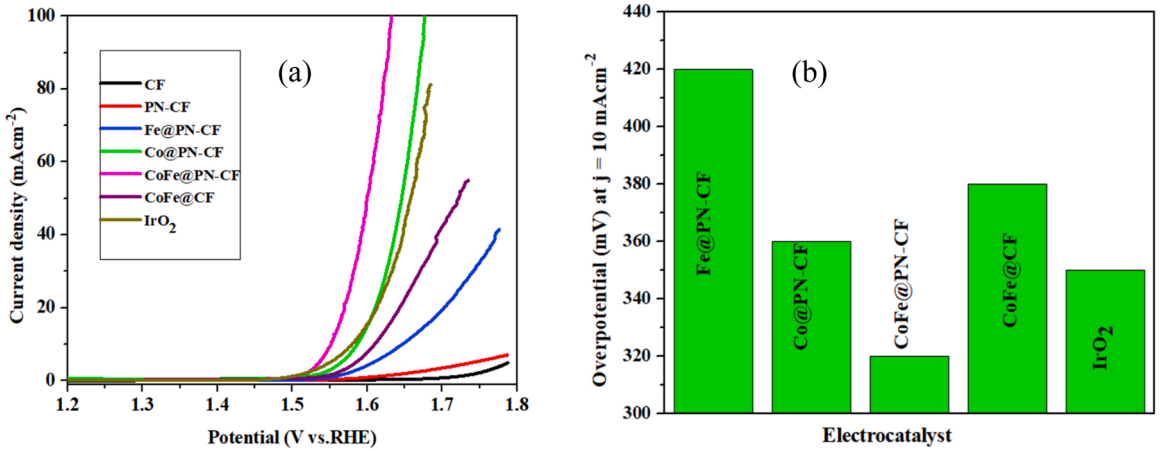

Fig. 6. (a) OER polarization curves of the electrocatalysts in the N2-saturated 1.0 M KOH and a scan rate of 5 mV s^{-1} at 1600 rpm, (b) Overpotential comparison at j = 10 $mAcm^{-2}$.

$$M + OH^- \leftrightarrow M{-}OH + e^- \quad (1)$$

$$M{-}OH^- + OH^- \leftrightarrow M{-}O{+}H_2O + e^- \quad (2)$$

$$M{-}O + M{-}O \rightarrow 2M + O_2 \quad (3)$$

$$M{-}O + OH^- \rightarrow M{-}OOH + e^- \quad (4)$$

$$M{-}OOH \rightarrow 2M + O_2 + e^- \quad (5)$$

To unravel further insight into the OER kinetics of the samples, the Tafel slope was determined by plotting overpotential (V) vs. Log (j), as shown in Fig. 7a. Tafel slope is commonly considered as a descriptor of OER kinetics. The CoFe@PN-CF sample reveals a small Tafel slope of 48 $mVdec^{-1}$, which is much lower than that of Fe@PN-CF (75 $mVdec^{-1}$ and 177 $mVdec^{-1}$), Co@PN-CF (70 $mVdec^{-1}$), CoFe@CF (77 $mVdec^{-1}$), CF (104 $mVdec^{-1}$), and PN-CF (163 $mVdec^{-1}$ and 266 $mVdec^{-1}$), and IrO_2 (72 $mVdec^{-1}$), implying the most rapid and expedite mass/charge transfer for OH^- oxidation at the CoFe@PN-CF catalyst surface.

To further illuminate the excellent OER catalytic activity of the CoFe@ PN-CF electrocatalyst, ECSAs of the materials were estimated using the double-layer capacitance layer (C_{dl}) as a descriptor. The C_{dl} was determined from the CV curves in the non-faradaic region (1.1–1.16 V vs.RHE) at various scan rates (20, 40, 60, 80, and 100 mVs^{-1}). Then, the ECSA was evaluated using the following equation: $ECSA = C_{dl}/C_s$, where C_s is the general specific capacitance (0.04 mF cm^{-2}) of metal electrodes in aqueous KOH solutions reported in the literature [52]. The CV curves of the different electrocatalysts at various scan rates are shown in Figure S5. By plotting the linear relationship between Δj/2 and scan rate at 1.13 V (vs. RHE), the value of C_{d1} can be obtained, which is the slope of the linear fitting (Fig. 7b). Accordingly, the value of C_{d1} for the different catalysts is determined to be as follows: CF (8.6 μFcm^{-2}), PN-CF (0.087 $mFcm^{-2}$), Fe@PN-CF (0.4 $mFcm^{-2}$), Co@PN-CF (2.4 $mFcm^{-2}$), CoFe@PN-CF (5.5 $mFcm^{-2}$), and CoFe@ CF (1.8 $mFcm^{-2}$). Using these results, it is straightforward to estimate the ECSA of each sample considering the C_s value and catalyst loading (1 mg/cm^2). Thus, the CoFe@PN-CF catalyst exhibits an ECSA of about 13.8 m^2/g, while the CF, PN-CF, Fe@PN-CF, Co@PN-CF, and CoFe@ CF catalyst shows a 0.02, 0.22, 1, 6 and 4.5 m^2/g, respectively. Evidently, the CoFe@PN-CF catalyst displays the highest ECSA revealing abundant or relatively more active sites for adsorption of the intermediates and accepting charge/electron through interface charge transfer, which is prominent for galvanizing OER activity. Based on these results, the relatively higher electrochemically active surface area of the CoFe@PN-CF catalyst could partially contribute to the improved OER catalytic activity achieved. Given the lowest Tafel slope, overpotential, charge transfer resistance, highest ECSA, and intrinsic OER activity, the CoFe@ PN-CF material herein is the most promising electrocatalyst for OER.

Considering the above results, ECSA normalized-OER polarization was plotted to determine the intrinsic activity of the individual active

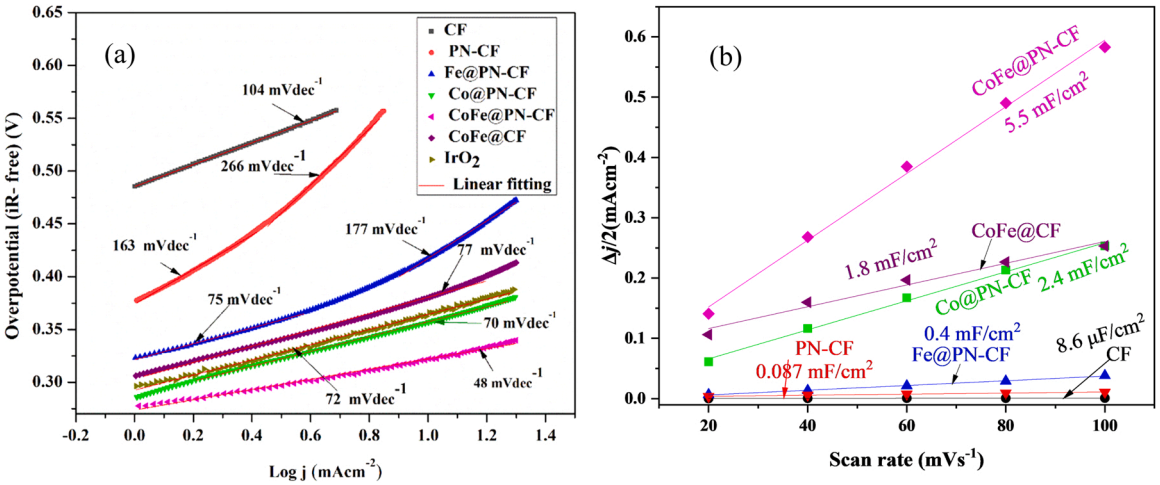

Fig. 7. (b) Tafel plots and (b) capacitive currents as a function of scan rate.

site. It is essential to mention that ECSA measurement helps quantifying the electrode-electrolyte interface area of the electrodes; nevertheless, not all interface is necessarily electrocatalytically active [53]. Figure S6 shows the ECSA-normalized OER polarization curves of the metal-based electrocatalysts. Notably, the ECSA normalized polarization curve exhibits different OER catalytic performance, which is in reversed trend compared to the geometric area normalized OER polarization curve (Fig. 6a). In this case, the Fe@PN-CF catalyst shows the highest ECSA-normalized polarization curve, and the CoFe@PN-CF catalyst presents relatively lower activity. This result suggests that the higher activity of CoFe@PN-CF mainly originates from the increased ECSA. CoFe@PN-CF catalyst has a large ESCA and favorable geometric area-normalized OER activity, meaning that the active sites are well distributed throughout the surface, and the atomic utilization is remarkably enhanced; all these factors play a critical role in promoting OER activity [54]. We also observed the same phenomena in our previous paper [75]. It has also been reported in elsewhere literature, clarifying ECSA normalized OER polarization curve, which results in reversed trend compared to the normalization by geometric surface area [55,56].

Electrocatalyst that comprises carbonaceous materials suffers from carbon corrosion at a high anodic potential. To this end, it is critical to differentiate the contribution of water oxidation to the total anodic current registered. There are several techniques employed to quantify the evolved oxygen, such as scanning electrochemical mass spectrometry [57], fluorescence oxygen sensors [58], gas chromatography [59,60], differential and online mass spectroscopy [61], rotating ring-disc electrode (RRDE) [62], etc. In this work, we employed the RRDE technique that has a low detection limit, and no sophisticated configuration is required. In this technique, the oxygen evolved at the disk electrode is detected at the ring by electrochemical reduction. This can estimate the OER efficiency of metal/carbon composite electrocatalysts. The dissolved oxygen produced at the disk electrode is diffused to the Pt ring electrode, where it is reduced. The rotating Pt-ring electrode was held at a constant oxygen reduction reaction (ORR) potential of 0.4 V vs.RHE. The faradaic oxygen efficiency ε was estimated using the following expression: $\varepsilon = (4/n_{ORR})\cdot i_{ring}/(N\cdot i_{disk})$ [63], where n_{ORR} denotes the number of electron transferred per O_2 molecule ($n_{ORR} = 4$ for Pt ring), N is the RRDE collection efficiency (0.248), and i_{ring} and i_{disk} are the ring and disk currents, respectively.

Fig. 8a and b show the disk and ring current profiles of the CoFe@PN-CF electrocatalyst as a function of time measured in 1.0 M KOH at 1600 rpm under N_2 saturation. The disk current at which it starts forming oxygen bubbles affects the accuracy of faradaic oxygen efficiency estimation. Therefore, it is crucial to limit the disk current for a proper assessment of faradaic oxygen efficiency. The faradaic efficiency was determined using chronoamperometry measurements by applying a constant disk potential of 1.51 V vs. RHE (equivalent to 1 $mAcm^{-2}$ OER current density) while the Pt ring was kept at 0.4 V vs. RHE. A current density 1.0 $mAcm^{-2}$ was chosen to evaluate the faradaic efficiency due to the fact that this current is enough to generate dissolved oxygen while maintaining a negligible local bubble formation rate on the disk electrode surface [64]. Fig. 8a and b display the disk and ring current as a function of time. At $E_{disk} = 0$ V vs.RHE, both disk and ring current show almost zero value, indicating no chemical response. When the disk potential was increased to 1.51 V vs. RHE, a current density equivalent to 1 $mAcm^{-2}$ was produced at the disk. As oxygen is generated at the disk electrode, it diffuses towards the surrounding Pt ring electrode, where it is rapidly reduced. Fig. 8**b** shows an apparent current registered from the Pt ring electrode, which indicates the evolved oxygen in the disk is being reduced at the ring electrode. The corresponding faradaic efficiency of CoFe@PN-CF and IrO_2 as a function of time is shown in Fig. 8c and Figure S3, respectively. At the start, at 1 $mAcm^{-2}$ current density (obtained by applying $E_{disk} = 1.50$ V for IrO_2 and $E_{disk} = 1.51$ V vs.RHE for CoFe@PN-CF catalyst), the faradaic efficiency of CoFe@PN-CF and IrO_2 catalyst was determined to be 95 %, and 99 %, respectively. The faradaic

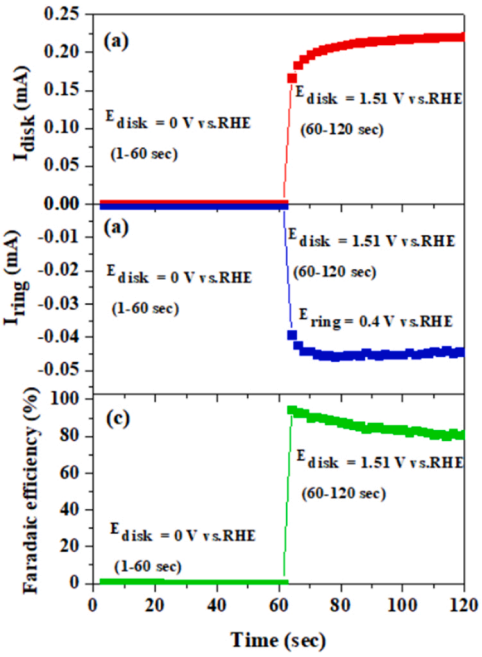

Fig. 8. Evaluation of faradaic efficiency CoFe@PN-CF electrocatalyst through RRDE technique: (a) disk current as a function of time, (b) ring current as a function of time, measured in 1 M KOH at 1600 rpm under N_2 saturation, and (c) faradaic oxygen efficiencies profile as a function of time.

efficiency of the IrO_2 catalyst determined in this work is comparable to the values reported in the literature [62]. The faradaic efficiency slightly decreases with increasing the time of operation. This can be due to different factors: oxygen bubbles can be formed in the pores of the electrocatalyst, and this takes time to dissolve and diffuse to the Pt ring electrode, subsequently decreasing the faradaic efficiency. Undissolved oxygen bubbles evolved at disk potentials cannot be collected and reduced at the Pt ring electrode [64]. Besides, several tiny bubbles would gather in the vicinity of the disk-ring interface, and these oxygen bubbles may limit the transfer of dissolved oxygen from the disk to the ring, resulting in reduced efficiency [62,65]. This can be observed in Fig. 8a, in which the disk current has to some extent, increased with increasing time while the Pt ring current remained constant. In this case, it is clear that it has influenced the faradic efficiency value since the i_{disk} in faradic efficiency ($\varepsilon = 4/n_{ORR})\cdot i_{ring}/(N\cdot i_{disk}$) has slightly increased. Henceforth, the 95 % Faradaic efficiency, which was attained at the beginning of the chronoamperometry measurement at 1.51 V (vs. RHE), is determined as the faradaic efficiency of the CoFe@PN-CF electrocatalyst, which is ascribed to the water oxidation rather than other side reactions.

EIS measurements were carried out to explore the interfacial properties of the as-prepared electrocatalysts. EIS is a non-destructive technique that enables to characterize of the state of a system in terms of three main electrical parameters: resistance, capacitance, and inductance [66]. Using these parameters, the state of the electronic conductivity and charge transfer process of the sample can be scrutinized. The EIS of the different electrocatalysts is measured and compared, as shown in Fig. 9 (Nyquist plot). All the samples share a semi-circle or an arc at a high frequency. The two most important parameters can be extracted from the plot: the total series resistance (R_s) and the charge transfer resistance (R_{ct}). The R_s is a sum of the resistance of the solution, active materials, and ohmic resistance, which can be extracted from the real axis intercept. The R_{ct}, which defines the oxidation kinetics of OH^- anions at the catalytic surface, can be obtained from the diameter of the semi-circle [38]. The value of the R_s for all samples is similar, with a slight difference. The major difference appears in the R_{ct}. The R_{ct} values

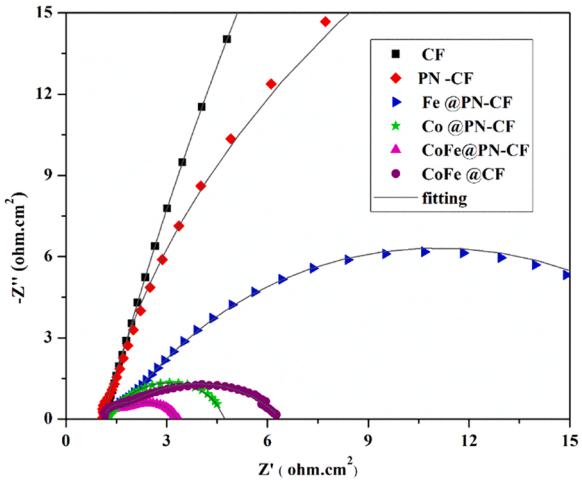

Fig. 9. EIS measurement measured at 1.6 V vs. RHE in 1 M KOH presented in Nyquist plot.

for the CF, PN-CF, Fe@PN-CF, Co@PN-CF, CoFe@PN-CF, and CoFe@CF samples are fitted to be 78.4, 67.6, 20.7, 3.6, 2.2 and 5.3 Ω.cm^2, respectively. Considering these results, among the samples, the lowest R_{ct} of CoFe@PN-CF (2.2 Ω.cm^2) catalyst further unveils the faster and more prominent OER activity. It reveals that the CoFe@PN-CF sample has an efficient electron transfer process which may be originated from the merit of the synergy between the graphitized carbon foam and bimetallic active sites.

Besides the electrocatalytic activity, stability is another key criterion for developing promising electrocatalysts for practical applications. Chronopotentiometry (*E-t* plot) measurement was carried out to assess the stability of the best-performing catalyst (CoFe@PN-CF) and the reference IrO_2 catalyst at a 10 mAcm^{-2} current density. The CoFe@PN-CF electrode presents a smooth potential increase after continuous operation for 20 h. As shown in Fig. 10a, the η_{10} of the CoFe@PN-CF catalyst elevates from 320 mV to 334 mV, which accounts for a 14 mV increase after 20 h OER measurements. In contrast, the IrO_2-based electrode shows severe activity deterioration or a substantial rise in potential after 6 h of continuous operation. These results reveal that the CoFe@PN-CF electrocatalyst retains an excellent performance and robust durability, opening a new avenue for the valorization of petroleum pitch for preparing treasured carbon support. To examine and compare the activity of the CoFe@PN-CF catalyst before and after stability measurements, we have also measured the OER polarization curve. As shown in Fig. 10b, only a slight shift towards a higher overpotential was observed, indicating that the CoFe@PN-CF has not only virtuous OER activity but also offers tremendous electrochemical durability. The superb electrocatalytic performance and durability of the CoFe@PN-CF catalyst may arise from the well-intertwined interface structure and synergetic effect of the active metals of Co, Fe, and P, N co-doped graphitized carbon foam.

The best-performing electrocatalyst was compared with similar materials recently reported in the literature. As shown in Table 4, the CoFe@PN-CF-based electrocatalyst outperformed most of the reported works; in particular, appealing OER activity and high stability are observed. Moreover, the carbon foam support used in this work was synthesized from the industrial waste material of petroleum pitch; as a result, the valorization of petroleum pitch-derived carbon foam offers a viable method for synthesizing cost-effective and active catalysts for water electrolysis. Because of its superior electrocatalytic performance, and low-cost raw material precursors, the CoFe@PN-CF catalyst has the potential to be utilized for the evolution of oxygen electrodes during the electrochemical process of water electrolysis.

Where; N-CNF: N-doped carbon nanofibers; CFP: carbon fiber paper; NPC: Nitrogen-enriched porous carbon; MWCNT: Multiwall carbon nanotube; NC: Nitrogen-doped carbon; GC: glassy carbon; NF: nickel foam; CP: Carbon paper; N-HCS: N-doped hollow carbon microspheres; and NCNFs: N-doped carbon nanoflowers.

For better elucidation of the physicochemical properties of the CoFe@ PN-CF catalyst after stability, the spent catalyst was recovered, and its microstructure was analyzed by TEM. As shown in Fig. 11, the original sample (Fig. 11a) shows a feathered-like structure with ultra-small particles immobilized in the carbon matrix. An ultrathin layer made up of Co/Fe covered the carbon substrate. The same phenomenon has been observed in the spent sample of CoFe@PN-CF (Fig. 11b), suggesting a robust morphology. Moreover, in both samples, no evident lattice fringes are observed, which confirms the low-crystalline nature of the sample again, as XRD elucidated it. (Fig. 3).

The outstanding electrocatalytic performance of CoFe@PN-CF electrocatalyst can be attributed to: i) the porous architecture of the carbon foam as a substrate, which can endow ample pores and rough surface to immobilize the active metals with an intertwined interface, meritoriously boosting the conductivity; ii) the bimetals coordinated with the P, N co-doped carbon foam can formulate a peculiar electronic environment with satisfactory active site distribution density and galvanize the inherent catalytic activity based on the coupling effect; iii) the open porous architecture of the carbon foam substrate immobilized with the active metal can expedite the infiltration of the electrolyte, promoting intimate contact and thus ensuring favorable catalytic kinetics at the

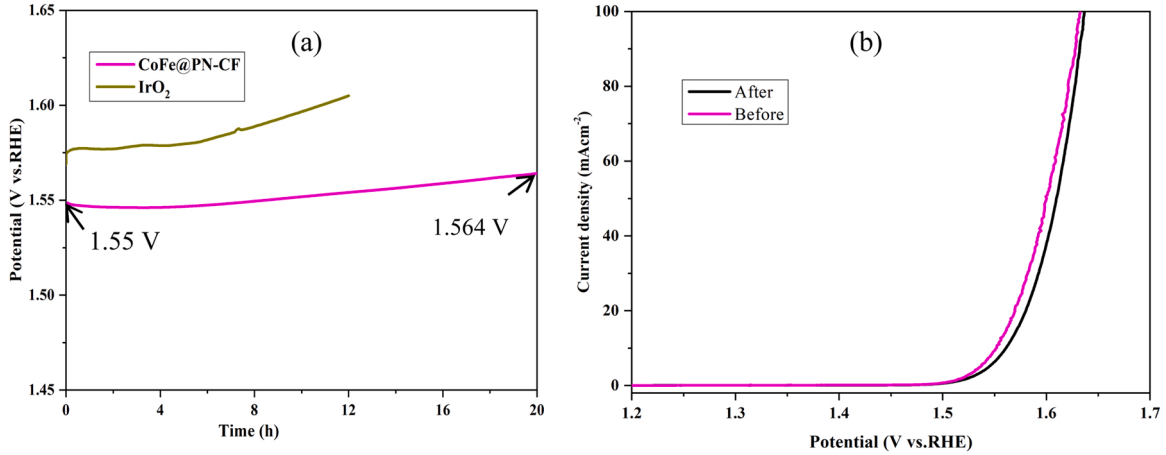

Fig. 10. Stability measurements: (a) Chronopotentiometry curve of CoFe@PN-CF and IrO_2 at a j = 10 mAcm^{-2}, and (b) OER polarization curve of CoFe@PN-CF catalyst before and after stability measurements.

Table 4
Comparison of OER electrocatalytic activity of CoFe/carbon-based catalysts reported in the literature. The η_{10} (mV) refers to the overpotential required to produce a current density of 10 mA cm^{-2}.

Electrocatalyst	Substrate	η_{10} (mV)	Tafel slope (mV dec^{-1})	Achieved stability	Ref.
CoFe@PN-CF	GC	320	48	Showed stable potential for 20 h during continued operation	This work
$CoFe_2O_4$ @N-CNFs	GC	349	80	Around 7.3 % decrease of current density after 40000 s operation	[67]
$Co_3Fe_7O_x$/NPC	GC	328	31.4	The potential at a $J = 10$ mA cm^{-2} remained stable for about 15 h	[68]
$FeCo_2$ P polyhedron	CFP	320	55	About 10 % drop of the initial current density after a 12 h continuous test.	[69]
FeCo-N/C	GC	370	52	Experienced 24 % of anodic current attenuation during 30,000 s continued operation.	[70]
CoFe/N-HCS	NF	292	58	Retained a high relative current of 84.3 % after 30 h operation.	[71]
Co_3O_{4-x} carbon@$Fe_{2-y}Co_yO$	GC	350	37.6	After 6000 cycles, a slight curve shift of about 20 mV at j = 50 mA cm^{-2} was observed.	[72]
CoFe@NC-700	GC	380	110	After 1000 s operation at 1.60 V, a 7 % current density decay was observed.	[73]
CoFe-$CoFe_2O_4$/N-CNTs	GC	334	80	After 1000 cycles, a 12 mV overpotential increase was recorded.	[74]
$CoFe_2O_4$/graphene	GCE	300	68	About 83 % relative current was obtained after 30,000 s testing.	[75]
CoFe-MWCNTs	NF	300	84	Exhibited stable potential for about 3 h, and after 1000 cycles, a 10 mV potential shift was observed.	[76]
$Co_{5.47}N/Co_3Fe_7$/NC	GC	380	62.68	After 4000 CV cycles, 10 mV of a potential shift was recorded.	[77]
Fe_3N @ Co_4N @ CoFe	NF	225	48	Showed stable potential for about 20 h.	[78]

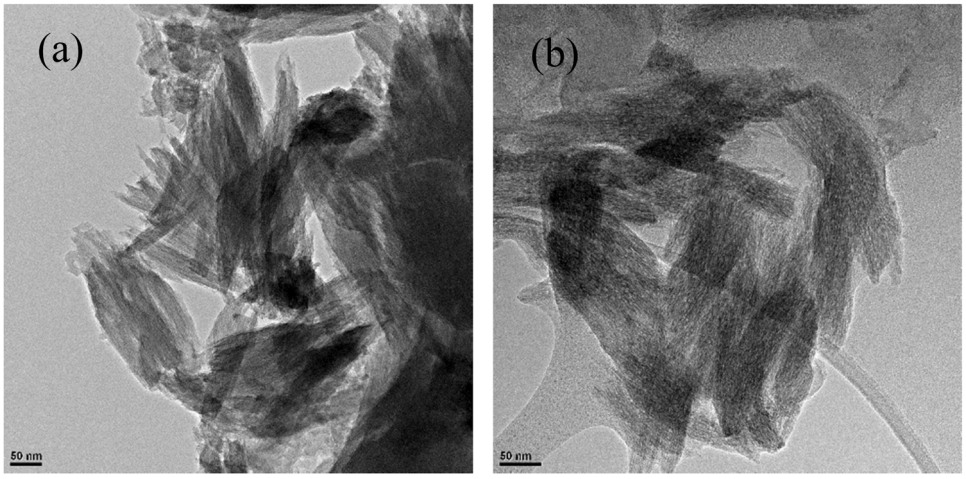

Fig. 11. TEM image of CoFe@PN-CF electrocatalysts (a) before and (b) after stability test.

electrolyte/electrode interface. In virtue of encouraging activity and durability of the CoFe@PN-CF electrocatalyst, alkaline water electrolysis using CoFe@ PN-CF as OER anodic electrode can be used for prospective renewable hydrogen production.

4. Conclusions

In summary, an effective route for valorizing petroleum pitch residues towards OER electrocatalyst is demonstrated. We have successfully synthesized CoFe-impregnated heteroatom (P, N) co-doped carbon foam derived from petroleum pitch. First, (P, N) co-doped carbon foam support was prepared through thermo-chemical treatment; then, the impregnation of Co and Fe metals into the as-prepared (P, N) co-doped carbon foam followed by carbonization was employed. This approach provides the merit of using petroleum pitch waste material to synthesize carbon foam support with a highly porous and defect-enriched structure upon incorporating P, N heteroatoms, in which electroactive metals can be immobilized in the carbon matrix. The as-prepared CoFe@PN-CF electrocatalyst shows excellent electrocatalytic activity, faster reaction kinetics, and a durable catalyst under OER measurements due to the excellent interaction between the PN-CF and the evolved Co_2P and iron carbide phases. Specifically, the as-synthesized CoFe@PN-CF catalyst requires a low overpotential of 320 mV to generate 10 $mAcm^{-2}$ current density, low Tafel slope of 48 $mV{\cdot}dec^{-1}$, relatively low charge transfer resistance, and high electrochemically active surface area. Most importantly, it remained stable for at least 20 h during continuous operation using a 1 M KOH aqueous solution, demonstrating its potential to be employed for large-scale water electrocatalysis. This research work offers a facile approach for fabricating low-cost alternative materials with high electroactivity and stability for enthralling water electrolysis toward green and clean H_2 production.

CRediT authorship contribution statement

Gebrehiwet Abrham Gebreslase performed data curation, writing – original draft preparation. David Sebastián performed supervision and writing-review and editing. María Victoria Martínez-Huerta performed conceptualization, supervision, writing-review and editing. María Jesús Lázaro project administration, funding acquisition.

Declaration of Competing Interest

The authors declare that they have no known competing financial interests or personal relationships that could have appeared to influence the work reported in this paper.

Data availability

No data was used for the research described in the article.

Acknowledgments

Financial support from the European Union's Horizon 2020 Research and Innovation programme under the Marie Skłodowska-Curie Actions–Innovative Training Networks (MSCA-ITN) Grant Agreement 813748 are gratefully acknowledged. Authors also acknowledge the use of instrumentation as well as the technical advice provided by the National Facility ELECMI ICTS, node "Laboratorio de Microscopias Avanzadas" at Universidad de Zaragoza.

Appendix A. Supporting information

Supplementary data associated with this article can be found in the online version at doi:10.1016/j.cattod.2022.12.022.

References

[1] P. Saravanan, M.R. Khan, C.S. Yee, D.V.N. Vo, An overview of water electrolysis technologies for the production of hydrogen, N. Dimens. Prod. Util. Hydrog. 8 (2020) 161–190, https://doi.org/10.1016/B978-0-12-819553-6.00007-6.

[2] B. Panigrahy, K. Narayan, B. Ramachandra Rao, Green hydrogen production by water electrolysis: a renewable energy perspective, Mater. Today Proc. 67 (2022) 1310–1314, https://doi.org/10.1016/j.matpr.2022.09.254.

[3] C. Yilmaz, M. Kanoglu, Thermodynamic evaluation of geothermal energy powered hydrogen production by PEM water electrolysis, Energy 69 (2014) 592–602, https://doi.org/10.1016/j.energy.2014.03.054.

[4] Y. Shi, X. Feng, H. Guan, J. Zhang, Z. Hu, Porous sunflower plate-like NiFe2O4/CoNi–S heterostructure as efficient electrocatalyst for overall water splitting, Int. J. Hydrog. Energy 46 (2021) 8557–8566, https://doi.org/10.1016/j.ijhydene.2020.12.062.

[5] N.T. Suen, S.F. Hung, Q. Quan, N. Zhang, Y.J. Xu, H.M. Chen, Electrocatalysis for the oxygen evolution reaction: recent development and future perspectives, Chem. Soc. Rev. 46 (2017) 337–365, https://doi.org/10.1039/c6cs00328a.

[6] G.A. Gebreslase, D. Sebastián, M.V. Martínez-Huerta, M.J. Lázaro, Nitrogen-doped carbon decorated-Ni3Fe@Fe3O4 electrocatalyst with enhanced oxygen evolution reaction performance, J. Electroanal. Chem. 925 (2022), 116887, https://doi.org/10.1016/j.jelechem.2022.116887.

[7] Y.P. Zhu, Y.P. Liu, T.Z. Ren, Z.Y. Yuan, Self-supported cobalt phosphide mesoporous nanorod arrays: a flexible and bifunctional electrode for highly active electrocatalytic water reduction and oxidation, Adv. Funct. Mater. 25 (2015) 7337–7347, https://doi.org/10.1002/adfm.201503666.

[8] Q. Ye, J. Li, X. Liu, X. Xu, F. Wang, B. Li, Surface pattern of Ni–Co hydroxide nanoplate arrays electrocatalysts for the oxygen evolution reaction, J. Power Sources 412 (2019) 10–17, https://doi.org/10.1016/j.jpowsour.2018.10.075.

[9] T. Gao, Z. Jin, Y. Zhang, G. Tan, H. Yuan, D. Xiao, Coupling cobalt-iron bimetallic nitrides and N-doped multi-walled carbon nanotubes as high-performance bifunctional catalysts for oxygen evolution and reduction reaction, Electrochim. Acta 258 (2017) 51–60, https://doi.org/10.1016/j.electacta.2017.07.172.

[10] J. Jiang, C. Yan, X. Zhao, H. Luo, Z. Xue, T. Mu, A. PEGylated, deep eutectic solvent for controllable solvothermal synthesis of porous NiCo2S4 for efficient oxygen evolution reaction, Green. Chem. 19 (2017) 3023–3031, https://doi.org/10.1039/c7gc01012e.

[11] J. Jiang, Q. Liu, C. Zeng, L. Ai, Cobalt/molybdenum carbide@N-doped carbon as a bifunctional electrocatalyst for hydrogen and oxygen evolution reactions, J. Mater. Chem. A 5 (2017) 16929–16935, https://doi.org/10.1039/C7TA04893A.

[12] C. Yu, Z. Liu, X. Han, H. Huang, C. Zhao, J. Yang, J. Qiu, NiCo-layered double hydroxides vertically assembled on carbon fiber papers as binder-free high-active electrocatalysts for water oxidation, Carbon N. Y. 110 (2016) 1–7, https://doi.org/10.1016/j.carbon.2016.08.020.

[13] Y. Li, B. Jia, Y. Fan, K. Zhu, G. Li, C.Y. Su, Bimetallic zeolitic imidazolite framework derived carbon nanotubes embedded with Co nanoparticles for efficient bifunctional oxygen electrocatalyst, Adv. Energy Mater. 8 (2018) 1–9, https://doi.org/10.1002/aenm.201702048.

[14] A.B. Jorge, R. Jervis, A.P. Periasamy, M. Qiao, J. Feng, L.N. Tran, M.M. Titirici, 3D carbon materials for efficient oxygen and hydrogen electrocatalysis, Adv. Energy Mater. 10 (2020), https://doi.org/10.1002/aenm.201902494.

[15] J. Zhang, Z. Zhao, Z. Xia, L. Dai, A metal-free bifunctional electrocatalyst for oxygen reduction and oxygen evolution reactions, Nat. Nanotechnol. 10 (2015) 444–452, https://doi.org/10.1038/nnano.2015.48.

[16] J. Lai, A. Nsabimana, R. Luque, G. Xu, 3D porous carbonaceous electrodes for electrocatalytic applications, Joule 2 (2018) 76–93, https://doi.org/10.1016/j.joule.2017.10.005.

[17] E. Mirzakulova, R. Khatmullin, J. Walpita, T. Corrigan, N.M. Vargas-Barbosa, S. Vyas, S. Oottikkal, S.F. Manzer, C.M. Hadad, K.D. Glusac, Electrode-assisted catalytic water oxidation by a flavin derivative, Nat. Chem. 4 (2012) 794–801, https://doi.org/10.1038/nchem.1439.

[18] C. Alegre, D. Sebastián, M.J. Lázaro, Carbon xerogels electrochemical oxidation and correlation with their physico-chemical properties, Carbon N. Y 144 (2019) 382–394.

[19] S. Pérez-Rodríguez, D. Sebastián, M.J. Lázaro, Electrochemical oxidation of ordered mesoporous carbons and the influence of graphitization, Electrochim. Acta 303 (2019) 167–175, https://doi.org/10.1016/j.electacta.2019.02.065.

[20] X. Lu, W.L. Yim, B.H.R. Suryanto, C. Zhao, Electrocatalytic oxygen evolution at surface-oxidized multiwall carbon nanotubes, J. Am. Chem. Soc. 137 (2015) 2901–2907, https://doi.org/10.1021/ja509879r.

[21] D.T. Tran, H.T. Le, V.H. Hoa, N.H. Kim, J.H. Lee, Dual-coupling ultrasmall iron-Ni2P into P-doped porous carbon sheets assembled CuxS nanobrush arrays for overall water splitting, Nano Energy 84 (2021), 105861, https://doi.org/10.1016/j.nanoen.2021.105861.

[22] Y. Zheng, Y. Jiao, S.Z. Qiao, Engineering of carbon-based electrocatalysts for emerging energy conversion: from fundamentality to functionality, Adv. Mater. 27 (2015) 5372–5378, https://doi.org/10.1002/adma.201500821.

[23] J. Liu, G. Ning, K. Shi, M. Zheng, Y. Sun, Y. Gao, Y. Zhang, H. Wang, N-doped hollow porous carbon spheres@Co Cu Fe alloy nanospheres as novel non-precious metal electrocatalysts for HER and OER, Int. J. Hydrog. Energy 47 (2022) 5947–5960, https://doi.org/10.1016/j.ijhydene.2021.11.204.

[24] Y. Wang, R. Dong, P. Tan, H. Liu, H. Liao, M. Jiang, Y. Liu, L. Yang, J. Pan, Investigating the active sites in molybdenum anchored nitrogen-doped carbon for alkaline oxygen evolution reaction, J. Colloid Interface Sci. 609 (2022) 617–626, https://doi.org/10.1016/j.jcis.2021.11.058.

[25] E. Vijayakumar, S. Ramakrishnan, C. Sathiskumar, D.J. Yoo, J. Balamurugan, H. S. Noh, D. Kwon, Y.H. Kim, H. Lee, MOF-derived CoP-nitrogen-doped carbon@NiFeP nanoflakes as an efficient and durable electrocatalyst with multiple catalytically active sites for OER, HER, ORR and rechargeable zinc-air batteries, Chem. Eng. J. 428 (2022), 131115, https://doi.org/10.1016/j.cej.2021.131115.

[26] X. Zheng, J. Wu, X. Cao, J. Abbott, C. Jin, H. Wang, P. Strasser, R. Yang, X. Chen, G. Wu, N-, P-, and S-doped graphene-like carbon catalysts derived from onium salts with enhanced oxygen chemisorption for Zn-air battery cathodes, Appl. Catal. B Environ. 241 (2019) 442–451, https://doi.org/10.1016/j.apcatb.2018.09.054.

[27] C. Zhang, N. Mahmood, H. Yin, F. Liu, Y. Hou, Synthesis of phosphorus-doped graphene and its multifunctional applications for oxygen reduction reaction and lithium ion batteries, Adv. Mater. 25 (2013) 4932–4937, https://doi.org/10.1002/adma.201301870.

[28] C. Yang, T. He, W. Zhou, R. Deng, Q. Zhang, Iron-Tuned 3D cobalt-phosphate catalysts for efficient hydrogen and oxygen evolution reactions over a wide pH range, ACS Sustain. Chem. Eng. 8 (2020) 13793–13804, https://doi.org/10.1021/acssuschemeng.0c04966.

[29] H.W. Choi, D.I. Jeong, S. Bin Kwon, S. Woo, J. Kim, J.H. Kim, W.S. Yang, B. Lim, B. K. Kang, D.H. Yoon, Nickel-Iron nitrides and alloy heterojunction with amorphous N-doped carbon Shell: High-efficiency synergistic electrocatalysts for oxygen evolution reaction, Appl. Surf. Sci. 566 (2021), 150706, https://doi.org/10.1016/j.apsusc.2021.150706.

[30] Z. Peng, H. Wang, X. Xia, X. Zhang, Z. Dong, Integration of CoFe Alloys and Fe/Fe3C nanoparticles into n-doped carbon nanosheets as dual catalytic active sites to promote the oxygen electrocatalysis of Zn-air batteries, ACS Sustain. Chem. Eng. 8 (2020) 9009–9016, https://doi.org/10.1021/acssuschemeng.0c01729.

[31] G. Abrham Gebreslase, M. Victoria Martínez-Huerta, D. Sebastián, M. Jesús Lázaro, Transformation of CoFe2O4 spinel structure into active and robust CoFe alloy/N-doped carbon electrocatalyst for oxygen evolution reaction, J. Colloid Interface Sci. (2022), https://doi.org/10.1016/j.jcis.2022.06.005.

[32] P. Chen, J.N. Metz, A.S. Mennito, S. Merchant, S.E. Smith, M. Siskin, S.P. Rucker, D.C. Dankworth, J.D. Kushnerick, N. Yao, Y. Zhang, Petroleum pitch: Exploring a 50-year structure puzzle with real-space molecular imaging, Carbon N. Y 161 (2020) 456–465, https://doi.org/10.1016/j.carbon.2020.01.062.

[33] C. Chen, E.B. Kennel, A.H. Stiller, P.G. Stansberry, J.W. Zondlo, Carbon foam derived from various precursors, Carbon N. Y. 44 (2006) 1535–1543, https://doi.org/10.1016/j.carbon.2005.12.021.

[34] M. Inagaki, J. Qiu, Q. Guo, Carbon foam: preparation and application, Carbon N. Y. 87 (2015) 128–152, https://doi.org/10.1016/j.carbon.2015.02.021.

[35] F. Dong, C. Liu, M. Wu, J. Guo, K. Li, J. Qiao, Hierarchical porous carbon derived from coal tar pitch containing discrete Co-Nx-C active sites for efficient oxygen electrocatalysis and rechargeable Zn-air batteries, ACS Sustain. Chem. Eng. 7 (2019) 8587–8596, https://doi.org/10.1021/acssuschemeng.9b00373.

[36] Y. Liu, Y. Hu, P. Ma, F. Li, F. Yuan, S. Wang, Y. Luo, J. Ma, Amorphous CoFe double hydroxides decorated with N-doped cnts for efficient electrochemical oxygen evolution, ChemSusChem 12 (2019) 2679–2688, https://doi.org/10.1002/cssc.201900754.

[37] G.A. Gebreslase, M.V. Martínez-Huerta, M.J. Lázaro, Recent progress on bimetallic NiCo and CoFe based electrocatalysts for alkaline oxygen evolution reaction: a review, J. Energy Chem. 67 (2022) 101–137, https://doi.org/10.1016/j.jechem.2021.10.009.

[38] J. Chang, S. Zang, J. Li, D. Wu, Z. Lian, F. Xu, K. Jiang, Z. Gao, Nitrogen-doped porous carbon encapsulated nickel iron alloy nanoparticles, one-step conversion synthesis for application as bifunctional catalyst for water electrolysis, Electrochim. Acta 389 (2021), https://doi.org/10.1016/j.electacta.2021.138785.

[39] B. Tsyntsarski, B. Petrova, T. Budinova, N. Petrov, M. Krzesinska, S. Pusz, J. Majewska, P. Tzvetkov, Carbon foam derived from pitches modified with mineral acids by a low pressure foaming process, Carbon N. Y. 48 (2010) 3523–3530, https://doi.org/10.1016/j.carbon.2010.05.048.

[40] W. Guo, C. Geng, Z. Sun, J. Jiang, Z. Ju, Microstructure-controlled amorphous carbon anode via pre-oxidation engineering for superior potassium-ion storage,

J. Colloid Interface Sci. 623 (2022) 1075–1084, https://doi.org/10.1016/j.jcis.2022.05.073.
[41] M. Hara, T. Yoshida, A. Takagaki, T. Takata, J.N. Kondo, S. Hayashi, K. Domen, A carbon material as a strong protonic acid, Angew. Chem. - Int. Ed. 43 (2004) 2955–2958, https://doi.org/10.1002/anie.200453947.
[42] L. Wang, B. Wen, H. Yang, Y. Qiu, N. He, Hierarchical nest-like structure of Co/Fe MOF derived CoFe@C composite as wide-bandwidth microwave absorber, Compos. Part A Appl. Sci. Manuf. 135 (2020), 105958, https://doi.org/10.1016/j.compositesa.2020.105958.
[43] D. Torres, J.L. Pinilla, R. Moliner, I. Suelves, On the oxidation degree of few-layer graphene oxide sheets obtained from chemically oxidized multiwall carbon nanotubes, Carbon N. Y. 81 (2015) 405–417, https://doi.org/10.1016/j.carbon.2014.09.073.
[44] Å. Björkman, Thermische Klärschlammbehandlung, Schweiz. Z. Für Hydrol. 31 (1969) 632–645, https://doi.org/10.1007/BF02543692.
[45] F. Te Tsai, H.C. Wang, C.H. Ke, W.F. Liaw, FeCo/FeCoPxOy(OH)z as bifunctional electrodeposited-film electrodes for overall water splitting, ACS Appl. Energy Mater. 1 (2018) 5298–5307, https://doi.org/10.1021/acsaem.8b00922.
[46] H.J. Niu, S.S. Chen, J.J. Feng, L. Zhang, A.J. Wang, Assembled hollow spheres with CoFe alloyed nanocrystals encapsulated in N, P-doped carbon nanovesicles: an ultra-stable bifunctional oxygen catalyst for rechargeable Zn-air battery, J. Power Sources 475 (2020), 228594, https://doi.org/10.1016/j.jpowsour.2020.228594.
[47] H.J. Niu, L. Zhang, J.J. Feng, Q.L. Zhang, H. Huang, A.J. Wang, Graphene-encapsulated cobalt nanoparticles embedded in porous nitrogen-doped graphitic carbon nanosheets as efficient electrocatalysts for oxygen reduction reaction, J. Colloid Interface Sci. 552 (2019) 744–751, https://doi.org/10.1016/j.jcis.2019.05.099.
[48] J. He, Z. Hu, J. Zhao, P. Liu, X. Lv, W. Tian, C. Wang, S. Tan, J. Ji, Ni-decorated Fe-/N- co-doped carbon anchored on porous cobalt oxide nanowires arrays for efficient electrocatalytic oxygen evolution, Chem. Eng. Sci. 243 (2021), 116774, https://doi.org/10.1016/j.ces.2021.116774.
[49] B. Peng, Y. Xu, K. Liu, X. Wang, F.M. Mulder, High-performance and low-cost sodium-ion anode based on a facile black phosphorus−carbon nanocomposite, ChemElectroChem 4 (2017) 2140–2144, https://doi.org/10.1002/celc.201700345.
[50] H.J. Niu, S.S. Chen, J.J. Feng, L. Zhang, A.J. Wang, Assembled hollow spheres with CoFe alloyed nanocrystals encapsulated in N, P-doped carbon nanovesicles: an ultra-stable bifunctional oxygen catalyst for rechargeable Zn-air battery, J. Power Sources 475 (2020), 228594, https://doi.org/10.1016/j.jpowsour.2020.228594.
[51] Y. Zhang, X. Gao, L. Lv, J. Xu, H. Lin, Y. Ding, C. Wang, Tailoring π-symmetry electrons in cobalt–iron phosphide for highly efficient oxygen evolution, Electrochim. Acta 341 (2020), 136029, https://doi.org/10.1016/j.electacta.2020.136029.
[52] T.V.M. Sreekanth, G.R. Dillip, P.C. Nagajyothi, K. Yoo, J. Kim, Integration of Marigold 3D flower-like Ni-MOF self-assembled on MWCNTs via microwave irradiation for high-performance electrocatalytic alcohol oxidation and oxygen evolution reactions, Appl. Catal. B Environ. 285 (2021), 119793, https://doi.org/10.1016/j.apcatb.2020.119793.
[53] D. Voiry, M. Chhowalla, Y. Gogotsi, N.A. Kotov, Y. Li, R.M. Penner, R.E. Schaak, P. S. Weiss, Best practices for reporting electrocatalytic performance of nanomaterials, ACS Nano 12 (2018) 9635–9638, https://doi.org/10.1021/acsnano.8b07700.
[54] X. Huang, L. Gong, H. Xu, J. Qin, P. Ma, M. Yang, K. Wang, L. Ma, X. Mu, R. Li, Hierarchical iron-doped CoP heterostructures self-assembled on copper foam as a bifunctional electrocatalyst for efficient overall water splitting, J. Colloid Interface Sci. 569 (2020) 140–149, https://doi.org/10.1016/j.jcis.2020.02.073.
[55] Y. Dang, P. Han, Y. Li, Y. Zhang, Y. Zhou, Low-crystalline mixed Fe-Co-MOFs for efficient oxygen evolution electrocatalysis, J. Mater. Sci. 55 (2020) 13951–13963, https://doi.org/10.1007/s10853-020-05026-2.
[56] M. Liu, L. Kong, X. Wang, J. He, X.H. Bu, Engineering bimetal synergistic electrocatalysts based on metal–organic frameworks for efficient oxygen evolution, Small 15 (2019), https://doi.org/10.1002/smll.201903410.
[57] A. Minguzzi, M.A. Alpuche-Aviles, J.R. López, S. Rondinini, A.J. Bard, Screening of oxygen evolution electrocatalysts by scanning electrochemical microscopy using a shielded tip approach, Anal. Chem. 80 (2008) 4055–4064, https://doi.org/10.1021/ac8001287.
[58] C. Xiao, Y. Li, X. Lu, C. Zhao, Bifunctional porous NiFe/NiCo2O4/Ni foam electrodes with triple hierarchy and double synergies for efficient whole cell water splitting, Adv. Funct. Mater. 26 (2016) 3515–3523, https://doi.org/10.1002/adfm.201505302.
[59] W. Liu, H. Liu, L. Dang, H. Zhang, X. Wu, B. Yang, Z. Li, X. Zhang, L. Lei, S. Jin, Amorphous cobalt–iron hydroxide nanosheet electrocatalyst for efficient electrochemical and photo-electrochemical oxygen evolution, Adv. Funct. Mater. 27 (2017), https://doi.org/10.1002/adfm.201603904.
[60] D. Senthil Raja, C.L. Huang, Y.A. Chen, Y.M. Choi, S.Y. Lu, Composition-balanced trimetallic MOFs as ultra-efficient electrocatalysts for oxygen evolution reaction at high current densities, Appl. Catal. B Environ. 279 (2020), 119375, https://doi.org/10.1016/j.apcatb.2020.119375.
[61] H. Baltruschat, Differential electrochemical mass spectrometry, J. Am. Soc. Mass Spectrom. 15 (2004) 1693–1706, https://doi.org/10.1016/j.jasms.2004.09.011.
[62] I.S. Filimonenkov, S.Y. Istomin, E.V. Antipov, G.A. Tsirlina, E.R. Savinova, Rotating ring-disk electrode as a quantitative tool for the investigation of the oxygen evolution reaction, Electrochim. Acta 286 (2018) 304–312, https://doi.org/10.1016/j.electacta.2018.08.056.
[63] I.S. Filimonenkov, C. Bouillet, G. Kéranguéven, P.A. Simonov, G.A. Tsirlina, E. R. Savinova, Carbon materials as additives to the OER catalysts: RRDE study of carbon corrosion at high anodic potentials, Electrochim. Acta 321 (2019), https://doi.org/10.1016/j.electacta.2019.134657.
[64] C.C.L. McCrory, S. Jung, J.C. Peters, T.F. Jaramillo, Benchmarking heterogeneous electrocatalysts for the oxygen evolution reaction, J. Am. Chem. Soc. 135 (2013) 16977–16987, https://doi.org/10.1021/ja407115p.
[65] A.T. Swesi, J. Masud, M. Nath, Nickel selenide as a high-efficiency catalyst for oxygen evolution reaction, Energy Environ. Sci. 9 (2016) 1771–1782, https://doi.org/10.1039/c5ee02463c.
[66] M.K. Cho, H.Y. Park, H.J. Lee, H.J. Kim, A. Lim, D. Henkensmeier, S.J. Yoo, J. Y. Kim, S.Y. Lee, H.S. Park, J.H. Jang, Alkaline anion exchange membrane water electrolysis: Effects of electrolyte feed method and electrode binder content, J. Power Sources 382 (2018) 22–29, https://doi.org/10.1016/j.jpowsour.2018.02.025.
[67] T. Li, Y. Lv, J. Su, Y. Wang, Q. Yang, Y. Zhang, J. Zhou, L. Xu, D. Sun, Y. Tang, Anchoring CoFe2O4 nanoparticles on N-doped carbon nanofibers for high-performance oxygen evolution reaction, Adv. Sci. 4 (2017), https://doi.org/10.1002/advs.201700226.
[68] X. Lin, X. Li, F. Li, Y. Fang, M. Tian, X. An, Y. Fu, J. Jin, J. Ma, Precious-metal-free Co-Fe-O: X coupled nitrogen-enriched porous carbon nanosheets derived from Schiff-base porous polymers as superior electrocatalysts for the oxygen evolution reaction, J. Mater. Chem. A 4 (2016) 6505–6512, https://doi.org/10.1039/c5ta10039a.
[69] J. Wang, J. Wang, M. Zhang, S. Li, R. Liu, Z. Li, Metal-organic frameworks-derived hollow-structured iron-cobalt bimetallic phosphide electrocatalysts for efficient oxygen evolution reaction, J. Alloy. Compd. 821 (2020), 153463, https://doi.org/10.1016/j.jallcom.2019.153463.
[70] H. Shui, T. Jin, J. Hu, H. Liu, In situ incorporation strategy for bimetallic FeCo-doped carbon as highly efficient bifunctional oxygen electrocatalysts, ChemElectroChem 5 (2018) 1401–1406, https://doi.org/10.1002/celc.201800013.
[71] J. Li, Y. Kang, W. Wei, X. Li, Z. Lei, P. Liu, Well-dispersed ultrafine CoFe nanoalloy decorated N-doped hollow carbon microspheres for rechargeable/flexible Zn-air batteries, Chem. Eng. J. 407 (2021), 127961, https://doi.org/10.1016/j.cej.2020.127961.
[72] W. Xu, W. Xie, Y. Wang, Co3O4-x-carbon@Fe2-yCoyO3 heterostructural hollow polyhedrons for the oxygen evolution reaction, ACS Appl. Mater. Interfaces 9 (2017) 28642–28649, https://doi.org/10.1021/acsami.7b09213.
[73] Y. Wang, T. Hu, Y. Qiao, Y. Chen, Synergistic engineering of defects and architecture in CoFe@NC toward highly efficient oxygen electrode reactions, Int. J. Hydrog. Energy 45 (2020) 8686–8694, https://doi.org/10.1016/j.ijhydene.2020.01.135.
[74] D. Xu, B. Liu, G. Liu, K. Su, C. Yang, H. Tong, D. Qian, J. Li, N-doped bamboo-like CNTs combined with CoFe–CoFe2O4 as a highly efficient electrocatalyst towards oxygen evolution, Int. J. Hydrog. Energy 45 (2020) 6629–6635, https://doi.org/10.1016/j.ijhydene.2019.12.180.
[75] Y. Ma, H. Zhang, J. Xia, Z. Pan, X. Wang, G. Zhu, B. Zheng, G. Liu, L. Lang, Reduced CoFe2O4/graphene composite with rich oxygen vacancies as a high efficient electrocatalyst for oxygen evolution reaction, Int. J. Hydrog. Energy 45 (2020) 11052–11061, https://doi.org/10.1016/j.ijhydene.2020.02.045.
[76] Z. Ali, M. Mehmood, J. Ahmed, A. Majeed, K.H. Thebo, CVD grown defect rich-MWCNTs with anchored CoFe alloy nanoparticles for OER activity, Mater. Lett. 259 (2020), 126831, https://doi.org/10.1016/j.matlet.2019.126831.
[77] L. Li, J. Chen, S. Wang, Y. Huang, D. Cao, MOF-derived CoN/CoFe/NC bifunctional electrocatalysts for zinc-air batteries, Appl. Surf. Sci. 582 (2022), 152375, https://doi.org/10.1016/j.apsusc.2021.152375.
[78] Z. Cui, X. Liang, P. Wang, P. Zhou, Q. Zhang, Z. Wang, Z. Zheng, Y. Liu, Y. Dai, B. Huang, In situ integration of Fe3N@Co4N@CoFe alloy nanoparticles as efficient and stable electrocatalyst for overall water splitting, Electrochim. Acta 395 (2021), 139218, https://doi.org/10.1016/j.electacta.2021.139218.

Supporting information

for

CoFe-loaded P, N co-doped carbon foam derived from petroleum pitch waste: an efficient electrocatalyst for oxygen evolution reaction

Gebrehiwet Abrham Gebreslase[a], David Sebastián[a], María Victoria Martínez-Huerta[b], Tanya Tsoncheva[c], B. Tsyntsarski[c], G. Georgiev[c], María Jesús Lázaro[a]

[a] Instituto de Carboquímica, CSIC. Miguel Luesma Castán 4, 50018, Zaragoza, Spain.

[b] Instituto de Catálisis y Petroleoquímica, CSIC. Marie Curie 2, 28049, Madrid, Spain.

[C] Institute of Organic Chemistry with Centre of Phytochemistry, Bulgarian Academy of Sciences, Acad. G. Bontchev, block 9, Sofia, 1113, Bulgaria.

* Corresponding authors: mmartinez@icp.csic.es, mlazaro@icb.csic.es

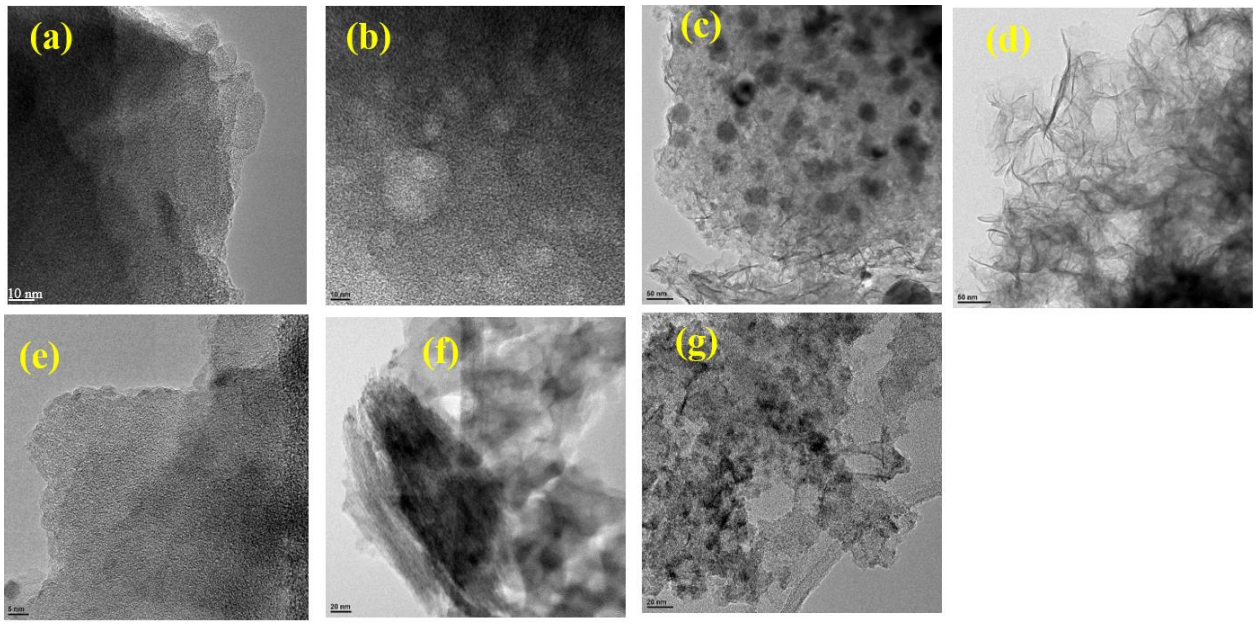

Figure S1. TEM image of (a) CF, (b) (PN-CF, (c) Fe@PN-CF, (d) Co@PN-CF, (e,f) CoFe@PN-CF, and (g) CoFe@CF sample

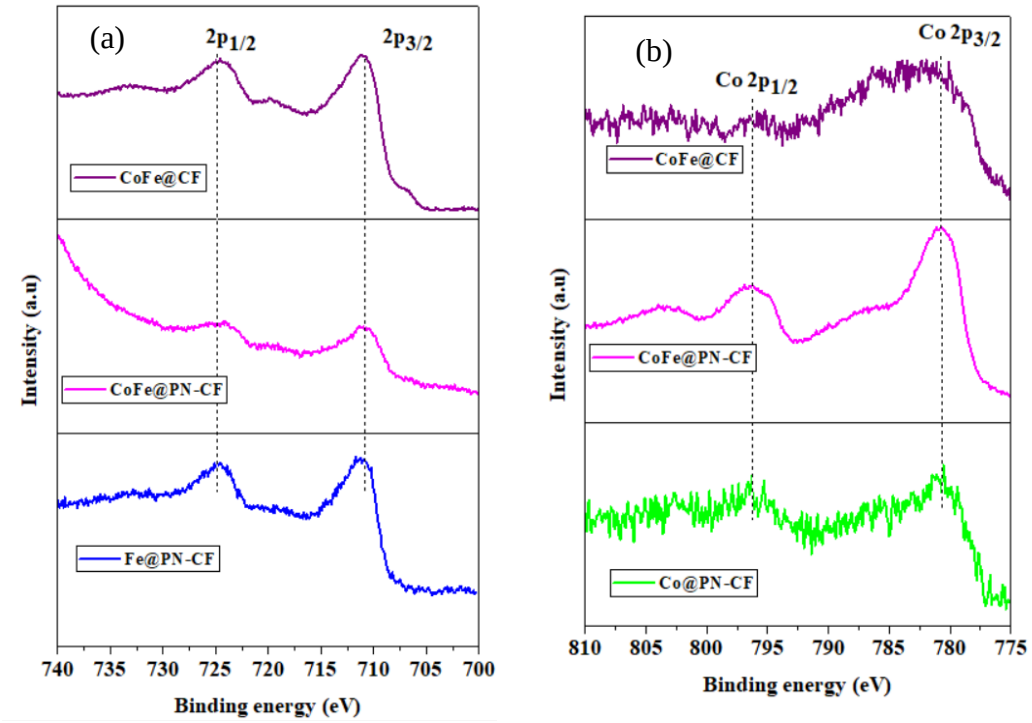

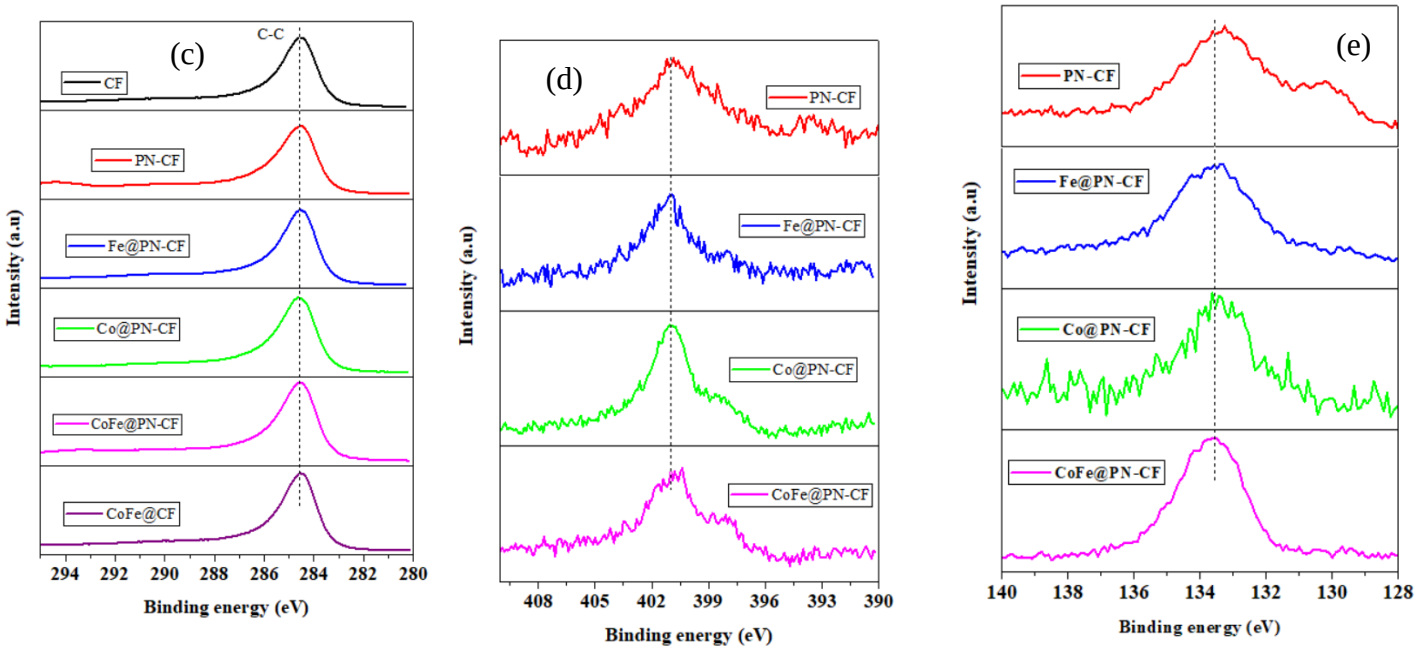

Figure S2. High resolution XPS of spectrum of Fe 2p (a), Co 2p (b), C 1s (c), N 1s (d), and P 2p (e).

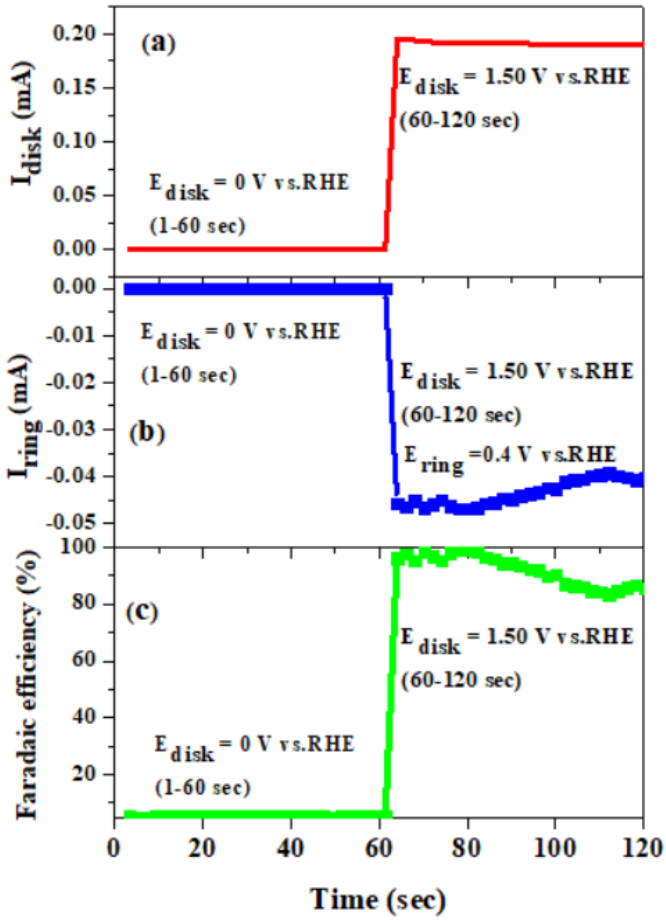

Figure S3. Chronoamperometry measurement of IrO_2 catalyst supported on RRDE at 1600 rpm in N_2-saturated 1.0 M KOH at a constant potential of 1.50 V vs.RHE (enough to produce 1.0 $mAcm^{-2}$): (a) disk current, (b) ring current at E_{ring} = 0.4 V vs.RHE, and (c) Oxygen faradaic efficiency profile.

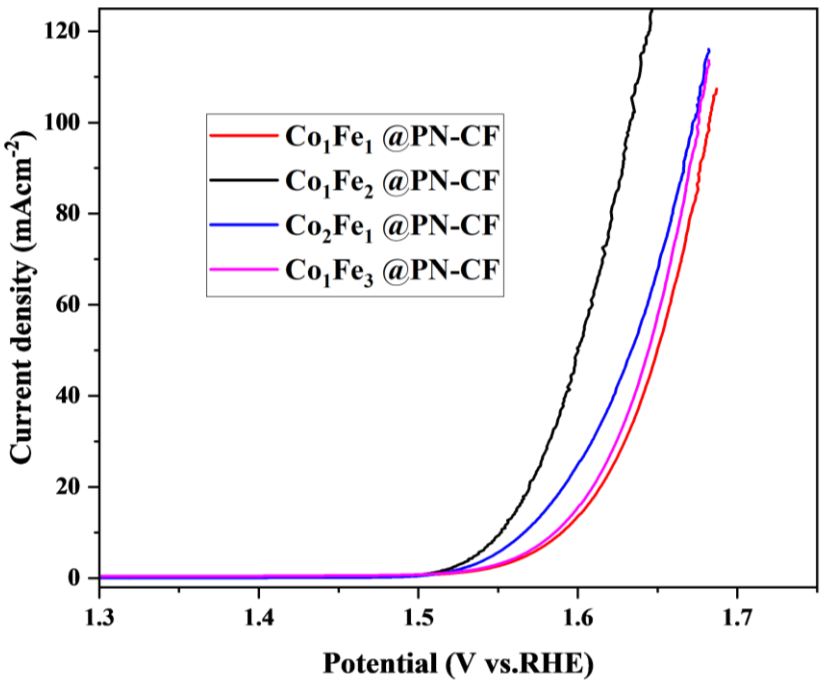

Figure S4. Comparison of OER polarization curve of CoFe@PN-CF prepared with different ratios of Co/Fe.

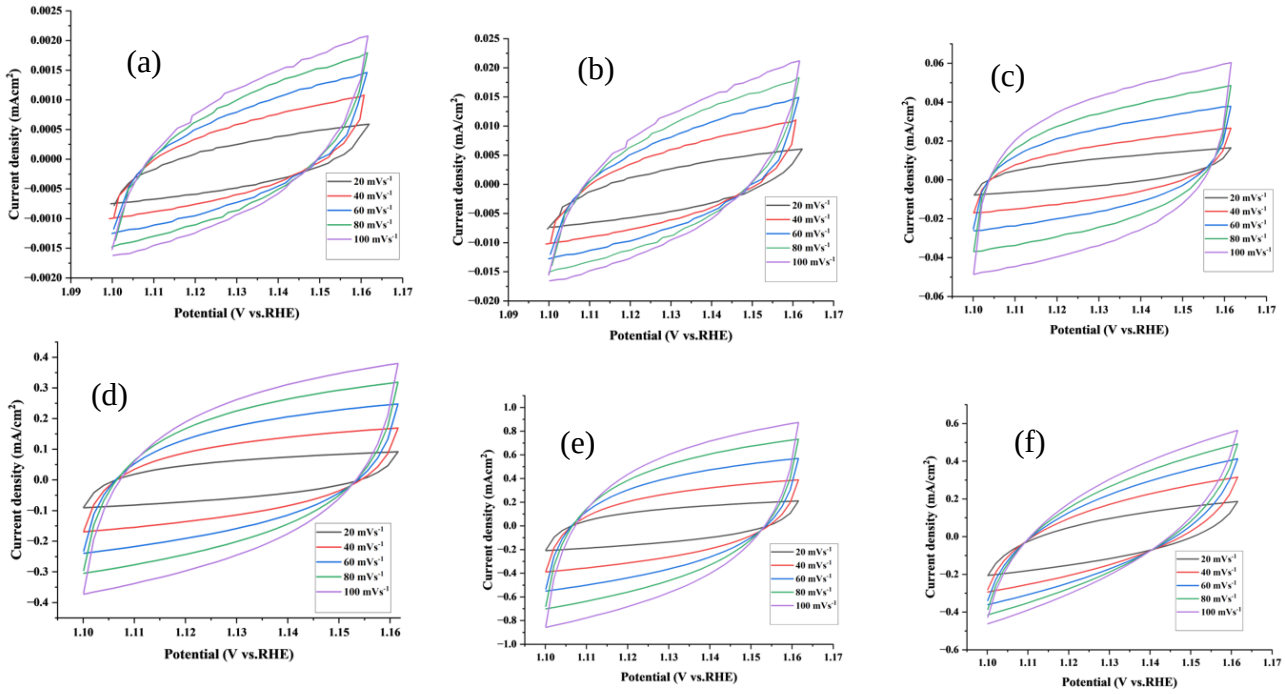

Figure S5. Cyclic voltammogram at different scan rates: (a) CF, (b) PN-CF, (c) Fe-PN-CF, (d) Co@PN-CF, (e) CoFe@PN-CF and (f) CoFe@CF.

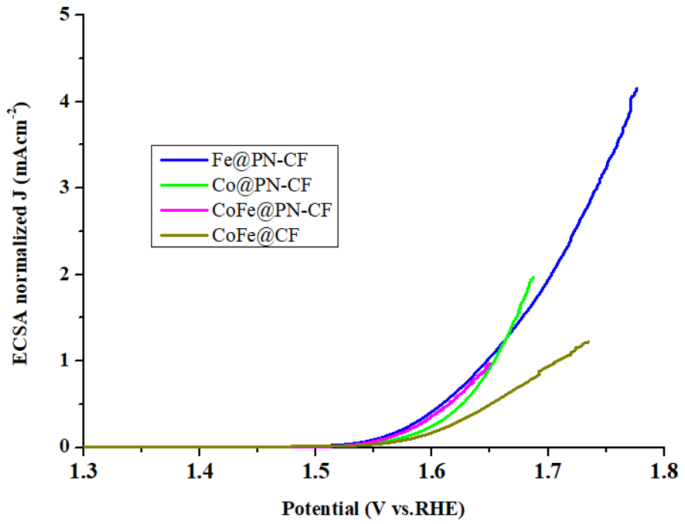

Figure S6. ECSA-normalized OER polarization curves of the as-prepared electrocatalyst.

Article V

Journal of Energy Chemistry 67 (2022) 101–137

Contents lists available at ScienceDirect

Journal of Energy Chemistry

journal homepage: www.elsevier.com/locate/jechem

http://www.journals.elsevier.com/journal-of-energy-chemistry/

Review

Recent progress on bimetallic NiCo and CoFe based electrocatalysts for alkaline oxygen evolution reaction: A review

Gebrehiwet Abrham Gebreslase [a], Maria Victoria Martínez-Huerta [b,*], Maria Jesus Lázaro [a,*]

[a] Instituto de Carboquímica, CSIC. Miguel Luesma, Castán 4, 50018, Zaragoza, Spain
[b] Instituto de Catálisis y Petroleoquímica, CSIC. Marie Curie 2, 28049, Madrid, Spain

ARTICLE INFO

Article history:
Received 20 April 2021
Revised 22 September 2021
Accepted 9 October 2021
Available online 25 October 2021

Keywords:
Water electrolysis
Oxygen evolution reaction
Bimetallic electrocatalyst
Nickel
Cobalt and iron

ABSTRACT

The deployment of hydrogen as an energy carrier is found to be a vital alternative fuel for the future. It is expected that water electrolysis, powered by renewable energy sources, be able to scale-up hydrogen production. However, the reaction kinetic of oxygen evolution reaction (OER) is a sluggish process, which predominantly limits the efficiency of water electrolysis. This review recapitulates the recent progress and efforts made in the design and development of two selected earth-abundant bimetallic electrocatalysts (NiCo and CoFe) for alkaline OER. Each bimetal electrocatalyst is thoroughly outlined and discussed in five sub-sections, including bimetal (oxy) hydroxides, Layered double hydroxides (LDHs) structures, oxides, composites, alloy and nanostructured electrocatalysts, and assembled with heteroatoms. Furthermore, a brief introduction to an in situ/operando characterization techniques and advantages for monitoring the structure of the electrocatalysts is provided. Finally, a summary outlining the challenges and conceivable approaches to advance OER performance is highlighted and discussed.

Gebrehiwet Abrham Gebreslase received his BSc. Degree in 2019 in the department of Chemical Engineering from Mekelle Institute of Technology-Mekelle University (MIT-MU), Tigray, Ethiopia. He obtained his master degree in 2019 in the Erasmus Mundus Master in Membrane Engineering for a Sustainable World (EM3E-4SW), specialization in Nanotechnology and Nanoscience from the University of Zaragoza, Spain. Currently, he is pursuing his PhD degree under the fellowship of Marie Skłodowska-Curie Action – International Training Network (MSCA-ITN) at the Instituto de Carboquímica-CSIC, Spain. His research interests focus on synthesis and characterization of nanomaterials for electrochemical water electrolysis (Oxygen Evolution Reaction (OER) and Hydrogen Evolution Reaction (HER)).

Dr. María Victoria Martínez Huerta got her PhD in Chemistry in 2001 from Universidad Autónoma de Madrid. She is Senior Scientist since 2010 and Head of the Electrocatalysis Group for Energy and Environment of the Institute of Catalysis and Petrochemistry (ICP) at the Spanish National Research Council (CSIC). Its lines of research are linked to the development of electrocatalysts for energy and environmental applications that involve a reduction in the environmental impact derived from the use of fossil fuels, mainly in those applications that use hydrogen as an energy carrier such as fuel cells, electrolysers and unitized regenerative fuel cells.

* Corresponding authors.
E-mail addresses: mmartinez@icp.csic.es (M.V. Martínez-Huerta), mlazaro@icb.csic.es (M.J. Lázaro).

https://doi.org/10.1016/j.jechem.2021.10.009

Dr. Mª Jesús Lázaro (Dr. in Chemistry) is Research Professor at the CSIC at the Instituto de Carboquímica (ICB_CSIC). She has participated in 75 Projects and 14 contracts, in which 45 has been the Principal Researcher. As a result, she has published 265 articles in indexed scientific journals (H Scopus = 50), has directed 17 doctoral theses and is the author of 6 patents. Since October 2015, she is the Institutional Delegate of CSIC in Aragon. In addition, she is the president of the Spanish Coal Group and the European Carbon Association and of the Association of Women Researchers and Technologists (AMIT).

1. Introduction

Energy shortage and environmental impact are among the world's contemporary challenges, instigated by the intensive exploitation of fossil fuels. The persistently propagating energy demand, the finite reservoir of fossil fuels, and ecological and societal glitches provoked an urgent need to hunt for an alternative energy source [1-5]. The deployment of hydrogen as an energy carrier was found to be the most vital alternative fuel for the future. Hydrogen is characterized by its superior thermal efficiency and gravimetric energy density, and it is environmentally friendly (zero emission of greenhouse gas) accompanied by good sustainability [6-8]. Moreover, hydrogen retains the highest specific energy density (140 MJ kg^{-1}), which is more than twofold superior to conventional solid fuels (50 MJ kg^{-1}). Currently, the overall global hydrogen production is reported to be around 500 bcm per year. A significant portion of this amount is utilized to synthesize ammonia, fertilizer production, fuel cells, and petroleum refining [9-11].

Hydrogen can be produced from numerous sources of renewable and non-renewable raw materials, including steam reforming, coal gasification, biomass, water electrolysis, and nuclear energy [8,9,11-13]. Among the various sources, it is expected that water electrolysis, powered by renewable energy sources, can scale up CO_2-free hydrogen production with high purity (99.9%). In water electrolysis, electricity is applied to split the water molecule into hydrogen and oxygen entities, and the cost of electricity determines the price of H_2 energy production [7,14,15]. The electrolysis technologies can be classified depending on the electrolyte: alkaline electrolysis cell (AEC), solid oxide electrolysis cell (SOEC), proton exchange membrane water electrolysis (PEMWE), and anion exchange membrane water electrolysis cell (AEMWE). The working principle, pros, and cons of all those mentioned technologies can be found in elsewhere myriads of books and review papers [11,12,15,16].

The liquid alkaline electrolysis cell (AEC) is the most mature hydrogen production technology, being used on a global commercial scale, possessing features of high suitability and high purity of hydrogen, which has imminently attracted worldwide devotion [17]. However, AEC needs to enhance energy efficiency and improve safety, operability, and stability as the liquid electrolyte can cause corrosion [10,18]. An anion exchange membrane used as an electrolyte in AEMWE takes certain advantages compared to AEC. In this case, it is unnecessary to use a concentrated KOH solution, making the installation less critical and easier to operate [17,19]. Furthermore, AEMWE retains certain advantages compared with PEMWE, such as using non-noble metal or earth-abundant metal oxides based electrocatalyst, due to the increased kinetics of electrochemical reactions in an alkaline [20,21]. Nevertheless, AEMWE is less developed compared with AEC and PEMWE, in which further improvements are required.

Electrochemical water splitting is accredited as an efficient and environmentally benign technology to obtain hydrogen. However, the water reduction and oxidation processes that occur at the cathode and anode, respectively, are kinetically sluggish, adversely affecting the overall efficiency of water electrolysis. Principally, the water electrolysis is mainly restricted by the indolent kinetics (high overpotential) of oxygen evolution reaction (OER) occurring at the anode electrode, ascended from the four-electron transfer: [$4OH^- \rightarrow 2H_2O + O_2 + 4e^-$] [22-30]. This impedes the widespread implementation of water-electrolysis for mass hydrogen production. To overcome the energy barrier of the OER process, it is indispensable to exploit electrocatalysts, which could convey a high current density at low overpotential accompanied by long-term stability.

The current benchmark of electrocatalysts for OER applications is based on precious metals (Ir and Ru) and their oxides (IrO_2 and RuO_2) [21,31-37]. Though those materials showed a magnificent catalytic activity for OER, their low abundance, high cost, poor chemical stability in alkaline media obstruct them from the tenable application. Therefore, it is vital to develop a more efficient, stable, and low-cost non-noble electrocatalyst for OER that could substitute the expensive Ir- and Ru-based catalysts for sustainable and high efficiency of alkaline water-electrolysis [38-42].

Over the past few years, remarkable efforts have been devoted to developing non-precious metal-based electrocatalysts for the OER process. Different transition metals have enthralled a considerable courtesy for voluminous investigators/academicians to develop a robust and efficient electrocatalyst due to their electronic modulator structure and tunable physicochemical properties. Transition metals such as Co [43-45], Ni [46-49], Fe [50,51], Mn [52,53] have been broadly explored for electrocatalytic OER [54]. Moreover, combining two or more metals offers high electrochemical activity toward oxygen evolution compared with monometallic counterparts. For example, bimetallic and multimetallic compounds based on transition metals such as $Co(Fe_x Ni_{1-x})_2P$ [38], $NiCo_2O_4$ [55], $CoFe_2O_4$ [39], CoFe-Co_8FeS_8 [56], P-$Co_{0.9}Ni_{0.9}Fe_{1.2}$ NCs (NCs: nanocubes) [57], W-NiCoP [29], MoCoNiS [58], have recently exhibited a noticeable electrocatalytic activity and stability. Among the different transition metals, Ni, Co, and Fe based catalysts were demonstrated to be the most prominent candidates to expedite the OER because of their ubiquitous availability in nature, low cost, peculiar redox characteristic, abundant active site, synergistic effects between the coupled metals [59-64].

Although remarkable progress has been made in investigating of low cost and high performance of electrocatalyst for OER, the efficiency of the current catalysts is still inadequate in terms of both catalytic activity and durability; hence, further research is needed yet to revolutionize catalysts with high catalytic activity and stability that is suitable for sustainable electrochemical water oxidation and reduction. This review paper will be encapsulating the recent progress and challenges in developing NiCo and CoFe bimetallic-based electrocatalysts for water oxidation. State of the art and electrocatalytic performance of two selected bimetallic transition metals (NiCo and CoFe,) in alkaline OER, the fundamental chemistry of OER, the general electrochemical evaluating parameter employed to probe OER electrocatalyst are reviewed. We believe that this review would be a flashpoint for researchers to design and develop a tremendous NiCo and CoFe based electrocatalyst for OER in the future.

2. Fundamental principles of alkaline water oxidation

In alkaline water electrolysis, the overall water splitting reaction mechanism consists of two half-reactions: hydrogen evolution reaction (HER) and OER, as described as follows [65]:

$$\text{Cathode: } 4H_2O + 4e^- \rightarrow 2H_2 + 4OH^-, \quad (1)$$

$$\text{Anode: } 4OH^- \rightarrow 2H_2O + O_2 + 4e^-, \quad (2)$$

$$\text{Overall: } 2H_2O \rightarrow 2H_2 + O_2. \quad (3)$$

OER process is a four-electron transfer system with sluggish reaction kinetics that sternly hinders oxygen formation. Researchers have proposed several reaction mechanisms for OER, and the most accepted and recognized electrochemical reaction pathways for oxygen evolution in alkaline media are given below, which is expressed by four consecutive steps [49,66,67]:

$$4OH^- \rightarrow OH^* + 3OH^- + e^-, \quad (4)$$

$$OH^* + 3OH^- \rightarrow O^* + 2OH^- + H_2O + e^-, \quad (5)$$

$$O^* + 2OH^- + H_2O \rightarrow OOH^* + OH^- + H_2O + e^-, \quad (6)$$

$$OOH^* + OH^- + H_2O \rightarrow O_2 + 2H_2O + e^-. \quad (7)$$

A schematic representation of the multi-electron transfer is presented in Fig. 1, which shows an additional O_2 formation possibility from the M–O instead of M–OOH. As evident from the above equations, four electrons are required to produce one mole of O_2, and multiple electron transfer at one time is kinetically slow, and the OER process contains numerous steps with one electron for each step [68]. The energy barrier originated from each step, deters the kinetics of OER, and demands high overpotential to overcome the energy barrier. Three intermediates of OH*, O*, and OOH* entities are formed during the OER process. As mentioned above, the four steps are thermodynamically non-spontaneous, requiring substantial energy to progress to the following step. The step with the superior energy barrier becomes the rate-determining step (RDS), which eventually governs the catalyst's efficiency [69].

An ideal catalyst that follows the Sabatier principle [71], a catalyst should bind oxygen neither too strong nor too weakly, is crucial to deliver low overpotential leading to the high energy efficiency of water splitting. The Sabatier idea gives a volcano-shaped relationship between catalyst activity and bond strength. For example, Man and co-workers [66] claimed that a free energy diagram could be developed using OH*, O*, and OOH* intermediate entities, in which O* binding energy to the metal oxide surface can be used as a descriptor. According to the Sabatier principle, a catalyst with moderate binding activity is essential since weak adsorption hinders intermediates formation. When the adsorption of the catalyst is too strong, then the formed intermediate will not be desorbed easily. Specifically, when the adsorption of O entities on the surface of the catalyst is too weak, then the intermediate OH* could not be easily formed, and also, when the adsorption of O entities on the surface of the catalyst is strong enough, the formed OH* could not quickly form OOH* [72]. Scaling ratio (the relationship between the energy barrier of each step) can be formed between the binding energies of HO*, HOO*, and O* species on metal oxide surfaces. The scaling ratio shows that only one parameter could govern the free energy diagram and hence the performance. The catalyst activity can be drawn as dependent on only one factor, such as using oxygen binding energy, which gives a volcano-shaped relationship between the activity of the catalyst and the determined oxygen binding energy. A surface that binds oxygen too strongly and too weakly, the potential is mainly restricted by the formation of HOO* and oxidation of HO* species, respectively [69].

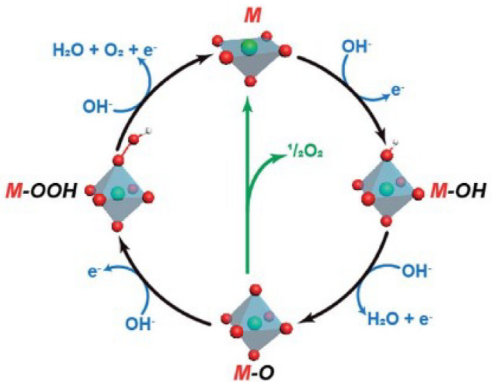

Fig 1. A schematic representation of an alkaline OER mechanism. The green line designates O_2 formation potential from M–O instead of forming an intermediate of M–OOH. M: Metal. Reproduced from Ref. [70] with permission from Royal Society of Chemistry.

3. Electrochemical evaluating parameters of electrocatalysts for the OER performance

The electrochemical performance of electrocatalyst material for OER can be assessed using various parameters. In the lab scale, the electrochemical measurements for OER are usually performed in a liquid environment in a three-electrode cell controlled by a potentiostat/galvanostat and using a rotating disc electrode (RDE) [73] or using another support stainless steel (SS) [74], substrate such as nickel foam (NF) [75]. For the case of RDE, a thin film of the electrocatalysts is prepared by coating a catalytic ink onto the glassy carbon of the RDE. The ink is obtained from a mixture of catalyst powder, a binder (Nafion ionomer), and solvent (water, ethanol) [76,77]. A carbon rod as a counter electrode and reference electrodes such as Ag/AgCl electrode, Hg/HgO electrode, the saturated calomel electrodes, and the reversible hydrogen electrode (RHE) in the supporting electrodes are usually used [78-81].

Electrocatalysts can be coated or directly grow on a conductive substrate such as NF [75,82-85], SS [74], carbon cloth (CC) [86], fluorine-doped tin oxide (FTO) [87], carbon fiber paper (CFP) [88], in which they act as a working electrode during the OER. Substrates such as NF and SS are highly porous materials with a large surface area, excellent electrical conductivity, and good corrosion resistance at high pH values [89-92]. Comparing RDE and the conductive substrate-based working electrode, it was demonstrated that those conductive substrates offer excellent catalytic performance. This is due to a high specific surface area which is essential to accelerate the diffusion of electrolytes and liberate oxygen from the material. Also, the substrate contains abundant active sites and defects for electrocatalysis, which boost electrocatalytic performance [90-93]. In the case of RDE, an ink of catalyst mixed with a polymeric binder is coated on the surface, and the use of binder lessens the contact area between the electrolyte and active site of the electrolyte, thus reduces the conductivity of the electrode, as a result, deteriorated OER performance is obtained.

Moreover, catalysts coated on the glassy carbon surface can be scratched or peel off and agglomerate/aggregate during long-term electrochemical measurements [93-95]. In general, the type of substrate used to grow or coat the catalyst highly affects the resulting electrocatalyst performance. It is noteworthy to mention that the substrates (glassy carbon, NF, SS, etc.) should be carefully investigated for their catalytic performance. NF and SS have substantial catalytic activity towards OER, while glassy carbon has a low response for OER. For example, Hu and co-workers [90] endeavored to examine the catalytic activity of NF and SS for OER. It

was reported both conductive substrates without catalyst unveiled a remarkable catalytic activity for alkaline OER. Thus, the catalytic contribution should not be disregarded during the catalyst evaluation by growing or coating on these substrates since these conductive substrates also contribute to the overall catalytic performance. Nowadays, few excellent electrocatalysts with extraordinary electrocatalytic performance have been reported using NF as a substrate without any binders [94]. The various conductive substrate utilized to grow or coat NiCo and CoFe based electrocatalyst are summarized in Tables (1–9).

In the following section, the most common parameters used for probing catalytic activity and efficiency, such as overpotential, Tafel slope, turnover frequency (TOF), electrochemical impedance spectrum (EIS), stability, and electrochemically active surface area (ECSA), are succinctly discussed.

3.1. Overpotential

Overpotential (η) is one of the most vital parameters that determine the electrochemical performance of an electrocatalyst. It is determined by the potential difference between the potential required to achieve specific current density and the theoretical potential (1.23 V), as shown in Eq. (8). The overpotential value needed to attain a 10 mA cm^{-2} current density is usually used as a reference [61], and a lower overpotential value indicates outstanding catalytic performance.

$$\eta = E_{RHE} - 1.23\ V. \quad (8)$$

3.2. Tafel slope

The electrochemical kinetic equation that relates the rate of chemical reaction and overpotential is known as a Tafel equation. It is used to investigate the reaction kinetics of the catalyst deposited on electrode materials. Tafel slope is used to comprehend the reaction mechanism and kinetics and compare the electrochemical performance of various catalysts. It can be determined by using Eq. (9) [73,96,97], which gives information about the RDS.

$$\eta = b\log(\tfrac{j}{j_0}) + a, \quad (9)$$

where b represents the Tafel slope, η is overpotential, j is current density, and j_o is an exchange current density. The exchange current density (j_0) reveals the intrinsic rate of electron transfer kinetics between the electrode and analyte. As elucidated in section 2, OER is a multi-step process comprising a sequence of reactions and numerous intermediate entities such as MO, MOOH. Many prospects toward the OER mechanism related to the Tafel slope have been proposed. One of the most well-recognized explanations for alkaline OER mechanism is Krasil'shchikov's Path which is given in Eq. (10–13) with their respective Tafel slope value [77,98]:

$$M + OH^- \leftrightarrow MOH + e^-,\ b = 120\ mV\ dec^{-1} \quad (10)$$
$$MOH + OH^- \leftrightarrow MO^- + H_2O,\ b = 60\ mV\ dec^{-1} \quad (11)$$
$$MO^- \rightarrow MO + e^-,\ b = 45\ mV\ dec^{-1} \quad (12)$$
$$2MO \rightarrow 2\ M + O_2,\ b = 19\ mV\ dec^{-1} \quad (13)$$

Electrocatalysts with lower Tafel slope are considered to be promising for the OER process. Different Tafel slopes indicate different RDSs. In a given reaction, a smaller Tafel slope specifies that the RDS is found at the last step of the electron transfer reaction, which eventually displays an excellent electrocatalyst. The lower Tafel slope shows a rapid increase of current density with increasing overpotential, signifying fast electrocatalyst kinetics for OER.

3.3. Electrochemically active surface area (ECSA)

ECSA embodies the electrode area accessible to the media/electrolyte used for transferring charges [99]. It helps quantify the area of the reacting surface of the electrode and allows to compare the intrinsic catalytic performance of materials. It can be calculated by the double-layer capacitance (C_{dl}) measured by cyclic voltammetry (CV) [100,101]. In this case, the CV is recorded in the non-Faradic potential region at different scan rates (υ). The CV curve is utilized to quantify the double-layer charging current (i_c). The current is directly proportional to the scan rates as equated in Eq. (14), which is vital to determine the double layer charging current (i_c) [102]:

$$i_c = \upsilon \times C_{dl}. \quad (14)$$

The slope of the graph of i_c vs. υ represents the value of the C_{dl}. Based on this, ECSA can be determined using Eq. (15):

$$ECSA = \frac{C_{dl}}{C_s}, \quad (15)$$

where C_s is the specific capacitance of alkaline electrolyte (e.g., 0.04 mF cm^{-2} for 1.0 M KOH) [103], high ECSA provides a higher surface density of active catalytic sites exposed to the OER related species, enhancing the mass transport rate. Hence, the overall catalytic activity could be promoted.

3.4. Turnover frequency (TOF) and mass activity

TOF is defined as the number of reactant molecules that one gram of electrocatalyst can convert into a product per time [104]. TOF and mass activity are also commonly used to study the electrochemical performance of the electrocatalyst. The TOF can be determined according to the following Eq. (16) [105]:

$$TOF\left(\frac{1}{s}\right) = \frac{J \times A}{4 \times F \times n}, \quad (16)$$

where J (mA cm^{-2}) represents the current density at a given overpotential, A is the active working electrode area, F is the Faradays constant (96485C mol^{-1}), and n is the number of moles. It is difficult to determine the exact value of TOF as all the elements in the catalyst may not be electrocatalytically active during the operation. Yet, it is essential for evaluating parameters to compare the catalytic activity of similar materials, and the high value of TOF embodies higher catalytic activity. The mass activity of the catalyst can be determined as mass activity = J g^{-1}, where m is the mass loading of the working electrode (mg cm^{-2}), and j is measured current density (mA cm^{-2}) at a particular potential [105].

3.5. Exchange current density (J_0)

Exchange current density (J_o) is also commonly used to scrutinize the catalytic efficiency, which can be determined using Eq. (17) [106].

$J_0 = RT/nFR_{ct}$, (17)

where R represents the gas mole constant (8.314 J mol^{-1} K^{-1}), T is the experimental temperature (298 K at room temperature), n is the electron transfer number, F is Faraday's constant (96485C mol^{-1}), and R_{ct} is the charge transfer resistance that can be obtained from EIS. High-performance electrocatalysts in OER should display low overpotential, low Tafel slope, and high exchange current density.

3.6. Faraday efficiency (FE)

Faradic efficiency (FE) describes the electrochemical performance of materials by interrelating the percentage of the actual and theoretical products. In OER, FE is the ratio of the amount of oxygen gas produced by the experiment to the amount of oxygen gas determined theoretically [107]. This parameter elucidates the conversion efficiency from electrons to oxygen molecules. FE can be defined as follows:

$$\mathrm{FE} = \frac{4Fn_{O_2}}{It} \times 100\%, \quad (18)$$

where F is the Faraday's constant (96485C mol^{-1}), n_{O2} is the amount of molecular oxygen produced, I is the current applied, and t is the reaction time.

3.7. Stability

Electrocatalyst stability is very indispensable for extensive scale application. Two methods are commonly employed to explore catalyst stability: chronoamperometry (E-t curve), chronopotentiometry test (I-t curve), and CV. In practice, the structure of catalyst and composition severally alters during the electrochemical reaction, and the fundamental phenomena that happen during the reaction are subtle. Recently, several cutting-edge instruments help us control the OER in situ or operando process to probing catalysts' structure, composition, and electrochemical behavior during the OER process [108]. Intended to compare electrocatalyst activity and stability for OER, Wang and co-workers [109] proposed a standard protocol to explore the real catalyst activity and stability simultaneously. A standard figure of merit depicted with the overpotential @10 mA cm^{-2} at the initial time plotted against overpotential @10 mA cm^{-2} at certain hours was proposed, as shown in Fig. 2. The protocol was designed to be applicable for alkaline and acidic media, a more practical application. During a comparison of various catalysts, precaution should be taken on the amount of mass loading and the intrinsic nature of the electrode.

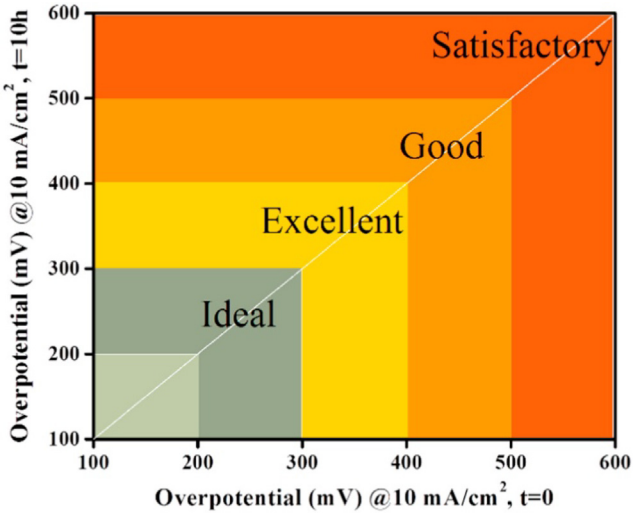

Fig 2. The standard figure of merit for comparative probing of electrocatalyst for OER system. Reproduced from Ref. [109] with permission from the Elsevier Ltd. Lies.

Any electrocatalyst materials that show a overpotential in the range of 200 to 300 mV would be the most promising material for the OER process, mainly if the overpotential remained less than 300 mV after a 10 h operation. Besides, any electrocatalyst material that lies its overpotential from 300 to 400 mV in any axis is very good for the OER process. If the overpotential remains in the stated range after 10 h, then this catalyst is considered excellent for OER application. If after 10 h operation lies its overpotential in the range of 400 to 500 mV, it is still a suitable catalyst with low stability. However, any electrocatalyst materials that exhibit an overpotential greater than 500 mV in either axis are not promising for the OER process. In general, the above discussion of OER catalysts can be grouped into different classes based on the overpotential: ideal class = 200 to 300 mV, excellent class = 300 to 400 mV, good class = 400 to 500 mV, and satisfactory class > 500 mV.

4. Synthesis method and ideal characteristic of electrocatalyst

The activity of an electrocatalyst is highly determined by its structure and morphology, which, in turn, depends on the route of the synthesis technique. Different synthesis methods might offer a distinct feature in the bulk and surface of the materials and the cation oxidation number/state [110]. In this review, we have attempted to encapsulate the various synthesis methods utilized to prepare NiCo and CoFe electrocatalysts, which are indicated throughout the tables (Tables 1–9) and schematically shown in Fig. 3, which highlights a snapshot of the various synthesis techniques, and the ideal characteristics of electrocatalyst for OER.

The synthesis methods can be generally categorized into two groups: physical and chemical methods. The chemical methods are based on the bottom-up approach, i.e., different distribution sizes of nanostructured materials are formed by an assembly of atoms or molecules. In contrast, the physical methods are based on the top-down approach in which nanomaterials are formed by unraveling bulk material counterparts [111,112]. Chemical synthe-

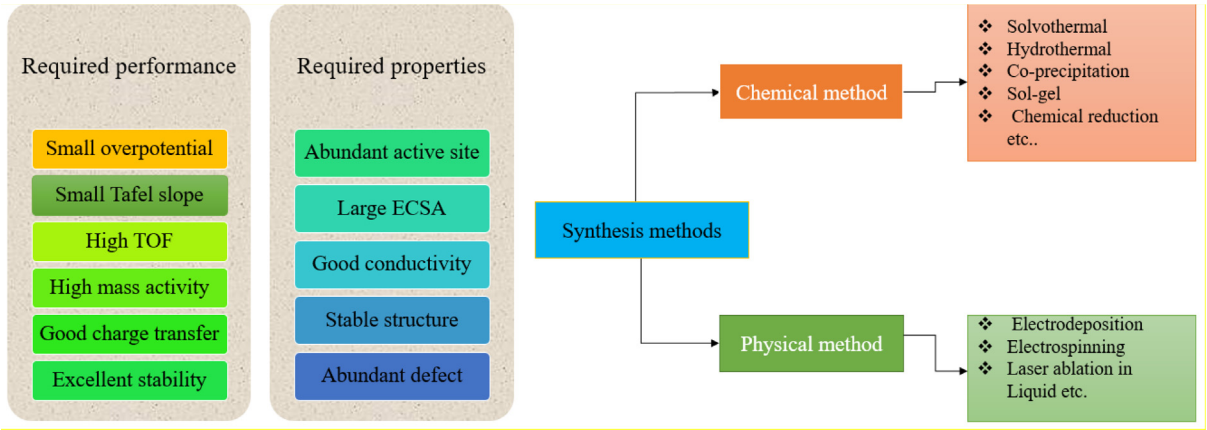

Fig 3. An overview of ideal electrocatalyst characteristics and different synthesis methods employed to synthesize NiCo and CoFe based electrocatalyst.

sis methods including hydrothermal [113-115], solvothermal [97,116,117], sol–gel [118], co-precipitation [119], chemical vapor deposition (CVD) [120], etc., are among the extensively used methods to synthesize bimetallic electrocatalysts.

A solvothermal method is a comprehensive synthesis method that occurs in a closed system, necessities a high temperature and pressure to provoke a chemical reaction or decomposition of the materials precursor to form the sought compound from the solution. It has advanced remarkably over the past decades and is reported to be a versatile strategy to obtain a well-controlled morphology and particle size of metal nanostructures. The predominant factors that govern the quality of the product prepared by the solvothermal route are temperature and time, solvent and ligand effect, reductant and capping agent effects. A detailed explanation of how all these key factors influence the synthesis process can be found in an elsewhere review paper [121]. This method is mainly applicable for nonaqueous forms or generally for organic solvents. When the solvent is water or aqueous solution, it is called hydrothermal. Solvothermal and hydrothermal involve mixing precursors in a given solvent and then sealing them in an autoclave, followed by heating at a high temperature above the solvent's boiling point. They are relatively facile in which the reaction can be completed in one pot or single step. This endows to control the structure and morphology of the electrocatalyst by tuning the reaction parameters such as time, composition, temperature, or pH. The pressure and temperature expedite the dissolution of the chemical reagent and crystallization formation of a product. With appropriate selection of the precursor composition, solvent, and reaction conditions, products with high purity, homogeneously dispersed nanoparticles with narrow size distribution can be obtained [122]. Polyol, part of the solvothermal method, is a promising route to obtain a product with well-controlled crystallinity, size, and morphology. This method involves heating the precursors with a stabilizer and reducing agent in an organic solvent such as ethyl glycol, diethyl glycol, pentanediol, glycerol, butanediol. It benefits to prepare high-quality metal nanoparticles and possesses several advantages such as low cost, ease of use, and already proven for large-scale applications [117]. General description of both solvothermal and hydrothermal can be read in ref. [123]. The sol–gel method is one of the wet-chemical techniques used to prepare nanostructured materials. The synthesis process of sol–gel comprises several steps, including hydrolysis of metal alkoxides to form sol, condensation, aging, and drying of the mixture. Finally, calcination is performed to obtain nanoparticles [111]. The co-precipitation method works by heat treatment of the precursor metal in a given solvent with a precipitant. The precipitant can be removed by post-treatment, such as washing during centrifugation and calcination. Particle aggregation-agglomeration can occur in this method, negatively affecting the resulting catalyst performance [124]. Likewise, CVD is a type of chemical synthesis method, which is a crucial tool to synthesize atomically thin 2D nanomaterials with high quality and controlled thickness. In this process, gaseous or vaporous materials react at a certain temperature in the gas or gas–solid interfaces to form solid products with certain structural defects. Detail working principles and descriptions, the merits of CVD over other synthesis methods can be found elsewhere [125].

Moreover, apart from the chemical synthesis methods, physical methods such as electrospinning [126,127], laser ablation in liquid (LAL) [114], and electrodeposition [128-130] are also employed to synthesize bimetallic electrocatalyst including NiCo and CoFe. Electrospinning is a promising synthetic route to prepare 1D nanofibers with different structural morphologies such as nanocables, porous tubes, and nanorods. These offer an effective route for large-scale electrocatalyst production and thus have immense potential application. In this technique, a polymer solution mixed with the desired metal precursors are first prepared, and then nanostructured materials are prepared by electrospinning the solution onto a given substrate. This technique is usually considered a low-cost, clean, and efficient synthetic method [131-134]. Few researchers have used LAL to prepared NiCo and CoFe based electrocatalysts for OER. This technique is rapid and can control different properties (size, composition, or crystal phase) independently, and surfactant is unnecessary. The detail underlying the synthesis procedure, its merits over other synthesis methods can be found elsewhere [135].

Furthermore, the electrodeposition technique is a relatively easy method, in which electrocatalysts such as layered double hydroxides (LDHs) forms can be prepared within a short period on the surface of the electrode such as NF, SS mesh (SSM), and CFP [136,137]. Despite its fast process, precisely controlling the morphology distribution of the catalyst on the substrate is yet perplexing. NF was demonstrated to be an ideal substrate to directly design electrocatalyst on it due to its robust macroporous structure with a high surface area and commendable electrical conductivity [138]. A substantial number of researchers have employed NF to grow materials for efficient electrocatalysis [113,139-144]. Besides, SSM and CFP were reported to be a remarkable potential for growing catalytic materials on the surface and showed a magnificent catalytic activity for OER [138,145-150]. This review has attempted to rummage the various substrate materials exploited to design and grow NiCo and CoFe bimetallic electrocatalysts, as shown in the following sections (section 5.1 and 5.2, in Tables 1–9). An electrocatalyst that displays low overpotential and Tafel slope and high stability/durability is required for stunning water oxidation. To obtain such appealing performance, it is necessary to produce a material with plenty of active catalytic sites, excellent electrical conductivity, and a robust structure with abundant defects.

5. Bimetallic (NiCo and CoFe) based electrocatalyst for OER application

In recent years, transition metals such as Ni, Co, and Fe based bimetallic electrocatalyst received an incredible devotion by researchers/scientists aimed to be used as an operative electrocatalyst for alkaline OER, owing to high intrinsic catalytic activity, eco-friendly and low cost (due to their earth abundance) [151]. Transition metal-based electrocatalysts in different combinations (mono metal, bimetal, and ternary metals) have been uncovered as promising candidates for OER due to their active sites, attractive electronic conductivity, and synergistic effect, affordable and environmental friendliness. Innumerable efforts have been made in probing and investigating monometallic Ni, Co, and Fe-based electrocatalyst for OER. For example, Lyons and co-workers [152] studied the electrocatalytic activity of Ni, Co, and Fe towards OER. The finding revealed that the catalytic activity of these metals in terms of decreased overpotential is ordered as follows: Ni > Co > Fe. Ni-based electrocatalyst displayed higher catalytic performance than Co and Fe. It was suggested that the difference catalytic activity originates from the bond strength of OH–$M^{2\delta}$,($0 \leq \delta \leq 1.5$) in which the order was claimed to be: Ni < Co < Fe, which is in the inverse of the activity. More information on the comparison of parameters associated with the OER catalytic activity of the monometallic Ni, Co, and Fe can be found elsewhere [153].

Incorporating a secondary metal into another metal can modify and modulate the local electronic structure, leading to an improved intrinsic catalytic activity towards water oxidation [154]. And also, simulations have uncovered that binary or ternary (oxy)hydroxides composed of Fe, Co, and Ni have the highest activities stemmed from the optimized M–OH bond strengths [155]. Moreover, an electrocatalyst prepared by combining two metals can

have unique morphology with an abundant active site, different crystallographic properties, and desired electronic structure. All these traits could boost catalytic activity [148,156,157].

It has been reported that the intrinsic catalytic activity of materials for OER strongly depends on adsorption Gibbs free energy for the binding strength of the reaction intermediate species of OH/O/OOH (ΔG_{OH^*}, ΔG_{O^*}, and ΔG_{OOH^*}), where * refers to the active site on the catalyst surface. As explained in section 2, the volcano plot for OER is used as the general explanatory scheme of the Sabatier principle in electrocatalysts, which states that superb catalytic activity can be attained if the material's surface possesses optimal binding energy for the reaction intermediates. The theoretical overpotential versus Gibbs free energy (η vs. ($\Delta G_{O^*}-\Delta G_{OH^*}$)) in the volcano plot reveals outstanding consistency with the electrocatalytic activity for OER [66]. Metal oxides such as IrO_2, RuO_2, and PtO_2, located at the top/apex of the volcano plot, possess optimal biding strength for OER intermediates and exhibited a small overpotential for OER. However, these aforementioned noble metal/metal oxides are expensive materials that hamper their extensive application. Metals next to the noble metals in the volcano plot, such as Ni, Co, and Fe, are getting a substantial devotion for an efficient OER electrocatalyst [158]. These three transition metals were discovered to be positioned close to the top of the Sabatier volcano curves, thereby displaying that these metals encompass optimal binding strengths with the OER reacting intermediate species and possess high active sites for OER. Due to the synergetic effect and other factors, the bimetals of NiCo and CoFe are demonstrated to be promising electrocatalysts towards OER.

There are specific review papers published devoted to NiFe-based electrocatalyst for alkaline OER, covering recent progress and advanced development of NiFe-based materials and their corresponding reaction mechanism, and its challenges and prospects on NiFe-based materials development electrocatalyst for OER [62,159]. However, no systematic review of the high performance of bimetallic (NiCo and CoFe) based electrocatalyst for the OER process has been reported yet.

In the last two decades, substantial research interest has been growing in developing NiCo and CoFe based electrocatalysts for the OER. This can be corroborated by the number of published papers per year increasing progressively every year, especially in the last 10 years, as shown in Fig. 4. It appears that in recent years, remarkable effort and progress have been made in preparing NiCo and CoFe based materials for water oxidation. In particular, the number of published papers has shown a steady increase in the last decade (2010–2021). A few hundred articles were published before 2010 (2000–2009, not included in Fig. 4). Among the two bimetals, NiCo based electrocatalyst was found to be extensively researched materials compared with CoFe counterparts by referring to the number of published papers.

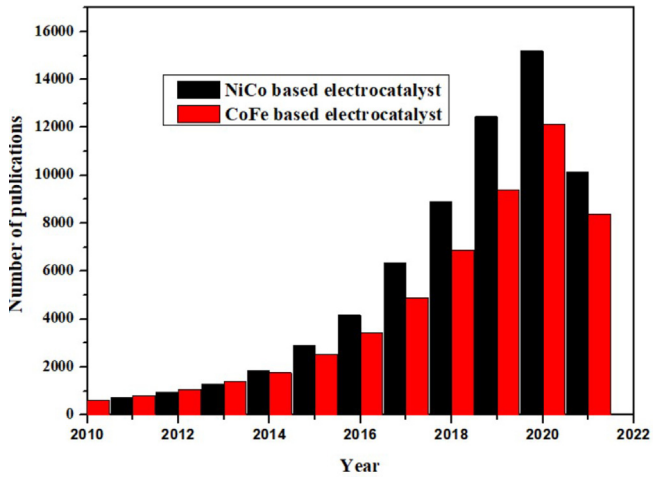

Fig 4. The number of publications per year (from 2000 to 2021) for NiCo and CoFe based electrocatalyst for OER, as derived from Scopus (Last checked on June 20, 2021).

OER can be performed under different electrolyte solutions: acidic, neutral, or alkaline. In acidic solutions, Ir and Ru oxides are considered a reference for OER electrocatalysis. Besides, transition metals, including NiCo and CoFe, have been responsive to OER under acidic media. However, due to the harsh acidic environment, these transition metals are not sable for long-term operation [160,161]. Currently, Ir and Ru are the principal metals exploited for OER electrocatalysis. OER under neutral conditions has also been practiced. The neutral solution is beneficial to the electrocatalyst and apparatus due to the minor corrosion issue. However, OER electrocatalysis under a neutral medium suffers from sluggish kinetics, compared with alkaline and acidic conditions, due to the lower proton/OH concentration [160]. Bimetals such as Co_xNi_yP [162], $CoFe_2O_4$ [163], CoFeP [164], are among the bimetals tested for OER under neutral media. Few review papers on transition metals, including NiCo and CoFe, based electrocatalyst for OER under neutral medium, can be found in ref. [165]. On the other hand, electrocatalysis under an alkaline solution is more favourable for water oxidation than acidic [166]. In addition to the precious metals of Ir, Ru, and their oxide, earth-abundant transition metals such as Ni, Co, and Fe have been demonstrated to be efficient OER under alkaline media [23,24].

For industrial applications, a catalyst with high catalytic activity and long-term stability under intermittent polarization in an alkaline environment is indispensable. A robust electrocatalyst that can efficiently deliver a current density above 500 mA cm^{-2} with long-term stability at an overpotential of less than 300 mV is required [167,168]. Few NiCo and CoFe based electrocatalysts have been reported that fulfil the requirements for a large-scale application. For example, Shao and co-workers [168] prepared Co–Fe–OH nanosheet arrays in-situ grown onto the iron foam (Co-FeF), unveiling an outstanding electrochemical performance towards OER. An ultralow overpotential of 208 and 298 mV was required to derive a current density of 10 and 500 mA cm^{-2}, demonstrating its potential for a commercial water electrolyzer. At a lab-scale, commonly, electrocatalysts are measured their electrochemical performance using a three-electrode system. However, measuring their performance in two-electrode systems that approach to the practical water electrolyzer is crucial. This review is dedicated to summarizing NiCo and CoFe based electrocatalysts used for alkaline OER. Each bimetal electrocatalyst is thoroughly outlined and discussed in five main sub-sections, including bimetal (NiCo or CoFe) assembled with heteroatoms of P/N/S, bimetal LDHs structure, bimetal-(oxy) hydroxide, bimetal oxide or spinel, and lastly, bimetal of composite, alloy, and other electrocatalysts.

5.1. NiCo based electrocatalysts for alkaline OER application

In this Section, the recent progress of NiCo based bimetallic electrocatalyst used for alkaline OER is reviewed. The state-of-the-art review is divided into five main subsections: NiCo (oxy) hydroxide, NiCo LDHs, NiCo oxide, and spinel, NiCo combined with hetero atoms of S/P/N, and finally composite, alloy, and other electrocatalyst containing Co and Ni.

5.1.1. NiCo (oxy) hydroxides based electrocatalysts

Substantial efforts have emphasized developing bimetallic (oxy) hydroxide for water oxidation. Theoretical calculation and experimental results have disclosed that M–OH (M: metal) with high valence cations offers outstanding electrochemical water splitting in an alkaline aqueous solution. This is due to the highly oxidized cation that expedites the adsorption process of the inter-

mediates and facilitates the kinetic reaction, thus stimulating the OER. Besides, the electrophilic nature of the high-valence cation is essential to adsorb and decompose water molecules, which is vital for the OER process [114,169,170]. It is generally recognized that materials with high-OH surface functional groups are effective catalysts for OER. Among the myriads of 3*d* transition metal-based electrocatalysts, Ni and Co in the state of oxide recently display a remarkable potential for water oxidation [171]. Preparing nanostructured bimetal NiCo oxide with low overpotential and rapid oxygen evolution kinetic have received significant attention due to their high earth abundance, high theoretical efficiency, and eco-friendly compared with a noble metal oxide such as IrO_2. However, the underlying route of preparing nanomaterials with augmented surface area and conductivity is yet challenging. Several researchers have been endeavored to design bimetal NiCo-(oxy) hydroxide with a nanostructured framework [114,115,171,172]. Zhao and co-workers [172] attempted to prepare bimetals of NiCoOH-based catalysts for water oxidation. A distinctive sandwich like the coaxial structure of the 3D [Ni $(^{2+/3+})$ $Co_2(OH)_{6-7}]_x$ nanotube arrays was prepared by thermal solution treatment followed by co-electrodeposition. A substrate of nickel nanotube arrays with an open channel coated with Ni and Co–OH nanosheets $[Ni(^{2+/3+})Co_2(OH)_{6-7}]_x$ is presented. The Ni substrate is vital to offer a large surface area and rapid charge transport, and it supports the active layer of $[Ni(^{2+/3+})Co_2(OH)_{6-7}]_x$. The distinctive feature of the large surface area boosted electron transport. The coupling effect of the two metals provided tremendous OER activity, reaching a current density of 10 mA cm^{-2} at 460 mV overpotential. It has also retained an excellent catalytic activity after 1000 cycles. Wang and co-workers [114] prepared an electrocatalyst of $Co_{0.75}Ni_{0.25}(OH)_2$ nanosheets via LAL for the alkaline OER process. It was reported that rich trivalent cations were propagated on the interior wall of porous nanosheet and the Co^{3+} enhanced electrical conductivity and the OER. According to He and co-workers [173], the OER of the Co-based electrocatalysts seems to be associated with the oxidation state of Co^{3+} and Co^{4+}, which are responsible for the adsorption of OH^-, while Co^{2+} would be responsible for the oxygen reduction reaction. Therefore, the novel catalyst of $Co_{0.75}Ni_{0.25}(OH)_2$ nanosheets exhibited a remarkable OER activity, demanding ultra-small overpotential of 235 mV to reach a current density of 10 mA cm^{-2}. Moreover, very recently, Wang and co-workers [115] prepared $Ni_{0.25}Co_{0.75}(OH)_2$ catalyst with different molar ratios of Ni and Co via hydrothermal method. They revealed that the dopant Ni was able to revolutionize the local electronic structure, tune the bandgap, morphology, surface area and the charge distribution of $Ni_xCo_y(OH)_2$ at microscale level. All these features enable the catalyst to exhibit a remarkably stimulated electrochemical reaction for OER. The optimum $Ni_{0.25}Co_{0.75}(OH)_2$ electrocatalyst displayed an overpotential of 352 mV to reach 10 mA cm^{-2}. Importantly, the as-made electrocatalyst displayed a remarkable current density stability for about 12 h without significant decay, operated at 1.60 V vs. RHE generating 12 mA cm^{-2}, this surpasses for the benchmark of RuO_2, in which the current density decreased fast when the RuO_2 was tested at the same condition.

On the other hand, it was claimed that preparing amorphous nanostructured material can stimulate catalytic activity. Materials with superaerophobic (extreme bubble repellency) propensity can be ideal for electrocatalysts for water oxidation [174]. Relieving the bubble-related issue in the catalyst is indispensable for OER since the accumulation of bubbles on the surface of the electrode consumes more operating voltage due to the ohmic loss, thus leading to poor efficiency of water electrolysis. This bottleneck can be mitigated by engineering the catalyst's surface to liberate the generated gas bubbles quickly [171]. One of the great methods to develop superaerophobic and nanostructured catalytic layers is electrodepositing of catalyst on a conductive substrate such as NF, which helps to control the morphology and alignment of the structure's building block and crystallinity [175]. This technique's principal problem is developing a deposit with suitable characteristics such as amorphous crystal structure, nanoscale alignment, and hierarchal morphology to exploit the catalyst exposure. Balram and co-workers [176] introduced a mechanism to grow nanodentrite amorphous metal hydroxide on 3D substrate via electrodeposition for the first time. The growth of this nanodendrite particle was expedited by adjusting the water content in the alcoholic deposition solution and employing high deposition voltage. A α-Ni-Co hydroxide deposited on the SS surface presented high OER catalytic activity with ultra-small potential (255 mV) to derive a current density of 10 mA cm^{-2} in 1.0 M KOH basic solution. Interestingly, the novel material showed encouraging stability over 10000 cycles of measurement, which could be stemmed from the superaerophobic nature of the catalytic layer underwater that repelled the produced gas bubbles and synergetic effect of the metals. This novel preparation approach could foster an avenue for future researchers to design new bimetallic hydroxide or oxide materials on other 3D substrates with superior catalytic activity for OER electrode and full water electrolysis electrode construction.

Moreover, it was demonstrated that generating oxygen vacancies in the catalyst structure is paramount to substantially boost the active site's reactivity and offer favorable binding energy to the oxygen intermediates, thus enhancing. However, the development of 3*d* transition metal catalyst that owns both well-defined nanostructures accompanied by abundant oxygen defects/vacancies is yet a perplexing phenomenon [177]. One study of Guo and co-workers [113] recently attempted to fabricate nanostructured materials with rich oxygen defects by doping nickel into cobalt hydroxide, giving CoNi-OH hexagonal nanoplates. It was reported that the existence of Ni in the CoNi-OH was vital to foster OER activity. A three-electrode system was employed to probe the electrocatalytic performance of the prepared materials. Fig. 5(a) shows the polarization curve of four different materials examined in 1.0 M KOH electrolyte using a 5 mV s^{-1} scan rate. The bimetallic NiCo hydroxide-based electrocatalyst unveiled superior OER activity generating a current density of 10 mA cm^{-2} at 238 mV (Fig. 5b), which is much higher than monometallic hydroxide of Ni and Co catalysts and the bare NF. This superior catalytic activity of CoNi–OH/NFs was supported by the lowest Tafel slope of 60.2 mV dec^{-1}, as shown in Fig. 5(c). Besides, long-term measurements were also conducted in chronoamperometry at a voltage of 1.53 V for 7500 s to examine their stability (Fig. 5d), where CoNi-OH/NF maintains a superior current density of 6.25 mA cm^{-2}, suggesting its exceptional stability. Besides, the long-term chronopotentiometry test at a current density of 10 mA cm^{-2} was also conducted to examine further the durability of the catalyst CoNi-OH/NF, where trivial potential change was observed during 40 h continuous measurement (Fig. 5e). These results confirmed an outstanding activity reinforced with the long-term stability of CoNi-OH/NF. Furthermore, various NiCo bimetallic (oxy) hydroxide-based electrocatalysts for OER have been reported and summarily presented in Table 1.

In summary, various NiCo (oxy) hydroxides-based electrocatalysts have been demonstrated to be responsive for OER in alkaline electrolytes. Preparing nanostructured materials with high surface area, tuning the local electronic structure, creating oxygen vacancies, and amorphous nanostructure are among the standard routes employed to obtain a promising electrocatalyst. Superior catalytic can be obtained by growing NiCo (oxy) hydroxides on porous conductive substrates such as NF, CFP. Few researchers have reported that NiCo (oxy) hydroxides-based electrocatalysts can deliver a current density of 10 mA cm^{-2} at a small overpotential (less than

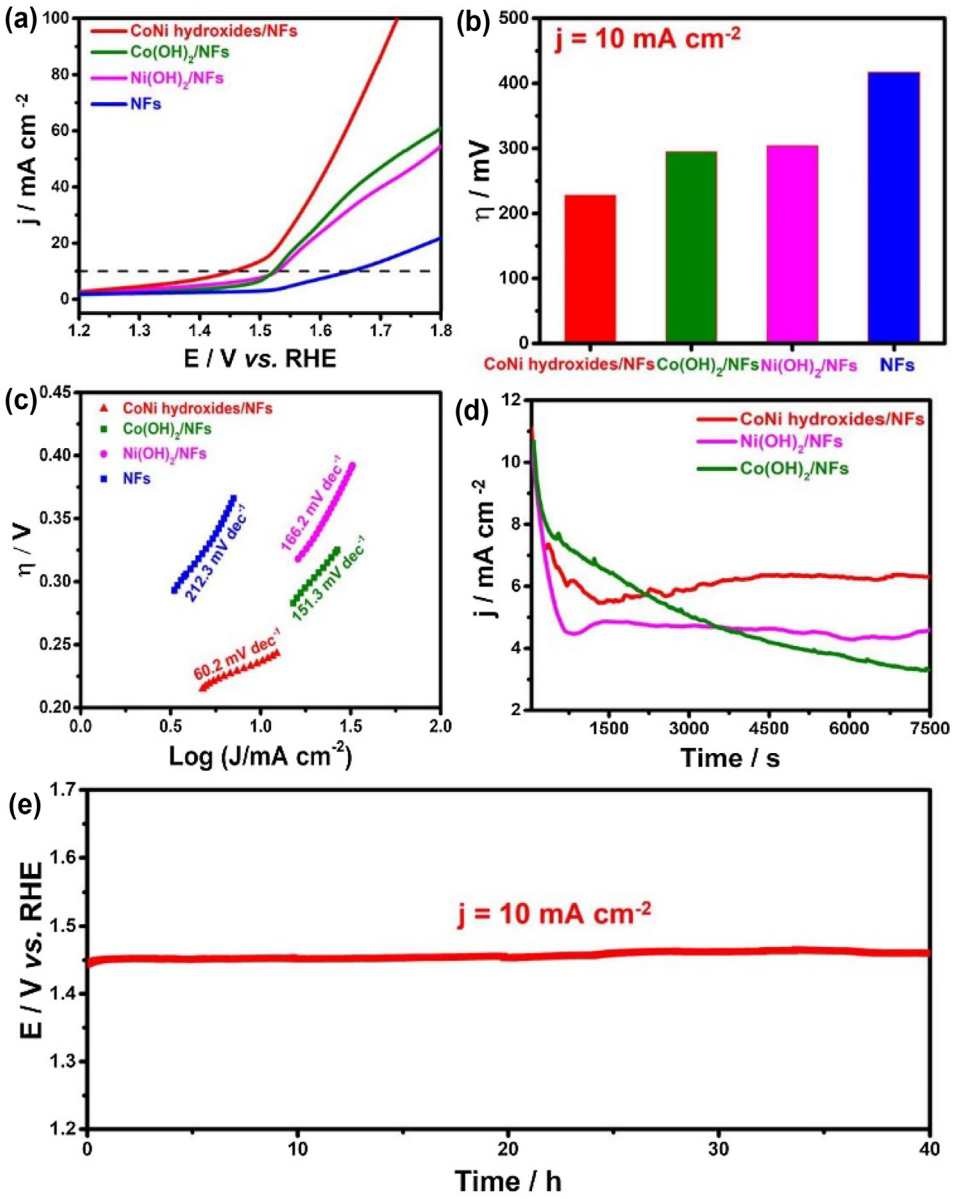

Fig 5. Comparison of OER activity (a) LSV polarization of curve of different materials, (b) comparison of overpotential at a current density of 10 mA cm^{-2}, (c) Tafel slope of the different catalyst, (d) chronoamperometry test of different catalyst at 1.53 V and (e) stability test for OER at a current density of 10 mA cm^{-2} using CoNi-OH/NFs as a catalyst. Reproduced from Ref. [113] with permission from Elsevier.

300 mV). Despite their profound OER activity, preparing a robust electrocatalyst for long-term and large-scale applications is challenging. The catalyst irreversibly or reversibly restructures into another phase during the reaction process, affecting the overall electrochemical performance. Hence, monitoring of catalysts' structure evolution during the reaction is imperative.

5.1.2. NiCo LDHs based electrocatalysts

LDHs based electrocatalysts were demonstrated to be one of the most competing categories of catalysts, presenting an unsettled electrochemical performance in energy storage and conversion, owing to a high active site accessible to the electrolyte solution by anion exchange. The flexibility and modulatory nature of LDHs endow to design of materials with different structures by tuning the cation and anion interlayer [178]. The general chemical formula of LDHs can be represented as $[M^{2+}_{1-x}M^{3+}_{x}(OH)_2]^{+}(A^{n-})_{x/n}{\cdot}mH_2O$, which entails positively charged brucite-like host layers accompanied with interlayer anion and water as charge balancing, enabling it to offer distinctive redox characteristics [179]. Few studies indicated that LDHs prepared using Ni/Co can be a tempting electrocatalyst for the OER system. In this frame, usually, catalysts are in situ grown onto the porous substrate (NF, SSM). This is essential to expedite electron transfer, boost electrolyte penetration to the porous architecture, and enrich ECSA [180]. For example, Jiang and co-workers [116] prepared NiCo LDHs electrocatalyst using NF as a substrate via a simple solvothermal process. Briefly, metal precursors of Ni and Co were dispersed in a mixture of methanol and distilled water, followed by adding clean NF for subsequent thermal treatment. Then, the active metals are in situ grown on the 3D macroscopically porous NF substrate. The prepared catalyst showed a remarkable activity toward OER, offering a low onset potential of 290 mV and a large current density with excellent stability for about 4000 s. Such high catalytic activity can result from the unique layered structure, interconnected layers with peculiar redox features of the NiCo-LDH nanosheet. Although this study brought a remarkable achievement, the catalytic activity of NiCo LDHs is limited by

Table 1
State-of-the-art review of Ni-Co-(oxy) hydroxide based electrocatalysts for OER.

Electrocatalyst	Substrate	Overpotential (mV) @10 mA cm^{-2}	Tafel slope (mV dec^{-1})	Synthesis method	Catalyst loading (mg cm^{-2})	Stability	Ref.
Ni_3S_2@$Co(OH)_2$	NF	330	53.2	Solvothermal	6.1	Stable for 20 h during CP[e] test at η_{10}[f] of 330 mV	[97]
$Ni_xCo_{1-x}(OH)_2$	NF	270	59	Hydrothermal	1.0	Nearly stable for 10 h, tested at 1.55 and 1.58 V @ 30 and 100 mA cm^{-2}.	[139]
SL[a]- $Ni_xCo_{1-x}(OH)_2$	GC[c]	329@5	49	Hydrothermal	0.02	Showed good stability for over 3000 s	[171]
α-Ni-Co hydroxide	–	255	24	Electrodeposition	–	Stable during 10,000 cycles at η_{10} of 255 mV	[176]
ML[b]- $Ni_xCo_{1-x}(OH)_2$	GC	341@5	54	Hydrothermal	0.02	Remained stable for few hours, deposited 1.2 μg of catalyst in GC (3 mm diameter)	[171]
$[Ni^{(2+/3+)}Co_2(OH)_{6-7}]_x$	ITO[d]	460	145	Electrodeposition	–	Remained stable during 1000 cycles of accelerated stability test,	[172]
Ni-doped Co $(OH)_2$	NF	238	60.2	Hydrothermal	–	Stable for over 40 h, tested at η_{10} of 238 mV	[113]
$Co_{0.75}Ni_{0.25}(OH)_2$	CFP	235	56	LAL	0.2	95% retention after 12 h	[114]
$Ni_{0.25}Co_{0.75}(OH)_2$	GC	352	72	Hydrothermal	0.1	Remained stable for over 12, tested at 1.60 V to produce 12 mA cm^{-2}.	[115]

[a] SL: single layer; [b] ML: multilayer; [c] GC: glassy carbon; [d] ITO: indium tin oxide; [e] CP: Chronopotentiometry; [f] η_{10}: overpotential at 10 mA cm^{-2}

its low electrical conductivity and durability. Also, there is inevitable aggregating and restacking of nanosheets. One typical route to overcome this problem is impregnating conductive substances such as metal and carbon to LDH materials. In another study, Xiang and co-workers [181] prepared novel 2D NiCo-LDH@NiCo-hydroxysulfide (NiCo-LDH@HOS) heterostructure nanosheets using NF as substrate by fast (30 s) in situ surface sulfurization of the NiCo-LDHs in Na_2S solution at ambient temperature. The electrochemical performance of the as-prepared NiCo-LDH@HOS electrocatalyst for the alkaline OER process is shown in Fig. 6(a–d). The

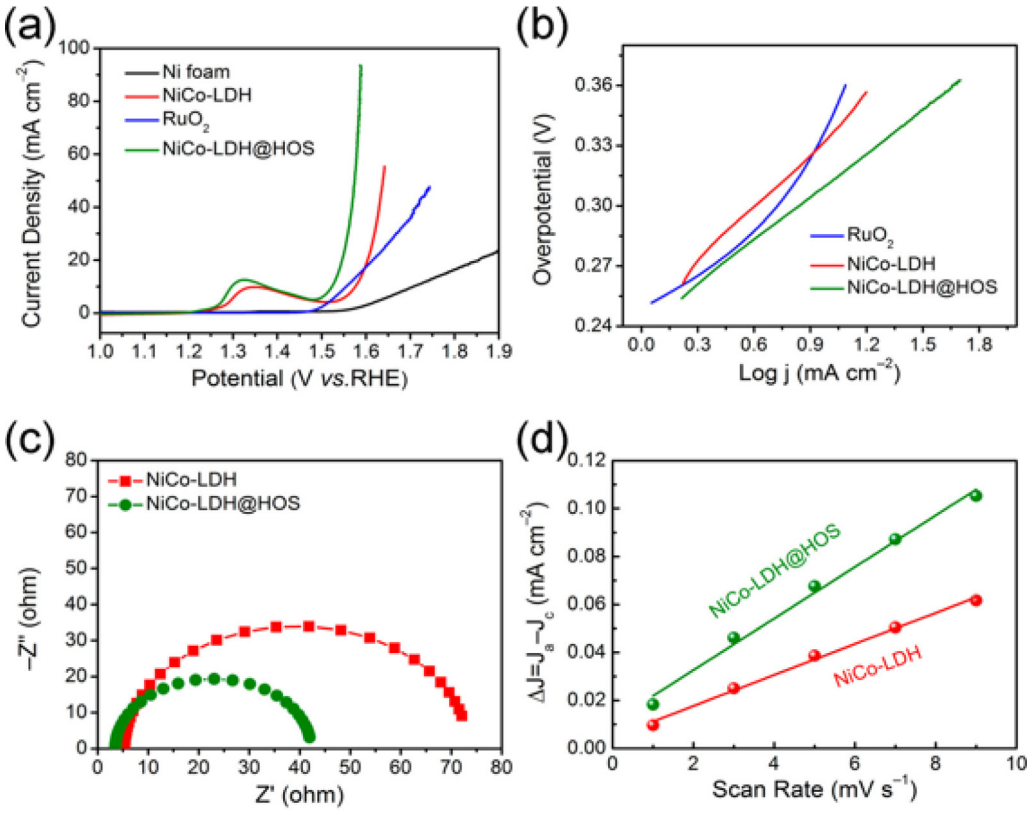

Fig 6. Schematic diagram of (a) polarization curves of various catalysts in 0.1 M KOH, (b) comparison of Tafel slopes of various catalysts, (c) EIS spectra of different electrodes, (d) graph the current density vs. the scan rate. Reproduced from Ref. [181] with permission from American Chemical Society.

figure explicitly compares the performance of the various prepared catalysts and the precious and commercial catalysts of RuO_2. The electrode catalytic activity of the NiCo-LDH@HOS exhibited excellent performance and stability for OER, demanding a low overpotential of 293 mV to obtain 10 mA cm^{-2} current density in 0.1 M KOH electrolyte and stable during 62 h continuous measurement. This galvanized OER activity and stability are higher than that of NiCo-LDH nanosheets and reference RuO_2 catalyst. The excellent electrocatalyst activity NiCo-LDH@HOS can be credited to the NiCo-hydroxy sulfides layer, which remarkably stimulates the electrical conductivity, thus boosting active sites' reactivity. Besides, Yu and co-workers [182] prepared NiCo-LDH material supported on CFP substrate without a binder. Carbon fiber is used as a current collector, and its robust feature is essential for stimulating mass diffusion and electron transport. The as-prepared NiCo-LDH nanoarrays exhibited a low overpotential of 307 mV to derive a current density of 10 mA cm^{-2} in an alkaline medium. Such superb activity was claimed to be originated from the large surface area arisen from the vertically aligned LDH nanoarrays, which promote intimate contact of the electrolyte with the catalytic layer. A breakthrough and an exceptional NiCo-LDH based electrode material were prepared by growing on 3D nickel–cobalt foam substrate [183]. N_2 and argon radio frequency plasma reformed the microstructure and physicochemical character of the NiCo-LDH. The plasma was helpful to nitridize the material, leading to improve electrocatalyst activity. The overpotential required to derive a current density of 10 mA cm^{-2} was only 190 mV in a 1.0 M KOH electrolyte solution. This novel material with ultra-small overpotential was able to outmaneuver numerous transition bimetallic-based electrocatalysts utilized for alkaline OER application. Other NiCo-LDH based electrode materials were also reported to be an effective and high catalytic performance for alkaline OER [119,183,184].

Moreover, it was explored that the active site of transition metals is predominantly found at the edge sites. The metals' electrochemical reaction site is stalled by the close pack basal planes. Therefore, working on the basal planes is essential to boost the materials' catalytic activity [185]. One possible route to galvanize the basal planes is through defect engineering and the nanostructure of the materials. Preparing 2D nanosheet-based LDH electrode material can galvanize the OER catalytic activity. For example, Song and co-workers [186] synthesized a nanosheet of NiCo LDH catalyst by exfoliation of bulk NiCo LDHs. Metal (oxy) hydroxide consists of edge-sharing octahedral MO_6 layers. The exfoliation helps to expose the edge-sharing MO_6 octahedral layers (which are the active sites) separated from the bulk materials.

After anion exchange, the prolonged inter-layer space endowed the bulk NiCo LDH materials delamination into a single layer nanosheet, which was confirmed by laser beam irradiation of the solution. Besides, the non-appearance of [00*n*] growth plane peak in the X-ray diffraction (XRD) pattern indicates single layer nature. The exfoliated NiCo LDHs showed a remarkable higher OER activity in 1.0 M KOH electrolyte, using an overpotential of 300 mV, a 3.4 fold of current density increment was recorded and compared with the bulk NiCo-LDHs. The excellent OER activity of the nanosheets compared with the bulk LDHs was probed due to proliferated several active edge sites and superb electronic conductivity while maintaining similar ECSA. Similarly, Jiang and co-workers [116] prepared NiCo-LDH nanosheet with improved OER catalytic activity in an alkaline environment. The electrode materials were prepared by in situ directly growing of bimetallic NiCo-LDHs on a substrate of NF. The substrate with a peculiar porous structure and meander architecture was essential to increase the active surface area. The nanosheet of NiCo-LDHs with the layered arrangements is interconnected to the surface of NF, forming 3D nanoarray networks which maintain both excellent structural stability and electrical connection, facilitating electron transport. It disclosed an appealing OER activity (670 mV@50 mA cm^{-2}) exceeding the commercial RuO_2 electrocatalyst. Besides, Liang and co-workers [187] reported NiCo-LDH nanoplate with an enhanced activity that was prepared via high pressure hydrothermal continuous flow reactor. The nanoplate materials offered a current density of 10 mA cm^{-2} at a small overpotential (367 mV) in 1.0 M KOH. Furthermore, remarkable stability has been achieved at 1.593 V, generating a current density of 10 mA cm^{-2}. After 6 h, the amount of potential required to generate the same current density has somewhat increased to 1.615 V. The superb OER activity could be stemmed from the high surface area and high content of putative active sites. Besides, X-ray photoelectron spectroscopy (XPS) confirmed that the NiCo-LDH nanoplate that was formed by exfoliation of bulk materials was found with a significant change in its electronic structure.

Overall, CoFe based electrocatalysts are among the most active for alkaline OER due to their high active site accesses to the electrolyte solution by anion exchange. Similar to metal hydro(oxy)oxides, LDHs contain stacked layers of edge shared octahedral MO_6. However, LDHs consist of positively charged brucite-like host layers and charge-balancing interlayer anions, differing from metal hydro(oxy)oxides. The flexible and tunning nature of LDHs enables designing materials with numerous structures by modulating the cation and anion interlayer. The close basal planes restrict NiCo-LDHs during water oxidation. Creating defects and nanostructured materials can circumvent such problems. The intercalated anions and water between the layers and various metals cations create larger interlayer space with peculiar redox characteristics. Such a unique structure enables to obtain super electrochemical performance. Some efforts have been made in preparing NiCo-LDHs for OER, and good performance has been achieved in both activity and stability. Table 2 presents some of the NiCo-LDH electrocatalysts employed for alkaline OER.

5.1.3. NiCo oxide-based electrocatalysts

Spinel oxide-based electrocatalysts have shown a tremendous performance for water oxidation because their peculiar physical and chemical properties stemmed from the tunable cations in the structure. The general formula of spinel oxide is expressed as AB_2O_4, where A and B are cation metals with tetrahedral and octahedral coordination, respectively [191-193]. Metal oxide and spinels are characterized by their surface-rich chemistry resulted from their various oxidation state. They are also known for their durability in an alkaline environment and have palpable electrical conductivity [194]. There are two types of spinel structures depending on the location of the metals in the crystallographic site (octahedral (O_h) and tetrahedral (T_d) sites). Spinel structure with the formula of $(A^{2+}_{Td})\ (B^{3+}_{Oh})_2\ O_4$ in which divalent cation resides in the tetrahedral site is known as normal spinel. The second type is called inverse spinel with a configuration of $(A^{2+}_{Oh})\ (B^{3+}_{Td})\ (B^{3+}_{Oh})_2\ O_4$, where divalent cation A^{2+} is located in the octahedral site. Unlike in perovskite, transition metals can be found in both tetrahedral and octahedral sites, leading to acquiring different d-band splitting frameworks [195,196]. Besides, in a spinel structure, electron hopping can take place between the different oxidation states that eventually enhance electrical conductivity [69]. Substantial research work has been conducted in the preparation and characterization of spinel oxide for OER electrocatalyst. Cui and co-workers [197] prepared a spinel oxide of $NiCo_2O_4$ nanoplatelets via a co-precipitation decomposition strategy using NaOH as a precipitant. By adjusting the molar ratio of the Ni and Co precursors, controlling the operating temperature and time, a spinel with a core-ring $NiCo_2O_4$ nanoplate was obtained (Ni/Co = 1:4 and decomposed at 200 °C for 1 h), which was confirmed by high-resolution transmission electron microscopy (HRTEM). A considerable Co content was observed in the inner core of the nanoplates, and the surface of the edge was found retaining Ni

Table 2
State-of-the-art review of NiCo-LDH based electrocatalyst for OER.

Electrocatalyst	Substrate	Overpotential (mV)@10 mA cm^{-2}	Tafel slope mV dec^{-1}	Synthesis method	Catalyst loading (mg cm^{-2})	Stability	Ref.
NiCo-LDH@HOS	NF	293	72	Hydrothermal	0.45	Overpotential increased by only 2.4% after 62 h of stability test	[181]
Co_9S_8@NiCo LDH	NF	278@30	103	Hydrothermal	1.8	Slight increase of overpotential after 12 h	[188]
NiCo LDHs	NF	367	40	Hydrothermal	0.17	Slightly increased from 1.593 to 1.615 V to produce 10 mA cm^{-2} after 6 h test	[187]
NiCo-LDH NS[a]	NF	420	113	Solvothermal	1.76	Steady current density at potential of 1.52, 1.76, and 1.96 V for about 4000 s.	[116]
NiCo-LDHs	GC	314	77	Solvothermal	0.35	Remained stable for over 8 h with 1.48% loss of potential.	[189]
3D-NICo-LDHs	SSM	270	61	Electrodeposition	–	85% current retention after 36 h test	[190]
N-doped NiCo LDHs	Carbon rod	190	123	PECVD[b]	–	Stable for 24 h at η of 190 mV	[183]
NiCo-LDH nanoplates	CFP	307	64	Wet thermal	0.8	Stable after 20 h testing at J[c] of 100 mA cm^{-2}	[182]
NiCo LDHs	GC	290	31	Co-precipitation	0.2	8.38% current loss after 30 h test	[119]
NiCo-LDHs	NF	334	41	exfoliation	1.0	nearly constant during 13 h test at J of 10 mA cm^{-2}	[186]
NiCo-LDH NSs	CFP	299	45	Hydrothermal	0.467	Stable for 10 h; at the potential of 1.53 V.	[191]
NiCo-LDHs	NF	271	72	Wet thermal	1.0	Showed 17 mA cm^{-2} stable current at 1.76 V for 18 h during water splitting	[140]

[a] NS: Nanosheet; [b] PECVD: plasma-enhanced chemical vapour deposition; [c] J: current density.

and Co at a molar ratio of 1:2. The peculiar core-ring nanostructure endows an enhanced active surface area and an abundant number of the active site of Co atoms, which remarkably stimulated the OER activity. Consequently, a small overpotential of 315 mV was required to generate a large current density of 100 mA cm^{-2} using core-ring $NiCo_2O_4$ as anodic materials for alkaline OER. In comparison, a large overpotential of 438 mV was claimed to reach the same current density using $NiCo_2O_4$ without a core-ring structure. The high electrocatalytic activity of the core-ring $NiCo_2O_4$ could be emanated from the high roughness factor (R_f = 870 ± 23) and high capacitance (C = 52.2 ± 1380 μF m^{-2}), which was higher than $NiCo_2O_4$ (without core-ring) with a roughness factor of 445 ± 8 and capacitance of 26.7 ± 480 μF m^{-2}. Shi and co-workers [87] prepared $NiCo_2O_4$ directly grown on FTO substrate. The electrochemical water oxidation potential of $NiCo_2O_4$ with needles and nanosheets was investigated. The anode with $NiCo_2O_4$ nanoneedle catalytic layer presented a noticeable performance, endowing a current density of 10 mA cm^{-2} at 223 mV of overpotential. State-of-the-art NiCo oxide and spinel-based electrocatalyst with their corresponding OER performance are summarized in Table 3. Recently, Alegre and co-workers [126] prepared an exceptional spinel bimetallic $NiCo_2O_4$ electrocatalyst for alkaline OER. An ultras-mall over-potential of 223 mV was observed to derive a current density of 10 mA cm^{-2}, which is hyper-performance compared with other bimetallic materials and even outshined for the state of the art precious metals employed for OER. The high performance was believed to be originated from the high oxidation state of the active metals (Ni and Co with + 3 oxidation state) and well-defined crystallographic structure.

Preparing electrocatalyst materials reinforced with 2D or 3D configuration could stimulate the catalytic activity for the electrochemical water splitting process because 2D and 3D substrates offer the maximum number of active units and upsurges the contact area with the solution. For example, Yan and co-workers [198] prepared $Ni_xCo_{3-x}O_4$ nanowires directly grown on NF conductive substrate by hydrothermal reaction. The as-developed $Ni_xCo_{3-x}O_4$ nanowires showed a remarkable potential for the OER process, attained a current density of 10 mA cm^{-2} by applying an overpotential of 335 mV. This high OER catalytic is ascended from the coupling effect of the material's two metal and amorphous oxide nature. In 2017, Deng and co-workers [199] prepared well-ordered mesoporous NiCo oxide via the nano-casting technique. At an optimum composition ratio of 4:1 (Co/Ni), CoNi was turned to be the most effective for alkaline water oxidation; an overpotential of 336 mV was required to fetch a current density of 10 mA cm^{-2}, which overwhelmed several other reported bimetallic electrocatalysts. Electrochemical measurements divulged that the embedded nickel was responsible for boosting the catalytic activity. The XPS characterization revealed that the content of $Ni(OH)_2$ species was augmented after testing for OER. Besides, Zhao and co-workers [75] prepared a hollow CoNi oxide microsphere anchored by nanosheet by controlling Co/Ni molar ratio via the self-template technique. The chemical composition and size of the hollow voids of the prepared materials can be modulated using the bimetallic precursors. The optimum Co_2-Ni_1-O material exhibited an overpotential of 310 mV to develop a current density of 10 mA cm^{-2} and a small Tafel slope of 57 mV dec^{-1} in 1.0 M KOH. The high performance for OER is stemmed from the large ECSA, and the charge conduction is enhanced due to the coupling effect of the two metals.

On the other hand, it was established that materials with a nanostructured framework exhibit a hyper catalytic wave of activity for OER process due to their peculiar architecture and chemical composition [200]. One way to fabricate nanostructured materials is based on a template. Wu and co-workers [74] synthesized nanostructured $NiCoO_x$ anchored on SS via electrodeposition method using silica as a template. Shortly, the NiCo-SiO_2 composite film was first synthesized through potentiostatic. Then, the silica template was chemically etched, and the bimetal NiCo was liberated and formed $NiCoO_x$ layer while scanning by CV in the alkaline medium. The prepared materials revealed a galvanized catalytic activity for OER, which demanded a 326 mV of overpotential to generate a high current density of 100 mA cm^{-2} in 1.0 M KOH medium accompanied with excellent stability for about 20 h. Besides, Elakkiya and co-workers [82] prepared nanoporous $NiCo_2O_4$ spinel with a flower-like structure for water oxidation. The nanoscaled spinel oxide materials with high ECSA, high porosity, and enriched active site exhibited a considerable OER and HER activity in alkaline medium, furnishing higher current density at lower overpotential.

Moreover, various NiCo bimetal oxide and spinel with nanostructured framework have been reported and showed a remarkable potential for sustainable OER [87,201-203]. In general, oxides, including spinels, are among the widely investigated mate-

Table 3
State-of-the-art review of NiCo Ni-Co-(oxy) hydroxide and oxide based electrocatalysts for OER.

Electrocatalyst	Substrate	Overpotential (mV)@10 mA cm^{-2}	Tafel slope (mV dec^{-1})	Synthesis method	Catalyst loading (mg cm^{-2})	Stability	Ref.
$NiCo_2O_4$ nanoneedles	FTO	323	292	Hydrothermal	0.53	Stable current density for 3 h	[87]
$NiCo_2O_3$@OMC[n]	GC	281	96.8	Solvothermal	0.567	Stable for 230 h	[204]
Core-ring $NiCo_2O_4$	Ni	315 @ 100	54	Co-precipitation	–	–	[197]
$NiCo_2O_4$/CNT-150	TFS[a]	360	129	Hydrothermal	7.3	Showed good current density stability after 3000 s.	[205]
Core-shell C/$NiCo_2O_4$	CC	168	57.6	Hydro/solvothermal	0.875	Showed stable potential after applying constant density of 10 mA cm^{-2}	[86]
NiCoalloy@C/$Ni_xCo_{1-x}O$/NF	NF	300	106	Solvothermal	0.32	–	[83]
$NiCo_2O_4$/NiO	GC	360	61	Hydrothermal	1.06	Unchanged current density for 11 h	[206]
HM[b] $NiCo_2O_4$ NP	GC	340	75	Template based	0.25	After 500 cycles, 20 mV increase of potential to generate 10 mA cm^{-2}	[202]
$NiCo_2O_4$-rGO	GC	390	63	Two-step solution	0.24	At 1.66 V maintains 94% of its original current density after 1000 CV cycles,	[207]
NiCo-$NiCoO_x$	SS	389	74	Deposition	–	Stable current density of 100 mA cm^{-2} for 20 h	[74]
$NiCo_2O_4$ 3D nanosheet	GC	360	50–60	Solvo/hydrothermal	0.4	Stable current density of 10 mA cm^{-2} for about 5 h	[208]
CS-Ni-Co NWN[c]	CFF[d]	302	43.6	Hydrothermal	–	Stable *J* of 10 mA cm^{-2} for 10 h	[209]
$NiCo_2O_4$/GNs[e]	GC	383	137	Solvothermal	–	Retained 47.1% of current density after 1 h operation	[210]
$NiCo_2O_4$@C	–	267	46.5	Hydrothermal	–	Potential increased from 1.50 to 1.55 V to produce *J* of 10 mA cm^{-2} after 30 h	[211]
$NiCo_2O_4$ NW	FTO-GP[f]	460	90	Hydrothermal	1.0	Stable *J* for over 10 h	[212]
$NiCo_2O_4$ nanoframe	GC	265	82	Hydrothermal	–	Stable *J* of 10 mA cm^{-2} for 10 h	[203]
HU[g]-$NiCo_2O_4$	GC	419.3	51.3	Thermal decomposition	0.069	Trivial decrease of anodic current after 1200 cycles	[213]
Ni-Co_2-O-HNSs[h]	GC	362	64.4	Thermal decomposition	0.2	–	[214]
$NiCo_2O_4$ PN[i]	PtF[j]	264	89.8	Hydrothermal	–	Almost no change of *J* at overpotential of 264 mV for over 12 h	[215]
N-doped graphene $NiCo_2O_4$ film	Graphene films	373	156	Heterogeneous reaction	–	Less than 10% anodic current loss after 1000 cycles	[216]
Co/Ni 4/1	GC	336	36	Nano-casting	2.0	Stable-current density of 10 mA cm^{-2} for 14 h	[199]
$NiCo_2O_4$	GC	398	49	Hard template	0.55 μg cm^{-2}	Stable current density of 10 mA cm^{-2} for 3 h	[194]
Co_2-Ni_1-O	NF	310	57	Solvothermal	1.0	6% current density loss after 12 h	[75]
$NiCo_2O_4$	CNF[k]	223	–	Electrospinning	–	Stable current density for over 24 h	[126]
Ni-Co-OH/$Ni_2P_2O_7$	NF	197	63	Chemical	–	Durable current density for over 12 h	[217]
Ni-Co_3O_4	GC	300	82	Aqueous chemical growth	–	Excellent stability of *J* for about 40 h	[218]
NP[l]-$NiCo_2O_4$	NF	360	150	Hydrothermal	0.12	Stable current density for about 10 h	[82]
$Ni_1Co_1O_2$ NWs[m]	GC	248	41.8	Hydrothermal	–	A slight shift of potential after 48 h test	[201]
$Ni_xCo_{3-x}O_4$	NF	335	75	Hydrothermal	0.7	A slight *J* decrease after 6000 s operation	[198]
NiO_x/$NiCo_2O_4$/Co_3O_4	Ni	315	76	De-alloying	–	Stable current density of 10 mA cm^{-2} for 12 h.	[219]
$NiCoO_x$-400	GCE	280	74	Hydrothermal	–	Stable current density at 1.5 V for over 3000 s	[220]

[a] TFS: Ti foil substrate; [b] HM: Hollow mesoporous; [c] CS/NWN: carbon-shelled/nanowire network; [d] CFF: carbon fiber fabric; [e] GNs: graphene nanosheets: [f] FTO-GP: fluorine-doped tin oxide glass plate; [g] HU: hollow urchins; [h] HNS: hollow nanosponges; [i] PN: porous nanotubes; [j] PtF: platinum foil; [k] CNF: carbon nanofiber; [l] NP: nanoporous; [m] NW: nanowires, [n] OMC: ordered mesoporous carbon.

rials for OER using NiCo bimetals. Substantial progress has been advanced in preparing NiCo based electrodes for water oxidation. Some of them surpassed the reference electrocatalysts, Ir and Ru. However, preparing NiCo-based oxide catalyst with a high active site, robust structure, and long-term stable for large-scale application is still challenging.

5.1.4. NiCo composite, alloy, and other electrocatalysts

Carbon material and its composites have been reported as a promising alternative to expedite electrochemical reactions in the water-splitting process. Primarily, graphene, carbon nanotube (CNT), and multi-wall carbon nanotube (MWCNT), have been broadly utilized to improve the conductivity of bimetallic electrocatalyst to facilitate the reaction and activity of the catalyst for OER [221,222]. NiCo bimetallic catalysts can be upgraded to their activity by incorporating foreign materials that retain large surface area and porous structure.

Metal-organic frameworks (MOF) have been utilized to construct enormous enhanced bimetallic electrocatalysts for anodic water oxidation. MOFs are notorious for their peculiar large surface area, high carbon content, well-defined structure, and adjusted pore texture. All those properties are very decisive to speed up electrochemical reactions [200,222,223], and many scientists have been extensively working with MOFs and MOFs-derived electrocatalysts for OER application. MOFs were demonstrated to be an essential sacrificial precursor or template to develop an excellent electrocatalyst [224]. Moreover, pristine MOFs were also discovered as potential electrocatalysts. Pristine MOFs contain numerous

redox-active metal centers such as Ni, Co, and Fe and functionalized ligands, expediting electron transfer. Furthermore, the porous structures of MOFs are imperative for mass and electron transfer. However, most pristine MOFs exhibit intrinsic low conductivity due to the inaccessibility of the active center restricted by the surrounding organic ligand and poor electronic coordination between the metal center and organic ligand, which hamper their electrocatalytic performance [225]. Hence, it is essential to mention that the direct employment of pristine MOFs for OER application is still at the early stage, and there is a big room for further improvement.

The recent development and progress made on Ni, Co, and Fe-based pristine MOFs utilized directly for OER can be found elsewhere [225-228]. This review predominantly focuses on two bimetallic NiCo and CoFe based electrocatalysts, including MOF-derived bimetals. Myriads of effort have been made in preparing NiCo MOFs derived electrocatalyst for OER. For example, Zhang and co-workers [229] prepared NiCoP/nitrogen-doped carbon polyhedral nanocage material via chemical etching, and it was found to be an active composite material to expedite the OER process. NiCo based bimetallic zeolite ZIF (ZIF: zeolitic imidazolate framework) polyhedra were transformed into NiCoP/N-doped polyhedral nanocages through tannic acid chemical etching and calcination. Interestingly, the prepared catalyst with a hollow structure exhibited excellent catalytic activity for water oxidation. A current density of 10 mA cm^{-2} was generated using an overpotential of 297 mV and showed appealing long-term stability. In 2018, Yu and co-workers [230] reported a porous hollow NiCoS derived from MOF-ZiF-67. The template of ZIF-67 was vital to fabricate a material with porous hollow architecture. NiCoS was synthesized via the hydrothermal/solvothermal sulfidation reaction method followed by the calcination process. Catalysts with various compositions of NiCoS were prepared and probed their catalytic wave of activity for OER. The as-developed NiCoS-3 exhibited a large surface area of 123 m^2 g^{-1}, which is favorable for exposure of the active sites and ease of transport electrolyte and oxygen, hence promoting the overall catalytic activity. A current density of 10 mA cm^{-2} was achieved using 320 mV of overpotential, which is comparable with the precious metal of RuO_2 (332 mV to reach the same current density) (Fig. 7a), and presented a low value of Tafel slope (Fig. 7b), which indicates favorable kinetic reaction for OER. Also, the charge transfer resistance of NiCoS-3 was determined to be lower than Co_3S_4, highlighting its rapid electron transfer rate (Fig. 7c). Moreover, the long-term stability of the NiCoS-3 electrocatalyst was investigated and exhibited tremendous durability (Fig. 7d). NiCoS-3 electrocatalyst showed insignificant decay (maintained over 95%) of initial current density during 40000 s measurement. Besides, in recent years, myriads of reports have been disclosed offering a profound capability of MOF-derived materials to enhance bimetallic electrocatalyst water oxidation (Table 4).

Moreover, preparing composite materials that comprise heteroatoms assembled with carbon materials can enhance catalytic activity. Singh and co-workers [231] prepared a composite material entailing of bimetals of NiCo doped with nitrogen and porous graphene oxide (NiCo/pNGr) via a hydrothermal reaction. The nitrogen-doped graphene oxide was essential for an excellent dis-

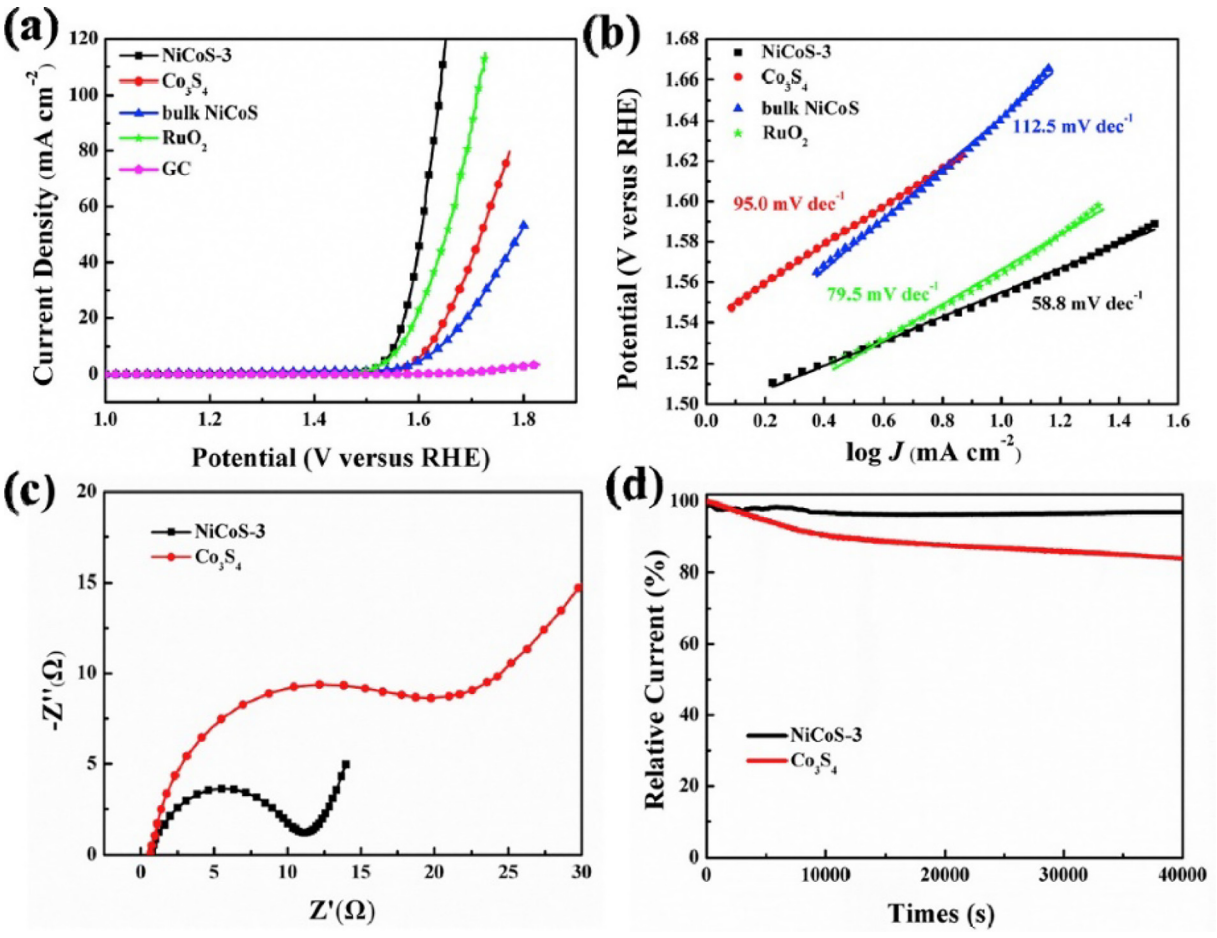

Fig 7. Schematic diagram of (a) LSV curve result of various catalysts tested in 1.0 M KOH, (b) comparison of Tafel slopes, (c) EIS Nyquist plot two selected catalysts, (d) stability test of two selected catalysts using Chronoamperometry. Reproduced from Ref. [230] with permission from Elsevier Ltd.

Table 4
State-of-the-art electrochemical performance of Ni/Co composite and alloy-based electrocatalyst for OER.

Catalyst	Substrate	Overpotential (mV) @10 mA cm^{-2}	Tafel slope (mV dec^{-1})	Synthesis method	Catalyst loading (mg cm^{-2})	Stability	Ref.
NiCo@$NiCoO_x$	SSD[a]	295	31	Hydrothermal	–	Increased its potential from 1.56 to 1.62 V after 20 h tested at *J* of 100 mA cm^{-2}	[235]
NiCoDH/NiCoS	GCE	303@20	77.6	Solvothermal	0.136	Trivial increase of overpotential ($\triangle V$ = 54.6 mV) after 50 h operation	[236]
NiCo-CH	GCE	343	66	Co-precipitation	–	Stable current for about 9000 s, tested at the potential of 1.573 V	[237]
NiCo/pNG_r[c]	GCE	260	87	Co-precipitation	1	30% activity loss after 12 h	[231]
U-NiCo[e]	GCE	387	49	Hydrothermal	0.40	Stable current for 3 h tested at the potential of 1.63 V	[238]
C-NiCo[d]	GCE	430	44	Hydrothermal	0.40	A slight shift of overpotential from 430 to 455 mV at *J* of 10 mA cm^{-2}	[238]
Ni-Co_3O_4 nanosheets	NF	310	59.5	Hydrothermal	0.62	Stable current for about 12 h	[239]
Co_3O_4@Ni_2P-CoP/NF	NF	298@50	75	Hydrothermal	–	Stable current for 40 h, tested at *J* of 1.56 V	[240]
$CoeNi_3C$/Ni @ C	GC	325	112.45	Solvothermal	0.2	A stable current density of 10 mA cm^{-2} at an overpotential of 325 mV after 100000 s	[241]
Ph[f] NiCoS-3 polyhedron	–	320	58.8	Solvothermal	–	Maintained above 95% of its initial current density after 40000 s testing,	[230]
PB[g] Ni-Co Oxide	GCE[b]	380	50	Chemical etching	–	Stable current for 10 h	[242]
$NiCo_2O_4$@NiO@Ni C/SNA[h]	NF	240	43	Hydrothermal	1.66	Stable current density of 20 mA cm^{-2} for over 10 h.	[143]
$Co_{0.5}Ni_{0.5})_3(PO_4)_2$/Ni	NF	273	59.3	Hydrothermal	4.4	Trivial decay after 30 h, tested at potential of 1. 57 V	[141]
NiO/$NiCo_2O$/NF	NF	264	79.3	Hydrothermal	0.5	Showed 9.40% increase of potential after 12 h testing	[142]
NiCoP NWAs[i]/NF	NF	370	54	Hydrothermal	8	Showed good stability for 28 h.	[243]
Ni-Co aerogels	–	184@100	–	Sol gel	–	–	[244]
$NiCo_2O_4$ NrA[l]	NF	320	69.4	Hydrothermal	4.0	Stable at potential of 1.7 V for over 12 h	[245]
$NiCo_2S_4$@$NiCo_2S_4$/NF	NF	200@40	31.1	Hydrothermal	–	Stable current density for over 12 h	[246]
NiCo-PBA[j]/NF	NF	280	97	Hydrothermal	1.9	93% retention of current density after 50 h testing	[247]
CdS@NiCo-LDHs	NF	132	39.3	Chemical oxidation	–	Stable current density for 45 h	[248]
$Ni_{2.3\%}$-CoS_2/CC	CC	370@100	106	Hydrothermal	0.97	Stable current density for 12 h	[249]
NiCoP/C	GC	330	96	Annealing	–	Showed stable current density for 10 h	[200]
NiCoP/NC[m] PHCs[k]	GC	297	51	Chemical etching	0.28	Constant potential of 1.55 V for 10 h	[229]
$NiCo_2O_4$/XC-72	Ni	419.3	51	Hard templating	0.069	Showed stable polarization curve after 1200th cycles.	[213]
$NiCo_2O_4$@$Ni_{0.796}$Co LDHs	NF	193	37.59	Hydrothermal	–	Stable current density of 25 mA cm^{-2}, for over 22 h operation	[233]
NiCo LDH@FeOOH	CFP	224	38	Hydrothermal	–	Superb stability at 100 mA cm^{-2} for 25 h	[234]
$NiCo_2S_4$@Co_1Ni_4-LDHs	CC	337@100	111.2	Co-precipitation	5	A slight shift of potential from 1.56 to 1.59 V after 40 h operation	[250]
Ni/Co_3 O_4@NC	GC	350	52.27	impregnation-calcination	0.2	The polarization curve remained unaltered after 1000 cycles	[251]
NiCo- MOF	NF	270@50	35.4	Solvothermal	–	Stable *J* of 10 mA cm^{-2} for about 30000 s	[252]

[a] SSD: stainless steel disk; [b] GCE: glassy carbon electrode; [c] PNGr: N-doped porous graphene; [d] C-NiCo: cetyltrimethyl ammonium chloride (CTAC) stabilization of $NiCo_2O_4$-NiCo; [e] U-NiCo: urea-stabilized $NiCo_2O_4$-NiCo: [f] Ph: porous hollow; [g] PB: Prussian-Blue; [h] C/SNA: core/shell nanocone Array; [i] NWA: nanowire arrays; [j] PBA: Prussian blue analogues: [k] NC-PHCs: nitrogen-doped carbon polyhedral nanocages; [l] NrA: nanorod arrays; [m] NC: nitrogen-doped carbon.

tribution of bimetal NiCo nanoparticles on the surface of the porous sheet. The porous structure is helpful to bring an extra benefit through the coupling effect of the interacting materials. Besides, dopant N in the porous structure is indispensable to establish synergetic interaction between the two metals of NiCo nanoparticle that tune the material's electronic structure and catalytic activity. The schematic illustration of the synthesis route for the composite material of NiCo/pNGr is shown in Fig. 8. A comparison of NiCo nanoparticle distribution in N-doped porous graphene oxide and without nitrogen doping was explored. It was found that NiCo nanoparticles were well dispersed in N-doped graphene oxide with smaller particle size distribution than in graphene oxide without doping nitrogen. The particle size of NiCo/pGr was found to be in the range of 30–50 nm, while NiCo/pNGr (75:25) as determined to be in the range of 5–10 nm particle size. Such a significant particle size discrepancy could primarily originate from the excellent interaction between the nitrogen-doped porous graphene oxide and the bimetals NiCo synergetic interaction during the preparation process. The prepared composite material of NiCo/pNGr (75:25) showed an insightful electrocatalytic performance for OER, which required a low overpotential of 260 mV to reach a current density of 10 mA cm^{-2} with long term stability. Recently, Zhang and co-workers [232] prepared CoS_2-$NiCo_2S_4$/N, S-co-doped graphene nanosheet (NSG) catalyst using NSG as a conductive substrate, and $CoCl_2{\cdot}6H_2O$ and $NiCl_2{\cdot}6H_2O$ as precursors of Co and Ni, respectively. Briefly, NSG was synthesized following of Hummers' method and hydrothermal route. Then, Ni-Co sulfide/NSG was prepared by dissolving of the NSG, and the Co and Ni precursors in distilled water and thioacetamide were added to that mixture. The prepared catalyst showed an excellent OER perfor-

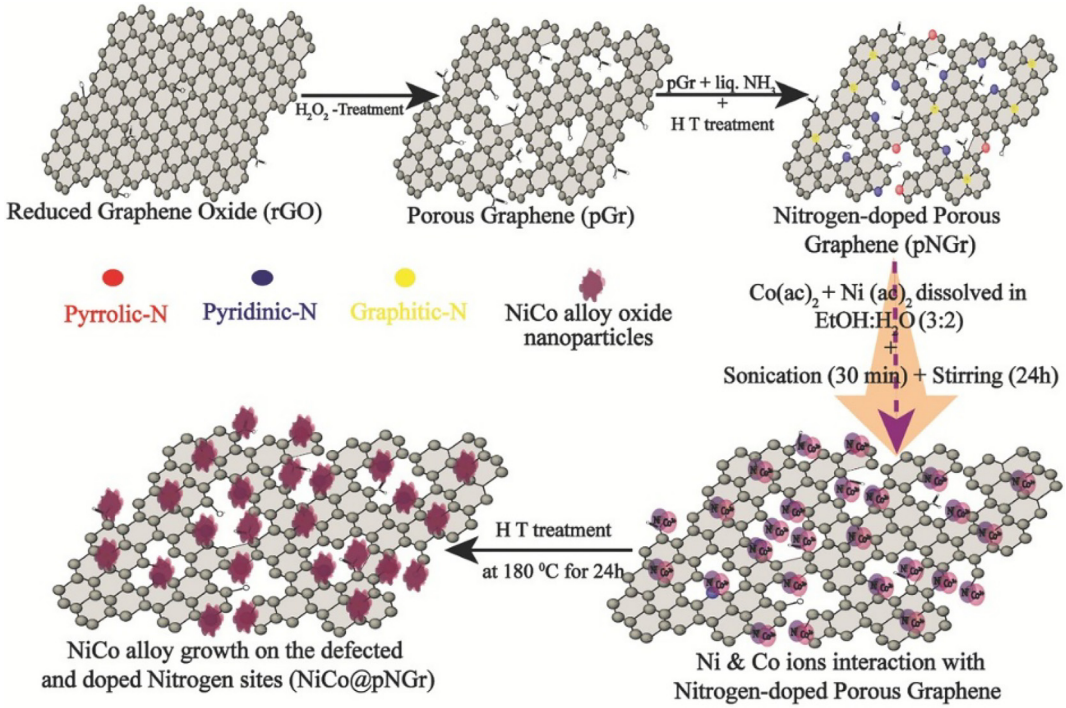

Fig 8. Schematic illustration of the preparation method for composite NiCo/pNGr electrocatalyst for OER. Reproduced from Ref. [231] with permission from WILEY-VCH.

mance with a small overpotential of 272 mV at 10 mA cm^{-2} current density. The hyper-performance of the catalyst could be attributed to the synergetic effect of the bimetallic and the suitable electrical conductive substrate has arisen from the N, S co-doped graphene. CoS_2-$NiCo_2S_4$/NSG electrocatalyst revealed long term stability during 10 h continuous testing at 1.50 V, showing loss of current density just not greater than 1.0%, suggesting that the electrocatalyst is durable and outperformed for the commercial catalyst of RuO_2, which exhibited ca. 6% of current density loss after 6 h during alkaline OER testing [35]. After 2000 cycle operations, CoS_2-$NiCo_2S_4$/NSG displayed a trivial potential increase to obtain 10 mA cm^{-2} current density, mesmerizing their great electrocatalyst wave activity for OER.

In summary, NiCo composite, alloys, and nanostructured based electrocatalyst have shown a tremendous catalytic activity for OER. NiCo bimetallic catalysts can be improved their activity by incorporating foreign materials that retain large surface area and electrically conductive. In this case, preparing NiCo composite doped with carbon, alloy with nanostructure is among the widely practiced methods. Surface engineering, incorporating foreign materials, creating oxygen vacancies, and nanostructure are among the followed routes to improve NiCo catalyst. Excellent electrocatalysts with lower overpotential (less than 250 mV) to derive a current density of 10 mA cm^{-2} have been reported. For example, $NiCo_2O_4$@$Ni_{0.796}Co$ LDHs [233], and NiCo LDH@FeOOH [234] catalyst exhibited an ultralow overpotential of 193 and 224 mV, respectively, to deliver a current density of 10 mA cm^{-2}. However, there is still ample room to investigate these catalysts for practical large-scale application.

5.1.5. N, S, and P doped NiCo based electrocatalysts

Findings revealed that doping/incorporating heteroatom or anions such as P, N, and S into NiCo bimetallic oxide or hydroxide can notably change the electronic structure and improve overall electrochemical performance, including activity and durability in alkaline OER. Modulating the electronic structure helps overcome the kinetic barrier persisted in the material, thus improving the activity [253,254]. It was demonstrated that phosphorization or sulfurization of metals could ameliorate the intermediate reactant's binding energy on the catalytic layer's surface, leading to ideal Gibbs free energy that is crucial for water electrolysis [255-257]. The peculiar e_g orbital occupancy of 3*d* transition metals, including metal phosphide /sulfide, oxide, and hydroxide, trigger them to retain high catalytic activity to adsorb the reactant intermediate (like *OOH, *OH), thus offers superior electrocatalysis [133,257]. Besides, doping of heteroatoms can accelerate the electron transfer from d-band to 2*p* orbitals of those O^{2-} to favor the adsorption potential of OH^- hence revolutionizing the materials' structure. Moreover, incorporation of heteroatom such as N into metals can create a defect or oxygen vacancy in the structure [113] which is vital for the adsorption of the intermediates. Table 5 shows myriads of attempts of bimetallic NiCo electrocatalysts with doped/incorporated heteroatoms of P, N, and S, which present a great OER activity in alkaline electrolytes.

Fang and co-workers [249] prepared $Ni_{2.3\%}$-CoS_2 electrocatalyst by directly growing on CC intended to use for both OER and HER electrodes. The prepared materials uncovered a profound electrocatalytic activity in which a high current density of 100 mA cm^{-2} was obtained using a low overpotential of 370 mV for OER. And also, during overall water splitting measurements, a 1.66 V of cell voltage was necessitated to provide a current density of 10 mA cm^{-2}. Besides, Yu and co-workers [257] reported an enhanced OER activity via bimetallic NiCo doped with phosphorous. At an optimum molar ratio of Ni/Co, $Ni_{0.51}Co_{0.49}P$, it was demonstrated that a small overpotential of 239 mV was required to fetch 10 mA cm^{-2} and exhibited a small Tafel slope (45 mV dec^{-1}) in 1.0 M KOH. Such superb performance was believed to be instigated by the enhanced electrical conductivity that boosted the reaction kinetics and the high surface area resulted from the layered architecture. Moreover, the development of a nanostructured NiCo bimetallic electrocatalyst reinforced with a heteroatom can stimulate the catalytic capability for water oxidation. Liu and co-workers [258] prepared nanowire arrays comprising of $NiCo_2S_4$ directly grown on the substrate of CC. This was obtained by converting

the spinel oxide $NiCo_2O_4$ nanowires into sulfide assembled NiCo bimetallic oxide supported on CC. For the synthesis of the nanowires, a piece of chemical cleaned CC was used to grow $NiCo_2O_4$ arrays on its surface through hydrothermal route. After that, $NiCo_2S_4$ nanowires array was prepared by sulfidation of the previously prepared spinel oxide. A mass of 0.4 mg cm^{-2} was calculated to be the mass load of $NiCo_2S_4$ on the CC. The two prepared materials and commercial RuO_2 were evaluated their OER activity using 1.0 M KOH electrolyte solution, as shown in Fig. 9. It is apparent from Fig. 9(a) that $NiCo_2S_4$ nanowire showed a remarkably higher current density than the $NiCo_2O_4$, which is comparable with RuO_2. The $NiCo_2S_4$ nanowire electrocatalyst generated a current density of 20 and 100 mA cm^{-2}, by applying an overpotential of 280 and 340 mV, respectively. In contrast, $NiCo_2O_4$ nanowires required an overpotential of 390 and 470 mV to reach the same current density. This was also supported with a Tafel slope in which 89 and 90 mV dec^{-1} Tafel slope was determined for $NiCo_2S_4$ and $NiCo_2O_4$, respectively (Fig. 9b). The outstanding OER catalytic activity was attributed to the low resistance of the catalyst that EIS confirmed. Moreover, the high value of capacitance ($NiCo_2S_4$ = 31.5 mF cm^{-2} while $NiCo_2O_4$ = 12.4 mF cm^{-2}) highlights high surface roughness and specific surface area are beneficial for OER process. The novel $NiCo_2S_4$ catalyst showed a trivial current density loss during 500 CV scans in 1.0 M KOH at 2 mV s^{-1} (Fig. 9c) due to its strong morphology integration, which led to good stability for about 12 h (Fig. 9d) [258].

Yan and co-workers [223] reported that Co_4Ni_1P NTs (NTs: nanotubes) electrocatalyst exhibits a remarkable higher catalytic activity and stability in alkaline OER system. Different Co_xNi_yP (x, y = 0, 1, 2, 3, 4, and 9) electrocatalysts were synthesized using two steps of solid-state reaction: (i) Co_xNi_yO was obtained by oxidation reaction at a temperature of 350 °C in air atmosphere, and (ii) Co_xNi_yP was obtained by the phosphorization calcination with NaH_2PO_2 at 300 °C in a nitrogen atmosphere. By varying the molar ratio of Co and Ni in MOFs precursors, different phases of NiCo bimetallic phosphides were synthesized. They noticed that Co_4Ni_1P NTs exhibit superior OER activity and active surface area than Co-P and Ni-P. The Co_4Ni_1P NTs contain nanotube-like structural morphology with crystalline Co_2P and hexagonal NiCoP phases, and it holds a porous structure with a high specific surface area (55.6 m^2 g^{-1}). Co_4Ni_1P NTs showed an outstanding electrochemical performance for alkaline OER, furnishing a current density of 10 mA cm^{-2} at 245 mV. Also, it required a low voltage of 1.59 mV to achieve 10 mA cm^{-2} current density for overall water splitting using both anode and cathode catalyst, which is comparable to the reference electrocatalysts of Pt/C and RuO_2 counterparts. Co_4Ni_1P NTs revealed a trivial decay after 3000 cycles of CV, with low current density decay (97.2% retention) at η of 245 mV operated for 20 h in 1.0 KOH, signifying its excellent stability. Besides, Yan and co-workers [259] prepared bimetallic NiCo nanorod doped with sulfur supported on NF via two-step steps. Firstly, NiCo-OH supported on NF was fabricated by electrodepositing of the metal precursor. Then, NiCoS was prepared by hydrothermal sulfurization of the previously prepared material. It was demonstrated that the bimetallic NiCoS/NF catalyst retained high OER activity compared with CoS_x/NF. A current density of 100 mA cm^{-2} was attained by applying an overpotential of 370 and 390 for NiCoS/NF and Co_xS/NF, respectively. The Tafel slope calculation also supported this. A low Tafel slope of 145 and 157 mV dec^{-1} was obtained for NiCoS/NF and CoS_x/NF, revealing a more favorable reaction kinetic in the bimetallic NiCoS/NF electrocatalyst. Qiu and co-workers [260] synthesized NiCoP nanocage electrocatalyst via template-based technique for electrode water oxidation. By tuning the molar ration of Co/Ni, an optimum electrocatalyst of $Ni_{0.6}Co_{1.4}P$ with nanocage structure was obtained and exhibited an unusual catalytic activity compared with the monometallic complements. It was validated that a low overpotential of 300 mV was demanded to derive an OER current density of 10 mA cm^{-2} with a small Tafel slope of 80 mV dec^{-1}. Density functional theory (DFT) calculation was used to inquiry about the superior performance of the prepared electrocatalyst, which revealed that the optimum molar ratio of Co/Ni was $Ni_{0.6}Co_{1.4}P$. This catalyst enhanced its charge density at the Fermi level. It enabled the d-state more proximal to the Fermi level, thus leading to high charge

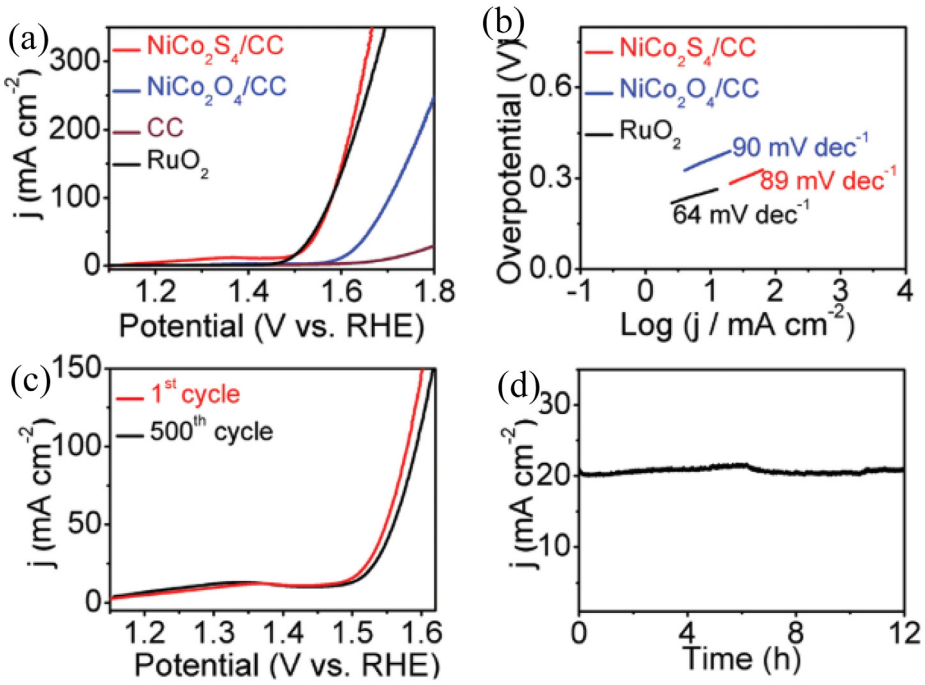

Fig 9. Comparison of OER activity (a) LSV curve of various electrocatalysts in 1 M KOH, (b) Tafel slope of different materials, (c) polarization curve obtained before and after 500 CV cycle at a scan rate of 2 mV s^{-1}, (d) stability test during 12 h continuous measurement. Reproduced from Ref. [258] with permission from the Royal Society of Chemistry.

carrier density and small adsorption energy. In general, nanotube, hollow nanostructure, and nanoparticles own large surface areas, which are essential to contact with the electrolyte solution, thus stimulating electrocatalytic performance. Saad and co-workers [261] observed mesoporous bimetallic catalysts impregnated with nitride enhanced catalytic activity and stability. A silica-based hard template was used to synthesize the 3D ordered mesoporous bimetallic $NiCo_2N$, followed by impregnation, silicon removal, and nitridation process. Due to the large surface area, uniform configuration, accessible pore texture, and improved electrolyte infiltration to the porous structure, the as-developed mesoporous $NiCo_2N$ showed excellent anodic electrode performance for oxygen evolution. For the geometric current density of 10 mA cm^{-2}, a small overpotential of 289 mV was necessitated. This outshines the benchmark catalyst of IrO_2 and the corresponding mesoporous monometallic of Ni_3N and CoN. Qin and co-workers [262] prepared an amorphous 2D nanosheet consisting of bimetallic Ni and Co accompanied with sulphurization. Due to the synergetic effect of Ni and Co, and 2D structure doped with S species, the NiCoS nanosheet exhibited superior catalytic activity for OER with a small overpotential of 280 mV at 10 mA cm^{-2} of current density. The catalyst also showed outstanding durability in a 1.0 M KOH alkaline electrolyte. Besides, NiCoS outperformed for the many electrocatalysts used for overall water splitting with a low overpotential of 1.58 V at a current density of 20 mA cm^{-2} with remarkable prolonged stability. Moreover, other NiCo doped with N, P, and S were reported as active and robust electrocatalysts for the evolution of oxygen in anode electrode [168,232,261,263-265].

Recently, Amorim and co-workers [266] found an optimum bimetallic NiCoP nanowire electrocatalyst for OER by controlling the molar ratio of the metal precursors. They found that the bimetallic CoNiP nanowire with a molar ratio of 1:1 disclosed the best performance in OER measurements, reached 10 mA cm^{-2} current density with an overpotential of 301 mV. A high value of TOF (0.022 s^{-1}) was obtained at an overpotential of 350 mV, which outstrips many other reported bimetallic catalysts and the precious metals utilized for OER. The superior value of TOF of the prepared materials denotes its high intrinsic OER activity. Besides, nitrogen-doped bimetallic nanostructured materials have also shown an extraordinary competency for OER. More recently, a discovery ultra-small an overpotential of 214 mV was recorded to derive a current density of 10 mA cm^{-2} using Ni_2Co-N as anode electrode for OER, which exceeded the myriads of transition metals used for OER and also for the commercial RuO_2 and IrO_2 electrocatalysts [267]. According to Table 5, the breakthrough and the lowest overpotential ever is reported with an overpotential of 133.8 mV to

Table 5
Electrochemical performance of Ni-Co S/P/N based electrocatalyst for OER.

Catalyst	Substrate	Overpotential (mV)@10 mA cm^{-2}	Tafel slope (mV dec^{-1})	Synthesis method	Catalyst load (mg cm^{-2})	Stability	Ref.
NiCoS	GC	280	112	Solvothermal	–	A slightly decrease of *J* after 15 h	[262]
$NiCo_2S_4$	CC	336@20	141	Hydrothermal	0.43	Stable *J* of 20 mA cm^{-2} for 12 h	[258]
Co_4Ni_1P NTs	–	245	61	Solid-state reaction	0.28	Stable *J* at potential of 1.55 V for over 10 h	[223]
$NiCo_2S_4$	GCE	337	64	Solvothermal	0.07	Trivial decay of *J* after 30 h operation, and 95.8% of FE	[269]
Co-Ni(1:1)/PI-CNT	GCE	365	59	Electrodeposition	–	Stable *J* of 10 mA cm^{-2} for 8 h	[270]
$Ni_{0.51}Co_{0.49}P$	NF	239	45	Electrodeposition	–	Stable *J* of 10 and 50 mA cm^{-2} for 100 h	[257]
Co-Ni hybrid oxides	ITO	203	87	Co-precipitation	–	Stable *J* of 20 and 40 mA cm^{-2} for 10 h	[263]
$CoNi_xSy$/NCP	GCE	280	71	Co-precipitation	2.5	Only 3.151% current reduction after 10 h operation	[264]
NiCo-$NiCoO_2$@NC	GC	318	136	Hydrothermal	0.26	After 12 h testing, 93.8% retention of current density	[271]
NiCoS/NF	NF	370@100	145	electrodeposition	–	no apparent decrease of *J* for over 10 h	[259]
NiCo/NiCoP	GC	290	55	hydrothermal	0.25	After 20 h operation and 1000 CV cycles, little decay was observed	[265]
NiCo/						$NiCo_2S4$@NiCo NF	
294	59.6			Electrodeposition	–	Superb stability for over 100000 s operation	[272]
Ni_1Co_1-P	NF	300@35	71	Wet thermal	0.35	Stable *J* for over 12 h	[222]
$CoNi_2S_4$	NF	328	129	Solvothermal	3.8	Constant potential after 10 h operation	[273]
Co_4Ni_1P	GC	245	61	Solid state reaction	0.19	Retention of 97.2% and 95.7% of the initial current was obtained for 10 and 20 mA cm^{-2} after 20 h operation	[223]
$Ni_{0.6}Co_{1.4}P$ nanocages	GC	300	80	Pearson's-HSAB[a]	0.35	a decay 10% in the current density after 10 h	[260]
$NiCo_2N$	GC	289	56	Nanocasting	0.2	–	[261]
$Co_xNi_{1-x}S_2$	GC	290	46	Solvothermal	0.285	Less than 5% current loss observed after 10 h operation	[274]
Ni_2Co-N	CC	214	53	Hydrothermal	2.0	Merely 3.3% increase of overpotential was exhibited after 60 h operation	[267]
Ni_{10}-CoPi	GC	320	44.5	An oil –phase	0.35	Stable *J* of 20 mA cm^{-2} was retained for 20 h with less than 5% decay	[275]
CoNiPP-600	NF	264	60	Hydrothermal	–	Only 3.46% current losses after 10 h	[276]
$Ni_{2.3\%}$-CoS_2	CC	370@100	106	Hydrothermal	0.97	91% *J* retention after 12 h operation	[249]
CoS_2-$NiCo_2S_4$/NSG	GC	272	62.8	Hydrothermal	0.22	After 10 h operation, a trivial *J* loss of 2.4 and 1.0% was observed for *J* of 10 and 50 mA cm^{-2}, produced at potential of 1.50 and 1.62 V, respectively	[232]
$Ni_{4.3}Co_{4.7}S_8$	NF	133.8@20	194.2	Hydrothermal	4	Good stability for about 8 h	[268]
NiCoP-NWAs	NF	270@20	116	Hydrothermal	8	On the 1st 20 min, the potential increased from 1.35 to 1.52 V and remained stable for 28 h	[243]
$NiCo_2S_4$ NW/NF	NF	260	40.1	Hydrothermal	–	Showed 85% of its initial activity retention after 50 h	[277]
NiCoP	Ti foil	310	52	One-pot hot-solution	–	Slight decrease of *J* of 10 mA cm^{-2} after 8 h operation	[278]
$Co_2NiS_{2.4}(OH)_{1.2}$	GC	279	52	Precipitation	0.25	long-term durability at *J* of 10 mA cm^{-2} for about 28000 s	[279]

[a] HSAB: hard and soft acid-base.

derive a current density of 20 mA cm^{-2}.which was achieved by bimetallic sulfide of $Ni_{4.3}Co_{4.7}S_8$ [268] (Table 5). This could be an essential avenue to design and develop an affordable, active, and stable electrocatalyst for large-scale water electrolysis applications that could substantially substitute the precious metals utilized to expedite OER.

In general, doping/incorporating heteroatom or anions such as P, N, and S into NiCo bimetals dramatically revolutionizes the microstructure, electronic structure, and electrical conductivity and improves the overall electrochemical performance. Modulating the electronic structure helps to overcome the kinetic barrier in the material, thus improving the activity. Combing heteroatoms with metals can also change the binding energy of the intermediate reactant on the catalytic surface, leading to ideal Gibbs free energy, which is essential for OER. Growing NiCo bimetals assembled with heteroatoms on conductive substrates, such as NF, is a promising strategy to acquire a good electrocatalyst for OER. Despite the substantial progress made in improving NiCo by incorporating heteroatoms, a robust NiCo electrocatalyst with high activity and stability suitable for extensive scale application is still required.

5.2. CoFe based electrocatalysts for alkaline OER application

Bimetallic electrocatalysts comprising cobalt and iron are among the widely scrutinized electrocatalysts for the alkaline OER realm due to their powerful catalytic capability. This section is devoted to reviewing the state-of-the-art CoFe based electrocatalysts employed for OER. To briefly elaborate state of the art, we made five main sub-sections similar to the NiCo section, including CoFe hydroxides, CoFe LDHs, CoFe oxide and spinel, CoFe composites alloy, and other electrocatalysts, and CoFe assembled with hetero atoms of S/P/N.

5.2.1. CoFe (oxy) hydroxides based electrocatalyst

CoFe based electrocatalysts with a hollow structure containing hydroxide can boost the catalyst reaction, activity, and stability for OER. Feng and co-workers [144] prepared a hollow hybrid electrocatalyst comprising FeOOH and Co supported on NF via electrodeposition routes. The synthesis process is schematically presented in Fig. 10. Briefly, the hybrid catalyst was prepared as follows: (i) the NF substrate was thoroughly cleaned and treated with various chemicals, including acetone, HCl, and distilled water; (ii) using the galvanostatic electrolysis technique, ZnO nanorod arrays were synthesized using 0.01 M zinc nitrate and 0.05 M ammonia nitrate solution; (iii) Co metal was coupled with ZnO by electrodeposition; (iv) the prepared ZnO@Co/NF was then immersed into NaOH for 3 h to remove ZnO nanoarrays, resulting in Co nanotube arrays, and (v) FeOOH/Co/FeOOH was synthesized by electrodepositing of FeOOH precursor solution on both the inner and outer surface of Co nanotubes arrays. The Co metal was designed to be placed between two FeOOH, and this was important for some reason. Firstly, the Co sited in the middle aids can achieve fast electron transfer due to its high electrical conductivity, alleviating the low electrical conductivity of the FeOOH. Secondly, the hollow structure of FeOOH/Co/FeOOH can facilitate ion transport. Lastly, due to the coupling effect of the two metals, the catalytic reaction, activity, and stability could be boosted. Electrochemical measurements showed high catalyst activity and durability, which demanded low overpotential for OER. EIS measurement demonstrated that the prepared hybrid electrocatalyst possesses high electrical conductivity, which was estimated by measuring the

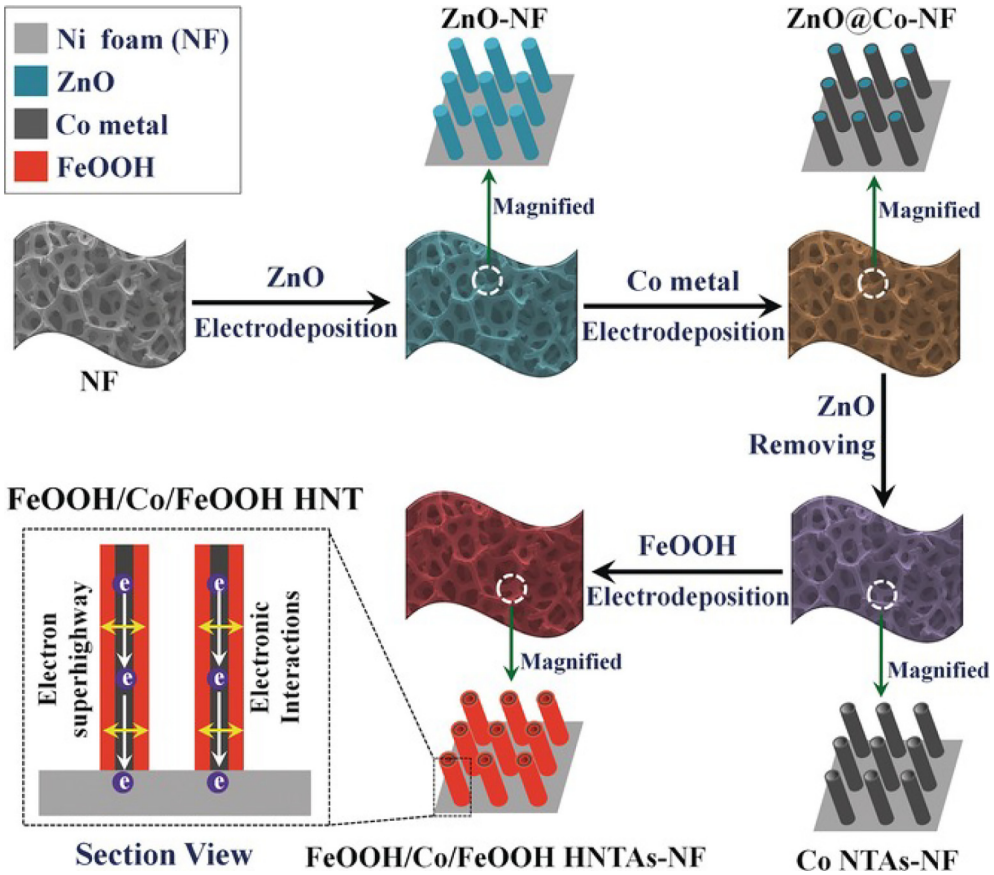

Fig 10. Synthesis route of FeOOH/Co/FeOOH-NF electrocatalysts. Reproduced from Ref. [144] with permission from WILEY-VCH.

capacitance of the electrical double layer (EDL) (using 5 mV s^{-1} around 306 mF cm^{-2} capacitance was obtained). The prepared hydride electrocatalyst showed an interesting essence of performance for OER with a low overpotential of 250 mV to furnish a current density of 20 mA cm^{-2} with a small Tafel slope of 32 mV dec^{-1}. Furthermore, it has also shown a fantastic catalytic activity for about 50 h in 1.0 M NaOH. Zhang and co-workers [280] also prepared Co-doped Fe-OOH through gelatin-assisted hydrothermal technique, which gave excellent electrocatalytic activity in OER, demanding 290 mV overpotential to generate a current density of 10 mA cm^{-2}. However, the reaction mechanism and role of Fe incorporated/doped into Co oxide remained subtle. More recent studies by Enman and co-workers [281] revealed that oxidized iron species participated as active sites in the OER on the CoFe (oxy) hydroxyl catalysts, that was probed by operando X-ray absorption spectroscopy (XAS) and DFT. They found that OER was different in the presence and absence of iron, being less active in Fe-free CoO_xH_y electrocatalyst.

On the other hand, Han and co-workers [282] prepared iron modulated cobalt hydroxide nanostructured electrocatalyst for alkaline OER. It was designed by a conversion tailoring technique, in which the iron modulated cobalt (oxy) hydroxide was anchored onto graphene oxide to develop two-dimensional nanohybrids. The iron was essential to change the micro sized sheet into the nanometer-sized particle, leading to a susceptible iron-influenced feature. Both iron and cobalt were crucial for catalytic activity. At the same time, graphene was essential for the dispersion of Fe-CoOOH nano-sized particles and helpful for linking the conducting networks, vital for fast electron transport during the reaction. The DFT calculations unveiled that the iron added into the Fe-CoOOH materials resulted in a quick catalytic response due to the boosted adsorption competence for the intermediate entities involved in OER. The as-prepared Fe-CoOOH connected in graphene oxide showed a remarkable electrochemical performance in OER, demanding only 330 mV overpotential to offer 10 mA cm^{-2} current density. Moreover, a small Tafel slope of 37 mV dec^{-1} was obtained, which denotes that fast reaction kinetics is persisted in the prepared catalyst. The existence of iron was able to alter the electronic structure of Co, leading to suitable adsorption of intermediates on the catalyst surface and hence accelerates the OER kinetics [283]. Besides, Wang and co-workers [284] prepared CoO@FeOOH core–shell nanowire grown directly on 3D CC by hydrothermal and electrodeposition process to obtain CC@CoO@-FeOOH. Taking advantage of the nanowires with good facet exposure to the reactant, the conductive 3D CC, which is vital for rapid electron transfer, and the synergetic effect of Co and Fe, CC@CoO@FeOOH electrocatalyst exhibited an excellent electrochemical wave of performance, demanding only 255 mV overpotential to produce a current density of 10 mA cm^{-2} along with good stability, Zhou and co-workers [285] prepared a bimetallic hydroxide catalyst comprising of Co and Fe.

By controlling the ratio of Fe and Co, $Co_{0.7}Fe_{0.3}(OH)_x$ was found to be the most appealing electrocatalyst for OER, requiring a quite low overpotential of 220 mV to afford a current density of 10 mA cm^{-2}. Co-Fe hydroxide nanosheet arrays were directly grown and incorporated into 3D copper foam. The resulting catalyst showed a low Tafel slope and less charge transfer resistance, confirming its right candidate for OER. Besides, the stability of the prepared electrocatalyst was appealing, which remained almost stable for around 100 h continuous measurements. Furthermore, Inohara and co-workers [286] developed an efficient electrocatalyst of Co-doped Fe-OOH for OER by modifying the ratio of Co and Fe. The prepared electrocatalyst showed low overpotential and excellent stability. The list of the state of the art of bimetallic electrocatalysts based on Co and Fe (oxy) hydroxide employed for alkaline OER is presented in Table 6.

Moreover, preparing amorphous Co-Fe hydroxide structures can enhance catalytic reactivity and activity for OER since amor-

Table 6
State-of-the-art review of CoFe (oxy) hydroxides based electrocatalyst for OER.

Catalyst	Substrate	Overpotential (mV)@10 mA cm^{-2}	Tafel slope (mV dec^{-1})	Synthesis method	Catalyst loading (mg cm^{-2})	Stability	Ref.
$Co_{0.20}Fe_{0.80}OOH$	GC	383	40	Precipitation	0.20	Nearly unaltered potential for over 12 h operation	[286]
FeOOH/Co/FeOOH HNTAs[a]-NF	NF	250@20	32	Electrodeposition	0.5	Constant overpotential of 250 mV to produce *J* of 20 mA cm^{-2} for over 50 h	[144]
CC@CoO@FeOOH-NWAs	CC	255	80	Hydrothermal/electrodeposition	1.9	After 20 h testing, the same operating potential was retained to produce a *J* of 10 mA cm^{-2} @255 mV, and 50 mA cm^{-2} @305 mV	[284]
$Co_{0.54}Fe_{0.46}OOH$	GC	290	47	Gelatin assisted soft template	0.20	89% retention of current density after 25000 s testing	[280]
$CoFe(OH)_x$	Cu-D[f]	275	34	Wet chemical	–	The potential changed from 1.505 to 1.507 V after 10 h operation to produce a *J* of 10 mA cm^{-2}	[291]
Fe-CoOOH/G	GC	330	37	Solvothermal	0.20	Showed stable operating potential of 1.58 V for over 5 h	[282]
$Co_{0.7}Fe_{0.3}(OH)_x$	CuF[b]	220	62.4	Anodic oxidation	–	no apparent decline in current density after 100 h operation	[285]
$Co_{0.875}Fe_{0.125}OOH$	CC	300@20	83	Hydrothermal	3.6	Revealed reveals negligible *J* loss after 1000 cycles, and after 50 h, stable *J* of 20 mA cm^{-2} was retained	[292]
Am[c].CoFe-OH	Graphite	280	28	Electrodeposition	0.035	Stable *J* of 10 mA cm^{-2} for over 36 h testing	[290]
Am.$CoFe(OH)_x$	GC	293	67.4	Template method	0.305	Stable current for over 10 h operation	[288]
Am.Co-Fe-OH NSA[d]	FeF[e]	208	47	Wet chemical	–	Superb stability of *J* for over 60 hMeasurements	[168]
FeCoOOH	CC	259	34.9	Hydrothermal	1.0	Superb operating potential stability for 100 h	[293]
$CoFe(OH)_x$	GC	293	67.4	CuO_2 Template based	0.306	After 10 h testing, a stable current was observed	[288]
CoFeOH/NF	NF	360@400	43.7	Electrochemical	–	After 320 operations, the potential remained below 1.6 V to achieve a *J* of 400 mA cm^{-2}	[294]
$Co_{0.5}Fe_{0.5}(OH)_x$	GC	320@100	58.3	Etching and precipitating	–	Stable *J* of 5 mA cm^{-2} for 10 h	[295]

[a] HNTAs: hybrid nanotube arrays; [b] CuF: copper foam; [c] Am.: amorphous: [d] NSA: nanosheet arrays; [e]FeF: iron foam; [f] Cu-D: copper disk.

phous materials retain high defects and active electrochemical sites than the corresponding crystalline structure [287], essential to augment the catalytic activity. And also, good structural stability and corrosion resistance in harsh environments can be found in amorphous materials, which can keep an interesting property such as superhydrophilic and superaerophobic states for controlling the bubble formation and release during OER [288]. Considering all these merits, myriads of researchers have been dedicated to fabricating Co-Fe hydroxide electrocatalysts with amorphous structure [288-290]. For example, Yue and co-workers [288] prepared amorphous material of $CoFe(OH)_x$ through a template-assisted route. The as-made electrocatalyst surpassed the benchmark of commercial RuO_2 electrocatalyst. A low overpotential of 293 mV was used to export an OER current density of 10 mA cm^{-2} in a 1.0 M KOH solution. Intriguingly, the as-prepared electrocatalyst $CoFe(OH)_x$ unraveled substantial stability for about 10 h continuous operation.

CoFe-hydroxide based electrocatalysts have shown an excellent activity towards OER due to their pleniful active site and versatile composition. Catalysts that could deliver a high current density and maintain their mechanical robustness and long-term operation stability are ideal for industrial applications. Few electrocatalysts meet all these requirements for large-scale applications. Growing CoFe-oxyhydroxide on a conductive substrate could deliver a remarkable high activity and stability. For example, growing of amorphous CoFe- oxyhydroxide nanosheet on iron foam offered an appealing activity and stability for alkaline OER, forthcoming to fulfil industrial application requirements. An ultralow overpotential of 208 and 298 mV was required to derive a current density of 10 and 500 mA cm^{-2}, respectively, demonstrating its super electrochemical activity for OER. the superb activity was believed to be originated from the nanosheet and amorphous nature, which facilitated to augment the ECSA and provide more active sites for OER, respectively [168]. Hence, shadowing a strategy to fabricate Nanosized particles on a given conductive substrate is indispensable for obtaining a suitable catalyst for water oxidation, particularly, for full water electrolysis in general.

5.2.2. CoFe LDHs based electrocatalysts

CoFe LDHs based electrocatalysts have been proved effective for OER, due to their high ECSA exposed to the electrolyte and possible to control the interlayer space by introducing different ionic moieties [178]. Han and co-workers [287] prepared CoFe-LDHs electrocatalysts for OER by co-precipitation and hydrothermal technique. The as-prepared CoFe-LDH electrocatalyst indicated an outstanding electrocatalytic activity for water oxidation due to the synergetic effect between Fe and Co metals in the LDH structure and the nanoscale dimension that triggered the distance for the ion transport to be short, and the broader interlayer space structure with anions and water intercalation enhanced for OER. A low overpotential of 340 mV is necessitated to derive a current density of 10 mA cm^{-2}. The same group also modified the CoFe-LDHs by assembling on reduced graphene oxide (rGO) to obtain 2D sheet-on-sheet binary architectures (CoFe-LDH/rGO), which increased the conductivity and activity of the catalyst. The resulting hybrid electrocatalyst offered a remarkable electrochemical performance for OER, requiring 325 mV overpotential to furnish a current density of 10 mA cm^{-2}. XPS elucidated the chemical composition and surface electronic state of the prepared electrocatalyst. Results indicate that Co and Fe species existed in the form of Co^{2+} and Fe^{3+} oxidation states. They concluded that Fe^{3+} was essential to modify the structure and components of the as-prepared materials, leading to a new phase of the hydrotalcite-like layer structure, which was vital for the high electrochemical water splitting.

Moreover, another approach to ameliorating the electrocatalytic performance of LDHs was proposed. The idea is to create an oxygen vacancy in the atomic structure of the catalysts, which could eventually revolutionize the adsorption of the OH^- intermediates and amend the electrical conductivity of the materials [296]. Inspired by this framework, Liu and co-workers [297] prepared CoFe-LDHs intercalated with formate ion by wet chemical method. The XPS analysis revealed that oxygen vacancies were identified in both the Fe and Co center; nevertheless, the oxygen vacancies are found mainly in the unsaturated Co center. In addition, in the O 1*s* peak, high defect sites with low oxygen coordination were also assigned. It is reported that these high defect sites or oxygen vacancies are essential to reduce the barriers for the adsorption of OH^- due to the low coordination sites of the MO_6 structure. DFT theory substantiates that the unoccupied bonding t_{2g} orbitals of MO_6 center (MO_{6-x}) could induce a high electron transfer conductivity and accelerate OH^- anions adsorption reaction. During testing in an H-type cell using the three-electrode cell connected to an electrochemical station, a current density of 10 mA cm^{-2} was produced by applying an overpotential of 260 mV. Besides, a voltage of 1.63 mV was required for the overall alkaline water spitting process to achieve a current density of 10 mA cm^{-2}, demonstrating its potential to replace the precious metals of Ru and Ir. Wang and co-workers [298] prepared an edge-riched nitrogen-doped ultrathin CoFe LDH nanosheets by exfoliating bulk CoFe LDHs via nitrogen plasma. The obtained catalyst contains several atomic-sized holes and abundant edge sites. These peculiar ultrathin CoFe LDH nanosheets with abundant reactive sites, atomic-sized holes, and edge sites remarkably enhance the catalytic activity and eventually lifts the overall OER performance. The prepared electrocatalyst showed high performance for OER, in which a small overpotential of 233 mV was needed to furnish a current density of 10 mA cm^{-2}. Moreover, it showed superb stability of LSV curve, remained stable after 2000 CV. The high catalytic activity of the prepared electrocatalyst was believed to be stemmed from the increased oxygen vacancies on the CoFe LDH surface, which favors the adsorption of the reacting intermediates of OER.

Table 6 shows the recent CoFe-LDH based electrocatalysts prepared for OER with their respective overpotential required to derive a specific current density, synthesis method, and Tafel slope obtained. As shown in Table 7, the most common preparation methods for the synthesis of CoFe-LDH electrocatalysts are solvothermal, hydrothermal, and co-precipitation, which are wet chemical methods that need a long time to prepare a desired material and demand high temperature and pressure. The electrodeposition method has been proposed and used to prepare CoFe bimetallic oxide and LDH electrocatalysts for different applications [245,246]. For example, Sakita and co-workers [299] prepared CoFe-LDH electrocatalysts by depositing metal precursors on glassy carbon substrate by potentiostatic mode in the continuous or pulsed regime. They observed that the electrosynthesis potential and pulses adjustment were fundamental to avoid pure alloy formation or excessive hydroxides. A different mass was loaded on the substrate by controlling the pulse deposition time, and an optimum mass load of CoFe at a pulse rate of 0.5 s was obtained. This material revealed an outstanding electrocatalytic performance for OER, in which a current density of 10 mA cm^{-2} was achieved at only 286 mV of overpotential. This fast and easy preparation technique can be an excellent way to prepare for further effective and promising electrocatalysts for OER and overall water splitting applications. Another study also explored an electrodeposition scheme to prepare 3D porous CoFe-LDH nanoshets on the NF for OER. The as-made material offered an overpotential of 250 mV to derive 10 mA cm^{-2} OER of current density [300].

Furthermore, adjusting hollow and nanostructured materials can boost the electrocatalyst performance for OER. Yuan and co-workers [295] prepared ultrathin hollow structured CoFe-LDH NCs by coupling etching and co-precipitation methods. The cat-

Table 7
State-of-the-art review of CoFe LDH based electrocatalysts for OER.

Catalyst	Substrate	Overpotential (mV)@10 mA cm^{-2}	Tafel slope (mV dec^{-1})	Synthesis method	Catalyst loading (mg cm^{-2})	Stability	Ref.
CoFe-LDHs	GC	286	48	Electrodeposition	–	The operating potential increases by 1.2 mV min^{-1}	[299]
Co_8Fe_1-LDHs	NF	262	42	Hydrothermal	2.0	After 20 h operation, a stable *J* of 10 and 50 mA cm^{-2} was observed	[303]
CoFe-LDHs	Ti_3C_2MXene	319	50	Heating and reflux method	–	A stable *J* of 2.7 mA cm^{-2} at an overpotential of 0.5 V was obtained after 10 h operation	[302]
CoFe-LDH/rGO	GC	325	43	Co-precipitation	0.204	Stable *J* of 5 mA cm^{-2} for about 10 h,	[287]
CoFe-LDHs	GC	340	43	Co-precipitation	0.204	A constant operating potential for 10 h	[287]
CoFe-35 LDHs	GC	350	49	Co-precipitation	4.50	Good stability for over 48 h	[304]
CoFe LDH-F	NF	260	47	Hydrothermal	0.20	Stable *J* at voltage of 1.63 V for 35 h	[297]
$Co_{0.4}Fe_{0.6}$ LDH/ g-CNx[a]	GC	280	29	Co-precipitation	0.14	Unaffected overpotential of 280 mV for oxygen evolution at 10 mA cm^{-2} for a day	[305]
N-CoFe LDHs	GC	233	40.03	Hydrothermal	0.20	Stable polarization curve after 2000 CV cycles	[298]
CoFe-LDHs	GC	286	45	Dealloying	0.20	Only a 1.5% potential increase was observed after 60 h operation	[306]
Co_4Fe_2-LDH/ $Co(OH)_2$-NWs	NF	220@50	51	Hydrothermal	–	Negligible change after 1000 cycles , and high stable *J* for 48 h	[301]
CoFe-LDHs	ITO	400	83	Co-precipitation	0.20	Stable *J* of 10 mA cm^{-2} from for 10 h	[307]
CoFe-LDHs	NF	300	83	Co-precipitation	0.20	In the first 1.5 h, a slight increment from 1.52 to 1.54 V to generate *J* of 10 mA cm^{-2}	[307]
CoFe-LDHs	GC	270	58.3	Etching and precipitating	–	A stable *J* of 5 mA cm^{-2} after 10 h	[295]
CoFe-LDH/ Co_3O_4(6:4)	GC	290	77	Solvothermal	0.35	A 10% decrease of original activity after 10 h operation	[308]
M−CoO/CoFe LDHs	CFP	254	34	Pulsed laser ablation	0.20	A 4% loss of current density after 12 h operation	[309]
CoFe-LDHs	NF	250	35	Electrodeposition	–	Stable *J* of 10 mA cm^{-2} for 50 h testing	[300]

[a] CNx: nitride composite.

alytic activity of the hollow CoFe-LDHs was probed with linear sweep voltammetry at a sweeping rate of 50 mV s^{-1} in alkaline media (1.0 M KOH). Different CoFe LDH materials were prepared by controlling the ratio of Co and Fe, and the optimum ratio with 50% of each metal exhibited a remarkable high wave of catalytic activity, achieved 10 mA cm^{-2} current density at 270 mV of overpotential. It unveiled a trivial change after 200 cycles, signifying good stability. Besides, other studies preparing nanoplate and nanowire structure of LDH materials can enhance the catalytic activity for OER. A material made by coupling of Co_4Fe_2-LDHs and $Co(OH)_2$ revealed extraordinary electrocatalytic performance in water oxidation, achieved 50 mA cm^{-2} OER current density with an ultra-small overpotential of 220 mV [301]. Moreover, synthesizing CoFe-LDH materials directly grown on conductive support such as MXene and NF has also provided an insightful catalytic activity for alkaline water oxidation application [302,303].

Overall, CoFe-LDH based electrocatalyst offers an excellent catalytic activity towards OER. Substantial efforts have been made in preparing CoFe-LDH structure using various methods, including electrodeposition, hydrothermal, solvothermal, etc. The challenges remain to obtain robust electrocatalysts with high activity accompanied with high stability that could essentially deploy for industrial application. Most of the reported electrocatalysts are tested at a lab scale using a three-electrode system. Therefore, further investigation using a two-electrode system must thoroughly scrutinize its potential for water electrolysis.

5.2.3. CoFe oxide-based electrocatalysts

CoFe bimetallic oxide and spinel-based electrocatalysts have shown notable performance to expedite OER. The spinel-type of CoFe bimetallic oxides are demonstrated to an appealing candidate for OER due to their earth abundance and environmental friendliness, rich redox activity, and good durability in alkaline media [127,310]. Many researchers have proposed various groundwork to synthesis metal oxide and spinel-based electrocatalysts for alkaline water oxidation. The catalyst prepared by hard templating/ nano-casting possesses attractive properties such as well-defined size, crystal structure, and possible particle size control and boost the surface area. All those mentioned characteristics are essential in catalytic reactions [311]. The desired replica's chemical and physical parameters can be modulated by changing the hard template and the operating condition, enabling us to prepare the

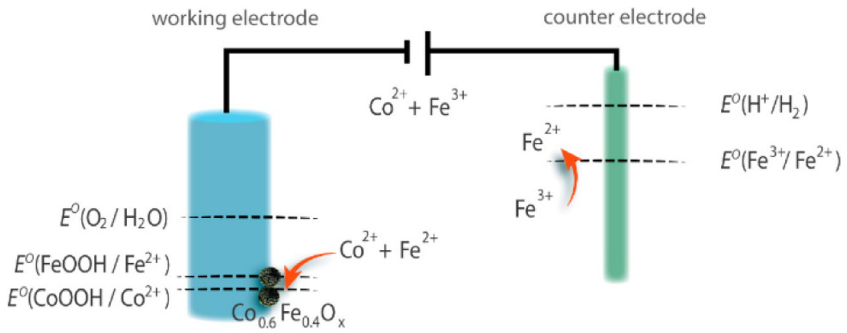

Fig 11. The proposed deposition mechanism $CoFeO_x$ using the electrodeposition technique. Reproduced from Ref. [130] with permission from the American Chemical Society.

selected materials. Using this frame, in 2014, Grewe and co-workers [312] prepared bimetallic electrocatalyst by doping iron into Co_3O_4, by controlling the ratio of the metal oxide precursors. It was designed by following specific reaction steps. Firstly, a cubic ordered mesoporous silica hard framework was prepared, followed by impregnation of different ratios of iron oxide and cobalt oxide precursors in the prepared framework to form Fe-Co_3O_4. The pristine Co_3O_4 electrocatalyst presented an overpotential of 526 mV to derive a current density of 10 mA cm^{-2} tested in 0.1 M KOH electrolyte.

In contrast, the iron-doped Co_3O_4 (at the ratio of Co/Fe = 32), displayed an overpotential of 486 mV to endow the same current density, suggesting that Fe dopant increased the catalytic activity of the resulting materials. This could be attributed to the change of the electronic structure that influences the electrical conductivity and charges transfer capability. Another approach for enhancing and controlling the catalytic activity was proposed by Morales-Gio and co-workers [130]. $CoFeO_x$ was oxidatively electrodeposited onto NF. This easy technique enables to control of the mass loading by changing the number of deposition rounds. The proposed preparation mechanism is presented in Fig. 11. The working electrode is used as an oxidation site for the CoFe bimetallic ions, and the counter electrode is used to reduce Fe (III) into Fe (II). Once the Fe (II) ion diffuses into the working electrode, $CoFeO_x$ commences electrodepositing on the substrate that could be observed by the mass increased in the quartz crystal. An optimum mass load was obtained by varying the depositing cycle and the bimetallic catalyst comprising $CoFeO_x$, which claimed an overpotential of 260 mV to attain a current density of 10 mA cm^{-2} and also presented a low Tafel slope of 36 mV dec^{-1}.

In recent years, CoFe spinel-based electrocatalyst has attracted a significant devotion in the realm of water oxidation due to its low cost, earth abundance, good catalytic activity. However, alone spinels are, in nature, poor electrical conductive, which hinders

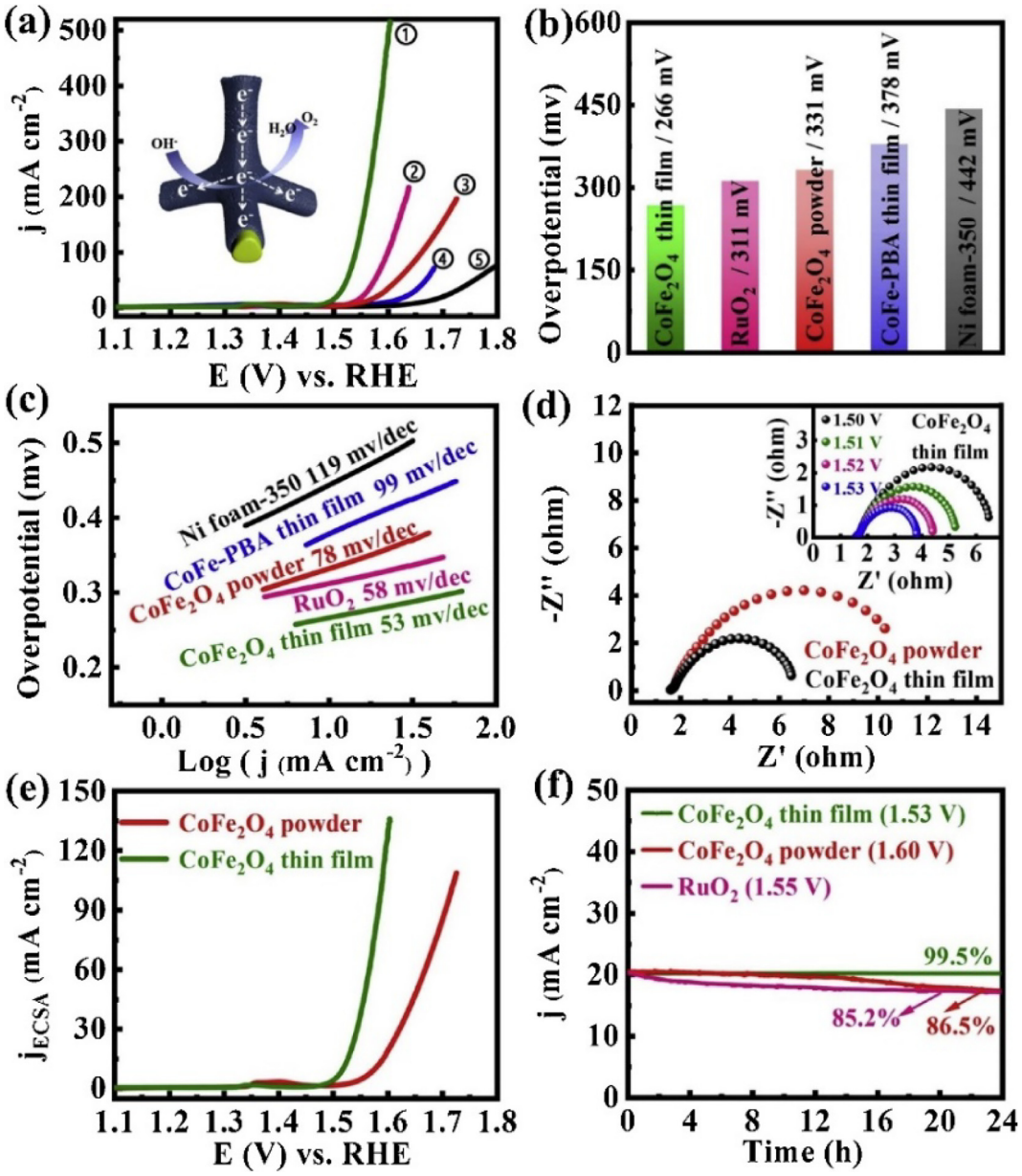

Fig 12. Comparison of OER activity of various electrocatalysts: (a) LSV polarization curves at a scan rate of 2 mV s^{-1}, (b) comparison of overpotential at 10 mA cm^{-2} of current density, (c) the needed overpotential at the different current density for the various electrocatalysts, (d) comparison of Tafel plots, and (e) Nyquist plots measured at different open-circuit potentials for various catalysts, (f) stability test in 1 M KOH. Reproduced Ref. [313] with permission from Elsevier. B.V.

them from competing with precious metals such as Ir and Ru. Many researchers have attempted to impregnate high electrical conductive agents, such as carbon materials [118]. Graphene has been extensively used among carbon materials due to its profound electrical conductivity and high specific surface area. One recent study reported a spinel of $CoFe_2O_4$ impregnated with graphene prepared by the sol–gel method [118]. The as-prepared catalyst showed an excellent activity with a lower overpotential of 300 mV to furnish 10 mA cm^{-2} current density, which surpassed the benchmark electrocatalyst of RuO_2. Zhang and co-workers [128] prepared $CoFe_2O_4$ spinel by electrodepositing onto NF substrate to enhance activity and stability. The electrocatalyst displayed a splendid electrochemical performance, requiring only 270 mV overpotential to fetch 10 mA cm^{-2} current density.

Moreover, Lei and co-workers [313] prepared various spinel forms of $CoFe_2O_4$ grown on NF and silicon substrate by liquid-phase epitaxy growth for OER. Among them, $CoFe_2O_4$ with a thin film was found to be an encouraging result with only 266 mV overpotential was needed to attain 10 mA cm^{-2} current density and excellent stability in 1.0 M KOH. An explicit comparison of the various prepared electrocatalyst with commercial RuO_2 is shown in Fig. 12(a–f). As apparent from the figure, a thin film of $CoFe_2O_4$ showed an attractive performance in OER, outperformed for the commercial RuO_2, showing low Tafel slope, low charge transfer resistance, highly ECSA, and low overpotential accompanied with fantastic stability. Other studies have also prepared electrocatalysts using CoFe oxide grown on NF substrate, showed tremendous performance in OER [314]. A list of state-of-the-art reviews on bimetallic CoFe oxide and spinel-based electrocatalyst is shown in Table 8.

Moreover, developing CoFe oxide electrode materials with defective surface architecture can considerably enrich catalyst activity since the materials can be tuned to its electronicbehavior and gap state in these frames, thus changing the charge transfer rate and adsorption energy for intermediate species. Having stimulated with this framework, Zhuang and co-workers [315] attempted to prepare CoFe based nanosheet with rich oxygen defects using a reductant of $NaBH_4$ intended to offer a more active site for reactant intermediates during OER. The atomically thin sheet formed was helpful to expedite the mass and charge transfer, thus boosting the activity. Only 308 mV of overpotential was demanded to achieve an OER current density of 10 mA cm^{-2} in 0.1 M KOH electrolyte. XPS explored the presence of the oxygen vacancies and the ample oxygen vacancies found in the thin sheets of CoFe oxides responsible for stimulating catalytic activity. Besides, in 2018, Huang and co-workers [316] prepared Fe/Co(oxides) with defective oxygen. It was demonstrated that the materials with defective surface structure showed a profound OER activity, requiring 329 mV to obtain 50 mA cm^{-2} OER current density.

In general, CoFe oxides are among the extensively investigated electrocatalyst for OER. Growing of these oxide materials on a conductive substrate such as SS and NF has attracted much attention and presented an outstanding performance. Among the well mesmerizing approach to enhance the overall electrochemical performance of CoFe-oxide electrocatalyst is fabricating nanostructured materials. In situ growing of CoFe oxide on these substrates or electrodeposition of Co and Fe precursors on the substrates was demonstrated to be an excellent strategy to obtain an appealing

Table 8
State-of-the-art review of CoFe oxide and spinel based electrocatalysts for OER.

Catalyst	Substrate	Overpotential (mV)@10 mA cm^{-2}	Tafel slope (mV dec^{-1})	Synthesis method	Catalyst loading (mg cm^{-2})	Stability	Ref.
$CoFeO_x$	NF	260	36	Electrodeposition	0.001	–	[130]
$CoFe_2O_4$	GC	698@100	42	Precipitation	3–5	–	[317]
CoFe-$CoFe_2O_4$/N-CNTs[a]	GC	334	80	Solvothermal	–	After 1000 cycles, 12 mV overpotential was increased to produce 100 mA cm^{-2}	[318]
Fe-Co_3O_4 (Co/Fe = 32)	GC	486	–	Hard template	0.12	Remained stable current after 10000 s	[312]
$CoFe_2O_4$ nanoplates	GC	410	61	Hydrothermal	1.06	Stable polarization curve after 500 cycles	[319]
$CoFe_2O_4$ NC	GC	450	61	Hydrothermal	1.06	Stable polarization curve after 500 cycles	[319]
$CoFe_2O_4$	CFP	280	42.1	Li reduction strategy	0.20	a small increase of about 20 mV at the first hour and remained-almost unaltered in the next few hours	[88]
$CoFe_2O_4$	Au	374	35	Electrochemical	–	Stable *J* of 10 mA cm^{-2} during 50 h measurements	[320]
$Co_3Fe_{1.5}$-O	GC	284	45	Chemical dealloying	0.20	During 60 h operation, only 1.5% of operating potential increment was observed	[306]
$CoFe_2O_4$	NF	270	31	Electrodeposition	1.20	–	[128]
$CoFe_2$ alloys/$CoFe_2O_4$	GC	300	73.34	Electrospinning	0.25	Constant potential during 12 h measurement	[131]
$CoFe_2O_4$	NF	266	53	liquid-phase epitaxy	1.60	13.5% current density (20 mA cm^{-2}) attenuation after 24 h operation	[313]
Fe-doped-Co_3O_4@C	Ni	260@20	70	Co-precipitation	5.0	After 100 h operation, 7% of current density degradation	[314]
$Co_{2.775}Fe_{0.225}O_4$	–	317	58	Nano casting	–	–	[321]
$CoFe_2O_4$	GC	342	57.1	Hard template	0.142	no attenuation after 1000 cycles, and no obvious *J* decay after 15 h operation	[322]
$CoFe_2O_4$ powders	NF	360	69.2	Sol-gel	0.0096	Stable various current density for over 10000 s operation	[323]
$CoFe_2O_4$ NP[b]	GC	335	76	Solvothermal	0.28	Good *J* stability after 500 cycles	[324]
$CoFe_2O_4$/graphene	GC	300	68	Sol-gel	0.33	83% retention of *J* of 10 mA cm^{-2} after 30000 s measurements	[118]
CoO_x + Fe^{3+}	GC	309	27.6	Electrodeposition	0.0095	the potential needed for 10 mA cm^{-2} augmented from 1.54 to 1.6 V in the first 5 h and then remained stable at 1.6 V for 20 h	[129]
Fe-Co_3O_4-H-NSs	NF	204	38	wet chemical reduction	1.25	After 30 h testing a slightly increase of overpotential (7.2 mV) was observed	[84]
FeCoO	NF	244	57	chemical bath deposition	1.70	Retained stable current density after 48 operation	[85]

[a] CNT: carbon nanotube; [b] NPs: nanoparticles.

CoFe oxide for OER. Despite their profound activity towards water oxidation, their stability remains subtle. There is still enormous room for further investigation, mainly on the issue of stability for long-term operation.

5.2.4. CoFe composite, alloy, and other electrocatalysts

Preparing of CoFe containing composite electrocatalysts can galvanize the catalytic activity. Numerous researchers have claimed that assembling CoFe bimetals with electrically conductive materials such as carbon can revitalize the conductivity, thus augmenting catalytic activity [325]. For example, Fang and co-workers [326] observed bimetallic CoFe assembled with carbon nanotubes increased its catalytic activity for OER. They prepared tubular bimetallic CoFeO/CNT electrocatalysts by pyrolysis of the Co and Fe precursor in triethylene glycol together with CNT. Briefly, the Co and Fe precursors and CNT were first ultrasonicated in triethylene glycol solvent to create a uniform solution; after that, the solution was heated to 278 °C at reflux for 30 min under argon flow, giving of $Co_{1-y}Fe_yO_x$/CNT electrocatalyst. Benefiting from the multi-walled architecture of CNTs, the outer layer of the bimetal oxide of $Co_{0.8}Fe_{0.2}O_x$ provides enough active sites for reactants, and the internal walls are interconnected, which are crucial for rapid mass and electron exchange. Interestingly, the novel $Co_{0.8}Fe_{0.2}O_x$/CNT electrocatalyst endowed an outstanding electrochemical performance, in which 10 mA cm^{-2} was generated by applying an extra potential of 280 mV overwhelmed numerous reported electrocatalyst for OER including the RuO_2 and IrO_2. Besides, Xu and co-workers [327] observed that the bimetallic CoFe hybrid embedded with carbon nanotube has superior catalytic activity for alkaline water splitting applications. Liu and co-workers [328] developed composite materials comprising bimetallic CoFe catalyst deposited onto CFPs via a technique of electro-conductive deposition. It exhibited excellent performance for OER application, necessitating a low overpotential of 283 mV to achieve 10 mA cm^{-2}. In 2019, Yang and co-workers [136] prepared extraordinary electrode materials using ternary metals CoFeNi. Two LDHs of CoFe and NiFe based electrocatalysts were integrated on to NF substrate by electrodeposition applying a constant potential of −1.0 V vs. Ag/AgCl for 50, 100, 200, 300 s, and the corresponding samples were labeled as CoFe@NiFe-50/NF, CoFe@NiFe-100/NF, CoFe@NiFe-200/NF, CoFe@NiFe-300/NF, respectively. The CoFe@NiFe-200 electrocatalyst assembled into NF offered a current density of 10 mA cm^{-2} at 190 mV of overpotential using 1.0 M KOH electrolyte (Fig. 13). Different techniques probed the electrochemical performance: EIS was used to elucidate the charge transfer resistance as shown in Fig. 13(b), where the smaller semicircle of CoFe@NiFe-200/NF indicates a less charge transfer resistance (R_t = 0.92 Ω) due to the rapid electron transfer kinetic between the interface of electrolyte and the electrode. The Tafel slope of CoFe@NiFe-200/NF was also determined to be around 46 mV dec^{-1}, which is smaller than the other catalysts, suggesting the high kinetic site for OER (Fig. 13a). The ECSA was also

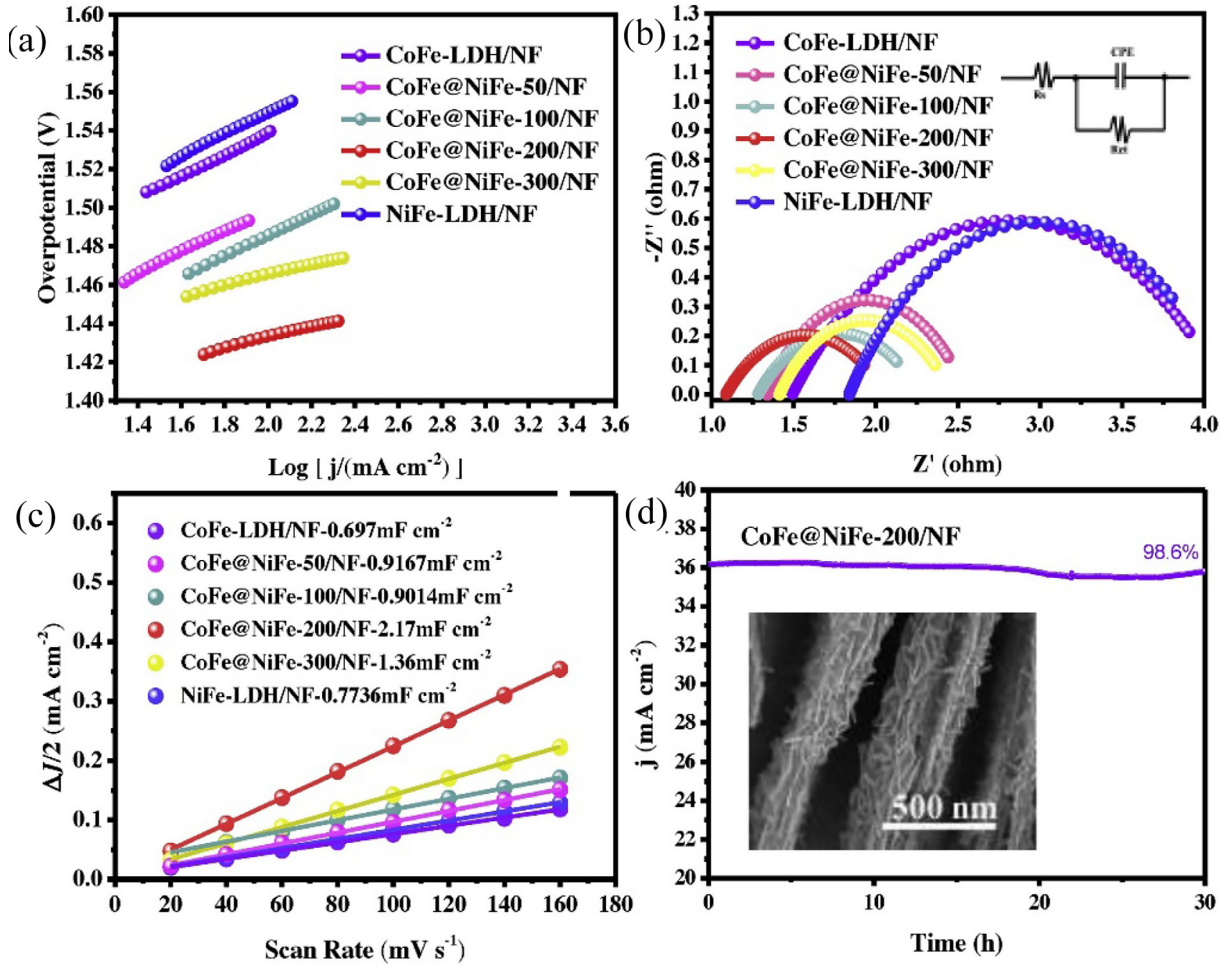

Fig 13. Comparison of OER performance: (a) Tafel slope of the various catalysts, (b) Nyquist plots of the different catalysts, (c) comparison of capacitance (slope of the graph) derived by capacitive vs. scan rate, (d) stability test using 320 mV overpotential. Reproduced from Ref. [136] with permission from Elsevier. B.V.

evaluated to probe the number of exposed sites for the reactants. As shown in Fig. 13(c), CoFe@NiFe-200/NF has the highest C_{dl} among all the materials prepared, which is around three-fold more elevated than the NiFe-LDH/NF, CoFe-LDH/NF, CoFe@NiFe-50/NF, CoFe@NiFe-100/NF, and CoFe@NiFe-300/NF, due to the intrinsic more active site persisted in the materials. As presented in Fig. 13(d), the stability of CoFe@NiFe-200/NF was also found to be promising for alkaline OER, remained stable for 30 h in 1.0 M KOH electrolyte. The catalyst also retains its morphology without changing its structure (as shown in Fig. 13d inset). More interestingly, the CoFe@NiFe-200/NF was determined to be helpful for the overall water splitting application, requiring a voltage of 1.59 V to derive a current density of 10 mA cm^{-2}. Moreover, other studies such as CoFeP TPAs/Ni [329], $Co_{1.2}Fe$/C [330], CoFe-/Co_8FeS_8/CNT [56], Am-CFDH/NCNTs [331] have shown a remarkable performance toward OER, which are comparable with the commercial electrocatalyst of RuO_2 and IrO_2.

Moreover, bimetallic electrocatalysts, such as CoFe LDHs, can enhance their catalytic activity by impregnating carbon materials such as CNTs and reduced graphene oxide (owning high surface area and electronic conductivity). This is to improve the low intrinsic electrical conductivity and change the electronic structure of the CoFe-LDHs, thus markedly boost the catalytic activity [56,331,332] Yang and co-workers [333] claimed that preparing CoFe-LDHs embedded with both MWCNTs and rGO can enhance the overall performance of the electrocatalyst toward water oxidation and oxygen reduction. Composite materials containing CoFe-LDH/MWCNT/rGO embraced porous hierarchical architecture with improved electrical conductivity. This is attributed to the assisted charge transport and the coupling effect of the bimetals, MWCNTs, and rGO. Moreover, MOFs coupled with CoFe bimetals, can enhance catalytic activity. MOFs own a high specific surface area, high carbon content, and tunable pore texture [333,334]. Besides, MOF can stimulate the dispersion of the metals and interconnect the particles forming a facile manner of transport channel in the materials. Hence, the embedding of bimetals with MOF can surge the overall performance for OER. Recently, Liu and co-workers [335] observed that combining CoFe with organic framework enhanced the essence of the catalytic activity toward oxygen evolution in an alkaline medium. An overpotential of 290 mV was required to export a current density of 10 mA cm^{-2} using an alkaline electrolyte of 1.0 M KOH. The high catalytic activity of the nanocomposite materials was deemed to be arising from the synergetic effect of the two metals and MOF, which was essential to tune/modulate the conductivity and electronic structure. Other composite materials such as CoFe@CNWs [151], CoFe/Co_8FeS_8/CNT [56], CoFeO/rGO, Co/Fe (2:1) [332], Co-Fe-N@MWCNT [204] were reported as an upright candidate to advance OER at relatively low overpotential compared with bimetallic electrocatalyst without carbon materials.

To substantially enhance and revolutionize the catalytic performance of materials, it is essential to augment the reactivity and the number of active core sites. For this case, there are two main strategies adapted to realize this framework: the first is to incorporate or dope other metal to the neat metal oxide, aiming to create oxygen vacancies and lessen the surface adsorption energy on the materials. The second technique is to engage in structural engineering and nanostructuring of the materials to enhance the catalytic activity in OER applications [335,336] For example, $Co_xFe_{3-x}O_4$ nanoarrays directly grown on CFP were prepared via hydrothermal and thermal treatment route. Results show that an iron-doped into spinel Co_3O_4 possesses a good catalytic activity and stability for OER. The composite materials of $Co_{2.3}Fe_{0.7}O_4$-NS/CFP noted an attractive result, obtained 10 mA cm^{-2} at 342 mV with profound stability for around 100 h, suggesting its scope for large scale application [336].

Overall, much work has been performed on the modification of bimetallic CoFe by introducing foreign materials. Transition metal oxide, such as CoFe oxide, possesses poor electrical conductivity. Doping/incorporating conductive supporting materials such as graphene and carbon nanotube with high surface area and conductivity could radically change the overall structure and performance. Integrating CoFe nanoparticles into the carbon skeleton can further enhance the stability and deter the aggregation of metal particles during the reaction. However, preparing these supporting carbon materials is delicate and expensive. Hence, a facile approach for preparing carbon materials to support metal oxide is imperative for practical OER application. Despite some achievements that have been reported, the overall electrochemical performance CoFe composite and alloy remains unsatisfactory compared with the reference electrocatalyst of Ru and Ir-based oxides due to the relatively inadequate active site and structural stability. Summary of the state of the art review of CoFe composites, alloys, and other electrocatalysts with their respective performance is presented in Table 9.

5.2.5. N, S, and P doped CoFe based electrocatalysts

It was demonstrated that the CoFe bimetallic electrocatalyst possesses an excellent electrocatalytic activity for water oxidation. However, they exhibit low electrical conductive originated from the intrinsic behaviors that hamper them for large-scale commercial applications. To overcome these bottlenecks, there are several ways of improving the performance, and one way is to impregnate hetero-atomic dopants such as nitrogen [357,373] phosphide [374,375] or sulfide [376] with the bimetallic, which amends the conductivity, adjust the electronic structure, durability and also boost the charge transfer, leading to enhanced electrochemical water oxidation. Forming of oxygen defects or heteroatoms dopants into metal oxide increases the charge mobility and conductivity and promotes electrons between neighboring catalytic sites [377]. In the year 2014, Shen and co-workers [378] prepared CoFe based bimetallic electrocatalyst by doping of S and N to enhance the conductivity of the materials. It was observed that a significant electrocatalyst activity was improved, in which 10 mA cm^{-2} of current density was attained using an overpotential of 410 mV. It was established that phosphorization of metal ameliorates the binding energy of the intermediate reactant on the surface of the catalytic layer, leading to ideal Gibbs free energy that is vital for H_2O electrolysis [256]. For example, Mendoza-Garcia and co-workers [379] observed that CoFe oxide modified by phosphorus presented high catalytic activity towards OER. A Co-Fe-P was prepared by phosphidation of the bimetallic oxide using trioctylphosphine as the P source. The synthesized materials showed 370 mV overpotentials to fetch a current density of 10 mA cm^{-2} in OER using 0.1 M KOH alkaline electrolyte. Xu and co-workers [256] observed that incorporating phosphorus into bimetallic CoFeOOH intensely ameliorated the overall performance of the resulting materials during the water oxidation test. The obtained two-dimensional CoFeP material endowed an alluring wave of performance for OER activity, demanding 305 mV of overpotential to accomplish 10 mA cm^{-2} of current density in 1.0 M KOH basic media, outstripping the benchmark of Ir/C electrocatalyst. Besides, Zhang and co-workers [154] prepared hollow porous Fe-Co-P nano boxes materials for OER in recent years. The study claimed that intramolecular charge transport between the two metals and the P–O is crucial for altering the catalytic activity. The hollow feature bargains short mass transport conduits and plentiful active surface sites, which ultimately greatly amplified the overall catalytic activity.

Preparing nanostructured CoFe electrode material, which holds high specific surface area materials, retains more active sites and good conductivity, can improve catalytic activity. Wang and co-

Table 9
State-of-the-art review of the CoFe composite, alloy and other electrocatalysts for OER.

Catalyst	Substrate	Overpotential (mV)@10 mA cm^{-2}	Tafel slope (mV dec^{-1})	Synthesis method	Catalyst loading (mg cm^{-2})	Stability	Ref.
CoFe@CNWs[f]	GCW	290	63	Hydrothermal	0.54	For over 12 h, showed constant operating potential of 1.55 V	[151]
Am-CFDH[e]/NCNTs	GC	270	56.88	Wet-chemical	0.285	Stable *J* of 10 mA cm^{-2} measured for about 20 h measurements	[331]
$CoFeWO_x$/C	GC	306	39	Pyrolysis	0.04	Stable *J* of 20 mA cm^{-2} for over 40 continuous OER test	[337]
Fe-Co/CFP	CFP	283	34	electroreductive deposition	1.20	A stable overpotential of 283 mV during 12 h continuous measurements	[328]
CO-Fe-1–1	CP	330	37	Electrodeposition	0.20	Remained stable for over 100 h operation	[338]
Co-Fe-8 min	CP	290	53.8	Electrodeposition	1.70	After 50 cycles, about 7.4% of current density decay was observed	[339]
CoFe LDH/ MWCNT/rGO	GC	430	77.73	Precipitation	0.140	At potential of 1.624 V, stable current density was obtained for about 20000 s	[333]
Fe-CoS/NC	GC	257	46.7	Hydrothermal	0.23	A stable *J* of 10 mA cm^{-2} for over 10 h operation, and only 2.82% decay was observed	[340]
CoFe/SN-C	GC	270	–	Ionothermal	1.0	Remained stable current density for over 5100 min	[341]
Fe-Co_9S_8NM/NF	NF	270	70	Hydrothermal	3.32	remained nearly unaffected current density after 10,000 continuous cycles of CVs test, and also stable for 10 h test	[342]
Co-Fe-phytate	GC	278	34	Co-precipitation	0.6	After 10 h operation, small current density loss of 5.6%	[343]
CoFe-LDH/ $NiCo_2O_4$/NF	NF	273@20	108	Hydrothermal	4.50	90% current density retention after 32 h continuous operation	[344]
CoFe-MWCNTs	NF	300	84	CVD	1.0	Constant overpotential of 300 mV for 3 h operation	[120]
CoFe@NiFe-200/ NF	NF	190	45.71	Electrodeposition	–	98.6% retention of current density after 30 continuous operation	[136]
CoFeG-HS[b]	GC	242	49.4	Solvothermal	0.26	showed stable current for over 50 h	[345]
CFO/rGO[c]; Co/Fe (2:1)	GC	340	310	Hydrothermal	0.10	The current density decreased after about 10 h	[332]
$Co_{0.8}Fe_{0.2}O_x$/ $CNTs_{25wt\%}$	GC	280	49	Pyrolysis	0.52	Stable current density for about 8 h	[326]
Co_3O_{4-x}-carbon@$Fe_{2-y}Co_yO$	GC	350	37.6	Thermal treatment	1.13	After 6000 cycles, it showed similar polarization curve with a small shift of about 20 mV at *J* of 50 mA cm^{-2}	[327]
CoFe-LDHs	–	270	58.3	Coordinating etching	–	Constant potential electrolysis at *J* of 5 mA cm^{-2} for about 10 h	[295]
NiCo-S@CoFeATT	GC	268	62	Hydrothermal	0.15	90% of the initial current density is retained after over 6 h operation	[253]
$Co_{0.75}Fe_{0.25}BO$/CP	GC	227	43.2	Hydrothermal	–	94% retention of the initial current density after 24 h successive operation	[346]
CoFe-based MOF	GC	290	40.9	Solution phase chemical	0.28	A slight decrease of 10% current density after 36 h continuous testing	[335]
CoFe/Co_8FeS_8/CNT	GC	290	38	Solvothermal	0.27	Stable current for about 18 h	[56]
CoFeP TPAs[g]/Ni	NF	198	96.7	Hydrothermal	4.0	Slight increase of 10 mV overpotential after 100 h operation	[329]
$Co_{2.7}Fe_{0.3}O_4$ NWs	CFP	342	64.4	Hydrothermal	4–5	After 100 h, a stable *J* of 1000 mA cm^{-2}	[336]
(Fe-Co)Se_2	GC	251	47.6	post-selenization	5.0	A stable *J* of 10 mA cm^{-2} for over 24 h	[347]
Am.Co_2Fe	GC	290	61	Mixing wet chemicals	0.28	A stable *J* of 14 mA cm^{-2} at the overpotential of 300 mV for about 36 h	[348]
B-NiCoFe	Fe wire	342	48	Bluing treatment	–	90.5% current retention was obtained after 1000 cycles	[349]
Co/Fe (2:1)	GC	570@130	42.39	Co-precipitation	0.20	Stable *J* of 130 mA cm^{-2} for about 16 h	[350]
FeCo-PM[h]12	GC	258	33	Co-precipitation	0.56	After 10 h operation at 1.52 V the current density decreased by only 8.3%	[351]
Co-Ni-Fe-51	GC	288	43	Solvothermal	0.12	11% decay of current density after 8 h	[352]
Co_7Fe_3	GC	365	60	DC[i] arc discharge technique	0.255	92.0% current density retention after long-term test	[353]
Fe_1Co_3/VO-800	GC	260	53	Plasma induced approach	–	Nearly no change of potential after 3000 cycles.	[354]
FeCo-N/C	GC	370	52	Solvothermal	0.32	After 3000 cycles, slight shift of overpotential by 7 mV was observed	[355]
$Co_{1.2}$Fe-MOF	GC	280	44.7	Wet chemical reduction	0.17	Only a slight increase of overpotential was observed during 15 h operation	[356]
CFO	GC	304	38	coordination-assisted-etching	0.50	No obvious of overpotential during 24 h continues measurements	[283]
Co-Fe-N@MWCNT	GC	290	32	Chemical reduction	1.0	stable current–time curve and 3% attenuation after 20000 s	[357]
CoFe-N-CN/CNT	GC	285	51.09	Lyophilisation and thermal	0.285	a stable *J* of 10 mA cm^{-2} at potential 1.52 V was during 20 h continuous testing	[358]
$Fe(OH)_3$@Co-MOF-74	CP[j]	292	44	Solvothermal	0.15	At overpotential of 331 mV, a stable *J* of 50 mA cm^{-2} for over 20 h	[359]
Fe-Co-F-400	GC	250	38.8	Co-precipitation and etching	–	Stable *J* of 10 mA cm^{-2} for 10 h testing	[360]
FeCoNi	NF	370@300	45	Electrodeposition	–	Retained constant potential after 8 h continuous electrolysis	[137]

(*continued on next page*)

Table 9 (*continued*)

Catalyst	Substrate	Overpotential (mV)@10 mA cm^{-2}	Tafel slope (mV dec^{-1})	Synthesis method	Catalyst loading (mg cm^{-2})	Stability	Ref.
$Ni_2CoFe_{0.5}$-LDHs	NF	240	65	Co-precipitation	–	A stable *J* of 10 mA cm^{-2} for about 72 h	[361]
NiFeCo-N_2	GC	320@9.06	72.9	Co-precipitation	0.038	Good stability for over 20 h	[362]
NiCoFe cations	CNTPE[k]	210	83	–	–	Remained stable for period of 10 h	[363]
FeCoNi-	N-CNF[d]	220	57	Electrospinning	–	Stable at *J* of 20 mA cm^{-2} for over 22 h	[364]
NiCoFe	NF	240	58	Hydrothermal	–	highly stable over 24 h	[365]
$NiCoFeO_x$	NF	232	58	Hydrothermal	1.0	Stable *J* for after 24 h	[366]
NiCoFe-LDHs	CFC	280	34	Co-precipitation	0.3–0.6	A slight increase from 1.53 to 1.55 V vs. RHE after 10 h test	[367]
NiCoFe-NC[a]	GC	250	31	Solvothermal	–	The *J* at 1.50 V increase at the initial of 4 h and then slight declined in the following 20 h	[368]
NiCoFe LTHs	CFC[l]	239	32	Electrodeposition	0.4	A slight decay (0.2%) after 20 h test	[369]
NiCoFe-LDHs	NF	276	56	templated in situ transformation	1.0	no apparent current loss after 12 h testing.	[370]
NiCoFe-OH	GC	230	72.7	Hydrothermal	–	Stable current at static potential of 230 V for about 10 h	[371]
PG-NiCoFe[m]-211 NAs	GC	313	51.9	cyanogel reduction	0.16	Stable potential after 12 continuous operation	[24]
NiCoFe-LDHs	CFP	288	92	Co-precipitation	0.532	Stable current after 12 h measurements	[372]

[a] NC: nitrogen-doped carbon layers; [b] G-HS: glycerate hollow spheres; [c] CFO/rGO: Co-Fe-O composites/reduced graphene oxides; [d] N-CNF: N-doped carbon nanofibers; [e] Am-CFDH/NCNTs: amorphous CoFe double hydroxides-decorated with N-doped carbon nanotubes; [f] CNWs: carbon nanowires: [g] TPA: triangular plate arrays; [h] PM: phosphomolybdate; [i] DC :direct current; [j] CP: carbon paper; [k] CNTPE: carbon nanotube paste electrode; [l] CFC: carbon fiber cloth; [m] PG-NiCoFe-211 NAs: pomegranate-like Fe-doped NiCo nanoassemblies.

workers [373] prepared 1D porous nanowire materials comprising of CoFeN as an effective electrocatalyst for the alkaline water splitting process. It was prepared by an ammonia annealing reaction of the CoFe double hydroxide source at 350 °C. The physicochemical characterization techniques such as XRD, XPS, and scanning electron microscopy (SEM) confirmed that nanoparticle anchored porous Co_3FeN_x nanowire was effectively produced using the route mentioned above. The as-made Co_3FeN_x materials unveiled an outstanding wave of electrocatalyst performance toward OER, succeeding 20 mA cm^{-2} at an ultra-small overpotential of 222 mV. More interestingly, the prepared electrocatalyst displayed a comparable catalytic performance with RuO_2 electrocatalyst for OER in an alkaline medium. Li and co-workers [380] synthesized a spinel $CoFe_2O_4$ nanoparticle stacked into N-assembled carbon fiber using a technique of electrospinning. Briefly, firstly, the solution of the precursors was electrospun onto the surface of the nanofiber membrane, followed by heat treatment to stabilize and calcined to carbonize the polymer precursor. Due to the nanostructure architecture and the synergy effect of the bimetals and the nitrogen-doped carbon fiber, the as-made $CoFe_2O_4$@N-CNFs electrode unveiled a noteworthy high wave of electrocatalyst performance toward OER, achieving a current density of 10 mA cm^{-2} using an overpotential of 349 mV, surpassing the commercial RuO_2 electrocatalyst. Numerous researchers have also prepared nanostructured and hollow materials doped with atomic of N, S, and P for anodic electrodes intended to use for OER in alkaline aqueous solution (Table 10). Besides, in recent years, Zhang and co-workers [374] prepared porous nanocuboid structured by doping of Fe into CoP. By controlling the composition of Fe and Co, an optimum content of Fe/Co was found to be $Co_{0.8}Fe_{0.2}P$, and this catalyst displayed a splendid performance for OER, requiring only 285 mV of overpotential to achieve an OER current density of 10 mA cm^{-2}. Good stability was also observed, which showed a small degradation of 5.78% during 10 h electrochemical measurement in 1.0 M KOH at a current density of 10 mA cm^{-2}. The impressive performance was claimed to have arisen from its porous architecture, optimized determining rate step, the well-integrated, and redistribution of π electron between Co and Fe cations.

Hollow nanostructured materials have peculiar properties with attractive activity and enhanced performance in electrolysis, ensued from their large surface area, which endows high catalytic site exposure to the reactants and the ultra-small dimension is also imperative for fast charge transfer. Zhang and co-workers [381] synthesized a hollow nanocage structured material using CoFe and Prussian blue analogs (PBA) bimetallic. The CoFe-PBA was used employed as a precursor template to fabricate CoFe-P, which was obtained by phosphidation of the precursors. SEM and TEM (Fig. 14) were used to elucidate the morphology and structure of the prepared materials. Fig. 14(b) shows a well-aligned nanocubodian structure with a uniform dimension size spanning from 250 to 350 nm. In comparison to the precursor CoFe-PBA (Fig. 14a), CoFeP cuboidal nanostructures unveiled more textured surface and hollow multivoid nanocages architecture (Fig. 14c and d)). CoFeP nanocages contain a hollow structure with voids in the interior and cubes and pyramids-looking walls. The creation of such a peculiar hollow structure might have resulted from variation of defect concentration in the surface and corner of the materials. Fig. 14(f) indicates the effective synthesize of CoFe-P, which EDX detected. Besides, XPS was used to explore the chemical oxidation state and composition of the prepared material. The XPS analysis also confirms the existence of the Co, Fe, N, and C elements in the product. Fig. 14(g) shows the Co 2*p* region of the CoFe-P multivoid nanocages. The binding energy of 778.8 and 793.6 eV region is attributed to the Co $2p_{3/2}$ and Co $2p_{1/2}$, respectively, assigned to Co^+ found in Co–P. Fig. 14(b–d) shows the existence of the Fe–P, metal phosphide, and N species, respectively. Both metals and the non-metal elements of P and N are very advantageous in enriching the prepared materials' catalytic activity. The novel prepared catalyst showed an extraordinary wave of electrocatalyst performance toward water oxidation, attaining a current density of 10 mA cm^{-2} at only 180 mV of overpotential, which surpassed various catalysts including the commercial IrO_2 and RuO_2 electrocatalysts.

Moreover, other studies disclosed that preparing a hybrid catalyst containing bimetallic CoFe-P/S and carbon materials can augment catalytic activity toward OER. Zhang and co-workers [334] synthesized bimetallic material hybridized with P, in which a superiors catalyst activity for OER was demonstrated. It was obtained via phosphorylation and thermal treatment of CoFe-MOFs. The hybrid electrocatalyst of CoFe-P uncovered notable electrocatalyst performance for OER, attained 10 mA cm^{-2} at a low overpotential of 244 mV. Other reports also claimed that preparing bimetallic

Table 10
State-of-the-art review of N, S and P doped CoFe based electrocatalysts for OER.

Catalyst	Substrate	Overpotential (mV)@10 mA cm^{-2}	Tafel slope (mV dec^{-1})	Synthesis method	Catalyst loading (mg cm^{-2})	Stability	Ref.
NSP-Co_3FeN_x	NF	222@20	46	Hydrothermal	–	After 2000 cycles, the polarization curve showed no attenuation of activity	[373]
$(Co_{0.54}Fe_{0.46})_2P$	GC	370	–	Phosphorylation	–	Stable current density after 1000 CV cycles	[379]
CoFeSP/CNT	CFP	262	68	Gas-phase sulfurization and Phphor.	–	a stable current of 10 and 20 mA cm^{-2} was maintained during continuous testing for 12 h at a constant overpotential of 280 and 300 mV, respectively	[384]
Co-Fe-P-1.7	NF	244	58	Solvothermal	1.0	Constant operating potential for over 40 h continuous operation	[334]
Fe-CoP cage	GC	300	35.2	Annealing	–	Stable polarization after 1000 cycles	[375]
$Co_{0.5}Fe_{0.5}S$@N-MC	GC	410	159	Hydrothermal	0.1	After 80 h operation, almost stable current was retained	[378]
$Co_{0.35}Fe_{0.17}P_{0.48}$/NC	GC	275	31	Gas-solid phase reaction	0.20	at operating potential of 1.53 V, a stable *J* of 10 mA cm^{-2} was recorded for about 17 h	[385]
$Co_{0.4}Fe_{0.6}P$	GC	270	25.6	Chemical-precipitation	0.20	Stable *J* of 30 mA cm^{-2} for about 3 h	[376]
CoFeP nanocage	GC	180	55	Co-precipitation	–	Stable polarization curve after 1000 cycles	[381]
Fe-CoS/NC	GC	257	46.7	Hydrothermal	0.23	2.82% increment of overpotential after 50 h measurement	[340]
CoFeP-1.8	NF	242@100	53	partial phosphating	3.41	88.24% retention of *J* of 100 mA cm^{-2} after 40 h test	[386]
CFeCoP	GP[a]	282	44	Electrodeposition	3.0	Stable *J* of 100 mA cm^{-2} for about 139 h	[382]
CoFeP/CF	CuF[b]	277.9@50	73	Hydrothermal	15.1	Maintained stable *J* of 10 mA cm^{-2} for more than 50 h	[387]
$Co_yFe_{10-y}O_x$/NPC[d]	GC	328	31.4	Hydrothermal	0.357	The potential at a *J* of 1 and 10 mA cm^{-2} remained stable for about 15 h	[388]
Fe-CoP HTPAs[e]	GC	230	69	ligand exchange reaction	–	Stable current density for over 50 h	[389]
$CoFe_2O_4$ @N-CNFs	GC	349	80	electrospinning	0.57	Around 7.3% decrease of current density after 40000 s operation	[127]
CoFe@NC-700	GC	380	110	Hydrothermal	–	Only 7% degradation after 10000 s	[390]
$Co_{0.8}Fe_{0.2}P$	GC	285	40	Phosphidation	0.255	only 5.78% degradation was observed after 10 h continuous test	[374]
S-d[c]-$FeCoO_x$	Graphite	300	40	Hydrothermal	0.45	–	[391]
CoFeP NSs	GC	305	49.6	co-reduction	–	Retained long-term stability with negligible decay at the *J* of 10 mA cm^{-2} for about 24 h	[256]
$Fe_{0.27}Co_{0.73}P$	NF	251	59.1	One pot-in situ co-reduction	3.0	Trivial attenuation of current density after 40 h continuous measurement	[383]
Fe-Co-P nanobox	CFP	269	31	chemical conversion	0.30	–	[154]
Co-Fe-Pyro	GC	276	31	Co-precipitation	1.0	Retention of 90% after 30000 s at 1.62 V	[392]
$FeCo_2$ P polyhedron	CFP	320	55	Solvothermal	0.50	only 10% drop of the initial current density after a 12 h test	[393]
$Co_{0.66}Fe_{0.33}P$	GC	294	69	Co-precipitation	0.25	No obvious attenuation of overpotential of 294 mV tested at 6 h	[394]
$Co_{0.7}Fe_{0.3}P_3$	CC	330@50	82.5	Hydrothermal	1.03	After 10 h continuous measurement, the current density was preserved at around 32 mA cm^{-2}	[395]

[a] GP: graphite plates; [b] CuF: copper foam; [c] S-d: sulfur-doped; [d] NPC: porous carbon nanosheets; [e] HTPAs: hollow triangle plate arrays.

CoFe doped with P or S and carbon material could boost the electrocatalyst wave of potential for OER [376,381].

Moreover, an affordable and easy method of cathodic deposition has attempted to synthesize P doped CoFe hydroxide bimetallic electrocatalyst with an outstanding performance [382]. The cathodically deposited CoFe-P on the graphite plate demonstrated a profound and superior electrochemical performance for alkaline OER, which attained 10 mA cm^{-2} @ low 282 mV of overpotential outstripped IrO_2 (IrO_2 demands an overpotential 320 mV to reach a current density of 10 mA cm^{-2}). Most significantly, the prepared electrocatalyst presented an extraordinary performance toward overall water splitting. A 1.56 V voltage is required to derive 10 mA cm^{-2} with a long operation lifetime (stable for around 139 h). Besides, in recent years, Lin and co-workers [383] proposed a one-pot approach to preparing novel material that can function for both OER and HER. By tweaking the molar ratio of Fe and Co, an optimum $Fe_{0.27}Co_{0.73}P$ electrocatalyst was found to be an enthralling catalyst for the overall water splitting process. The prepared mate ails entailed an outstanding catalytic competency showing an over the potential of 251 and 186 mV to harvest a current density of 10 mA cm^{-2} for OER and HER, respectively, in 1.0 M KOH solution. Good electrochemical stability was observed during 40 h continuous operation, signifying its potential for large-scale commercialization.

In summary, incorporating hetero atoms, such as N, P, and S, into bimetallic CoFe catalysts could tune the electronic structure, composition, and coordination environment, eventually altering the catalytic activity. Besides, doping of heteroatoms into carbon lattice could improve the positive charge density of the adjacent carbon atoms due to their strong electron-donating capability and high electronegativity. This eventually enhances the electrical conductivity, expedites intermediate reactants' adsorption, and further amplifies catalytic activity. However, ration design, facile, and controllable synthesis method of CoFe doped with hetero atoms with homogenous integration is still a challenging phenomenon.

6. Recent advances in situ/operando electrocatalyst characterization techniques

Discovering the connection between catalyst surface structure and active phase/reactivity is an imperative phenomenon in heterogeneous catalysts. Such foundational knowledge would empower researchers to rational design and develop advanced catalysts [396]. Nowadays, there are powerful, cutting-edge instru-

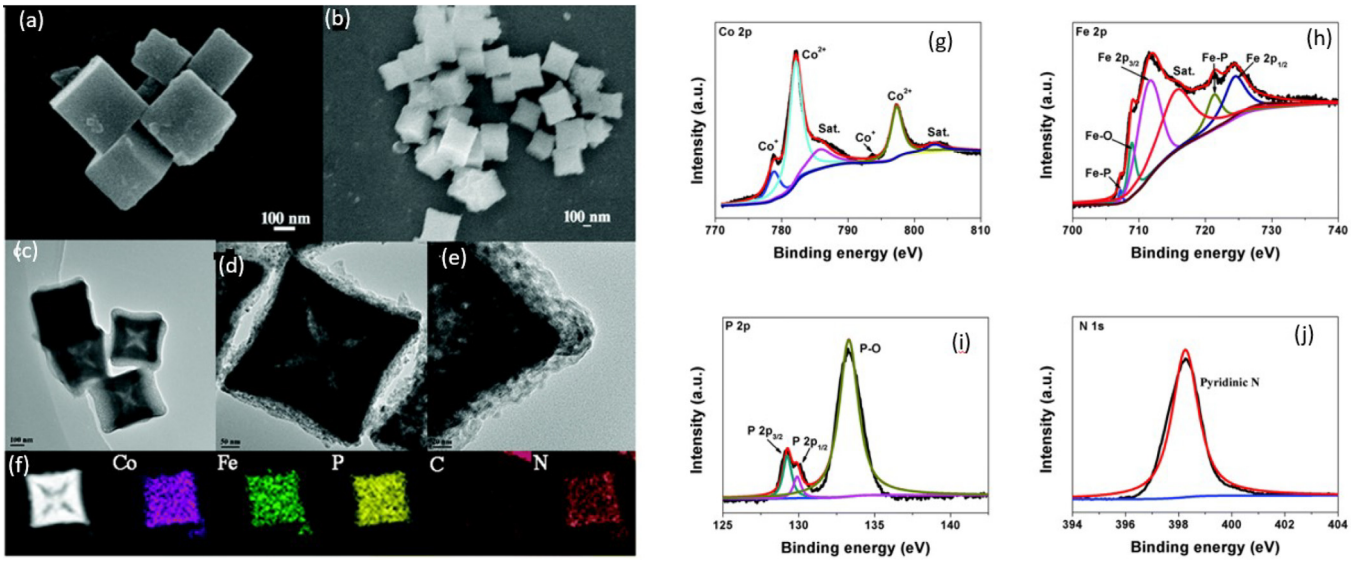

Fig 14. (a) SEM image of the precursor CoFe-PBA, (b) SEM image of the nanocage CoFe-P, (c–e) TEM images of CoFeP multivoiced nanocages, (f) EDX of Co, Fe, N, P, C revealing their uniform distribution, and high-resolution XPS spectra of (g) Co 2*p*, (h) Fe 2*p*, (i) P 2*p*, and (j) N 1*s* regions of CoFeP multi-void nanocages with fitting curves. Reproduced from Ref. [381] with permission from the Partner Organisations.

ments that enable us to monitor the catalyst structure and activity. The development of in situ/operando characterization techniques has brought enormous momentum to elucidate and unravel the enigma heterogeneous catalyst (such as electrocatalyst) structure and performance [108,396-398]. The term in situ is derived from a Latin word, referring to "on-site" or "on location", denoting that materials characterization is undertaken under meticulously controlled atmosphere (reaction condition, reducing/oxidizing, or vacuum) in a definite chemical reactor or cell. In situ-based probing of electrocatalyst has enabled researchers to expound catalyst evolution structure under a controlled environment; however, a direct relationship between catalyst structure and performance cannot be obtained since in situ technique has a limitation in analyzing the corresponding reaction products. The in situ spectroscopy probing bottleneck can be solved by concurrently gathering catalyst characterization and integrating online product analysis data, which is known as operando spectroscopy. This technique is emerging spectroscopy that allows to concurrently cartel the spectroscopic surface framework with catalytic activity/reactivity for a given material under actual reaction conditions [108,396,397,399]. Numerous operando spectroscopies have been used to monitor the catalyst structure change during the real phenomena of the reaction condition. For example, XAS is a powerful modern instrument that helps to extract crucial information of the local atomic and electronic structure of materials [400]. A particular example application of XAS for OER electrocatalyst can be found in different studies [279,398-407]. Few researchers have used XAS to unravel and monitor NiCo and CoFe based catalyst surface and activity during the reaction process.

Calvillo and co-workers [402] employed operando XAS to scrutinize the chemical and structure change of fresh and aged Co-Fe spinel powder. It was found that Co-Fe spinel exhibited higher energy value at both Fe K and Co K edge after the potential was augmented, showing that an increased oxidation state for both metals. An irreversible change was observed on the metal oxides, which gradually determined their durability for OER. Enman and co-workers [281] employed operando X-ray absorption spectroscopy and DFT to investigate the atomic and electronic structure of $Co(Fe)O_xH_y$ during OER. It was found that a high valance of state Fe participates in the OER process. They demonstrated partial Fe oxidation and a shortening of the Fe–O bond length during OER operating potential. The findings confirm that Co oxidation has prevailed only in the absence of Fe.

In the year 2018, Chen and co-workers [408] employed operando Raman spectroscopy to study the composition and structure of CoO_xH_y and $NiCoO_xH_y$ electrocatalyst during OER. The catalysts were electrodeposited on the surface of the FTO substrate. They observed an irreversible spinel transformation to the amorphous α-CoO phase, followed by a reversible conversion between α-CoO and the active phase NiOOH-h-CoO_2 at 0.2 and 0.3 V vs. Ag/AgCl, respectively. Besides, this technique has been used recently to probe the catalytic activity and change of other electrocatalyst surface structures during the OER [404,409,410].

XPS has been demonstrated to be a promising instrument for probing surface solids in a vacuum state and can offer important information such as the composition and chemistry of the surface materials. Nowadays, the working window of XPS is upgraded from high vacuum circumstance into a high pressure, allowing the investigation of surface materials under the actual working and near working conditions. An operando ambient pressure XPS (APXPS) enables us to study the catalyst evolution during OER at ambient pressure. For example, Favaro and co-workers [407] employed an APXPS to study the role and function of each transition metal and Ce oxide during OER. It uses "tender" X-rays, which is beneficial to probe materials surface concealed in the nanometer-thick solution layer. APXPS experiment requires low current, and this is in good alignment to investigate the activity of $Ni_{0.3}Fe_{0.07}Co_{0.2}Ce_{0.43}O_x$ at a lower overpotential. To directly monitor the catalyst chemistry under particular applied potential, the material $Ni_{0.3}Fe_{0.07}Co_{0.2}Ce_{0.43}O_x$ was analyzed by APXPS at operando conditions of 0.55 V vs. Ag/AgCl, which is tantamount to 340 mV overpotential and 1 mA cm^{-2} current density. Operando XAS has also been used to study the coordination shell structure of the metals distributed throughout the material. In this case, the sample was immersed in a bulk electrolyte, facilitating the diffusion rate and catalyst current density that is essentially suitable to study the electrocatalyst at the desired overpotential. The combination of both APXPS and XAS is a superb strategy for comprehending the active site of the catalyst and the role of ceria in improving the activity at small overpotential. Schematic represen-

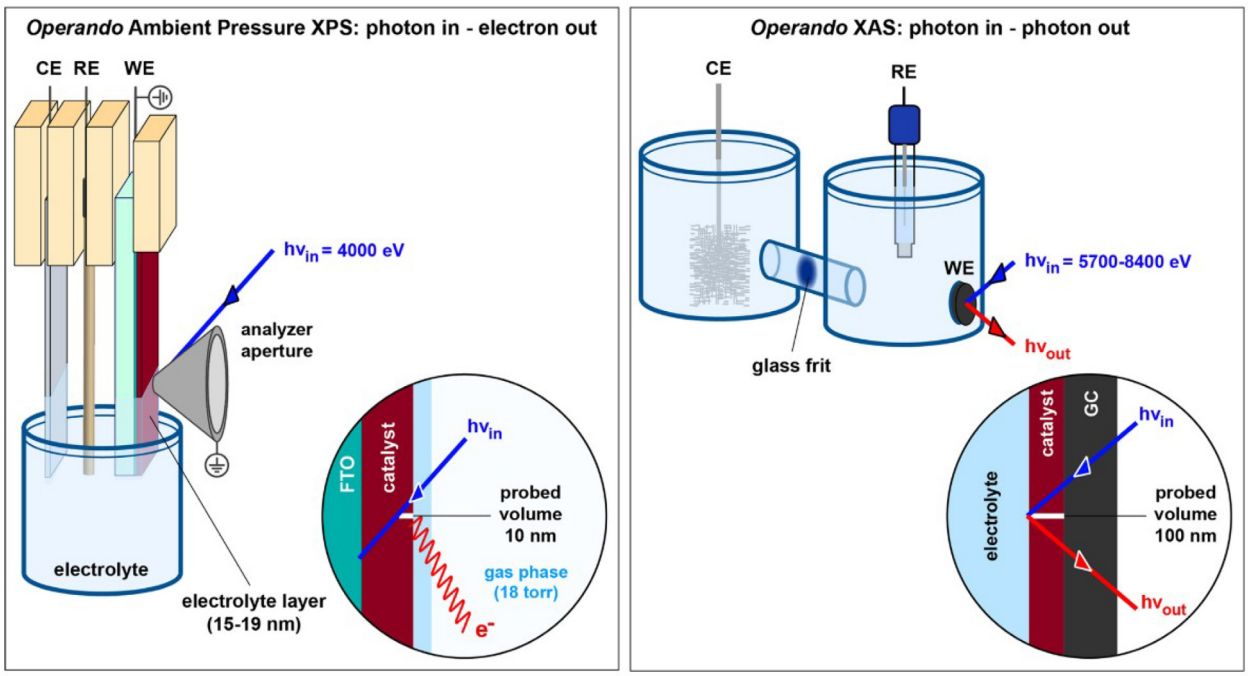

Fig 15. Schematic illustration of both APXPS and XAS configuration employed for an operando characterization of metal oxide OER electrocatalyst. CE: counter electrode; RE: reference electrode and WE: working electrode; Reproduced from Ref. [407] with permission from the American Chemical Society.

tation of both APXPS and XAS set up, utilized for the operando characterization of the prepared metal oxide for OER electrocatalyst, is shown in Fig. 15.

Moreover, the same authors [411] endeavored APXPS to study the chemical and structural change of different CoO_x electrocatalyst layers as a function of applied potential. APXPS was crucial to track the catalyst surface evolution of cobalt oxide during the OER process. The findings revealed that new spectral were observed at low binding energy within the Co 2*p* and O 1*s* regions. In addition to the aforementioned operando characterizations, other spectroscopy such as small-angle X-ray scattering (SAXS) [401], quartz crystal microbalance (QCM) spectroscopy [410], time-resolved Fourier transform infrared spectroscopy [412], EIS [406], synchrotron radiography [413] have also been considerably used to investigate and track the structural evolution and activity of electrocatalyst during the actual reaction condition. Furthermore, in situ spectroscopy such as Raman spectroscopy [414-417] in situ XAS [415,418], in situ grazing-angle XRD (GA-XRD) [415,418] in situ XRD [417] in situ XPS [402], in situ X-ray absorption near edge structure spectroscopy (XANES) [415,419,420], APXPS [421] and others have also been remarkably practiced to monitor and obtain information on bimetal electrocatalysts during OER process.

7. Conclusions and outlook

This review paper encapsulates the recent development and progress of two bimetallic (NiCo and CoFe) based electrocatalysts for alkaline OER. The underlying reaction mechanism of anodic OER, the broadly utilized parameters to evaluate the activity and stability of electrocatalyst in the alkaline water electrolysis process, have been momentarily reviewed. Typically, the activity and durability of two selected earth-abundant bimetals of NiCo and CoFe in various forms, including Oxy(hydroxide), oxide, doped with heteroatoms of P/N/S, spinel, LDH structure, composite, alloy, are systematically reviewed. These two bimetals electrocatalysts showed a notable OER activity (required < 300 mV of overpotential to generate 10 mA cm^{-2} current density), which overwhelmed the precious metals based electrocatalysts.

Myriads of strategies such as preparing of hollow porous or nanostructured materials, doping heteroatoms of nitrogen/phosphorous//sulfide into bimetals, preparing of catalyst deposited in 3D/2D structured substrate, preparing of bimetals with abundant oxygen defects/vacancies, integrating of a conductive material such as carbon into bimetals and preparing of amorphous structured bimetallic electrocatalyst are among the most promising approach to amplify the activity, stability, and durability of OER electrocatalyst. The recapitulated recent state of the art and progress of NiCo and CoFe based electrocatalysts are briefly presented in Tables (1–9). In general, the electrocatalyst performance is mainly constrained by three factors: the intrinsic nature of conductivity, active surface area, and electronic structure. To revolutionize the constraints mentioned above and others, numerous promising approaches have been established to achieve outstanding OER electrocatalyst. To mention some of them:

(1) A material with high electrical conductivity is vital for electrocatalyst to reduce the ohmic loss, minimize interface resistance, and expedite the electron transfer between the catalyst surface and current collector. Myriads of efforts have been divulged to developing new materials with hyper electrical conductivity, which are strong enough to maintain the electron exchange during the OER process. One common strategy to prepare a catalyst with robust electrical conductivity is to synthesize mixed oxide/stoichiometric oxide or impregnate with conductive materials (such as NF, graphene oxide, carbon nanotube).

(2) The ECSA of a material adversely influences the overall performance of catalytic proficiency. Materials with high ECSA could offer ample active sites, substantially stimulating the performance of the OER process. A catalyst with high ECSA can be attained by developing nanostructured material or

controlling the material size and shape. NiCo and CoFe based electrocatalysts retaining high ECSA can be obtained by constructing various morphologies such as nanowire array, holey sheet design, a nanoplate, core–shell assembly, nanofoam, microsphere, nanotube array, hollow porous configuration, nanoparticle and nanomesh.

(3) The electronic or atomic structure of material governs the intrinsic activity, which is profoundly related to the adsorption properties of oxygen-containing entities. The adsorption energy of the catalyst surface for the intermediate should be neither too strong nor too weak. Modifying the electronic structure of the active phase of material is critical to realize higher intrinsic activity for robust electrocatalysis. The electronic structure of NiCo and CoFe can be regulated by fabricating nanostructured NiCo/CoFe LDHs with OH interlayer, doping of cation or anion into the LDHs, creating defects/vacancies, integrating graphene, incorporating heteroatoms such as P/S/N into NiCo or CoFe oxide, assembling of NiCo or CoFe into MOF, doping of Ni into Co oxide and doing of Fe into Co oxide.

(4) Preparing amorphous nanostructured material was demonstrated to be a promising avenue to obtain an enormously boosted electrocatalyst. The gas evolution issue could affect the overall activity and stability of a material. A material with superaerophobic surface phenomena can be achieved by designing and developing amorphous nanostructured materials, which could reduce the formation and adhesion of gas bubbles on the catalytic layer of the electrode surface, thus improving the OER performance. Eradicating the gas bubbles from the electrode surface bestows plenty of active sites that can propagate the activity and stability of the OER system.

(5) Predictive modeling such as DFT could be vital to design and develop a new catalyst with ideal binding energy for intermediates of OER to achieve hyperactivity. Hence, the exploitation of predictive modeling and experimental work could facilitate designing and developing a novel material for appealing electrocatalysts.

Though substantial advancement has been made yet, finding a viable OER electrocatalyst for practical purposes with high performance, inexpensive, and stable/durable features is a perplexing phenomenon that necessitates further exploration. The following aspects are outlined for future endeavors that should be considered to design and develop a perfect bimetallic (e.g., NiCo and CoFe) based electrocatalyst for OER and overall water splitting process.

(1) The fundamental underlying of self-reconstruction of bimetallic-based electrocatalyst during the OER process and the reason that provokes the self-initiated reconstruction into different forms is not yet wholly comprehended. Hence, scientists should give more devotion to the mechanism of catalyst reconstruction to fully unveil the governing factor. Besides, developing advanced tools for in situ/-operando surveillance is vital to gain an insight into phase transformation, morphology change, and variation of valence state during the reaction process.

(2) The electrocatalysis reaction mechanism of OER and the active sites that play a crucial role in catalysis is not fully elucidated. This is important for rational design and the development of ideal materials for OER electrolysis. For example, the interconnection of electronic structure and catalytic activity requires advanced research. In situ/operando studies help unveil the molecular framework of the catalyst's active site and the catalyst surface reaction intermediate during the catalysis process. Both surface structure and activity/reactivity are scrutinized simultaneously. For an actual exploration and regulation process of electronic structure and catalysis mechanism, it could be essential to employ an in situ or operando method for future endeavors.

Declaration of Competing Interest

The authors declare that they have no known competing financial interests or personal relationships that could have appeared to influence the work reported in this paper.

Acknowledgments

Financial support from the European Union's Horizon 2020 Research and Innovation programme under the Marie Skłodowska-Curie Actions-Innovative Training Networks (MSCA-ITN) Grant Agreement 813748 (Bike project) are gratefully acknowledged. The authors also wish to acknowledge the Ministerio de Ciencia, Innovación y Universidades (MICINN), and FEDER for the received funding in the project of reference ENE2017-83976-C2-1-R.

References

[1] J. Lelieveld, K. Klingmüller, A. Pozzer, R.T. Burnett, A. Haines, V. Ramanathan, Proc. Natl. Acad. Sci. U. S. A. 116 (2019) 7192–7197.
[2] W.J. Ripple, C. Wolf, T.M. Newsome, P. Barnard, W.R. Moomaw, Bioscience. 70 (2019) 8–12.
[3] P.C. Stern, B.K. Sovacool, T. Dietz, Nat. Clim. Chang. 6 (2016) 547–555.
[4] D. Apfel, S. Haag, C. Herbes, Renew. Sustain. Energy Rev. 148 (2021) 111228.
[5] U.K. Pata, Renew. Energy. 173 (2021) 197–208.
[6] J.O.M. Bockris, Int. J. Hydrogen Energy. 38 (2013) 2579–2588.
[7] R. Chaubey, S. Sahu, O.O. James, S. Maity, Renew. Sustain. Energy Rev. 23 (2013) 443–462.
[8] A. Ahmed, A.Q. Al-Amin, A.F. Ambrose, R. Saidur, Int. J. Hydrogen Energy. 41 (2016) 1369–1380.
[9] P. Nikolaidis, A. Poullikkas, Renew. Sustain. Energy Rev. 67 (2017) 597–611.
[10] M.A. Khan, H.B. Zhao, W.W. Zou, Z. Chen, W.J. Cao, J.H. Fang, J.Q. Xu, L. Zhang, J.J. Zhang, Electrochem. Energ. Rev. 1 (2018) 483–530.
[11] M. Balat, M. Balat, Int. J. Hydrogen Energy. 34 (2009) 3589–3603.
[12] S. Shiva Kumar, V. Himabindu, Mater. Sci. Energy Technol. 2 (2019) 442–454.
[13] F. Barbir, Energy. 34 (2009) 308–312.
[14] S.E. Hosseini, M.A. Wahid, Renew. Sustain. Energy Rev. 57 (2016) 850–866.
[15] J. Chi, H. Yu, Chinese J. Catal. 39 (2018) 390–394.
[16] Q. Feng, X.Z. Yuan, G. Liu, B. Wei, Z. Zhang, H. Li, H. Wang, J. Power Sources 366 (2017) 33–55.
[17] M. David, C. Ocampo-Martínez, R. Sánchez-Peña, J. Energy Storage. 23 (2019) 392–403.
[18] K. Praveen, M. Sethumadhavan, Int. Conf. Adv. Comput Commun. Informatics IEEE 2017 (2017) 219–222.
[19] J.E. Park, S.Y. Kang, S.H. Oh, J.K. Kim, M.S. Lim, C.Y. Ahn, Y.H. Cho, Y.E. Sung, Electrochim. Acta. 295 (2019) 99–106.
[20] D. Xu, M.B. Stevens, M.R. Cosby, S.Z. Oener, A.M. Smith, L.J. Enman, K.E. Ayers, C.B. Capuano, J.N. Renner, N. Danilovic, Y. Li, H. Wang, Q. Zhang, S.W. Boettcher, ACS Catal. 9 (2019) 7–15.
[21] F.M. Sapountzi, J.M. Gracia, C.J. (Kees-Jan)Weststrate, H.O.A. Fredriksson, J.W. (Hans) Niemantsverdriet, Prog. Energy Combust. Sci. 58 (2017) 1–35.
[22] J. Guo, X. Li, Y. Sun, Q. Liu, Z. Quan, X. Zhang, J. Solid State Chem. 262 (2018) 181–185.
[23] G. Hao, W. Wang, G. Gao, Q. Zhao, J. Li, J. Energy Chem. 24 (2015) 271–277.
[24] Z.-J. Wang, M.-X. Jin, L. Zhang, A.-J. Wang, J.-J. Feng, J. Energy Chem. 53 (2021) 260–267.
[25] M. Görlin, P. Chernev, J.F. De Araújo, T. Reier, S. Dresp, B. Paul, R. Krähnert, H. Dau, P. Strasser, J. Am. Chem. Soc. 138 (2016) 5603–5614.
[26] H. Fu, Y. Liu, L. Chen, Y. Shi, W. Kong, J. Hou, F. Yu, T. Wei, H. Wang, X. Guo, Electrochim. Acta. 296 (2019) 719–729.
[27] W. Dai, T. Lu, Y. Pan, J. Power Sources 430 (2019) 104–111.
[28] Z. Li, B. Li, C. Yang, S. Lin, Q. Pang, P. Shen, Appl. Surf. Sci. 491 (2019) 723–734.
[29] S.S. Lu, L.M. Zhang, Y.W. Dong, J.Q. Zhang, X.T. Yan, D.F. Sun, X. Shang, J.Q. Chi, Y.M. Chai, B. Dong, J. Mater. Chem. A 7 (2019) 16859–16866.
[30] W. Liu, H. Zhang, C. Li, X. Wang, J. Liu, X. Zhang, J. Energy Chem. 47 (2020) 333–345.
[31] R.V. Genova-Koleva, F. Alcaide, G. Álvarez, P.L. Cabot, H.-J. Grande, M.V. Martínez-Huerta, O. Miguel, J. Energy Chem. 34 (2019) 227–239.
[32] M. Roca-Ayats, E. Herreros, G. García, M.A. Peña, M.V. Martínez-Huerta, Appl. Catal. B Environ. 183 (2016) 56–60.
[33] T. Zhang, S.-C. Li, W. Zhu, Z.-P. Zhang, J. Gu, Y.-W. Zhang, Nanoscale 9 (2017) 1154–1165.

[34] G. García, M. Roca-Ayats, A. Lillo, J.L. Galante, M.A. Peña, M.V. Martínez-Huerta, Catal. Today 210 (2013) 67–74.
[35] T. Reier, M. Oezaslan, P. Strasser, ACS Catal. 2 (2012) 1765–1772.
[36] E.J. Kim J. Shin J. Bak S.J. Lee K. hyun Kim, D.H. Song, J.H. Roh, Y. Lee, H.W. Kim, K.S. Lee, E.A. Cho, Appl. Catal. B Environ. 280 (2021) 119433.
[37] S. Cherevko, S. Geiger, O. Kasian, N. Kulyk, J.-P. Grote, A. Savan, B.R. Shrestha, S. Merzlikin, B. Breitbach, A. Ludwig, K.J.J. Mayrhofer, Catal. Today 262 (2016) 170–180.
[38] B. Zhang, Y.H. Lui, H. Ni, S. Hu, Nano Energy. 38 (2017) 553–560.
[39] X. Zhao, Y. Fu, J. Wang, Y. Xu, J.H. Tian, R. Yang, Electrochim. Acta. 201 (2016) 172–178.
[40] W. Yan, X. Cao, K. Ke, J. Tian, C. Jin, R. Yang, RSC Adv. 6 (2016) 307–313.
[41] Y. Huang, Y.E. Miao, H. Lu, T. Liu, Chem. - A Eur. J. 21 (2015) 10100–10108.
[42] J.C. Ruiz-Cornejo, D. Sebastián, M.V. Martínez-Huerta, M.J. Lázaro, Electrochim. Acta. 317 (2019) 261–271.
[43] Z. Zhou, N. Mahmood, Y. Zhang, L. Pan, L. Wang, X. Zhang, J.J. Zou, J. Energy Chem. 26 (2017) 1223–1230.
[44] M. Zhang, Q. Dai, H. Zheng, M. Chen, L. Dai, Adv. Mater. 30 (2018) 1–10.
[45] J.M. Luque-Centeno, M.V. Martínez-Huerta, D. Sebastián, G. Lemes, E. Pastor, M.J. Lázaro, Renew. Energy. 125 (2018) 182–192.
[46] J. Ren, Z. Hu, C. Chen, Y. Liu, Z. Yuan, J. Energy Chem. 26 (2017) 1196–1202.
[47] Y. Wu, Y. Liu, G.D. Li, X. Zou, X. Lian, D. Wang, L. Sun, T. Asefa, X. Zou, Nano Energy. 35 (2017) 161–170.
[48] Y. Jin, S. Huang, X. Yue, C. Shu, P.K. Shen, Int. J. Hydrogen Energy. 43 (2018) 12140–12145.
[49] B. Aghabarari, J.M. Luque-Centeno, M. Capel-Sánchez, M.J. Lázaro Elorri, M.V. Martínez-Huerta, Catalysts 9 (2019) 471.
[50] H. Li, P. Wen, Q. Li, C. Dun, J. Xing, C. Lu, S. Adhikari, L. Jiang, D.L. Carroll, S.M. Geyer, Adv. Energy Mater. 7 (2017) 1–12.
[51] X. She, J. Wu, H. Xu, J. Zhong, Y. Wang, Y. Song, K. Nie, Y. Liu, Y. Yang, M.T.F. Rodrigues, R. Vajtai, J. Lou, D. Du, H. Li, P.M. Ajayan, Adv. Energy Mater. 7 (2017) 1–7.
[52] M.M. Najafpour, S. Madadkhani, M. Tavahodi, Int. J. Hydrogen Energy. 42 (2017) 60–67.
[53] Y. Zhao, C. Chang, F. Teng, Y. Zhao, G. Chen, R. Shi, G.I.N. Waterhouse, W. Huang, T. Zhang, Adv. Energy Mater. 7 (2017) 1–7.
[54] R. Subbaraman, D. Tripkovic, K.C. Chang, D. Strmcnik, A.P. Paulikas, P. Hirunsit, M. Chan, J. Greeley, V. Stamenkovic, N.M. Markovic, Nat. Mater. 11 (2012) 550–557.
[55] J. Béjar, L. Álvarez-Contreras, J. Ledesma-García, N. Arjona, L.G. Arriaga, J. Electroanal. Chem. 847 (2019) 113190.
[56] B. Wang, Y. Hu, B. Yu, X. Zhang, D. Yang, Y. Chen, J. Power Sources 433 (2019) 126688.
[57] W.K. Gao, M. Yang, J.Q. Chi, X.Y. Zhang, J.Y. Xie, B.Y. Guo, L. Wang, Y.M. Chai, B. Dong, Sci. China Mater. 62 (2019) 1285–1296.
[58] J.F. Qin, M. Yang, T.S. Chen, B. Dong, S. Hou, X. Ma, Y.N. Zhou, X.L. Yang, J. Nan, Y.M. Chai, Int. J. Hydrogen Energy. 45 (2020) 2745–2753.
[59] J. Hou, Y. Wu, B. Zhang, S. Cao, Z. Li, L. Sun, Adv. Funct. Mater. 29 (2019) 1–39.
[60] T. Tian, M. Zheng, J. Lin, X. Meng, Y. Ding, Chem. Commun. 55 (2019) 1044–1047.
[61] W. Zhang, D. Li, L. Zhang, X. She, D. Yang, J. Energy Chem. 39 (2019) 39–53.
[62] J. Mohammed-Ibrahim, J. Power Sources 448 (2020) 227375.
[63] J. Kundu, S. Khilari, K. Bhunia, D. Pradhan, Catal. Sci. Technol. 9 (2019) 406–417.
[64] S. Anantharaj, S. Kundu, S. Noda, Nano Energy. 80 (2021) 105514.
[65] P. Acharya, Z.J. Nelson, M. Benamara, R.H. Manso, S.I.P. Bakovic, M. Abolhassani, S. Lee, B. Reinhart, J. Chen, L.F. Greenlee, ACS Omega 4 (2019) 17209–17222.
[66] I.C. Man, H.Y. Su, F. Calle-Vallejo, H.A. Hansen, J.I. Martínez, N.G. Inoglu, J. Kitchin, T.F. Jaramillo, J.K. Nørskov, J. Rossmeisl, ChemCatChem 3 (2011) 1159–1165.
[67] M. Bajdich, M. García-Mota, A. Vojvodic, J.K. Nørskov, A.T. Bell, J. Am. Chem. Soc. 135 (2013) 13521–13530.
[68] V.I. Birss, A. Damjanovic, P.G. Hudson, J. Electrochem. Soc. 133 (1986) 1621–1625.
[69] K.J. Seong, K. Byunghoon, K. Hyunah, K. Kisuk, Adv. Energy Mater. 8 (2018) 1702774.
[70] Z. Cai, X. Bu, P. Wang, J.C. Ho, J. Yang, X. Wang, J. Mater. Chem. A 7 (2019) 5069–5089.
[71] A.J. Medford, A. Vojvodic, J.S. Hummelshøj, J. Voss, F. Abild-Pedersen, F. Studt, T. Bligaard, A. Nilsson, J.K. Nørskov, J. Catal. 328 (2015) 36–42.
[72] Y. Mao, J. Chen, H. Wang, P. Hu, Chinese J. Catal. 36 (2015) 1596–1605.
[73] M. Kroschel, A. Bonakdarpour, J.T.H. Kwan, P. Strasser, D.P. Wilkinson, Electrochim. Acta. 317 (2019) 722–736.
[74] L.K. Wu, W.Y. Wu, J. Xia, H.Z. Cao, G.Y. Hou, Y.P. Tang, G.Q. Zheng, J. Mater. Chem. A 5 (2017) 10669–10677.
[75] J. Zhao, X.R. Wang, X.J. Wang, Y.P. Li, X.D. Yang, G.D. Li, F.T. Li, Inorg. Chem. Front. 5 (2018) 1886–1893.
[76] M. Roca-Ayats, M.D. Roca-Moreno, M.V. Martínez-Huerta, Int. J. Hydrogen Energy. 41 (2016) 19656–19663.
[77] G. Li, L. Anderson, Y. Chen, M. Pan, P.Y. Abel Chuang, Sustain. Energy Fuels 2 (2018) 237–251.
[78] N. Elgrishi, K.J. Rountree, B.D. McCarthy, E.S. Rountree, T.T. Eisenhart, J.L. Dempsey, J. Chem. Educ. 95 (2018) 197–206.
[79] A. Ashok, A. Kumar, J. Ponraj, S.A. Mansour, F. Tarlochan, Int. J. Hydrogen Energy 44 (2019) 16603–16614.
[80] K. Nejati, S. Davari, A. Akbari, K. Asadpour-Zeynali, Z. Rezvani, Int. J. Hydrogen Energy 44 (2019) 14842–14852.
[81] M. Al-Mamun, X. Su, H. Zhang, H. Yin, P. Liu, H. Yang, D. Wang, Z. Tang, Y. Wang, H. Zhao, Small 12 (2016) 2866–2871.
[82] R. Elakkiya, R. Ramkumar, G. Maduraiveeran, Mater. Res. Bull. 116 (2019) 98–105.
[83] D. Ping, X. Feng, J. Zhang, J. Geng, X. Dong, ChemElectroChem 4 (2017) 3037–3041.
[84] Y. Li, F.M. Li, X.Y. Meng, X.R. Wu, S.N. Li, Y. Chen, Nano Energy 54 (2018) 238–250.
[85] H.A. Bandal, A.R. Jadhav, A.H. Tamboli, H. Kim, Electrochim. Acta. 249 (2017) 253–262.
[86] X. Zhang, X. Li, R. Li, Y. Lu, S. Song, Y. Wang, Small 15 (2019) 1–13.
[87] H. Shi, G. Zhao, J. Phys. Chem. C 118 (2014) 25939–25946.
[88] G. Ou, F. Wu, K. Huang, N. Hussain, D. Zu, H. Wei, B. Ge, H. Yao, L. Liu, H. Li, Y. Shi, H. Wu, ACS Appl. Mater. Interfaces 11 (2019) 3978–3983.
[89] B. Pierozynski, T. Mikolajczyk, M. Luba, A. Zolfaghari, J. Electroanal. Chem. 847 (2019) 113194.
[90] X. Hu, X. Tian, Y.W. Lin, Z. Wang, RSC Adv. 9 (2019) 31563–31571.
[91] M. Yao, B. Sun, N. Wang, W. Hu, S. Komarneni, Appl. Surf. Sci. 480 (2019) 655–664.
[92] F. Yu, F. Li, L. Sun, Int. J. Hydrogen Energy. 41 (2016) 5230–5233.
[93] M. Yao, N. Wang, W. Hu, S. Komarneni, Appl. Catal. B Environ. 233 (2018) 226–233.
[94] X. Lu, C. Zhao, Nat. Commun. 6 (2015) 6616.
[95] S.H. Ahn, I. Choi, H.Y. Park, S.J. Hwang, S.J. Yoo, E. Cho, H.J. Kim, D. Henkensmeier, S.W. Nam, S.K. Kim, J.H. Jang, Chem. Commun. 49 (2013) 9323–9325.
[96] S. Trasatti, Electrochim. Acta. 29 (1984) 1503–1512.
[97] Z. Wang, H. Wang, S. Ji, X. Wang, B.G. Pollet, R. Wang, J. Power Sources 446 (2020) 227348.
[98] Y. Matsumoto, E. Sato, Mater. Chem. Phys. 14 (1986) 397–426.
[99] M. Dupont, A.F. Hollenkamp, S.W. Donne, Electrochim. Acta. 104 (2013) 140–147.
[100] E. Cossar, M.S.E. Houache, Z. Zhang, E.A. Baranova, J. Electroanal. Chem. 870 (2020) 114246.
[101] S. Trasatti, O.A. Petrii, Pure Appl. Chem. 63 (1991) 711–734.
[102] H.S. Jadhav, A. Roy, G.M. Thorat, W.J. Chung, J.G. Seo, J. Ind. Eng. Chem. 71 (2019) 452–459.
[103] S.K. Bikkarolla, P. Papakonstantinou, J. Power Sources 281 (2015) 243–251.
[104] M. Liang, R. Su, W. Qi, Y. Zhang, R. Huang, Y. Yu, L. Wang, Z. He, Ind. Eng. Chem. Res. 53 (2014) 13635–13643.
[105] F. Zheng, Z. Zhang, D. Xiang, P. Li, C. Du, Z. Zhuang, X. Li, W. Chen, J. Colloid Interface Sci. 555 (2019) 541–547.
[106] A. Xie, J. Zhang, X. Tao, J. Zhang, B. Wei, W. Peng, Y. Tao, S. Luo, Electrochim. Acta. 324 (2019) 134814.
[107] B. Iandolo, B. Wickman, B. Seger, I. Chorkendorff, I. Zorić, A. Hellman, Phys. Chem. Chem. Phys. 16 (2014) 1271–1275.
[108] Y. Yang, Y. Xiong, R. Zeng, X. Lu, M. Krumov, X. Huang, W. Xu, H. Wang, F.J. Disalvo, J.D. Brock, D.A. Muller, ACS Catal. 11 (2021) 1136–1178.
[109] M. Tahir, L. Pan, F. Idrees, X. Zhang, L. Wang, J.J. Zou, Z.L. Wang, Nano Energy. 37 (2017) 136–157.
[110] V. Rashkova, S. Kitova, I. Konstantinov, T. Vitanov, Electrochim. Acta. 47 (2002) 1555–1560.
[111] N. Baig, I. Kammakakam, W. Falath, I. Kammakakam, Mater. Adv. 2 (2021) 1821–1871.
[112] M. Parashar, V.K. Shukla, R. Singh, J. Mater. Sci. Mater. Electron. 31 (2020) 3729–3749.
[113] X. Guo, G. Liang, A. Gu, J. Colloid Interface Sci. 553 (2019) 713–719.
[114] X. Wang, Z. Li, D.-Y. Wu, G.-R. Shen, C. Zou, Y. Feng, H. Liu, C.-K. Dong, X.-W. Du, Small 15 (2019) 1804832.
[115] Y. Wang, C. Yang, Y. Huang, Z. Li, Z. Liang, G. Cao, J. Mater. Chem. A 8 (2020) 6699–6708.
[116] J. Jiang, A. Zhang, L. Li, L. Ai, J. Power Sources 278 (2015) 445–451.
[117] F. Fievet, S. Ammar-Merah, R. Brayner, F. Chau, M. Giraud, F. Mammeri, J. Peron, J.Y. Piquemal, L. Sicard, G. Viau, Chem. Soc. Rev. 47 (2018) 5187–5233.
[118] Y. Ma, H. Zhang, J. Xia, Z. Pan, X. Wang, G. Zhu, B. Zheng, G. Liu, L. Lang, Int. J. Hydrogen Energy. 45 (2020) 11052–11061.
[119] B.J. Waghmode, A.P. Gaikwad, C.V. Rode, S.D. Sathaye, K.R. Patil, D.D. Malkhede, ACS Sustain. Chem. Eng. 6 (2018) 9649–9660.
[120] Z. Ali, M. Mehmood, J. Ahmed, A. Majeed, K.H. Thebo, Mater. Lett. 259 (2020) 126831.
[121] J. Lai, W. Niu, R. Luque, G. Xu, Nano Today 10 (2015) 240–267.
[122] G. Demazeau, Res. Chem. Intermed. 37 (2011) 107–123.
[123] J. Li, Q. Wu, J. Wu, T.S. Division, O. Ridge, O. Ridge, C. Sciences, E. Division, Handbook of Nanoparticles, Springer International Publishing, Cham, 2015.
[124] S. Gyergyek, M. Drofenik, D. Makovec, Mater. Chem. Phys. 133 (2012) 515–522.
[125] Q. Wang, Y. Lei, Y. Wang, Y. Liu, C. Song, J. Zeng, Y. Song, X. Duan, D. Wang, Y. Li, Energy Environ. Sci. 13 (2020) 1593–1616.
[126] C. Alegre, C. Busacca, A. Di Blasi, O. Di Blasi, A.S. Aricò, V. Antonucci, V. Baglio, ChemElectroChem 7 (2020) 124–130.

[127] T. Li, Y. Lv, J. Su, Y. Wang, Q. Yang, Y. Zhang, J. Zhou, L. Xu, D. Sun, Y. Tang, Adv. Sci. 4 (2017) 1700226–1700234.
[128] C. Zhang, S. Bhoyate, C. Zhao, P.K. Kahol, N. Kostoglou, C. Mitterer, S.J. Hinder, M.A. Baker, G. Constantinides, K. Polychronopoulou, C. Rebholz, R.K. Gupta, Catalysts 9 (2019) 176.
[129] L. Gong, X.Y.E. Chng, Y. Du, S. Xi, B.S. Yeo, ACS Catal. 8 (2018) 807–814.
[130] C.G. Morales-Guio, L. Liardet, X. Hu, J. Am. Chem. Soc. 138 (2016) 8946–8957.
[131] L. Wu, L. Shi, S. Zhou, J. Zhao, X. Miao, J. Guo, Energy Technol. 6 (2018) 2350–2357.
[132] B. Jeong, D. Shin, J.K. Lee, D.H. Kim, Y.D. Kim, J. Lee, Phys. Chem. Chem. Phys. 16 (2014) 13807–13813.
[133] Z. Guo, W. Ye, X. Fang, J. Wan, Y. Ye, Y. Dong, D. Cao, D. Yan, Inorg. Chem. Front. 6 (2019) 687–693.
[134] Z. Zhang, J. Zhang, T. Wang, Z. Li, G. Yang, H. Bian, J. Li, D. Gao, RSC Adv. 8 (2018) 5338–5343.
[135] R.C. Forsythe, C.P. Cox, M.K. Wilsey, A.M. Müller, Chem. Rev. (2021) 7568–7637.
[136] R. Yang, Y. Zhou, Y. Xing, D. Li, D. Jiang, M. Chen, W. Shi, S. Yuan, Appl. Catal. B Environ. 253 (2019) 131–139.
[137] Y. Li, S. Yang, H. Li, G. Li, M. Li, L. Shen, Z. Yang, A. Zhou, Colloids Surfaces A Physicochem. Eng. Asp. 506 (2016) 694–702.
[138] Y. Wei, C.H. Shin, E.B. Tetteh, B.J. Lee, J.S. Yu, ACS Appl. Energy Mater. 3 (2020) 822–830.
[139] Q. Ye, J. Li, X. Liu, X. Xu, F. Wang, B. Li, J. Power Sources 412 (2019) 10–17.
[140] W. Liu, J. Bao, M. Guan, Y. Zhao, J. Lian, J. Qiu, L. Xu, Y. Huang, J. Qian, H. Li, Dalt. Trans. 46 (2017) 8372–8376.
[141] J. Li, W. Xu, D. Zhou, J. Luo, D. Zhang, P. Xu, L. Wei, D. Yuan, J. Mater. Sci. 53 (2018) 2077–2086.
[142] C. Chang, L. Zhang, C.W. Hsu, X.F. Chuah, S.Y. Lu, ACS Appl. Mater. Interfaces 10 (2018) 417–426.
[143] L. Wang, C. Gu, X. Ge, J. Zhang, H. Zhu, J. Tu, Part. Part. Syst. Charact. 34 (2017) 1–9.
[144] J. Feng, H. Xu, Y. Dong, S. Ye, Y. Tong, G. Li, Angew. Chemie Int. Ed. 55 (2016) 3694–3698.
[145] K. Zhang, Y. Liu, B. Wang, F. Yu, Y. Yang, L. Xing, J. Hao, J. Zeng, B. Mao, W. Shi, S. Yuan, Int. J. Hydrogen Energy. 44 (2019) 1555–1564.
[146] M.S. Balogun, W. Qiu, Y. Huang, H. Yang, R. Xu, W. Zhao, G.R. Li, H. Ji, Y. Tong, Adv. Mater. 29 (2017) 1702095.
[147] J. Shen, M. Wang, L. Zhao, P. Zhang, J. Jiang, J. Liu, J. Power Sources 389 (2018) 160–168.
[148] M. Yao, H. Hu, N. Wang, W. Hu, S. Komarneni, J. Colloid Interface Sci. 41 (2019) 576–584.
[149] S. Anantharaj, M. Venkatesh, A.S. Salunke, T.V.S.V. Simha, V. Prabu, S. Kundu, ACS Sustain. Chem. Eng. 5 (2017) 10072–10083.
[150] F. Moureaux, P. Stevens, G. Toussaint, M. Chatenet, Appl. Catal. B Environ. 258 (2019) 117963.
[151] X. Wang, B. Zheng, D. Yang, B. Sun, W. Zhang, Y. Chen, Energy Technol. 7 (2019) 1–8.
[152] M.E.G. Lyons, M.P. Brandon, J. Electroanal. Chem. 641 (2010) 119–130.
[153] H. Osgood, S.V. Devaguptapu, H. Xu, J. Cho, G. Wu, Nano Today 11 (2016) 601–625.
[154] H. Zhang, W. Zhou, J. Dong, X.F. Lu, X.W.D. Lou, Energy Environ. Sci. 12 (2019) 3348–3355.
[155] J. Zhang, R. García-Rodríguez, P. Cameron, S. Eslava, Energy Environ. Sci. 11 (2018) 2972–2984.
[156] C. Zhou, J. Mu, Y.F. Qi, Q. Wang, X.J. Zhao, E.C. Yang, Int. J. Hydrogen Energy. 44 (2019) 8156–8165.
[157] B. Yang, N. Zhang, G. Chen, K. Liu, J. Yang, A. Pan, M. Liu, X. Liu, R. Ma, T. Qiu, Appl. Catal. B Environ. 260 (2020) 118184.
[158] S. Sultan, J.N. Tiwari, A.N. Singh, S. Zhumagali, M. Ha, C.W. Myung, P. Thangavel, K.S. Kim, Adv. Energy Mater. 9 (2019) 1–48.
[159] J. Zhao, J.J. Zhang, Z.Y. Li, X.H. Bu, Small 16 (2020) 1–23.
[160] L. Zhang, Q. Fan, K. Li, S. Zhang, X. Ma, Sustain. Fuels. 4 (2020) 5417–5432.
[161] N.B. Halck, V. Petrykin, P. Krtil, J. Rossmeisl, Phys. Chem. Chem. Phys. 16 (2014) 13682–13688.
[162] Q. Zhou, Z. Chen, L. Zhong, X. Li, R. Sun, J. Feng, G. Wang, X. Peng, ChemSusChem 11 (2018) 2828–2836.
[163] H. Fang, T. Huang, D. Liang, M. Qiu, Y. Sun, S. Yao, J. Yu, M.M. Dinesh, Z. Guo, Y. Xia, S. Mao, J. Mater. Chem. A 7 (2019) 7328–7332.
[164] X. Zhang, X. Zhang, H. Xu, Z. Wu, H. Wang, Y. Liang, Adv. Funct. Mater. 27 (2017) 1606635.
[165] J. Peng, W. Dong, Z. Wang, Y. Meng, W. Liu, P. Song, Z. Liu, Mater. Today Adv. 8 (2020) 100081.
[166] N. Yuan, Q. Jiang, J. Li, J. Tang, Arab. J. Chem. 13 (2020) 4294–4309.
[167] H. Zhou, F. Yu, J. Sun, R. He, S. Chen, C.W. Chu, Z. Ren, Proc. Natl. Acad. Sci. U. S. A. 114 (2017) 5607–5611.
[168] B. Shao, W. Pang, X.Q. Tan, C. Tang, Y. Deng, D. Huang, J. Huang, J. Electroanal. Chem. 856 (2020) 113621.
[169] T.H. Nguyen, J. Lee, J. Bae, B. Lim, Chem. – A Eur. J. 24 (2018) 4724–4728.
[170] Q. Liu, H. Wang, X. Wang, R. Tong, X. Zhou, X. Peng, H. Wang, H. Tao, Z. Zhang, Int. J. Hydrogen Energy. 42 (2017) 5560–5568.
[171] L. Wang, C. Lin, D. Huang, F. Zhang, M. Wang, J. Jin, ACS Appl. Mater. Interfaces 6 (2014) 10172–10180.
[172] Z. Zhao, H. Wu, H. He, X. Xu, Y. Jin, Adv. Funct. Mater. 24 (2014) 4698–4705.
[173] X. He, F. Yin, G. Li, Int. J. Hydrogen Energy. 40 (2015) 9713–9722.
[174] D. Jeon, J. Park, C. Shin, H. Kim, J.W. Jang, D.W. Lee, J. Ryu, Sci. Adv. 6 (2020) 1–8.
[175] S. Zhu, J. Lei, L. Zhang, L. Lu, Int. J. Hydrogen Energy. 44 (2019) 16507–16515.
[176] A. Balram, H. Zhang, S. Santhanagopalan, ACS Appl. Mater. Interfaces 9 (2017) 28355–28365.
[177] L. Feng, H. Xue, ChemElectroChem 4 (2017) 20–34.
[178] M. Shao, R. Zhang, Z. Li, M. Wei, D.G. Evans, X. Duan, Chem. Commun. 51 (2015) 15880–15893.
[179] A.C. Thenuwara, N.H. Attanayake, J. Yu, J.P. Perdew, E.J. Elzinga, Q. Yan, D.R. Strongin, J. Phys. Chem. B 122 (2018) 847–854.
[180] Z. Lu, W. Xu, W. Zhu, Q. Yang, X. Lei, J. Liu, Y. Li, X. Sun, X. Duan, Chem. Commun. 50 (2014) 6479–6482.
[181] K. Xiang, J. Guo, J. Xu, T. Qu, Y. Zhang, S. Chen, P. Hao, M. Li, M. Xie, X. Guo, W. Ding, ACS Appl. Energy Mater. 1 (2018) 4040–4049.
[182] C. Yu, Z. Liu, X. Han, H. Huang, C. Zhao, J. Yang, J. Qiu, Carbon N. Y. 110 (2016) 1–7.
[183] T. Chen, R. Zhang, G. Chen, J. Huang, W. Chen, X. Wang, D. Chen, C. Li, K. Ostrikov (Ken), Catal. Today 337 (2019) 147–154.
[184] Y. Zhang, B. Cui, C. Zhao, H. Lin, J. Li, Phys. Chem. Chem. Phys. 15 (2013) 7363–7369.
[185] Q. Zhou, Y. Chen, G. Zhao, Y. Lin, Z. Yu, X. Xu, X. Wang, H.K. Liu, W. Sun, S.X. Dou, ACS Catal. 8 (2018) 5382–5390.
[186] F. Song, X. Hu, Nat Commun 5 (2014) 4477–4485.
[187] H. Liang, F. Meng, M. Cabán-Acevedo, L. Li, A. Forticaux, L. Xiu, Z. Wang, S. Jin, Nano Lett. 15 (2015) 1421–1427.
[188] J. Yan, L. Chen, X. Liang, Sci. Bull. 64 (2019) 158–165.
[189] S. Sun, C. Lv, W. Hong, X. Zhou, F. Wu, G. Chen, ACS Appl. Energy Mater. 2 (2019) 312–319.
[190] H.S. Jadhav, A.C. Lim, A. Roy, J.G. Seo, ChemistrySelect 4 (2019) 2409–2415.
[191] Y. Liu, M. Zhang, D. Hu, R. Li, K. Hu, K. Yan, ACS Appl. Energy Mater. 2 (2019) 1162–1168.
[192] Y. Zhou, S. Sun, C. Wei, Y. Sun, P. Xi, Z. Feng, Z.J. Xu, Adv. Mater. 1902509 (2019) 1902509.
[193] D. Ni, S. Liu, M. Wu, X. Lei, B. Xu, S.-C. Jun, C. Ouyang, Phys. Lett. A 560 (2019) 126114.
[194] P. Stelmachowski, A.H.A. Monteverde Videla, K. Ciura, S. Specchia, Int. J. Hydrogen Energy. 42 (2017) 27910–27918.
[195] S. Dey, G.C. Dhal, Mater. Sci. Energy Technol. 2 (2019) 575–588.
[196] N.-T. Suen, S.-F. Hung, Q. Quan, N. Zhang, Y.-J. Xu, H.M. Chen, Chem. Soc. Rev. 46 (2017) 337–365.
[197] B. Cui, H. Lin, J.-B. Li, X. Li, J. Yang, J. Tao, Adv. Funct. Mater. 18 (2008) 1440–1447.
[198] X. Yan, K. Li, L. Lyu, F. Song, J. He, D. Niu, L. Liu, X. Hu, X. Chen, ACS Appl. Mater. Interfaces 8 (2016) 3208–3214.
[199] X. Deng, S. Öztürk, C. Weidenthaler, H. Tüysüz, ACS Appl. Mater. Interfaces 9 (2017) 21225–21233.
[200] P. He, X.Y. Yu, X.W.D. Lou, Angew. Chemie - Int. Ed. 56 (2017) 3897–3900.
[201] H. Xu, J. Wei, M. Zhang, J. Wang, Y. Shiraishi, L. Tian, Y. Du, Nanoscale 10 (2018) 18767–18773.
[202] X. Lv, Y. Zhu, H. Jiang, X. Yang, Y. Liu, Y. Su, J. Huang, Y. Yao, C. Li, Dalt. Trans. 44 (2015) 4148–4154.
[203] Z. Chen, B. Zhao, Y.C. He, H.R. Wen, X.Z. Fu, R. Sun, C.P. Wong, Mater. Chem. Front. 2 (2018) 1155–1164.
[204] Y. Zhang, X. Wang, F. Luo, Y. Tan, L. Zeng, B. Fang, A. Liu, Appl. Catal. B Environ. 256 (2019) 117852.
[205] Z. Ma, H. Fu, C. Gu, Y. Huang, S. Hu, Q. Li, H. Wang, RSC Adv. 8 (2018) 28209–28215.
[206] C. Mahala, M. Basu, ACS Omega 2 (2017) 7559–7567.
[207] E. Umeshbabu, G. Ranga Rao, Electrochim. Acta. 213 (2016) 717–729.
[208] Y. Xiao, L. Feng, C. Hu, V. Fateev, C. Liu, W. Xing, RSC Adv 5 (2015) 61900–61905.
[209] S.H. Bae, J.E. Kim, H. Randriamahazaka, S.Y. Moon, J.Y. Park, I.K. Oh, Adv. Energy Mater. 7 (2017) 1–11.
[210] Z. Li, B. Li, J. Chen, Q. Pang, P. Shen, Int. J. Hydrogen Energy. 44 (2019) 16120–16131.
[211] J. Deng, H. Zhang, Y. Zhang, P. Luo, L. Liu, Y. Wang, J. Power Sources 372 (2017) 46–53.
[212] X. Yu, Z. Sun, Z. Yan, B. Xiang, X. Liu, P. Du, J. Mater. Chem. A 2 (2014) 20823–20831.
[213] J. Wang, T. Qiu, X. Chen, Y. Lu, W. Yang, J. Power Sources 268 (2014) 341–348.
[214] C. Zhu, D. Wen, S. Leubner, M. Oschatz, W. Liu, M. Holzschuh, F. Simon, S. Kaskel, A. Eychmüller, Chem. Commun. 51 (2015) 7851–7854.
[215] L. Zhang, Y. Li, J. Peng, K. Peng, Electrochim. Acta. 318 (2019) 762–769.
[216] S. Chen, S.Z. Qiao, ACS Nano 7 (2013) 10190–10196.
[217] N.R. Chodankar, I.V. Bagal, S. Ryu, Y. Han, D. Kim, ChemCatChem 11 (2019) 4256–4261.
[218] A.L. Bhatti, U. Aftab, A. Tahira, M.I. Abro, M. Kashif samoon, M.H. Aghem, M.A. Bhatti, Z. Hussainlbupoto, RSC Adv. 10 (2020) 12962–12969.
[219] J. Chen, Y. Ling, Z. Lu, X. Huai, F. Qin, Z. Zhang, Electrochim. Acta. 322 (2019) 134753.
[220] B. Chen, Z. Yang, Q. Niu, H. Chang, G. Ma, Y. Zhu, Y. Xia, Electrochem. Commun. 93 (2018) 191–196.
[221] Z. Ali, M. Mehmood, J. Ahmed, A. Majeed, K.H. Thebo, Mater. Res. Express 6 (2019) 105627.
[222] C. Shuai, Z. Mo, X. Niu, P. Zhao, Q. Dong, Y. Chen, N. Liu, R. Guo, J. Electrochem. Soc. 167 (2020) 026512.

[223] L. Yan, L. Cao, P. Dai, X. Gu, D. Liu, L. Li, Y. Wang, X. Zhao, Adv. Funct. Mater. 27 (2017) 1703455.
[224] X.F. Lu, L.F. Gu, J.W. Wang, J.X. Wu, P.Q. Liao, G.R. Li, Adv. Mater. 29 (2017) 1604437.
[225] Q. Liang, J. Chen, F. Wang, Y. Li, Coord. Chem. Rev. 424 (2020) 213488.
[226] K. Zhang, W. Guo, Z. Liang, R. Zou, Sci. China Chem. 62 (2019) 417–429.
[227] H.F. Wang, L. Chen, H. Pang, S. Kaskel, Q. Xu, Chem. Soc. Rev. 49 (2020) 1414–1448.
[228] Q. Shi, S. Fu, C. Zhu, J. Song, D. Du, Y. Lin, Mater. Horizons 6 (2019) 684–702.
[229] X. Zhang, L. Huang, Q. Wang, S. Dong, J. Mater. Chem. A 5 (2017) 18839–18844.
[230] Z. Yu, Y. Bai, S. Zhang, Y. Liu, N. Zhang, K. Sun, Int. J. Hydrogen Energy. 43 (2018) 8815–8823.
[231] S.K. Singh, D. Kumar, V.M. Dhavale, S. Pal, S. Kurungot, Adv. Mater. Interfaces 3 (2016) 1600532.
[232] R. Zhang, S. Cheng, N. Li, W. Ke, Appl. Surf. Sci. 503 (2020) 144146.
[233] M. Li, L. Tao, X. Xiao, X. Jiang, M. Wang, Y. Shen, ACS Sustain. Chem. Eng. 7 (2019) 4784–4791.
[234] X. Han, Y. Niu, C. Yu, Z. Liu, H. Huang, H. Huang, S. Li, W. Guo, X. Tan, J. Qiu, Nano Energy. 69 (2020) 104367.
[235] L.K. Wu, W.Y. Wu, J. Xia, H.Z. Cao, G.Y. Hou, Y.P. Tang, G.Q. Zheng, Electrochim. Acta. 254 (2017) 337–347.
[236] H. Zhao, Y. Yang, X. Dai, H. Qiao, J. Yong, X. Luan, L. Yu, C. Luan, Y. Wang, X. Zhang, Electrochim. Acta. 295 (2019) 1085–1092.
[237] S. Wang, T. Wang, X. Wang, Q. Deng, J. Yang, Y. Mao, G. Wang, Int. J. Hydrogen Energy. (2020) 12629–12640.
[238] A. Cetin, E.N. Esenturk, Mater. Today Chem. 14 (2019) 100215.
[239] L. Zeng, K. Zhou, L. Yang, G. Du, L. Liu, W. Zhou, ACS Appl. Energy Mater. 1 (2018) 6279–6287.
[240] M. Guo, Y. Li, L. Zhou, Q. Zheng, W. Jie, F. Xie, C. Xu, D. Lin, Electrochim. Acta. 298 (2019) 525–532.
[241] X. Jia, M. Wang, G. Liu, Y. Wang, J. Yang, J. Li, Int. J. Hydrogen Energy. 44 (2019) 24572–24579.
[242] L. Han, X.Y. Xu, X.W. Lou (David), Adv. Mater. 28 (2016) 4601–4605.
[243] J. Li, G. Wei, Y. Zhu, Y. Xi, X. Pan, Y. Ji, I.V. Zatovsky, W. Han, J. Mater. Chem. A 5 (2017) 14828–14837.
[244] H.C. Chien, W.Y. Cheng, Y.H. Wang, T.Y. Wei, S.Y. Lu, J. Mater. Chem. 21 (2011) 18180–18182.
[245] B. Zhang, X. Zhang, Y. Wei, L. Xia, C. Pi, H. Song, Y. Zheng, B. Gao, J. Fu, P.K. Chu, J. Alloys Compd. 797 (2019) 1216–1223.
[246] X. Du, W. Lian, X. Zhang, Int. J. Hydrogen Energy. 43 (2018) 20627–20635.
[247] L. Ma, B. Zhou, L. Tang, J. Guo, Q. Liu, X. Zhang, Electrochim. Acta. 318 (2019) 333–341.
[248] A. Pirkarami, S. Rasouli, E. Ghasemi, Appl. Catal. B Environ. 241 (2019) 28–40.
[249] W. Fang, D. Liu, Q. Lu, X. Sun, A.M. Asiri, Electrochem. Commun. 63 (2016) 60–64.
[250] F. Yuan, J. Wei, G. Qin, Y. Ni, J. Alloys Compd. 830 (2020) 154658.
[251] B. Dong, J.Y. Xie, Z. Tong, J.Q. Chi, Y.N. Zhou, X. Ma, Z.Y. Lin, L. Wang, Y.M. Chai, Chinese J. Catal. 41 (2020) 1782–1789.
[252] P. Thangasamy, S. Shanmuganathan, V. Subramanian, Nanoscale Adv. 2 (2020) 2073–2079.
[253] M. Hafezi Kahnamouei, S. Shahrokhian, ACS Appl. Mater. Interfaces 12 (2020) 16250–16263.
[254] K. Choi, I.K. Moon, J. Oh, J. Mater. Chem. A 7 (2019) 1468–1478.
[255] L. Peng, J. Wang, Y. Nie, K. Xiong, Y. Wang, L. Zhang, K. Chen, W. Ding, L. Li, Z. Wei, ACS Catal. 7 (2017) 8184–8191.
[256] H. Xu, J. Wei, C. Liu, Y. Zhang, L. Tian, C. Wang, Y. Du, J. Colloid Interface Sci. 530 (2018) 146–153.
[257] J. Yu, Q. Li, Y. Li, C.Y. Xu, L. Zhen, V.P. Dravid, J. Wu, Adv. Funct. Mater. 26 (2016) 7644–7651.
[258] D. Liu, Q. Lu, Y. Luo, X. Sun, A.M. Asiri, Nanoscale 7 (2015) 15122–15126.
[259] K.-L. Yan, X. Shang, Z. Li, B. Dong, J.-Q. Chi, Y.-R. Liu, W.-K. Gao, Y.-M. Chai, C.-G. Liu, Int. J. Hydrogen Energy. 42 (2017) 17129–17135.
[260] B. Qiu, L. Cai, Y. Wang, Z. Lin, Y. Zuo, M. Wang, Y. Chai, Adv. Funct. Mater. 28 (2018) 1706008.
[261] A. Saad, Z. Cheng, X. Zhang, S. Liu, H. Shen, T. Thomas, J. Wang, M. Yang, Adv. Mater. Interfaces 6 (2019) 1900960.
[262] C. Qin, A. Fan, D. Ren, C. Luan, J. Yang, Y. Liu, X. Zhang, X. Dai, M. Wang, Electrochim. Acta. 323 (2019) 134756.
[263] G. Mohan Kumar, P. Ilanchezhiyan, C. Siva, A. Madhankumar, T.W. Kang, D.Y. Kim, Int. J. Hydrogen Energy. (2019) 391–400.
[264] Y. Zheng, L. Zhang, H. Huang, F. Wang, L. Yin, H. Jiang, D. Wang, J. Yang, G. Zuo, Int. J. Hydrogen Energy. 44 (2019) 27465–27471.
[265] Z.Y. Shao, H. Qi, X. Wang, J. Sun, N.K. Guo, K. Huang, Q. Wang, Electrochim. Acta. 296 (2019) 259–267.
[266] I. Amorim, J. Xu, N. Zhang, D. Xiong, S.M. Thalluri, R. Thomas, J.P.S. Sousa, A. Araújo, H. Li, L. Liu, Catal. Today 358 (2019) 196–202.
[267] X. Gao, Y. Yu, Q. Liang, Y. Pang, L. Miao, X. Liu, Z. Kou, J. He, S.J. Pennycook, S. Mu, J. Wang, Appl. Catal. B Environ. 270 (2020) 118889.
[268] Y. Tang, H. Yang, J. Sun, M. Xia, W. Guo, L. Yu, J. Yan, J. Zheng, L. Chang, F. Gao, Nanoscale 10 (2018) 10459–10466.
[269] J. Jiang, C. Yan, X. Zhao, H. Luo, Z. Xue, T. Mu, Green Chem. 19 (2017) 3023–3031.
[270] X. Li, T. Wang, C. Wang, J. Alloys Compd. 729 (2017) 19–26.
[271] Y. Xiao, P. Zhang, X. Zhang, X. Dai, Y. Ma, Y. Wang, Y. Jiang, M. Liu, Y. Wang, J. Mater. Chem. A 5 (2017) 15901–15912.
[272] Y. Ning, D. Ma, Y. Shen, F. Wang, X. Zhang, Electrochim. Acta. 265 (2018) 19–31.
[273] J. Li, Q. Zhuang, P. Xu, D. Zhang, L. Wei, D. Yuan, Chinese J. Catal. 39 (2018) 1403–1410.
[274] Y.-R. Hong, S. Mhin, K.-M. Kim, W.-S. Han, H. Choi, G. Ali, K.Y. Chung, H.J. Lee, S.-I. Moon, S. Dutta, S. Sun, Y.-G. Jung, T. Song, H. Han, J. Mater. Chem. A 7 (2019) 3592–3602.
[275] L. Yang, H. Ren, Q. Liang, K.N. Dinh, R. Dangol, Q. Yan, Small 16 (2020) 1906766.
[276] P. Feng, X. Cheng, J. Li, X. Luo, ChemistrySelect 3 (2018) 760–764.
[277] A. Sivanantham, P. Ganesan, S. Shanmugam, Adv. Funct. Mater. 26 (2016) 4661–4672.
[278] C. Wang, J. Jiang, T. Ding, G. Chen, W. Xu, Q. Yang, Adv. Mater. Interfaces 3 (2016) 1–5.
[279] B. Wang, C. Tang, H.F. Wang, X. Chen, R. Cao, Q. Zhang, J. Energy Chem. 38 (2019) 8–14.
[280] X. Zhang, L. An, J. Yin, P. Xi, Z. Zheng, Y. Du, Sci. Rep. 7 (2017) 43590.
[281] L.J. Enman, M.B. Stevens, M.H. Dahan, M.R. Nellist, M.C. Toroker, S.W. Boettcher, Angew. Chemie Int. Ed. 57 (2018) 12840–12844.
[282] X. Han, C. Yu, S. Zhou, C. Zhao, H. Huang, J. Yang, Z. Liu, J. Zhao, J. Qiu, Adv. Energy Mater. 7 (2017) 1602148.
[283] F. Lyu, Y. Bai, Q. Wang, L. Wang, X. Zhang, Y. Yin, Mater. Today Chem. 11 (2019) 112–118.
[284] Y. Wang, Y. Ni, B. Liu, S. Shang, S. Yang, M. Cao, C. Hu, Electrochim. Acta. (2017) 356–363.
[285] T. Zhou, Z. Cao, H. Wang, Z. Gao, L. Li, H. Ma, Y. Zhao, RSC Adv. 7 (2017) 22818–22824.
[286] D. Inohara, H. Maruyama, Y. Kakihara, H. Kurokawa, M. Nakayama, ACS Omega 3 (2018) 7840–7845.
[287] X. Han, C. Yu, J. Yang, C. Zhao, H. Huang, Z. Liu, P.M. Ajayan, J. Qiu, Adv. Mater. Interfaces 3 (2016) 1500782.
[288] X. Yue, W. Ke, M. Xie, X. Shen, Z. Yan, Z. Ji, G. Zhu, K. Xu, H. Zhou, Catal, Sci. Technol. 10 (2020) 215–221.
[289] R.D.L. Smith, M.S. Prévot, R.D. Fagan, S. Trudel, C.P. Berlinguette, J. Am. Chem. Soc. 135 (2013) 11580–11586.
[290] W. Liu, H. Liu, L. Dang, H. Zhang, X. Wu, B. Yang, Z. Li, X. Zhang, L. Lei, S. Jin, Adv. Funct. Mater. 27 (2017) 1603904.
[291] S. Liu, B. Liu, C. Gong, Z. Li, Appl. Surf. Sci. 478 (2019) 615–622.
[292] Y. Li, W. Zhang, Z. Song, Q. Zheng, F. Xie, E. Long, D. Lin, Chempluschem 84 (2019) 1681–1687.
[293] G. Chen, J. Du, X. Wang, X. Shi, Z. Wang, H.P. Liang, Chinese J. Catal. 40 (2019) 1540–1547.
[294] K. Sliozberg, Y. Aniskevich, U. Kayran, J. Masa, W. Schuhmann, Zeitschrift. Für. Phys. Chemie (2020) 1466.
[295] H. Yuan, Y. Wang, C. Yang, Z. Liang, M. Chen, W. Zhang, H. Zheng, R. Cao, ChemPhysChem 20 (2019) 2964–2967.
[296] J. Bao, X. Zhang, B. Fan, J. Zhang, M. Zhou, W. Yang, X. Hu, H. Wang, B. Pan, Y. Xie, Angew. Chemie - Int. Ed. 54 (2015) 7399–7404.
[297] P.F. Liu, S. Yang, B. Zhang, H.G. Yang, ACS Appl. Mater. Interfaces 8 (2016) 34474–34481.
[298] Y. Wang, C. Xie, Z. Zhang, D. Liu, R. Chen, S. Wang, Adv. Funct. Mater. 28 (2018) 1–6.
[299] A.M.P. Sakita, R. Della Noce, E. Vallés, A.V. Benedetti, Appl. Surf. Sci. 434 (2018) 1153–1160.
[300] Y. Pei, Y. Ge, H. Chu, W. Smith, P. Dong, P.M. Ajayan, M. Ye, J. Shen, Appl. Catal. B Environ. 244 (2019) 583–593.
[301] L. Zhou, M. Guo, Y. Li, Q. Gu, W. Zhang, C. Li, F. Xie, D. Lin, Q. Zheng, Chem. Commun. 55 (2019) 4218–4221.
[302] C. Hao, Y. Wu, Y. An, B. Cui, J. Lin, X. Li, D. Wang, M. Jiang, Z. Cheng, S. Hu, Mater. Today, Energy. 12 (2019) 453–462.
[303] J. Zhao, X. Wang, F. Chen, C. He, X. Wang, Y. Li, R. Liu, X. Chen, Y. Hao, M. Yang, F. Li, Inorg. Chem. Front. 7 (2020) 737–745.
[304] F.K. Yang, K. Sliozberg, I. Sinev, H. Antoni, A. Bähr, K. Ollegott, W. Xia, J. Masa, W.G. Grünert, B.R. Cuenya, W.G. Schuhmann, M. Muhler, ChemSusChem 10 (2017) 156–165.
[305] T. Bhowmik, M.K. Kundu, S. Barman, ACS Appl. Energy Mater. 1 (2018) 1200–1209.
[306] L. Han, C. Dong, C. Zhang, Y. Gao, J. Zhang, H. Gao, Y. Wang, Z. Zhang, Nanoscale 9 (2017) 16467–16475.
[307] L. Feng, A. Li, Y. Li, J. Liu, L. Wang, L. Huang, Y. Wang, X. Ge, Chempluschem 82 (2017) 483–488.
[308] P. Ma, H. Yang, Y. Luo, Y. Liu, Y. Zhu, S. Luo, Y. Hu, Z. Zhao, J. Ma, ChemSusChem 12 (2019) 4442–4451.
[309] Z.W. Gao, T. Ma, X.M. Chen, H. Liu, L. Cui, S.Z. Qiao, J. Yang, X.W. Du, Small 14 (2018) 1–8.
[310] J. Zhao, Y. He, Z. Chen, X. Zheng, X. Han, D. Rao, C. Zhong, W. Hu, Y. Deng, ACS Appl. Mater. Interfaces 11 (2019) 4915–4921.
[311] H. Yang, D. Zhao, J. Mater. Chem. 15 (2005) 1217–1231.
[312] T. Grewe, X. Deng, H. Tüysüz, Chem. Mater. 26 (2014) 3162–3168.
[313] S. Lei, Q.H. Li, Y. Kang, Z.G. Gu, J. Zhang, Appl. Catal. B Environ. 245 (2019) 1–9.
[314] C. He, X. Han, X. Kong, M. Jiang, D. Lei, X. Lei, J. Energy Chem. 32 (2019) 63–70.
[315] L. Zhuang, L. Ge, Y. Yang, M. Li, Y. Jia, X. Yao, Z. Zhu, Adv. Mater. 29 (2017) 1606793.
[316] Y. Huang, R. Yang, G. Anandhababu, J. Xie, J. Lv, X. Zhao, X. Wang, M. Wu, Q. Li, Y. Wang, ACS Energy Lett. 3 (2018) 1854–1860.

[317] R.N. Singh, N.K. Singh, J.P. Singh, Electrochim. Acta. 47 (2002) 3873–3879.
[318] D. Xu, B. Liu, G. Liu, K. Su, C. Yang, H. Tong, D. Qian, J. Li, Int. J. Hydrogen Energy. 45 (2020) 6629–6635.
[319] C. Mahala, M.D. Sharma, M. Basu, Electrochim. Acta. 273 (2018) 462–473.
[320] C. You, Y. Ji, Z. Liu, X. Xiong, X. Sun, ACS Sustain. Chem. Eng. 6 (2018) 1527–1531.
[321] X. Gao, J. Liu, Y. Sun, X. Wang, Z. Geng, F. Shi, X. Wang, W. Zhang, S. Feng, Y. Wang, K. Huang, Inorg. Chem. Front. 6 (2019) 3295–3301.
[322] Y. Huang, W. Yang, Y. Yu, S. Hao, J. Electroanal. Chem. 840 (2019) 409–414.
[323] L.S. Ferreira, T.R. Silva, J.R.D. Santos, V.D. Silva, R.A. Raimundo, M.A. Morales, D.A. Macedo, Mater. Chem. Phys. 237 (2019) 121847.
[324] R. Valdez, A. Olivas, D.B. Grotjahn, E. Barrios, N. Arjona, R. Antaño, M.T. Oropeza-Guzman, Appl. Surf. Sci. 426 (2017) 980–986.
[325] Y.M. Zhao, F.F. Wang, P.J. Wei, G.Q. Yu, S.C. Cui, J.G. Liu, ChemistrySelect 3 (2018) 207–213.
[326] Y. Fang, X. Li, S. Zhao, J. Wu, F. Li, M. Tian, X. Long, J. Jin, J. Ma, RSC Adv. 6 (2016) 80613–80620.
[327] W. Xu, W. Xie, Y. Wang, A.C.S. Appl, Mater. Interfaces 9 (2017) 28642–28649.
[328] W. Liu, K. Du, L. Liu, J. Zhang, Z. Zhu, Y. Shao, M. Li, Nano Energy. 38 (2017) 576–584.
[329] L. Zhang, X. Wang, A. Li, X. Zheng, L. Peng, J. Huang, Z. Deng, H. Chen, Z. Wei, J. Mater. Chem. A 7 (2019) 17529–17535.
[330] J. Du, G. Liu, F. Li, Y. Zhu, L. Sun, Adv. Sci. 6 (2019) 2–8.
[331] Y. Liu, Y. Hu, P. Ma, F. Li, F. Yuan, S. Wang, Y. Luo, J. Ma, ChemSusChem 12 (2019) 2679–2688.
[332] J. Geng, L. Kuai, E. Kan, Q. Wang, B. Geng, ChemSusChem 8 (2015) 659–664.
[333] Y.J. Yang, M. Duan, C. Yan, D. Zhao, C. Jiang, X. Duan, X. Song, J. Electroanal. Chem. 856 (2020) 113697.
[334] T. Zhang, J. Du, P. Xi, C. Xu, ACS Appl. Mater. Interfaces 9 (2017) 362–370.
[335] Y. Liu, C. Wang, S. Ju, M. Li, A. Yuan, G. Zhu, Prog. Nat. Sci. Mater, Int, 2020, pp. 185–191.
[336] Z. Ye, C. Qin, G. Ma, X. Peng, T. Li, D. Li, Z. Jin, ACS Appl. Mater. Interfaces 10 (2018) 39809–39818.
[337] J. Sun, H. Li, Y. Huang, Z. Zhuang, Mater. Lett. 223 (2018) 246–249.
[338] M. Xiong, D.G. Ivey, Electrochim. Acta. 260 (2018) 872–881.
[339] M. Xiong, D.G. Ivey, Electrochem. Commun. 75 (2016) 73–77.
[340] C. Tian, T. Yang, Z. Liu, Y. Qing, B. Zhang, J. Zhou, Y. Wu, Appl. Surf. Sci. 510 (2020) 145484.
[341] C. Li, E. Zhou, Z. Yu, H. Liu, M. Xiong, Appl. Catal. B Environ. 269 (2020) 118771.
[342] W.K. Gao, J.F. Qin, K. Wang, K.L. Yan, Z.Z. Liu, J.H. Lin, Y.M. Chai, C.G. Liu, B. Dong, Appl. Surf. Sci. 454 (2018) 46–53.
[343] Y. Zhang, T. Gao, Z. Jin, X. Chen, D. Xiao, J. Mater. Chem. A 4 (2016) 15888–15895.
[344] Y. Zhang, M. Yang, X. Jiang, W. Lu, Y. Xing, J. Alloys Compd. 818 (2020) 153345.
[345] Z. Dong, W. Zhang, Y. Xiao, Y. Wang, C. Luan, C. Qin, Y. Dong, M. Li, X. Dai, X. Zhang, ACS Sustain. Chem. Eng. 8 (2020) 5464–5477.
[346] H. Liu, L. Yang, K. Qiao, L. Zheng, X. Cao, D. Cao, ChemSusChem 12 (2019) 3524–3531.
[347] W. Zhang, H. Zhang, R. Luo, M. Zhang, X. Yan, X. Sun, J. Shen, W. Han, L. Wang, J. Li, J. Colloid Interface Sci. 548 (2019) 48–55.
[348] W. Zhu, G. Zhu, C. Yao, H. Chen, J. Hu, Y. Zhu, W. Liang, J. Alloys Compd. 828 (2020) 154465.
[349] J. Xie, S. Cao, L. Gao, F. Lei, P. Hao, B. Tang, Chem. Commun. 55 (2019) 9841–9844.
[350] G.-C. Chen, T.H. Wondimu, H.-C. Huang, K.-C. Wang, C.-H. Wang, Int. J. Hydrogen Energy. 44 (2019) 10174–10181.
[351] H. Zhai, T. Gao, T. Qi, Y. Zhang, G. Zeng, D. Xiao, Chem. - An Asian J. 12 (2017) 2694–2702.
[352] G. Zeng, M. Liao, C. Zhou, X. Chen, Y. Wang, D. Xiao, RSC Adv. 6 (2016) 42255–42262.
[353] X. Yuan, X. Wang, M.S. Riaz, C. Dong, Z. Zhang, F. Huang, Catal, Catal. Sci. Technol. 8 (2018) 2427–2433.
[354] W. Chen, Y. Zhang, G. Chen, R. Huang, Y. Zhou, Y. Wu, Y. Hu, K. Ostrikov, J. Mater. Chem. A 7 (2019) 3090–3100.
[355] H. Shui, T. Jin, J. Hu, H. Liu, ChemElectroChem 5 (2018) 1401–1406.
[356] S. Xie, F. Li, S. Xu, J. Li, W. Zeng, Chinese J. Catal. 40 (2019) 1205–1211.
[357] T. Gao, Z. Jin, Y. Zhang, G. Tan, H. Yuan, D. Xiao, Electrochim. Acta. 258 (2017) 51–60.
[358] Y. Liu, F. Li, H. Yang, J. Li, P. Ma, Y. Zhu, J. Ma, ChemSusChem 11 (2018) 2358–2366.
[359] Z. Gao, Z.W. Yu, F.Q. Liu, C. Yang, Y.H. Yuan, Y. Yu, F. Luo, ChemSusChem 12 (2019) 4623–4628.
[360] C. Pei, H. Chen, B. Dong, X. Yu, L. Feng, J. Power Sources 424 (2019) 131–137.
[361] Q. Ma, B. Li, F. Huang, Q. Pang, Y. Chen, J.Z. Zhang, Electrochim. Acta. 317 (2019) 684–693.
[362] R. Attias, K. Vijaya Sankar, K. Dhaka, W. Moschkowitsch, L. Elbaz, M. Caspary Toroker, Y. Tsur, ChemSusChem 14 (2021) 1737–1746.
[363] A.H. Imani, R. Ojani, J.B. Raoof, Int. J. Hydrogen Energy. 46 (2021) 449–457.
[364] C. Li, Z. Zhang, M. Wu, R. Liu, Mater. Lett. 238 (2019) 138–142.
[365] M.A.Z.G. Sial, H. Lin, X. Wang, Nanoscale 10 (2018) 12975–12980.
[366] M.A.Z.G. Sial, S. Baskaran, A. Jalil, S.H. Talib, H. Lin, Y. Yao, Q. Zhang, H. Qian, J. Zou, X. Zeng, Int. J. Hydrogen Energy. 44 (2019) 22991–23001.
[367] T. Wang, W. Xu, H. Wang, Electrochim. Acta. 257 (2017) 118–127.
[368] W.J. Liu, X. Hu, H.C. Li, H.Q. Yu, Small. 14 (2018) 1–11.
[369] A.-L. Wang, H. Xu, G.-R. Li, ACS Energy Lett. 1 (2016) 445–453.
[370] Y. Qin, F. Wang, J. Shang, M. Iqbal, A. Han, X. Sun, H. Xu, J. Liu, J. Energy Chem. 43 (2020) 104–107.
[371] Z. Guo, Y. Wang, M. Li, S. Wang, F. Du, J. Alloys Compd. 832 (2020) 155012.
[372] M. Zhang, Y. Liu, B. Liu, Z. Chen, H. Xu, K. Yan, ACS Catal. 10 (2020) 5179–5189.
[373] Y. Wang, D. Liu, Z. Liu, C. Xie, J. Huo, S. Wang, Chem. Commun. 52 (2016) 12614–12617.
[374] Y. Zhang, X. Gao, L. Lv, J. Xu, H. Lin, Y. Ding, C. Wang, Electrochim. Acta. 341 (2020) 136029.
[375] J.Y. Xie, Z.Z. Liu, J. Li, L. Feng, M. Yang, Y. Ma, D.P. Liu, L. Wang, Y.M. Chai, B. Dong, J. Energy Chem. 48 (2020) 328–333.
[376] Z. Cao, T. Zhou, W. Xi, Y. Zhao, Electrochim. Acta. 263 (2018) 576–584.
[377] Y. Li, L. Hu, W. Zheng, X. Peng, M. Liu, P.K. Chu, L.Y.S. Lee, Nano Energy. 52 (2018) 360–368.
[378] M. Shen, C. Ruan, Y. Chen, C. Jiang, K. Ai, L. Lu, ACS Appl. Mater. Interfaces 7 (2015) 1207–1218.
[379] A. Mendoza-Garcia, D. Su, S. Sun, Nanoscale 8 (2016) 3244–3247.
[380] T. Li, Y. Lv, J. Su, Y. Wang, Q. Yang, Y. Zhang, J. Zhou, L. Xu, D. Sun, Y. Tang, Adv. Sci. 4 (2017) 1700226.
[381] X. Zhang, Y. Wu, Y. Sun, Q. Liu, L. Tang, J. Guo, Inorg. Chem. Front. 6 (2019) 604–611.
[382] F. Te Tsai, H.C. Wang, C.H. Ke, W.F. Liaw, ACS Appl. Energy Mater. 1 (2018) 5298–5307.
[383] C. Lin, P. Wang, H. Jin, J. Zhao, D. Chen, S. Liu, C. Zhang, S. Mu, Dalt. Trans. 48 (2019) 16555–16561.
[384] L. Huang, H. Wu, H. Liu, Y. Zhang, Electrochim. Acta. 318 (2019) 892–900.
[385] R. Yao, Y. Wu, M. Wang, N. Li, F. Zhao, Q. Zhao, J. Li, G. Liu, Int. J. Hydrogen Energy. 44 (2019) 30196–30207.
[386] W. Zhang, Y. Li, L. Zhou, Q. Zheng, F. Xie, K.H. Lam, D. Lin, Electrochim. Acta. 323 (2019) 134595.
[387] X. Huang, L. Gong, H. Xu, J. Qin, P. Ma, M. Yang, K. Wang, L. Ma, X. Mu, R. Li, J. Colloid Interface Sci. 569 (2020) 140–149.
[388] X. Lin, X. Li, F. Li, Y. Fang, M. Tian, X. An, Y. Fu, J. Jin, J. Ma, J. Mater. Chem. A 4 (2016) 6505–6512.
[389] E. Hu, J. Ning, D. Zhao, C. Xu, Y. Lin, Y. Zhong, Z. Zhang, Y. Wang, Y. Hu, Small. 14 (2018) 1–9.
[390] Y. Wang, T. Hu, Y. Qiao, Y. Chen, Int. J. Hydrogen Energy. 45 (2020) 8686–8694.
[391] S. Lalwani, A. Joshi, G. Singh, R.K. Sharma, Electrochim. Acta. 328 (2019) 135076.
[392] M. Liu, Z. Qu, D. Yin, X. Chen, Y. Zhang, Y. Guo, D. Xiao, ChemElectroChem 5 (2018) 36–43.
[393] J. Wang, J. Wang, M. Zhang, S. Li, R. Liu, Z. Li, J. Alloys Compd. 821 (2020) 153463.
[394] L. Zhang, W. Wang, G. Xu, H. Song, L. Yang, D. Jia, J. Colloid Interface Sci. 554 (2019) 202–209.
[395] L. Lin, Q. Fu, Y. Han, J. Wang, X. Zhang, Y. Zhang, C. Hu, Z. Liu, Y. Sui, X. Wang, J. Alloys Compd. 808 (2019) 151767.
[396] A. Chakrabarti, M.E. Ford, D. Gregory, R. Hu, C.J. Keturakis, S. Lwin, Y. Tang, Z. Yang, M. Zhu, M.A. Bañares, I.E. Wachs, Catal. Today 283 (2017) 27–53.
[397] H. Topsøe, J. Catal. 216 (2003) 155–164.
[398] Y. Zhu, J. Wang, H. Chu, Y.-C. Chu, H.M. Chen, ACS Energy Lett. 5 (2020) 1281–1291.
[399] M.A. Bañares, Catal. Today. 100 (2005) 71–77.
[400] A.N. Kravtsova, L.V. Guda, A.A. Guda, A.L. Trigub, D.D. Badyukov, A.V. Soldatov, Radiat. Phys. Chem. 175 (2019) 108097.
[401] M. Povia, J. Herranz, T. Binninger, M. Nachtegaal, A. Diaz, J. Kohlbrecher, D.F. Abbott, B.J. Kim, T.J. Schmidt, ACS Catal. 8 (2018) 7000–7015.
[402] L. Calvillo, F. Carraro, O. Vozniuk, V. Celorrio, L. Nodari, A.E. Russell, D. Debellis, D. Fermin, F. Cavani, S. Agnoli, G. Granozzi, J. Mater. Chem. A. 6 (2018) 7034–7041.
[403] N. Kornienko, J. Resasco, N. Becknell, C.-M. Jiang, Y.-S. Liu, K. Nie, X. Sun, J. Guo, S.R. Leone, P. Yang, J. Am. Chem. Soc. 137 (2015) 7448–7455.
[404] X. Su, Y. Wang, J. Zhou, S. Gu, J. Li, S. Zhang, J. Am. Chem. Soc. 140 (2018) 11286–11292.
[405] D.F. Abbott, E. Fabbri, M. Borlaf, F. Bozza, R. Schäublin, M. Nachtegaal, T. Graule, T.J. Schmidt, J. Mater. Chem. A 6 (2018) 24534–24549.
[406] H.Y. Wang, S.F. Hung, H.Y. Chen, T.S. Chan, H.M. Chen, B. Liu, J. Am. Chem. Soc. 138 (2016) 36–39.
[407] M. Favaro, W.S. Drisdell, M.A. Marcus, J.M. Gregoire, E.J. Crumlin, J.A. Haber, J. Yano, ACS Catal. 7 (2017) 1248–1258.
[408] Z. Chen, L. Cai, X. Yang, C. Kronawitter, L. Guo, S. Shen, B.E. Koel, ACS Catal. 8 (2018) 1238–1247.
[409] Z. Qiu, Y. Ma, T. Edvinsson, Nano Energy. 66 (2019) 104118.
[410] N. Kornienko, N. Heidary, G. Cibin, E. Reisner, Chem. Sci. 9 (2018) 5322–5333.
[411] M. Favaro, J. Yang, S. Nappini, E. Magnano, F.M. Toma, E.J. Crumlin, J. Yano, I.D. Sharp, J. Am. Chem. Soc. 139 (2017) 8960–8970.
[412] M. Zhang, M. De Respinis, H. Frei, Nat. Chem. 6 (2014) 362–367.
[413] O. Panchenko, M. Carmo, M. Rasinski, T. Arlt, I. Manke, M. Müller, W. Lehnert, Mater. Today Energy. 16 (2020) 100394.
[414] M.W. Louie, A.T. Bell, J. Am. Chem. Soc. 135 (2013) 12329–12337.
[415] Y. Zhu, H.-C. Chen, C.-S. Hsu, T.-S. Lin, C.-J. Chang, S.-C. Chang, L.-D. Tsai, H.M. Chen, ACS Energy Lett. 4 (2019) 987–994.
[416] M. Steimecke, G. Seiffarth, M. Bron, Anal. Chem. 89 (2017) 10679.

[417] R. Chen, S.F. Hung, D. Zhou, J. Gao, C. Yang, H. Tao, H. Bin Yang, L. Zhang, L. Zhang, Q. Xiong, H.M. Chen, B. Liu, Adv. Mater. 31 (2019) 1–7.
[418] H.-Y. Wang, S.-F. Hung, Y.-Y. Hsu, L. Zhang, J. Miao, T.-S. Chan, Q. Xiong, B. Liu, J. Phys. Chem. Lett. 7 (2016) 4847–4853.
[419] D. Wang, J. Zhou, Y. Hu, J. Yang, N. Han, Y. Li, T.K. Sham, J. Phys. Chem. C. 119 (2015) 19573–19583.
[420] S. Raabe, D. Mierwaldt, J. Ciston, M. Uijttewaal, H. Stein, J. Hoffmann, Y. Zhu, P. Blöchl, C. Jooss, Adv. Funct. Mater. 22 (2012) 3378–3388.
[421] H.G.S. Casalongue, J.D. Benck, C. Tsai, R.K.B. Karlsson, S. Kaya, M.L. Ng, L.G.M. Pettersson, F. Abild-Pedersen, J.K. Nørskov, H. Ogasawara, T.F. Jaramillo, A. Nilsson, J. Phys. Chem. C 118 (2014) 29252–29259.

Chapter IV: Global discussion

This chapter presents the global discussions and summary of the doctoral Thesis, including an overview of the doctoral Thesis, additional results pertinent to electrocatalysts performance measured in single-cell anion exchange membrane water electrolysis, and the main conclusion of the Thesis.

This section provides a summary of the primary outcomes of the research works of the doctoral Thesis, which are compiled in **Chapter 3**, and additional results pertinent to full water electrolysis performance measured in a single cell anion exchange membrane water electrolysis. In this doctoral Thesis, four series of electrocatalysts, including three for anode electrode (OER) and one for cathode electrode (HER), have been developed. In all, Ni, Co, and Fe metals were selected as base metals for the preparation of the electrocatalysts, considering their main merits of relatively good catalytic activity, high abundance, and low cost. In particular, three bimetallic-based electrocatalysts, $CoFe_2O_4$ and $NiFe_2O_4$ spinel oxides modified by carbonized polydopamine and CoFe loaded in carbon foam substrate, have been prepared for the OER electrode. In addition, NiCo bimetal-based electrocatalyst modified by phosphorus was also obtained for HER.

Due to their low surface area, poor electrical conductivity, and propensity for particle aggregation during preparation and dissolution during electrolysis, bimetal oxides and alloys perform poorly in many applications, including water electrolysis. In this regard, one promising strategy for prompting surface area and conductivity is assembling the electroactive metals with carbonaceous materials. Polydopamine was chosen as a carbon and nitrogen precursor to modify the $CoFe_2O_4$ and $NiFe_2O_4$ spinel oxide. Polydopamine is a biodegradable polymer distinguished by its remarkable affinity to virtually all solid materials, including transition metals, through chemical bonding due to the variety of functional groups in its structure. Besides, it is an inexpensive and environmentally benign source of carbon, which opens up a wide variety of doors for modifying different materials, which can easily be converted to a unique type of nitrogen-doped graphitized carbon. Considering these merits, $CoFe_2O_4$ and $NiFe_2O_4$ were modified by polydopamine through two facile processes of *in situ* polymerization of dopamine monomer followed by carbonization.

Moreover, apart from polydopamine, another carbonaceous material was also employed to improve the electrochemical properties of CoFe. Petroleum pitch, a low-cost and abundant industrial residue material, was used as a carbon precursor to prepare carbon foam to immobilize electroactive metals of Co/Fe. Carbon foam derived from petroleum pitch was obtained through a simple thermo-chemical and carbonization process. The carbon foam possesses intriguing features, including a large surface area with a porous and open-cell structure, lightweight, good strength, and tailorable thermal and electrical conductivity. In addition, it has an open-pore network, where macrospores are connected, forming micropores and having space/holes in their cell wall, which helps

incorporate foreign materials to alter their functionality. Doping heteroatoms (e.g., N, P) into carbon structure can further the surface chemistry and electronic configuration. To investigate the potential of carbon foam for alkaline oxygen evolution reactions, we developed and investigated composite materials consisting of Co/Fe integrated with P, N co-doped carbon foam (PN-CF) generated from petroleum pitch.

In addition to the three electrocatalysts for OER mentioned above, efforts have also been paid to prepare electrocatalysts for HER electrode. Using stainless steel mesh (SSM) in hydrogen and oxygen evolution reactions has garnered much attention. It was known that SSM excels in electrocatalysis for the oxygen evolution reaction (OER), whereas its catalytic activity for the hydrogen evolution reaction (HER) remains relatively low. This prevents the application of SSM-based catalysts for long-term and complete water electrolysis. This work transformed commercially available SSM materials into high-performance and stable electrocatalysts for alkaline HER by a simple hydrothermal approach followed by a phosphorization procedure. Detailed information, including the synthesis method, physicochemical and electrochemical characterization for each material, can be found in the corresponding sections in chapter 2.

Aimed at exploring the potential application of the electrocatalysts mentioned above for complete water electrolysis, the best-performing materials from each article were also tested in Anion exchange membrane water electrolysis (AEMWE). The following section summarizes the most important findings, including the electrochemical result obtained using a three-electrode system (already published) and further water electrolysis performance evaluated in a single AEMWE (not included in the publications, which are additional data).

1. Electrocatalyst for HER electrode

a) NiCoP/CoP sponge-like structure grown on stainless steel mesh as a high-performance electrocatalyst for hydrogen evolution reaction

This study used stainless steel mesh (SSM) with a three-dimensional network structure substrate to grow an electroactive catalyst. The commercially available SSM material was transformed into an active and stable electrocatalyst following a hydrothermal route and a phosphorization process. Briefly, mono and bimetals of Ni and Co were grown through a hydrothermal way; then, the as-prepared material was subjected to further phosphorization. The prepared catalysts were characterized by physicochemical, including scanning electron microscopy (SEM), transmission electron microscopy (TEM), X-ray diffraction (XRD), X-ray photoelectron spectroscopy (XPS), and electrochemical characterization. According to the findings of the electrochemical analysis, the NiCoP@SSM catalyst demonstrates an excellent wave of catalytic activity for HER measured in 1M KOH aqueous solution. In particular, the current density of 10 mA cm^{-2} can be obtained at a low overpotential of 138 mV. In addition, it presented the lowest Tafel slope in the series, relatively low charge transfer resistance, and the highest ECSA of the entire set. More interesting, it maintained its stability for about 24 hours of continuous operation. The high performance of the NiCoP@SSM catalyst could be attributed to several factors. First and foremost, the three-dimensional structure of the SSM provides a large surface area and myriads of active catalytic sites during the reaction. Secondly, the synergistic effect of nickel and cobalt and the electronic hybridization between these metals and phosphorus can optimize the energy barrier of a redox reaction and change the electronic structure, which effectively expedites the electrocatalysis. In addition, taking into account the $P^{\delta-}$ species found in the NiCoP and CoP structures, which have a high affinity towards proton-acceptor and, consequently, for hydrogen, and also taking into account the $Co^{\delta+}$/$Ni^{\delta+}$ hydride-acceptors, which have a moderate interaction with hydrogen, demonstrates that there is a significant synergistic effect that helps to accelerate the catalytic process. This synthesis method provides a simple fabrication procedure that is not only simple but also devoid of polymer binders and easy to scale up. It paves the way for developing HER-active electrocatalysts made from commercially available and low-cost SSMs.

2. Electrocatalysts for OER electrode

a) Transformation of $CoFe_2O_4$ spinel structure into active and robust CoFe alloy/N-doped carbon electrocatalyst for oxygen evolution reaction.

In this study, nitrogen-doped carbon-coated CoFe electrocatalysts were synthesized by the hydrothermal method and *in-situ* polymerization of dopamine, followed by carbonization. A comprehensive investigation was carried out to investigate the impact of the carbonized polydopamine on the physicochemical and electrochemical activities of CoFe. The change of the $CoFe_2O_4$ spinel structure into a CoFe alloy was observed when the ratio of the contents of $CoFe_2O_4$ and dopamine was carefully controlled and optimized. The morphology, crystalline structure, and chemical composition of the catalysts were characterized by scanning electron microscopy (SEM), transmission electron microscopy (TEM), X-ray diffraction (XRD), X-ray photoelectron spectroscopy (XPS), and inductively coupled plasma (ICP). The as-prepared electrocatalysts were measured for their electrochemical performance in a three-electrode system controlled by a potentiostat/galvanostat. It was discovered that the $CoFe/NC_{30\%}$ mixture (prepared with 30% dopamine) possesses an appealing electrocatalytic activity toward OER. A relatively low overpotential of 340 mV was required to produce a current density of 10 $mAcm^{-2}$, accompanied by a small Tafel slope of 77 $mVdec^{-1}$ measured in an electrolyte containing 1M KOH. More importantly, the $CoFe/NC_{30\%}$ catalyst demonstrated outstanding durability for at least 24 hours. The EIS analysis confirms that the optimal dopamine content integration is responsible for the high OER activity and stability of $CoFe/NC_{30\%}$, which may be due to (i) the synergetic effect of CoFe and N-doped carbon coating layer and (ii) the lowered charge transfer resistance. Findings from this study hold promise for advancing the development of a robust, cost-effective electrocatalyst for industrial-scale water electrolysis.

b) Nitrogen-doped carbon decorated-$Ni_3Fe@Fe_3O_4$ electrocatalyst with enhanced oxygen evolution reaction performance

In this work, a spinel oxide composed of $NiFe_2O_4$ was transformed into nitrogen-doped carbon-decorated $Ni_3Fe@NiFe_2O_4$ nanocomposite (denoted as $NiFe/NC_x$) electrocatalysts through three subsequent steps comprising hydrothermal, polymerization, and carbonization. It was determined to what extent the carbonized dopamine had an impact on the electrocatalytic activity and the structure of the $NiFe_2O_4$ precursor. The NiFe electrocatalyst that contained 10 wt.% dopamine ($NiFe/NC_{10\%}$) exhibited relatively higher catalytic activity for OER measured under 1M KOH aqueous solution. It revealed a low overpotential (350 mV at 10 $mAcm^{-2}$), a low Tafel slope (56 $mVdec^{-1}$), a low charge transfer resistance, and a relatively higher electrochemically active surface area. The most notable feature is that it did not change for at least 12 hours.

The following characteristics of $NiFe/NC_{10\%}$ could be responsible for its outstanding electrocatalytic activity as well as its good stability: (i) the surface functionality and structural character of the N-doped carbon that was constructed with dual phases (Ni_3Fe and Fe_3O_4) could be tuned to expose abundantly accessible active sites, expedite mass diffusion and electron transfer, and thereby stimulate OER activity. (ii) The presence of N-doped carbon causes changes in the morphology, crystal phase, and electronic structure of $NiFe_2O_4$, all of which have the potential to contribute to the improvement in OER activity positively. (iii) The synergetic effect of the developed Ni_3Fe alloy and Fe_3O_4 combined with the N-doped carbon can potentially increase OER activity and durability. The unusual OER electrocatalytic activity of the $NiFe/NC_{10\%}$ electrocatalyst may be attributable, at least in part, to all of the factors above. This research offers a vital strategy for functionalizing metal oxides and paves the way for developing an electrocatalyst for alkaline oxygen evolution reaction electrodes that is simple to synthesize, inexpensive, efficient, and stable.

c) CoFe-loaded P, N co-doped carbon foam derived from petroleum pitch waste: an efficient electrocatalyst for oxygen evolution reaction

In this study, we prepared a promising electrocatalyst for alkaline oxygen evolution reaction (OER) that consists of cobalt and iron introduced into a phosphorus and nitrogen co-doped carbon foam (CF) derived from petroleum pitch. It demonstrates a practical method for valorizing petroleum pitch waste materials into an OER electrocatalyst. Using petroleum pitch as a starting material, we successfully synthesized a CoFe-loaded heteroatom (P, N) co-doped carbon foam. First, a support material consisting of (P, N) co-doped carbon foam was prepared by subjecting it to a thermo-chemical process; next, the incorporation of mono and bimetals consisting of Co and Fe into the (P, N) co-doped carbon foam was performed, and finally, the resulting composite was subjected to carbonization process. Because of the critical carbon foam support that enabled immobilization of the electroactive metals of Co and Fe, the as-prepared electrocatalysts have shown appealing electrocatalytic activity, faster reaction kinetics, and good stability for OER electrodes. In particular, the as-synthesized CoFe@PN-CF electrocatalyst requires a low overpotential of 320 mV to create 10 $mAcm^{-2}$ current density, a low Tafel slope of 48 $mVdec^{-1}$, relatively low charge transfer resistance, and a large electrochemically active surface area. Most notably, it maintained stability for at least 20 hours while continuously operated with a 1M KOH aqueous solution, suggesting that it can be exploited for large-scale water electrocatalysis.

Figure 1 shows the OER polarization curve of IrO_2 and the best-performing electrocatalyst selected from each as-synthesized electrocatalyst aforementioned. We can appreciate the progressed electrocatalytic activity of the prepared electrocatalyst (CoFe@PN-CF, $CoFe@NC_{30\%}$, and $NiFe/NC_{10\%}$) compared to the commercial IrO_2. In the state of the art, the overpotential required to achieve 10 $mAcm^{-2}$ current density is used to evaluate and compare electrocatalysts for water electrolysis. Accordingly, the overpotential required to obtain10 $mAcm^{-2}$ current density for each electrocatalyst is given as follows: CoFe@PN-CF (320 mV), $CoFe@NC_{30\%}$ (340 mV), $NiFe/NC_{10\%}$ (350 mV), and IrO2 (350 mV). This demonstrates that the as-prepared electrocatalysts have a significant potential for accelerating the sluggish reaction kinetics of the OER electrode. This is supported by the fact that the electrocatalysts have exhibited splendid activity comparable with or even superior to that of the standard IrO_2 catalyst. In addition, the mentioned electrocatalysts are inexpensive because of their relatively high abundance on the earth. In particular, among the as-

prepared electrocatalysts, the CoFe@PN-CF-based was the most promising electrocatalyst for OER.

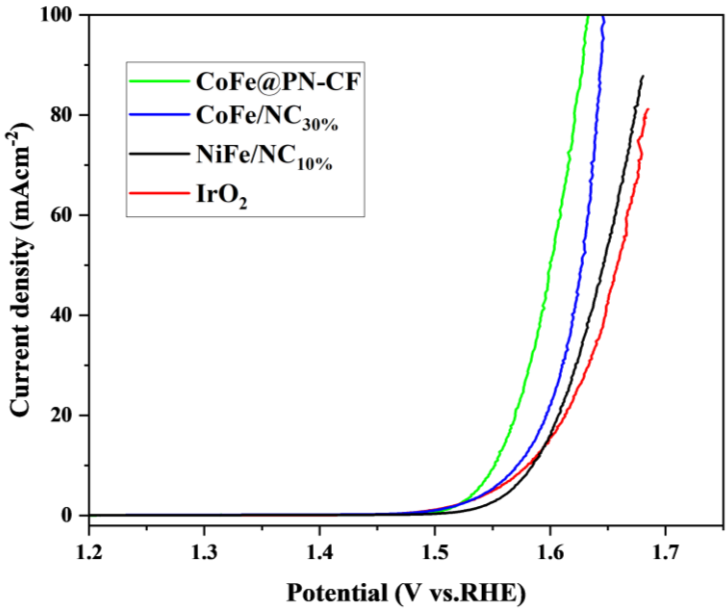

Figure 1. OER polarization curve of different electrocatalysts, measured in 1M KOH at 5 mVs^{-1} scan rate and 1600 rpm.

In addition to the activity, one of the most important criteria to consider when evaluating an electrocatalyst for comprehensive, large-scale applications is its long-term stability. Thus, each electrocatalyst was subjected to long-term measurement to assess its stability. **Figure 2** presents the chronopotentiometry stability test of the different electrocatalysts for OER under 1M KOH aqueous solution at 10 $mAcm^{-2}$ current density. It appears that the as-prepared electrocatalyst displayed relatively high stability for OER, further demonstrating the significant potential for long-term, extensive application.

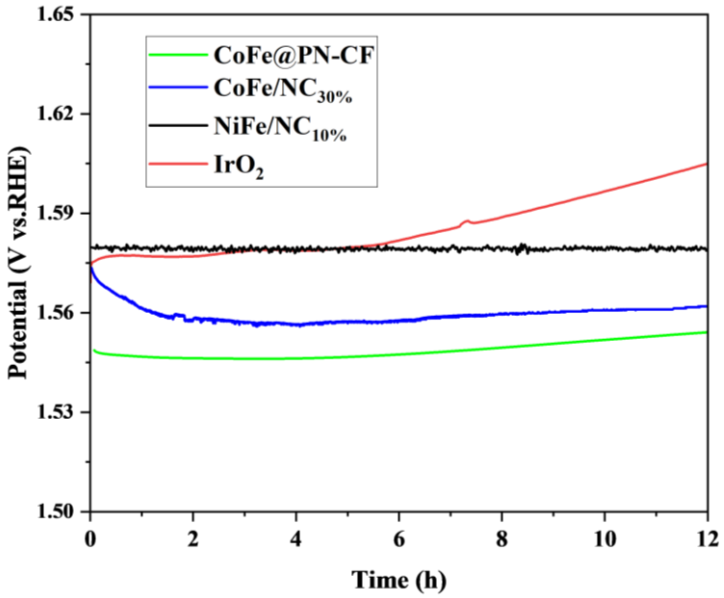

Figure 2. Chronopotentiometry stability test of various electrocatalysts for OER under 1.0 M KOH aqueous solution at 10 $mAcm^{-2}$ current density.

It is essential to mention here that all the previous results were obtained using a three-electrode system. Therefore, it is crucial to test the materials in complete water electrolysis to gain further insight into the catalysts for practical hydrogen production through water electrolysis. The following sub-section presents the full water electrolysis performance of the aforementioned electrocatalyst in a single-cell set-up using AEM.

3. Electrocatalyst testing in Anion exchange membrane water electrolysis

The performance of the as-prepared electrocatalysts was tested in an anion exchange membrane water electrolysis (AEMWE) single cell. AEMWE encompasses oxygen/hydrogen evolution electrodes, anion exchange membrane (AEM), gas diffusion layer (GDL) or porous transport layer (PTL), gaskets, monopolar plates, end plates, and current collectors. The schematic and actual image of the AEMWE system used for experiments is shown in **Figure 3**. **Figure 3 (a, b)** shows a detailed schematic illustration of the system, whereas **Figure 3 (c and d)** shows an actual AEMWE system available at the ICB-CSIC laboratory. A brief explanation for each component is presented as follows.

The primary function of the endplate is to distribute the pressure between the various components of the electrolyzer (GDL, bipolar, etc.) in such a way as to lower the contact resistance between those components. The monopolar plate that contains the flow field functions as the transmission channel for the water circulation and gas-releasing processes.

The current collector plates, typically composed of copper and inserted between the monopolar plate and end plate of the anode and cathode, are crucial to the system's operation. It is essential to keep in mind that copper plates are susceptible to corrosion in alkaline environments. Therefore, it is of the utmost importance to ensure the unit is well sealed so that the alkaline solution does not seep in from the electrolyzer's edge and onto the current collector plates.

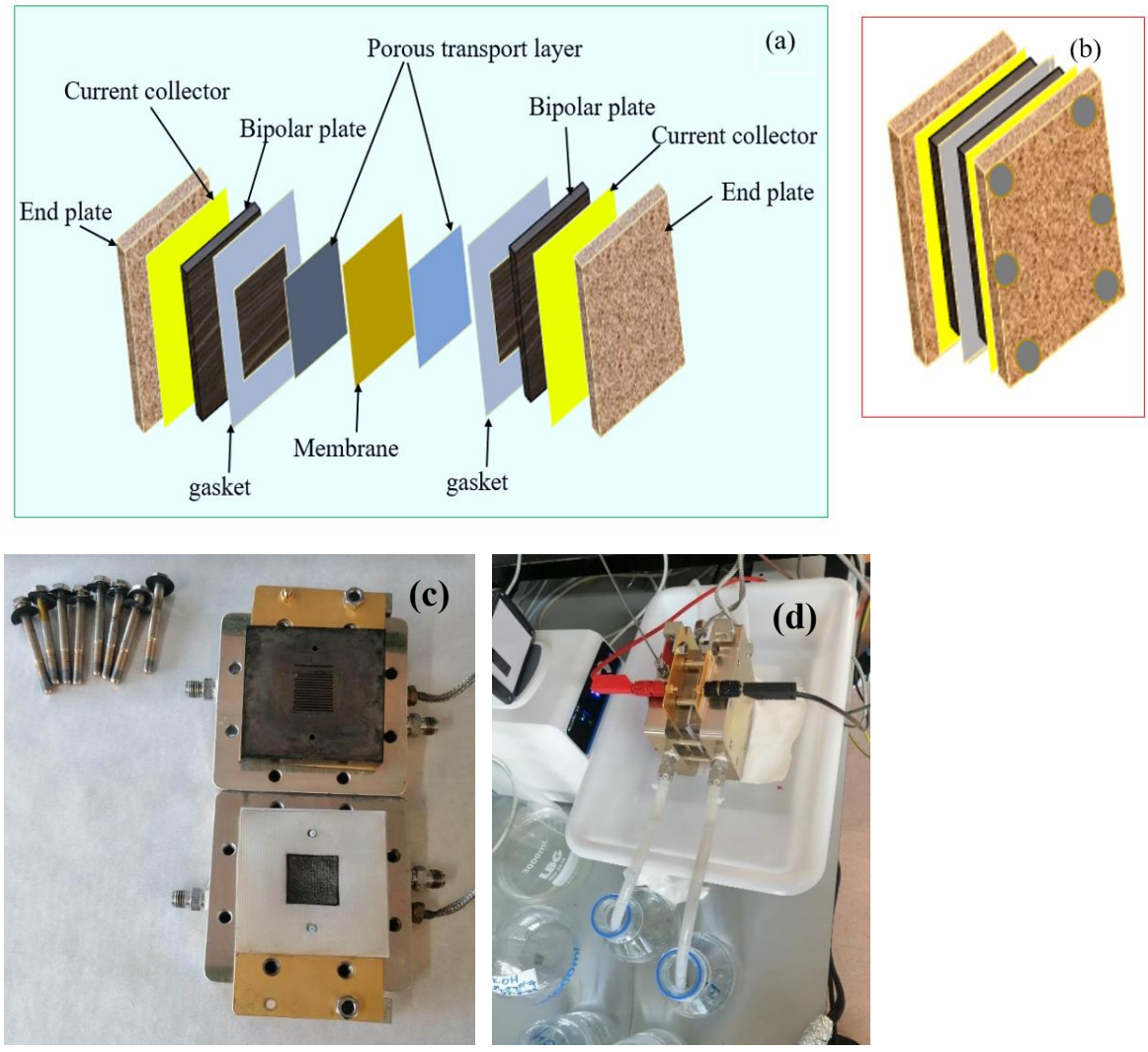

Figure 3. Schematic and actual photo of an AEMWE single cell system: (a) overview of the components of AEMWE set-up consisting of the end plates, monopolar plates, membrane, porous

transport layer, gaskets, and current collectors; (b) schematic illustration of assembled AEMWE, and (c) the actual AEMWE system consisting of the monopolar and end plates, current collectors, and MEA components and (d) the actual AEMWE set-up connected with inlet and outlet feed, electrical connections, heating resistors, and thermocouple.

It is necessary to insert gaskets between the membrane and the monopolar plate to alleviate unequal pressure within the cell caused by the thickness of the GDL and prevent membrane tears and internal leaking. The gasket thickness significantly influences the penetration of electrodes into the membrane and the pressure distribution throughout the MEA; hence, adjusting the gasket thickness is highly crucial to achieving an excellent electrode-membrane interaction, uniform pressure distribution, and ensuring that the necessary sealing is achieved. In actual practice, the thickness of the gaskets required is determined by gradually increasing or decreasing the number of gaskets used until the desired level of performance is reached.

Besides, the catalytic layer at each electrode helps improve the system's efficiency by lowering the overpotential of the oxygen/hydrogen evolution reactions. The GDL or PTL components facilitate the transport of reactants and the emission of generated gases. AEM is responsible for exchanging anions during the operation under wet conditions. The KOH aqueous solution is employed as an electrolyte to promote ion transfer.

The performance of AEMWE can be impacted by a wide variety of parameters, such as the membrane type and conductivity, membrane treatment, electrode preparation, ionomers utilized, the kind of catalyst, and the electrolyte concentration. In this PhD thesis, we focus on the impact of the electrodes on the overall water electrolysis, where the actual chemical reaction occurs. The as-prepared electrocatalysts' water electrolysis performance is measured and compared with the state-of-the-art.

The water electrolysis performance of the different electrocatalysts was measured using membrane electrode assembly (MEA). The MEA was prepared according to the ref. [1] with slight modification. Briefly, an anion exchange process was performed on a Fumasep® FAA3-50 membrane (Fumatech BWT GmbH) in a bromide form before the membrane was put into operation. The membrane was immersed in 1 M KOH solution for 1 h to make it in hydroxyl form. The electrodes for the anode and cathode were prepared as follows. The cathode electrode was prepared by mixing a commercial 40 wt.% platinum on carbon (Pt/C) (Alfa Aesar) and Fumion

(Fumion®FAA-3-solut-10, Fumatech) (20 wt.% of the total solid content) in ultrasonication for 30 min. The ink was deposited by spray coating technique onto a Sigracet 39BC gas diffusion layer (Ion Power, GmbH) to receive the cathodic gas diffusion electrode (GDE). A 0.2 mg/cm^2 platinum loading was used. The anode electrode was obtained by mixing commercial IrO_2 (Alfa Aesar) and Fumion (50 wt.% of the total solid content). Homogenous catalytic ink was obtained by dispersing and mixing the electrocatalyst and ionomer in ultrasonication for 30 min. The ink was also deposited by spray coating technique onto a nickel felt (Bekaert) acting as PTL to obtain the anodic GDE, and different catalyst loading was used (1.0 mg/cm^2 and 2.0 mg/cm^2). Using the same procedure, an anode electrode using the as-prepared electrocatalysts was also set with a catalyst loading of 2.7 mg/cm^2.

The MEA was obtained by sandwiching the membrane between the as-prepared electrodes with a geometrical area of 5 cm^2. Before the assembly, the GDEs were subjected to 1 h soak in an aqueous solution containing 1 M KOH at room temperature. The electrochemical characterizations were carried out in single cell configuration with a size of 5 cm^2, in terms of polarization curves at 60 ^{0}C temperature. A pump supplied a 1 M KOH solution to both electrodes at a flow rate of 4.2 mL/min. The electrochemical performance was measured in an AEMWE system controlled by a power supply (KEPCO®).

Water electrolysis polarization curves measured using the different electrocatalysts applied at the anode and cathode electrodes are shown in **Figure 4**. For comparison purposes, both anode and cathode electrodes were prepared and measured polarization curves using the commercial IrO_2 and Pt/C catalyst. On the one hand, the performance of the as-prepared electrocatalysts (CoFe@PN-CF, CoFe/$NC_{30\%}$, and NiFe/$NC_{10\%}$) was measured by applying them on the cathode electrode, and the Pt/C was used for the cathode electrode. On the other hand, to evaluate the water electrolysis performance of the as-prepared NiCoP@SSM electrocatalyst, IrO_2 was applied on the anode, and NiCoP@SSM catalyst was used on the cathode electrode. The I-V polarization curve (**Figure 4**) revealed that at 1.8 V cell potential, a current density of 0.35 Acm^{-2} can be achieved for the MEA developed using IrO_2 and Pt/C catalysts. To get insight into the performance of CoFe@PN-CF for the anode electrode, MEA was constructed by employing CoFe@PN-CF and Pt/C. In this case, a higher current density of 0.45 Acm^{-2} was observed at 1.8 V cell potential, indicating better performance than the MEA developed using IrO_2 and Pt/C catalysts. For the CoFe/$NC_{30\%}$ and

$NiFe/NC_{10\%}$ based electrocatalyst, a 0.3 and 0.2 Acm^{-2} current was obtained at the same cell potential, attesting significant electroactivity for water electrolysis; nevertheless, there is still room for further investigation to upgrade the overall performance. In addition, MEA made up of NiCoP@SSM on the cathode and IrO_2 on the anode electrode was applied. In this case, a current density of 0.1 A/cm^2 was obtained at 1.8 V. Aimed to leverage the potential of the as-prepared electrocatalyst for water electrolysis, we have also analyzed MEA-constructed from the PGM-free CoFe@PN-CF and NiCoP@SSM, a current density of about 0.11 Acm^{-2} was achieved at 1.8 V potential. The operating conditions (temperature and feed), the type of membrane, the materials used in the anode and cathode electrode, and the activity recorded at specific potential are shown in **Table 1**.

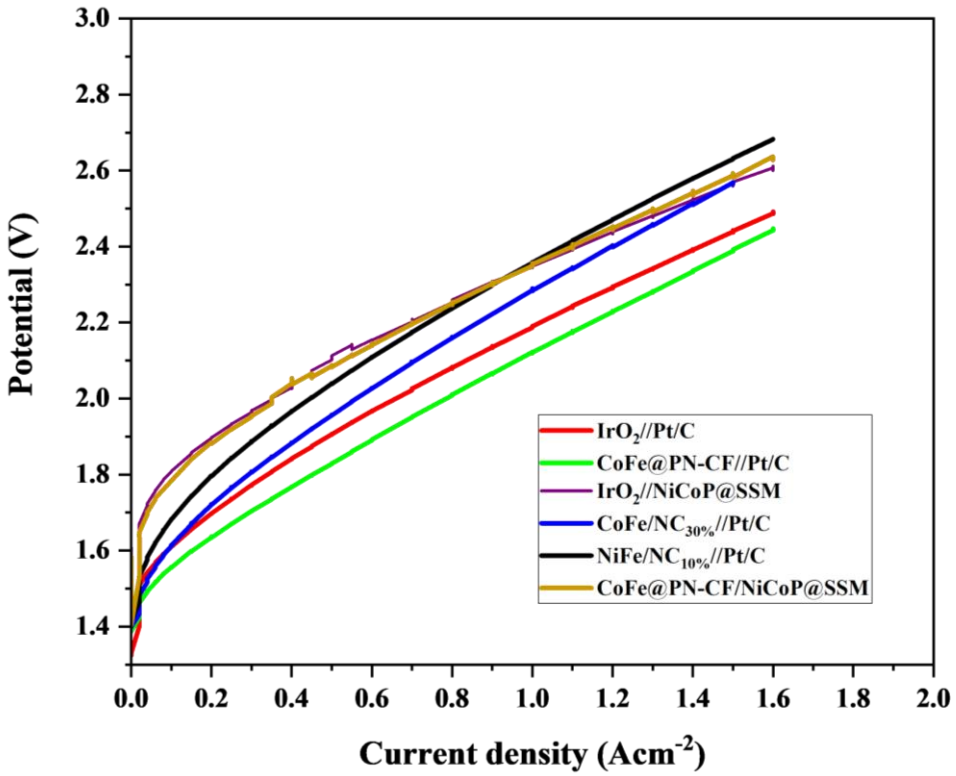

Figure 4. Water electrolysis performances of MEAs with different electrocatalysts.

Moreover, the fabricated MEAs were compared with the state-of-the-art. It is essential to mention that it is difficult to compare them directly with the catalyst reported in the literature as each author uses different means of testing configuration and conditions, including the type of membrane, and temperature, and current density at a different cell potential, electrolyte concentration, etc.

Nonetheless, we have attempted to compare the result obtained using the as-prepared electrocatalyst with the results reported in the literature. **Table 1** shows a comprehensive list of electrocatalysts (applied in both anode and cathode) tested in single-cell AEMWE. We can appreciate the performance of our MEA made up of CoFe@PN-CF //Pt/C, comparable to what was reported in the literature when the same membrane type was applied.

Table 1. A literature review on water electrolysis performance using AEM in 1 M KOH solution.

Label	**Membrane type**	**Anode**	**Cathode**	**T (^{0}C)**	**Activity**	**Ref.**
A	Fumasep® FAA3	CoFe@PN-CF	Pt/C	60	0.45 A/cm^2 @ 1.8 V	This work
B	Fumasep® FAA3	IrO_2	Pt/C	60	0.35 A/cm^2 @ 1.8 V	
C	Fumasep® FAA3	CoFe/$NC_{30\%}$	Pt/C	60	0.3 A/cm^2 @ 1.8 V	
D	Fumasep® FAA3	NiFe/$NC_{10\%}$	Pt/C	60	0.2 A/cm^2 @ 1.8 V	
E	Fumasep® FAA3	IrO_2	NiCoP@SSM	60	0.1 A/cm^2 @ 1.8 V	
F	Fumasep® FAA3	CoFe@PN-CF	NiCoP@SSM	60	0.11 A/cm^2 @ 1.8 V	
G	Fumasep® FAA3	IrO_2	Pt/C	60	0.32 A/cm^2 @ 1.8 V	[2]
H	Fumasep® FAA3	g–CN–CNF-800	Pt/C	60	0.48 A/cm^2 @ 1.8 V	
I	Fumasep® FAA3	$NiMn_2O_4$/C	Pt/C	50	0.18 A/cm^2 @ 1.8 V	[3]
J	Fumasep® FAA3	$NiMn_2O_4$/CNF	Pt/C	60	0.10 A/cm^2 @ 1.8 V	[4]
K	Fumasep® FAA3	$(NiCo)_3Se_4$	Pt/C	60	1 A/cm^2 @ 1.75 V	[5]

L	SustainionX37-50	NiFe-LDH	Pt/C	50	1 A/cm^2 @ 1.7 V	[6]
M	SustainionX37-50	Cr-NiFe-LDH	NiMoCo/NF	40	1 A/cm^2 @ 2.11 V	[7]
N	SustainionX37-50	NiCoO-NiCo/C	CuCoO/NF	50	504 mA/cm^2 at 1.85 V	[8]
O	SustainionX37-50	Ni-Fe-Co	Ni-Fe-O_x/NF	60	1 A/cm^2 @ 1.9 V	[9]
P	SustainionX37-50	$Cu_{0.81}Co_{2.19}O_4$/NF	Co_3S_4/NF	48	431 mA/cm^2 at 2 V	[10]
Q	SustainionX37-50	IrO_2/CP	Cu-Co-P/C	50	700 mA/cm^2 at 1.9 V	[11]
R	mm-qPVBz/Cl^-	Ni	$Cu_{0.7}Co_{2.3}O_4$	55	100 mA/cm^2 @ 2.0 V	[12]

Where; mm-qPVBz/Cl^-: Methylated melamine grafted polyvinyl benzyl chloride; NF: nickel foam; LDH: Layered double hydro-oxide; CNF: carbon nanofiber; CP: carbon paper.

However, it is easier to make an accurate performance comparison for different electrocatalysts if one takes into account the contribution of the ohmic resistance of the testing system. To compare with other results reported in the literature in which different membrane type was used, it was essential to consider the ohmic resistance. In this scenario, subtracting the ohmic resistance could provide a fair comparison. This is because every configuration has its resistance originating from the membrane and other component differences.

Figure 5 compares the catalysts prepared in this PhD thesis and the results reported in the literature using a single-cell AEMWE set-up. The raw data reported in the literature (**Figure 5a**) and ohmic resistance subtracted data (**Figure 5b**) are plotted to compare the activity profile of the catalysts. **Table 1** is labelled from A-F for the as-prepared MEA and G-R letters for the MEA results reported in the literature to make it easier when referring to the works.

The ohmic resistance of the AEMWE system available in our lab was determined to be about 300 mΩ.cm^2, which this resistance is higher compared to the literature (varies from 45-230 mΩ.cm^2).

As a result, it was essential to consider the ohmic resistance to get a fair activity comparison. Accordingly, the MEA equipped with the best-performing catalyst of CoFe@PN-CF//Pt/C prepared in this PhD thesis requires a potential of 1.66 V to obtain 0.45 A/cm^2 current density when the ohmic resistance was subtracted (**Figure 5b**), and it has even demonstrated an appealing activity without removing the ohmic resistance (**Figure 5a**). This made the as-prepared MEA more competitive than the other results reported in the literature. We can notice the activity difference before and after ohmic resistance elimination, in which CoFe@PN-CF//Pt/C shows an excellent water electrolysis performance, outperforming most of the results reported in the literature except with a few reports. This demonstrates the potential application of CoFe@PN-CF electrocatalyst for anode electrodes for full water electrolysis.

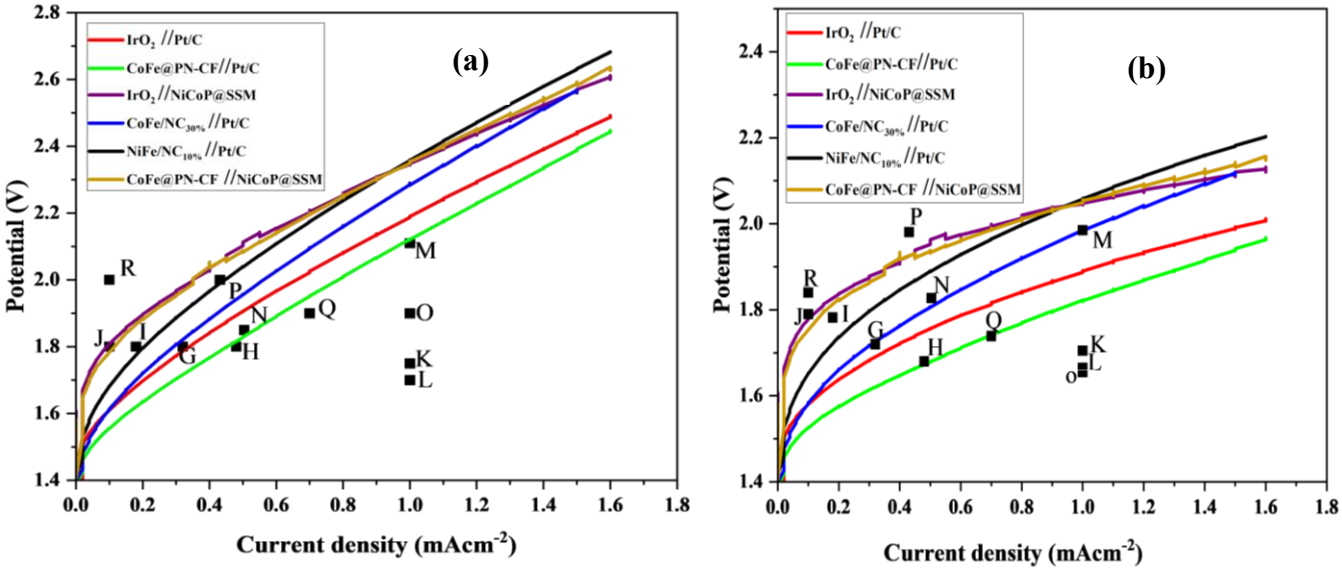

Figure 5. Comparison of MEA performance prepared in this PhD thesis and results reported in the literature (G-R) using single-cell AEMWE system. (a) Results plotted without iR-correction and (b) results plotted with an iR correction.

References for chapter IV

[1] I. Gatto, A. Caprì, C. Lo Vecchio, S. Zignani, A. Patti, V. Baglio, Optimal operating conditions evaluation of an anion-exchange-membrane electrolyzer based on FUMASEP® FAA3-50 membrane, Int. J. Hydrogen Energy. (2022). https://doi.org/10.1016/j.ijhydene.2022.04.176.

[2] J.E. Park, M.-J. Kim, M.S. Lim, S.Y. Kang, J.K. Kim, S.-H. Oh, M. Her, Y.-H. Cho, Y.-E. Sung, Graphitic carbon nitride-carbon nanofiber as oxygen catalyst in anion-exchange membrane water electrolyzer and rechargeable metal–air cells, Appl. Catal. B Environ. 237 (2018) 140–148. https://doi.org/10.1016/j.apcatb.2018.05.073.

[3] A. Carbone, S.C. Zignani, I. Gatto, S. Trocino, A.S. Aricò, Assessment of the FAA3-50 polymer electrolyte in combination with a NiMn2O4 anode catalyst for anion exchange membrane water electrolysis, Int. J. Hydrogen Energy. 45 (2020) 9285–9292. https://doi.org/10.1016/j.ijhydene.2020.01.150.

[4] C. Busacca, S.C. Zignani, A. Di Blasi, O. Di Blasi, M. Lo Faro, V. Antonucci, A.S. Aricò, Electrospun NiMn2O4 and NiCo2O4 spinel oxides supported on carbon nanofibers as electrocatalysts for the oxygen evolution reaction in an anion exchange membrane-based electrolysis cell, Int. J. Hydrogen Energy. 44 (2019) 20987–20996. https://doi.org/10.1016/j.ijhydene.2019.02.214.

[5] J. Abed, S. Ahmadi, L. Laverdure, A. Abdellah, C.P. O'Brien, K. Cole, P. Sobrinho, D. Sinton, D. Higgins, N.J. Mosey, S.J. Thorpe, E.H. Sargent, In Situ Formation of Nano Ni–Co Oxyhydroxide Enables Water Oxidation Electrocatalysts Durable at High Current Densities, Adv. Mater. 33 (2021) 1–11. https://doi.org/10.1002/adma.202103812.

[6] S.S. Jeon, J. Lim, P.W. Kang, J.W. Lee, G. Kang, H. Lee, Design Principles of NiFe-Layered Double Hydroxide Anode Catalysts for Anion Exchange Membrane Water Electrolyzers, ACS Appl. Mater. Interfaces. 13 (2021) 37179–37186. https://doi.org/10.1021/acsami.1c09606.

[7] M.H. Wang, Z.X. Lou, X. Wu, Y. Liu, J.Y. Zhao, K.Z. Sun, W.X. Li, J. Chen, H.Y. Yuan,

M. Zhu, S. Dai, P.F. Liu, H.G. Yang, Operando High-Valence Cr-Modified NiFe Hydroxides for Water Oxidation, Small. 18 (2022). https://doi.org/10.1002/smll.202200303.

[8] Y.S. Park, J. Jeong, Y. Noh, M.J. Jang, J. Lee, K.H. Lee, D.C. Lim, M.H. Seo, W.B. Kim, J. Yang, S.M. Choi, Commercial anion exchange membrane water electrolyzer stack through non-precious metal electrocatalysts, Appl. Catal. B Environ. 292 (2021) 120170. https://doi.org/10.1016/j.apcatb.2021.120170.

[9] I. Vincent, E.C. Lee, H.M. Kim, Highly cost-effective platinum-free anion exchange membrane electrolysis for large scale energy storage and hydrogen production, RSC Adv. 10 (2020) 37429–37438. https://doi.org/10.1039/d0ra07190k.

[10] Y.S. Park, J.H. Lee, M.J. Jang, J. Jeong, S.M. Park, W.S. Choi, Y. Kim, J. Yang, S.M. Choi, Co3S4 nanosheets on Ni foam via electrodeposition with sulfurization as highly active electrocatalysts for anion exchange membrane electrolyzer, Int. J. Hydrogen Energy. 45 (2020) 36–45. https://doi.org/10.1016/j.ijhydene.2019.10.169.

[11] W. Guo, J. Kim, H. Kim, S.H. Ahn, Cu–Co–P electrodeposited on carbon paper as an efficient electrocatalyst for hydrogen evolution reaction in anion exchange membrane water electrolyzers, Int. J. Hydrogen Energy. 46 (2021) 19789–19801. https://doi.org/10.1016/j.ijhydene.2021.03.120.

[12] Y.C. Cao, X. Wu, K. Scott, A quaternary ammonium grafted poly vinyl benzyl chloride membrane for alkaline anion exchange membrane water electrolyzers with no-noble-metal catalysts, Int. J. Hydrogen Energy. 37 (2012) 9524–9528. https://doi.org/10.1016/j.ijhydene.2012.03.116.

Chapter V: General Conclusions

In this chapter, the general conclusion of the doctoral thesis is presented.

General conclusions

This Doctoral Thesis has primarily devoted to investigating and designing bimetallic electrocatalysts for oxygen evolution reactions (OER) and hydrogen evolution reactions (HER) electrodes involved in an anion exchange membrane water electrolyzer employing earth-abundant transition metals. The work carried out in this Doctoral Thesis has produced the following results.

1. Hydrothermal route followed by *in situ* polymerization and carbonization have transformed spinel oxide ($NiFe_2O_4$ and $CoFe_2O_4$) into nitrogen-doped carbon-coated metal alloys (NiFe and CoFe) with enhanced properties. It was found that dopamine was an effective polymer to revolutionize the physicochemical and electrochemical properties of the spinel structure toward oxygen evolution reaction in 1M KOH electrolyte measured in a three-electrode electrochemical cell.
2. The impact of dopamine on structure and activity varied depending on the type of spinel oxide precursor. $CoFe/NC_{30\%}$ (obtained by mixing 30wt. % dopamine with $CoFe_2O_4$) and $NiFe/NC_{10\%}$ (obtained by mixing 10 wt. % dopamine with $NiFe_2O_4$) were found to be the optimal combination with stimulated activity and stability. In particular, overpotential of 340 mV at 10 mA cm^{-2} and Tafel slope of 77 mV dec^{-1} were obtained for $CoFe/NC_{30\%}$, and overpotential of 350 mV at 10 $mAcm^{-2}$ and Tafel slope of 56 mV dec^{-1} were obtained for $NiFe/NC_{10\%}$.
3. Carbon foam (CF) derived from petroleum pitch was also used to immobilize Co and Fe electroactive metals by carbonization process. The carbon foam presents interesting physicochemical properties to host the metals and enables to obtain of electrocatalysts with improved electrochemical properties.
4. Incorporating heteroatoms (P, N) into the carbon foam (PN-CF) has changed the structure and functionality of the CoFe electrocatalyst. OER measurements in 1 M KOH aqueous solution demonstrated that the bimetallic CoFe loaded in the PN-CF (CoFe@PN-CF) has the highest electrocatalytic activity (320 mV overpotential at j = 10 $mAcm^{-2}$) and lower Tafel slope (48 $mVdec^{-1}$) accompanied with excellent durability. Its outstanding electrocatalytic performance can be attributed to the synergetic effect of the bimetals coordinated with the P, N co-doped carbon foam that can formulate a unique electronic environment, with good active site distribution density and stimulate the inherent catalytic activity.

5. For the HER electrode, a NiCoP/CoP electrocatalyst with a unique sponge-like structure was successfully fabricated on a three-dimensional stainless steel mesh substrate through a hydrothermal route followed by a phosphorization process. Electrochemical results reveal that the NiCoP@SSM catalyst presents an excellent electrocatalytic activity for HER in 1 M KOH aqueous solution, requiring a low overpotential of 138 mV to derive a current density of 10 mA cm^{-2} and small Tafel slope of 74 mV dec^{-1}.
6. A single-cell AEMWE system was also used to examine the feasibility of the electrocatalysts mentioned above for full water electrolysis application. Accordingly, the electrocatalysts exhibit promising activity, especially for the OER electrode.
7. Among the best electrocatalysts of each of the series (CoFe@PN-CF, $CoFe/NC_{30\%}$, $NiFe/NC_{10\%}$, and NiCoP@SSM), it was found that CoFe@PN-CF has the highest activity in single-cell AEMWE, produced a current density of 0.45 Acm^{-2} at 1.8 V cell potential when MEA was prepared using CoFe@PN-CF in the anode and Pt/C in the cathode electrode.
8. This dissertation demonstrates the great potential of the transition metal-N, P modified carbon materials for oxygen evolution reaction. The CoFe@PN-CF-based electrocatalyst was found to have higher performance than the commercial IrO_2-based electrocatalyst.
9. The as-prepared electrocatalysts in this Doctoral Thesis can be applied as an alternative to the conventional precious metals-based electrocatalysts to produce clean and green hydrogen through water electrolysis.

Conclusiones generales

Esta tesis doctoral se ha centrado principalmente en investigar y diseñar electrocatalizadores bimetálicos para las reacciones de evolución de oxígeno (OER) y de evolución de hidrógeno (HER) que tienen lugar en un electrolizador de agua de membrana intercambiadora de aniones utilizando metales de transición abundantes en la corteza terrestre. El trabajo realizado en esta tesis doctoral ha producido los siguientes resultados:

1. La ruta de síntesis hidrotermal seguida de polimerización y carbonización in situ ha transformado las espinelas de $NiFe_2O_4$ y $CoFe_2O_4$ en aleaciones metálicas de NiFe y CoFe, respectivamente, recubiertas de carbono dopado con nitrógeno con propiedades mejoradas. La dopamina ha demostrado ser un polímero efectivo para modificar las propiedades fisicoquímicas y electroquímicas de la estructura de espinela hacia la reacción de evolución de oxígeno en un electrolito de KOH 1 M medido en una celda electroquímica de tres electrodos.
2. El impacto de la dopamina en la estructura y actividad varió en función de las espinelas. Se encontró que $CoFe/NC_{30\%}$ (obtenido mezclando el 30% en peso de dopamina con $CoFe_2O_4$) y $NiFe/NC_{10\%}$ (obtenido mezclando el 10% en peso de dopamina con $NiFe_2O_4$) eran las combinaciones óptimas que producían un aumento en la actividad y estabilidad de la reacción. En particular, se obtuvieron sobrepotenciales de 340 mV a 10 mA cm^{-2} y pendientes de Tafel de 77 mV dec^{-1} para $CoFe/NC_{30\%}$, y sobrepotenciales de 350 mV a 10 $mAcm^{-2}$ y pendientes de Tafel de 56 mV dec-1 para $NiFe/NC_{10\%}$.
3. La espuma de carbono (CF) derivada de la brea del petróleo también se utilizó para inmovilizar metales electroactivos de Co y Fe mediante el proceso de carbonización. La espuma de carbono presenta interesantes propiedades fisicoquímicas para alojar los metales y permite obtener electrocatalizadores con propiedades electroquímicas mejoradas.
4. La incorporación de heteroátomos (P, N) en la espuma de carbono (PN-CF) ha cambiado la estructura y funcionalidad del electrocatalizador de CoFe. La caracterización electroquímica hacia la reacción de evolución de oxígeno en una solución acuosa de KOH 1 M ha demostrado que el electrocatalizador bimetálico CoFe soportado en PN-CF (CoFe@PN-CF) tiene la mayor actividad electrocatalítica (320 mV de sobrepotencial a j = 10 $mAcm^{-2}$) y una pendiente de Tafel menor (48 $mVdec^{-1}$) acompañada de una excelente durabilidad. Su destacado rendimiento electrocatalítico puede atribuirse al efecto sinérgico de los metales coordinados con la espuma

de carbono co-dopada con P y N que da lugar a un entorno electrónico único y con una buena distribución de sitios activos estimulando de esta forma la actividad catalítica inherente.

5. Para la reacción de evolución de hidrógeno, se ha fabricado con éxito un electrocatalizador NiCoP/CoP con una morfología única tipo esponja sobre un sustrato de malla de acero inoxidable tridimensional mediante un proceso hidrotermal seguido de un proceso de fosforización. Los resultados electroquímicos revelan que el catalizador NiCoP@SSM presenta una excelente actividad electrocatalítica para HER en una solución acuosa de KOH 1 M, requiriendo un bajo sobrepotencial de 138 mV a una densidad de corriente de 10 mA cm^{-2} y una pequeña pendiente de Tafel de 74 mV dec^{-1}.
6. También se utilizó una monocelda de electrolizador de agua de membrana intercambiadora de aniones (AEMWE) para examinar la viabilidad de los electrocatalizadores preparados anteriormente. Se ha observado que los electrocatalizadores exhiben una actividad prometedora, especialmente para el electrodo OER.
7. De entre los mejores electrocatalizadores de cada una de las series (CoFe@PN-CF, $CoFe/NC_{30\%}$, $NiFe/NC_{10\%}$ y NiCoP@SSM), se ha visto que CoFe@PN-CF presenta la mayor actividad en la monocelda AEMWE, produciendo una densidad de corriente de 0,45 Acm^{-2} a un potencial de celda de 1,8 V usando una MEA con CoFe@PN-CF en el electrodo anódico y Pt/C en el electrodo catódico.
8. En esta tesis doctoral se demuestra el gran potencial de los materiales de carbono dopados con N y P con metales de transición incorporados para la reacción de evolución de oxígeno. Se ha podido determinar que el electrocatalizador basado en CoFe@PN-CF presenta un rendimiento superior al electrocatalizador comercial de IrO_2.
9. Los electrocatalizadores preparados en esta tesis doctoral pueden aplicarse como alternativa a los electrocatalizadores convencionales basados en metales preciosos para producir hidrógeno limpio y verde mediante la electrólisis de agua.

Appendixes

List of abbreviations

AEMWE	Anion Exchange Membrane Water Electrolysis
AWE	Alkaline Water Electrolysis
BET	Brunauer, Emmett And Teller
C_{dl}	Double-Layer Capacitance
CE	Counter Electrode
CF	Carbon foam
CV	Cyclic Voltammetry
EA	Elemental Analysis
EASS	Etched And Anodized Stainless Steel
ECSA	Electrochemical Active Surface Areas
EDS-STEM	Energy Dispersive Spectroscopy-Scanning-Transmission Electron Microscopy
EIS	Electrochemical Impedance Spectroscopy
GCE	Glassy Carbon Electrode
GDL	Gas Diffusion Layer
HER	Hydrogen Evolution Reaction
HRTEM	Transmission Electron Microscopy
ICP-AES	Inductively Coupled Plasma-Atomic Emission Spectroscopy
LSV	Linear Sweep Voltammetry
M	Metal
MEA	Membrane-Electrode-Assembly
NASSM	N-Doped Anodized Stainless-Steel Mesh
NC	Nitrogen-Doped Carbon
OER	Oxygen Evolution Reaction
PD	Polydopamine
PEMWE	Proton Exchange Membrane Water Electrolysis
PN-CF	Phosphorus and Nitrogen Co-Doped Carbon Foam

RDE	Rotating Disk Electrode
RDS	Rate-Determining Step
RE	Reference Electrode
RHE	Reversible Hydrogen Electrode
RRDE	Rotating Ring Disk Electrode
SEM	Transmission Scanning Electron Microscopy
SOEC	Solid Oxide Electrolysis Cell
SSM	Stainless Steel Mesh
STEM	Scanning Electron Microscopy
TEM	Transmission Electron Microscopy
WE	Working Electrode
XPS	X-Ray Photoelectron Spectroscopy
XRD	X-Ray Diffraction
EDX	Energy Dispersive X-Ray Spectroscopy